Terms and Conditions of Use of Digitised Theses from Trinity College Library Dublin

Copyright statement

All material supplied by Trinity College Library is protected by copyright (under the Copyright and Related Rights Act, 2000 as amended) and other relevant Intellectual Property Rights. By accessing and using a Digitised Thesis from Trinity College Library you acknowledge that all Intellectual Property Rights in any Works supplied are the sole and exclusive property of the copyright and/or other IPR holder. Specific copyright holders may not be explicitly identified. Use of materials from other sources within a thesis should not be construed as a claim over them.

A non-exclusive, non-transferable licence is hereby granted to those using or reproducing, in whole or in part, the material for valid purposes, providing the copyright owners are acknowledged using the normal conventions. Where specific permission to use material is required, this is identified and such permission must be sought from the copyright holder or agency cited.

Liability statement

By using a Digitised Thesis, I accept that Trinity College Dublin bears no legal responsibility for the accuracy, legality or comprehensiveness of materials contained within the thesis, and that Trinity College Dublin accepts no liability for indirect, consequential, or incidental, damages or losses arising from use of the thesis for whatever reason. Information located in a thesis may be subject to specific use constraints, details of which may not be explicitly described. It is the responsibility of potential and actual users to be aware of such constraints and to abide by them. By making use of material from a digitised thesis, you accept these copyright and disclaimer provisions. Where it is brought to the attention of Trinity College Library that there may be a breach of copyright or other restraint, it is the policy to withdraw or take down access to a thesis while the issue is being resolved.

Access Agreement

By using a Digitised Thesis from Trinity College Library you are bound by the following Terms & Conditions. Please read them carefully.

I have read and I understand the following statement: All material supplied via a Digitised Thesis from Trinity College Library is protected by copyright and other intellectual property rights, and duplication or sale of all or part of any of a thesis is not permitted, except that material may be duplicated by you for your research use or for educational purposes in electronic or print form providing the copyright owners are acknowledged using the normal conventions. You must obtain permission for any other use. Electronic or print copies may not be offered, whether for sale or otherwise to anyone. This copy has been supplied on the understanding that it is copyright material and that no quotation from the thesis may be published without proper acknowledgement.

Lanthanide-Directed Self-Assembly Formations from Novel Dipicolinic Acid Derivatives

Dawn E. Barry, B.A. (Mod.)

January 2014

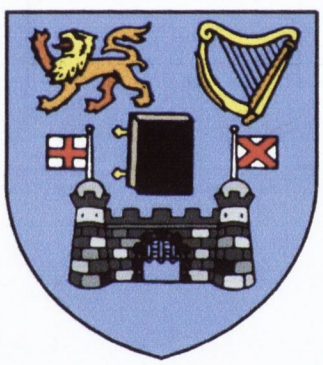

University of Dublin

Trinity College

Based on research carried out under the direction of

Prof. Thorfinnur Gunnlaugsson

A thesis submitted to the School of Chemistry, University of Dublin, Trinity College for the degree of Doctor of Philosophy

Declaration

This thesis is submitted for the degree of Doctor of Philosophy to the University of Dublin, Trinity College, and has not been submitted before for any degree or examination to this or any other university. Other than where acknowledged, all work described herein is original and carried out by the author alone. Permission is granted so that the Library may lend or copy this thesis upon request. This permission covers only single copies made for study purposes, subject to normal conditions of acknowledgment.

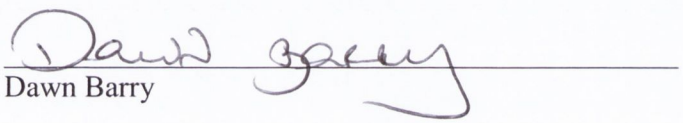

Dawn Barry

Acknowledgements

Firstly, I'd like to say a big thank you to my supervisor Thorri, for your continuous enthusiasm and support, particularly in these last few months. I really appreciate your patience and understanding throughout this special time in my life!

I'd also like to thank our collaborators Prof. Stephen Faulkner and Dr. Manuel Tropiano for their help with NIR lifetime measurements. It was great to get the opportunity to experience student life in Oxford. Also thanks to Prof. Martin Albrecht and Dr. Laszlo Mercs for all their help with the Langmuir project and for always making us feel welcome out in UCD.

I'd also like to say a big thank you to the TCD technicians John, Manuel, Martin and Gary. I'm sure I've given you your fair share of headaches at some time or another!

I don't think I'd be able to fit all past, present and visiting members of the group onto this page alone but I'd like to say a huge thank you to everyone for playing their part in making my time in the group what it was. When chemistry wasn't going well or when times were tough there was always time for a bit of craic and banter in the lab!

Fortunately, since day one we've had a number of fantastic postdocs who were always willing to share their knowledge and advice – thanks a million Emma, Steve, Oxana, Jon Komala, Miguel, Jenn and Salvador. Thank you all for always being there to teach me new techniques and answer my countless questions; but more importantly, thank you for your friendship. Emma and Komala, thanks for all your support, especially this past year, you always gave me great encouragement and assured me that I'd be well able to make it to the finish line even though there was an extra little one to think about! Thanks Jon, for taking me under your wing for the first two years of my PhD, and to Jenn for the much needed wine dates! Steve, Oxana and Miguel, the three of you have gone above and beyond the past few months; I can't put into words how much I appreciate all your help and guidance. You are three of the kindest people I've been lucky enough to befriend and I hope you get everything you deserve ☺ Rob, Brian, Sam, Laura, Elaine and Swagata, during your time in the group we managed to have the most memorable nights out and fun in the lab! It really hasn't been the same since you guys left, but I wish you all the best with your future endeavours. Dave, I've been really lucky to have had you to share most of my college experience with. I've really noticed since you've finished how much I've depended on your witty charm to get me through the hard times. We've had such a laugh with so many memories; you've been a true friend!

And to the rest of the guys who are next in line – Joe, go raibh maith agat as ucht na comhráite as Gaeilge faoi gach rud agus aon rud, they were always a breath of fresh air! Esther, my gym buddy, I really missed you and our workouts together in the last few months, keep up the good work! Fergus, thank you for your relentless enthusiasm and positivity, it really is admirable. To Helen, Sachi, Sam, Eoin and Bjorn, best of luck with the rest of your PhDs, it'll all be over before you know it, so enjoy….!

Mam, Dad and David, would you believe it – no more studying!!!! It's because of you guys I've gotten to where I am. Thank you for your unconditional love and support throughout. Without question you put up with all the ups and downs I brought home and lived every reaction/exam with me. What other family would've continued to pretend to be interested in chemistry after all this time?!

To the in-laws – Mary, Tony, Keith and Olga thank you all so much. I am so lucky to be a part of the Boland clann too, I've always been made feel so welcome into the family.

Dec, my other, better half!! I can't begin to explain how eternally grateful I am to you for your continuous encouragement, love and support, not just throughout this PhD but since day one. I think you deserve an honorary degree for all that I've put you through! You have been my rock; picking me up along the way, always making sure we had fun no matter what the challenge and never letting me forget what was important! You've been by my side cheering me on but now finally you can take a breather before we embark on our next big adventure together!

Abstract

This thesis, entitled "Lanthanide-Directed Self-Assembly Formations from Novel Dipicolinic Acid Derivatives" is divided into six chapters. Chapter 1, the introduction, gives an overview of the lanthanide ions including their unique photophysical properties and the strategies employed for ligand design in the development of lanthanide luminescent complexes. Ln^{III}-directed self-assembly is central to the work described within this thesis and hence the following two sections are devoted to a discussion of those monometallic and multimetallic Ln^{III}-directed self-assembled systems reported in the literature. Work in this area which has recently been published by the Gunnlaugsson group and therefore serves as the platform from which this research has been based is then described. Since the main chapter of this thesis focuses on the use of the Langmuir-Blodgett technique for the solid state fabrication of monometallic Ln^{III}-directed self-assembled systems a section detailing the theory behind this technique is then given. A section is dedicated to the advances made in the area of lanthanide containing Langmuir-Blodgett films while the concluding section of the chapter gives an outline of the work described within this thesis.

The main goal of Chapter 2 was to design optically active compounds capable of Ln^{III} coordination, sensitisation and Langmuir monolayer formation. The synthesis of an amphiphilic C_{16} enantiomeric pair of tridentate ligands, based on the 2,6-pyridine dicarboxylic acid framework is described. The Ln^{III}-directed self-assembly behaviour of these compounds was evaluated spectroscopically with the elucidation of the various stoichiometric species produced in CH_3CN solution and their corresponding binding constants calculated. The chirality of both the ligands and their corresponding 1:3 (M:L) complexes (M = Eu^{III}, Nd^{III}, Tb^{III}, Sm^{III}, Dy^{III} and Lu^{III}) was also probed by Circular Dichroism and Circularly Polarised Luminescence measurements. The six pairs of amphiphilic enantiomeric 1:3 (M:L) complexes were then synthesised and photophysically characterised followed by the investigation into their ability to form stable Langmuir monolayers at an air-water interface. Chapter 2 also details the photophysical results obtained following studies conducted on immobilised monolayers (Langmuir-Blodgett films) of visibly emitting (Eu^{III}, Tb^{III} and Sm^{III}) and NIR (Nd^{III}) emitting monometallic tris chelate complexes.

Chapter 3 focuses on the functionalisation of an enantiomeric pair of helicate ligands for the improved solubility of their corresponding 2:3 Ln^{III}-directed chiral helical assemblies in more competitive solvent media. The synthesis of the helicate ligands, which have been modified at the 4-*para* position of the pyridine moiety backbone (extending away from the Ln^{III} binding pocket), is described, followed by an in-depth study on the self-assembly process by means of a series of photophysical titrations in CH_3CN, CH_3OH and CH_3OH:H_2O solvent mixtures. Data was

analysed in order to establish the various stoichiometric species in solution and calculate their corresponding binding constants. The enantiomeric dimetallic triple stranded 2:3 solid helicate complexes were also synthesised and photophysically evaluated with chiro-optical studies confirming retention of chirality upon complex formation. Since the Eu^{III}-directed self-assembly of the ligands in a partial aqueous environment could not be clearly interpreted a number of stability measurements were then carried out on the dimetallic triple stranded helicates in a CH_3OH:H_2O mixed solvent medium.

For the purpose of enhancing both the water solubility and biological activity of previously developed mononuclear Ln^{III}-directed self-assembled systems a chiral asymmetric 2,6-pyridine dicarboxylic acid analogue was modified at the 6-*ortho* position with a positively charged pyridinium side chain and also with a Pt(terpyridine) moiety. This yielded 2 pairs of novel enantiomeric ligands bearing a Ln^{III} tridentate coordinating pocket, an antenna group and a side chain with the potential to enhance water solubility and/or biological relevance. Chapter 4 documents the synthesis of these derivatives and the spectrophotometric solution studies employed to investigate the ability of these ligands to self-assemble in solution under the direction of Eu^{III}. It was suggested from these studies that the close proximity of the pyridinium side chain to the binding pocket was hampering the ability of these ligands to assemble in a 1:3 manner. Photophysical titrations also indicated that the Pt(terpyridine) functionalised complexes did not assemble to give the desired 1:3 monometallic complex in CH_3OH or H_2O. This was postulated as being due to the presence of the sterically bulky Pt(terpyridine) moiety adjacent to the NO_2 coordinating unit. It was concluded from these results that, although it was possible to append novel substituents to these relatively simple asymmetric structures, the location of the additional charge and/or large metal group plays an important role in determining the behaviour of these systems in solution.

The objective of the project described in Chapter 5 was to graft a C_{12} thiol-terminated chain to the 4-*para* position of 2,6-pyridine dicarboxylic acid for the tethering of the ligand onto the surface of AuNPs and subsequent formation of luminescent hybrid Ln^{III}-directed self-assembly-AuNP conjugates. The synthesis of the compound and its Ln^{III}-directed self-assembly behaviour (Ln^{III} = Eu^{III} and Tb^{III}) in 0.1 M Tris-HCl buffered solution was monitored spectroscopically and analysed by non-linear regression analysis. The photophysical properties of the 1:3 Eu^{III} and Tb^{III} assemblies were then evaluated with quantum yield and q value determination carried out at different ligand concentrations due to the sensitivity of the ligand concentration on its solubility. Quantum yield values were however comparable to those of the unsubstituted parent 2,6-pyridine dicarboxylic acid structure. Preliminary studies, including DLS and TEM measurements, following the functionalisation of the AuNPs with the ligand concluded its successful adsorption onto the surface of the AuNPs.

Chapter 6 details the experimental procedures used in Chapters 2, 3, 4 and 5 and the characterisation of the compounds prepared. The remainder sections include the literature references and appendices to support the relevant chapters.

Abbreviations

Å	angstrom (1×10^{-10} m)
AcOEt	ethyl acetate
A_L	absorbance of left-handed polarised light
aq.	Aqueous
A_R	absorbance of right-handed polarised light
Ar	aryl
AuNPs	gold nanoparticles
BnBr	benzyl bromide
BSA	bovine serum albumin
CD	circular dichroism
cm	centimetre
COSY	correlation spectroscopy
CPL	circularly polarised luminescence
ct-DNA	calf thymus DNA
cyclen	1,4,7,10-tetracyclododecane
d	doublet
D_2O	deuterium oxide
DLS	dynamic light scattering
DMAP	4-(dimethylamino)pyridine
DMF	*N*,*N*-dimethyl formamide
DMSO	dimethyl sulfoxide
DNA	deoxyribonucleic acid
H_2dpa	dipicolinic acid
ε	molar extinction coefficient
EDCI·HCl	*N*-(3-Dimethylaminopropyl)-*N'*-ethylcarbodiimide hydrochloride
EDS	energy-dispersive X-ray spectroscopy
equiv.	equivalents
ES^+	electron spray (positive mode)
Et_3N	triethylamine
EtOH	ethanol
G	gaseous state
H_2dpa	2,6-pyridine-dicarboxylic acid (dipicolinic acid)

HEPES	4-(2-hydroxyethyl)-1-piperazineethanesulfonic acid
hrs	hours
HMBC	heteronuclear multi-bond correlation spectroscopy
HOBt	1-Hydroxybenzotriazole hydrate
HRMS	high resolution mass spectrometry
HPLC	high-performance liquid chromatography
HSQC	heteronuclear single-quantum correlation spectroscopy
hν	energy
Hz	Hertz
IC	internal conversion
ICLD's	immobilised chiral luminescent devices
ILCT	intra-ligand charge transfer
IR	infrared
ISC	intersystem crossing
J	coupling constant (expressed in Hz)
L	ligand
LC	liquid condensed phase
LE	liquid expanded phase
LLBs	lanthanide luminescent bioprobes
LMCT	ligand-to-metal charge transfer
Ln	lanthanide
Ln^{III}	lanthanide(s) ion
m	multiplet
M	metal
mdeg	milli ($\times 10^{-3}$) degree
MeI	methyl iodide
mins	minutes
mL	millilitre
M:L	metal:ligand ratio
mN m^{-1}	milli Newton per metre
MM2	molecular mechanics
MOF	metal organic framework
mol	mole
MRI	magnetic resonance imaging
ms	millisecond(s) (1 x 10^{-3} s)

MS-LD$^+$	matrix-assisted laser desorption/ionization
m.p.	melting point
m/z	mass to charge ratio
nap	naphthalene
NIR	near infrared
nm	nanometre (1×10^{-9} m)
ns	nanosecond(s) (1×10^{-9} s)
NMR	nuclear magnetic resonance
NPs	nanoparticles
OMe	methoxy
Pd/C	palladium on carbon catalyst
pH	$-\log[H_3O]^+$
Phta	phthalimide
ppm	parts per million
Pybox	pyridine-bis(oxazoline)
q	hydration state
r	donor-acceptor distance
RBF	round bottom flask
RT	room tempertature
s	singlet
S_0	singlet ground state
S_1	singlet excited state
SEM	scanning electron microscopy
SPR	surface plasmon resonance
T_1	triplet excited state
t	triplet
TEM	transmission electron microscopy
THF	tetrahydrofuran
TLC	thin layer chromatography
TMS	tetramethylsilane
TOAB	tetraoctylammonium bromide
TRIS	tris(hydroxymethyl)aminomethane
TRD	time resolved detection
UV-visible	ultraviolet-visible

XO	xylenol orange
β	overall stability constant
λ	wavelength
λ_{max}	wavelength of maximum absorbance
τ	lifetime
τ	transfer ratio
π	surface pressure
γ	surface tension
δ	chemical shift
μs	microsecond(s) (1×10^{-6} s)
g_{lum}	dissymmetry factor value
η_{sens}	efficiency of lanthanide sensitisation
$\eta_{isc\ is}$	efficiency of intersystem crossing
η_{et}	efficiency of energy transfer
Φ_{tot}	quantum yield
τ_R	radiative lifetime
τ_{obs}	observed lifetime
μL	microlitre

Table of Contents

Chapter One - Introduction

Chapter Two - Emissive Langmuir–Blodgett films formed from chiral lanthanide-directed self-assemblies

Chapter Three - Chiral helical assemblies for enhanced solubility in competitive solvent media

Chapter Four - Functionalisation of half-helicate precursors for potential biological activity

Chapter Five - Self-assembly of a thiol H_2dpa unit for AuNP surface attachment

Chapter Six - Experimental

Chapter One

Introduction

1. Introduction

'Supramolecular chemistry', a term first coined by Lehn in 1978,[1] refers to the pre-organisation, recognition and binding of complimentary host–guest chemical species for the development of 'supermolecules'.[2-5] Analogous to the biochemical 'lock and key' theory first conceived by Fischer in 1894 to explain size and shape complementarity between an enzyme and its substrate[1] supramolecular chemistry involves 'chemistry beyond the molecule' whereby host ligand receptors are designed with binding sites which satisfy the geometric size, shape and electronic character of the receptor for the construction of higher order complex architectures *via* intermolecular interactions.[1-5] As described by Lehn, supramolecular chemistry aims at developing highly complex chemical systems from molecular components interacting *via* a number of non-covalent interactions such as hydrogen bonding, Van der Waals forces, ion-dipole interactions, π-π stacking *etc.* and so pre-organisation and complementarity are crucial in the design of such systems.[2-5] The area of supramolecular chemistry has undergone immense acceleration in the past 40 years with developments stemming from the construction of systems such as crown ethers,[6] cryptands,[7] lariat ethers[8] and podands[9] with a continuous expansion towards larger complex architectures such as rotaxanes, catenanes,[10-15] multimetallic helicates,[16-29] metal organic frameworks (MOF's) and clusters[30-35] in more recent years. Functional supermolecules have found applications in many diverse disciplines such as analytical methods,[36] gas storage,[31,33] biological probes and imaging agents,[19,37-46] light emitting devices,[34,47-49] catalysis[34] and molecular logic switches[50-55] to name but a few.

The self-assembly of these pre-organised systems can be driven by metal coordination to the transition metals[56,57] but also the lanthanide ions, bringing with them their fascinating photophysical and magnetic properties.[39,46,47,58-63] This not only allows for the creation of visually appealing and exquisite architectures but further extends their potential use as functional supramolecular devices. Lanthanide-directed self-assembly of appropriately designed ligands for the development of novel chiral assemblies has been a major topic of interest within the Gunnlaugsson group and has led to the formation of lanthanide luminescent systems such as helicates and bundles.[21,64-69] Much emphasis has been placed not only on the investigation of the self-assembly behaviour and photophysical properties of these assemblies but also on encouraging their potential incorporation into biological and materials based applications such as those mentioned above.[70,71]

With the aim of building upon work previously carried out within our research group the objective of this PhD was to form mononuclear and dinuclear chiral luminescent Ln^{III}-

directed self-assembled systems, based on the pyridine-2,6-dicarboxylic acid (dipicolinic acid (H_2dpa)) framework, possessing novel functionalisation for Langmuir-Blodgett monolayer formation, increased water solubility (with a view to extend into biological media) and for surface attachment to gold nanoparticles (AuNPs). By further functionalising previously investigated and relatively well documented systems the chiral luminescent properties of these assemblies may then be explored. For example, by immobilising these systems into organised monolayers their use as chiral analytical sensors and/or optical devices may be investigated, while the ability to function as chiral sensors in an aqueous environment opens up an avenue towards biologically relevant sensing capabilities.

1.1 Lanthanide metal ions

The lanthanide metal ions are a group of elements of the periodic table known as 'rare earth elements'. They include the 15 elements lanthanum through to lutetium (atomic numbers 57 to 71) and are located between the third row elements barium and hafnium. Contrary to their name, elements such as cerium and lanthanum are found quite abundantly in nature (crustal abundance data: Ce = 66 ppm, La = 35 ppm).[72] Currently the constant requirement to develop new and more efficient magnetic and luminescent materials for application in biomedical analysis, MRI contrast agents, NMR shift reagents, electroluminescent materials for LEDs, optical fibres for telecommunications and lasers has led to a recent surge of interest in lanthanide ion incorporation in functional supermolecules in order to take advantage of the unique magnetic and photophysical properties these metals have to offer.[38,47,59,60,73,74]

1.1.1 Photophysical properties and advantages of the lanthanides

The photophysical properties of the lanthanides are governed by their electronic configurations where a general trend of gradual filling of the 4*f* orbitals is observed. Their electronic configurations are described by [Xe]$4f^n$, where (n = 0-14), as they tend to exist primarily in their trivalent lanthanide state (Ln^{III}). As electrons successively occupy the valence 4*f* orbitals they do so according to Hund's rule whereby each orbital in the 4*f* sub-shell is singly occupied with one electron before any one orbital is doubly occupied. Since the 4*f* sub-shell is located in closer proximity to the nuclear core than the outer filled $5s^25p^6$ orbitals poor shielding of the nuclear charge by the electrons in the 4*f* orbitals leads to a decrease in ionic radii across the series, known as the 'lanthanide contraction', *i.e.* as nuclear charge increases a greater nuclear effect is felt by the $5s^25p^6$ electrons resulting in a 'contraction' of the ionic radius. This feature gives rise to a similar size and reactivity profile within the lanthanide metal series.[75]

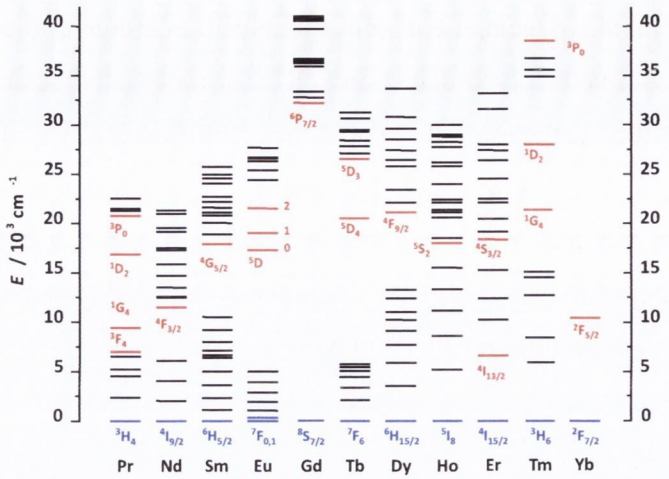

Figure 1.1. *Partial energy diagrams for the lanthanide aquo ions.*[73]

As the Ln^{III} 4*f* electrons are located within the filled $5s^2$ and $5p^6$ sub-shells they are 'hidden' from their external environment and so ligand perturbations in the first and second coordination sphere are limited giving rise to characteristic narrow line-like emission spectra upon Ln^{III} excitation by electromagnetic radiation.[47] Electronic transitions involve a redistribution of electrons within the 4*f* sub-shell, formally Laporte forbidden *f-f* transitions. However, these selection rules may become relaxed by a number of mechanisms such as vibronic coupling (which causes a change in geometry and thus symmetry around the metal ion), *J*-mixing and mixing with opposite parity wavefunctions such as 5*d* orbitals[76], and as such weak luminescence results.

A partial energy diagram illustrating energy gaps for the lanthanide aquo ions is shown in Figure 1.1 and displays the main luminescence transitions observed for each.[63] As shown, the energy gap for Gd^{III} is the largest of all the Ln^{III} with $\Delta E = 32200$ cm^{-1} (for $^6P_{7/2} \rightarrow {}^8S_{7/2}$) corresponding to UV emission. The most commonly encountered Ln^{III} in luminescent sensor development are Eu^{III} and Tb^{III}, with energy gaps of $\Delta E = 12300$ cm^{-1} (for $^5D_0 \rightarrow {}^7F_6$) and $\Delta E = 14800$ cm^{-1} (for $^5D_4 \rightarrow {}^7F_6$) corresponding to the emission of red and green visible light respectively. The energy levels of the excited and ground states in Nd^{III} ($^4F_{3/2} \rightarrow {}^4I_J$) and Yb^{III} ($^3F_{5/2} \rightarrow {}^3F_{7/2}$) however are closer together, and so the emission generated is in the near-infrared region of the electromagnetic spectrum.[63,75]

Additionally, the Ln^{III} exhibit extremely long luminescence lifetimes, ranging from $10^{-2} \sim 10^{-6}$ s (in the millisecond (ms) range for Eu^{III} and Tb^{III} and the microsecond (μs) range for Sm^{III} and Dy^{III}, for example), compared to those of common organic dyes which are in the nanosecond (ns) range and those of biological media which have excited state lifetimes typically in the submicrosecond (<μs) range.[39,46,47,77-79] These two photophysical features offer distinct advantages for responsive probes in cellular imaging and analyte detection in

biological media in the development of lanthanide luminescent bioprobes (LLBs) in a technique known as time resolved detection (TRD) or time-gated detection. Implementation of TRD avoids the detection of short-lived autofluorescence from the biological background.[37] Figure 1.2 displays how by exciting the Ln^{III} and measuring its long lived Ln^{III}-centred luminescence after a particular time interval detection of background autofluorescence from biological organic fluorophores and light scattering may be avoided, elucidating an intense signal (good signal to noise ratio).[38,80]

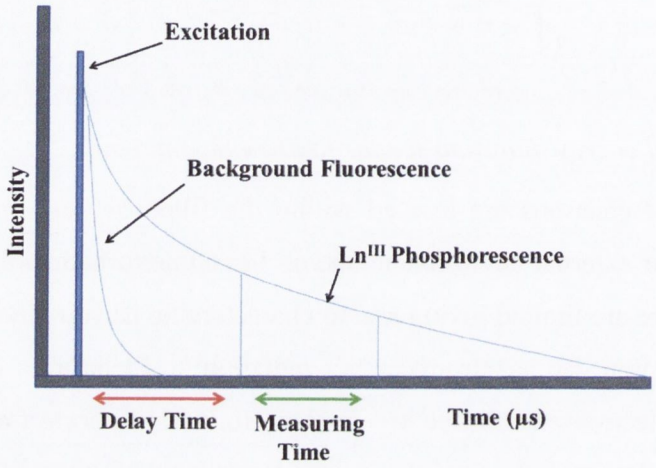

Figure 1.2. *A time delay between excitation and Ln^{III} phosphorescence detection allows background fluorescence to decay to negligible levels.*

The low probability of occurrence of the formally Laporte forbidden *f-f* transitions accounts for their weak absorption extinction coefficients (less than 4 M^{-1} cm^{-1})[39,59,81] and resultant low intensity luminescence. In order to overcome this obstacle and efficiently populate the Ln^{III} excited state a sensitising chromophore (known as an 'antenna') may be incorporated into the ligand complexing the Ln^{III}. As illustrated in Figure 1.3 the function of the sensitising antenna is to absorb electromagnetic radiation and transfer this energy to the (triplet) excited state of the lanthanide, generating an excited Ln^{III}, where energy is then emitted either as light (luminescence) or undergoes non-radiative deactivation (quenching). This indirect excitation of the Ln^{III} excited state allows for the significant photophysical properties of the Ln^{III} to be utilised or probed more efficiently.[59,63] Energy may be fed onto the Ln^{III} centre by a number of routes, most notably from the triplet excited state of the ligand (T_1) to the Ln^{III} excited state. However, other energy migration pathways have also been encountered such as the direct transfer from the ligand singlet excited state (S_1), intra-ligand charge transfer (ILCT) or ligand-to-metal charge transfer (LMCT) states.[59,63,82] However, these avenues of energy transfer play a less prominent role in the antenna effect, and as such are considered to a much lesser extent.

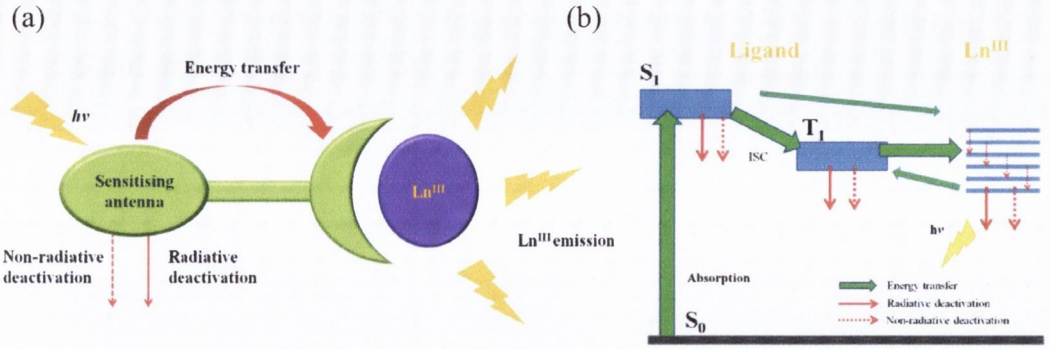

Figure 1.3. *(a) Simplified diagram illustrating how the 'antenna effect' is used to indirectly sensitise the Ln^{III} generating lanthanide emission. (b) Jablonski diagram illustrating the energy transfer from the 'antenna' to the Ln^{III} centre.*[49,83]

Two mechanisms to depict the energy transfer process from the ligand T_1 to the Ln^{III} ion have been commonly accepted and are known as Dexter's and Förster's mechanisms. The Dexters mechanism involves a double electron exchange whereby, following excitation and subsequent efficient intersystem crossing (ISC), an electron is transferred from the ligand T_1 excited state to the excited state of the Ln^{III}; while simultaneously, an electron is transferred from the highest occupied energy level of the metal ion to the vacant gap created by the initial photo-excitation of the ligand (as shown in Figure 1.4 (a)) with a distance dependency of e^{-r}. Förster's mechanism, which is more likely for the Ln^{III}, [63,80] comprises of energy transfer from the donor to the acceptor *via* dipole-dipole coupling of the dipole moment associated with the de-excitation of the ligand T_1 with the dipole moment associated with the 4*f* orbitals, as shown in Figure 1.4 (b),[60,76] with a distance dependency of r^{-6}.[80,84] Consequently, for both sensitisation processes, energy transfer is more efficient when the donor antenna group is located in close proximity to the acceptor Ln^{III}.

Not only is the efficiency of the sensitisation process dependent on the donor-acceptor distance but it also relies on a number of other factors such as:

1) The energy difference between the antenna S_1 and its T_1 where $\Delta E = 5000\ cm^{-1}$ is ideal for efficient ISC and thus efficient T_1 population.[76]

2) An optimal energy difference between the antenna T_1 and the Ln^{III} excited state to avoid fluorescence from the antenna (if the energy difference is too high) and non-radiative quenching *via* back energy transfer (if the energy difference is too low) (for Eu^{III}: $2500\ cm^{-1} < \Delta E\ (^3\pi\pi^*\text{-}\ ^5D_0) < 3500\ cm^{-1}$ and for Tb^{III}: $2500\ cm^{-1} < \Delta E\ (^3\pi\pi^*\text{-}\ ^5D_4) < 4000\ cm^{-1}$).[76]

3) Minimisation of deactivation by non-radiative processes such as vibrational collisions with local solvent molecules.[79,85]

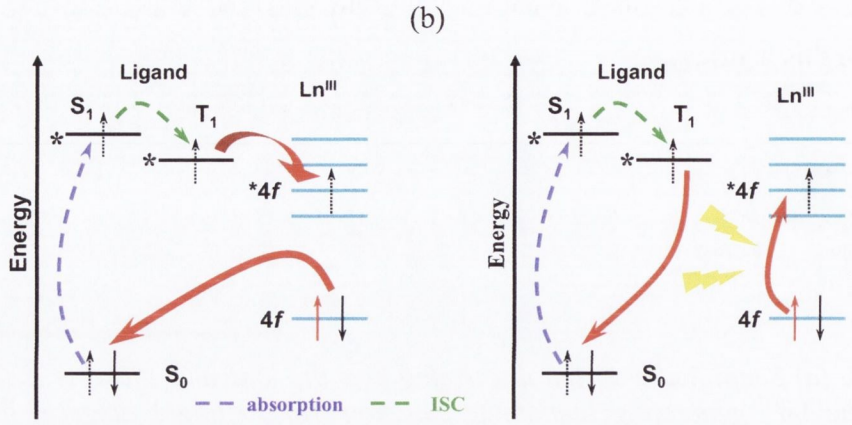

Figure 1.4. *Example of sensitisation mechanisms of energy transfer from the ligand S_1 via T_1 to Ln^{III} excited state. (a) Dexter's and (b) Förster's mechanism.*

Competing with radiative luminescence deactivation is non-radiative deactivation *via* collisions with high energy vibrating O-H, N-H and C-H oscillators within the Ln^{III} coordination sphere. This quenching process involves energy transfer from the Ln^{III} excited state to solvent molecules through vibrational collisions, or with ligand O-H, N-H and C-H oscillators. With regards to designing highly luminescent Ln^{III} complexes this deactivation pathway can be quite detrimental. On the other hand, however, it offers an impartial route to probe the coordination environment of the Ln^{III} by determining the number of solvent molecules directly bound to the Ln^{III} centre (q value or hydration state) in such complexes. Horrocks *et al.* developed an equation to determine the hydration state of a Eu^{III} or Tb^{III} complex based on the observation that O-D isotopic oscillators reduce the excited state lifetimes of Eu^{III} and Tb^{III} to a far lesser extent than the O-H oscillator.[86] This equation was further modified by Parker *et al.* to include the effect of other oscillators such as N-H and C-H on this deactivation process; these are given by Equations 1 and 2 (for Eu^{III} and Tb^{III}) where an additional correction factor of 0.075 ms^{-1} should be made for each carbonyl-bound amide NH oscillators with Eu^{III}:[82,87]

Equation 1: $$q^{EuIII} = 1.2[(1/\tau_{H2O})-1/\tau_{D2O})-0.25]$$

Equation 2: $$q^{TbIII} = 5[(1/\tau_{H2O})-1/\tau_{D2O})-0.06]$$

This non-radiative deactivation process reduces the energy of the excited state and thus competes with radiative luminescence. Consequently, it is usually advantageous to minimise this energy transfer process by protecting the Ln^{III} and preventing surrounding solvent vibrating oscillators from entering the first coordination sphere and binding to the Ln^{III}. This may be achieved by designing polydentate ligands which fully occupy the high coordinative

environments of the Ln^{III} and 'shield' them from potential undesirable deactivation *via* processes of this nature.

The dependence of Ln^{III} luminescence on the above parameters means that careful ligand design for appropriate Ln^{III} complexation and sensitisation must be taken into account to achieve full exposure of the photophysical properties of the Ln^{III} in the formation of novel applicable lanthanide luminescent systems.

1.2 Ligand design for lanthanide luminescent complex systems

Ionisation energy data reveal that the lanthanides exist primarily in their +3 oxidation state with high charge density causing them to act as hard Lewis acids. Hence, they tend to possess variable and large coordination numbers (from between 9 and 12) forming labile ionic complexes with donor ligands which are hard Lewis bases.[72] The development of systems incorporating the Ln^{III} therefore entail the design of ligands containing functional groups such as amides, carboxylates and nitrogen based heterocycles that facilitate their high coordination requirements.[39,72] Moreover, it is essential that ligand-Ln^{III} bond formation results in both kinetically and thermodynamically stable complex formation to ensure that the Ln^{III} remains tightly bound. Unfavourable enthalpic processes such as ligand dehydration in solution are generally not counteracted by favourable ligand-Ln^{III} bond formation and it is thus understood that the assembly process and subsequent bond formation is entropically driven.[63] Polydentate acyclic chelating ligands such as podands offer enhanced stability over monodentate ligands due to the 'chelate effect' (*i.e.* reduced entropy of disorder loss and ring formation upon complexation). In such instances a number of flexible functionalised pendant arms containing appropriately located coordinating groups (usually bidentate/tridentate) are generally grafted onto such structures in a pre-organised manner for Ln^{III} encapsulation.[63,88-90] However, this strategy lacks the pre-disposition macrocyclic ligands have to offer as complexation requires a large conformational entropic factor in comparison. Polydentate macrocyclic ligands containing a pre-organised cavity, such as cyclen[39] and calixarenes,[91] further reduce the entropic cost compared to their acyclic counterparts by maintaining a pre-determined cavity size and optimised coordinating sites for Ln^{III} selectivity. This is known as the 'macrocyclic effect', a specific case of the 'chelate effect'. Furthermore, pendent arms are often attached to the cavity encouraging further pre-organisation, coordinative saturation and Ln^{III} stability.

Another strategy implemented to develop more sophisticated complex supramolecular systems is that of self-assembly. Self-assembly comprises of the fine tuning of ligand design such that complimentary weak non-covalent interactions drive the manifestation of hierarchal molecular edifices.[4] By pre-organising ligands in a specific manner one can take advantage

of the intermolecular forces between functional groups on adjacent ligands and control the assembly of these coordinating building blocks around one or several ions. This self-assembly process has led to the generation of elegant systems such as catenanes, rotaxanes,[10-15] metal-directed molecular cages and boxes.[92] Whilst much emphasis has been placed on the development of transition metal based supramolecular systems[56,57] Ln^{III}-directed self-assembly formation has only recently experienced considerable attention.

Ln^{III}-directed self-assembly incorporates the use of the Ln^{III} to drive the self-assembly process offering a route towards large molecular fabrications such as bundles,[93] helicates[94-97] or hierarchical systems such as clusters[98,99] or metal organic frameworks (MOFs).[35,100,101] Since the Ln^{III} possess larger coordination numbers than the transition metal ions, ligand binding sites and metal coordination geometries play an important role in determining and controlling the overall structure of the resulting system.

Since this thesis primarily deals with the development of novel chiral Ln^{III}-directed self-assembly formations, based on the 2,6-pyridinedicarboxylic acid (H_2dpa) framework, the following sections of this chapter are divided into the most relevant examples of monometallic and multimetallic Ln^{III} -directed self-assembly systems currently in the literature with discussions broadly focusing on functionalised pyridine ligands. Some recent examples developed within the Gunnlaugsson group, a brief overview of the Langmuir-Blogett technique and theory followed by a summary of the work described within this thesis are then given.

1.3 Monometallic Ln^{III}-directed self-assembled systems

Several different types of sensitisers for the development of monometallic Ln^{III}-directed self-assembled systems have been reported and recently reviewed.[58,67] However, it is the pyridine unit and its analogues which offer appreciable comparison to the systems under investigation within this thesis and so, as mentioned above, current research in related fields is thus discussed accordingly with a primary focus on the H_2dpa framework.

The extensive employment of the basic tridentate dipicolinate (H_2dpa) backbone as a Ln^{III} chelating unit originates from its ability to form nine-coordinate 1:3 (Ln:dpa) tris(dipicolinate) complexes bearing high stability constants.[102] The crystal structures of many such complexes have been reported[103,104] while the capacity of H_2dpa, **1**, to deliver sufficient photophysical properties for efficient lanthanide luminescent sensitisation encourages its continued study and derivatisation for further application. Relatively large luminescent quantum yields are exhibited by, in particular, Eu^{III} and Tb^{III} tris(dipicolinates) where $Cs_3[Eu(dpa)_3]$ and $Cs_3[Tb(dpa)_3]$ for example display quantum yields of 24% ± 2.5%

and 22% ± 2.5%, respectively, in TRIS-HCl buffered solution (0.1 M). The intense luminescence observed is a result of sensitisation occurring through the dpa^{2-} triplet excited state with an efficiency of 85% for the tris complex in the solid state and 61% in solution and as such these systems have been proposed by Chauvin *et al.* for implementation as secondary standards for quantum yield determination.[105-108]

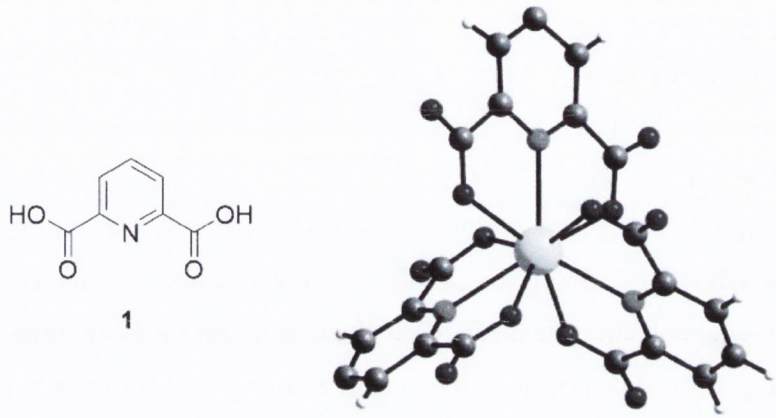

Figure 1.5. *2,6-pyridinedicarboxylic acid* ***1*** *(H_2dpa) and X-ray crystal structure of $Cs_3[Eu(dpa)_3]$.*[105]

A great deal of knowledge of the Ln^{III} tris(dpa) system has clearly been acquired. Consequently, it is now of particular interest to modify the simple H_2dpa structure ligand core to enhance its potential applicability. In order to make use of perhaps a sensing functionality interacting/receptor moieties and/or groups enhancing water solubility can be attached for imaging purposes and/or for solid state fabrication. It is critical, however, to investigate the effects H_2dpa derivatisation has on the overall stability and desirable photophysical properties of these Ln^{III} complex systems in solution.

George *et al.* reported the synthesis of H_2dpa (**1**) analogues **2** - **4** where the 4 and 3, 5 positions of the pyridine ring were derivatised with hydroxy, chloro and bromo substituents. A photophysical study was carried out to investigate the effect these simple modifications have on the sensitisation and emission properties of the $Eu(\mathbf{L})_3$ (where **L** = **1** - **3**) and Eu(**4**) complexes.[107] Findings were compared to results previously reported for analogous Tb^{III} systems and following substitution of the four position in the order Cl > H > OH it was found that the ability to sensitise Eu^{III} emission was increased, in contrast to OH > H > Cl for Tb^{III}.[107,109] In the case of **4**, the dibromo-4-hydroxy derivative, no sensitisation was observed and so results were inconclusive due to incomplete saturation of the Eu^{III} coordination sphere as a Eu:**L** ratio of 1:1 was found. Long luminescence lifetimes were also determined for $Eu(\mathbf{L})_3$ (where **L** = **1** - **3**) ranging from 1.16 to 2.9 ms (in CH_3OH and H_2O) - an attractive feature for the development of luminescent biological probes.

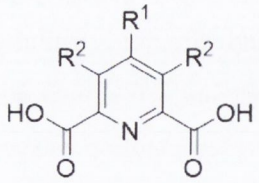

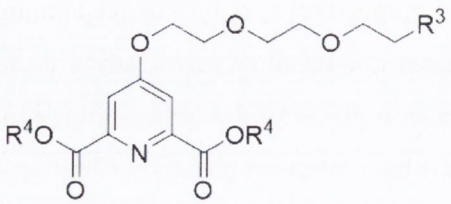

2: R^1 = OH, R^2 = H
3: R^1 = Cl, R^2 = H
4: R^1 = OH, R^2 = Br

5: R^3 = OMe, R^4 = H
6: R^3 = OH, R^4 = Na
7: R^3 = NH_2, R^4 = H
8: R^3 = Phta, R^4 = Na

Phta: 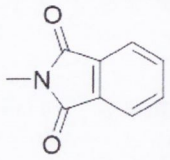

With an eventual coupling to biological molecules in mind Chauvin *et al.* synthesised four novel derivatives of H_2dpa where the 4-*para* position of the pyridine unit was functionalised with a polyethylene chain, each chain differing by the terminal substituent (*i.e.* either by an alcohol, methoxy, phthalimide or an amine group), to react with Eu^{III} and Tb^{III} forming tris chelate complexes.[106] Not only did these ligands form thermodynamically stable 1:3 monometallic complexes at physiological pH ($\log\beta_{13} \approx 19 - 20$ ($Eu(\mathbf{L})_3$); **L** = **5** - **8**) but also, depending on the terminal substituent of the pendant arm, the photophysical properties were tuned. Substitution at the 4-*para* position always displayed a detrimental effect on Tb^{III} sensitisation where luminescence quantum yields (in H_2O) did not exceed 18%, compared to that of 22% for $[Tb(\mathbf{1})_3]^{3-}$. Nevertheless, sensitising efficiencies of 70% gave rise to quantum yields of up to 29% (for **L** = **7**) for the Eu^{III} tris complexes, 5% larger than that observed for $[Eu(\mathbf{1})_3]$.[105] This data may be assumed as a model system for the modification of the 4-*para* position of H_2dpa illustrating that with careful consideration of the grafting moiety a gateway towards the incorporation of biomolecules into such systems may be opened, without completely diminishing the optical properties of the complex core.[106]

More recently three tridentate 6-phosphoryl picolinic acid derivatives (**9** - **11**) were developed as ligands for Eu^{III} and Tb^{III} sensitisation by Chauvin *et al.* in which one of the carboxylate side groups of H_2dpa has been replaced by a phosphoryl-based functional group. Compounds **9** and **10** where shown to form water soluble 1:3 complexes while that of **11** precipitates in the presence of Ln^{III}.[110] Stability constants greater than those observed for the parent H_2dpa compound were determined where $\log\beta_{13}$ = 23.8 and 24.3 for $Eu(\mathbf{9})_3$ and $[Eu(\mathbf{10})_3]^{3-}$ were calculated, respectively, in comparison to $\log\beta_{13}$ = 22.4 for $[Eu(\mathbf{1})_3]^{3-}$. The emission spectra of $Eu(\mathbf{9})_3$ and $[Eu(\mathbf{10})_3]^{3-}$ were also measured as a function of pH displaying the highest luminescence at pH 4.8 for $Eu(\mathbf{9})_3$ whereas $[Eu(\mathbf{10})_3]^{3-}$ was more luminescent at pH 9.0. Obtaining maximum emission at these pH extremities is uncommon yet quite interesting for self-assembled systems of this nature. Another more notable feature displayed

by the Tb(**9**)$_3$ complex was that it exhibited a quantum yield of 40% in water, much larger than the corresponding Eu(**9**)$_3$ complex (15%). This highlights the significance that simple substitution has not only on complex thermodynamic stability but also on the possibility of altering luminescent properties.[110]

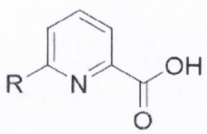

9: R = $PO(OEt)_2$
10: R = PO(OEt)OH
11: R = $PO(OH)_2$

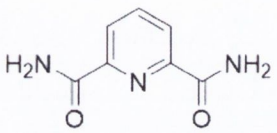

12

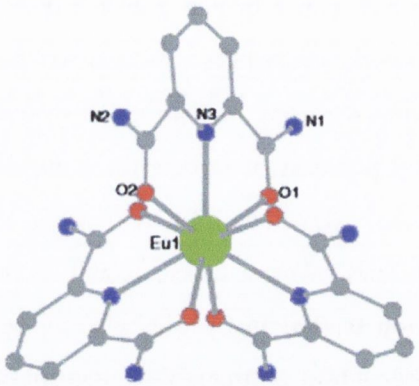

$[Eu(\mathbf{12})_3]^{3+}$

Figure 1.6. *Ligands* ***9*** *–* ***12*** *designed for monometallic* Ln^{III}*-directed self-assembly and X-ray crystal structure of* $[Eu(\mathbf{12})_3]^{3+}$.[111]

The versatility attainable by simple modification of the H_2dpa framework, while still retaining a fully saturated luminescent 1:3 tris chelate complex, has also been confirmed by Tanase *et al.* (as well as by Muller *et al.* as shall be discussed in later sections) by the facile conversion of both the carboxylate groups to amide groups, as shown in **12**.[111] Again a tridentate cavity provides hard nitrogen and oxygen donor atoms to form a nine-coordinate mononuclear species. A tricapped trigonal prismatic arrangement in both $[Eu(\mathbf{12})_3]^{3+}$ and $[Tb(\mathbf{12})_3]^{3+}$ crystal structures were shown and both Eu^{III} and Tb^{III}-centred emission was exhibited by solid samples of both upon excitation of the pyridine-2,6-dicarboxamide antenna. Lifetime measurements (carried out on solid samples) further confirmed the presence of a single luminescent species with values of 1.9 ms and 2.2 ms obtained for $[Eu(\mathbf{12})_3]^{3+}$ and $[Tb(\mathbf{12})_3]^{3+}$, respectively.

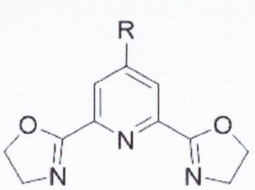

13: R = H

14: R = 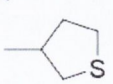

15: R = Br
16: R = OMe

17: R = 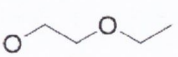

Pyridine-bis(oxazoline) ligands, also known as Pybox (**13**), are another class of simple precursors which have experienced considerable attention as competent chromophores for

Ln^{III} sensitisation in recent years, in particular by de Bettencourt-Dias *et al.* The thiopene-derivatised-Pybox, **14**, was the first published Pybox Ln^{III} sensitiser forming the 1:1, 1:2 and the 1:3 (Ln:L) species in CH_3CN solution.[112] Substantial quantum yields (in CH_3CN) of 76% and 59% for Eu(**14**)$_3$ and Tb(**14**)$_3$ and a 1:2 crystal structure of the Eu(**14**)$_2$ species were obtained. This further fuelled the progressive study and modification of the Pybox framework eventually leading to the evolution of compounds **15** and **16**. An electron donating methoxy and an electron withdrawing bromo moiety were attached to the 4-*para* pyridyl position of Pybox for comparison with the parent Pybox ligand **13** as well as the previously developed **14**. A number of crystal structures suitable for X-ray diffraction were grown and in most cases displayed the anticipated 1:3 stoichiometries for these examples. Solution studies in CH_3CN also evidenced the existence of the 1:1, 1:2 and the 1:3 (Ln:L) species, while appreciable quantum yield values were obtained for these in CH_3CN (for Eu(**15**)$_3$ = 36%, Tb(**15**)$_3$ = 23%, Eu(**16**)$_3$ = 24% and Tb(**16**)$_3$ = 21%).[113] Furthermore, subsequent tailoring of the Pybox structure, by attachment of an ethylene glycolethyl ether to the 4-*para* position afforded **17** and successfully demonstrated the ability of these Pybox ligands to sensitise the Ln^{III} in a fully aqueous environment.[114]

Other *N*-donor chelating units, which have been well established for Ln^{III}-directed self-assemblies include bipyridine,[115-117] terpyridine[118,119] and more recently tetrazole ligands.[119-121] However, for the purpose of relevance and concision, only two recent examples published by Mazzanti *et al.* incorporating the tetrazole unit are discussed.[121] Both tridentate chelating building blocks **18** and **19**, analogous to the well-known H_2dpa system, were shown to form helical tris-chelate Ln^{III} complexes, as evidenced by X-ray crystallography and ^{1}H NMR analysis. It was also found that by changing the counterion for these self-assemblies the solubility of both complexes could be tuned. Of these, the bis-tetrazolate-pyridine ligand **18** offered the most promising photophysical properties as it was not only capable of sensitising both visible and near-IR emitting Ln^{III} but replacement of the carboxylate group with the tetrazolate substituent also significantly extended the absorption window of the corresponding complexes towards the visible region (up to 330 nm), relative to the parent H_2dpa system itself.[121]

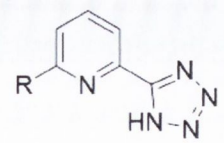

18: R =

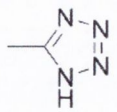

19: R = COOH

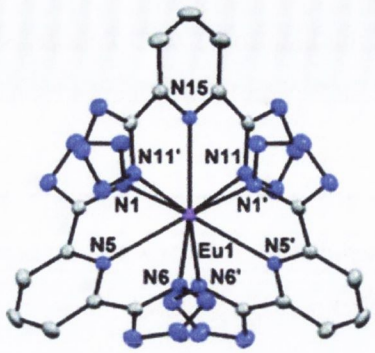

$[Eu(\mathbf{18})_3]^{3-}$

Figure 1.7. *Ligands* ***18*** *and* ***19*** *designed for monometallic* Ln^{III}*-directed self-assembly and X-ray crystal structure of* $[Eu(\mathbf{18})_3]^{3+}$ [121]

Another similar *N*-donor type tridentate ligand which has been intensively investigated is the bis(benzimidazole)pyridine ligand. It has been implemented for the formation of both mononuclear and multinuclear Ln^{III}-directed self-assembled systems. These studies have been mainly conducted by Bünzli *et al.* who have synthesised a large library of bis(benzimidazole)pyridine precursors, five examples of which are shown here **20** – **24**.[122-127] Substituents of varying steric and electronic character where appended to different positions of both the pyridine and benzimidazole subunits and the effect their incorporation has on the photophysical characteristics and overall size and shape of the final system evaluated. Ligands **20** – **22** react with lanthanide nitrates to give neutral 1:1 nitrato luminescent complexes $[Ln(NO_3)_3(\mathbf{L})(solv)]$ (**L** = **20** – **22**, & **24**) while simply choosing non-competitive lanthanide perchlorate salts instead yields tris $[Ln(\mathbf{L})_3]^{3+}$ (**L** = **20** – **23**) complexes with a coordination geometry close to the ideal tricapped trigonal prism.

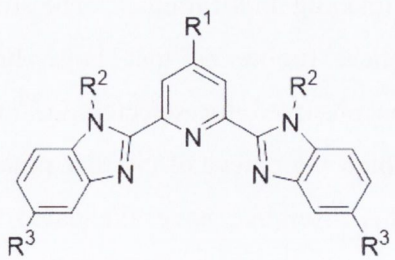

20: R^1 = H, R^2 = CH_3, R^3 = H
21: R^1 = H, R^2 = C_2H_5, R^3 = H
22: R^1 = H, R^2 = C_8H_{17}, R^3 = H
23: R^1 = H, R^2 = $(CH_3O)_2C_6H_3$, R^3 = H
24: R^1 = C_6H_5, R^2 = $(CH_3O)_2C_6H_3$, R^3 = H

In addition to the bis(benzimidazole)pyridine ligands, mono derivatised benzimidazole-, benzothiazole- and benzoxazole-substituted pyridine-2-carboxylic acids have also been shown to be capable of providing a nine-coordinate environment for the Ln^{III} while the heteroaromatic side groups act as efficient antennae for sensitising Ln^{III} luminescence.[128,129]

It has been established, from these in depth studies, that substitution at the R^3 position of the ring imparts the electronic and photophysical properties of the final complex system while substitutions at R^1 and R^2 influences its overall structure and stability as steric bulk at these positions affects the co-planarity of the aromatic rings in the final complexes, severely limiting their stabilities in solution.[122-127] This set of observations emphasises the importance of careful ligand design for rationally controlling the shape, stability and properties of the resulting Ln^{III}-directed self-assemblies.

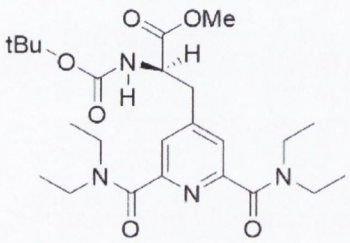

25

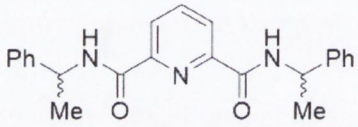

26: (*S*, *S*)
27: (*R*, *R*)

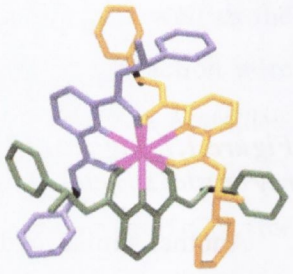

$[Eu(\mathbf{26})_3]^{3+}$

Figure 1.8. *Ligands* ***25*** *-* ***27*** *designed for monometallic* Ln^{III}*-directed self-assembly and X-ray crystal structure of* $[Eu(\mathbf{26})_3]^{3+}$ *.*[130]

Crucial to modern drug discovery is the recognition of chiral molecules, the determination of the absolute configuration of an unknown chiral compound.[131] Since the observation of the Pfeiffer effect - the induction of optical activity in a solution of a labile racemic mixture by the addition of a secondary chiral substance,[132] a growing interest in the development of chiral luminescent probes has occurred and led to the generation of monometallic Ln^{III} directed self-assemblies such as **25**, **26** and **27**.[130,133,134]

In luminescent Ln^{III} complexes ligand field structure is sensitively reflected in the sign and magnitude of Circularly Polarised Luminescence (CPL) and therefore CPL active Ln^{III} complexes have potential use in chiral sensing and imaging applications.[135] The advantage of using luminescent Ln^{III} complexes as chiro-optical probes is that large luminescent dissymmetry values (g_{lum}) as high as 0.5 may be observed for selected Ln^{III} transitions compared to other chiral organic molecules for which the extent of circular polarisation is less than 1 x 10^{-2}.[135,136] Preliminary studies in this discipline have elucidated that **25**, a tridentate ligand bearing a bulky chiral group in the 4-*para* position of the pyridine ring, forms thermodynamically stable $[Ln(\mathbf{25})_3]^{3+}$ (Ln = La^{III}, Eu^{III}, Lu^{III}) complexes in CH_3CN with logβ values in the range 19-20. However, only a very small excess of one diastereoisomer was induced in solution, reflected by weak CPL signals for $[Eu(\mathbf{25})_3]^{3+}$ and $[Tb(\mathbf{25})_3]^{3+}$ (calculated luminescence dissymmetry factor for $[Tb(\mathbf{25})_3]^{3+}$ $^5D_4 \rightarrow {}^7F_5$ transition

g_{lum} = 0.02).[130,133] This encouraged the introduction of more influential functional groups capable of inducing pronounced diastereoisomerism in such structures.

Enantiomers **26** and **27** were developed and shown to form stable 1:3 $[Eu(\mathbf{L})_3]^{3+}$ (**L** = **26**, **27**) optical isomers *in situ* possessing constant CPL activity over a long period of time in CH_3CN (calculated luminescence dissymmetry factor for $[Eu(\mathbf{26})_3]^{3+}$ $^5D_0 \rightarrow {}^7F_1$ transition g_{lum} = 0.19).[133,134] Due to the long shelf life exhibited by these chiral emitting species they have been proposed as reliable CPL calibration standards.[134] Further study on these systems have revealed the formation of stable tris complexes in CH_3CN (logβ in the range 23.8) while X-ray crystal structures of $[Ln(\mathbf{L})_3]^{3+}$ (**L** = **26**, **27**; (Ln = Eu^{III}, Gd^{III}, Tb^{III} and Yb^{III}) are isostructural for the Ln^{III} series studied in the solid state. Most importantly, this study illustrates that the chiral nature of the ligand may induce Δ or Λ stereochemistry in the final complex product.[130] Attentive ligand design may therefore be exploited to build upon these chiral Ln^{III} complex bioprobe foundations, as shall be discussed in later sections.

Although podand ligand structures **28** and **29** are quite dissimilar to those systems discussed up until this point they are worth mentioning as they also represent ideal candidates for the development of Ln^{III} luminescent chiral CPL probes and have received considerable attention by researchers such as Raymond and co-workers in recent times.[137,138] Enantiomeric octadentate chiral 2-hydroxyisophthalamide chelating ligands **28** and **29** have been shown to form chiral 1:1 complexes with Tb^{III}, Eu^{III}, Sm^{III} and Dy^{III}. Ln^{III}-centred luminescence was exhibited by all eight complexes with quantum yield measurements (carried out in CH_3OH) indicating a significantly high value for the Tb.**28** complex (63%). Eu.**28** possessed a rather low quantum yield value (2.3%) however CPL analysis displayed relatively large dissymmetry factor values for both enantiomeric complexes with g_{lum} values of +0.30 and -0.29 obtained for the $^5D_0 \rightarrow {}^7F_1$ transition in Eu.**28** and Eu.**29** (in CH_3OH), respectively. Excited state lifetime measurements were also conducted in both CH_3OH and CD_3OD and confirmed that in the cases of the Eu^{III} and Tb^{III} complexes (Eu.**28**, Eu.**29**, Tb.**28** and Tb.**29**) a *q* value of 1 was obtained in which all eight ligand coordinating groups are directly bound to the Ln^{III} with the remaining coordination site occupied by a solvent molecule.

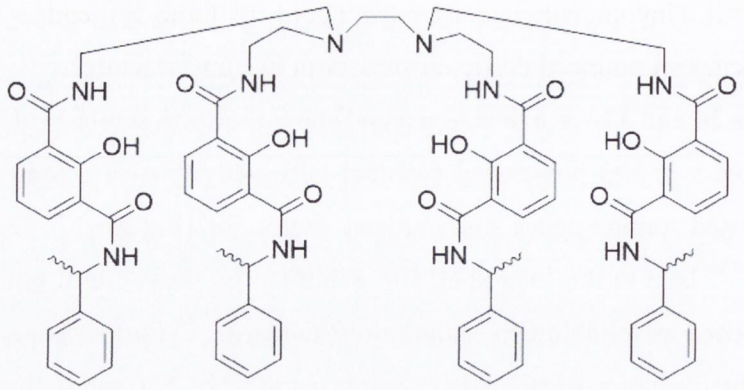

28: (*R*, *R*, *R*, *R*)
29: (*S*, *S*, *S*, *S*)

With regard to those monometallic self-assembly systems discussed above it is clear that key factors such as the choice in metal ion, M:L ratios and concentrations, the number and location of ligand coordinating groups and even the nature of the solvent play an even more prominent role in the development of multimetallic Ln^{III}-directed self-assemblies as one can generate a wide variety of supramolecular edifices such as MOFs,[139] helicates,[21,64,140-145] coordination polymers[146-148] and extravagant clusters, as shall be discussed below. Once again, those examples of multimetallic Ln^{III}-directed self-assembled systems most applicable to the work described within this thesis are discussed in the following section with other less relevant examples briefly touched upon in order to give a more representative overview of this area of research.

1.4 Multimetallic Ln^{III}-directed self-assembled systems

On account of the lability and relatively unpredictable nature of the Ln^{III} coordination preferences the construction of discrete synthetically controlled polymetallic Ln^{III} containing architectures as new functional materials can prove quite a challenge to the supramolecular chemist. Nonetheless, by manipulating ligand design for pre-organisation the variable coordination numbers and stereochemical inclination of the Ln^{III} may be accommodated for. This is reflected by the growing number and diverse range of emerging multimetallic Ln^{III} containing superstructures in recent times.[21,64,140-144,149]

Work by Mazzanti *et al.* highlights the diversity of such systems by selectively obtaining elegant cluster superstructures utilising the simple assymetric tetradentate terpyridine carboxylate ligand unit **30** by precisely controlling species concentration.[149] Preliminary work involved a stepwise synthetic strategy leading to the selective assembly of large hexameric Eu^{III} wheels.[149] Reaction of $Eu(CF_3SO_3)_3$ with two equivalents of **30** in the presence of triethylamine in CH_3OH led to the formation of the mononuclear eight coordinate complex $[Eu(\mathbf{30})_2](CF_3SO_3)$, which was confirmed by X-ray crystallography.

Addition of small aliquots of $Eu(CF_3SO_3)_3$ to $[Eu(\mathbf{30})_2](CF_3SO_3)$ leads to the self-assembly of the polynuclear hexameric Eu^{III} wheel $[Eu\subset(Eu(\mathbf{30})_2)_6]^{9+}$ possessing an encapsulated Eu^{III} cation in its centre.[149]

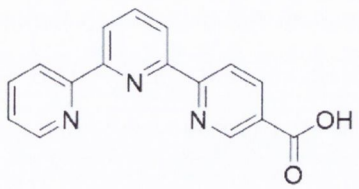

30:

$[Lu\subset(Eu\mathbf{30})_2)_6]^{9+}$

Figure 1.9. *Compound **30** designed for the development of the heterometallic cluster superstructure* $[Lu\subset(Eu(\mathbf{30})_2)_6]^{9+}$.[150]

By investigating the inclusion of different *f* elements in these systems selective recognition and thus incorporation of two different Ln^{III} into the polymetallic ring was achieved.[150] It was found that the formation and size of the cyclic assembly was controlled by the ionic radius and the coordination number of the Ln^{III}. The addition of Ln^{III} possessing smaller ionic radii to $[Eu(\mathbf{30})_2](CF_3SO_3)$ led selectively to the formation of a species with the Eu^{III} located on the peripheral sites of the ring with the smaller ion occupying only the central site. This is shown for the X-ray crystal structure of the heterometallic $[Lu\subset(Eu(\mathbf{30})_2)_6]^{9+}$ complex above.[150]

As mentioned in the previous section, Ln^{III} based chiral supramolecular architectures are attractive for chiral sensing purposes. In view of this the chiral carboxylate-derivatised bipyoxazoline tetradentate ligand **31** was synthesised for use in the diastereoselective self-assembly synthesis of an enantiopure trinuclear Eu^{III} complex *via* a concentration-dependent process. The evolution of the diastereomeric self-assemblies (Δ)-$[Eu(\mathbf{31})_2]^+$ and (Λ)-$[Eu(\mathbf{31})_2]^+$ were formed with partial stereoselectivity ($\Lambda/\Delta \approx 1.8$) at low concentrations while at higher concentrations selective homochiral recognition affords the trinuclear $[(\Delta\Delta\Delta)$-$Eu(\mathbf{31})_2)_3]^{3+}$ triangular complex exclusively.[98] Moreover, Mazzanti *et al.* have further enhanced the controlled complexity of these systems by synthesising **32** (the enantiomer of **31**) and assembled, by the addition of Eu^{III} to a mixture of diastereoisomers of either the bis ligand **31** complex or the bis ligand **32** complex, large multimetallic enantiopure wheels. The

addition of Eu^{III} to a mixture of (Δ)-$[Eu(\mathbf{32})_2]^+$ and (Λ)-$[Eu(\mathbf{32})_2]^+$ gives rise to the selective self-assembly of the enantiopure heptameric Eu^{III} wheel $[Eu\subset(\Lambda\text{-}Eu(\mathbf{32})_2\Delta\text{-}Eu(\mathbf{32})_2)_3(CF_3SO_3)_9]$, which is shown below, while the addition of Eu^{III} to a mixture of (Δ)-$[Eu(\mathbf{31})_2]^+$ and (Λ)-$[Eu(\mathbf{31})_2]^+$ yields the corresponding enantiomeric heptameric Eu^{III} $[Eu\subset(\Delta\text{-}Eu(\mathbf{31})_2\Lambda\text{-}Eu(\mathbf{31})_2)_3(CF_3SO_3)_9]$ ring. Both structures were elucidated by solid state X-ray crystallography and were shown to be isostructural while Eu^{III}-centred CPL emission was detected from the mononuclear, trimeric and heptanuclear species. Of these, the trimeric complexes showed remarkable CPL activity in comparison to the mono- and heptanuclear species with g_{lum} values (for the $^5D_0 \rightarrow {}^7F_1$ transition) of -0.04 and +0.06 (for the mononuclear species), ±0.45 (for the trimeric species) and +0.1 (for the heptameric species) obtained.[150,151]

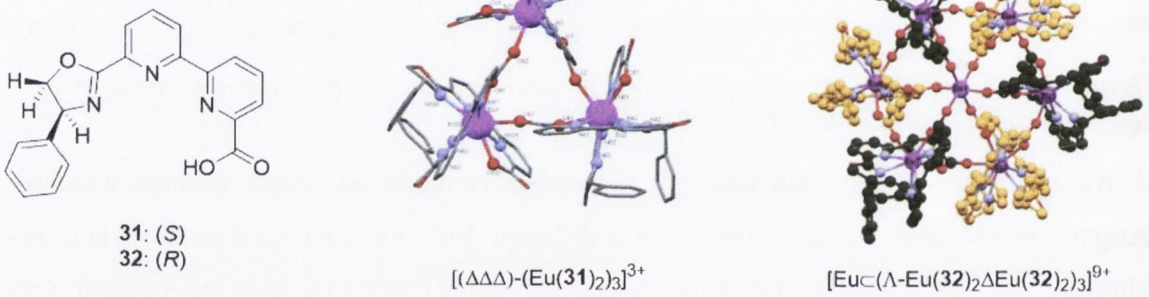

Figure 1.10. *Compounds* ***31*** *and* ***32*** *designed for the formation of the trimeric* $[(\Delta\Delta\Delta)\text{-}Eu(\mathbf{31})_2)_3]^{3+}$ *and heptanuclear* $[Eu\subset(\Lambda\text{-}Eu(\mathbf{32})_2\Delta\text{-}Eu(\mathbf{32})_2)_3(CF_3SO_3)_9]^{9+}$ *self-assembly cluster structures.*[98,150,151]

The chiral bipyridine derivative **33**, which possesses a pinene unit and an appended carboxylate donor group, has also been implemented for the diastereocontrolled synthesis of enantiopure trinuclear Eu^{III} complexes.[152] In the presence of Eu^{III} **33** has been shown by Lama *et al.* to transfer its chirality into the final supramolecular polymetallic structure $[Eu_3(\mathbf{33})_6(\mu_3\text{-}OH)(H_2O)_3](ClO_4)_2{\cdot}3H_2O$ inducing diastereoselectivity upon self-assembly. As shown from the crystal structure of $[Eu_3(\mathbf{33})_6(\mu_3\text{-}OH)(H_2O)_3](ClO_4)_2{\cdot}3H_2O$ the three Eu^{III} are bridged by a central hydroxide ion. Three of the ligands coordinate through both of their carboxylate and bipyridine donor groups; the carboxylate group linking two Eu^{III} centres, while the remaining ligands coordinate solely through their carboxylate groups, again bridging two Eu^{III} centres. This gives rise to an interesting mode of helical chirality, which is reflected in the CD spectrum of the complex, where the ligands adopt a propeller like arrangement around the trinuclear Eu^{III} core.[152]

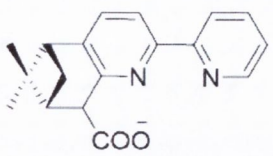

33: (+)
34: (-)

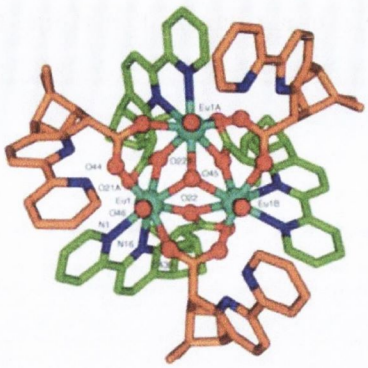

$[Eu_3(\mathbf{33})_6(\mu_3\text{-}OH)(H_2O)_3](ClO_4)_2.3H_2O$

Figure 1.11. *Compounds **33** and **34** designed for mulitmetallic cluster structure formation and X-ray crystal structure of* $[Eu_3(\mathbf{33})_6(\mu_3\text{-}OH)(H_2O)_3](ClO_4)_2 \cdot 3H_2O$.[152]

Furthermore, a solvent-dependent study was conducted and revealed a process in which Pr^{III} and **33**, with the same M:L ratio (1:2.25), can follow one of two distinct diastereoselective self-assembly pathways.[153] In CH_3OH a two dimensional trinuclear array was self-assembled upon the reaction of $Pr(ClO_4)_3$ with **33** in the presence of triethylamine, while in CH_3CN, a three dimensional tetranuclear pyramidal polyhedron was observed. Most interestingly was the reversibility of the interconversion between the two species by simple addition or removal of H_2O from the CH_3CN system.[153] Lama *et al.* have also carried out in-depth investigations into the incorporation of a number of other Ln^{III} into this system and evaluated the photophysical and chiro-optical properties of these tris $[Ln_3(\mathbf{L})_6(\mu_3\text{-}OH)\text{-}(H_2O)_3](ClO_4)_2$ (Ln = La^{III}, Pr^{III}, Nd^{III}, Sm^{III}, Eu^{III}, Gd^{III}, Tb^{III}, Dy^{III}, Ho^{III}, Er^{III}) (**L** = **33**, **34**) complexes. Sufficient sensitisation of metal-centred luminescence was observed in all cases and the self-recognition capabilities of the system were also tested. CPL emission was also exhibited by the enantiomeric Eu^{III} tris complexes with g_{lum} values of ±0.088, ±0.058, ±0.003 and ±0.003 calculated for the $^5D_0 \rightarrow {}^7F_J$ (J = 0 - 4) transitions respectively.[154]

The development of trinuclear Ln^{III} cluster complexes possessing luminescent and relaxivity properties has also been accomplished by Hamacek *et al.*[155-157] However, the importance of ligand pre-programming for the design and construction of pre-determined higher order molecular edifices has been markedly emphasised in a more recent publication.[158] The self-assembly of the first pentanuclear Ln^{III} helicate has been driven by metal coordination of one symmetric tridentate ligand **35** and three unsymmetric tripodal tetradentate ligands **36** to five Ln^{III}. As shown, **35** forms the tetrahedron base while the three **36** ligands form the side faces and linear part of the supramolecular structure. By precisely combining previously studied chemical motifs[159,160] (in a 5:1:3 Eu:**35**:**36** ratio) the assembly of $[Eu_5(\mathbf{35})(\mathbf{36})_3]^{15+}$ (molecular model shown) was achieved and verified by NMR and ESMS

studies, demonstrating the successful application of pre-disposition for controlled synthesis of Ln^{III} containing multinuclear assemblies.[158]

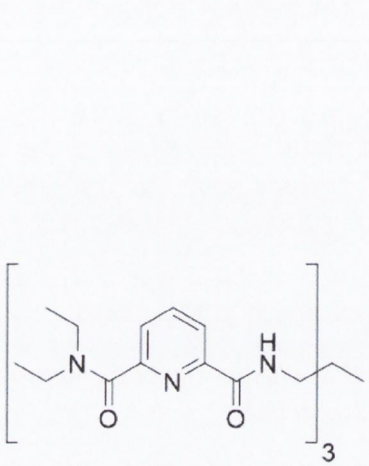

35

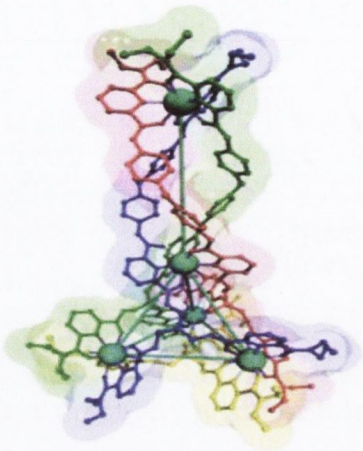

$[Eu_5(\mathbf{35})(\mathbf{36})_3]^{15+}$

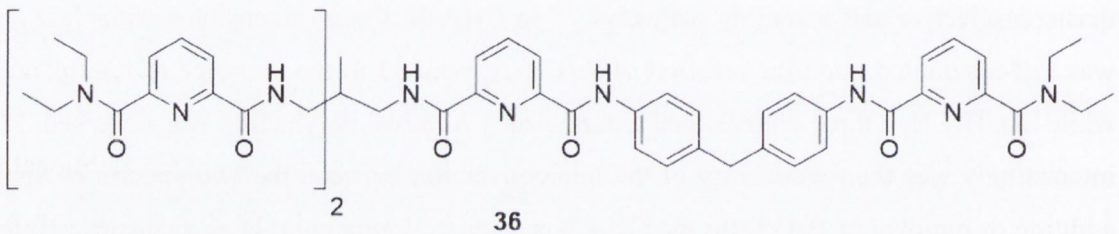

36

Figure 1.12. *Ligands **35** and **36** developed for the self-assembly of the first pentanuclear Ln^{III} helicate $[Eu_5(\mathbf{35})(\mathbf{36})_3]^{15+}$ (molecular model shown).*[158]

In relation to the controlled synthesis of multinuclear assemblies the Ln^{III}-directed self-assembly of polymetallic triple stranded helicates has been pioneered by Piguet *et al.* and Bünzli *et al.* in recent times.[20,141,161-165] Since the research groups of Piguet *et al.* and Bünzli *et al.* have worked so closely together in recent times the progress both groups have made in this area shall be discussed collectively in the following sections.

The emergence of the first self-assembled dinuclear triple helical Ln^{III} complex[166] inspired both research groups to progressively alter and tune their original ligand structure, based on a bis(benzimidazole)pyridine unit, to strive for a better understanding of the thermodynamically controlled self-assembly process and for an enhancement in the structural and photophysical properties of the system for eventual biological/materials based application purposes.

A detailed study of the bis(benzimidazole)pyridine framework for the development of *f*-element containing helicates seems to have originated from a publication in the early 1990's by Piguet *et al.* in which a bis(bidentate) bis(1-methyl-2-(6'-methyl-2'-pyridyl)benzimida-zol-5-yl)methane ligand formed a dimetallic triple helical complex upon self-assembly with

Co^{II}.[167] Since then, the bis(benzimidazole)pyridine unit has undergone tremendous study and derivatisation for the incorporation of the luminescent Ln^{III}.

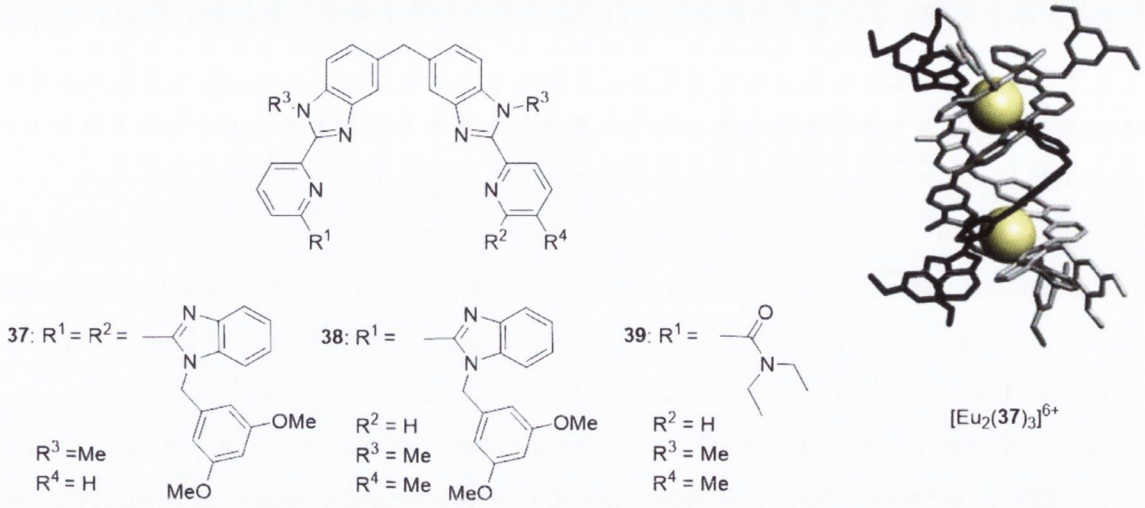

Figure 1.13. *Bis(benzimidazole)pyridine compounds* ***37*** *–* ***39*** *designed for the formation of dimetallic triple stranded helical complexes via* Ln^{III}*-directed self-assembly and X-ray crystal structure of* $[Eu_2(\mathbf{37})_3]^{6+}$.

Initially, the bis(benzimidazole)pyridine scaffold was functionalised by an additional two terminal benzimidazole units (which bear 3,5-dimethoxybenzyl groups to increase solubility), affording the symmetric ligand **37**, which is pre-organised such that two tridentate units are well defined, separated by a flexible $-CH_2$ spacer and available for Ln^{III} coordination. An X-ray crystal structure of the first self-assembled dinuclear triple-helical Ln^{III} complex $[Eu_2(\mathbf{37})_3](ClO_4)_6 \cdot 9CH_3CN$ shows **37** wrapped around a helical axis defined by two Eu^{III} and aromatic stacking between the three ligand strands. In each coordination sphere the Eu^{III} was nine-coordinated by the six nitrogen atoms of the benzimidazole units and by the three nitrogen atoms of the pyridine groups respectively This gives a structure with a slightly distorted tricapped trigonal prismatic geometry; confirming the formation of the triple stranded bimetallic helicate.[166] However, quenching of Ln^{III}-centred luminescence was observed as the ligand strands were not sufficiently "rigid enough" to fully protect the metal centre from interacting with solvent/anion molecules in the surrounding environment.[162] The formation mechanism of this supramolecular system $[Eu_2(\mathbf{37})_3]^{6+}$ was studied in great detail with three major species characterised in CH_3CN solution possessing global binding constants of $\log\beta_{12} = 11.6$, $\log\beta_{22} = 18.1$ and $\log\beta_{23} = 24.3$ for $Eu\mathbf{37}_2$, $Eu_2\mathbf{37}_2$ and $Eu_2\mathbf{37}_3$, respectively. This study also indicated that the self-assembly process was mainly governed by electrostatic interactions between the ligands and the Eu^{III}.[168]

Supramolecular devices expressing dual functionality opens up new opportunities for the development of multi-responsive probes. The combination of two or more different luminescent centres, or a luminescent and a magnetic centre, within one sensing probe would therefore be advantageous for the selective detection of different analytes. In light of this, the inclusion of two or more different *d*- or *f*- block metal ions into heteropolymetallic triple stranded helicates has received appreciable attention from Bünzli *et al.*[141,164,165,169,170]

Ligand **38** (an analogue of **37**) was synthesised for the self-assembly of the first *d-f* heterodinuclear triple helix in solution.[164] Ligand **38** possesses a bidentate binding unit suitable for coordination of *d*-block metals and an identical tridentate unit to that seen in **37**, suitable for Ln^{III} coordination. The evolution of the heteronuclear $[LaZn(\mathbf{38})_3]^{5+}$ complex was evidenced by spectroscopic data as being the predominant species in solution (when mixed in a 3:1:1 **38**:La:Zn ratio); illustrating the ability to complex *f*- and *d*- elements selectively by pre-disposing selective bind sites. Following the analysis of spectrophotometric titrations, by using non-linear regression analyses, which was carried out with an equimolar mixture of the La^{III} and Zn^{III} salts in the range M_{tot}:**38** = 0.1 – 2.5:1, a binding constant of $\log\beta_{113} = 26.2$ for the $[LaZn(\mathbf{38})_3]^{5+}$ species was obtained.[141,164] Grafting *N,N*-diethylcarboxamido groups in place of the benzimidazole group in **38**, yielded **39**, for which an increase in both selectivity and Ln^{III}-centred luminescence quantum yield was observed.[165] Additionally, replacement of the benzimidazole group with a *N,N*-diethylcarboxamido group resulted in a crystalline material that was suitable for X-ray crystallographic analysis in the case of $[EuZn(\mathbf{39})]^{5+}$; this was the first luminescent self-assembled helical *d-f* complex to be structurally characterised.[17,165]

Significant effort to pre-programme helicate ligands for the selective recognition and self-assembly of *f-f* heterodimetallic triple stranded helicates, based on Ln^{III} size discrimination, has been made by the implementation of the ditopic ligand **40**. The unsymmetric bis(tridentate) ligand **40** bears a benzimidazole-pyridine-carboxamide tridentate moiety coded to preferentially coordinate smaller Ln^{III} and a less strongly coordinating bis(benzimidazole)pyridine unit which preferentially binds larger Ln^{III}. The formation of the heterodimetallic species, which were prepared in CH_3CN solution in a 1:1:3 (Ln:Ln′:**40**) (Ln = La^{III}, Pr^{III}, Eu^{III}, Ln′ = Eu^{III}, Tb^{III}, Er^{III}, Yb^{III}, Lu^{III}) ratio, were evaluated by both ^1H NMR and ESMS spectroscopy. Substantial percentage yields of the heterodimetallic species were elucidated from both measurements and point to the formation of stable heterodimetallic species in solution. In particular, it was evidenced by ESMS spectroscopy and by ^1H NMR that $[LaLu(\mathbf{40})_3]$ was formed in solution in 90% yield with respect to ligand concentration.

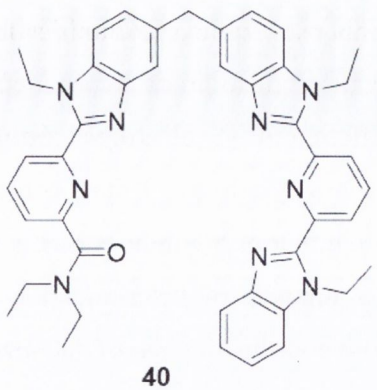

40

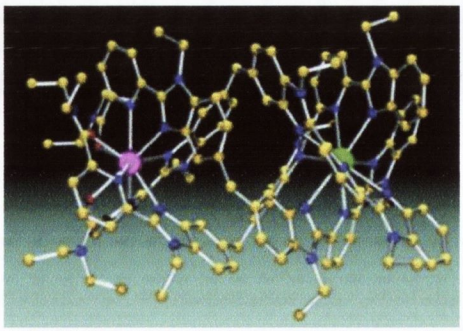

$[LaEu(\mathbf{40})_3](ClO_4)_{6.3}MeCN.3EtCN$

Figure 1.14. *Unsymmetric bis(tridentate) ligand* ***40*** *synthesised for the formation of heterodimetallic species and the X-ray crystal structure of* $[LaEu(\mathbf{40})_3](ClO_4)_6{\cdot}3MeCN{\cdot}3EtCN$.[169,170]

X-ray crystal structures of a number of heterodimetallic species were grown and evaluated, $[LaEu(\mathbf{40})_3](ClO_4)_6{\cdot}3CH_3CN{\cdot}3CH_3CH_2CN$ is shown in Figure 1.14, and confirm structural data obtained from solution studies in which three ligands are shown wrapping helically around two Ln^{III} with the three amide moieties coordinating to the heavier Eu^{III} (smaller radius) and the benzimidazole-pyridine-carboxamide units of the three ligands bound to the larger La^{III}. Compound **40** represents the first unsymmetric ditopic ligand pre-organised to selectively bind heteropairs of Ln^{III} based on the difference in their ionic radii.[169,170]

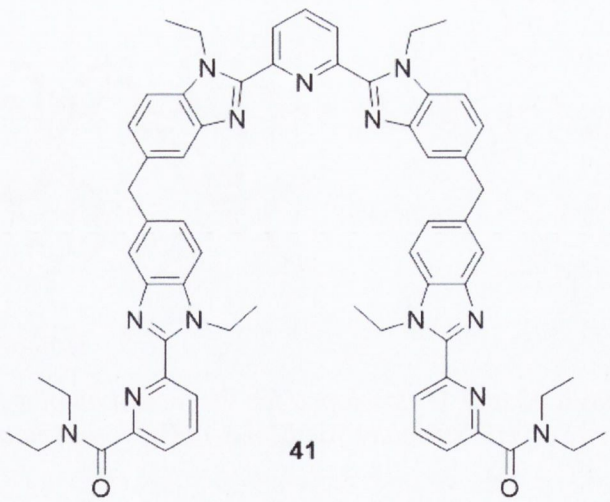

41

An extension of the bis(benzimidazole)pyridine backbone to integrate three tridentate binding units led to the development of ligand **41**, a symmetric tritopic ligand capable of accommodating three Ln^{III} for the formation of trimetallic triple stranded helicates. In the self-assembly of the homometallic $Eu_3(\mathbf{41})_3$ complex coordination of the third Ln^{III}, and thus final structure, is driven to completion by positive cooperativity, as evidenced by Scatchard plots, despite an increase in intermetallic repulsion upon the addition of another Eu^{III} to the system. The X-ray crystal structure of $[Eu_3(\mathbf{41})_3](CF_3SO_3)_9(CH_3CN)_9(H_2O)_2$ displayed again

the three ligand strands wrapping around each metal ion in a pseudo-threefold axis with each Ln^{III} coordinated by nine donor atoms giving rise to a pseudo-trigonal prismatic arrangement. Interestingly, the terminal sites (EuN_6O_3) display differences in electronic properties compared to the central site (EuN_9) in that the presence a low lying LMCT state resulted in luminescence from the two terminal EuN_6O_3 sites only. Furthermore, under stoichiometric conditions, **41** assembles with different Ln^{III} to give a mixture of heterometallic triple stranded helicates in CH_3CN $[(Ln)_x(Ln')_{3-x}(\mathbf{41})_3]^{9+}$ with both coordinating sites (N_6O_3 and N_9) exhibiting different affinities for each specific Ln^{III}, again illustrating the dependence of the self-assembly process on the Ln^{III} size. Similarly to that corroborated above for **40**, the generally favoured heterotrimetallic helicate was that in which the central Ln^{III} site was preferentially occupied by the larger Ln^{III} with the two terminal N_6O_3 sites occupied by the smaller Ln^{III}.[140,171]

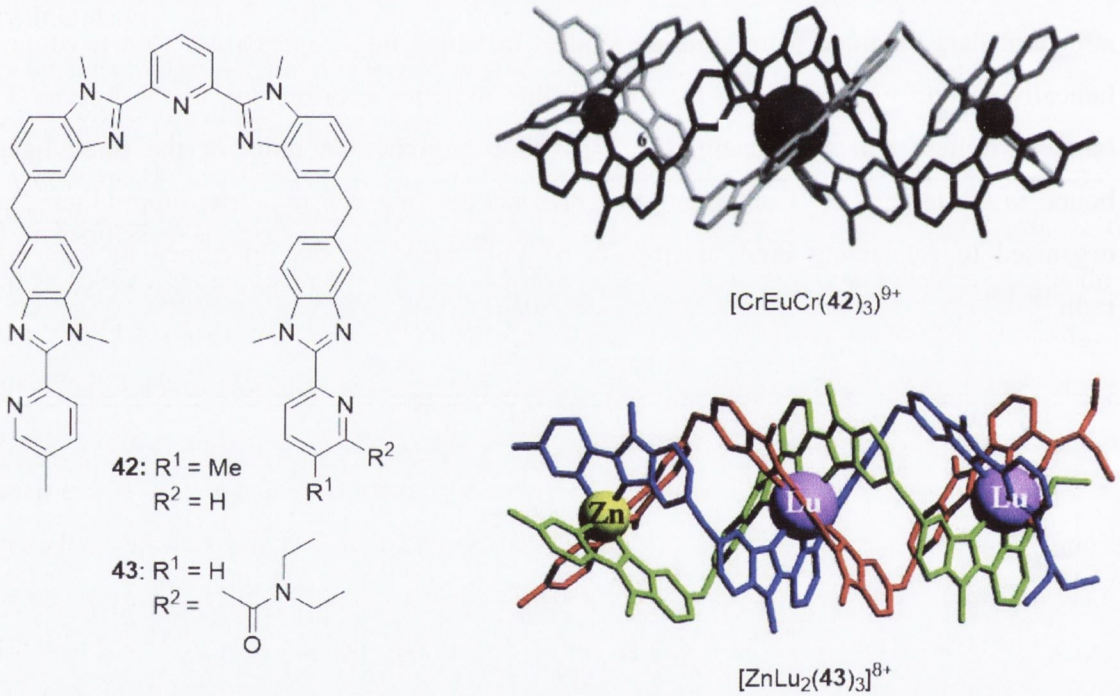

Figure 1.15. *Compounds **42** and **43** developed for the formation of d-f heterotrinuclear triple helical structures. X-ray crystal structure for* $[ZnLu_2(\mathbf{43})_3]^{8+}$ *and model for* $[CrEuCr(\mathbf{42})_3]^{9+}$ *structure are shown.* [172,173]

Derivatives of **38**, ligands **42** and **43** were synthesised for the formation of *d-f* heterotrinuclear triple helical structures.[172,173] As shown, ligand **42** possesses a tridentate central N_3 binding site connected to two terminal bidentate N_2 binding sites which is suitable for selective *d-f-d* block self-assembly formation of heterotrimetallic triple stranded helicates of the form $[MLnM(\mathbf{42})_3]^{7+}$ (M = Cr^{II}, Zn^{II}) and (Ln = La^{III}, Eu^{III}, Gd^{III}, Tb^{III}, Lu^{III}). For $[ZnLnZn(\mathbf{42})_3]^{9+}$ (Ln = Eu^{III}, Tb^{III}) Ln^{III}-centred luminescence was observed. However, in the case of $[CrLnCr(\mathbf{42})_3]^{9+}$ (Ln = Eu^{III}, Tb^{III}), Cr^{II} underwent rapid oxidation to Cr^{III}, resulting in

the generation of non-emissive inert complexes.[172] Compound **43** on the other hand, was designed with the intention of forming *d-f-f* metal ion self-assembly of heterotrimetallic triple stranded helicates. The X-ray crystal structure of the $[ZnLu_2(\mathbf{43})_3]^{8+}$ complex was obtained, as shown in Figure 1.15.[173]

Evidently, tremendous effort has been employed in order to extend and tailor the relatively simple bis(benzimidazole)pyridine core for the selective recognition of *d*- and *f*-block metal ions for subsequent formation of multifunctional heteropolymetallic triple stranded helicates. In conjunction with this an investigation into the applicability of water soluble Ln^{III} based homobimetallic helicates as biological sensors/imaging agents was undertaken by Bünzli *et al.*, and is discussed below.[16,19,96,143,144,161,174-176]

The stability and photophysical properties of homodinuclear triple stranded helicates of **37** were improved by replacing the two terminal benzimidazole groups with carboxyamide binding units yielding the symmetric bis(tridentate) chelating ligand **44**.[177] Quantum yield measurements suggested that the carboxyamide group in **44** favours energy transfer to the Eu^{III}-centre in $[Eu_2(\mathbf{44})_3]^{6+}$ compared to the benzimidazole units in $[Eu_2(\mathbf{37})_3]^{6+}$ giving rise to strong Eu^{III}-centred emission. The quantum yield of $[Eu_2(\mathbf{44})_3]^{6+}$ (relative to $[Eu(terpy)_3]^{3+}$ at the same concentration) was determined as $Q_{rel} = 0.27$ – a significant enhancement to that obtained for $[Eu_2(\mathbf{37})_3]^{6+}$ ($Q_{rel} = 0.005$, a 54 –fold increase in relative quantum yield). A more significant aspect of the helicate ligand analogue **44** was its ability to form highly stable dimetallic triple stranded helicates which were resistant to hydrolysis in moist CH_3CN up to 2.5 M H_2O. These steps towards water stable Ln^{III}-directed dimetallic triple stranded helicates led to the generation of **45**, which was responsible for the first lanthanide-containing helicate self-assembled in water.[178] Ligand **45** was shown to react with the entire Ln^{III} series forming neutral carboxylate homodinuclear triple stranded helicates of the form $[Ln_2(\mathbf{45}\text{-}2H)_3]$. These were found to be stable in water in the pH range of 3-12[179] while a competitive titration with 1,4,7,10-tetraazacyclododecane-N,N′,N″,N‴-tetraacetic acid (dota) shows that the stability of the Eu^{III} helicate $[Eu_2(\mathbf{45}\text{-}2H)_3]$ is comparable to that of $[Eu(dota)]^-$. Spectrophotometric data obtained at pH 7.2 in 100% H_2O were analysed by non-linear regression analysis giving stability constants of $\log\beta_{23} = 26.1$ and $\log \beta_{23} = 30$ for the $[Eu_2(\mathbf{45}\text{-}2H)_3]$ and $[Lu_2(\mathbf{45}\text{-}2H)_3]$ self-assembly species, respectively. Furthermore, solid state X-ray crystallography of $[Ln_2(\mathbf{45}\text{-}2H)_3]$ complexes (Ln = Eu^{III}, Tb^{III}) confirmed the helicity of the three ligand strands wrapped around two nine-coordinate Ln^{III} to be of pseudo-D_3 symmetry, as shown by the Eu^{III} complex below.[179,180]

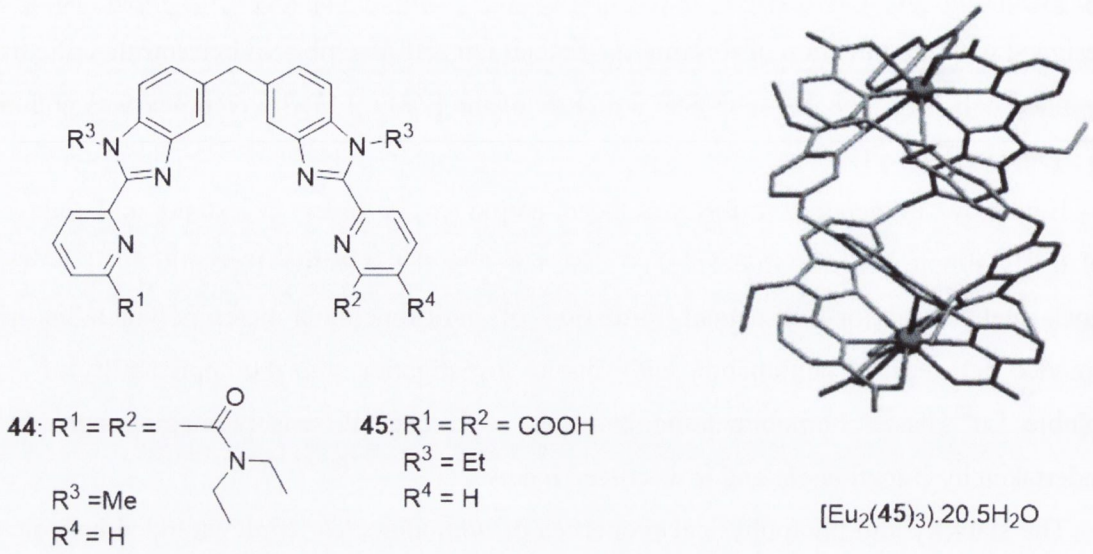

Figure 1.16. *Bis(tridentate) chelating ligands **44** and **45** synthesised for the formation of homodinuclear triple stranded helicates and X-ray crystal structure of* $[Eu_2(\mathbf{45})_3]\cdot 20.5H_2O$.[178,179]

Because of the high thermodynamic stability of the luminescent dimetallic triple stranded helicate $[Ln_2(\mathbf{45}\text{-}2H)_3]$ (Ln = Eu^{III}, Tb^{III}) in water, analogues of **45** were postulated by the authors as being ideal candidates for sensing/imaging capability studies in biological media. For these, water solubility was even further enhanced by grafting a polyoxyethylene chain to the four pyridyl position of the ligand, yielding **46**.[176] Ligand **46** was shown to exist as H_2L and HL^- at physiological pH and, as was seen for **45**, formed thermodynamically stable neutral $[Ln_2(\mathbf{46})_3]$ complexes ($\log\beta_{23}$ = 26 – 30 for Ln = La^{III}, Eu^{III}, Lu^{III}) upon self-assembly in TRIS-HCl buffered solution. The biological application of these structures were investigated in human cervical adenocarcinoma (HeLa) cells which were loaded with a 500 μM solution of $[Eu_2(\mathbf{46})_3]$ for 6 hrs, after which emission spectra and luminescence lifetime measurements confirmed cell permeation and also that the complex remained intact within the cells. Not only was staining of the cell cytoplasm achieved by permeation of $[Eu_2(\mathbf{46})_3]$ into the cells but cell viability after 24 hrs in the presence of $[Eu_2(\mathbf{46})_3]$ remained unaltered compared to cell viability in the absence of $[Eu_2(\mathbf{46})_3]$. This indicated that the proliferation of the helicate complex into the HeLa cells had no noticeable influence on the health of the cells.[176] Furthermore, $[Eu_2(\mathbf{46})_3]$ has also found use, in conjunction with acridine orange, as a pH insensitive luminescent probe for the analysis and quantification of DNA and PCR based products.[144]

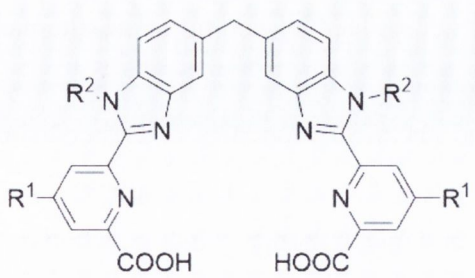

46: R^1 = $-(OCH_2CH_2)_3OMe$

R^2 = Me

47: R^1 = H

R^2 = $-(OCH_2CH_2)_3OMe$

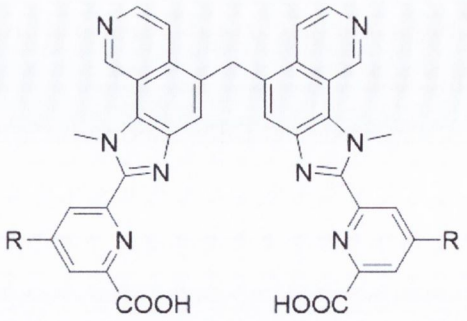

R = $-(OCH_2CH_2)_3OMe$

48

Derivatisation of the initial ligand structure **45** with a polyoxyethylene group appended to both benzimidazole rings, afforded the related analogue **47**, where the water solubility was again enhanced and the formation in water of the highly stable neutral dimetallic triple stranded helicate $Eu_2(\mathbf{47})_3$ ($\log\beta_{23}$ = 23.4) at physiological pH also allowed for the study of this complex as a cell staining agent. Luminescence microscopy detected Eu^{III}-centred emission from the cell cytoplasm at concentrations >50 μM after loading times of 20-30 mins. Again, the $Eu_2(\mathbf{47})_3$ complex remained un-dissociated following permeation *via* endocytosis into the cell cytoplasm of several cancerous cell lines (MCF-7, HeLa, Jurkat and 5D10) while its effect on cell viability was estimated and concluded not to be significant. However, attachment of the polyoxyethylene chain to the benzimidazole ring did have an effect on the photophysics of the ligand excited state, resulting in a reduction in quantum yield from 18% to 11% for $Eu_2(\mathbf{46})_3$ and $Eu_2(\mathbf{47})_3$, respectively.[16,176,181]

Unfortunately a drawback to the use of both $Eu_2(\mathbf{46})_3$ and $Eu_2(\mathbf{47})_3$ as biological luminescent tags was their short excitation wavelengths, which lie in the UV region at ~ 320 - 325 nm. Since it has been proven that substitution of the benzimidazole unit permits tuning of the photophysical properties of the resulting complex a series of compounds bearing different functional groups appended to the benzimidazole rings were developed, including ligand **48**, and the influence these different substituents have on the photophysical properties were then evaluated. The most promising results from this study were displayed by **48** where a compromise between the shifting of the excitation wavelength towards the visible range (330 nm → 365 nm) and a minimisation of quantum yield decrease was achieved.[174] In an effort to further shift the excitation wavelength of these systems towards the visible and NIR

range multiphoton-excitation has also been probed and proved successful as an alternative method.[161]

By systematically altering both the physical and chemical properties of earlier helicate ligands designed by Bünzli and Piguet *et al.*, these researchers have, in a stepwise manner, enabled their enhancement and employment in biological media. This novel class of luminescent compounds offers a number of distinctive advantages for implementation as imaging agents and as detection probes in bio-assays such as thermodynamic stability, kinetic inertness, appreciable luminescence quantum yields, long lifetimes, cell permeability, non-cytotoxicity, slow egression times and versatility for derivatisation. More recently binuclear Ln^{III} luminescent helicates of this type have been bio-conjugated to avidin and tested for their specific recognition of a mucin-like protein receptor expressed on the surface of human breast cancer MCF-7 tumour cells.[96,175] This work highlights that elegant and exquisite superstructures are not solely the fruits of Ln^{III}-directed self-assembly but that by calculated ligand design and perseverance one may create and advance towards exciting new functional supramolecular devices. For this reason this area of Ln^{III} encapsulation and property exploitation for the construction of functional higher order structures, in particular multimetallic triple stranded helicates, is currently a highly topical and fast growing area of interest with those such as Pikramenou *et al.*,[182] Faulkner *et al.*[142] and Albrecht *et al.*[94,95,183] applying their own strategies for the formation of Ln^{III} based helicate assemblies and as such are discussed below.

The bis(β-diketonate) **49** has been developed by Pikramenou *et al.* for the formation of luminescent neutral triple stranded homodinuclear helicates Ln_2**49**$_3$ (Ln = Nd^{III}, Sm^{III}, Eu^{III}, and Gd^{III}) and anionic quadruple stranded Eu^{III} homodimetallic helicates Eu_2**49**$_4$.[182] The bis(bidentate) ligand **49** consists of two conjugated diketonate sites linked by a 1,3-phenylene spacer suitable for the coordination of six carbonyl oxygen atoms to each Ln^{III} upon self-assembly. The formation of the Ln_2**49**$_3$ species was monitored by ^{1}H NMR and mass spectrometry and points to the evolution of a single, highly symmetric species in solution. Lifetime measurements and q value calculations carried out on Eu_2**49**$_3$ in CH_3OH and CD_3OD elucidated that three solvent molecules are bound to each Eu^{III} centre. Photophysical investigations of the energy of the donor $^3\pi\pi^*$ state of the ligand were examined and confirm **49** as a suitable sensitizer for Sm^{III}, Eu^{III}, and Nd^{III} but not Tb^{III} and Dy^{III} which possess higher energy excited states. The tetrastranded dinuclear lanthanide complex Eu_2**49**$_4$ was prepared by altering the **49**:Ln ratio to 2:1 and using piperidine to act as a counterion. Mass spectrometry of freshly prepared solutions of $(Hpip)_2[Eu_2$**49**$_4]$ showed a peak for the doubly charged species $[Eu_2$**49**$_4]^{2-}$, confirming formation of the complex.[182]

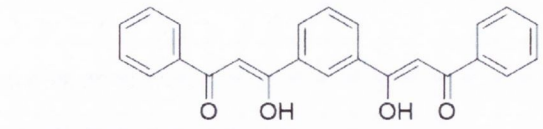

49

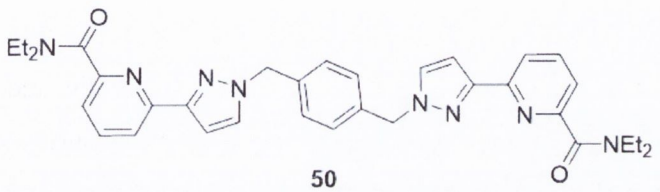

50

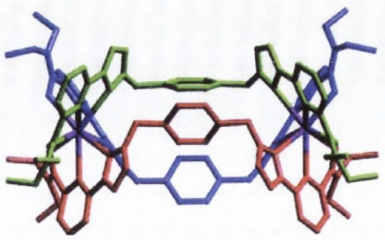

$[Nd_2(\mathbf{50})_3](ClO_4)_6$

$[Nd_4(\mathbf{50})_4]^{12+}$

Figure 1.17. *Ligands **49** and **50** developed for the formation of luminescent homonuclear assemblies. X-ray crystal structures for $[Nd_2(\mathbf{50})_3](ClO_4)_6$ and $[Nd_4(\mathbf{50})_4]^{12+}$ are also displayed.*[142,182]

Faulkner *et al.* again made use of the heterocyclic pyridine moiety in **50** in which two amide-pyridine-pyrazole tridentate binding pockets are connected through a phenyl spacer group for the formation of polynuclear coordination compounds. A range of architectures such as dimetallic triple stranded cylindrical mesocates $Ln_2(\mathbf{50})_3$ ($Ln = Nd^{III}$, La^{III}), dimetallic double stranded mesocates $Ln_2(\mathbf{50})_2$, cyclic tetranuclear helicates $Ln_4(\mathbf{50})_4$ or a one-dimensional coordination polymer, in which metal ions and bridging ligands alternate along the sequence, may result depending upon the **50**:Ln ratio and reaction conditions implemented. Reaction of **50** with $Nd(ClO_4)_3$ in a 3:2 ratio in CH_3CN followed by diisopropyl ether diffusion yields crystals suitable for X-ray crystal structure determination.

As shown above for $[Nd_2(\mathbf{50})_3](ClO_4)_6$ the complex contained two nine-coordinate Nd^{III} centres each located within a N_6O_3 site and, contrary to previously discussed helicates above, has a cylindrical (non-helical) 'mesocate' architecture in which the three ligands are arranged in a side-by-side manner. In contrast, reaction of **50** with $Nd(ClO_4)_3$ in a 1:1 ratio in CH_3CN followed by diisopropyl ether diffusion yielded the 4:4 cyclic tetranuclear helicate $[Nd_4(\mathbf{50})_4(H_2O)_{11}(CH_3CN)](ClO_4)_{12}\cdot 2.5H_2O\cdot 4CH_3CN$, as shown in Figure 1.17. Luminescence measurements on the Nd^{III} complexes revealed that excitation into the ligand π-π^* excited state gives rise to characteristic near-infrared luminescence at 1060 nm.[142]

Another approach towards the self-assembly of homo- and heteropolymetallic helicates which has received considerable attention by Albrecht *et al.* involved the use 2-amido-8-

hydroxyquinoline ligands.[94,95,183,184] This class of ligands, including the symmetric bis(tridentate) chelating ligand **51** and the unsymmetric tridentate-bidentate ligand **52**, have been shown to form homo- Ln^{III} and hetero- mixed metal dimetallic triple stranded helicates.

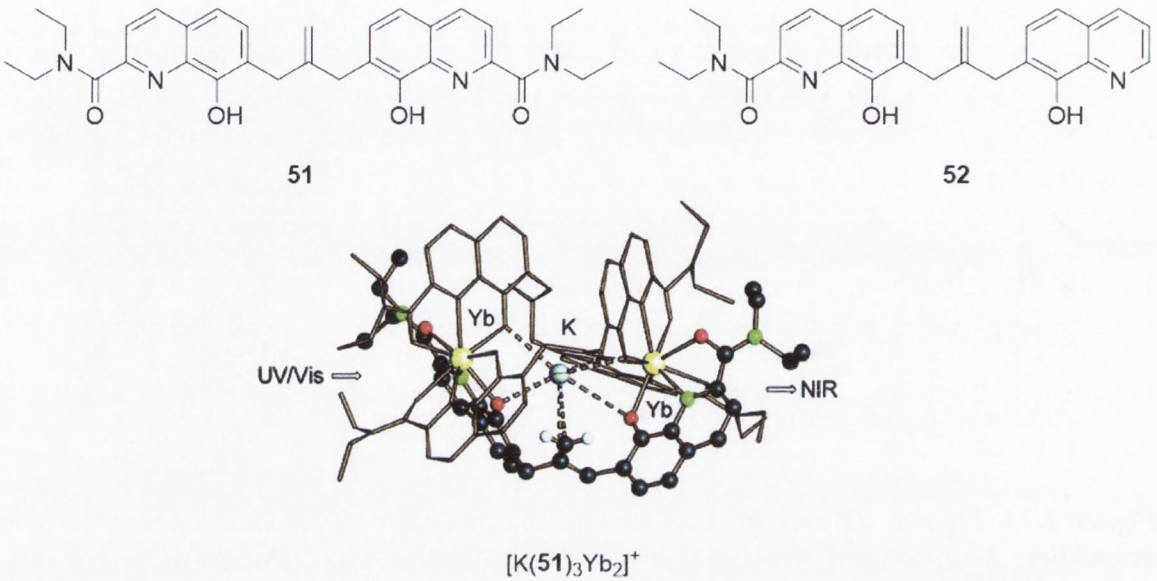

Figure 1.18. *2 -amido-8-hydroxyquinoline ligands **51** and **52** developed for the self-assembly of homo- and heterpolymetallic helicates. X-ray crystal structure of $K(\mathbf{51})_3(Yb)_2]^+$ is also shown.*[94,95,183]

Reaction of **51** with Ln^{III} triflate salts in the presence of alkali carbonates (added to deprotonate the hydroxyl proton and provide a cation to template the self-assembly process) in a 3:2 (**51**:Ln) ratio affords the desired homodinuclear coordination compound. On the other hand, by reacting three equivalents of ligand **52** with mixed Ln^{III} and Al^{III} salts it was possible to obtain heterodinuclear triple stranded complexes. The use of NMR spectroscopy of diamagnetic homo- La/La and Y/Y and hetero- La/Al and La/Zn species demonstrated the stability of such systems in solution. As shown above for $[K(\mathbf{51})_3(Yb)_2]^+$, a series of X-ray crystal structures of the homo 3:2 species of **51** indicated the formation of triple stranded helicates with each ligand wrapped around two Ln^{III} (coordination number nine) in a helical manner bearing an encapsulated alkali metal ion within its central cavity. Crystal structures of heterodinuclear species such as $[(\mathbf{52})_3AlYbK]^+$ were unattainable and so these self-assemblies were structurally characterised by ^1H NMR and mass spectrometry alone. These quinolone derivatives possess a low lying excited state providing efficient sensitisation of the NIR emitting Ln^{III}, such as Nd^{III}, Er^{III} and Yb^{III}. For example the complex $[K(\mathbf{51})_3(Yb)_2]^+$ displays expected NIR Yb^{III}-centred emission and also weak red emission from incomplete energy transfer from the ligand to the metal ion. Interestingly, an enhancement in the NIR luminescence emission and the excited state lifetime was exhibited by $[K(\mathbf{52})_3AlYb]^+$ due to

an internal quenching process of the Al^{III} quinolinate unit by the Yb quinolinate moiety as a result of a difference in excited state energy levels.[94,95,183]

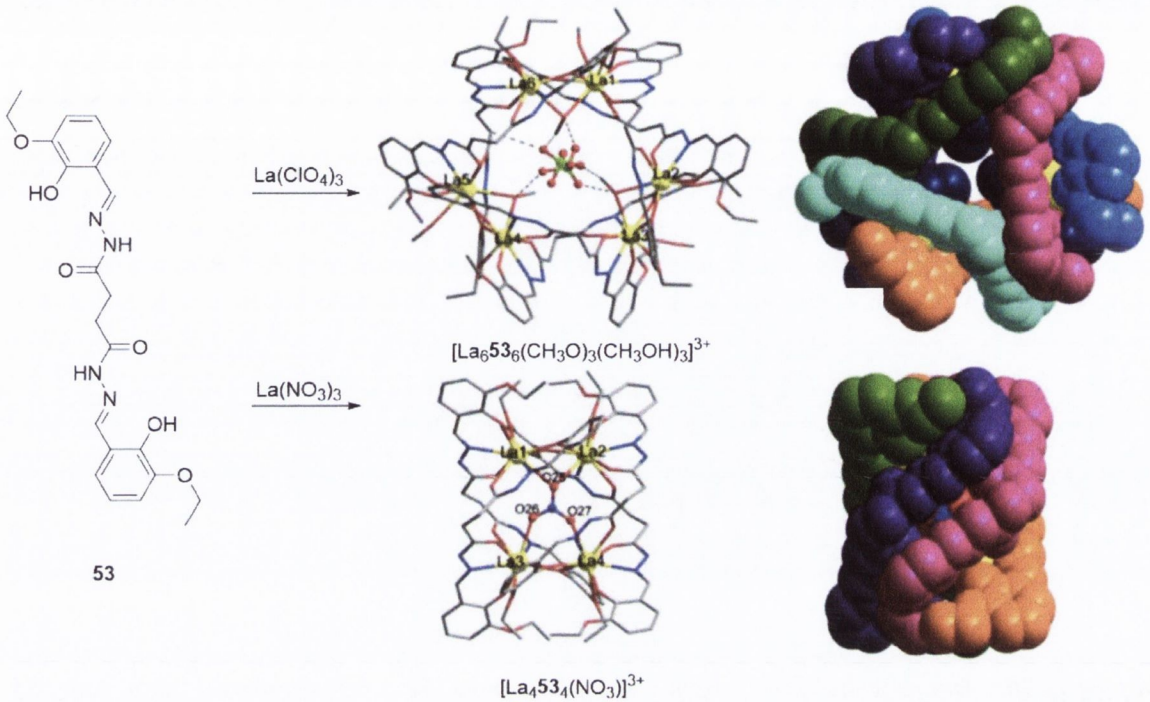

Figure 1.19. *Compound* ***53*** *developed for the self-assembly of the circular helicate species* $[La_6\mathbf{53}_6(CH_3O)_3(CH_3OH)_3]^{3+}$ *and the tetranuclear stranded helicate complex* $[La_4\mathbf{53}_4(NO_3)]^{3+}$. *X-ray crystal structures of* $[La_6\mathbf{53}_6(CH_3O)_3(CH_3OH)_3]^{3+}$ *and* $[La_4\mathbf{53}_4(NO_3)]^{3+}$ *are shown.*[185]

Research recently published by Wang and co-workers on the development of multiple lanthanide helicate clusters highlighted the significance the templating effect of the counter anion employed can impose upon the stereochemistry of the supramolecular architecture manifested.[185] The bis(tridentate) compound **53** was shown to self-assemble and form a novel hexanuclear Ln^{III} circular helicate ($[La_6\mathbf{53}_6(CH_3O)_3(CH_3OH)_3]^{3+}$) in the presence of $La(ClO_4)_3$, as shown in Figure 1.19. However, upon addition of $La(NO_3)_3$, which possesses a trigonal planar NO_3^- as opposed to a tetrahedral ClO_4^- counter anion, a tetranuclear stranded helicate complex ($[La_4\mathbf{53}_4(NO_3)]^{3+}$) was preferentially formed. Furthermore, the system was shown to undergo dynamic conversion from the circular helicate to the tetranuclear stranded helicate species upon NO_3^- stimulus. These results signify that simple key factors, such as the size, shape and the binding mode of the counter anion, can play a crucial role in determining the stereochemistry of the resulting self-assembly species.[185]

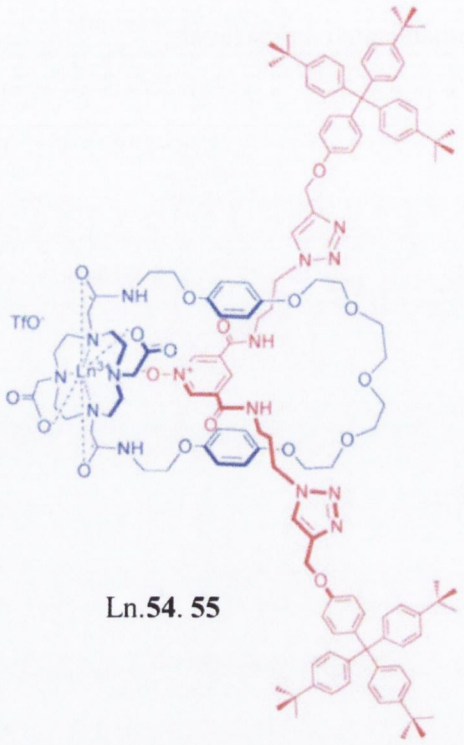

Ln.54. 55

Figure 1.20. *Macrocyclic Ln^{III} complexed compound **54** and stoppered axle unit **55** synthesised for the formation of novel lanthanide [2] rotaxanes Lu.**54.55** and Eu.**54.55**.*[186]

In order to fully convey the contribution Ln^{III}-directed self-assembly synthesis has made in advancing supramolecular chemistry towards the fabrication of novel functional self-assemblies it is worth briefly discussing the first interlocked rotaxane structure synthesised *via* Ln^{III}-templated synthesis recently developed by Faulkner and co-workers (Figure 1.20).[186] In this study the authors succeeded in assembling the Ln^{III} [2]rotaxanes (where Ln^{III} = Lu^{III} and Eu^{III}) shown in Figure 1.20. Compound **54** consists of a Ln^{III}-complexed dota cyclen moiety which was integrated into a macrocyclic framework. Compound **54** was initially used to form a pseudo-rotaxane by assembling it with an appropriately functionalised pyridine *N*-oxide threading component where the *N*-oxide serves to satisfy the Ln^{III} coordination sphere. The threading unit was then stoppered by a copper(I) catalysed azide-alkyne 'click' reaction yielding **55** and the novel Ln^{III} containing interlocked system Ln.**54.55**. The structure was characterised by NMR spectroscopy in which donor-acceptor aromatic stacking interactions between the electron rich hydroquinone groups and the electron deficient pyridine *N*-oxide axle motif are observed. Eu^{III}-centred excited state luminescence lifetime measurements for the rotaxane system were conducted in a CH_2Cl_2:CH_3OH (1:1) and a CD_3Cl_2:CD_3OD (1:1) solvent mixture allowing the calculation of *q*, the number of Ln^{III}-bound solvent molecules. A *q* value of 0 was estimated equating to the

exclusion of CH_3OH from the inner coordination sphere of Eu^{III}, again suggesting coordination of the *N*-oxide to the Ln^{III} ion.[186]

Bearing in mind that only a select few examples by some of the leading researchers within this field have been discussed herein it is evident that a substantial effort is currently ongoing to develop more effective ligand scaffolds in order to widen the scope of these mononuclear and multinuclear Ln^{III} based systems. These research groups have gained a greater insight into the self-assembly process of a number of different ligand classes' and have fine-tuned the chemical and physical properties of the resultant entities accordingly in order to exploit the versatility these simple building blocks have to offer for their eventual promotion into various disciplines for functional application.

The main goal of the Gunnlaugsson research group is to design, synthesise, characterise and spectroscopically evaluate novel chiral monometallic and multimetallic Ln^{III}-directed self-assemblies based on the 2,6-dipicoline amide framework. With a view to expand upon and improve our basis structure, the chiral mononuclear 'Trinity Sliotar', a variety of mononuclear systems have been designed in which the antenna group has been altered/removed or changed and/or a new functional group has been appended. These results together with a number of publications on chiral dimetallic triple stranded helicate derivatives which have also been prepared by the group are discussed in the following section.

1.5 Recent examples of Ln^{III}-directed self-assemblies within the Gunnlaugsson group

The synthesis of elegant self-assemblies such as bundles and helicates has been a highly topical area of research within the Gunnlaugsson group in recent years. Not only does it allow one to explore supramolecular chemical artistry but these systems offer the potential for functionalisation and utilisation as luminescent probes for imaging and sensing purposes.

Novel self-assembled bundles, the so-called 'Trinity Sliotar' systems, were initially synthesised in which three chiral pyridyldiamide tridentate chelating ligands are organised around a Ln^{III} (Ln^{III} = Nd^{III}, Sm^{III}, Eu^{III}, Tb^{III}, and Yb^{III}) centre in a tightly packed helical manner, as depicted by $[Tb(\mathbf{56})_3]^{3+}$ below.[93] Ligands **56** and **57** consist of two chiral naphthalene antenna groups (*R,R* or *S,S*) connected through the 1-naphthyl position to a central Ln^{III} tridentate picolinic centre made up of two carbonyl oxygen atoms and a pyridyl nitrogen atom to give an overall symmetric ligand. Spectroscopic investigations of the self-assembly process of **56** and **57** with $Eu(CF_3SO_3)_3$ in both CH_3CN and CH_3OH solutions indicated the presence of a 1:1, a 1:2 and a 1:3 Ln:**L** (**L** = **56**, **57**) species in solution possessing large stability constants of $\log\beta_{13} \approx 19$ (in CH_3OH) and ≈ 20 (in CH_3CN) for both enantiomeric 1:3 species.[187] The 1:3 Ln:**L** complexes were found to be highly symmetrical,

with the ligand chirality transferred to the complex upon self-assembly, as evidenced by CD, CPL and X-ray crystallography, to give either Δ or Λ stereoisomers. Solid state X-ray crystallography confirmed the appreciable stability of these bundles, as face-to-face π-π stacking interactions existed between the pyridine unit of one ligand and one naphthalene unit from each of the other ligands upon complexation. Both excited state lifetime measurements and X-ray crystallography confirmed that the Ln^{III} sits in a fully saturated coordinative environment, protected from interacting external solvent molecules, with a coordination sphere comprising of three pyridyl nitrogen atoms and six carboxyl oxygen atoms (N_3O_6) giving an overall coordination number of nine.[93,187]

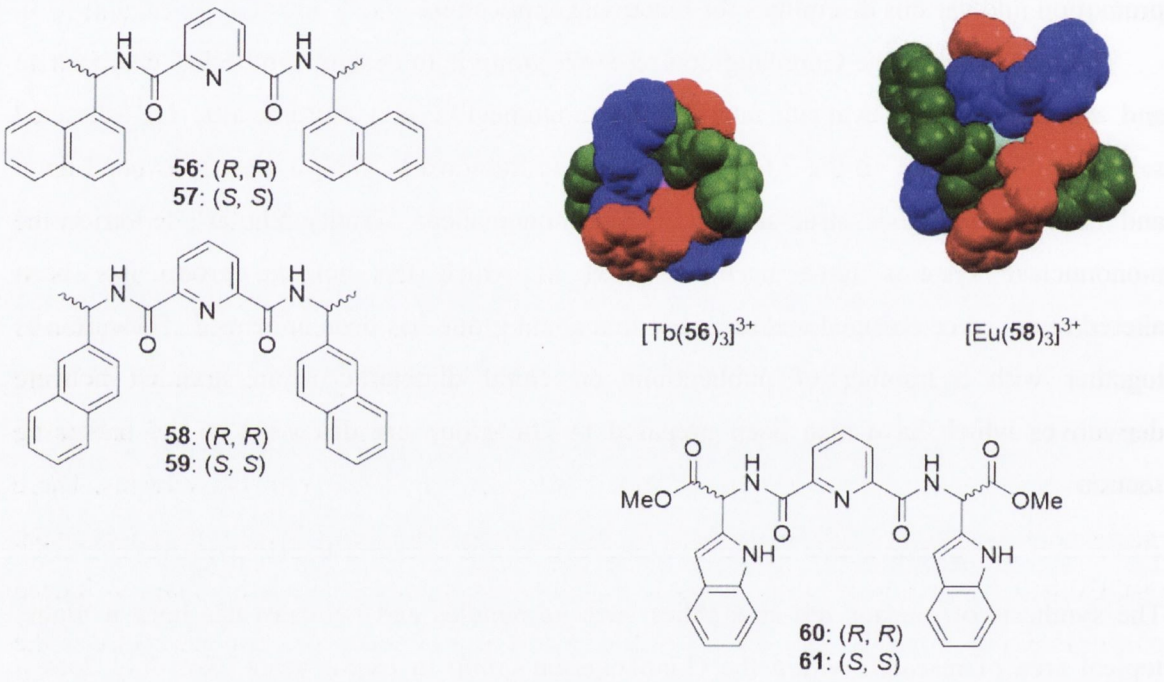

Figure 1.21. *Compounds* ***56*** *–* ***61*** *developed for the* Ln^{III}*-directed self-assembly of monometallic system and X-ray crystal structure of* $[Tb(\mathbf{56})_3]^{3+}$ *and* $[Eu(\mathbf{58})_3]^{3+}$*.*[93,187]

Although factors such as thermodynamic stability, kinetic inertness, sizable luminescence quantum yields and long excited state lifetimes – prime specifications for the construction of Ln^{III} containing luminescent devices – were appreciable for **56** and **57** it was still crucial to fully elucidate the extent to which these systems could be modified and how minor changes to the original structure might influence these parameters. Consequently, it was critical to investigate the effect that isomerism has on ligand sensitisation efficiency *etc.* and so the 2-naphthalene isomers **58** and **59** were synthesised in order to probe such queries.

The NO_2 tridentate chelating unit and antenna groups remain the same for **58** and **59** however attachment of the chromophore occurs through the 2-napthyl position in contrast to the 1-naphthyl position as seen for **56** and **57**. Synthesis and spectroscopic studies were conducted on the ligands with Eu^{III} only and compared to previously documented results. X-

ray crystal structures of the enantiomeric pair $Eu(\mathbf{L})_3(ClO_4)_3$ (**L** = **58**, **59**) were grown and shown to be isomorphous and isostructural to one another, similarly to the enantiomeric triflate complex pair of **56** and **57**. In contrast, π-π stacking, which is responsible for the tightly packed nature of the $Eu(\mathbf{L})_3(CF_3SO_3)_3$ (**L** = **56**, **57**) complexes, was not observed for $Eu(\mathbf{L})_3(ClO_4)_3$ (**L** = **58**, **59**) giving rise to a more flattened and open structure, as can be seen for $Eu(\mathbf{58})_3(ClO_4)_3$ in Figure 1.21. This subtle change to the original framework not only plays a role in dictating the structure of the solid state but self-assembly stability and complex photophysical features were also affected following this minor modification. Thermodynamic stability constants obtained from spectroscopic investigations of the 1:3 Eu:**L** (**L** = **58**, **59**) self-assembly species were comparable to those obtained for **56** and **57** in CH_3CN ($\log\beta_{13} \approx 20$) however in protic CH_3OH solution a decrease in stability was evident from the reduction in $\log\beta_{13}$ values from $\log\beta_{13} \approx 19$ for $Eu(\mathbf{L})_3$ (**L** = **56**, **57**) to $\log\beta_{13} \approx 17$ for $Eu(\mathbf{L})_3$ (**L** = **58**, **59**). The higher binding constants obtained for the Eu^{III} tris complexes with **56** and **57** were attributed to the presence of stabilising π-π stacking interactions in the 1-naphthyl derivatives – a feature which is absent in the 2-naphthyl derivative analogues. It has to be stated that the solvation effects can also play an important role in the desolvation of ligands which can also affect the binding model.[188] Luminescence quantum yields were measured and antenna-to-ion energy transfer (η_{sens}) values calculated with Φ_{tot} found to be four times higher for $Eu(\mathbf{L})_3$ (**L** = **56**, **57**) than for $Eu(\mathbf{L})_3$ (**L** = **58**, **59**) in both solvents. These values confirm that the efficiency of sensitisation is in fact five times less for $Eu(\mathbf{L})_3$ (**L** = **58**, **59**). Excited state lifetimes were similar for both of the complexes, indicating that it is indeed more likely that the efficiency of energy transfer from the ligand to the metal centre is the main cause of quantum yield deterioration and not quenching processes *via* interacting oscillators in the surrounding environment.[187]

It has thus been illustrated by this detailed study that minor changes to the primary bundle ligand structure can have a dramatic effect on the chemical and physical behaviour of the complex. Nonetheless, by changing the antenna unit entirely, from a naphthalene group to a tryptophan, the ability to successfully coordinate and sensitise Tb^{III} and Eu^{III} was not completely diminished in the case of **60** and **61**.[65] As for **56** – **59** the tridentate coordinating unit of the enantiomeric pair **60** and **61** comprised of an NO_2 unit – the pyridyl nitrogen and two flanking carbonyl oxygen atoms - with the possibility of additional coordination from the methyl esther groups appended to the tryptophan amino acid moiety. The chromophoric naphthalene was exchanged for the biologically relevant tryptophan with a view to perhaps grafting biomolecules such as peptide-based derivatives to the carboxyl terminus. Mass spectrometry and fitting of spectroscopic data, obtained following the addition of either

$Eu(CF_3SO_3)_3$ or $Tb(CF_3SO_3)_3$ to either **60** or **61** in CH_3CN, suggested the formation of only the 1:1 and the 1:2 species in solution but not the predicted 1:3 species. As crystals grown were not of high enough quality to confirm the exact stoichiometry and binding mode in the solid state it can be concluded that the absence of the 1:3 species may either be due to steric hindrance or participation of two additional donor atoms from the amino ester functionality fully occupying the coordination sphere of the Ln^{III}. In this instance, the structural integrity of the bundle analogue has been shown to impede the stoichiometry of the system as neither Tb^{III} nor Eu^{III} directed the formation of the expected 1:3 nine-coordinate complex in solution.[65]

In parallel to modifying the chromophoric portion of the initial bundle structure attempts to functionalise the four pyridyl position are also on-going and have been conducted primarily by Dr. David Caffrey. Efforts to improve water solubility and introduce biologically active groups, by means of appending a polyethoxy chain and sugar moieties respectively, are thought to open up new prospects for these systems. A detailed study of the effects substitution at this position has on the stability and photophysical properties of a small library of four pyridyl functionalised derivatives is currently in preparation and soon to be published. Other analogues discussed within the thesis of Dr. David Caffrey include bundle ligands grafted with a macrocyclic cavity and ditopic bundle ligands linked *via* a polyethoxy chain, the latter of which has displayed anion sensing capabilities by utilising a cyclen ternary complex.

Based on a similar framework to that described above, pre-organised ligands for the Ln^{III}-directed self-assembly of triple stranded homodimetallic helicates ($\mathbf{L}_3$:Ln_2) (**L = 62 – 66**) have also been synthesised and extensively studied by Drs. Floriana Stomeo, Christophe Lincheneau, Steve Comby.[21,64,69] Ligand design of **62 – 66** entailed the incorporation of two 2,6-pyridinedicarboxamide functionalities for bis(tridentate) binding and two chiral naphthalene moieties for sensitisation of the two Ln^{III}, differing by the linking spacer group only. As shown for the chiral ditopic ligand **62** a 1,3-xylene based spacer linked two tridentate diamide pyridyl (NO_2) chelating units together allowing both Ln^{III} ions (Ln^{III} = Sm^{III}, Eu^{III}, Tb^{III}, Lu^{III}) to attain a nine-coordinate binding sphere upon self-assembly, ensuring complete saturation. Evolution of the self-assembled species was monitored spectroscopically as the photophysical properties of the antennae and Ln^{III} were perturbed upon helicate formation. Excitation into the naphthalene antennae (λ_{ex} = 281 nm) and subsequent characteristic Ln^{III}-centred emission confirmed effective sensitisation and thus successful complexation. Emission intensity increased with each additional aliquot of metal ion until the most highly emissive $\mathbf{62}_3$:Ln_2 (Ln^{III} = Sm^{III}, Eu^{III}, Tb^{III}) species became the

predominant species in solution, followed by a rapid decrease as the less emissive $\mathbf{62}_2$:Ln_2 species evolved. Fitting of spectroscopic data using non-linear regression analysis indicated that in the presence of 0.2→0.8 equiv. of Eu^{III} the $\mathbf{62}_3$:Eu_2 species was the most dominant in solution with it being formed in over 80% at 0.67 equiv. of Eu^{III}. High thermodynamic stability constants were elucidated for all of the 3:2 and 2:2 L:Ln assemblies ($\log\beta_{32} \approx 27$ and $\log\beta_{22} \approx 20$ for Ln^{III} = Sm^{III}, Eu^{III}, Tb^{III}, Lu^{III}) encouraging further studies involving these systems.[21]

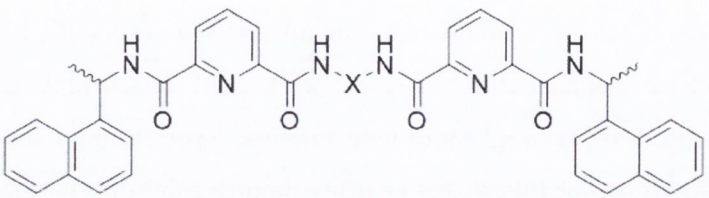

62: (*S*, *S*) X =

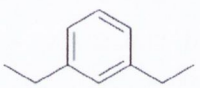

63: (*R*, *R*) X =
64: (*S*, *S*) X =

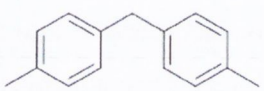

65: (*R*, *R*) X =
66: (*S*, *S*) X =

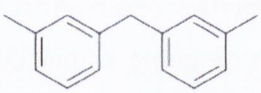

The inherent chirality of *para*-diphenyl spacer analogues **63** and **64** was exploited for the Eu^{III}-directed formation of one of the first examples of highly stable enantiomerically pure dinuclear triple stranded helicates *via* asymmetric induction.[69,189,190] Solid complexes $Eu_2(\mathbf{L})_3(CF_3SO_3)_6$ (**L** = **63**, **64**) were synthesised by refluxing in CH_3CN and isolated by diethyl ether diffusion. Both ^1H NMR and CD spectroscopic studies signified that the complexes were formed as a pair of enantiomers with a high degree of symmetry. The CPL spectra, displaying bands of opposite sign and equal magnitude, further confirmed that the chirality of the ligands had indeed been transferred to the Eu^{III} centre upon complexation, giving rise to chiral Eu^{III}-centred emission. The CPL dissymmetry factors of the measured transitions for $Eu_2(\mathbf{L})_3(CF_3SO_3)_6$ (**L** = **63**, **64**) were almost identical in both magnitude and sign to those calculated for the corresponding original mononuclear bundle structures, whose absolute configurations have been determined by X-ray crystallography.[93,187] This implied that each dimetallic triple stranded species was formed as a single helical homochiral species possessing either ΔΔ or ΛΛ stereochemistry, respectively.[69]

Variations on this diphenyl linker moiety, namely **65** and **66,** have also been examined with findings suggesting that the stability of the resulting helicate can be greatly affected by

the size of the Ln^{III} binding cavity available upon complexation which, in turn, is dictated by the location of connection to the diphenyl spacer.[64] Structural isomers **65** and **66**, which possess two identical binding sites to those of **63** and **64** are linked *via* a *meta*-diphenyl spacer, were also synthesised for the formation of enantiomerically pure dimetallic triple stranded helicates $Eu_2(\mathbf{L})_3$ (**L** = **65**, **66**). Interestingly, a greater stability than that seen for $Eu_2(\mathbf{L})_3$ (**L** = **63**, **64**) was observed for these which is believed to arise from the fact that the central cavity is more "*squeezed*" enabling tighter binding (confirmed using MM2 molecular modelling) of the Eu^{III} upon self-assembly.

Facile modification of these simple monometallic and multimetallic ligand structures may open up new opportunities for use in biological or materials based applications, such as chiral luminescent sensing, bio-imaging, logic gate mimics, light emitting devices *etc.*, although many of these aforementioned applications often require solubility in water, bio-conjugation or immobilisation onto solid substrates – three areas of significant interest within the supramolecular lanthanide community. Not only must the Ln^{III} system be appropriately functionalised/conjugated or incorporated into the solid support but the desirable features of the Ln^{III} must be retained, *i.e.* surface attachment for example should not markedly alter the attractive luminescent properties observed in the bulk solid or in solution. To this end, a substantial effort has been on-going within the Gunnlaugsson group to strategically attach biologically active functional groups[41,42,191] to Ln^{III} luminescent complexes and/or to incorporate them into solid supports such as gels[71,192,193] and gold nanoparticles[194-198] with studies proving that upon transfer from solution to a functional/solid state there may be retention and subsequent appliance of the Ln^{III} luminescent characteristics.

With these exciting new ideas in mind it was our intention (in Chapter 2) to develop similar modified chiral mononuclear self-assemblies in an attempt to form highly organised Langmuir monolayers at an air-water interface and to further attach these monolayers onto solid supports, generating Langmuir-Blodgett films. Considering this technique is central to the main chapter of this thesis the following section is dedicated to Langmuir monolayer and Langmuir-Blodgett (LB) film theory, apparatus and application. A few examples of Ln^{III} containing LB films will follow while a brief overview of the work described within this thesis shall conclude this chapter.

1.6 Langmuir-Blodgett technique: theory and applications

In 1917 Irving Langmuir first reported studies carried out on the ability of a variety of oils to form thin films at an air-water interface.[199] He hypothesised that "a portion of the oil molecule is attracted to the water, while the remainder is more attracted to other oil molecules than to water" and that "the spreading of an oil upon water is due to the presence of an 'active group' in the molecule".[199] Research into this field was undertaken by Langmuir, and later in collaboration with Katherine Blodgett, to extend the applicability of these thin film monolayers by attaching them to solid substrates - later to become known as 'Langmuir-Blodgett films'. [200-203] In later years this technique was further extended by Kuhn in which he implemented the LB method to study energy transfer interactions between layers of chromophoric dyes which were organised into thin film arrangements.[204-206]

(a) (b)

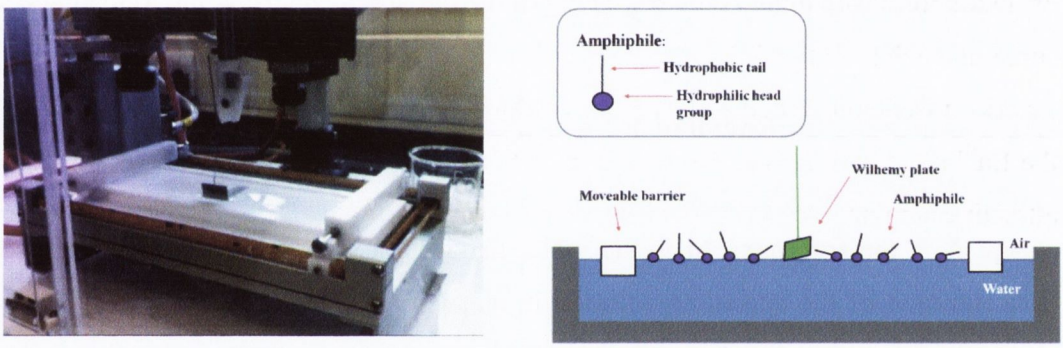

Figure 1.22. *(a) Picture of Langmuir trough, used in collaboration with Prof. Martin Albrecht, in UCD laboratory. (b) Simplified illustration of a Langmuir trough displaying features such as moveable barriers and Wilhelmy plate. Amphiphile is spread onto surface using water-immiscible solvent - note amphiphiles are displaying gaseous state behaviour.*

It is now a well-established criterion that, in general, for a substance to successfully form a monolayer at an air-water interface it must possess both an 'active' hydrophilic head group to confer intermolecular interaction with the water subphase and a hydrophobic portion to prevent water solubility.[207] Compounds bearing such characteristics (soaps and phospholipids for example) are known as surfactants or amphiphiles. Designing amphiphiles for Langmuir film formation requires a great deal of consideration for the hydrophilic/hydrophobic ratio within the molecule as it is this factor which dictates whether monolayer formation will prove successful or not.[207]

The apparatus employed for the assembly of Langmuir monolayers and subsequent LB film formation was used in collaboration with Prof. Martin Albrecht in UCD Dublin and is known as a Langmuir trough, as shown above in Figure 1.22 (a). For monolayer formation at an air-water interface the amphiphilic material is initially dissolved in a water-immiscible solution (usually chloroform or hexane)[208] and is dispensed from a microsyringe onto the

water surface leaving a disordered layer of non-interacting molecules on the surface of the subphase analogous to a three-dimensional gaseous state (G), see Figure 1.22 (b). The moveable barriers are then compressed and the area available to the floating surfactant is reduced, forcing the molecules closer together and the system to undergo several phase transitions. The nonpolar hydrocarbon chains begin to orientate away from the subphase and the polar headgroups interact with one another and with the water resulting in a phase transition to the liquid expanded phase (LE). These phase changes are signified by a surface pressure change illustrated by a surface pressure-area isotherm, see Figure 1.23 (a), which plots surface pressure (π) (monitored by means of a Wilhelmy plate) versus area per molecule (a). Surface pressure (π) is defined as the difference in surface tension of the clean surface (γ_o) with respect to the surface tension of the surface in the presence of the floating amphiphile (γ), ($\pi = \gamma_o - \gamma$), while the area per molecule is calculated by the Langmuir trough software from data input at the beginning of the measurement, using the following equation:

Equation 3: $$a = \frac{AM}{CN_A V}$$

where A is the film area, M is the molecular weight of the monolayer material, C is the concentration of the spreading solution in mass per unit volume, V is its volume and N_A Avogadro's number. Another phase transition occurs upon further compression and is known as the liquid condensed phase (LC). In this state the chains are orientated perpendicular with respect to the surface with strong intermolecular interactions causing the formation of a closely packed, one molecule thick layer known as a Langmuir monolayer. Over compression of this state may result in film collapse which is identified by a sharp decrease in surface pressure. By extrapolating the steepest part of the curve prior to collapse, a minimum cross-sectional area per molecule can be obtained.[207,208]

Monolayer stability may be evaluated by holding the film in the LC phase for a fixed period of time and monitoring its surface pressure. A stable film will hold its surface pressure over the time interval while unstable films usually collapse, displaying a decrease in surface pressure. Factors such as temperature and alkyl chain length must be considered when generating an ideal phase transition surface pressure-area isotherm as a monolayer's characteristics are highly dependent on these two parameters.[207,208]

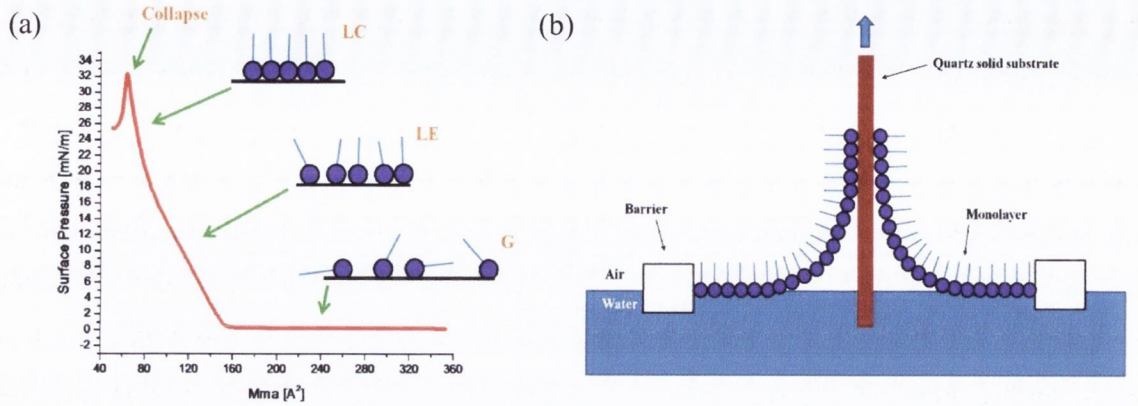

Figure 1.23. *(a) Surface pressure-area isotherm graph indicating different phase transitions for an ideal Langmuir monolayer. (b) Deposition of monolayer onto solid substrate as support is passed upward through air-monolayer interface.*

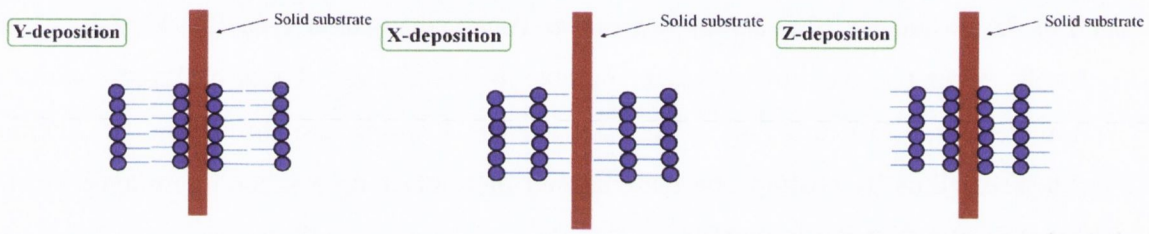

Figure 1.24. *Y-type, X-type and Z-type deposition. Y-type deposition is most common for fatty acid and fatty acid salt monolayers.*

Once it has been verified that it is possible for the surface active substance to form a stable Langmuir monolayer at the air-water interface deposition onto a solid support, such as a glass or quartz slide for example, may be accomplished by vertical dipping of a thin slide through the monolayer-subphase interface, see Figure 1.23 (b). Solid substrate hydrophobicity/hydrophilicity dictates whether dipping begins with the substrate positioned above or submersed below the monolayer. For hydrophilic substrates the slide is lowered and submerged through the subphase before the amphiphile is spread onto the surface. Removal of the slide by means of an upward stroke results in monolayer attachment to the slide *via* hydrophilic interactions between the polar headgroups and slide. Hydrophobic coated slides remain above the subphase/monolayer interface before the material is deposited onto the water surface. A downward stroke of the slide causes attachment of the hydrophobic chains to the slide upon submersion.[207,208]

This process of slide emersion (upstroke) and immersion (downstroke) gives rise to one of three packing patterns known as deposition architecture type. The three types of film architectures available to multilayered systems are described as Y-type (most common), X-type and Z-type, as shown in Figure 1.24.

The quality of film transfer is measured by evaluating the deposition transfer ratio (τ) and is given by:

$$\textbf{Equation 4:} \quad \tau = \frac{A_L}{A_S}$$

where A_L is the decrease in the area occupied by the monolayer and A_S the coated area of the solid substrate. Values obtained between 0.95 – 1.05 for deposition transfer ratio represent high quality transfer from the subphase to the substrate with excellent homogeneity.

Maintaining a single phase state is critical during the deposition process in order to obtain molecular-level control over the structure of the resultant film. Using the Langmuir-Blodgett technique enables the deposition of well-ordered and highly structured ultrathin immobilised layers. Attachment of monolayers onto solid substrates in this way has many advantages over other solid matrix immobilisation techniques in that it offers precise control over parameters such as layer number (number of monolayer coats), deposition type (X, Y, Z-type) and molecule amount (deposition of exact number of molecules). Layer-by-layer coating of monomolecular films also opens up an avenue towards the formation of alternate multilayered films by coating one material and then attaching a second substance bearing different functions and/or properties.[207,208]

As just stated, the LB technique offers the availability to, in a stepwise three-dimensional manner, combine layers exhibiting different functions for the fabrication of hybrid LB systems for multifunctional purposes. Since the early 1970's much interest has been centred on the incorporation of molecule-based conducting and magnetically active compounds into LB films for the purpose of molecular engineering of electronic switching devices and memory storage at the nanomolecular level.[209-227] The distinct resemblance of the biological membrane – composed of a bilayer of amphiphilc phospholipid molecules - to artificial monolayers assembled *via* the Langmuir method has also inspired researchers to build biomimetic systems as representative models due to the great interest in developing highly sensitive biosensors.[228-232] However, the application of the LB technique in these areas is not detailed here as, more relevant to the work described within this thesis are those optically active compounds which are incorporated into LB films, in particular Ln^{III} containing LB films, which is the theme of the following section.

1.7 Lanthanide containing Langmuir monolayers and Langmuir-Blodgett films

Despite the fact that fabrication of attractive luminescent Ln^{III} materials into ordered ultrathin films provides an alternative route towards solid state emitting devices there are very few examples of Ln^{III} luminescent LB films in the literature. The majority of research groups working within the area of Ln^{III} based energy transfer luminescent LB films use β-diketonates[233-239] although polyoxametalates (known as POMs),[240-242] calixarenes[243] and heterocyclic pyridine ligands[244] have also been reported.

Other systems have been identified in which Ln^{III} have been incorporated into LB films for purposes other than energy transfer luminescence including films of a hemicyanine Eu^{III} complex which has been shown to exhibit good second harmonic generation,[245] and the films of double-decker-type bisphthalocyanines compounds whose electrochromic and electrochemical behaviour has been studied in great depth by de Saja *et al.* for gas-sensing purposes (NO_2/N_2O_4, selected herbicides, volatile organic compounds and tobacco smoke in particular).[246-251] The main focus herein is that of Ln^{III} complex containing LB films expressing luminescence *via* energy transfer from surrounding excited antennae ligands, most notably the β-diketonate systems.

There are generally three main methods by which Ln^{III} luminescent systems may be fabricated into LB films. By dissolving the metal ion salt into the aqueous subphase the metal ion can be adsorbed onto/into the surfactant Langmuir monolayer upon assembly at the air-water interface.[237,243,244] Another method by which Ln^{III} complexes may be incorporated into LB films is to deposit a mixture of classical film-forming molecules with non-amphiphilic functional molecules onto the subphase, allowing the surfactant substance to act as a mediator in the film-forming process.[233,235,236] Chemical modification of the functional complex (either the parent (metal-complexing) ligand or a counter anion) is the third method by which Ln^{III} materials may be incorporated into LB films. Through initial design and synthesis to attain double functional systems – both amphiphilic and luminescent character – pure LB films are obtainable.[237-239,244,252]

As shown below, thenoyltrifluoroacetone (TTA) β-diketonates in particular have been employed by a number of research groups for Ln^{III} complexation, sensitisation and subsequent LB film incorporation.[233] Qian *et al.* designed **67** such that the complex counter anion displayed amphiphilicity to facilitate stable Langmuir monolayer formation at the air-water interface.[233] Stable monolayer formation was confirmed by a *s*urface pressure-area isotherm of **67**. However, the difficultly in depositing pure monolayers of **67** onto solid substrates led to the investigation of the Langmuir monolayer forming abilities of mixtures of **67** with arachidic acid (AA) and octadecane (OD). Higher collapse pressures were observed

when mixtures of **67** with OD were deposited onto the surface with an increase in OD molar fraction giving rise to larger π collapse values – suggesting closer packing of the molecules in the presence of OD. Mixed monolayers with AA (in molar ratios of 1:16 and greater) could be deposited onto hydrophobic quartz slides by vertical dipping while mixed monolayers of **67** and OD (molar ratio 1:4) were deposited by a horizontal lifting technique. Absorption and emission spectra of **67** in the mixed monolayer assemblies (50 layers) with OD (molar ratio 1:4) and AA (molar 1:16) in comparison to organic solutions ($CHCl_3$ and CH_3OH) of **67** reflect the difference in symmetry in going from the solution to the solid state. Not only was the $^5D_0 \rightarrow {}^7F_2$ transition split into two peaks but emission from the higher energy exited $^5D_1$ state was observed and the usually weakly observed symmetry forbidden transition $^5D_0 \rightarrow {}^7F_0$ was enhanced upon organisation into the LB film.[233] Moreover, Qian *et al.* have carried out a study illustrating the effect that different chain lengths and different hydrophilic β-diketonate head groups have on the monolayer morphology and collapse processes of monolayers of Eu^{III} complexes.[234]

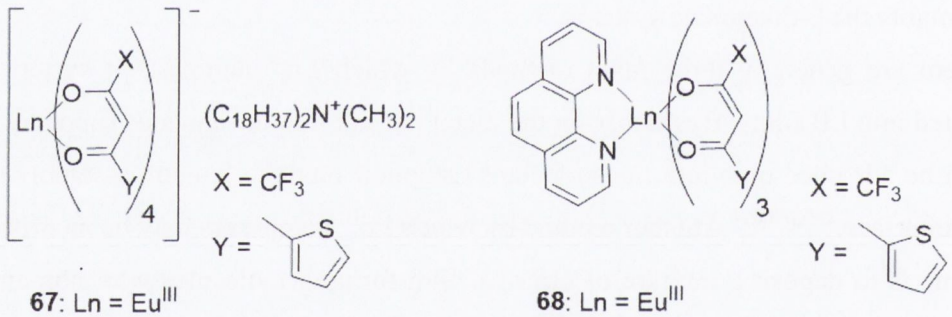

67: Ln = Eu^{III}

68: Ln = Eu^{III}
69: Ln = Sm^{III}

Zhang *et al.* developed a method to assemble non-amphiphilic complexes **68** and **69** at the air-water interface in which an appropriate composite subphase is selected.[235] When the aqueous subphase solution is saturated with TTA, 1,10-phenanthroline (Phen) and **68** dissolution and dissociation of **68** was effectively inhibited by the components and so by adding the fatty acid AA (to aid assembly) and depositing a mixture of **68**:AA/**69**:AA (molar ratio 1:1) onto the composite subphase surface homogeneously dispersed stable monolayers were formed and successfully transferred onto hydrophobic glass substrates. UV-visible absorption spectra of $CHCl_3$ solutions of **68**:AA and **69**:AA (1:1) were compared to those obtained from LB films of **68**:AA and **69**:AA (1:1) with shifting of bands upon immobilisation into LB films attributed to the superior organization and interaction of the molecules in the LB film. A linear dependence of the absorbance on the number of layers was also obtained indicating that the films have vertical uniformity. Ln^{III}-centred emission *via* energy transfer from the coordinating chromophores was preserved upon LB fabrication

with the emission intensity exhibited from **68** LB films being stronger than that of **69** LB films, the intensity of the former being nearly 25 times the intensity of the latter.[235] These results suggest that not only can Ln^{III} luminescence be preserved upon LB film fabrication but that the organisational structure of the monolayer can have an effect on the photophysical properties. Furthermore, the influence of the β-diketonate on the excited state lifetimes and energy transfer process was studied on a series of analogous of **68** and **69** which were immobilised into molecular LB films. It was concluded that fluorescence lifetime of the rare earth complexes varied with the β-diketonate ligand (those studied were (acetylacetone), trifluoroacetylacetone, hexafluoroacetylacetone and thenoyltrifluoroacetone) while the lifetime was also shown to be longer in the LB film than that in solution and solid powder.[236]

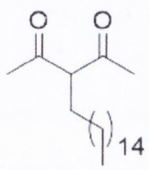

70

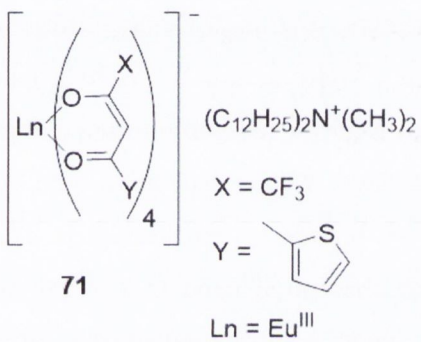

71

For the fabrication of thin Eu^{III}-centred luminescent films of **70**, de Gomes *et al.* combined the methods of introducing a long aliphatic chain into the parent ligand structure for spreading ability and assembly of the amphiphilic ligands into Langmuir films on a Eu^{III} 0.1 mmol L^{-1} solution subphase.[237] Following an appropriate time interval (120 mins), to allow complexation of **70** to Eu^{III}, monolayers were then transferred to quartz slides yielding Z-type architecture with three layers of $Eu(\mathbf{70})_n \cdot xH_2O$ deposited by means of three vertical withdrawals of the slide. Eu^{III} distribution within the films was verified by SEM images, EDS analysis and the exhibition of characteristic Eu^{III} luminescence upon excitation at 353 nm.[237]

More recently, de Adati *et al.* have developed a similar system to **67** in which a functional group to impart amphiphilicity has been introduced to the counter anion (didodecyldimethyl ammonium) to eliminate the need for a co-spreading surfactant or a composite subphase.[238] **71** comprises of Eu^{III} coordinated to four TTA β-diketonates bearing a negative charge which is neutralised by the amphiphilic cation didodecyldimethyl ammonium. Upon spreading $CHCl_3$ solutions of **71** onto water pure stable Langmuir monolayers of **71** were obtained. Subsequent attachment of monolayers of **71** onto a quartz solid substrate afforded Y-type deposition which, following excitation of the sensitising

antenna (λ = 307 nm), was shown to retain the desirable Ln^{III} luminescent properties following LB fabrication.[238]

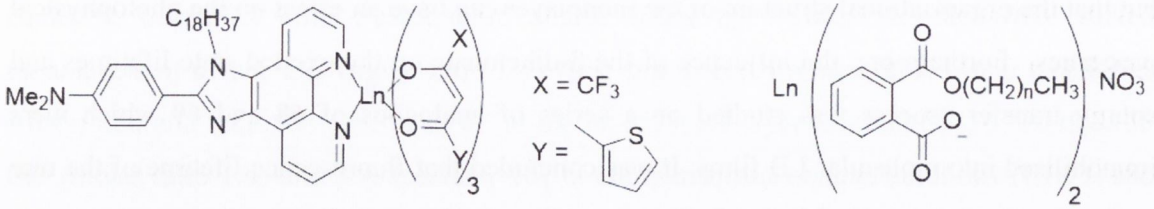

72: Ln = Eu^{III}

73: Ln = Tb^{III}, n = 15
74: Ln = Tb^{III}, n = 17
75: Ln = Tb^{III}, n = 19

The film-forming ability of **72** was analysed by surface-pressure area isotherm measurements, low angle X-ray diffraction and UV-visible and emission spectroscopy by Bian *et al.*[239] Introduction of the hydrophobic alkyl chain onto one of the Ln^{III} coordinating units allows for the assembly of the complex into pure stable monomolecular films at an air-water interface. Y-type deposition onto hydrophilically treated glass substrates was achieved with up to thirteen layers fabricated. The UV-visible spectra of the LB films exhibited a maximum absorption band at λ = 328 nm which was blue shifted relative to **72** in THF possibly due to the arrangement of **72** in an ordered environment. A linear dependence of the absorbance on the number of layers was again obtained for **72** indicating that the transfers were uniform and reproducible. The Eu^{III}-centred luminescence was preserved upon LB film formation as the emission spectrum, exhibited from a thirteen layered LB film, displayed characteristic Eu^{III} peaks at λ = 579, 592, 612, 652 and 701 nm corresponding to the $^5D_o \rightarrow {}^7F_j$ ($J = 0 - 4$) transitions.[239]

Other ligand systems for LB film formation of Ln^{III} luminescent systems *via* energy transfer other than the β-diketonates are uncommon despite the wide range of antenna moieties available for Ln^{III} coordination and sensitisation. The remaining literature examples discussed, **73** - **78**, highlight the versatility of the LB technique and how, with a greater understanding, a broad spectrum of functional systems may be integrated into the solid state for practical applications. Yan *et al.* developed nine Ln^{III} complex systems for LB film fabrication, the three Tb^{III} complexes of which are shown (**73** – **75**), where the coordinating ligand itself possesses both the chromophoric sensitising unit and the long chain ester group for the induction of amphiphilicity.[252] Again, there was no need for a co-spreading agent or a composite subphase so Langmuir monolayers of the appropriate complex were assembled by spreading their $CHCl_3$ solutions onto a water subphase. The monolayer forming ability of these systems was shown to be greatly affected by the length of the substituted chain with an

increase in chain length correlating to an increase in collapse surface pressure values. Immobilisation onto quartz solid substrates with Z-type architecture was achieved with low-angle X-ray diffraction illustrating the layered structure of the films. The ordered arrangement in the LB films was again confirmed by UV-visible absorption spectroscopy in which absorption peaks located at 252 nm (**73**), 250 nm (**74**) and 245 nm (**75**) for the $CHCl_3$ solutions were shifted to 230 nm, 233 nm and 235 nm when immobilised into their LB films (twelve layers), respectively. Furthermore, a linear relationship between layer number and absorption intensity was displayed upon subsequent layer attachment. Emission spectra obtained for solid state samples of **73** - **75** compared to those obtained for the LB films show differences in emission peak position and emission peak ratios, again revealing the influence ordering and immobilisation can have on the properties of the resultant structure.[252]

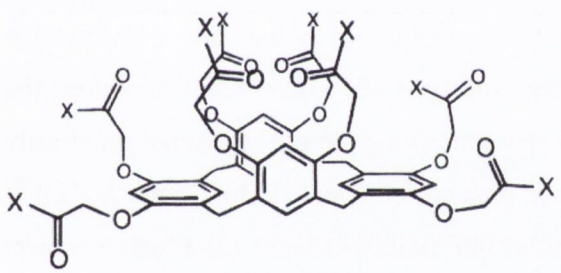

76: X = OMe
77: X = NEt_2

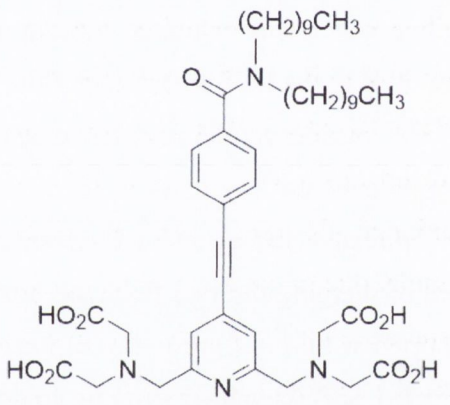

78

The first calixarene based systems, **76** and **77**, exhibiting energy transfer luminescence in LB films were reported by Dutton *et al.*[243] Solutions of **76** or **77** were spread onto either a pure water or a 2 x 10^{-4} M $TbCl_3$ solution subphase and assembled into stable Langmuir monolayers. The stability of **76** on the 2 x 10^{-4} M $TbCl_3$ solution subphase was monitored over an 8 hr period with very little fluctuation in π, indicative of good monolayer stability. Single monolayers of Tb.**76** and Tb.**77** were transferred onto solid substrates from the 2 x 10^{-4} M $TbCl_3$ subphase on the upward stroke of a quartz slide, affording films with transfer ratios close to unity. Multilayers of Tb.**76** and Tb.**77** were unattainable however but single layers did display excellent luminescent properties. The UV-visible absorption spectra of 10% CH_3OH/CH_3CN solutions of Tb.**76** and Tb.**77** were compared to those of their corresponding LB films with no noticeable differences in the spectra obtained from the solutions to the immobilised films. This similarity between the solution and monolayer

spectra indicates that the same species are present in both solution and in the solid monolayers. Characteristic Tb^{III}-centred emission was also displayed upon excitation into the ligand π-π* band confirming an energy transfer luminescence mechanism.[243]

A time-resolved study of the mechanism of the energy transfer from **78** to Ln^{III} (Ln = Eu^{III}, Gd^{III}, Tb^{III}) in LB films was carried out by Lemmetyinen *et al.*.[244] Langmuir monolayers of **78** were assembled on a $LnCl_3$ subphase and films were deposited onto quartz solid substrates with transfer ratios of ~ 1. No change in shape of the surface pressure-area isotherm graphs were observed upon monolayer formation although there was a slight shift in mean molecular area with changing Ln^{III}. The absorption spectrum of **78** in CH_3OH solution experienced a 10 nm redshift following complexation to the Ln^{III} but no noticeable difference in the absorption spectrum of the complex in solution compared to that obtained from the LB was seen. Upon excitation of the ligand (λ = 300 nm) characteristic Eu^{III} and Tb^{III} luminescence was exhibited indicating energy transfer *via* sensitisation of the coordinating ligand **78** to the Ln^{III} within each film.[244]

By considering the very few examples of Langmuir monolayers and LB films containing luminescent Ln^{III} systems in the literature and the abundance of mono- and multimetallic Ln^{III}-directed self-assembled systems, which have received such significant attention, the idea of merging the two fields became apparent. By modifying simple structures previously reported within our group it was assumed that the generation of novel chiral emitting Ln^{III}-directed self-assembled systems could be organised into highly ordered LB films, a project which shall be discussed in detail in Chapter Two.

1.8 Work described within this thesis

The main objective of the work reported within this thesis was to build upon previously developed Ln^{III}-directed self-assembled systems for potential use in biological/materials based luminescent applications. It was envisioned that suitable modification of ligand structures which have been developed within our group, and hence are relatively well understood, would enable the aforementioned advantageous properties of the Ln^{III} ions to be exploited, further fuelling the applicability of systems of this nature.

Chapter 2 focuses on the functionalisation of the H_2dpa framework for the solid state fabrication of mononuclear Ln^{III} luminescent systems. Amphiphilic asymmetric tridentate ligands based on **56** and **57** were synthesised with the aim of providing three significant features – the ability to fully coordinate the Ln^{III} in a 1:3 fashion; to efficiently sensitise the Ln^{III} *via* indirect excitation; and to enable the assembly of monomolecular Langmuir monolayers at an air-water interface for subsequent immobilisation into ultra-thin Langmuir-

Blodgett films. Two optically active amphiphilic compounds were synthesised, fully characterised and their Ln^{III}-directed self-assembly behaviour (Ln^{III} = Eu^{III}, Nd^{III}, Tb^{III}, Sm^{III}, Dy^{III} and Lu^{III}) was photophysically evaluated in CH_3CN solution. 1:3 (M:L) complexes $Ln.L_3$ were synthesised and their ability to form Langmuir monolayers at an air-water interface was established. Furthermore, Langmuir monolayer stability was investigated and, following attachment to a solid quartz substrate, immobilised monolayers of visibly ($Ln.L_3$ (Ln = Eu^{III}, Tb^{III} and Sm^{III}) and NIR ($Nd.L_3$) emitting mononuclear complexes were shown to exhibit Ln^{III}-centred emission.

Chapter 3 is based on the modification of the ditopic helicate ligand **62** for the formation of dinuclear Ln^{III} luminescent chiral helical assemblies. Attachment of two polyoxyethylene chains to the helicate ligand backbone structure was expected to enhance the solubility of such systems in more competitive solvent media. This chapter details the progress made in synthesising two such chiral helicate ligands and the spectroscopic measurements which were implemented in order to 1) probe the chirality of the ligands and their resulting 2:3 M:L assemblies and 2) establish their Eu^{III}-directed self-assembly behaviour *in situ* in solvent media of varying competitiveness with a view to bringing these studies into a fully aqueous environment.

The versatility of simple "half helicate" chiral ligand precursors is examined in Chapter 4 by incorporating two novel functionalities - a positively charged pyridinium side chain and a Pt(terpy) functionality - into the 6-*ortho* position of an asymmetric analogue of the sliotar compounds **56** and **57**. It was anticipated that grafting of a pyridinium side chain would primarily enhance water solubility while the attachment of the biologically active Pt(terpy) group could also allow the Ln^{III} luminescence of these systems to be utilised as a probe in biological media, for instance in DNA binding/reporting. Four novel chiral tridentate ligands were synthesised, fully characterised and their Eu^{III}-directed self-assembly behaviour was investigated by spectroscopic methods.

Chapter 5 gives an account of preliminary studies carried out on a H_2dpa derivative which was functionalised with a C_{12} thiol-terimated chain at the 4-*para* position of **1**. The intention of such an attachment was to tether, through a thiol-Au linkage, a Ln^{III} coordinating unit/sensitising moiety to the surface of AuNPs for the formation of ligand-AuNPs conjugates which display Ln^{III} luminescence upon Ln^{III}-directed self-assembly. Few examples of such conjugates exist and, given the unique and advantageous properties both the Ln^{III} ions and the AuNPs have to offer, bridging such fields proved fascinating. With the development of a luminescent sensing device in mind, ligand synthesis, Eu^{III}- and Tb^{III}-

directed self-assembly studies in H_2O and preliminary studies on the adsorption of the Ln^{III}coordinating/sensitising ligand onto the surface of AuNPs are described.

Chapter 6 details the experimental procedures and techniques employed throughout the research described in the preceding chapters.

Chapter Two

Emissive Langmuir–Blodgett films formed from chiral lanthanide-directed self-assemblies

2. Introduction

For the supramolecular chemist, great interest lies in the design and synthesis of beautifully extravagant and elegant superstructures. In addition to this, the creation of functional molecular structures is highly attractive for the construction of novel materials and new technologies. As a result of structural and functional integration of such supramolecular (chemical) entities, exciting new developments have emerged in applications as far afield as molecular machinery to analytical optical sensing and biological cell imaging agents.[53-55,96,253] As mentioned in chapter one, it was envisaged that with appropriate functionalisation, the chiral Ln^{III}-directed self-assembled supramolecular structures developed within our research group may be exploited for use in such biological or materials based applications. To date studies carried out on these systems have been conducted primarily in solution; focusing on the photophysical properties of the complex and the self-assembly process *in situ*. The use of Langmuir and Langmuir-Blodgett techniques however, allows for the translation of these systems from solution to the solid state with the additional benefit of offering control at the molecular level over the organisation of these complexes into thin monomolecular films. Deposition of these Ln^{III} systems onto solid supports in this manner may open up new prospects in the development of immobilised chiral luminescent devices. Therefore, the principle aim of this project was to develop highly organised self-assembled monolayers (SAMs) of systems of this type at an air-water interface, and to further transfer these monolayers to quartz solid supports in order to generate immobilised Ln^{III} luminescent Langmuir-Blodgett films. Developments in this area originated from the recently reported Ln^{III}-directed self-assembled "half-helicate" systems which were based on chiral ligands **79** (*S*) and **80** (*R*).[66]

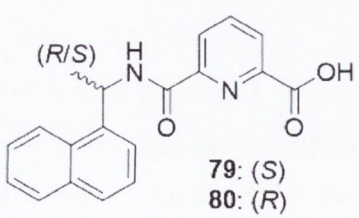

79: (*S*)
80: (*R*)

The interaction of these ligands with Ln^{III}, such as Eu^{III}, have recently been shown to give rise to the formation of Ln^{III} luminescent "half-helicates" in a 1:3 metal:ligand (M:L) stoichiometry.[66] The formation of the self-assemblies Eu.$\mathbf{79}_3$ and Eu.$\mathbf{80}_3$ was monitored *in situ* using spectroscopic techniques while Circularly Polarised Luminescence (CPL)

measurements were employed to illustrate the exhibition of chiral Ln^{III}-centred luminescence from such self-assembled structures. Molecular modelling calculations (MM2) were also implemented in order to gain insight into the stereochemistry of these mononuclear systems. The results from these calculations indicated that these structures all had the three naphthalene antennae residing on the same side, directed towards the inside of a "half-helicate", with the methyl groups outside the coordination sphere of the Ln^{III} ion, giving rise to the most stable complex arrangement.[66]

This chapter deals with the synthesis of amphiphilic analogues of chiral ligands **79** and **80** and the photophysical properties of the resulting 1:3 Ln^{III} complexes (Ln^{III} = Eu^{III}, Nd^{III}, Tb^{III}, Sm^{III}, Dy^{III} and Lu^{III}). Spectroscopic measurements were employed to re-evaluate the Ln^{III}-directed self-assembly of these amphiphilic ligand derivatives in CH_3CN solution while the ability of both chiral ligands (**81** and **82**) and their corresponding 1:3 Ln^{III} complexes to form Langmuir monolayers and Langmuir-Blodgett films at an air-water interface was also established. Since the intention of this project was to retain functionality for future application appropriate modification for solid state incorporation was required but it was also crucial, following derivatisation, that the unique photophysical properties of the Ln^{III} system were preserved and so the photophysical properties exhibited by the Langmuir-Blodgett films have also been probed.

The first section of this chapter focuses on studies carried out on the Eu^{III} 1:3 mononuclear systems while the second section discusses those studies performed on the NIR-emitting Nd^{III} systems. The remaining sections detail results obtained for the Tb^{III}, Sm^{III}, Dy^{III} and Lu^{III} monometallic species.

2.1 Design and synthesis of ligands 81 (*S*) and 82 (*R*)

As discussed above, previous studies on the "half-helicate" ligands **79** and **80** demonstrated that the carboxylic group at the 6 pyridyl position was available for substitution and hence an enhancement in the potential applicability of these systems. The importance of amphiphilicity for the formation of Langmuir monolayers at an air-water interface has previously been stressed in chapter one and so it was anticipated therefore that the incorporation of a long alkyl hydrophobic hydrocarbon chain into the "half-helicate" ligand system would induce sufficient amphiphilicity for monolayer formation. Firstly, by grafting a hexadecyl alkyl chain onto the 6 pyridyl position of **79** and **80** it was assumed that it would be possible for both chiral ligands themselves to self-assemble at the air-water interface. Furthermore, since MM2 calculations elucidated that all three antennae were shown to preferentially reside on one side in the resulting 1:3 complex, it was expected that the three

hexadecyl alkyl chains would align together, enabling monolayer formation of the Ln^{III} complexes on the Langmuir trough.

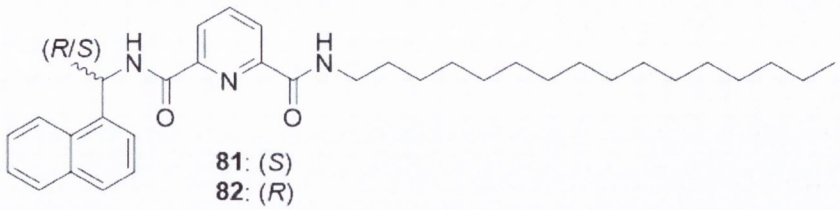

81: (*S*)
82: (*R*)

When designing chiral amphiphilic ligands **81** (*S*) and **82** (*R*) it was critical to achieve the implementation of three functionalities, *i.e.* a tridentate binding unit to efficiently host the large Lewis acidic Ln^{III} ion, a Ln^{III} sensitising antenna and a hydrophobic long alkyl chain to induce amphiphilicity. Ligand design was based on that applied to **79** and **80** entailing the incorporation of a chiral naphthalene chromophore, a pyridyl diamide group (based on the 2,6-pyridine dicarboxylic acid (dpa) framework) and a hexadecyl aliphatic alkyl chain. The chiral naphthalene group was employed for efficient chiral Ln^{III} sensitisation *via* the 'antenna effect' (as described in the previous chapter) while binding was expected to occur between the Ln^{III} and tridentate chelating functionality which consisted of two amido carbonyl oxygens and a pyridyl nitrogen atom. As displayed for **79** and **80**, self-assembly was expected to give rise to the formation of 1:3 M:L stoichiometric species with the Ln^{III} residing in a fully saturated chiral coordinating environment. Attachment of the hexadecyl alkyl chain was the only variation on the "half helicate" structure but it was still vital to re-evaluate its behaviour in solution before extending studies to the self-assembly process at the air-water interface.

A point to note is that this project has been carried out in collaboration with Dr. Jonathan A. Kitchen in which all syntheses and measurements of the (*R*) enantiomer **82** have been conducted by him. For the purpose of this chapter results obtained for the (*S*) enantiomer **81** shall be more heavily discussed with regular relevant referencing to results obtained for **82** as necessary for comparison.

Synthesis of ligands **81** and **82** involved a four step synthetic pathway, depicted in Scheme 2.1. The first three steps of which have previously been reported by Gardiner *et al.*[254] and Stomeo *et al.*.[69] An initial monoprotection of 2,6-pyridine dicarboxylic acid **83** was required to allow exposure of only one carboxylic acid site for subsequent peptide coupling. Monoprotection was achieved by adding 1.2 equiv. of benzyl bromide (BnBr) to a stirring solution of **83** and $NaHCO_3$ in DMF at 60 °C.

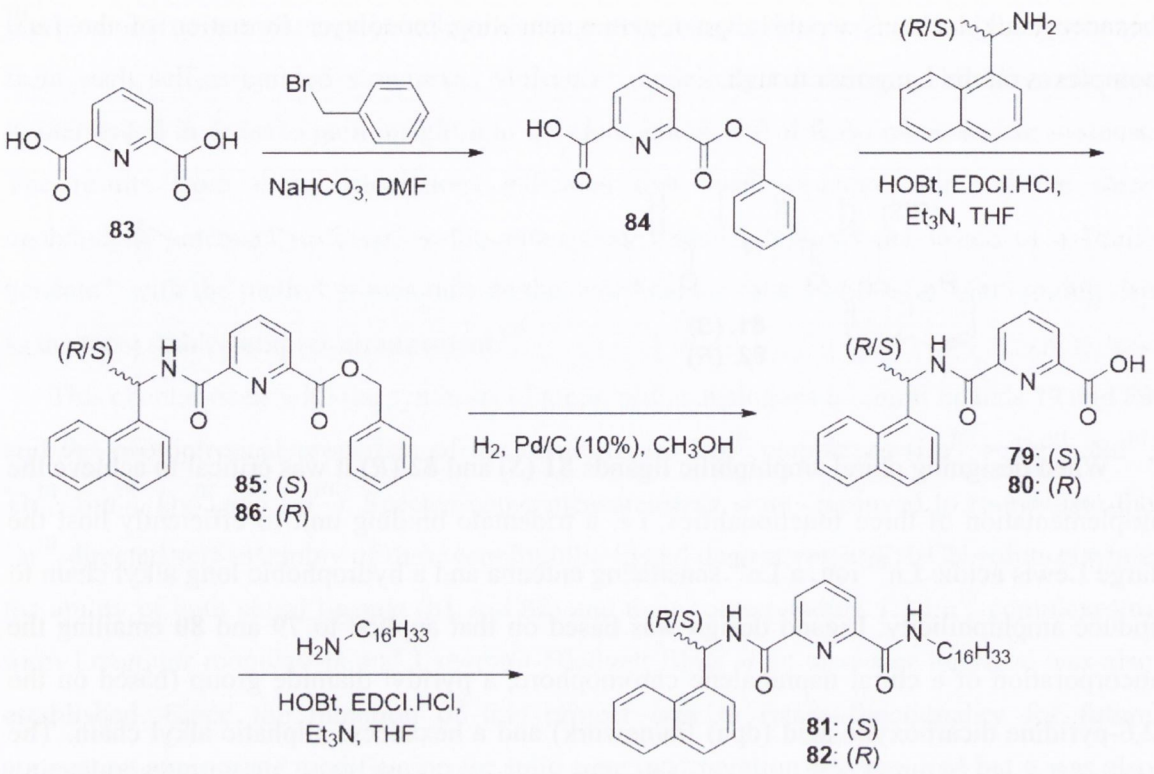

Scheme 2.1. *Synthetic pathway towards amphiphilic ligands* ***81*** *(S) and* ***82*** *(R).*

The reaction mixture was heated at 60 °C for a further 5 hrs and then cooled to RT before being diluted with H_2O and neutralised to pH = 7 with sat. aq. $NaHCO_3$ solution. The diester side product was then extracted with ethyl acetate and the aqueous layer acidified to pH = 3. The monoprotected product was extracted with ethyl acetate before being washed with H_2O, brine and dried over $MgSO_4$. Volatiles were removed under reduced pressure yielding compound **84** as a white solid in 52% yield. Successful product formation was indicated by the appearance of a sharp singlet peak in the ^1H NMR spectrum (400 MHz, $CDCl_3$) resonating at 5.48 ppm, corresponding to the CH_2 group of the benzyl ester **84** while the benzyl aromatic protons were located between 7.40 ppm and 7.51 ppm. The ^{13}C NMR (100 MHz, $CDCl_3$) and high resolution mass spectrometry (HRMS) data for **84** also correlated well with previously reported literature values.[254]

Introduction of the appropriate (*S* or *R*) chiral 1-(1-naphthyl)-ethylamine antenna moiety was achieved *via* an EDCI·HCl ((3-Dimethylaminopropyl)-3-ethylcarbodiimide Hydrochloride) peptide coupling reaction. A mixture of 6-(benzyloxycarbonyl)picolinic acid (**84**), HOBt, NEt_3 and 1 equiv. of (*S*)-(-)-1-(1-naphthyl)ethylamine (or (*R*)-(-)-1-(1-naphthyl)ethylamine) in THF were placed under argon and cooled to 0 °C. After 30 mins of stirring EDCI·HCl was added to the reaction mixture and stirred at 0 °C for a further 30 mins. The reaction mixture was then allowed to reach RT and stirred for 48 hrs leaving a yellow solution with a white solid residue. The solution was filtered and the THF was removed

under reduced pressure to give an orange oil which was redissolved in CH_2Cl_2. The solution was then washed with 1.0 M HCl, sat. aq. $NaHCO_3$, H_2O and brine and the organic phase dried over $MgSO_4$. Solvent was removed under reduced pressure affording **85** and **86** as an orange oil in 84% and 81% yields, respectively. Characteristic peaks verifying the successful synthesis of compound **85** were found to resonate at 1.82 ppm and 6.19 ppm in the ^{1}H NMR spectrum (400 MHz, $CDCl_3$) representing the CH_3 and CH groups of the naphthalene moiety, respectively. Aromatic CH protons were also observed occurring at 8.23, 7.84, 7.64 and between 7.57 – 7.38 ppm, respectively.[69]

Hydrogenolysis was then implemented in order to remove the benzyl protecting group. This method involved the use of a Parr hydrogen shaker apparatus in which compound **85**/**86** was placed under 3 atm of H_2 in the presence of a 10% Pd/C catalyst in CH_3OH. The reaction mixture was then filtered through celite and volatiles were removed *in vacuo* affording the deprotected moieties **79** (*S*) and **80** (*R*) in 76% and 83% yields, respectively. The disappearance of the aromatic signals and CH_2 signal at 5.48 ppm in the ^{1}H NMR spectrum (400 MHz, DMSO-d_6) of **79** confirmed the successful removal of the benzyl ester protecting group.[69]

Compounds **79** and **80** were then coupled to hexydecyl amine in the final step using a peptide coupling method identical to that described above for the synthesis of compounds **85** and **86**. The desired amphiphilic ligands **81** and **82** were synthesised in 51% and 59% yields, respectively and fully characterised by 1D and 2D NMR spectroscopy using H-H COSY, C-H COSY, HSQC and HMBC experiments.

As shown in the ^{1}H NMR spectrum (600 MHz, $CDCl_3$) of **81** in Figure 2.1, resonances corresponding to the long alkyl chain reside at 3.20 ppm, 3.31 ppm, 1.44 ppm, 1.27 – 1.22 ppm and 0.9 ppm (see Appendix Figure A2.1 for ^{1}H NMR spectrum of **82**). Interestingly the two CH_2 protons next to the amide group of the long chain (CH_2 group **13**) resonate individually as a pair of multiplets at 3.20 ppm and 3.31 ppm. The remaining characteristic peaks have been discussed for those compounds previous and can be observed in the ^{1}H NMR spectrum (600 MHz, $CDCl_3$) in Figure 2.1. ^{13}C NMR (150 MHz, $CDCl_3$), HRMS and IR spectroscopy were also employed to verify formation of the desired amphiphilic ligands **81** and **82**. In addition, the solid state crystal structures of both compounds **81** and **82** were determined by X-ray crystallography.

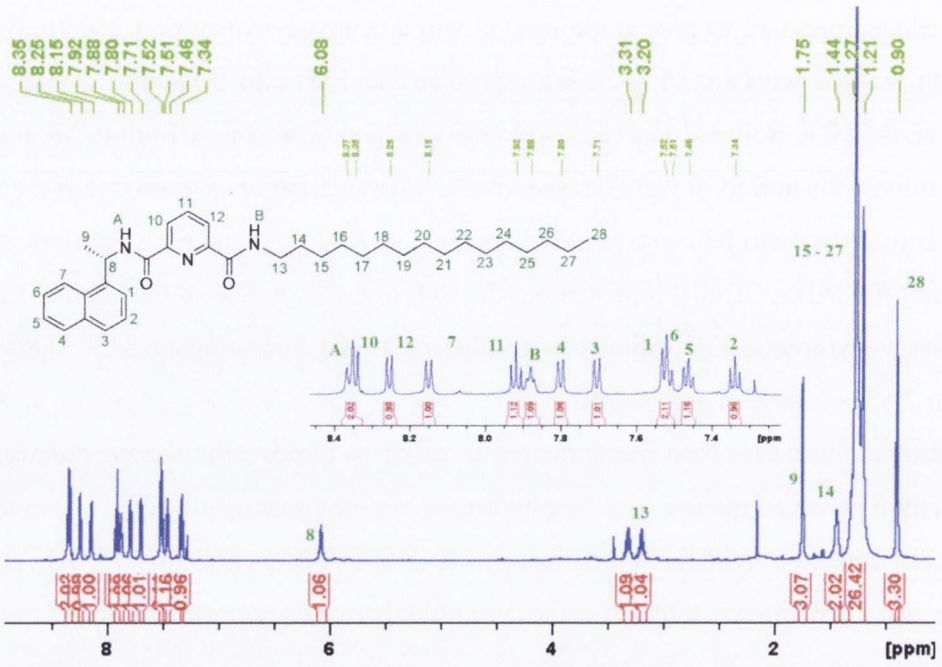

Figure 2.1. *^{1}H NMR spectrum (600 MHz, $CDCl_3$) of **81** (S).*

2.2 X-ray crystal structure analysis of 81 (*S*) and 82 (*R*)

Single crystals of ligand **81** were grown by the slow evaporation of CH_2Cl_2/CH_3CN solution in the presence of CH_3I and its solid state structure determined at 150 K. Compound **81** crystallised in the chiral, monoclinic space group $P2_1$ and contained two crystallographically independent molecules in the asymmetric unit in which the hexadecyl chain of one molecule remains relatively trans coplanar (retaining a 'straight' chain conformation) while the chain of the second molecule acquires a square "bent-like' structure.

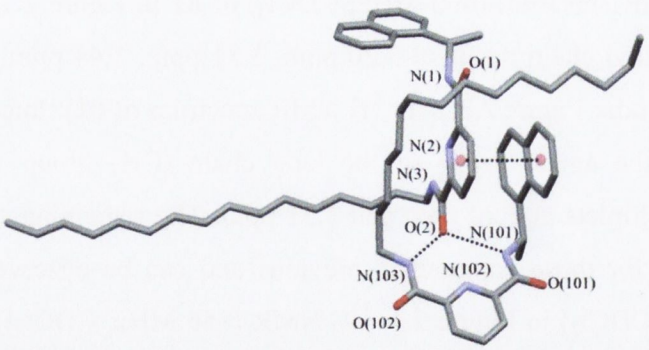

Figure 2.2. *Perspective view of ligand **81** (S) illustrating dimeric nature of packing. Note that π-π stacking and hydrogen bonding exist between the two crystallographically independent molecules. Hydrogen atoms have been omitted for clarity.*

The dimeric nature of the packing is governed by interactions through NH···O hydrogen bonds (see also Table 2.1 for bond angles and lengths) and offset face to face π-π stacking between the pyridyl ring of one molecule and the naphthalene ring of the other, as shown in

Figure 2.2 (see also Appendix Table A2.1), with a centroid-centroid distance of 3.650 Å for **81** (and a centroid-centroid distance of 3.658 Å for **82**, see below).

Crystals of ligand **82** were also grown by means of the slow evaporation of CH_2Cl_2/CH_3CN solution in the presence of CH_3I (determined at 108K) and are displayed in Figure 2.3 (b) (see also Appendix Table A2.2 and A2.3). Evidently these crystals were shown to be isomorphous to **81** and also clearly illustrate the enantiomeric relationship between the two isomers **81** and **82**. The absolute configuration of **82** was not determined by crystallographic means, however, **81** was collected using Cu κ-α radiation thus allowing refinement of the flack parameter. This was able to confirm that the crystal was of the *S* isomer, as expected. Both solid state structures were analysed by Dr. Jonathan A. Kitchen.

Table 2.1. *Hydrogen bonds lengths and angles for ligand **81** (Å and °). Symmetry transformations used to generate equivalent atoms:* [a] *-x+1,y+1/2,-z+2* [b] *x+1,y,z*

D-H...A	d(D-H)	d(H...A)	d(D...A)	<(DHA)
N(1)-H(1X)...O(102)[a]	0.89	2.19	3.0500(18)	162.0
N(3)-H(3X)...O(102)[a]	0.87	2.12	2.9447(18)	158.3
N(101)-H(10X)...O(2)[b]	0.9	2.18	3.0192(18)	154.9
N(103)-H(10Y)...O(2)[b]	0.9	2.15	3.0105(17)	158.2

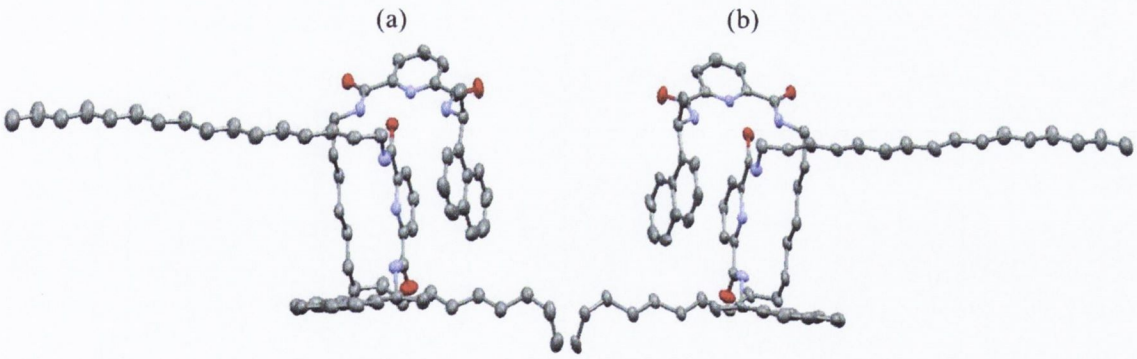

Figure 2.3. *Crystal structures of ligands **81** (a) and **82** (b) with thermal ellipsoids shown at 50% probability. Both enantiomers pack in an identical manner, as mirror images of one another, displaying the enantiomeric relationship between the two isomers. Hydrogen atoms have been omitted for clarity.*

2.3 Formation of mononuclear tris chelate complexes $Eu.81_3$ (*S*) and $Eu.82_3$ (*R*)

Preparation of the mononuclear Eu^{III} complexes was achieved by reacting either **81** or **82** with $Eu(CF_3SO_3)_3$ in a 1:3 stoichiometric M:L ratio in HPLC grade CH_3OH. Application of microwave irradiation for 10 mins at 70 °C (see Scheme 2.2) followed by isolation by vapour

diffusion of diethyl ether afforded the desired complexes Eu.**81**$_3$ and Eu.**82**$_3$ as white solids in yields of 56% and 42%, respectively. Both complexes were characterised by ^{1}H NMR (see Figure 2.4 and Appendix Figure A2.2), IR and elemental analysis. Broadening and shifting of signals in the ^{1}H NMR spectrum (400 MHz, CD_3OD-d_4) signified complexation of the paramagnetic Eu^{III} ion.

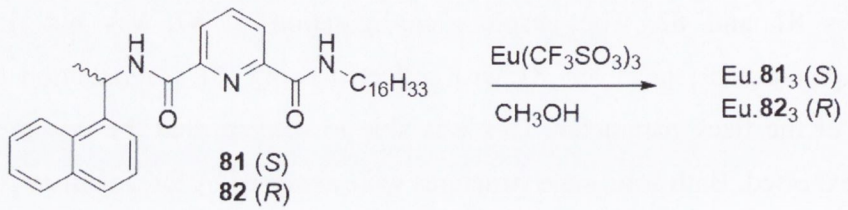

Scheme 2.2. *Preparation of Eu^{III} complexes Eu.**81**$_3$ (S) and Eu.**82**$_3$ (R) carried out under microwave irradiation at 70 °C.*

IR is representative of complexation of the ligand to the Eu^{III} *via* a shift in the amide carbonyl group stretching frequency. The IR is a useful tool in coordination chemistry as a change in the vibrational frequency of a group that is directly coordinated to the Ln^{III} usually indicates successful complexation. A shift in the IR stretching frequency of the amide carbonyl band (from 1654 cm^{-1} to 1633 cm^{-1} for Eu.**81**$_3$ and from 1650 cm^{-1} to 1631 cm^{-1} for Eu.**82**$_3$) verified complexation on both occasions.

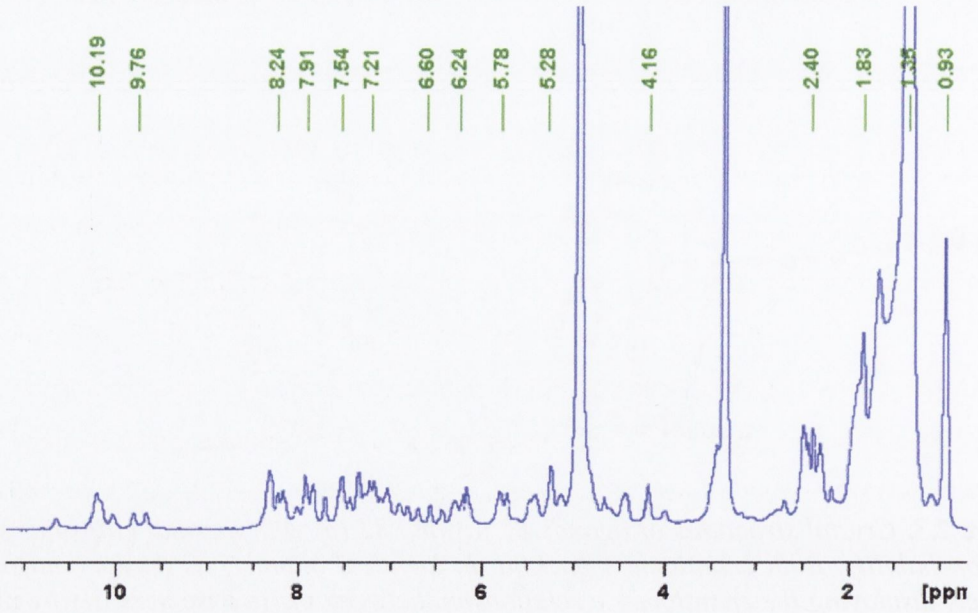

Figure 2.4. *^{1}H NMR spectrum (400 MHz, CD_3OD-d_4) of Eu.**81**$_3$.*

Elemental analysis (C, H, N) also supported formation of Eu.**81**$_3$ and Eu.**82**$_3$ in the solid state. Unfortunately neither of the 1:3 complexes Eu.**81**$_3$ nor Eu.**82**$_3$ were detectable by HRMS in the range of solvents investigated (CH_3OH, CH_2Cl_2, CH_3CN), however their 1:2 counterparts were observed (see Appendix Figure A2.3 for calculated and experimental

isotopic distribution pattern for Eu.**81**$_3$). This is probably due to the fact that sample preparation for HRMS analysis requires very low concentrations (0.1 mg/mL) which may have led to disassociation of the complexes. Moreover, the self-assembly species is subjected to a harsh environment during HRMS analysis which may cause removal of the third ligand.

2.4 Photophysical characterisation of complexes Eu.81$_3$ (*S*) and Eu.82$_3$ (*R*)

Having successfully synthesised both ligands **81** and **82** and their corresponding 1:3 Eu^{III} complexes, Eu.**81**$_3$ and Eu.**82**$_3$, we next evaluated their photophysical properties in CH_3CN, as shown in Figures 2.5 – 2.7 and Appendix Figure A2.4.

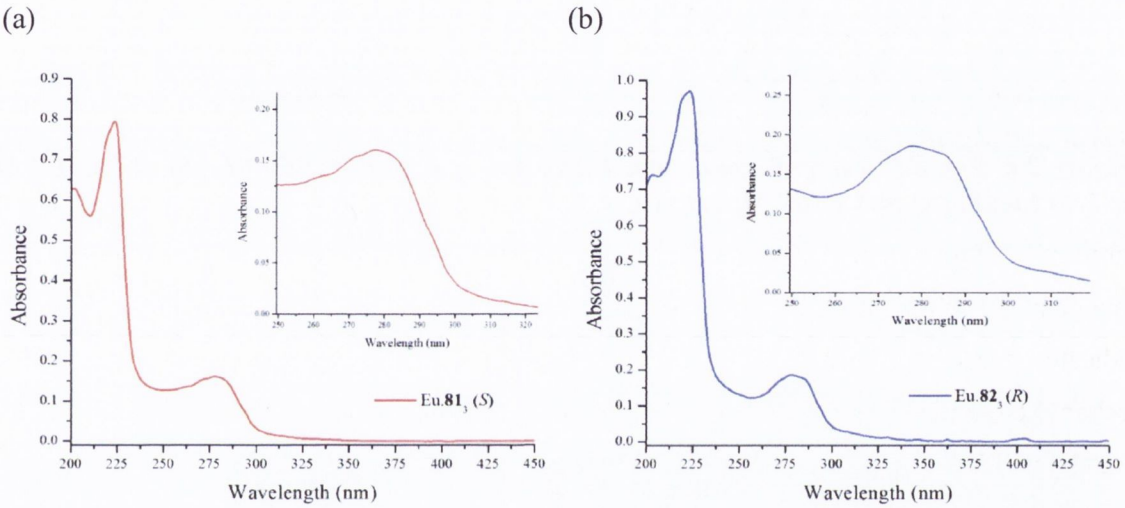

Figure 2.5. *The UV-visible absorption spectra of (a) Eu.**81**$_3$ (S) (4.1 x 10^{-6} M) and (b) Eu.**82**$_3$ (R) (4.8 x 10^{-6} M) in CH_3CN.*

The UV-visible absorption spectra of Eu.**81**$_3$ and Eu.**82**$_3$ were dominated by a high energy absorption band located at λ_{max} = 223 nm. This band is assigned to the singlet ground to the singlet second excited state ($S_0 \rightarrow S_2$) $\pi - \pi^*$ transition while the longer wavelength absorption band occurring at λ_{max} = 281 nm represents the singlet ground to the singlet first excited state ($S_0 \rightarrow S_1$) $\pi - \pi^*$ transition of the antenna moiety.

Upon excitation of the naphthalene antenna at λ_{max} = 281 nm characteristic Eu^{III}-centred time-delayed luminescence was displayed, as shown in Figure 2.6 and Appendix Figure A2.4. Line-like emission bands located at 595 nm, 615 nm, 650 nm and 695 nm are assigned to deactivation from the Eu^{III} $^5D_0$ excited state to ^7F_J states (where J = 1 – 4) indicating effective sensitisation *via* energy transfer from the naphthalene antenna group to the Eu^{III} centre. Luminescence measurements were also carried out in CH_3OH (see Appendix Figure A2.4) where a band centred at λ = 580 nm is also observed representing the J = 0 transition. The presence of this band represents the high degree of symmetry at the Eu^{III} centre, *i.e.* C_3

symmetry is achieved by coordinative saturation at the Eu^{III} centre *via* binding to three tridentate ligands.[69]

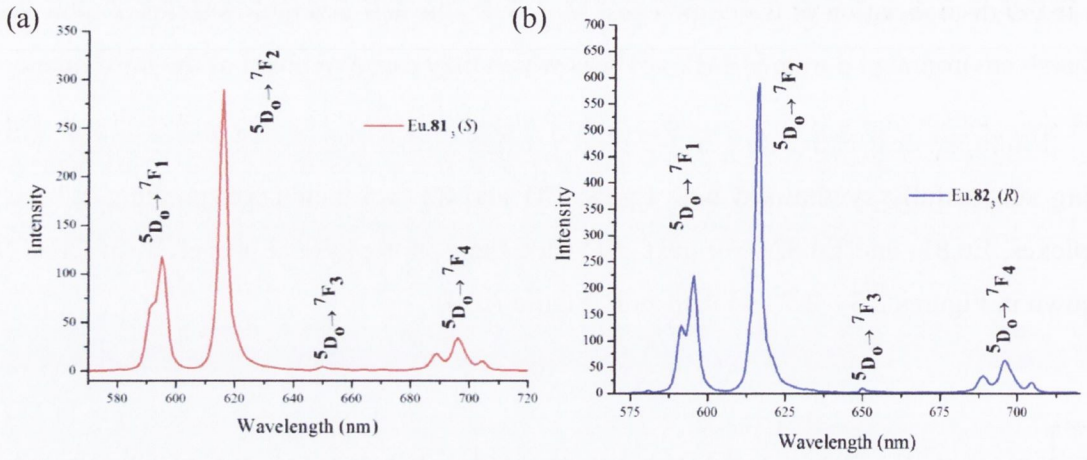

Figure 2.6. *The Eu^{III}-centred luminescence emission spectra of (a) Eu.**81**$_3$ (S) (4.1 x 10^{-6} M) and (b) Eu.**82**$_3$ (R) (4.8 x 10^{-6} M) in CH_3CN.*

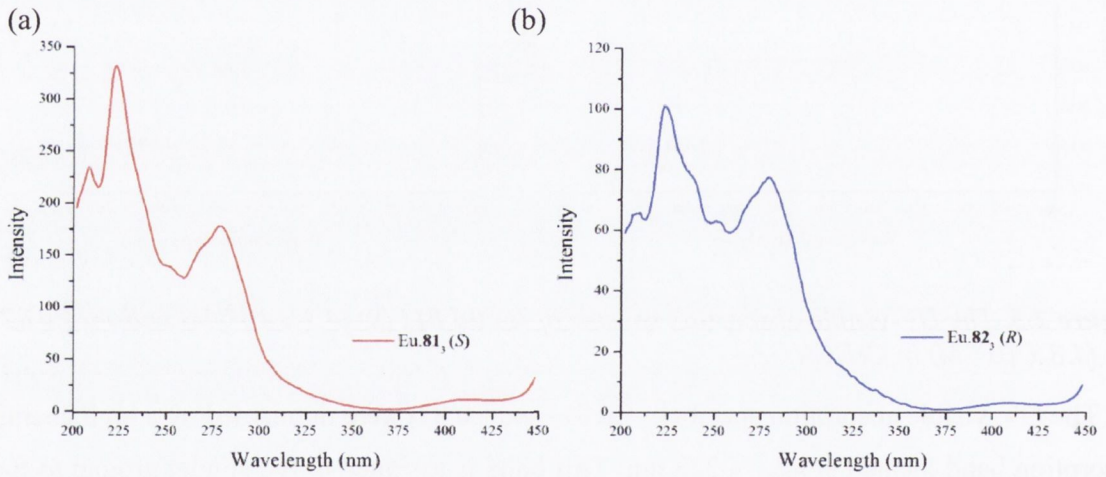

Figure 2.7. *Excitation spectra of (a) Eu.**81**$_3$ (S) (4.1 x 10^{-6} M) and (b) Eu.**82**$_3$ (R) (4.8 x 10^{-6} M) in CH_3CN (λ_{em} = 615 nm).*

Excitation spectra were also recorded for Eu.**81**$_3$ and Eu.**82**$_3$ in CH_3CN displaying maximum intensity (λ_{em}= 615 nm) at 223 nm and 281 nm (see Figure 2.7). These spectra closely resembld the UV-visible absorption spectra, further suggesting successful sensitisation of the Eu^{III} centre by indirect excitation of the antenna moiety.

As previously stated non-radiative deactivation of the Ln^{III} excited state can have a detrimental effect on Ln^{III} luminescence. However, it offers a route to determining the number of bound water molecules (hydration state, *q*) of a Ln^{III} complex. This is based on the fact that O-D isotopic oscillators reduce the excited state lifetime of Eu^{III} to a far lesser extent than the O-H oscillator.[87] Excited state lifetime measurements for Eu.**81**$_3$ and Eu.**82**$_3$ were conducted in H_2O and D_2O in which these complexes were only sparingly soluble. The

excited state lifetimes of Eu.**81**$_3$ and Eu.**82**$_3$ in both solutions were best fit to a mono-exponential decay function, indicating the presence of only one major luminescent species in H_2O and D_2O for both complexes.

Table 2.2. *Excited state lifetime values for complexes Eu.**81**$_3$ and Eu.**82**$_3$ in H_2O and D_2O and hydration state (q) values calculated using equation 1.*

Complex	τ_{H2O} (ms)	τ_{D2O} (ms)	*q* values
Eu.**81**$_3$	1.49	1.54	-0.3 ± 0.5
Eu.**82**$_3$	1.47	1.60	-0.2 ± 0.5

Excited state lifetime values of 1.49 and 1.47 ms in H_2O and 1.54 and 1.60 ms in D_2O were calculated for Eu.**81**$_3$ and Eu.**82**$_3$, respectively (see Table 2.2). Equation 1 (see section 1.1.1), first developed by Horrocks and co-workers,[87] was used for calculation of hydration state *q* values for Eu.**81**$_3$ and Eu.**82**$_3$ (see Table 2.2). *q* values of ~ 0 were calculated in each case indicating that the Eu^{III} centre is fully coordinated to three tridentate ligands in aqueous solution, free from any coordinating solvent oscillators.

2.5 Chiro-Optical properties of Eu^{III} complexes Eu.**81**$_3$ (*S*) and Eu.**82**$_3$ (*R*) – Circular Dichroism

The differential absorption of right- and left- circularly polarised light by an optically active asymmetric chromophore (or a symmetric chromophore in an asymmetric environment) is known as circular dichroism (CD). Circular dichroism is a spectroscopic technique in which measurements are carried out in the visible and ultra-violet region of the electromagnetic spectrum monitoring electronic transitions within a molecule. Since molecules containing chiral chromophores possess electrons residing in a chiral environment they will interact with and absorb the right- and left- 'handed' components of electromagnetic radiation to different extents resulting in a CD signal which is given by:

Equation 5: $\Delta A = A_L - A_R$

where A_L is the absorbance of left-handed circularly polarised light and A_R is the absorbance of right-handed circularly polarised light. A graph displaying ΔA for a given asymmetric structure may therefore possess both positive and negative signals characteristic of the chiral compound. Enantiomeric compounds give rise to CD absorption bands at equal wavelengths but of opposite sign as their structures are mirror images of one another. This technique was

implemented to probe the chiral nature of both the ligand and complex isomer structures and to verify the enantiomeric relationship between each pair.

CD spectra for ligands **81** (*S*) and **82** (*R*) and complexes Eu.**81**$_3$ (*S*) and Eu.**82**$_3$ (*R*) were recorded in CH_3CN to investigate the enantiomeric relationship between the chiral ligands and their corresponding 1:3 tris chelate Eu^{III} complexes with the latter being formed in solution upon the addition of 0.33 equiv. of $Eu(CF_3SO_3)_3$. The spectra of **81** (*S*) and **82** (*R*) were mirror images of one another, confirming structural isomerism and the enantiomeric purity of each in solution (see Figure 2.8 (a)). Positive bands were centred at λ = 205 nm, 229 nm and 286 nm, with a broad shoulder at 250 nm, and a negative band occurred at λ = 221 nm for the *S* enantiomer **81** while the opposite CD spectrum was observed for the *R* enantiomer **82**.

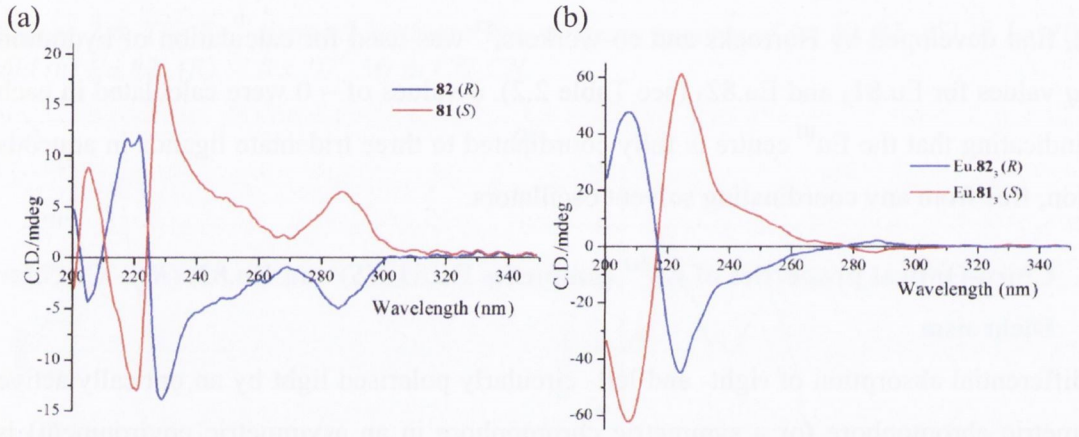

Figure 2.8. *Circular dichroism spectra of ligands* ***81*** *(S) and* ***82*** *(R) (2 x 10^{-5} M) recorded in CH_3CN at RT (a) before and (b) after the addition of 0.33 equiv. of $Eu(CF_3SO_3)_3$ - note that slight discrepancies in intensities can be derived from differences in concentrations.*

Retention of chirality upon complex formation *in situ* was confirmed by the CD spectra of Eu.**81**$_3$ (*S*) and Eu.**82**$_3$ (*R*) where their circular dichroism bands were equal in magnitude but opposite in sign (Figure 2.8 (b)). A dramatic change in both CD spectra was exhibited upon complex formation in which a large negative band was located at 208 nm and a large positive band occurred at 225 nm for Eu.**81**$_3$ (*S*). Concomitantly, the band centred at 286 nm experienced a significant decrease in intensity, appearing as a small negative absorption band, following formation of the 1:3 tris chelate Eu.**81**$_3$ (*S*) complex in solution. Concurrently, for the CD spectrum of the corresponding Eu.**82**$_3$ (*R*) complex, a large positive band was located at 208 nm while a large negative band occurred at 225 nm. The absorption band associated with the naphthalene chromophore again experienced a notable decrease in absorption, appearing as a positive band centred at 286 nm.

These profound CD changes upon complexation influenced us to monitor the CD spectra as a function of metal concentration in order to gain further insight into the structural changes of the various species generated in the self-assembly process. The overall changes in the CD spectra of **81** (*S*) and **82** (*R*) upon titrating with increasing concentrations of $Eu(CF_3SO_3)_3$ (from 0 – 4 equiv.) in CH_3CN at RT are shown below in Figure 2.9.

These studies illustrate that the most notable changes occur upon the formation of the 1:3 M:L species in solution. A significant enhancement in the relative intensity of absorption was exhibited by the band located at 229 nm, with it being slightly shifted to 225 nm after the addition of 0.33 equiv. of $Eu(CF_3SO_3)_3$ for ligand **81** (*S*) (see Figure 2.9 (a)). Between additions 0→0.33 equiv. a disappearance in the negative band centred at 221 nm occurred which was accompanied by the emergence of a negative signal located at 208 nm. With further aliquots of Eu^{III} a decrease in absorption intensity was evident for these bands at 208 nm and 225 nm suggesting a change in ligand conformation and a shift in stoichiometry towards the 1:2 and 1:1 species – both species which consequently possess different structural integrity to that of their 1:3 counterpart. An opposite trend was displayed by **82** (*R*) (Figure 2.9 (b)), verifying the enantiomeric structural relationship between the two systems.

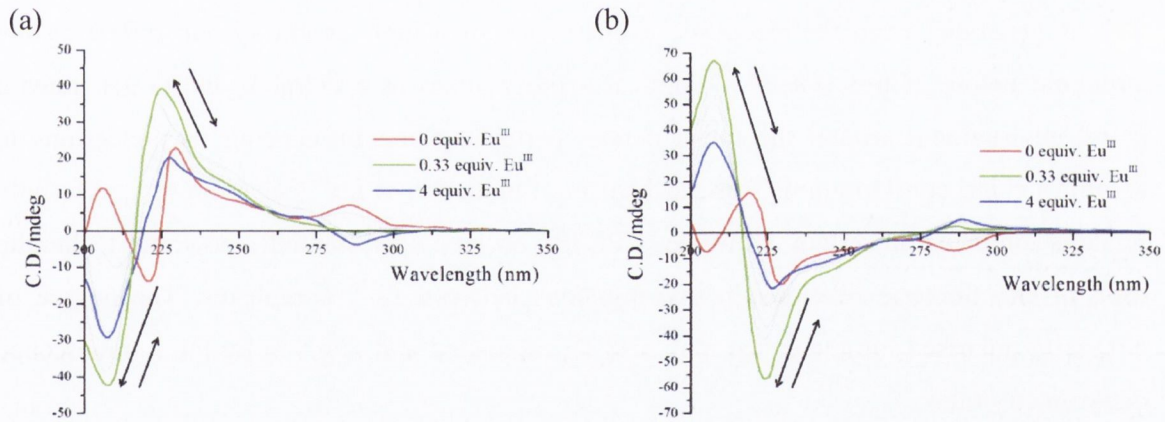

Figure 2.9. *The overall changes in the circular dichroism spectrum of (a)* ***81*** *(S) (3.2 x 10^{-5} M) and (b)* ***82*** *(R) (3.7 x 10^{-5} M) upon titrating against increasing concentrations of $Eu(CF_3SO_3)_3$ (0→4 equiv.) in CH_3CN at RT.*

Exciton coupling features arise in CD spectra when chromophores, which possess chiral disposition, are brought into close spatial proximity and their excited states are coupled together to give excitonic states.[255] A bisignate curve, termed an exciton couplet, in the CD spectrum is indicative of this phenomenon and arises because electronic transitions of the excitonic states are excited to different degrees by right and left circularly polarised light.[255] Parker and co-workers have investigated the use of these same chiral naphthalene antennae (as well as the 2-isomers) in C_4 symmetry based tetranaphthyl based cyclen ligands and Eu^{III} complexes.[256] Although the structures are quite different to those presented herein, some

similarities exist; enabling us to draw some correlations between our results and those obtained in Parker's studies. First, both results indicate the presence of single chiral stereoisomers in solution for the ligands and second both show the appearance of distinctive bisignate profiles upon formation of the metal ion complexes with crossover points at 218 nm, which, as mentioned above, suggesting the occurrence of exciton coupling between the naphthyl chromophores.[256]

2.6 Chiro-Optical properties of Eu^{III} complexes Eu.81_3 (*S*) and Eu.82_3 (*R*) - Circularly Polarised Luminescence (CPL)

Analogous to CD, circularly polarised luminescence (CPL) is the differential emission of right circularly polarised light versus left circularly polarised light by chiral luminescent molecular systems.[257] The main parameter encountered in CPL measurements is the emission circular intensity differential (ECID) and is given by:

Equation 6: $$\Delta I(\lambda) = I_L(\lambda) - I_R(\lambda)$$

where I_L and I_R denote left and right circularly polarised light emission intensity, respectively. CPL is generated from the electronic excited state of a luminescent system reflecting the structural nature of this state. Ln^{III} optical activity arises as a chiral ligand(s) generates a chiral environment around the metal centre, perturbing and influencing its *f* electrons to assume a chiral configuration. This mechanism of induction of Ln^{III} *f* electron optical activity remains somewhat uncertain. However, CPL has become a substantially powerful technique used in enantiomeric relationship investigations between Ln^{III} complexes. The degree of circularly polarised luminescence may also be calculated and is given by the luminescence dissymmetry ratio:

Equation 7: $$g_{lum} = \frac{2\Delta I}{I}$$

where ΔI is the difference in the intensities of left and right circularly polarised emissions and I is the total emission intensity.[134,257-259]

CPL spectra of complexes Eu.**81**$_3$ (*S*) and Eu.**82**$_3$ (*R*) were recorded in CH_3CN at the Department of Chemistry, University of Glasgow, in collaboration with Prof. Robert Peacock (as were all CPL measurements within this thesis) to evaluate whether chirality had been transferred from the ligands to the Eu^{III} centre upon complexation and to determine if the metal ion was sitting in a chiral environment. The CPL spectra of complexes Eu.**81**$_3$ (*S*) and Eu.**82**$_3$ (*R*) displayed chiral Eu^{III}-centred emission with positive and negative bands

representative of deactivation from the $^5D_0$ excited state to the ^7F_J ground states (J = 0-4) (Figure 2.10). Opposite trends were observed for each transition, evidencing that the Eu^{III} metal was residing in a chiral environment of opposite handedness in each case.

Comparison of these CPL spectra with those obtained previously in our laboratory for the parent structures Eu.**56**$_3$ and Eu.**57**$_3$, for which the crystal structures of the 1:3 complexes are known, allowed us to assign the absolute stereochemistry of these self-assemblies as being Λ and Δ for Eu.**81**$_3$ (*S*) and Eu.**82**$_3$ (*R*), respectively.[93] Dissymmetry factor values (g_{lum}) were also determined for these complexes with values of -0.18 and 0.11 and 0.18 and -0.10 calculated for the ΔJ = 1 and ΔJ = 2 transitions for Eu.**81**$_3$ (*S*) and Eu.**82**$_3$ (*R*), respectively (Table 2.3).

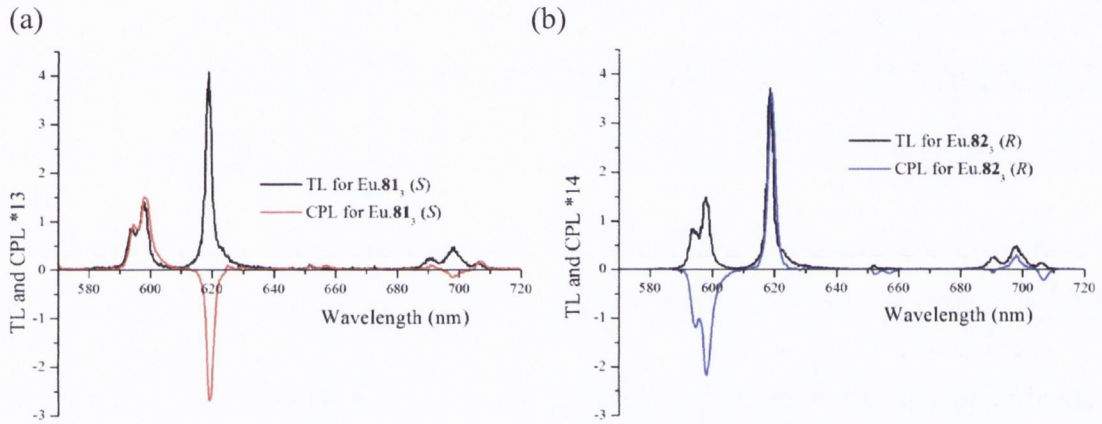

Figure 2.10. *Total Eu^{III}-centred emission and CPL spectra of complexes (a) Eu.**81**$_3$ (S) and (b) Eu.**82**$_3$ (R) recorded in CH_3CN (excitation at λ = 281nm).*

The g_{lum} values obtained for the ΔJ = 1 and ΔJ = 2 transitions of Eu.**81**$_3$ (*S*) and Eu.**82**$_3$ (*R*) complexes were slightly lower to those evaluated for Eu.**56**$_3$ and Eu.**57**$_3$ (-0.24 and 0.25 and 0.22 and -0.26 for the ΔJ = 1 and ΔJ = 2 transitions for Eu.**56**$_3$ and Eu.**57**$_3$, respectively)[187] which might reflect the unsymmetrical nature of complexes Eu.**81**$_3$ (*S*) and Eu.**82**$_3$ (*R*) in comparison to the symmetrical complexes Eu.**56**$_3$ and Eu.**57**$_3$.

Table 2.3. *Summary of dissymmetry factors obtained for Eu.**81**$_3$ (S) and Eu.**82**$_3$ (R) in CH_3CN.*

Complex	(g_{lum}) 598 nm	(g_{lum}) 619 nm
Eu.**81**$_3$	-0.18	0.11
Eu.**82**$_3$	0.18	-0.10

2.7 Solution studies on the Eu^{III}-directed self-assembly of 81 (*S*) and 82 (*R*) in CH_3CN

A series of UV-visible absorption and luminescence photophysical titrations were also conducted in CH_3CN in order to investigate the self-assembly of ligands **81** and **82** with Eu^{III} *in situ*. This procedure involves monitoring the changes in the ligand UV-visible absorption spectrum and the evolution of Eu^{III}-centred emission upon the addition of known equiv. aliquots of $Eu(CF_3SO_3)_3$ to a solution of either **81** or **82**. By fitting this data using the non-linear regression analysis program SPECFIT, species stoichiometry and their corresponding binding constant values may be elucidated.

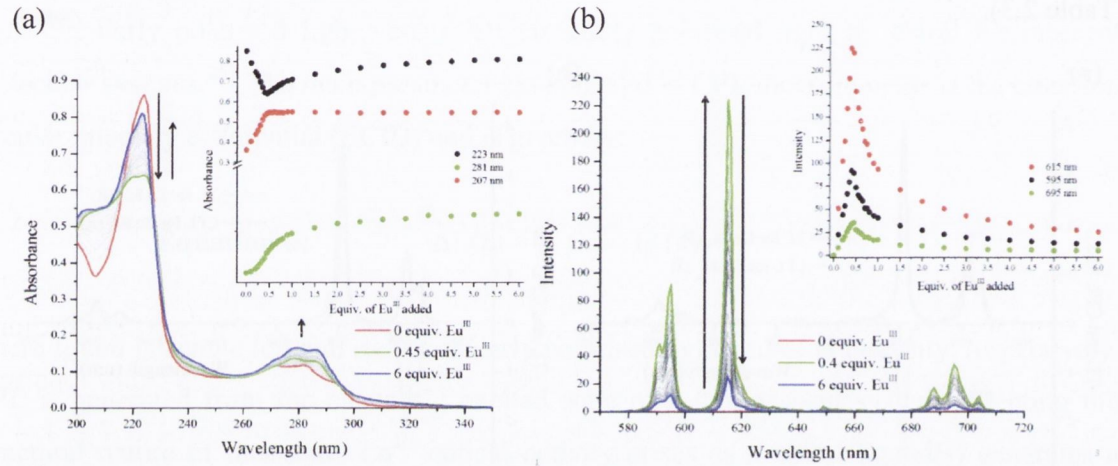

Figure 2.11. *The overall changes in the (a) UV-visible absorption spectra and (b) Eu^{III}–centred phosphorescence spectra upon titrating* ***81*** *(1 x 10^{-5} M) against $Eu(CF_3SO_3)_3$ (0→6 equiv.) in CH_3CN at RT.* ***Inset****: corresponding experimental binding isotherm of (a) absorbance at λ = 223 and 281 nm and (b) Eu^{III} phosphorescence emission intensity at λ = 595, 615 and 695 nm.*

The overall changes observed in the UV-visible absorption spectrum of **81** follwing the addition of increasing concentrations of Eu^{III} are displayed in Figure 2.11 (a). The UV-visible absorption spectrum of ligand **81** consists of a long wavelength absorption band centred at λ_{max} = 281 nm (ε = 8969 M^{-1} cm^{-1}). As mentioned above, this band represents the $S_0 \rightarrow S_1$ $\pi - \pi^*$ transition of the antenna moiety presenting hyperfine structure with two shoulders located at 271 nm and 293 nm while the higher energy absorption band was again evident at λ_{max} = 223 nm, which is assigned to the $S_0 \rightarrow S_2$ $\pi - \pi^*$ transition. Significant changes were observed in the UV-visible absorption spectra upon increasing concentrations of Eu^{III}, including the formation of several isosbestic points at 216, 226 and 294 nm, respectively. A hypochromatic effect was experienced by the band located at λ_{max} = 223 nm up until the addition of 0.45 equiv. of $Eu(CF_3SO_3)_3$, as can be observed from the binding isotherm graph (Figure 2.11 (a) inset). Subsequent additions gave rise to a small absorption increase between

0.45→1 equiv. of Eu^{III} followed by an absorbance plateau at higher metal concentrations. These changes are indicative of equilibrium displacement and evolution of different stoichiometric species in solution as the Eu^{III} concentration is increased. Concurrently, an enhancement in absorption in the band centred at λ_{max} = 281 nm was evident upon Eu^{III} additions between 0→1 equiv.. The peak centred at λ = 281 nm was shifted to 278 nm while the shoulder, located at λ = 293 nm, was also shifted; occuring at 285 nm following the addition of 1 equiv. of $Eu(CF_3SO_3)_3$. At higher metal concentrations no noticeable changes were observed at this absorption band.

The fluorescence emission spectrum of ligands **81** and **82** was very weak being affected to only a small extent throughout the self-assembly process (see Appendix Figure A2.5 for overall changes in the fluorescence spectra of ligand **81**). Therefore, only the emergence of Eu^{III}-centred emission from each solution was investigated throughout the titration since these changes were substantial enough to analyse. This was achieved by exciting into the sensitising moiety at λ_{ex} = 281 nm and measuring the delayed Eu^{III}-centred luminescence. A gradual enhancement in a typical Eu^{III}-centred luminescence spectrum was observed upon the addition of 0→0.4 equiv. of Eu^{III} with characteristic transitions appearing at λ = 595 nm, 615 nm, 650 nm and 695 nm, respectively (Figure 2.11 (b)). These emission bands represent deactivation from the Eu^{III} $^5D_0$ excited state to the ^7F_J ground states, where J = 1 – 4, signifying effective energy transfer from the ligand to the metal centre and thus successful complexation in solution. Further additions of Eu^{III} result in a sharp decrease in the emission intensity of these transitions with an eventual plateau exhibited by the self-assembly system at metal equiv. greater than 1 (Figure 2.11 (b)). The above quenching results display a shift in species equilibrium as the titration proceeds suggesting that the most emissive 1:3 (M:L) species (Eu.$\mathbf{81}_3$) evolves in solution between additions 0→0.4 equiv. with the lesser emissive 1:1 species (Eu.**81**) predominating in solution at higher metal concentrations.

The overall changes observed in both the UV-visible absorption and the luminescence spectra upon titrating the corresponding *R* enantiomer **82** with increasing concentrations of Eu^{III} were identical to that observed for **81**, as shown in Appendix Figure A2.6, confirming that both enantiomers behave in the same manner in CH_3CN solution. For verification of the stoichiometry of the various species present in solution this data was fit by means of non-linear regression analysis as described below.

2.8 Fitting of titration data and determination of complex stability constants

In order to gain a better understanding of the self-assembly process in solution the global changes in both the UV-visible absorption and Ln^{III}-centred emission spectra were fit by using the non-linear regression analysis program SPECFIT.[260,261] SPECFIT uses a non-linear

least squares regression method to minimise the differences between experimental data obtained from spectroscopic data and theoretical data calculated from a proposed model. The stepwise equilibrium equations used as a model for the formation of the various Ln^{III}-directed self-assembly species in solution encountered in this chapter and subsequent chapters can be expressed as follows:

$$M + L \underset{}{\overset{K_{11}}{\rightleftharpoons}} ML \qquad K_{11} = \frac{[ML]}{[M][L]}$$

$$ML + L \underset{}{\overset{K_{12}}{\rightleftharpoons}} ML_2 \qquad K_{12} = \frac{[ML_2]}{[ML][L]}$$

$$ML_2 + L \underset{}{\overset{K_{13}}{\rightleftharpoons}} ML_3 \qquad K_{13} = \frac{[ML_3]}{[ML_2][L]}$$

Thus the cumultative stability constant β_{13} can be expressed as the product of the step-by-step equilibrium constants given by:

$$\beta_{13} = K_{11} \times K_{12} \times K_{13}$$

The general equation for:

$$mM + nL \underset{}{\overset{\beta_{13}}{\rightleftharpoons}} M_mL_n$$

can be written as:

Equation 8: $$\beta_{mn} = \frac{[M_mL_n]}{[M]^m[L]^n}$$

Stability binding constants are usually quoted as their logarithmic values however and as such, shall be reported as $\log\beta_{mn}$ throughout this thesis.

Analysis of the UV-visible absorption data pointed to the presence of four absorbing species in solution, namely the ligand itself (**81**), the 1:1 (Eu.**81**), the 1:2 (Eu.$\mathbf{81}_2$) and the 1:3 (Eu.$\mathbf{81}_3$) species. The speciation distribution graph obtained following fitting the UV-visible absorption titration data, (Figure 2.12 (a)), indicates that upon the addition of 0→0.4 equiv. of Eu^{III} the predominant species in solution was the 1:3 (Eu.$\mathbf{81}_3$) species with a binding constant value of $\log\beta_{13} = 20.9 \pm 0.3$ calculated.

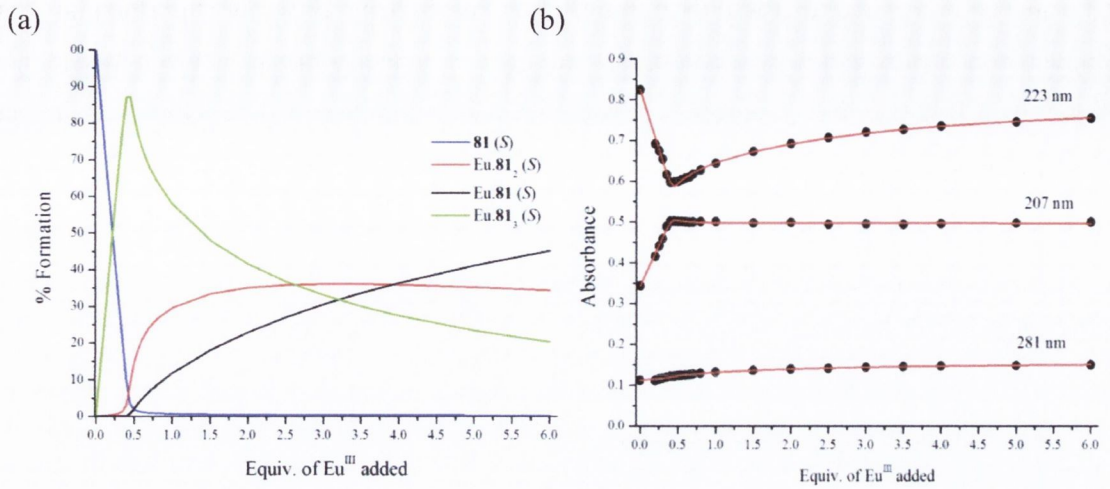

Figure 2.12. *(a) The speciation distribution diagram obtained from UV-visible absorption titration data fit (upon titrating ligand* ***81*** *against Eu(CF_3SO_3)$_3$ in CH_3CN) and (b) the fit of the experimental binding isotherms using the non-linear regression analysis program SPECFIT.*

A speciation distribution percentage value of 87% for the Eu.**81**$_3$ species after the addition of 0.4 equiv. of Eu^{III} was evident, accounting for the significant changes occurring at this point in the titration. Additional aliquots of Eu^{III} shifts the equilibrium towards the formation of a second 1:2 Eu.**81**$_2$ species, with it being formed in 30% yield following the addition 1 equiv. of Eu^{III}, with a binding constant value of $\log\beta_{12} = 13.8 \pm 0.0$ calculated. These results direct us to the conclusion that between these two equivalence values, equilibrium is distributed between the formation of both species, consequently giving rise to the maximum changes in absorbance occurring in this region. Subsequent aliquots gave rise to the formation of the 1:1 Eu.**81** species with it being formed in 37% yield after the addition of 4 equiv. of the metal ion, with a binding constant value of $\log\beta_{11} = 6.6 \pm 0.2$. Binding isotherms for this data analysis confirmed that a good fit was obtained. A summary of all the binding constants calculated for this chapter are found in Table 2.7.

Analysis of the UV-visible absorption data following the titration of **82** with $Eu(CF_3SO_3)_3$ gave rise to the elucidation of binding constant values of $\log\beta_{11} = 6.7 \pm 0.2$, $\log\beta_{12} = 13.8 \pm 0.0$ and $\log\beta_{13} = 20.5 \pm 0.3$ for the Eu.**82**, Eu.**82**$_2$ and the Eu.**82**$_3$ species respectively, (see Appendix Figure A2.7), confirming the same behaviour for both enantiomers in solution.

The solution formation of Eu.L$_n$ (where L = **81**/**82** and n = 1-3) was also analysed by fitting the changes in the characteristic Eu^{III}-centred emission spectra. The matching of the binding isotherms with the theoretical fit, (Figure 2.13 (b), evidenced that a good fit was obtained while, as mentioned above, a summary of all the binding constants calculated for this chapter are found in Table 2.7.

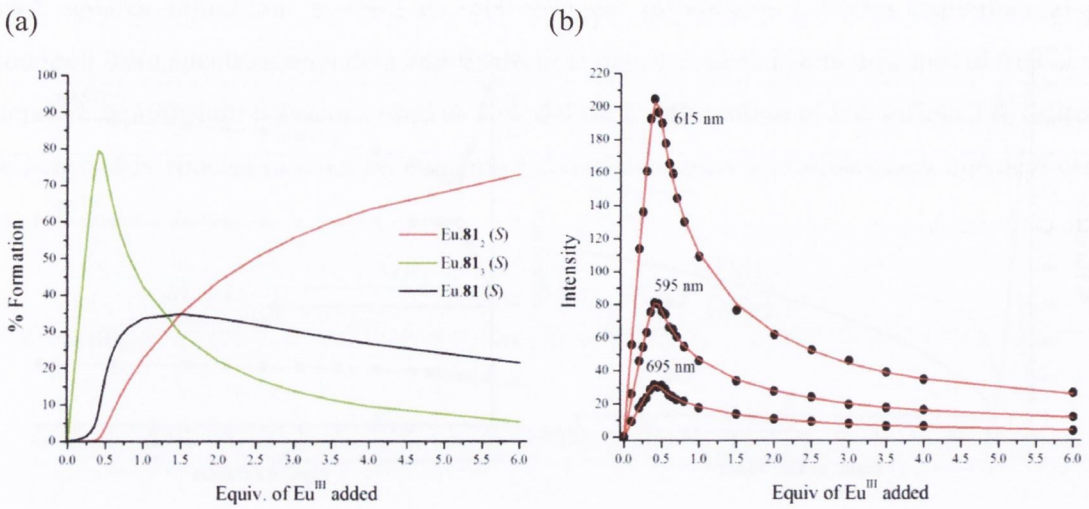

Figure 2.13. *The speciation distribution diagram obtained from the luminescence titration data fit (upon titrating ligand **81** against $Eu(CF_3SO_3)_3$ in CH_3CN) and (b) the fit of the experimental binding isotherms using the non-linear regression analysis program SPECFIT.*

From the speciation distribution diagram shown in Figure 2.13 (a) it is evident that an almost identical trend was observed to that shown following fitting of the UV-visible absorption titration data. A speciation distribution formation value of 80% was observed for the Eu.**81**$_3$ species after the addition of 0.4 equiv. of Eu^{III} with a binding constant value of $\log\beta_{13} = 19.9 \pm 0.2$. Subsequent additions of Eu^{III} is again shown to give rise in a shift in equilibrium with the evolution of the lesser emissive 1:2 Eu.**81**$_2$ species evident at higher Eu^{III} concentrations. A speciation distribution formation value of 34% was observed for this species after the addition of 1 equiv. of Eu^{III} with a binding constant value of $\log\beta_{12} = 13.3 \pm 0.2$ calculated. The least emissive 1:1 Eu.**81** complex then becomes the most predominant in solution with it being formed in 63% following the addition of 4 equiv. of Eu^{III}, with a binding constant of $\log\beta_{11} = 6.7 \pm 0.1$.

Fitting of the overall changes in the luminescence spectra for the titration of **82** with Eu^{III} again indicated an identical behaviour for **82** (see Appendix Figure A2.8) with binding constant values of $\log\beta_{11} = 6.7 \pm 0.2$, $\log\beta_{12} = 14.3 \pm 0.3$, $\log\beta_{13} = 21.9 \pm 0.4$ obtained for Eu.**82**, Eu.**82**$_2$ and the Eu.**82**$_3$ species respectively, again demonstrating the similar behaviour for both systems in solution.

2.9 Langmuir monolayer formation of Eu.81$_3$ (*S*) and Eu.82$_3$ (*R*) complexes

In order to assess if complexes Eu.**81**$_3$ and Eu.**82**$_3$ were suitable for forming Langmuir monolayers at an air-water interface it was vital to first examine monolayer formation of ligands **81** and **82** to ensure that the hydrophilic/hydrophobic ratio chosen in the design of the ligands induced sufficient amphiphilicity. This process was carried out in collaboration with Dr. Laszlo Mercs and Prof. Martin Albrecht in the School of Chemistry and Chemical

Biology, Belfield, UCD. The process involved the spreading of a 20 μL sample of ligand **81** (6.62×10^{-4} M) (or ligand **82**) in $CHCl_3$ onto the surface of a water subphase at RT. Solvent was allowed to evaporate before the barriers were closed (at a speed of 6 mm min^{-1}) and the surface pressure was closely monitored. A typical surface pressure-area isotherm graph was obtained for both ligands (Figure 2.14 (a)).

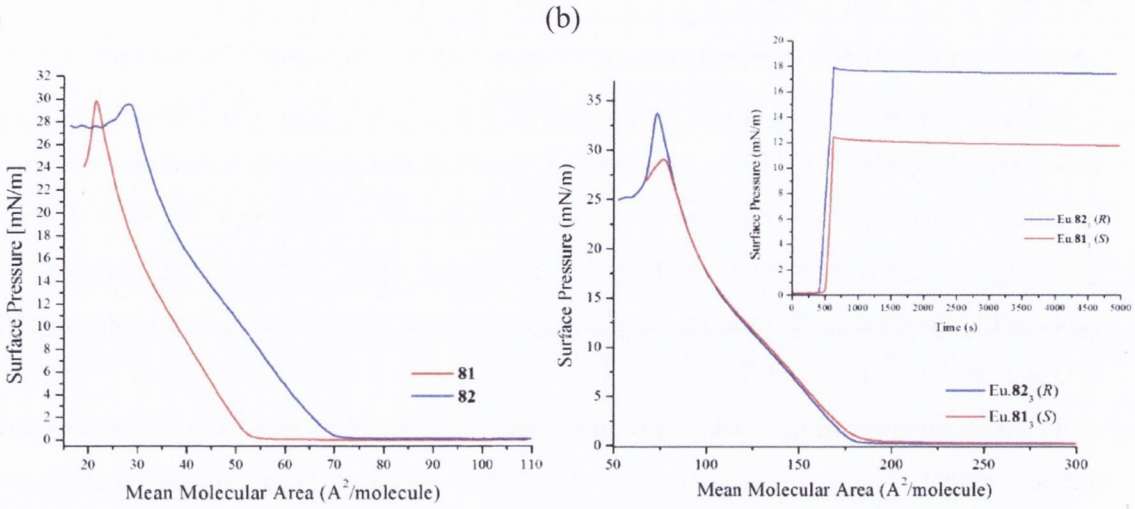

Figure 2.14. *Surface pressure-area isotherms of (a) ligands **81** (S) and **82** (R) and (b) Eu.**81**$_3$ (S) and Eu.**82**$_3$ (R).* ***Inset****: (b) surface pressure-time profiles for Langmuir monolayers of Eu.**81**$_3$ (S) and Eu.**82**$_3$ (R).*

Upon area decrease an exponential increase in surface pressure evidenced the different phase transitions, *i.e.* gaseous (G), liquid expanded (LE), liquid condensed (LC) and film collapse. These results confirmed monolayer formation at the air-water interface for **81** and **82**. A G phase state was observed at areas greater than 55 $Å^2$ up until a thin monomolecular film of ligand **81** began to form and existed in the LE phase within the area range 55 – 33 $Å^2$, as is evident from the aforementioned sharp increase in surface pressure between these two values. As this area was further decreased interfacial molecules began to interact, becoming more densely packed and forming a LC phase, known as a Langmuir monolayer, between the area range 26 – 22 $Å^2$. The exact nature of the Langmuir monolayer is unknown, however, film collapse occurs at 30 mN m^{-1} corresponding to an area occupancy of 22 $Å^2$ for ligand **81**, while film collapse for **82** occurs at 29 mN m^{-1} (corresponding to an area occupancy of 28 $Å^2$). This is assigned to the cross-sectional area of approximately one alkyl chain[207] so it can be assumed that in this LC state the polar head groups are orientated towards the water phase, strongly interacting with one another, with their hydrophobic alkyl chains orientated perpendicular to the subphase plane. A similar profile was observed for ligand **82** (see Figure 2.14 (a)) confirming the ability of both ligands to self-assemble into Langmuir monolayers at the air-water interface. Once it had been established that ligands **81** and **82** had the ability to

self-assemble in this manner it was predicted that complexes Eu.**81**$_3$ and Eu.**82**$_3$ would be capable of exhibiting this property also.

Monolayer formation of complexes Eu.**81**$_3$ and Eu.**82**$_3$ was monitored in an identical manner to that described above. A 20 μL volume of Eu.**81**$_3$ (2.5 x 10^{-4} M) (or complex Eu.**82**$_3$), using $CHCl_3$:MeOH (9:1) as the spreading solvent, was spread onto the water subphase at RT and solvent allowed to evaporate. A surface pressure-area isotherm was obtained upon barrier compression (at a speed of 6 mm min^{-1}), indicating successful monolayer formation for Eu.**81**$_3$ and Eu.**82**$_3$, see Figure 2.14 (b). The various phase transitions were observed as the area was reduced and the material was compressed into an organised monolayer in both cases. Eu.**81**$_3$ amphiphiles displayed disordered gaseous behaviour at areas greater than 160 $Å^2$. However, upon further compression a steep exponential increase in surface pressure was observed (LE phase) where the molecules begin to organise by self-assembling at the interface. A phase transition to the LC phase was signified by changes in the surface pressure-area isotherm at an area of 90 $Å^2$ where surface pressure steeply increased upon organisation of the molecules. Film collapse takes place at a surface pressure of 29 mN m^{-1} for Eu.**81**$_3$ (while film collapse for Eu.**82**$_3$ occurs at 34 mN m^{-1}) corresponding to a cross-sectional area occupancy for approximately three alkyl chains. We can therefore assume that the polar Eu^{III} coordination spheres are closely packed and orientated towards the water phase with the hexadecyl chains pointing out, perpendicular to the plane of the subphase.

To assess the stability of the Langmuir monolayers of Eu.**81**$_3$ and Eu.**82**$_3$ the barriers were kept at a fixed position for an extended period of time (>1 h). Surface pressure was monitored over time, as shown in Figure 2.14 (b) inset, confirming film stability as there was no significant decrease in surface pressure evident. These results indicate that the monolayers of Eu.**81**$_3$ and Eu.**82**$_3$ display excellent stability properties. Having obtained these promising results it was our intention to then apply the Langmuir-Blodgett technique to immobilise our complexes onto a solid support allowing us to take our studies from solution to the solid state in a highly controllable, organised manner.

2.10 Langmuir-Blodgett film formation of Eu.81$_3$ (*S*) and Eu.82$_3$ (*R*) complexes

As it was necessary to use a quartz solid support for eventual spectroscopic investigations, it was anticipated that deposition would occur through hydrophilic interactions between the polar head groups of the amphiphilic complexes and the surface of the quartz. As described in chapter one, solid substrate hydrophobicity/hydrophilicity dictates whether dipping begins with the substrate positioned above or submersed below the monolayer. As the surface of the quartz slide (10 mm x 1 mm x 35 mm) is hydrophilic the slide was lowered and submerged

into the subphase before the amphiphilic complex was spread onto the surface. The amphiphile was then organised into the LE phase (by compressing the barriers until a surface pressure of 12 mN m^{-1} was obtained (for Eu.**81**$_3$)) and allowed to stabilise (20 mins) before emersion of the slide by means of an upward stroke (at a speed of 4 mm min^{-1}) resulted in monolayer transfer.

Films possessing dimensions of 1 cm (h) x 1 cm (w) were successfully transferred and attached to the slide with transfer ratios of ~ 1, indicating high quality transfer from the subphase to the substrate with excellent order and uniformity. As this deposition process had not yet been investigated for complexes of this nature it was necessary to 'fine tune' the deposition technique to elucidate the resulting architecture type. That is, as deposition architecture type could not be predicted a number of trial measurements were required before the type of deposition was established and determined as being Z-type. It was critical that the quartz slide be thoroughly cleaned prior to monolayer transfer by means of submersion in piranha solution (3:1 concentrated sulfuric acid to 30% hydrogen peroxide solution) to ensure successful immobilisation of the Langmuir-Blodgett film.

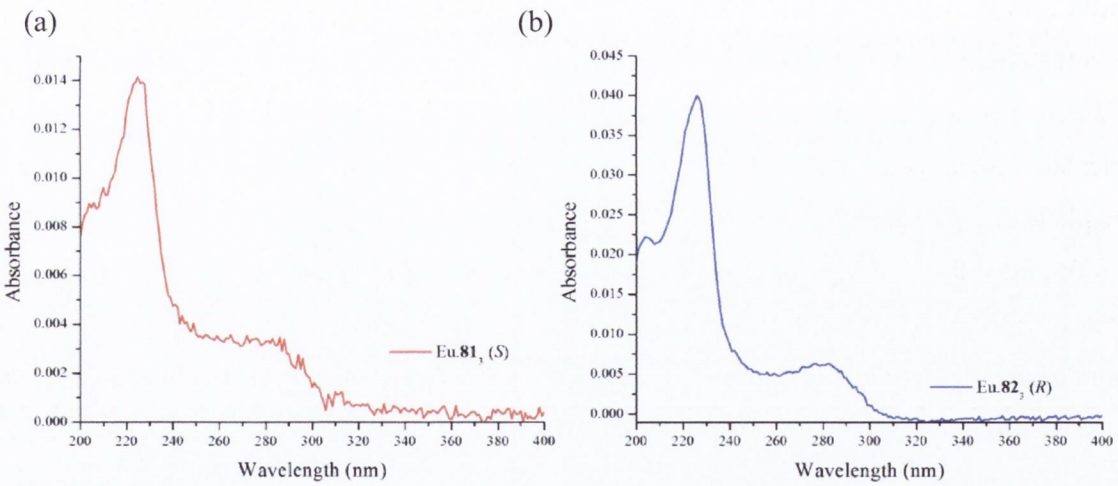

Figure 2.15. *UV-visible absorption spectra of (a) Eu.**81**$_3$ (S) and (b) Eu.**82**$_3$ (R) immobilised on quartz slide.*

The photophysical properties of the immobilised Eu.**81**$_3$ and Eu.**82**$_3$ monolayers (two monolayers, *i.e.* one monolayer attached to each side of the slide) were next evaluated (see Figure 2.15 - Figure 2.18). The UV-visible absorption spectrum of Langmuir-Blodgett films of Eu.**81**$_3$ and Eu.**82**$_3$ were recorded, as shown in Figure 2.15 displaying an identical profile to that observed for these systems in solution with two λ_{max} bands located at 223 nm and 281 nm. Upon excitation at λ = 281 nm Eu^{III}-centred time-delayed luminescence was also exhibited by both immobilised films with bands centred at λ = 593 nm ($^5D_0 \rightarrow {}^7F_1$), 615 nm ($^5D_0 \rightarrow {}^7F_2$) and 695 nm ($^5D_0 \rightarrow {}^7F_4$), as shown in Figure 2.17.

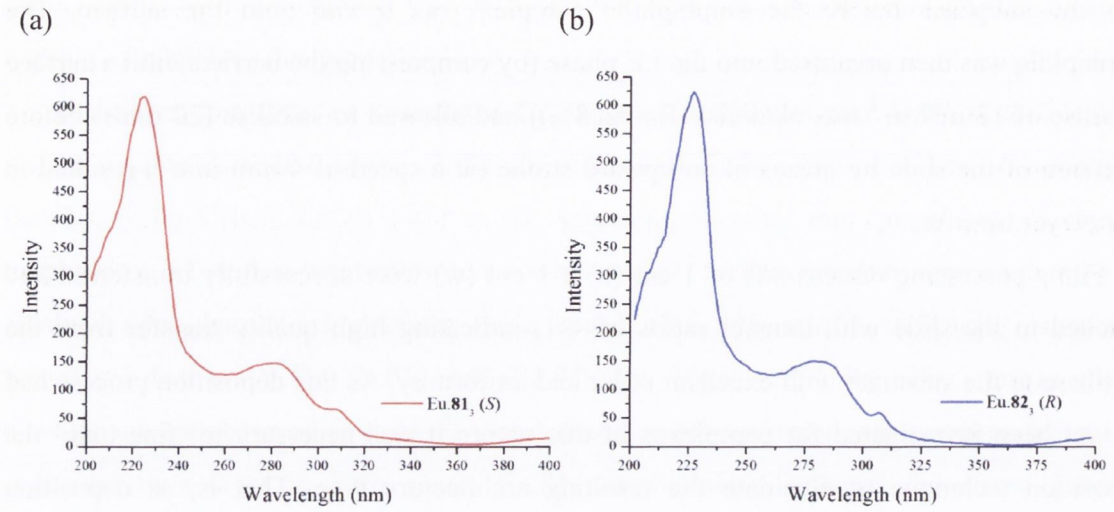

Figure 2.16. *Excitation spectra (emission at λ_{em} -= 615 nm) of (a) Eu.**81**$_3$ (S) and (b) Eu.**82**$_3$ (R) immobilised on quartz slide.*

These results, in addition to the excitation spectra recorded for both LB films (see Figure 2.16) which closely resemble the UV-visible absorption spectra, clearly confirms successful sensitisation of the Eu^{III} centre by the ligand in the solid state and thus retention of the desirable photophysical properties of the self-assembled system.

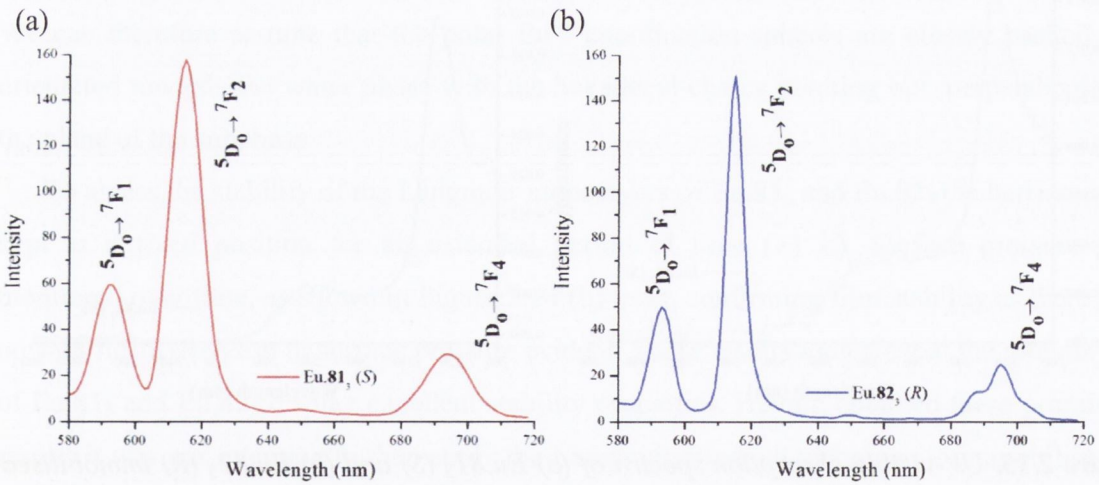

Figure 2.17. *Eu^{III}-centred phosphorescence spectra of (a) Eu.**81**$_3$ (S) and (b) Eu.**82**$_3$ (R) immobilised on quartz slide (excitation at λ_{ex} = 281 nm).*

The enantiomeric relationship between the monolayers was also investigated using CD and CPL spectroscopy. Unfortunately a CD signal was not detectable from either LB film however CPL spectra from the two monolayers displayed chiral Eu^{III}-centred luminescence each with signals, corresponding to the ΔJ = 1 and 2 transitions, of equal amplitude but opposite sign (Figure 2.18 (a)). The band representing the ΔJ = 1 transition appears as a positive signal for the Eu.**81**$_3$ monolayer but as a negative signal for the Eu.**82**$_3$ monolayer.

The opposite is true for the signal associated with the $\Delta J = 2$ transition with it appearing as a negative signal for the Eu.**81**$_3$ complex but positive for Eu.**82**$_3$. These results confirm that the monolayers are in fact enantiomeric with each Eu^{III} centre reporting the chiral nature of the local environment. Furthermore, dissymmetry factor values were determined for the $\Delta J = 1$ and 2 transitions for the immobilised Eu.**82**$_3$ layer with values of g_{lum} =0.161 and 0.068 for $\Delta J = 1$ and $\Delta J = 2$, respectively. This slight difference from the solution results is most likely related to the formation of the LB films in which the packing of the molecules may have had an effect on the local coordination environment of the Ln^{III} or, it also may be due to the effect of the solid surface.

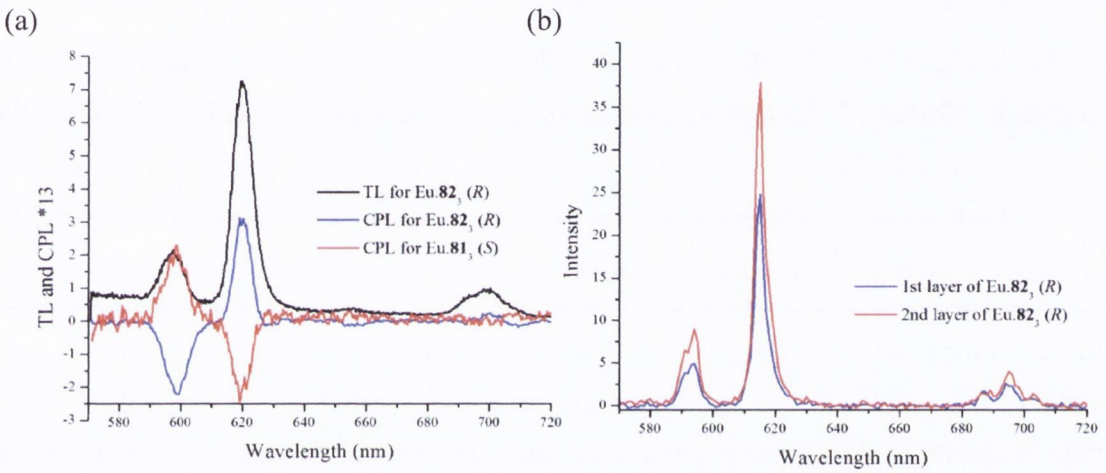

Figure 2.18. *(a) Total Eu^{III}-centred emission (from Eu.**82**$_3$ (R)) and CPL spectra from monolayer of Eu.**81**$_3$ (S) and (b) Eu.**82**$_3$ (R) immobilised on quartz solid support (excitation at λ = 281nm). (b) Eu^{III}-centred luminescence exhibited from one monolayer and two monolayers of Eu.**82**$_3$ (R).*

The excited-state decay of Eu^{III}-centred emission was also determined for immobilised monolayers of Eu.**81**$_3$ and Eu.**82**$_3$ and in both cases were best fit to a bi-exponential decay function indicating the presence of possibly two luminescent species within each film. Lifetimes values of 1.502 ms and 0.35 ms were calculated for Eu.**81**$_3$ while values of 1.477 ms and 0.0988 ms were obtained for Eu.**82**$_3$. The longer excited lifetime values (1.502 and 1.477 ms) are comparable to those obtained in solution in which q values of 0 were calculated. This confirms the presence of the fully saturated complex species within the LB films. The second, shorter lived species, may be due to a partial dissociation of the complex during the LB process. Interestingly these films were found to be stable under ambient conditions over a period of many months.

It was also possible to transfer multiple layers of films of the Eu.**82**$_3$ complex onto a quartz slide with transfer ratios close to unity obtained for the deposition of the first two monolayers. As demonstrated in Figure 2.18 (b) emission was enhanced upon the deposition

of a second monolayer (*i.e.* two immobilised monolayers on each side of the solid substrate). The attachment of a third layer however did not render uniformity with transfer ratios reflecting the deterioration of transfer efficiency as a subsequent monolayer was coated. Sequential attempts to attach more than three monolayers were unsuccessful as it was noticed that upon emersion of the solid support layers were affixed however as the slide was once again immersed the film was instantly detached.

Due to the relatively weak emissive properties of these films it was not possible to observe the typical red Eu^{III}-centred emission by the naked eye under the UV lamp. These results did however provide a model system evidencing the potential applicability of this technique to Ln^{III}-directed self–assemblies of this type. In more recent times Langmuir and Langmuir-Blodgett films of highly emissive cyclen based complexes have been developed by Dr. Laura K. Truman.[262] Moreover, monolayers of these complexes can be seen under the UV lamp by the naked eye and have also been shown to display dual Eu^{III} and Tb^{III}-centred emission. Furthermore, preliminary studies for the selective sensing of amino acids, by means of monolayer Ln^{III} emission modulation, have proven promising.

2.11 Summary – Visibly emitting Eu^{III}-directed self-assembled systems

The aim of this project was to build upon previous work carried out on the "half-helicate" ligands **79** and **80** by synthesising amphiphilic analogues **81** and **82** for Langmuir monolayer formation at an air-water interface and subsequent immobilisation onto a quartz solid substrate for the generation of solid state Ln^{III} emissive materials.

Compounds **81** and **82** were synthesised and fully characterised, and in addition their molecular structures were determined by X-ray crystallography elucidating their solid state packing interactions. Complexation of ligands **81** and **82** with 0.33 equiv. of Eu^{III} resulted in isolation of luminescent solid state complexes Eu.$\mathbf{81}_3$ and Eu.$\mathbf{82}_3$ with hydration state values of $q \sim 0$ calculated, confirming that the Eu^{III} was indeed residing in a fully saturated coordinative environment bound to three tridentate ligands within the 1:3 complexes. CD and CPL analysis confirmed that the chirality of ligands **81** and **82** was retained and transferred to the Eu^{III} centre upon complexation and that complexes Eu.$\mathbf{81}_3$ and Eu.$\mathbf{82}_3$ exist as a pair of enantiomers, displaying chiral Eu^{III}-centred long-lived emission. Detailed CD titrations gave further insight into the structural changes of the various species generated in the self-assembly process with the most significant changes observed upon the formation of the 1:3 species. The Eu^{III}-directed self-assembly process of both **81** and **82** with $Eu(CF_3SO_3)_3$ was monitored in CH_3CN solution using spectroscopic techniques and illustrated that three stoichiometric species were present in solution (1:1, 1:2 and 1:3), with the 1:3 species predominantly formed upon the addition of approximately 0.4 equiv. of Eu^{III}. Langmuir

monolayers of ligands **81** and **82** and their corresponding complexes Eu.**81**$_3$ and Eu.**82**$_3$ were then prepared and the photophysical properties of the luminescent films investigated. Attachment of the complexes onto a quartz solid substrate was achieved *via* Z-type deposition with good transfer ratios of ~ 1 obtained in both cases. These Langmuir-Blodgett films were found to display Eu^{III}-centred long-lived luminescence while CPL measurements were employed to verify that the luminescence emitted from the films was chiral. Multiple layers of up to two monolayers of Eu.**82**$_3$ were successfully deposited onto the quartz supports with an increase in Eu^{III}-centred emission displayed upon additional monolayer coating. Further layering did not result in high enough quality films to increase the number of LB layers for an increased luminescent signal and eventually gave rise to a simultaneous attachment/detachment process. From these studies it has been shown that complexes of Eu.**81**$_3$ and Eu.**82**$_3$ can be successfully assembled into Langmuir monolayers at an air-water interface and organised into ultra-thin films. The photophysical properties of these surface bound chiral Ln^{III} luminescent assemblies have also been shown to be unaltered upon incorporation into LB films.

2.12 Moving towards NIR emitting Nd^{III} -directed self-assembled systems

The above sections have detailed developments made to novel chiral Eu^{III}-directed self-assemblies and their immobilisation into visibly emitting chiral monomolecular ultra-thin films. The NIR emitting lanthanides, such as Pr^{III}, Yb^{III}, Er^{III}, and Nd^{III}, however offer major advantages over the visibly emitting Ln^{III} for applications in biology,[48] such as in the development of luminescent imaging agents and bioprobes, as the NIR emission (800–1000 nm) is transparent to biological tissue allowing imaging through relatively thick tissue samples. Moreover, from an optical devices point of view, the NIR emissive Ln^{III} can be employed in telecommunications optical networks, again owing to their emission in the transparent window of silica fibers (1000–1600 nm).[62,263-265] Of the NIR emitting lanthanides, Nd^{III} and Er^{III} are particularly interesting as their luminescent behaviour is highly sensitive to the external environment.[62,264,265] In particular, the high density of states in the excited state manifolds of Nd^{III} and Er^{III} ensures that non-radiative quenching of the lanthanide emissive state by associated C–H and O–H oscillators is more important in complexes with these ions than any other Ln^{III}, as they are quenched to a greater extent through closely associated C–H oscillators (in addition to N–H and O–H oscillators).[82,264-267] As well as introducing a strong dependence of luminescence quantum yield and lifetime upon structure, this phenomenon also means that ternary assemblies, involving guests such as biomolecules and complexes, will change the luminescence quantum yields of such species.[268,269] Such assemblies have already been widely exploited in systems where inner

sphere solvation is changed when the assembly is formed.[198,270] However, there is also clear potential to exploit the more subtle effects inherent to the presence of local oscillators in lifetime resolved imaging. For practical sensing application, Nd^{III} complexes are ideal as luminescence quantum yields from Er^{III} complexes in aqueous media tend to be very low as a consequence of the small energy gap between the emissive state and ground state. Only a small number of examples of LB films composed of thermodynamically and kinetically stable Ln^{III} based complexes have been developed to date, as discussed in the chapter one,[234,243] and to the best of our knowledge no examples of NIR emitting Ln^{III} based LB films (or NIR luminescent monolayers) have been developed.

On account of these observations it was therefore our intention to extend our interest to the development of functional Ln^{III} luminescent structures involving NIR emitting Nd^{III}. We set out to form highly organised Langmuir monolayers and LB films in a similar manner to that described above for the Eu^{III} system in which amphiphilic chiral ligands **81** and **82** were again implemented. Studies on these systems were conducted in a similar manner to that described for the Eu^{III}-directed self-assembled systems above and as such are detailed herein.

2.13 Formation of mononuclear tris chelate complexes Nd.81$_3$ (*S*) and Nd.82$_3$ (*R*)

The mononuclear 1:3 Nd^{III} complexes were synthesised by reacting either **81** or **82** with $Nd(CF_3SO_3)_3$ in a 1:3 stoichiometric M:L ratio in HPLC grade CH_3OH. Microwave irradiation was applied to the reaction mixture for 10 mins at 70 °C (see Scheme 2.3). Both Nd.**81**$_3$ and Nd.**82**$_3$ were isolated by vapour diffusion of diethyl ether yielding the desired products, Nd.**81**$_3$ and Nd.**82**$_3$, as white solids in yields of 50% and 59%, respectively.

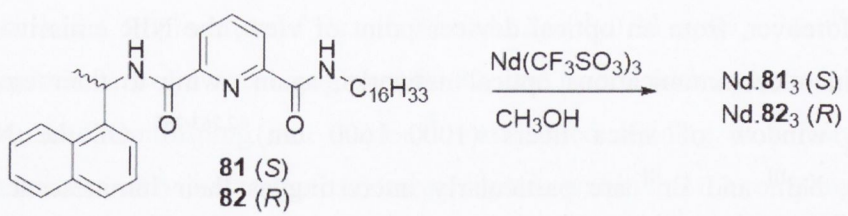

Scheme 2.3. *Preparation of Nd^{III} complexes Nd.**81**$_3$ (S) and Nd.**82**$_3$ (R) carried out under microwave irradiation at 70 °C.*

As shown for Eu.**81**$_3$ and Eu.**82**$_3$ broadening and shifting of signals in the ^1H NMR spectrum (400 MHz, CD_3OD- d_4) (see Appendix Figure A2.9 and A2.10) indicates complexation of the paramagnetic Nd^{III} ion while a shift in IR stretching frequency of the amide carbonyl band (from 1654 cm^{-1} to 1631 cm^{-1} for Nd.**81**$_3$ and from 1650 cm^{-1} to 1633 cm^{-1} for Nd.**82**$_3$) also verified formation of the 1:3 Nd^{III} complexes. Elemental analysis was also employed to confirm complexation in both cases. Neither Nd.**81**$_3$ nor Nd.**82**$_3$ were

detectable by HRMS in the range of solvents investigated (CH_3OH, CH_2Cl_2, CH_3CN), however their 1:2 counterparts were observed again possibly due to complex dissociation at the low concentration required for HRMS analysis (see Appendix Figure A2.11 for calculated and experimental isotopic distribution pattern for Nd.**81**$_3$).

2.14 Photophysical characterisation of complexes Nd.81$_3$ (*S*) and Nd.82$_3$ (*R*)

The photophysical properties of complexes Nd.**81**$_3$ and Nd.**82**$_3$ were evaluated in CH_3CN and CH_3OH, as shown in Figure 2.19 and Appendix Figures A2.12 – 2.16. As illustrated for the analogous Eu^{III} systems Eu.**81**$_3$ and Eu.**82**$_3$ above, the UV-visible absorption spectrum displayed a major absorption band located at λ_{max} = 281 nm, associated with the $S_0 \rightarrow S_1$ π - π^* transition, while a second peak, assigned to the the $S_0 \rightarrow S_2$ π - π^* transition, was centred at λ_{max} = 223 nm, see Figure 2.19 (a).

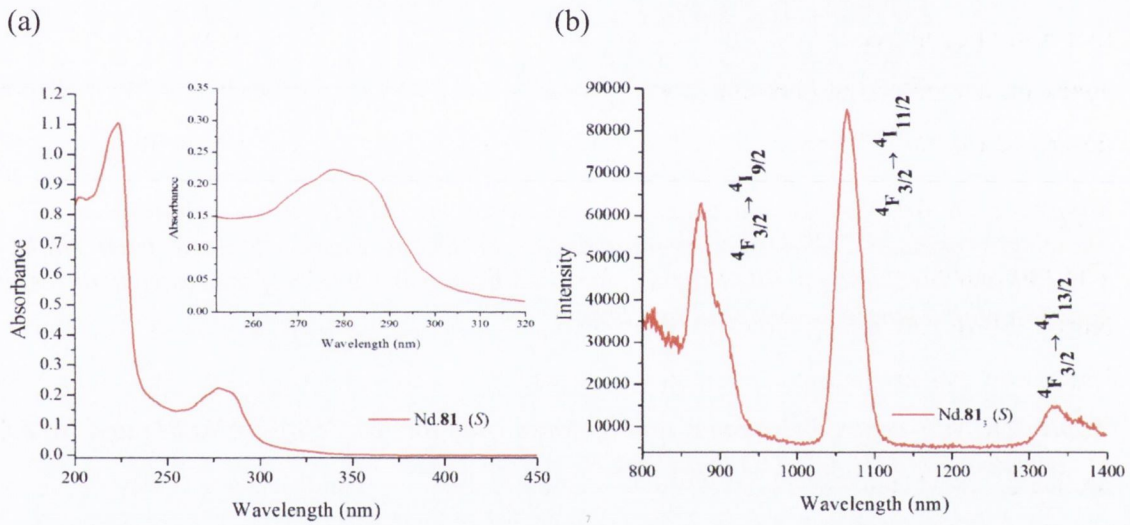

Figure 2.19. *The (a) UV-visible absorption spectra and (b) corrected luminescence spectra of Nd.**81**$_3$ (S) (6.3 x 10^{-6} M) in CH_3CN.*

Characteristic Nd^{III}-centred luminescence was exhibited from both Nd.**81**$_3$ and Nd.**82**$_3$, as shown in Figure 2.19 (b) and Appendix Figures A2.12 (b) and A2.14 – A2.16, following excitation into the naphthalene sensitising moiety at λ_{max} = 281 nm. A typical Nd^{III} line-like emission spectrum was displayed with bands occurring at 880 nm, 1064 nm and 1334 nm, indicative of efficient energy transfer from the chromophore to the Nd^{III} $^4F_{3/2}$ excited state and subsequent deactivation to the ^4I_J ground states (where J = 9/2, 11/2 and 13/2).

Time resolved emission spectra (TRES) were also recorded for both Nd.**81**$_3$ and Nd.**82**$_3$ in CH_3CN, CH_3OH, and CD_3OD as shown in Figure 2.20 (a) and Appendix Figure A2.17. These measurements were conducted in collaboration with Prof. Stephen Faulkner at the University of Oxford in which Dr. Manuel Tropiano assisted with the set-up of the instrument while experiments were primarily carried out by Dr. Jonathan A. Kitchen and

myself. The Nd^{III} luminescence decays (excitation at 337 nm) of the three transitions 880 nm ($^4F_{3/2} \rightarrow {}^4I_{9/2}$), 1064 nm ($^4F_{3/2} \rightarrow {}^4I_{11/2}$), and 1334 nm ($^4F_{3/2} \rightarrow {}^4I_{13/2}$) were observed. Lifetime measurements evaluated at 1064 nm fit well to a model in which the data was fit to components for rise time and decay time by reconvolution with the detector response (see Figure 2.20 (b), Figure 2.21 and Appendix Figure A2.18).

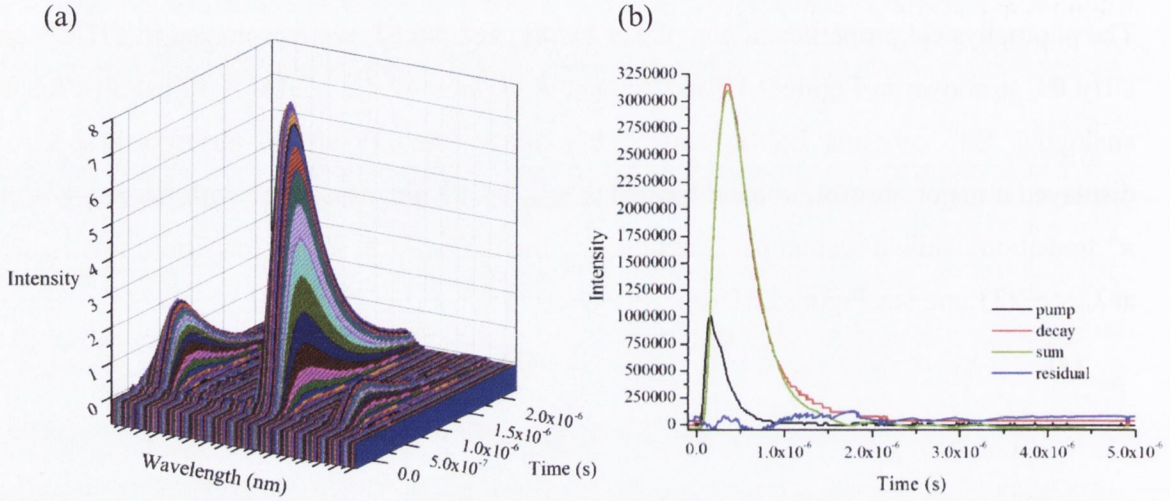

Figure 2.20. *(a) Time-resolved emission spectrum of Nd.**81**$_3$ after excitation at 337 nm, showing sensitised Ln^{III}-based luminescence. (b) Decay curve obtained from Nd.**81**$_3$ in CH_3OH and residuals for fitted curve generated by deconvulution of the instrument response function with a single exponential function.*

Table 2.4. *Nd^{III}-centred rise times and lifetimes (/ns) for Nd ($^4F_{3/2}$) in Nd.**81**$_3$ and Nd.**82**$_3$ as measured in CH_3OH, CD_3OD and CH_3CN.*

	MeOH		CD_3OD		MeCN	
	$\tau_{rise\ time}$ (ns)	τ (ns)	$\tau_{rise\ time}$ (ns)	τ (ns)	$\tau_{rise\ time}$ (ns)	τ (ns)
Nd.**81**$_3$	16	206	45	775	22	491
Nd.**82**$_3$	12	251	40	865	22	460

Similar behaviour for both complexes was observed in the three solvent media studied, as can be seen from the data in Table 2.4, and the typical fitted temporal profiles shown in Figure 2.20 (b), Figure 2.21 and Appendix Figure A2.18. The rise time in such systems generally arises from the involvement of the triplet excited state of the donor chromophore in the energy transfer process to the Ln^{III}. This is supported by the differences between the rise time values evaluated in CH_3OH and in CD_3OD, *i.e.* longer rise times were observed in deuterated media (45 and 40 ns for Nd.**81**$_3$ and Nd.**82**$_3$ in CD_3OD in comparison to 16 and 12 ns for Nd.**81**$_3$ and Nd.**82**$_3$ in CH_3OH respectively). These rise time values reflect the

imperfect overlap between the triplet state of the donor chromophore and phonon assistance involving the solvent vibrational manifold, *i.e.* the lower energy (and less effective spectral overlap) of C–D and O–D vibrational oscillators with the donor triplet state relative to the spectral overlap with analogous C–H and O–H oscillators found in non-deuterated CH_3OH. It is clear from this data that both Nd^{III} containing systems exhibit similar luminescence lifetimes in each of the solvent systems studied.

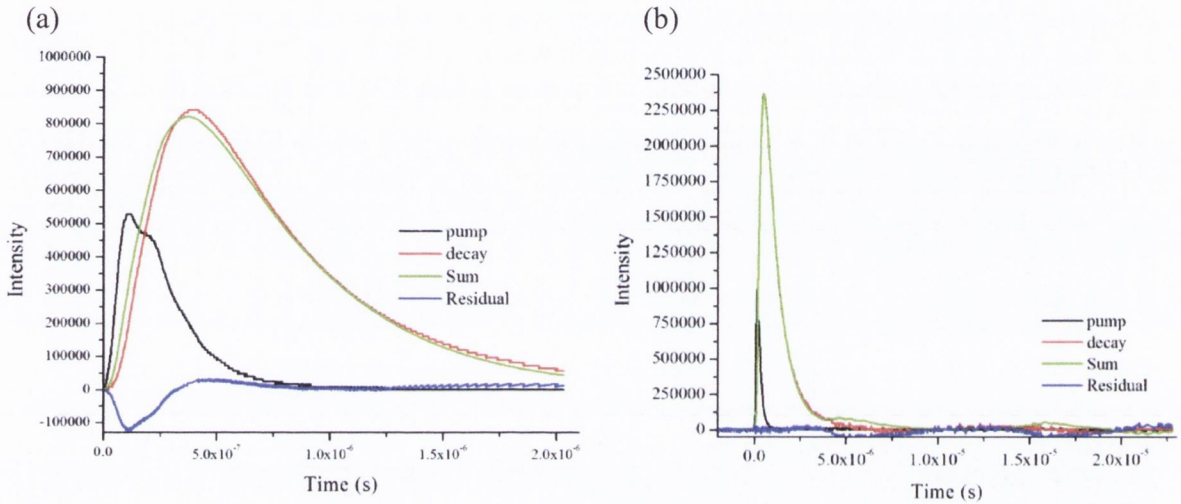

Figure 2.21. *Decay curves obtained from Nd.**81**$_3$ in (a) CH_3CN and (b) CD_3OD and residuals for fitted curve generated by deconvulution of the instrument response function with a single exponential function.*

Due to the profound dependence of the luminescence lifetime of Nd^{III} complexes upon ligand structure, it is unwise to use the published equations which were established for aminocarboxylate ligand systems derived from cyclen to calculate the number of inner sphere water molecules (q).[264,265] However, lifetime values are consistent with a low degree of solvation at the metal centre as those calculated in CH_3OH are very long for a Nd^{III} complex. If we accept that three tridentate diamidopyridyl ligands fill the inner coordination sphere, the differences between the values for the decay components of the luminescence lifetimes obtained in CH_3OH and CD_3OD are highly instructive. Clearly, two complexes do not constitute a sufficient body of data to establish meaningful relations that define q in dipicolinate systems, but it may be useful to consider an equation of the form:

$$q = A(1/\tau_{CH3OH} - 1/\tau_{CD3OD} - B)$$

In a system in which there is no coordinated solvent, the difference between $1/\tau_{CH3OH}$ and $1/\tau_{CD3OD}$ should reflect B, the outer sphere solvent contribution to non-radiative deactivation

of the excited state. On this basis, Nd.**81**$_3$ and Nd.**82**$_3$ give values of 3.5 ± 0.6 and 2.8 ± 0.5 μs^{-1}, respectively which are within error of one another and imply that the coordination environments and the nature of the solvation of the two complexes are very similar. These values for B differ significantly from the value of the outer sphere correction value obtained for aminocarboxylate ligand systems (1.4 μs^{-1}),[265] suggesting that there may be significant variations in outer sphere solvent effects between different classes of complex.

2.15 Chiro-Optical properties of Nd^{III} complexes – CD and CD titrations

In order to investigate the enantiomeric nature of the ligands and inspect whether chirality had been retained in their corresponding complexes Nd.**81**$_3$ (*S*) and Nd.**82**$_3$ (*R*) CD spectra were recorded in CH_3CN in a similar manner to that described for Eu.**81**$_3$ (*S*) and Eu.**82**$_3$ (*R*) where the complexes were formed *in situ* upon the addition of 0.33 equiv. of $Nd(CF_3SO_3)_3$.

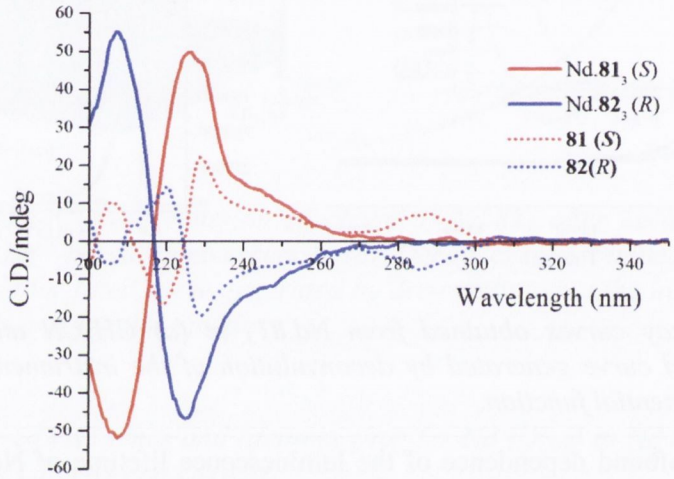

Figure 2.22. *Circular dichroism spectra of ligands* ***81*** *(S) and* ***82*** *(R) (3.3 x 10^{-5} M) recorded in CH_3CN at RT before and after the addition of 0.33 equiv. of $Nd(CF_3SO_3)_3$ - note that slight discrepancies in intensities can be derived from differences in concentrations.*

Again CD spectra for the ligands **81** (*S*) and **82** (*R*) alone were mirror images of one another, confirming their enantiomeric relationship (Figure 2.22). Following the addition of 0.33 equiv. of Nd^{III} and subsequent formation of the 1:3 complexes *in situ* CD spectra were recorded and indicated that the chirality of the system had been retained upon complexation. Moreover the CD spectra corresponding to complexes Nd.**81**$_3$ (*S*) and Nd.**82**$_3$ (*R*) experienced significant structural changes in comparison to that seen for the CD spectra of the ligands. Only two major bands were observed for both enantiomeric complexes with the CD spectrum of Nd.**81**$_3$ (*S*) displaying a large negative band centred at 207 nm and a large positive band located at 224 nm. Nd.**82**$_3$ (*R*) gave a CD spectrum also possessing signals at 207 nm and 224 nm of equal magnitude but opposite in sign, thus demonstrating that the two complexes were formed as a structurally identical pair of enantiomers. The bisignate profiles exhibited by

Nd.**81**$_3$ and Nd.**82**$_3$ again suggest the possibility of exciton coupling between chromophores as they are arranged in close proximity around the metal centre; however the existence of this characteristic requires more in depth studies to be carried out for full confirmation. Consequently, CD spectra for complexes Nd.**81**$_3$ and Nd.**82**$_3$ were also recorded between -10 and +25 °C. However, only minor changes were observed within this temperature range for both systems, as shown in Appendix A2.19.

As investigated for the corresponding Eu^{III} systems above, the appreciable changes observed in the CD spectra upon complexation prompted us to examine the CD spectra as a function of metal concentration in order to gain further insight into the structural changes of the various species generated in the self-assembly process. The overall changes in the CD spectra of **81** (*S*) and **82** (*R*) upon titrating with increasing concentrations of $Nd(CF_3SO_3)_3$ (from 0→4 equiv.) in CH_3CN at RT are shown in Figure 2.23.

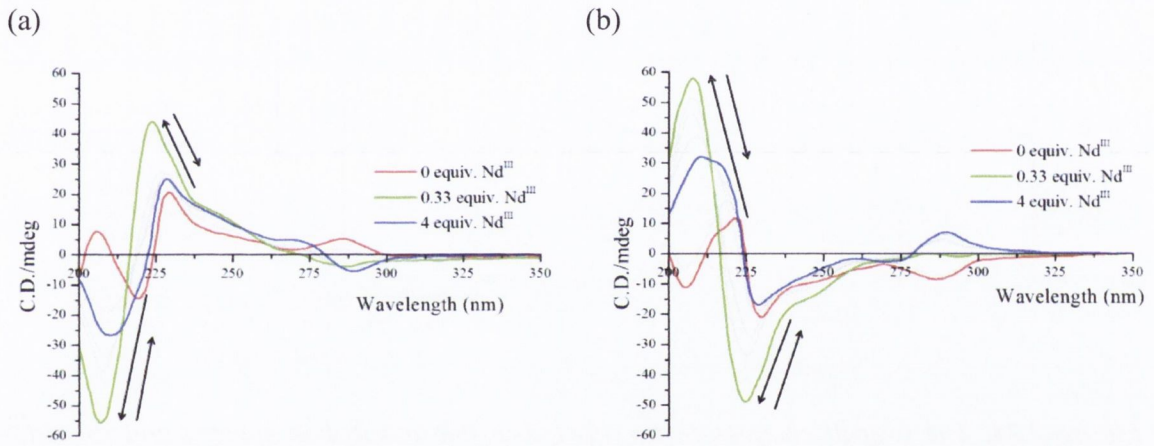

Figure 2.23. *The overall changes in the CD spectra of (a)* ***81*** *(S) (3.4 x 10^{-5} M) and (b)* ***82*** *(R) (3.6 x 10^{-5} M) upon titrating against increasing concentrations of $Nd(CF_3SO_3)_3$ (0→4 equiv.) at RT in CH_3CN.*

From these analyses it was clear that a similar behaviour to that displayed for the Eu^{III} self-assembly system was occurring. Evidently, those transitions associated with the ligand CD spectra experience significant changes throughout the titration, specifically within the Nd^{III} concentration range of 0→0.33 equiv., indicating the formation of primarily the 1:3 species in solution. For ligand **81** an increase in relative intensity of the positive band located at 229 nm and a shift to 224 nm occurred within this metal concentration range. Concurrently, the band located at 218 nm disappeared while a new negative band emerged at 207 nm. At higher Nd^{III} concentrations, between 0.33 – 4 equiv. of metal, the bands centred at 207 nm and 224 nm shifted to 210 nm and 228 nm, respectively, while simultaneously experiencing a decrease in relative intensity. These pronounced changes are reflective of the structural nature of the various self-assembled species in solution with the most notable

changes correlating to the formation of the 1:3 assembly. The formation of the 1:2 and the 1:1 species at higher Nd^{III} is more likely, giving rise to different CD spectra to that shown for the corresponding 1:3 complex.

2.16 Solution studies on the Nd^{III}-directed self-assembly of 81 (*S*) and 82 (*R*) in CH_3CN

A series of photophysical titrations (UV-visible absorption and luminescence) were next conducted in CH_3CN solution in order to gain an insight into the stoichiometry of the self-assembly process of **81** and **82** with Nd^{III} in solution, and to further quantify the binding affinity of the various complexes formed *in situ* which was achieved by fitting the changes observed using nonlinear regression analysis.

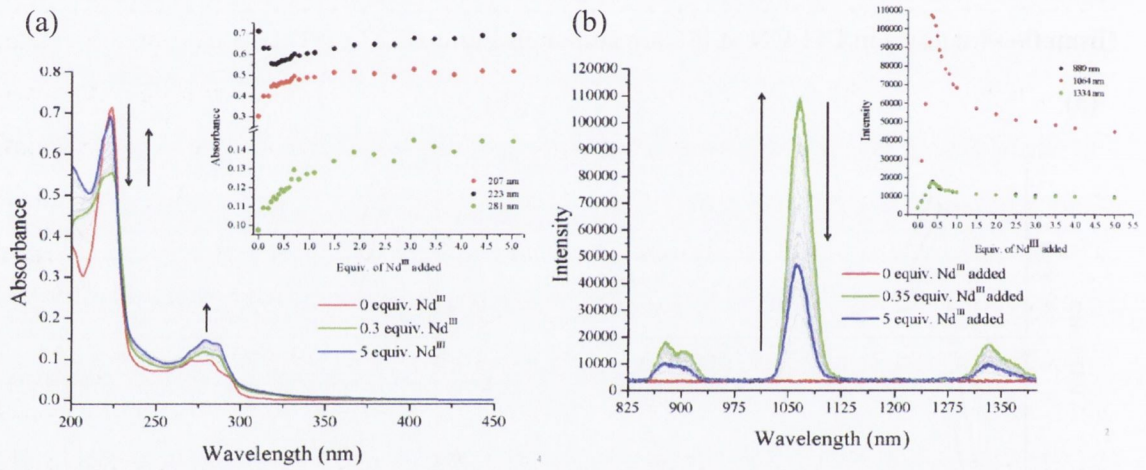

Figure 2.24. *The overall changes in the (a) UV-visible absorption spectra and (b) Nd^{III}–centred phosphorescence spectra upon titrating* ***81*** *(1 x 10^{-5} M) against $Nd(CF_3SO_3)_3$ (0→5 equiv.) in CH_3CN at RT.* ***Inset****: corresponding experimental binding isotherm of (a) absorbance at λ = 207, 223 and 281 nm and (b) Nd^{III} phosphorescence emission intensity at λ = 880, 1064 and 1334 nm.*

The overall changes in the UV-visible absorption spectrum of **81** upon titrating against $Nd(CF_3SO_3)_3$ in CH_3CN are shown in Figure 2.24 (a). Here, the high energy absorption band centred at λ = 223 nm experienced a hypochromatic effect within the addition of 0→0.33 equiv. of the metal salt. As we had anticipated from both the CD results and studies carried out on the Eu^{III} system in previous sections, subsequent additions of Nd^{III} then gave rise to a small increase in the absorbance up until the addition of 1 equiv. of Nd^{III}, after which the equilibrium of the system was reached. Similarly, the longer wavelength absorption band centred at λ = 281 nm experienced a sharp increase in absorbance between additions of 0→1 equiv. of Nd^{III}, reaching a plateau after the addition of 1 equiv. of $Nd(CF_3SO_3)_3$. An identical behaviour was observed upon titrating **82** with Nd^{III} (see Appendix Figure A2.21 – A2.22).

These changes are similar to those observed for the Eu^{III} system above and from previously documented results from our laboratory.[66]

The emergence of long-lived Nd^{III} centred luminescence was also monitored and clearly visible, with the appearance of characteristic line-like emission bands centred at 880 nm, 1064 nm, and 1334 nm upon excitation at $\lambda = 281$ nm. These bands represent deactivation of the Nd^{III} $^4F_{3/2}$ excited state to ^4I_J ground states (where $J = 9/2$, 11/2 and 13/2), see Figure 2.24 (b) and Appendix Figure A2.20). As anticipated, the NIR emission gradually enhanced between the addition of 0→0.35 equiv. of Nd^{III}, confirming the formation of the most emissive 1:3 stoichiometric species in solution and, at the same time, verifying efficient energy transfer from the antenna to the Nd^{III} centre. As was observed in the CD spectra, significant modulation was also shown at higher equiv. (greater than 0.35), indicative of the formation of the different self-assembly species in solution. The corresponding titration profile in which the emission at 880 nm, 1064 nm, and 1334 nm was monitored, is shown in Figure 2.24 inset, and demonstrates that after the addition of 0.35 equiv. of Nd^{III} the emission intensity sharply decreases, reaching a plateau after the addition of *ca.* 1 equiv. of metal. This is indicative of the evolution of the lesser emissive 1:2 species, and eventually the 1:1 species as a function of increasing Nd^{III} concentration (see also Appendix Figure 2.20).

A luminescence titration profile matching that shown for **81** was illustrated upon the addition of $Nd(CF_3SO_3)_3$ to ligand **82** in CH_3CN, as shown in Appendix Figure A2.21 – A2.22, where an initial gradual enhancement in intensity was displayed, followed by a sharp decrease in Nd^{III}-centred emission. The similarity between the UV-visible absorption and luminescence spectra changes for both **81** and **82** point to an identical Nd^{III}-directed self-assembly behaviour. These results were also compared to the Eu^{III} titrations above, indicating that the self-assembly behaviour of ligands **81** and **82** are relatively independent of the nature of the Ln^{III} ion employed.

2.17 Fitting of titration data and calculation of complex stability constants

The global changes in both the UV-visible absorption and NIR emission spectra were again fit by non-linear regression analysis using the program SPECFIT in order to elucidate the various stoichiometric species present in solution and their corresponding binding constants.

The speciation distribution diagram obtained from fitting the UV-visible absorption experimental data is shown in Figure 2.25 (a). Upon the addition of 0.33 equiv. of Nd^{III} the predominant species observed is the 1:3 Nd.**81**$_3$ species, formed in 79% yield. The fit at three different wavelengths (207 nm, 223 nm and 281 nm) is also shown Figure 2.25 (b). Additional aliquots of Nd^{III} drive equilibrium towards the formation of the 1:1 species, Nd.**81**, until it becomes the most dominant species in solution. An almost identical titration

behaviour was exhibited by **82**, as shown by the fit of the overall changes in the UV-visible absorption spectra of **82** (Appendix Figure A2.23) with the Nd.$\mathbf{82}_3$ species being formed in 74% following the addition of 0.33 equiv. of Nd^{III}. Binding constant values obtained from the analyses of the UV–visible absorption and luminescence titration data of both systems are summarised in Table 2.7, and show that the Nd.$\mathbf{81}_3$ species is formed with a binding constant value of log $\beta_{13} = 18.3 \pm 0.6$ while for Nd.$\mathbf{82}_3$ a binding constant value of log $\beta_{13} = 17.8 \pm 0.4$ was elucidated. Interestingly, the formation of the 1:2 species was not observed in either case, an indication that it is possibly short-lived, but formation of the 1:1 complex gave log $\beta_{11} = 6.0 \pm 0.3$ for Nd.**81** and log $\beta_{11} = 6.1 \pm 0.2$ for Nd.**82**.

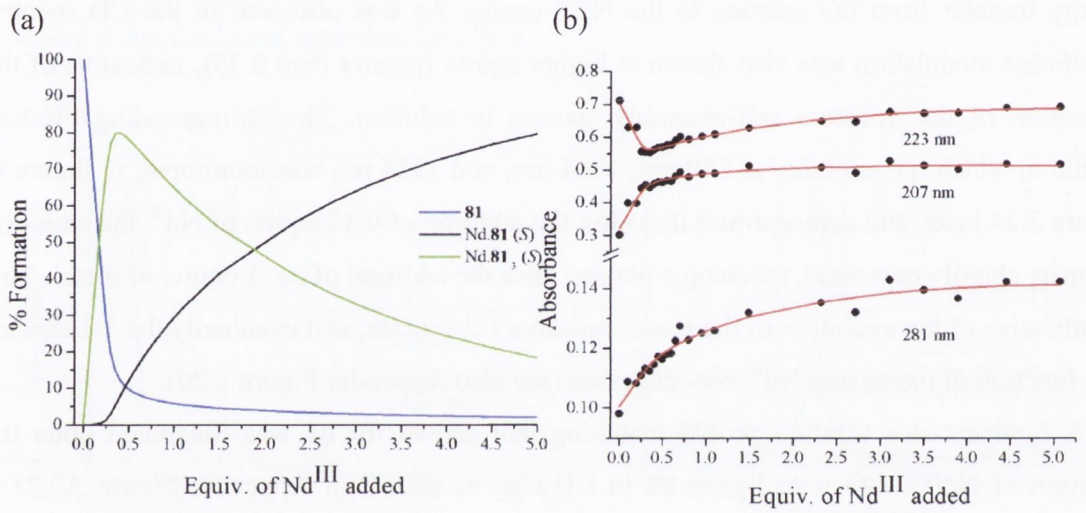

Figure 2.25. *(a) The speciation distribution diagram obtained from the UV-visible absorption titration data fit (upon titrating ligand* ***81*** *against* $Nd(CF_3SO_3)_3$ *in* CH_3CN*) and (b) the fit of the experimental binding isotherms using the non-linear regression analysis program SPECFIT.*

In a similar manner, the global changes in the Nd^{III}-centred emission were analysed using SPECFIT (as shown in Appendix Figures A2.24 and A2.25). As observed upon fitting the overall changes in the ground state of the system, the titration of both **81** and **82** confirmed formation of the 1:3 species in solution upon the addition of 0.33 equiv., with log $\beta_{13} = 17.2 \pm 0.4$ and log $\beta_{13} = 17.8 \pm 0.3$ calculated for Nd.$\mathbf{81}_3$ and Nd.$\mathbf{82}_3$, respectively. From the speciation distribution diagram it was again evident that at higher metal concentrations the lesser emissive 1:1 species becomes the predominant species in solution with binding constants of log $\beta_{11} = 6.2 \pm 0.2$ and log $\beta_{11} = 6.5 \pm 0.2$ obtained for Nd.**81** and Nd.**82**, respectively. These values are comparable to those evaluated above calculated from fitting the changes in the UV-visible absorption titrations and also in relation to the Eu^{III} based self-assembly systems.

Having established the Nd^{III}-directed self-assembly behaviour of ligands **81** and **82** *in situ* and analysed the photophysical properties of the solid state 1:3 complexes we then investigated the capability of these systems to form Langmuir monolayers at an air-water interface using the same procedure to that described above.

2.18 Langmuir monolayer formation of Nd.81_3 (*S*) and Nd.82_3 (*R*) complexes

The ability of complexes Nd.$\mathbf{81}_3$ and Nd.$\mathbf{82}_3$ to self-assemble at an air-water interface was investigated in an identical manner to that described above for Eu.$\mathbf{81}_3$ and Eu.$\mathbf{82}_3$. 20 μL aliquots of each complex was spread (~2.4×10^{-4} M), using $CHCl_3/CH_3OH$ (9:1) as the spreading solvent, onto the surface of a water subphase at room temperature.

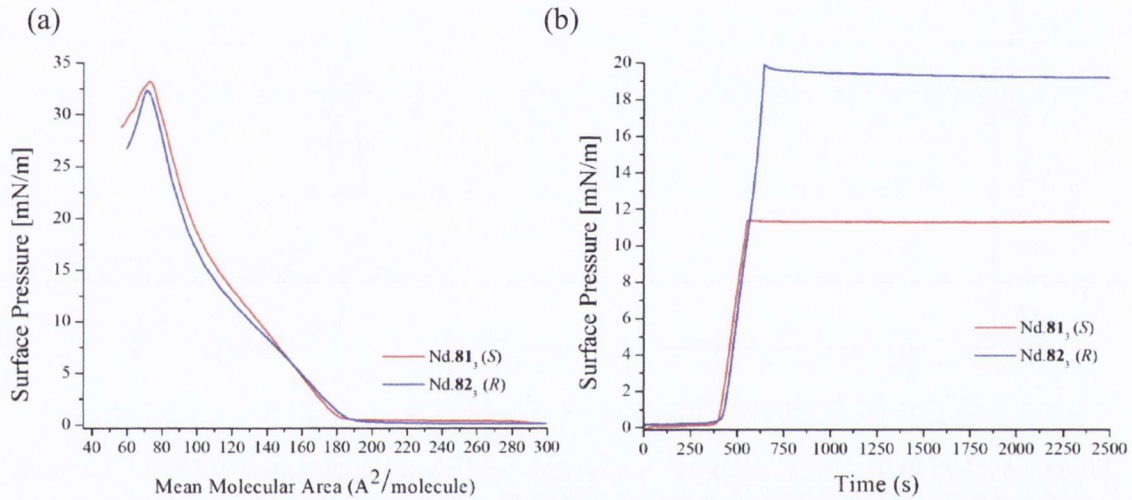

Figure 2.26. *(a) Surface pressure-area isotherms of Nd.$\mathbf{81}_3$ (S) and Nd.$\mathbf{82}_3$ (R). (b) Surface pressure-time profiles for Langmuir monolayers of Nd.$\mathbf{81}_3$ (S) and Nd.$\mathbf{82}_3$ (R).*

A typical surface pressure–area isotherm was obtained in each case; see Figure 2.26 (a), in which an exponential increase in surface pressure evidenced the different phase transitions, that is, G, LE, LC, and C, upon area decrease. The films collapsed at 33 mN m^{-1} for Nd.$\mathbf{81}_3$ and 32 mN m^{-1} for Nd.$\mathbf{82}_3$ with areas of 70 ± 5Å^2 per molecule. The areas of these Nd^{III} complexes are approximately those expected for three alkyl chains (*ca.* 66 Å^2 per molecule) and indicate that the complexes remain intact at the air-water interface with supramolecular organisation into monolayers. The isotherm features as well as the average area per molecule are similar, within experimental error, to the Eu^{III} systems above implying that the supramolecular packing is unaffected by changes in the Ln^{III} ion implemented. The stability of each Langmuir monolayer was also assessed by maintaining the monolayers in the LC phase for an extended period of time (exceeding 40 mins) and monitoring the surface pressure over that time interval. The results are depicted in Figure 2.26 (b), demonstrating

excellent stability properties for films of both the Nd.**81**$_3$ and the Nd.**82**$_3$, as had been observed for the Eu^{III} complexes above.

2.19 Langmuir-Blodgett film formation of Nd.81$_3$ (*S*) and Nd.82$_3$ (*R*) complexes

Having successfully formed Langmuir monolayers of Nd.**81**$_3$ and Nd.**82**$_3$, each film was then transferred onto a quartz slide with transfer ratios of ~1, generating LB films of high quality possessing good uniformity and homogeneity. Deposition was achieved upon the emersion of the solid support, as was described for the Eu^{III} systems above, giving rise to Z-type deposition of Nd.**81**$_3$ and Nd.**82**$_3$.

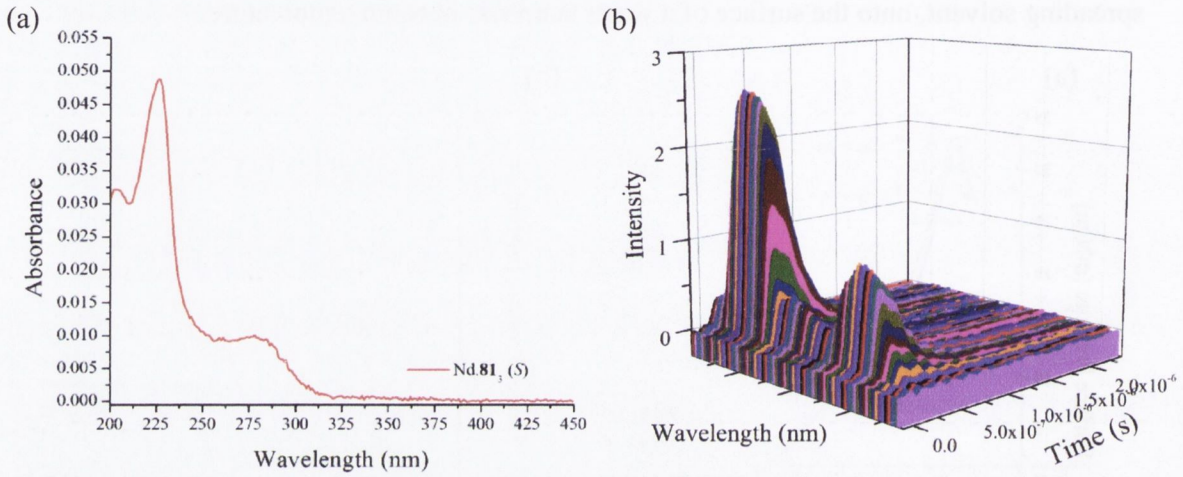

Figure 2.27. *(a) UV-visible absorption spectrum of Langmuir-Blodgett Nd.**81**$_3$ (S) monolayer and (b) time-resolved emission spectrum of Nd.**81**$_3$ (S) monolayer after excitation at 337 nm, showing sensitised Nd^{III}-based luminescence.*

The photophysical properties of the monomolecular solid state structures were then evaluated. The UV–visible absorption spectra were recorded and their NIR emission properties were also probed by recording time resolved emission spectra; see Figure 2.27 and Appendix A2.26. We were, however, unable to obtain reliable CD spectra of these (single monolayer based) LB films.

The UV-visible absorption spectra displayed by both films were structurally identical to those obtained for the solid compounds Nd.**81**$_3$ and Nd.**82**$_3$ with bands associated with the main absorption transitions found at λ_{max} = 223 nm and λ_{max} = 281 nm. NIR emission, although weak, was detected from each (upon excitation at 337 nm) with bands centred at λ = 880 nm and 1064 nm, representing deactivation from the Nd^{III} $^4F_{3/2}$ excited state to ground states $^4I_{9/2}$, and $^4I_{11/2}$. The weaker $^4F_{3/2} \rightarrow {}^4I_{13/2}$ transition at 1334 nm, which was detected for the solid complexes, was not observed due to significant noise in the spectrum arising from scattered light from the fourth harmonic of the excitation pulse. Attempts to remove the signal arising from scatter by using bandpass or interference filters merely resulted in a

diminution of the overall signal. However, it is clear from comparison of the relative intensities of the 880 nm and 1064 nm peaks in solution and on the surface that the complex symmetry is very similar on both occasions, since the 1064 nm transition is hypersensitive to symmetry ($\Delta J = 4$). These results demonstrate that Nd^{III} NIR emission can be recorded even from only a single monolayer, clearly demonstrating the sensitivity of the system. As for the Eu^{III} based LB films, they have been found to be stable under ambient conditions over a period of many months.

2.20 Summary – NIR emitting Nd^{III}-directed self-assembly systems

The main goal of this area of the project was to extend our studies to include the NIR emitting Nd^{III}. Measurements were conducted in a similar manner to that described for the Eu^{III} systems above in that the solid complexes Nd.**81**$_3$ and Nd.**82**$_3$ were first prepared under microwave irradiation and their photophysical properties analysed; the Nd^{III}-directed self-assembly process of ligands **81** and **82** was again re-evaluated *in situ* in order to gain insight into the main stoichiometric species in solution; and the ability of the 1:3 complexes to assemble at an air-water interface and form Langmuir monolayers for the eventual affixing to solid quartz slides was then assessed.

Spectroscopic techniques, including UV-visible absorption, luminescence and CD, gave an indication of the various species produced in the self-assembly system, notably the 1:3 and the 1:1 components. Interestingly, fitting of titration data did not elucidate the presence of the 1:2 complex in solution, although it is highly likely that it is formed, possibly in very low undetectable yields. Assembly of both enantiomeric 1:3 complexes at an air-water interface was successful with stability measurements confirming the resilience of the monolayers over a long period of time. Furthermore, organisation of these monolayers into solid state LB films gave rise to NIR centred luminescence that, by comparing to the solution state measurements, remained relatively unchanged upon immobilisation.

The fabrication of chiral, visibly emitting Eu^{III} and NIR emitting Nd^{III} assemblies into solid state architectures in this manner may open up a new direction in the development of Ln^{III} luminescent materials. By bridging our solution based luminescent systems with the Langmuir-Blodgett technique advances towards more applicable, highly sensitive optical devices may be acquired. These exciting new results prompted us to further continue work in this area by including other Ln^{III} metal ions, namely Tb^{III}, Sm^{III}, Lu^{III} and Dy^{III}. The inclusion of other Ln^{III} metals not only presents an opportunity to delve into the possibility of producing dual emitting edifices but by investigating other Ln^{III} systems the robustness and versatility of this technique, in relation to the incorporation of Ln^{III} luminescent self-assemblies into LB films, may be ascertained.

2.21 Formation of mononuclear tris chelate complexes Ln.81$_3$ (*S*) and Ln.82$_3$ (*R*) complexes (Ln = Tb^{III}, Sm^{III}, Dy^{III}, Lu^{III})

In a similar manner to that described for the previously discussed Eu^{III} and Nd^{III} systems mononuclear complexes Ln.**81**$_3$ (*S*) and Ln.**82**$_3$ (*R*) (Ln = Tb^{III}, Sm^{III}, Lu^{III}, Dy^{III}) were synthesised by refluxing either **81** or **82** in HPLC grade CH_3OH under microwave irradiation at 70 °C for 10 mins in the presence of 0.33 equivalents of the appropriate metal triflate salt (see Scheme 2.4). Each solid complex was isolated *via* diethyl ether vapour diffusion yielding all complexes as white solids, see Table 2.5 for % yields.

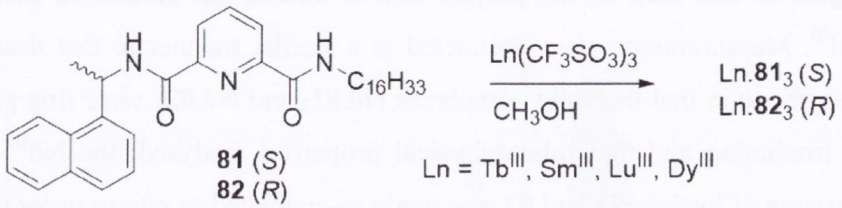

Scheme 2.4. *Preparation of Ln^{III} complexes Ln.**81**$_3$ (S) and Ln.**82**$_3$ (R) carried out under microwave irradiation at 70 °C (Ln = Tb^{III}, Sm^{III}, Lu^{III}, Dy^{III}).*

Formation of the desired products was verified using NMR spectroscopy in which broadening and shifting in the ^{1}H NMR spectrum was observed; see Appendix Figures A2.27 – A2.31. IR analysis also confirmed complexation; see Table 2.6 for amide carbonyl stretching frequency shifts, while only the 1:2 species was detectable by HRMS (see Appendix Figures A2.32 - A2.35 for calculated and experimental isotopic distribution pattern for Ln.**81**$_3$ (Ln = Tb^{III}, Sm^{III}, Dy^{III} and Lu^{III}). Elemental analysis was again employed, supporting formation of the 1:3 complex in each case.

Table 2.5. *% yields calculated for solid complexes Ln.**81**$_3$ (S) and Ln.**82**$_3$ (R) (Ln = Tb^{III}, Sm^{III}, Lu^{III}, Dy^{III}) following preparation under microwave irradiation and isolation via diethyl ether diffusion.*

Complex	Yield (%)	
	L = **81**	L = **82**
Tb.L$_3$	52	71
Sm.L$_3$	46	50
Lu.L$_3$	53	52
Dy.L$_3$	36	50

Table 2.6. *Amide carbonyl stretching frequencies shifts upon complexation of ligands* ***81*** *and* ***82*** *with 0.33 equiv. of* $Ln(CF_3SO_3)_3$ *(Ln =* Tb^{III}, Sm^{III}, Lu^{III}, Dy^{III}*).*

Compound	Amide carbonyl stretching frequency (cm^{-1})	
	L = **81** (*S*) (1654 cm^{-1})	L = **82** (*R*) (1650 cm^{-1})
$Tb.L_3$	1634	1634
$Sm.L_3$	1633	1633
$Lu.L_3$	1638	1635
$Dy.L_3$	1635	1634

2.22 Photophysical characterisation of complexes $Ln.81_3$ (*S*) and $Ln.82_3$ (*R*) (Ln = Tb^{III}, Sm^{III}, Dy^{III}, Lu^{III})

The photophysical properties of complexes Ln.**81**$_3$ and Ln.**82**$_3$ (Ln = Tb^{III}, Sm^{III}, Lu^{III}, Dy^{III}) were next evaluated in CH_3CN, see Figures 2.28 – 2.30 and Appendix Figures A2.36 – A2.41. Ligand based UV-visible absorption bands were displayed for all eight complexes as before at λ_{max} = 223 nm and λ_{max} = 281 nm. Furthermore, excitation into the sensitising chromophore moiety at λ = 281 nm gave rise to Tb^{III}-centred and Sm^{III}-centred emission in the cases of Tb.**L**$_3$ and Sm.**L**$_3$ (**L** = **81** and **82**), demonstrating successful population of the Ln^{III} excited states in these instances (see Figure 2.29 and Appendix Figure A2.39). Characteristic line-like emission peaks occurred at λ = 490 nm, 545 nm, 585 nm and 620 nm following energy transfer to the Tb^{III} centre, which are associated with deactivation from the Tb^{III} $^5D_4$ excited state to the ^7F_J ground states, where J = 6 – 3.

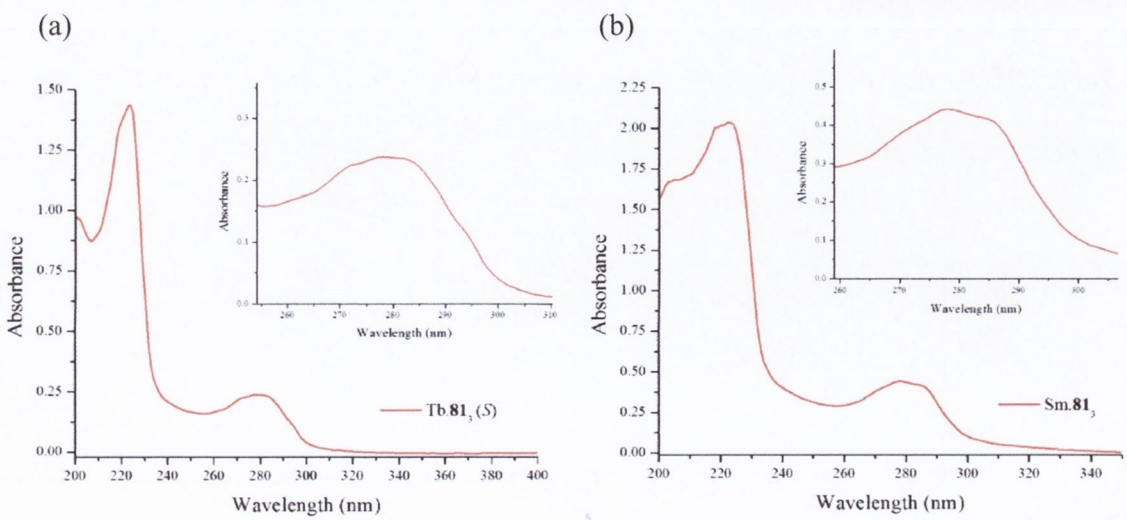

Figure 2.28. *UV-visible absorption spectra of (a) Tb.***81**$_3$ *(S) (5.7 x* 10^{-6} *M) and (b) Sm.***81**$_3$ *(S) (1.1 x* 10^{-5} *M) in* CH_3CN*.*

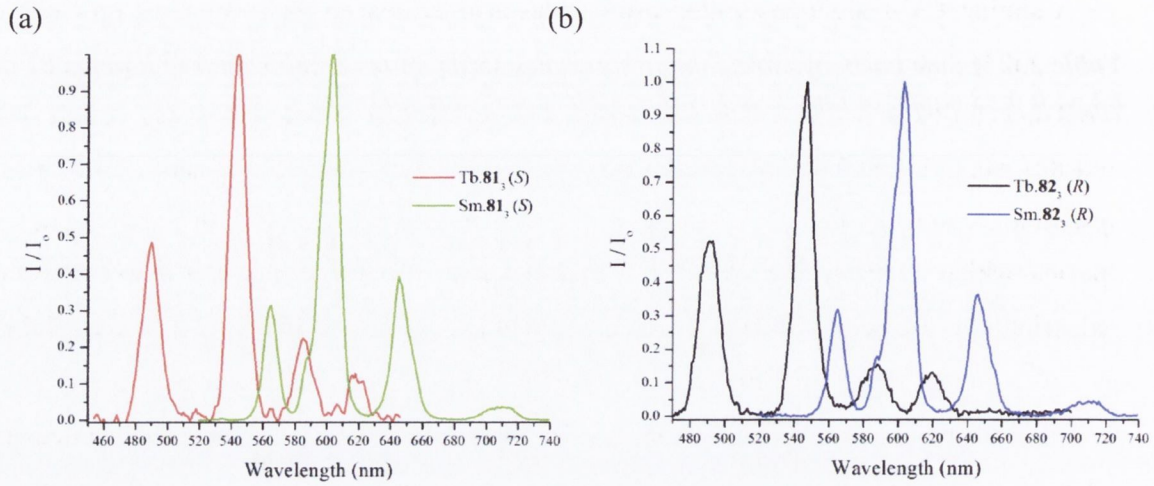

Figure 2.29. *Normalised phosphorescence spectra of (a) Tb.**81**$_3$ (S) and Sm.**81**$_3$ (S) and (b) Tb.**82**$_3$ (R) and Sm.**82**$_3$ (R) recorded in CH_3CN.*

Efficient energy transfer and Sm^{III} sensitisation *via* excitation of the covalently appended naphthalene chromophore at λ = 281 nm was also verified for Sm.$\mathbf{L}_3$ (**L** = **81** and **82**), as shown in Figure 2.29 and Appendix Figure A2.39. A typical Sm^{III} emission spectrum was exhibited on both occasions with bands centred at 565 nm, 600 nm, 645 nm and 708 nm corresponding to the $^4G_{5/2} \rightarrow {}^6H_J$ electronic transitions, where J = 5/2, 7/2, 9/2, 11/2.

Excitation spectra (λ_{em} = 545 nm for Tb.$\mathbf{L}_3$ and λ_{em} = 645 nm for Sm.$\mathbf{L}_3$, **L** = **81** and **82**) were also recorded for Ln.$\mathbf{L}_3$ (where Ln = Tb^{III} and Sm^{III} and **L** = **81** and **82**) with the structure of the excitation spectra closely matching that of the UV-visible absorption spectra (Figure 2.30 and Appendix Figure A2.40). These results clearly confirm successful sensitisation of both the Tb^{III} and Sm^{III} centres in the four complexes by indirect excitation of the naphthalene group.

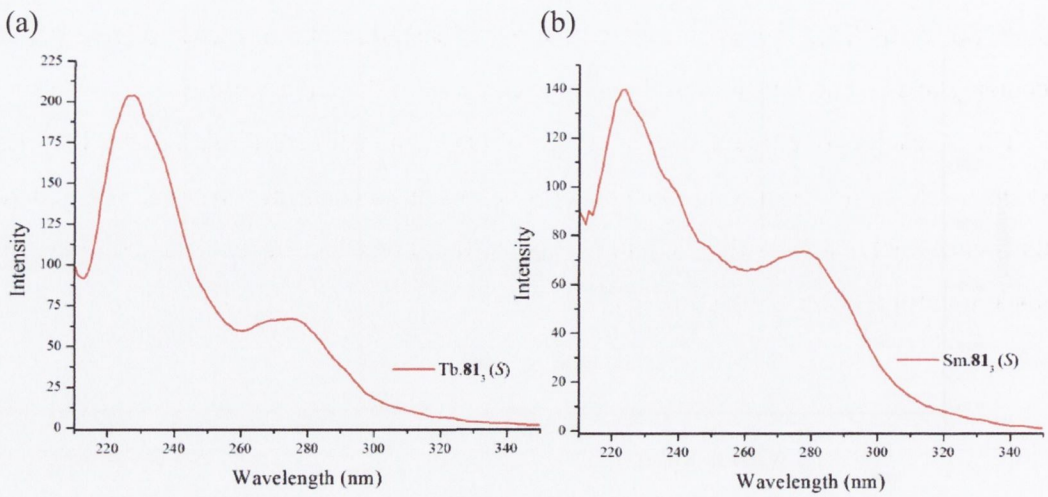

Figure 2.30. *Excitation spectra of (a) Tb.**81**$_3$ (S) (5.7 x 10^{-6} M) (λ_{em} = 545 nm) and (b) Sm.**81**$_3$ (S) (1.1 x 10^{-5} M) (λ_{em} = 645 nm) in CH_3CN.*

A similar UV-visible absorption profile was also evidenced for complexes Ln.$\mathbf{L}_3$ (Ln = Lu^{III} and Dy^{III} and **L** = **81** and **82**) with bands appearing at λ_{max} = 223 nm and λ_{max} = 281 nm, see Appendix Figure A2.41. However, in the case of Ln.$\mathbf{L}_3$ (Ln = Lu^{III} and Dy^{III} and **L** = **81** and **82**) excitation at λ = 281 nm did not give rise to Ln^{III}-centred emission. For the Lu^{III} system this can be explained by considering the electronic configuration of the trivalent Lu^{III} species which is given by [Xe] $4f^{14}$. The inherent 'filled' 4*f* subshell does not allow redistribution of electrons within this energy level and so line-like emission is not exhibited by Lu^{III}. The electronic configuration of Dy^{III} on the other hand, given by [Xe] $4f^{9}$, does permit electronic redistribution within the 4*f* subshell but population of the $^4F_{9/2}$ excited state often results in energy dissipation *via* non-radiative pathways due to the small energy gap between then ground and excited states. Another plausible reason for a lack of Dy^{III} emission detected in this particular system may be that the energy of the ligand triplet excited state is not well suited for efficient energy transfer and subsequent population of the $^4F_{9/2}$ excited state.

2.23 Chiro-Optical properties of Ln^{III} complexes – CD and CPL

CD spectra were recorded for complexes Ln.$\mathbf{81}_3$ and Ln.$\mathbf{82}_3$ (Ln = Tb^{III}, Sm^{III}, Lu^{III}, Dy^{III}), which were formed *in situ* by adding 0.33 equiv. of the appropriate metal triflate salt to either **81** or **82** in CH_3CN solution (see Figure 2.31 and Appendix Figure A2.42). As before, a bisignate profile was displayed for each of these Ln.$\mathbf{L}_3$ (Ln = Tb^{III}, Sm^{III}, Lu^{III}, Dy^{III} and **L** = **81** and **82**) complexes. For the four *S* enantiomeric complexes Ln.$\mathbf{81}_3$ (Ln = Tb^{III}, Sm^{III}, Lu^{III}, Dy^{III}), a negative CD signal was located at 207 nm while a positive CD band centred at 224 nm, with a broad shoulder located at 250 nm. CD spectra, which were equal in magnitude but opposite in sign, were detected for the four corresponding *R* enantiomeric complexes Ln.$\mathbf{82}_3$ (Ln = Tb^{III}, Sm^{III}, Lu^{III}, Dy^{III}) in which the peak located at 207 nm was positive but the band occurring at 224 nm appeared in the negative region of the CD spectrum.

These results conclude a similar trend to that demonstrated above for the Eu^{III} and Nd^{III} systems, *i.e.* similar conformational species is present in each Ln^{III} system. The generation of significant bisignate profiles again suggests the presence of exciton coupling between adjacent chromphores upon complexation.[255,256]

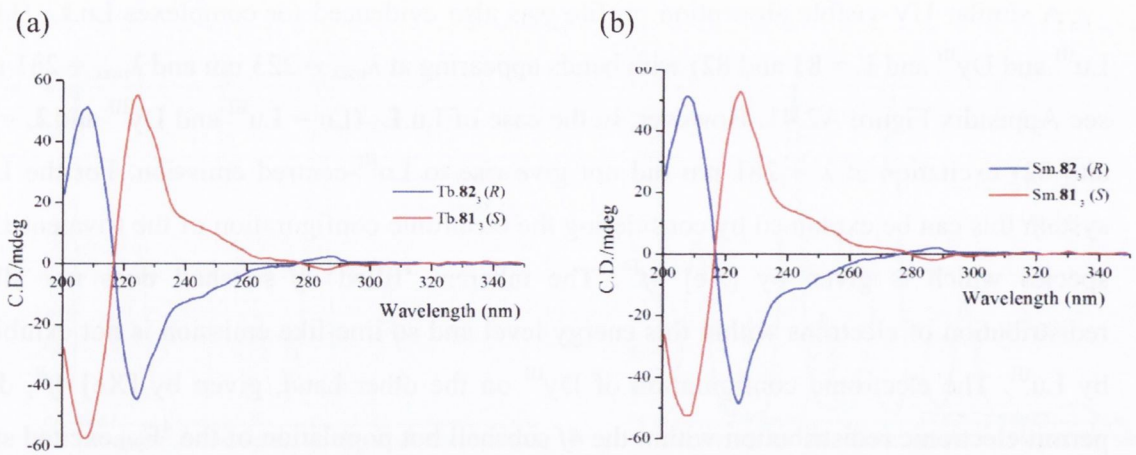

Figure 2.31. *The circular dichroism spectra of ligands* ***81*** *(S) and* ***82*** *(R) (2 x 10^{-5} M) recorded in CH_3CN at RT after the addition of 0.33 equiv. of (a) $Tb(CF_3SO_3)_3$ and (b) $Sm(CF_3SO_3)_3$ - note that slight discrepancies in intensities can be derived from differences in concentrations.*

CD titrations, which were carried out by titrating either ligand **81** or **82** with increasing concentrations of the appropriate $Ln(CF_3SO_3)_3$ salt, were implemented to further investigate these CD observations. As shown in Figure 2.32 and Appendix Figures A2.43 – A2.45, each data set matched those of the previously studied Eu^{III} and Nd^{III} systems. In each case, the prominent CD changes were displayed when 0.33 equiv. of Ln^{III} were added to the system, indicative of the 1:3 species exhibiting the most significant chiral structural behaviour. For the *S* enantiomeric systems (Figure 2.32) the ligand positive CD signal located at 229 nm experienced a substantial relative increase in absorption and small shift to 224 nm between additions 0→33 equiv. of $Ln(CF_3SO_3)_3$ (Ln = Tb^{III} and Sm^{III}). Concurrently, the band located at 218 nm disappeared while a new negative band emerged at 207 nm, experiencing an enhancement in relative absorption intensity also. As was seen before for the Eu^{III} and Nd^{III} systems, additional aliquots of Ln^{III} (0.33→5 equiv. of Ln^{III}) caused these two bands to decrease in relative intensity which is conclusive of the evolution of different stoichiometric species in solution, namely the 1:1 and the 1:2 species, as equilibrium is driven towards their formation at higher Ln^{III} concentrations.

The overall changes observed in the CD spectra following the titration of **81** with $Lu(CF_3SO_3)_3$ and $Dy(CF_3SO_3)_3$ matched those illustrated above. Moreover, the overall changes in the CD spectra following the titration of **82** with $Ln(CF_3SO_3)_3$ (Ln = Tb^{III}, Sm^{III}, Lu^{IIII} and Dy^{III}) displayed a mirror image (see Appendix Figure A2.43 and A2.45), in each case, to results obtained for the *S* enantiomeric systems. In summary, it can be assumed, that in all eight systems similar structural character is exhibited by the various species in solution, with the most definitive chiral complex formed at a M:L ratio of 1:3.

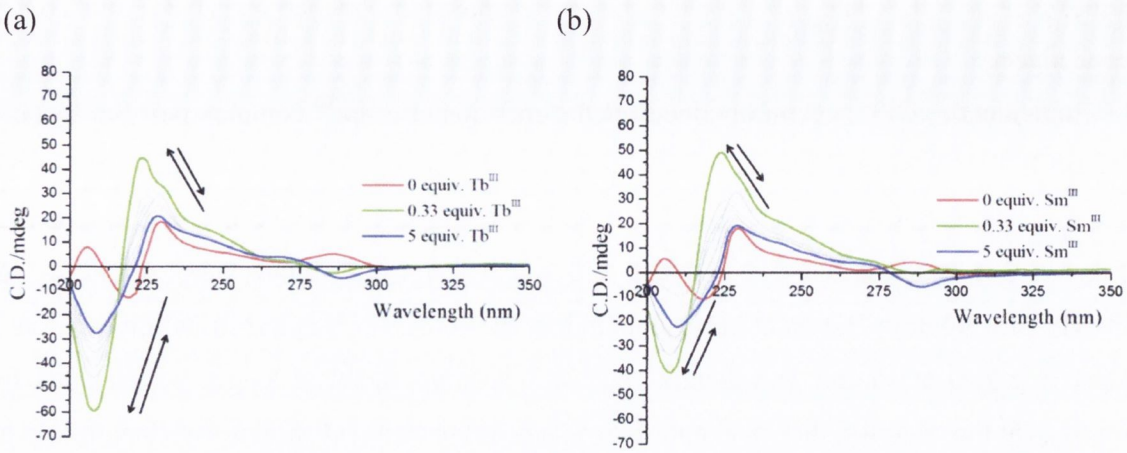

Figure 2.32. *The overall changes in the CD spectra of* ***81*** *(S) (3.4 x 10^{-5} M for (a) and 3.3 x 10^{-5} M for (b)) upon titrating against increasing concentrations of (a) $Tb(CF_3SO_3)_3$ (0→5 equiv.) and (b) $Sm(CF_3SO_3)_3$ (0→5 equiv.) at RT in CH_3CN.*

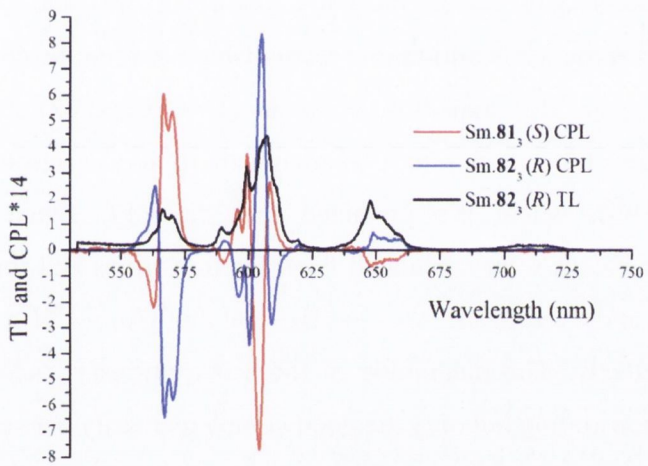

Figure 2.33. *Total Sm^{III}-centred emission and CPL spectra of complexes Sm.**81**$_3$ (S) and Sm.**82**$_3$ (R) recorded in CH_3CN (excitation at λ = 281nm).*

CPL analysis was again employed to verify whether chirality had been preserved and transferred to the local environment of the Ln^{III} (Ln^{III} = Tb^{III} and Sm^{III}) centre upon complexation. CPL measurements were evaluated in CH_3CN for Tb.$\mathbf{L}_3$ and Sm.$\mathbf{L}_3$ (**L** = **81** and **82**) and are shown in Appendix Figure A2.46 and Figure 2.33.

Excitation of the chiral antennae gave rise on all occasions to Ln^{III}-centred chiral emission with spectral bands of the enantiomeric complexes appearing at identical wavelengths but of opposite sign, confirming the enantiomeric relationship between the complex pairs Tb.$\mathbf{L}_3$ and Sm.$\mathbf{L}_3$ (**L** = **81** and **82**). As shown in Appendix Figure A2.46 for the Tb^{III} 1:3 complexes transitions representing deactivation from the $^5D_4$ excited state to the ^7F_J ground states, where J = 6 – 3, were observed with each band split, appearing as a negative and positive signal. Dissymmetry factor values for the J = 6 and 5 transitions were calculated for both complexes with g_{lum} = -0.05 and 0.05 for the $^5D_4 \rightarrow {}^7F_6$ transition and

values of g_{lum} = 0.21 and -0.24 for the $^5D_4 \rightarrow {}^7F_5$ transition obtained for Tb.**81**$_3$ and Tb.**82**$_3$, respectively.

Equivalently, CPL spectra obtained for the enantiomeric Sm^{III} complex pair Sm.$\mathbf{L}_3$ (**L** = **81** and **82**) were mirror images of one another with bands, correlating to the $^4G_{5/2} \rightarrow {}^6H_J$ electronic transitions where J = 5/2, 7/2, 9/2, were displayed for both chiral compounds (Figure 2.33). Both the $^4G_{5/2} \rightarrow {}^6H_{5/2}$ and $^4G_{5/2} \rightarrow {}^6H_{7/2}$ transition bands were split in two for Sm.**81**$_3$ and Sm.**82**$_3$. The band corresponding to the $^4G_{5/2} \rightarrow {}^6H_{5/2}$ transition appeared as a negative signal at shorter wavelengths but as a positive signal at longer wavelengths for Sm.**81**$_3$. On the contrary, this band appeared as a positive signal at shorter wavelengths but as a negative signal at longer wavelengths for Sm.**82**$_3$. The opposite was true for the $^4G_{5/2} \rightarrow {}^6H_{7/2}$ transition bands. The band representing the $^4G_{5/2} \rightarrow {}^6H_{9/2}$ transition appeared as a positive signal for the Sm.**82**$_3$ enantiomeric complex but as a negative signal for the Sm.**81**$_3$ complex. These results again reflect the chiral nature of the local environment the Sm^{III} resides within, confirming the enantiomeric relationship between the complex pair. The $^4G_{5/2} \rightarrow {}^6H_{5/2}$ and the $^4G_{5/2} \rightarrow {}^6H_{7/2}$ transitions of Sm.$\mathbf{L}_3$ (**L** = **81** and **82**) are well suited for CPL measurements as these transitions satisfy the magnetic dipole selection rules, where $\Delta J = 0, \pm 1$ (except for $0 \leftrightarrow 0$), where it's predicted that the CPL signal should be large.[137] Dissymmetry factor values were calculated for these transitions and found to be g_{lum} = 0.45 and -0.23 and -0.44 and 0.29 for the $^4G_{5/2} \rightarrow {}^6H_{5/2}$ and the $^4G_{5/2} \rightarrow {}^6H_{7/2}$ transitions of Sm.**81**$_3$ and Sm.**82**$_3$, respectively. The magnitude of these dissymmetry factors are thought to be relatively large demonstrating not only the good complementarity between the chiral emitting complexes but also that these values are in close agreement with those previously calculated for the related Sm^{III} complex analogues Sm.**56**$_3$ and Sm.**57**$_3$ (being 0.50 and 0.28 0.28 for the $^4G_{5/2} \rightarrow {}^6H_{5/2}$ and $^4G_{5/2} \rightarrow {}^6H_{7/2}$ and transitions, respectively).[93]

2.24 Solution studies on the Ln^{III}-directed self-assembly of 81 (*S*) and 82 (*R*) in CH_3CN

The formation of the monometallic Ln^{III}-directed self-assemblies (Ln^{III} = Tb^{III}, Sm^{III}, Lu^{III} and Dy^{III}) were then monitored *in situ* by analysing the changes in the UV-visible absorption and luminescence spectra. This process was carried out in a similar manner to that described above for the Eu^{III} and Nd^{III} systems in which a 1 x 10^{-5} M solution of either ligand **81** or **82** was titrated against specific known aliquots of a $Ln(CF_3SO_3)_3$ stock solution of the particular Ln^{III} under investigation, *i.e.* either Tb^{III}, Sm^{III}, Lu^{III} or Dy^{III}. Data was then fit using non-linear regression analysis as described before in order to elucidate the stoichiometric species in solution and their corresponding binding constants, as shall be discussed in the following sections.

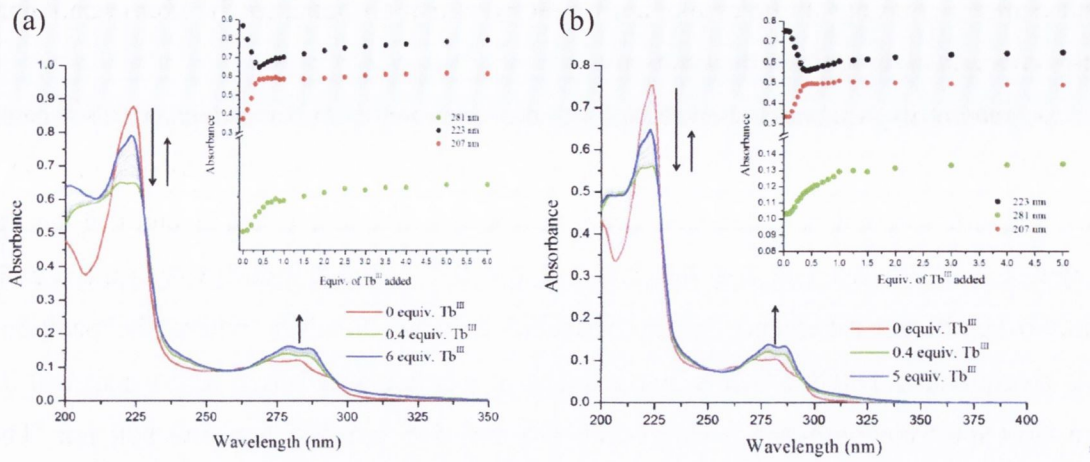

Figure 2.34. *The overall changes in the UV-visible absorption spectra upon titrating (a)* ***81*** *(0 - 6 equiv.) and (b)* ***82*** *(0→5 equiv.) (1 x 10^{-5} M) against $Tb(CF_3SO_3)_3$ in CH_3CN at RT.* ***Inset****: corresponding experimental binding isotherm of absorbance at λ = 207, 223 and 281 nm.*

The overall changes observed in the UV-visible absorption spectra following the titration of ligand **81** with $Tb(CF_3SO_3)_3$ in CH_3CN are displayed in Figure 2.34 (a). Between additions 0→0.4 equiv. of the $Tb(CF_3SO_3)_3$ metal salt the most pronounced changes occur, as indicated by the binding isotherms plotted for 207 nm, 223 nm and 281 nm in the graph inset in Figure 2.34 (a). The major absorption band assigned to the $S_0 \rightarrow S_2$ π-π^* transition (at λ_{max} = 223 nm) experienced a large hypochromatic effect within this metal concentration range, followed by a small absorption enhancement and then an eventual plateau upon the addition of subsequent Tb^{III} aliquots. The peak located at λ_{max} = 281 nm, representative of the $S_0 \rightarrow S_1$ π-π^* transition of the aromatic naphthalene functionality, experienced the most significant changes upon the addition of 0→1 equiv. of $Tb(CF_3SO_3)_3$. The absorption of this band was increased while, concurrently, slightly shifted to 278 nm. The shoulder of the 281 nm band was also redshifted to 285 nm following the addition of 1 equiv. of metal; again an absorbance plateau at higher Tb^{III} concentrations was evident.

Similarly, the UV-visible absorption spectra changes for **82** upon the titration of $Tb(CF_3SO_3)_3$ were analysed and shown to give rise to an identical trend, as shown in Figure 2.34 (b). This supports the conclusion that the same self-assembly process occurs in both instances with the same constituent species present in solution as equilibrium is altered and the self-assembly process proceeds for both ligands **81** and **82**.

Again the fluorescence emission spectra of ligands **81** and **82** was very weak being affected to only a small extent throughout the self-assembly process (see Appendix Figure A2.47 and A2.48 for overall changes in the fluorescence spectra of ligand **81** upon titrating against $Ln(CF_3SO_3)_3$ (Ln = Tb^{III}, Sm^{III}, Lu^{III} and Dy^{III}). Therefore, only the emergence of

Ln^{III}-centred emission (in the case of $Ln(CF_3SO_3)_3$ (Ln = Tb^{III} and Sm^{III})) from each solution was investigated throughout the titrations.

As shown in Appendix Figure A2.49, the emergence of time-delayed Tb^{III}-centred luminescence was monitored for both systems. In contrast to the changes observed in the Eu^{III} and Nd^{III}-centred emission spectra in previous sections the global changes in the Tb^{III}-centred emission were markedly different. At low Tb^{III} concentrations (0→0.4 equiv.) there was no significant emergence in luminescence evident, however, within the addition of 0.4→1 equiv. of $Tb(CF_3SO_3)_3$ a sharp intensity increase was observed in a typical Tb^{III} emission spectrum with bands centred at 490 nm, 545 nm, 585 nm and 620 nm. These emission bands are characteristic of deactivation from the $^5D_4$ excited state to the ^7F_J ground states, where J = 6 – 3. Upon subsequent additions of Tb^{III}, from 1→6 equiv., a more subtle but steady increase in emission intensity was observed. It was not possible to fit this unusual luminescence behaviour by non-linear regression analysis suggesting that a more complicated process is occurring. This observation was made with the previously studied helicate system involving ligand **62**,[21] in which an identical luminescence trend was observed for our amphiphilic ligands **81** and **82**. Again luminescence titration data was not possible to fit and measurements with **62** were repeated with samples that had been equilibrated over a period of 24 hrs. This gave rise to the same luminescence behaviour, and hence, confirmed that this difference was not due to slow kinetics. It was suggested that a back energy pathway is present, due to the close proximity of the ligand triplet state to the metal excited state, in which energy is transferred to the metal centre *via* sensitisation but is then transferred back to the triplet state of the ligand. This is definitely a plausible explanation as another energy migration pathway would indeed complicate the system, *i.e.* changes in solution equilibrium would not exactly be reflected in the luminescence changes observed. Another point to consider is the direct excitation of $Tb(CF_3SO_3)_3$. If $Tb(CF_3SO_3)_3$ is in fact directly excited by excitation at λ = 281 a continuous enhancement in Tb^{III}-centred emission would be expected as the metal salt concentration is continuously increased.

The overall changes observed in the UV-visible absorption spectra of ligand **81** following titration with $Sm(CF_3SO_3)_3$ in CH_3CN are depicted in Figure 2.35 (a), see Appendix Figure A2.50 for those changes observed for compound **82**. The binding isotherm graphs, see plots for 207 nm, 223 nm and 281 nm inset in Figure 2.35 (a) and Appendix Figure A2.50 (a), display an identical trend to previously investigated Ln^{III} systems. The Sm^{III}-centred emission of the system was also monitored and, as displayed above for titrations with Eu^{III} and Nd^{III}, was shown to exhibit a gradual enhancement in intensity upon the addition of 0.35 equiv. of $Sm(CF_3SO_3)_3$. Characteristic bands assigned to the $^4G_{5/2} \rightarrow {}^6H_J$ electronic transitions, where

J = 5/2, 7/2, 9/2, 11/2, were located at 565 nm, 600 nm, 645 nm and 708 nm. The gradual enhancement is indicative of formation of the most emissive 1:3 Sm.**81**$_3$ species in solution while the sharp decrease in emission intensity at -these characteristic wavelengths at higher equivalents (between 0.35→1 equiv.) of metal, and eventual plateau in emission (at Sm^{III} concentrations greater than 1 equiv.), suggest displacement of solution equilibrium towards the formation of the lesser emissive 1:2 (Sm.**81**$_2$) and 1:1 (Sm.**81**) species in solution.

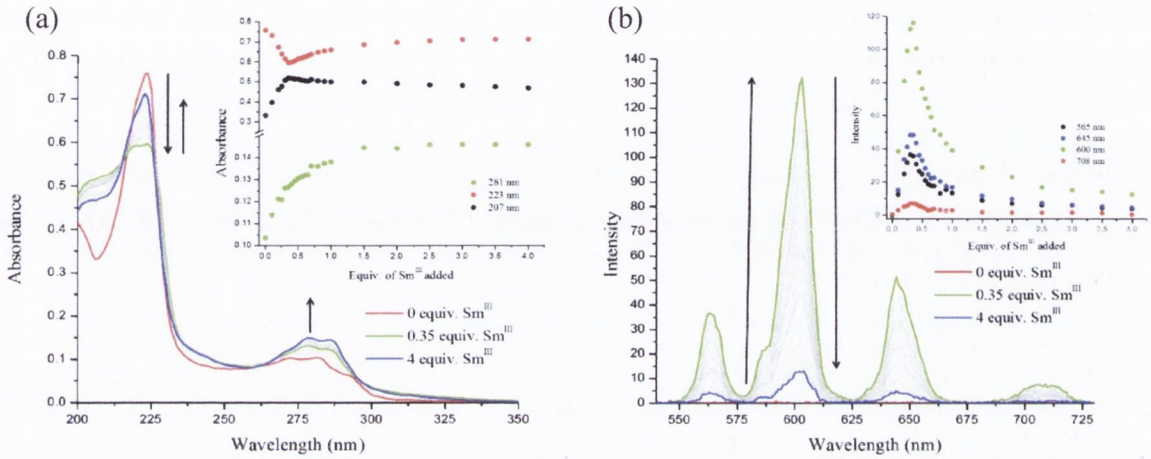

Figure 2.35. *The overall changes in the (a) UV-visible absorption spectra and (b) Sm^{III}–centred phosphorescence spectra upon titrating* ***81*** *(1 x 10^{-5} M) against $Sm(CF_3SO_3)_3$ (0→4 equiv.) in CH_3CN at RT.* ***Inset****: corresponding experimental binding isotherm of (a) absorbance at λ = 207, 223 and 281 nm and (b) Sm^{III} phosphorescence emission intensity at λ = 565, 600, 645 and 708 nm.*

The Ln^{III}-directed self-assembly of ligands **81** and **82** with $Lu(CF_3SO_3)_3$ and $Dy(CF_3SO_3)_3$ in CH_3CN were also evaluated spectroscopically, the overall changes in the UV-visible absorption spectra of which are shown in Appendix Figure A2.51 and A2.52. Results obtained for these titrations are comparable to those described above implying that the Ln^{III}-directed self-assembly process is identical for both amphiphilic isomers regardless of the metal ion employed. In order to gain a better understanding of each self-assembly system, *i.e.* to elucidate the stoichiometric species formed in solution and their corresponding binding constants, the global changes in the above titrations for **L** = **81** and **82** for Ln^{III} = Tb^{III}, Sm^{III}, Lu^{III} and Dy^{III} were further analysed by fitting the data using SPECFIT. The results obtained using SPECFIT are discussed below in the following section.

2.25 Fitting of titration data and calculation of complex stability constants

Analysis of the UV-visible absorption data recorded for the titration of **81** with $Tb(CF_3SO_3)_3$ pointed to the presence of three absorbing species in solution, the ligand itself (**81**), the 1:1 (Tb.**81**), and the 1:3 (Tb.**81**$_3$) species.

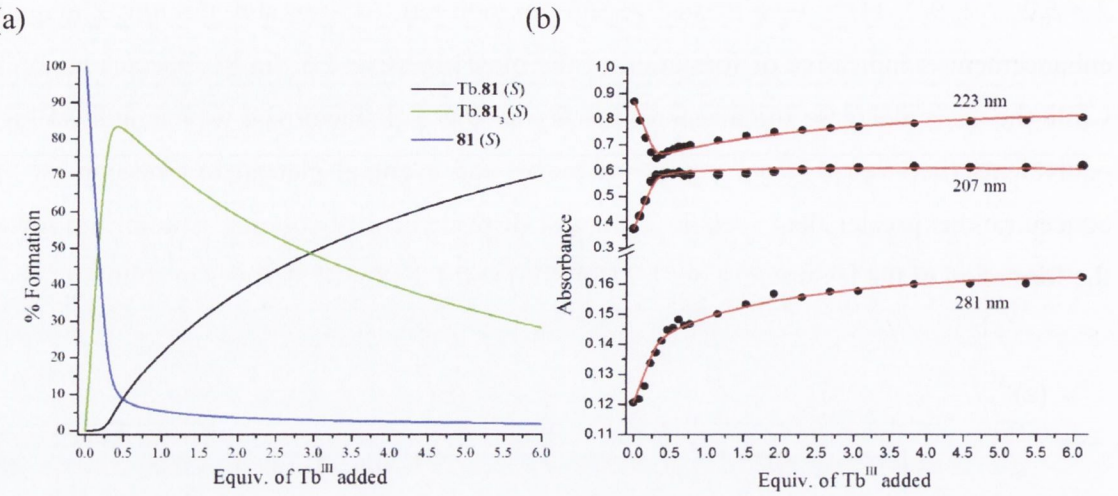

Figure 2.36. *(a) The speciation distribution diagram obtained from the UV-visible absorption titration data fit (upon titrating ligand* ***81*** *against $Tb(CF_3SO_3)_3$ in CH_3CN) and (b) the fit of the experimental binding isotherms using the non-linear regression analysis program SPECFIT.*

The speciation distribution graph and the binding isotherms obtained following fitting of this data are shown in Figure 2.36. From the speciation distribution graph it is clear that as the titration proceeds ligand **81** concentration quickly diminishes while the formation of the 1:3 Tb.**81**$_3$ species in 83% upon the addition of 0.4 equiv. of $Tb(CF_3SO_3)_3$ is observed, with a binding constant value of log β_{13} = 18.1 ± 0.3. An increase in Tb^{III} concentration leads to an equilibrium displacement with the 1:1 Tb.**81** species becoming the predominant species in solution towards the end of the titration when the metal concentration is high - Tb.**81** is formed with a binding constant value of log β_{11} = 5.8 ± 0.2 with it being formed in 66% yield following the addition of 5 equiv. of Tb^{III}.

Fitting of the UV-visible absorption data recorded for the titration of **82** with $Tb(CF_3SO_3)_3$ gave similar results with binding constant values of log β_{11} = 6.4 ± 0.0 and log β_{13} = 18.3 ± 0.2 calculated for the Tb.**81** and Tb.**82**$_3$ complexes, respectively (see Appendix Figure A2.53 for **82** fit and Table 2.7 for summary of binding constants). As mentioned in the previous section fitting of luminescence titration data involving $Tb(CF_3SO_3)_3$ was not possible and so shall not be discussed.

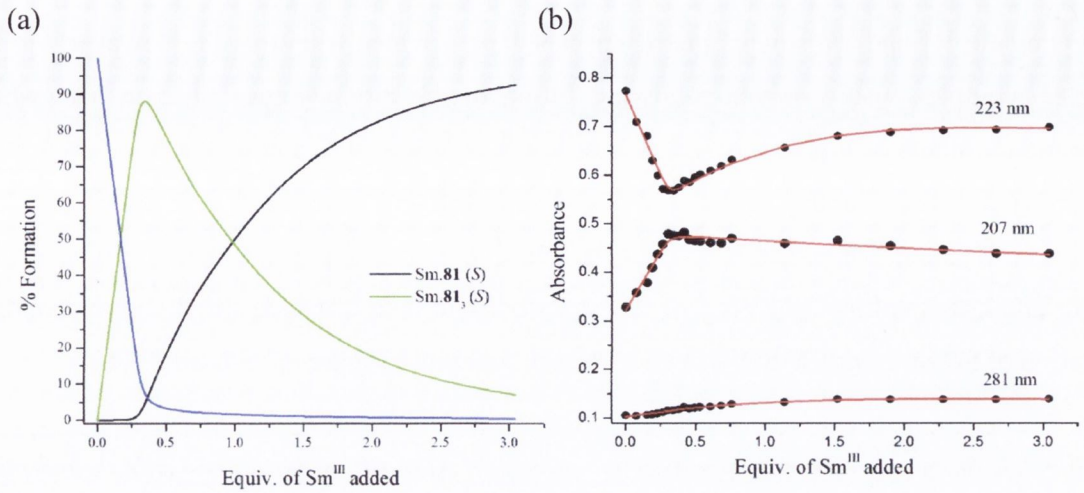

Figure 2.37. *(a) The speciation distribution diagram obtained from the UV-visible absorption titration data fit (upon titrating ligand* ***81*** *against $Sm(CF_3SO_3)_3$ in CH_3CN) and (b) the fit of the experimental binding isotherms using the non-linear regression analysis program SPECFIT.*

Changes in both the UV-visible absorption and luminescence titration data obtained for the titration of ligands **81** and **82** with $Sm(CF_3SO_3)_3$ were also examined using SPECFIT. The speciation distribution diagram and fit of the binding isotherms obtained from fitting the UV-visible absorption spectra following the titration of **81** with $Sm(CF_3SO_3)_3$ are shown in Figure 2.37. At approximately 0.35 equiv. of Sm^{III} the Sm.**81**$_3$ species is formed in 88% with a binding constant value of log β_{13} = 19.8 ± 0.5. Additional aliquots of the metal give rise to the predominant formation of the Sm.**81** complex with it being formed, with a binding constant value of log β_{11} = 6.8 ± 0.2, in 92% upon the addition of 3 equiv. of $Sm(CF_3SO_3)_3$.

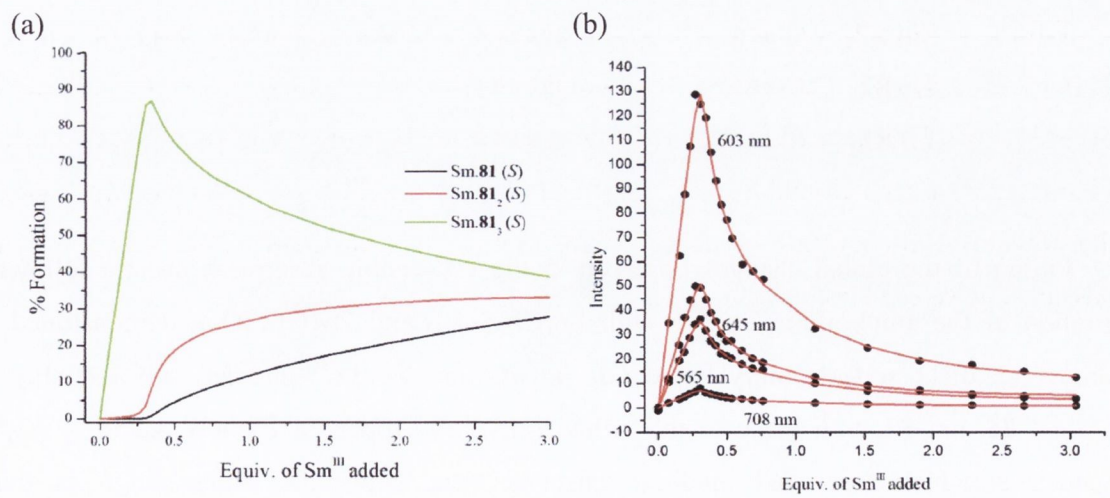

Figure 2.38. *(a) The speciation distribution diagram obtained from the luminescence titration data fit (upon titrating ligand* ***81*** *against $Sm(CF_3SO_3)_3$ in CH_3CN) and (b) the fit of the experimental binding isotherms using the non-linear regression analysis program SPECFIT.*

Only the 1:1 and 1:3 stoichiometric species were detected from this fit. However, the 1:2 Sm.**81**$_2$ complex was observed following fitting of the luminescence titration data where binding constants of log β_{11} = 6.2 ± 0.2, of log β_{12} = 13.2 ± 0.2 and of log β_{13} = 20.3 ± 0.2 were evaluated for Sm.**81**, Sm.**81**$_2$ and Sm.**81**$_3$, respectively (see Figure 2.38 and Table 2.7), with Sm.**81**$_3$ being formed in 87% after the addition of 0.35 equiv. of metal. Similar results were elucidated following fitting of the spectroscopic data obtained for the corresponding titration of **82** with $Sm(CF_3SO_3)_3$ in CH_3CN, see Appendix Figure A2.54 and A2.55.

Table 2.7. *Summary of binding constants calculated from fitting both UV-visible absorption and Ln^{III}-centred luminescence titration data for both R and S enantiomers **81** and **82**. *Value fixed, otherwise convergence not reached.*

Ln.L_3	UV-visible absorption			Luminescence		
	log β_{11}	log β_{12}	log β_{13}	log β_{11}	log β_{12}	log β_{13}
Eu.**81**$_3$	6.6 ± 0.2	13.8*	20.9 ± 0.3	6.7 ± 0.1	13.3 ± 0.2	19.9 ± 0.2
Nd.**81**$_3$	6.0 ± 0.3	-	18.3 ± 0.6	6.2 ± 0.2	-	17.2 ± 0.4
Tb.**81**$_3$	5.8 ± 0.2	-	18.1 ± 0.3	-	-	-
Sm.**81**$_3$	6.8± 0.2	-	19.8 ± 0.5	6.2 ± 0.2	13.2 ± 0.2	20.3 ± 0.2
Dy.**81**$_3$	6.7 ± 0.2	-	19.4 ± 0.4	-	-	-
Lu.**81**$_3$	6.3 ± 0.2	-	18.3 ± 0.3	-	-	-
Eu.**82**$_3$	6.7 ± 0.2	13.8*	20.5 ± 0.3	6.7 ± 0.2	14.3 ± 0.3	21.9 ± 0.4
Nd.**82**$_3$	6.1 ± 0.2	-	17.8 ± 0.4	6.5 ± 0.2	-	17.8 ± 0.3
Tb.**82**$_3$	6.4*	-	18.3 ± 0.2	-	-	-
Sm.**82**$_3$	6.8 ± 0.2	-	19.4 ± 0.4	6.2 ±0.2	13.4 ± 0.1	20.4 ± .2
Dy.**82**$_3$	6.6 ± 0.2	-	19.4 ± 0.4	-	-	-
Lu.**82**$_3$	6.2 ± 0.2	-	18.3 ± 0.3	-	-	-

Fitting of the global changes observed in the UV-visible absorption spectra following titration of the amphiphilic ligands with $Lu(CF_3SO_3)_3$ and $Dy(CF_3SO_3)_3$ demonstrated an almost identical self-assembly behaviour *in situ* for the Ln^{III}-directed self-assembly of ligands **81** and **82** with these metal triflate salts, see Appendix Figures A2.56 – A2.59. Species stoichiometries and binding constants were within the same range as those previously discussed, see Table 2.7 for summary of results.

It was reasonable to consider the possibility of a marked trend across the Ln^{III} series; from the largest Ln^{III} ion towards the smallest ion in the order Nd^{III}, Sm^{III}, Eu^{III}, Tb^{III}, Dy^{III}, Lu^{III}

i.e. did the size of the metal ion have an effect on the coordination environment and subsequently the species formed in solution and/or their stability in solution? By examining the SPECFIT data and binding constants generated it was evident that no noticeable trend occurred, *i.e.* the size of the Ln^{III} radius had no apparent influence on species stoichiometry or complex stability. All Ln^{III}-directed self-assembly systems were shown to progress in the same manner (within experimental error).

2.26 Langmuir monolayer formation of Ln.81$_3$ (*S*) and Ln.82$_3$ (*R*) complexes (Ln = Tb^{III}, Sm^{III}, Dy^{III}, Lu^{III})

For the sake of examining the adaptability and broadening the scope of LB films composed of Ln^{III}-directed self-assemblies of this nature the ability of the remaining four pairs of enantiomeric complexes to assemble at an air-water interface and form thin monomolecular Langmuir films was established.

The graph shown in Figure 2.39 (a) displays a typical pressure-area isotherm profile in each case following the investigation of the four *S* enantiomeric complexes (Tb.**81**$_3$, Sm.**81**$_3$, Lu.**81**$_3$ and Dy.**81**$_3$). Each isotherm displays the various phase transitions as the barriers are compressed and the monolayer is assembled. In the case of Tb.**81**$_3$ a disordered gaseous behaviour is displayed by the amphiphilic complex at areas greater than 160 $Å^2$. Further compression results in a steep exponential increase in surface pressure (during which the system enters the LE phase) where the molecules begin to organise and assemble at the interface. The Tb.**81**$_3$ material undergoes a phase transition to the LC phase which is signified by a change in the surface pressure-area isotherm at an area of 91 $Å^2$ where surface pressure steeply increases upon organisation of the molecules. The exact nature of the complex Langmuir monolayer is again unknown; however, film collapse takes place at a surface pressure of 30 mN m^{-1} for Tb.**81**$_3$ (while film collapse for Tb.**82**$_3$ occurs at 33 mN m^{-1}) which corresponds to a cross-sectional area occupancy for approximately three alkyl chains, as was shown for Eu^{III} and Nd^{III} systems in previous sections above. We can therefore assume that the system assumes a similar structural behaviour to the Eu^{III} and Nd^{III} systems in which the polar Tb^{III} coordination spheres are closely packed and orientated towards the water phase with the hexadecyl chains pointing out. All eight complexes organise into Langmuir monolayers of the same structural integrity, evidenced by their surface-pressure area isotherm graphs in Appendix Figure A2.60 – see Table 2.8 for mean molecular area values estimated upon Langmuir monolayer collapse.

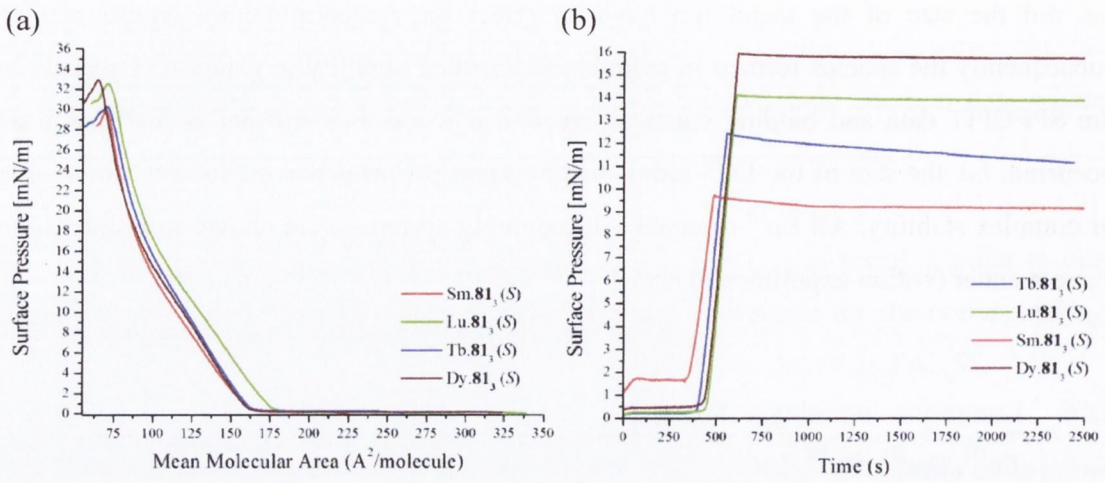

Figure 2.39. *(a) Surface pressure-area isotherms of Ln.**81**$_3$ (S). (b) Surface pressure-time profiles for Langmuir monolayers of Ln.**81**$_3$ (S), Ln = Tb^{III}, Sm^{III}, Lu^{III}, Dy^{III}.*

The stability of each monomolecular film was surveyed by maintaining the film in the LC state and monitoring the surface-pressure at the interface over an extended period of time (>30 mins). As shown by the surface pressure-time profiles for the Langmuir monolayers of Ln.**81**$_3$ (*S*) and Ln.**82**$_3$ (*R*), (Ln = Tb^{III}, Sm^{III}, Lu^{III}, Dy^{III}) (see Figure 2.39 (b) and Appendix Figure A2.60 (b)) all films remain stable and intact over this time interval.

These encouraging results inspired us to further expand our studies by then applying the Langmuir-Blodgett technique to organise these complexes into LB films with the additional prospect of developing multilayers composed of different visibly/NIR emitting (Eu^{III}/Nd^{III}/Tb^{III}/Sm^{III}) immobilised layers.

Table 2.8. *Surface-pressure and corresponding mean molecular area values upon film collapse for Ln.L$_3$ (Ln = Eu^{III}, Nd^{III}, Tb^{III}, Sm^{III}, Lu^{III}, Dy^{III} and L = **81** and **82**).*

Complex	Surface-pressure at collapse (mN/m)		Mean molecular area (A²/molecule)	
	L = **81**	L = **82**	L = **81**	L = **82**
Eu.**L**$_3$	29	34	76	74
Nd.**L**$_3$	33	32	74	71
Tb.**L**$_3$	30	33	71	66
Sm.**L**$_3$	30	35	70	70
Lu.**L**$_3$	33	34	71	62
Dy.**L**$_3$	33	32	65	58

2.27 Langmuir-Blodgett film formation of Ln.81$_3$ (*S*) and Ln.82$_3$ (*R*) complexes (Ln = Tb^{III}, Sm^{III}, Dy^{III}, Lu^{III})

High quality films possessing dimensions of 1 cm (h) x 1 cm (w) were successfully transferred and attached to the quartz substrate as before whereby the hydrophilic slide (10 mm x 1 mm x 35 mm) was lowered and submerged into the subphase before the amphiphilic complex was spread onto the surface. The amphiphile was then organised into the LE phase and allowed to stabilise (20 mins) before emersion of the slide by means of an upward stroke (at a speed of 4 mm min^{-1}) resulted in monolayer transfer with transfer ratios of ~ 1 obtained in all cases, indicating transfer of high quality films possessing Z-type architecture.

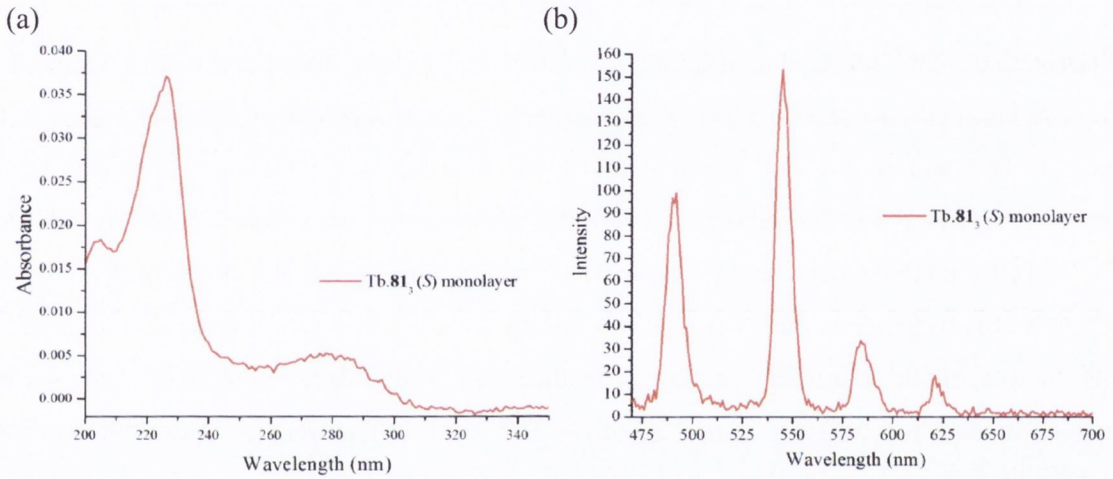

Figure 2.40. *(a) UV-visible absorption spectra and (b) Tb^{III}-centred phosphorescence spectra of Tb.**81**$_3$ (S) immobilised on quartz slide (excitation at λ_{ex} = 281 nm).*

The photophysical properties of the LB films were then evaluated and as before showed retention of UV-visible absorption and emissive characteristics upon solid state fabrication. The photophysical properties of both Tb^{III} complex monolayers are shown in Figure 2.40 (a) and Appendix Figure A2.61 - A2.62. The UV-visible absorption spectrum in each case is again dominated by the two main absorption bands at λ = 223 nm and λ = 281 nm while excitation into the sensitsing naphthalene moiety again gives rise to a typical Tb^{III}-centred luminescence spectrum. Excitation spectra (λ_{em} = 545 nm) were also recorded for both monomolecular complex films, both matching closely the structure of the UV-visible absorption spectra. Tb^{III} excited state lifetime measurements were also conducted giving rise to luminescence decays which were best fit to a bi-exponential function indicating the presence of two luminescent species in the film. Lifetime values of 1.312 ms and 0.071 ms were obtained for the Tb.**81**$_3$ monolayer and values of 1.514 ms and 0.225 ms were obtained for the Tb.**82**$_3$ monolayer. The longer lived excited state species (possessing lifetimes of 1.312 ms and 1.514 ms) is representative of the fully saturated 1:3 complexes Tb.**81**$_3$ and

Tb.**82**$_3$ within the film, *i.e.* these measurements support the assumption that the majority of the 1:3 complexes remain intact within the LB films.[105] The second shorter lived excited state species may be a partially dissociated species within the film which has lost 1 or 2 tridentate ligands during the LB process leaving the metal centre exposed and available for H_2O subphase coordination. The chiral nature of these Ln^{III}-based LB films was also probed using CD and CPL analysis. Unfortunately no signal was detected from either technique. These results do however illustrate that immobilisation of these films is not at the complete detriment of the desirable photophysical features.

Typical UV-visible absorption spectra were exhibited by LB films of Sm.**81**$_3$ and Sm.**82**$_3$, as shown in Appendix Figures A2.63 (a) and A2.64 (a), while upon excitation at $\lambda = 281$ nm characteristic Sm^{III}-centred emission was detected. In these instances it was difficult to achieve luminescence due to a less efficient energy transfer mechanism from the ligand to the metal centre and so the Sm^{III}-centred emission observed was very noisy. For this reason reliable excitation and luminescence lifetime measurements were unattainable. In addition, CD and CPL analysis were again implemented but could not verify the chirality of the films.

Attempts to generate dual light emitting multi-layered LB systems were also undertaken. Efforts were made to initially coat a quartz slide with a monolayer of the Eu^{III} complex and then to attach a second layer composed of the Tb^{III} system. The transfer of two films (Tb.**81**$_3$ and Eu.**81**$_3$) was achieved with good transfer ratios (~1) but examination of the photophysical properties of such immobilised films elucidated that the sensitisation *via* energy transfer from the ligand to the Ln^{III} centre was much more efficient for Eu^{III} in comparison to the Tb^{III} system, *i.e.* Tb^{III}-centred emission could not be detected using the same parameters as those implemented for the exhibition of Eu^{III}-centred emission. To overcome this limitation it would be necessary to coat the slide with additional layers of the Tb^{III} complex, however, from above investigations it was noted that following the deposition of a third LB film transfer quality deteriorates substantially. The deposition of layer numbers greater than three is not reliably possible as it had been observed above. Once the third layer was attached subsequent layering efforts saw an attachment/detachment cycle. At this point, due to the above findings, the extent to which this project could be taken was limited requiring a fundamental change in strategy whereby the ligand required re-evaluation and perhaps re-design, in which the incorporation of a more efficient Tb^{III} sensitising moiety may in fact overcome this obstacle.

2.28 Conclusion

The main objective for this project was to functionalise the relatively simple "half helicate" framework with a hexadecyl alkyl chain to produce amphiphilic ligands **81** and **82** for the

formation of 1:3 Ln^{III}-based luminescent systems capable of Langmuir monolayer assembly at an air-water interface with a view to then fabricate highly ordered Ln^{III} luminescent monomolecular LB films.

Following the successful results obtained for the visibly emitting Eu^{III} and NIR emitting Nd^{III} systems (which have been discussed and summarised in Sections 2.11 and 2.20) this project was then expanded to include a number of other Ln^{III} metal ions, namely Tb^{III}, Sm^{III}, Lu^{III} and Dy^{III}, all of which demonstrated the ability to self-assemble ligands **81** and **82** in an identical manner *in situ*, forming conclusively the 1:1 Ln.**L** and the 1:3 Ln.$\mathbf{L}_3$ (Ln = Tb^{III}, Sm^{III}, Lu^{III} and Dy^{III}, **L** = **81** and **82**) species in CH_3CN. All eight Ln.$\mathbf{L}_3$ 1:3 complexes exhibited facile monolayer formation at an air–water interface. LB films of Tb.$\mathbf{L}_3$ and Sm.$\mathbf{L}_3$ (**L** = **81** and **82**) were then deposited onto quartz slides with high quality transfer ratios (~1) while spectroscopic measurements depicted the exhibition of both UV-visible absorption and Ln^{III}-centred luminescence from each monolayer. However, the limit of these LB systems was reached at this point since no CPL emission was detectable from LB films of Tb.$\mathbf{L}_3$ or Sm.$\mathbf{L}_3$ (**L** = **81** and **82**). The inability to coat a large number of layers onto the solid substrate further prevented the succession of this project in the development of dual/multi light emitting ultrathin solid structures.

The merging of Ln^{III}-directed self-assemblies with solid state fabrication techniques has experienced a remarkable advancement as a result of this study. Previous to this work Ln^{III} luminescent systems have been incorporated, by our group and others, into materials using solid state techniques such as hydrogel incorporation and AuNP attachment. The implementation of the LB technique however has received much less attention for systems of this type, as is evidenced by the few examples discussed in chapter one. Future prospects for this project are limitless with adjustments to the current amphiphilic ligands **81** and **82** currently underway. Furthermore, Ln^{III}-based cyclen systems have been incorporated into LB films by other members of our group, displaying significantly improved emissive properties and amino acid sensing capabilities.

Chapter Three

Chiral helical assemblies for enhanced solubility in competitive solvent media

3. Introduction

Synthetic supramolecular helicates are of current interest because they are reminiscent of biomolecules, such as the double-helical arrangement of nucleic acids in DNA and α-helices of polypeptides, representing the complexity of self-organisation and cooperativity found in nature.[17,26,271] By pre-programming individual constituents for metal-directed self-assembly and selective formation of helical systems case studies can be provided; presenting model systems for the mechanisms, thermodynamics, kinetics and dissociation of biologically relevant double-helical macromolecules.[26] The potential variations in such structures has led to the development of a vast number of transition metal based helicates,[167,271-275] and to a lesser extent, Ln^{III} based helicates.[21,162,165,174,276] As mentioned in chapter one, the large coordination requirements and the unique photophysical and magnetic properties of the Ln^{III} have ignited a surge of interest in the controlled spontaneous association of chiral Ln^{III}-directed helical assemblies.

The rationale behind moving self-assemblies into water based solvent systems stems from the fact that biological processes are dominated by chemistry in an aqueous environment. It is crucial therefore to move supramolecular chemistry from organic media into water (or more aqueous media *i.e.* mixed alcohol/H_2O solvent systems) for a better understanding of biochemical mechanisms in nature.[277] In addition to this, water serves as a 'greener' more environmentally friendly non-toxic alternative solvent system.[278] Furthermore, water solubilisation of functional supermolecules is of utmost importance for the development of supramolecular technologies in biological diagnostic applications such as optical biosensors, bioprobes and cellular imaging agents.[277]

As shown in chapter one, attachment of an ethylene glycol ethyl ether water solubilising functionality to the 4-*para* position of Pybox, affording **17**, has been developed by de Bettencourt-Dias *et al.* and shown to self-assemble, *via* Ln^{III}-directed coordination, and successfully sensitise Ln^{III} in a 100% aqueous environment.[114] Carboxylic acid and polyoxyethylene functional groups have also been appended to the bis(benzimidazole)pyridine framework, by Bünzli and co-workers, and shown to confer water solubility in helicate ligands **44** – **48**, enabling the implementation of highly stable homodinuclear triple stranded helicate assemblies as cell imaging agents and detection probes.[174,176-179,181,276] Evidently, appropriate functionalisation of self-assembly constituents can harness stable water soluble Ln^{III} architectures which not only retain their photophysical properties but which possess luminescent features which can be employed as a functioning tool.

As discussed in chapter one the Ln^{III}-directed self-assembly of **62** – **66** gave rise to highly stable enantiomerically pure dinuclear triple stranded helicates with CPL spectra confirming transfer of chirality to the metal centre upon complexation.[64,69] These previous studies carried out within the Gunnlaugsson group on the formation of enantiomerically pure triple stranded dimetallic helicates have all been conducted in either CH_3CN or in an CH_3CN:$CHCl_3$ (50:50) mixed organic meda. Modification of this system for future advances towards bio-conjugation and/or exploitation of complex chirality requires water solubility. By carefully considering the introduction of substituents to the 4 pyridyl position of such systems an enhancement in solubility in more competitive media may be achieved while a detrimental effect to the photophysical properties may be simultaneously avoided.[106] With a view to eventually obtaining fully water soluble systems it was envisaged that grafting a polyoxyethylene chain onto the Gunnlaugsson helicate framework would have an insignificant effect on the overall photophysical properties of the system while imparting some degree of water solubilisation. The current chapter focuses on developments made to the original helicate ligand **62** in which a polyoxyethylene chain has been introduced to the 4-*para* position to aid solubility in more competitive media and the effect this additional functionality has on the self-assembly process.

3.1 Design, synthesis and characterisation of ligands 87 (*S*,*S*) and 88 (*R*,*R*)

The design of ditopic ligands **87** (*S*,*S*) and **88** (*R*,*R*) for Ln^{III}-directed self-assembly of dimetallic triple stranded helicates was based on the aforementioned chiral ligand **62**. Both **87** and **88** consist of a symmetric bis(tridentate) structure in which both diamidopyridyl (NO_2) chelating units are linked *via* an *m*-xylylenediamine spacer group.

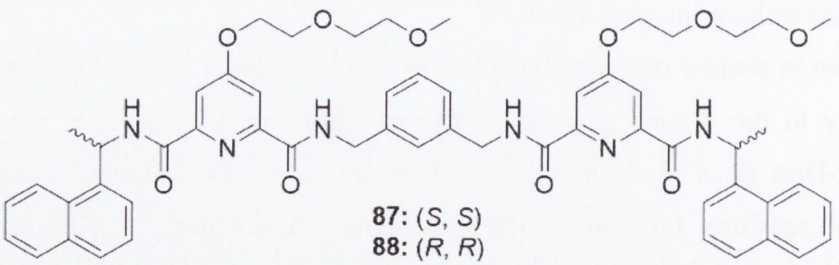

87: (*S*, *S*)
88: (*R*, *R*)

As seen for **62**, the 1-(1-naphthyl)-ethylamine antenna functionality incorporated for both Ln^{III} sensitisation and structure conformation stability in the corresponding complex, also bestows ligand chirality giving rise to either (*S*,*S*) or (*R*,*R*) ligand stereochemistry. Derivatisation of the 4-*para* position of the two pyridine units with polyoxyethylene groups shall, in theory, enhance the solubility of such systems in more competitive media. Preparation of ligands **87** and **88** involved a two part synthetic procedure in which the

polyoxyethylene chain precursor 1-iodo-2-(2-methoxyethoxy)ethane **91** was synthesised in parallel to the enantiomeric pair **94** (*S*) and **95** (*R*).

The first step in the synthetic pathway towards **91** was an S_N2 substitution reaction, as illustrated in Scheme 3.1 in which diethylene glycol methyl ether **89** (in THF) was added to a solution of NaOH in H_2O at 0 °C followed by the addition of tosyl chloride. This mixture was allowed to reach RT and then left stirring for a further three days after which solvent was removed under reduced pressure yielding a white solid. The solid residue was then redissolved in $CHCl_3$ and washed with 1 M aq. NaOH, H_2O and dried over $MgSO_4$. Solvent was again removed *in vacuo* affording 2-(2-methoxyethoxy)ethyl 4-methylbenzenesulfonate **90** as a colourless oil in 53% yield. ^{1}H NMR (400 MHz, $CDCl_3$), ^{13}C NMR (100 MHz, $CDCl_3$) and high resolution mass spectrometry (HRMS) data for **4** correlated well with previously reported literature values.[279,280]

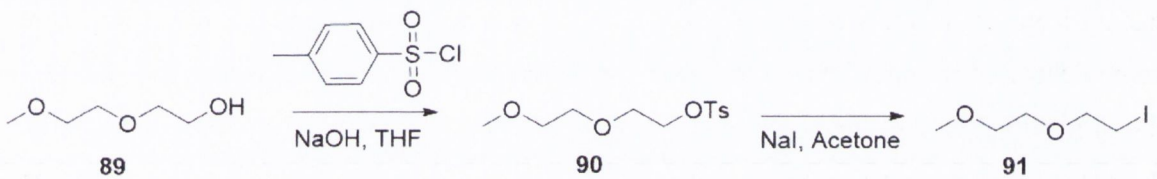

Scheme 3.1. *Synthetic pathway towards polyoxyethylene chain precursor **91**.*

The tosyl group of **90** was converted to the corresponding iodo compound by means of a second S_N2 substitution reaction by refluxing **90** and NaI in acetone for 16 hrs. The solution was then filtered by suction filtration and solvent evaporated under reduced pressure. The resulting brown residue was dissolved in $CHCl_3$ and washed with H_2O, brine and dried over $MgSO_4$. Solvent was removed *in vacuo* yielding a brown oil, **91**, in 85% yield which was characterised by ^{1}H NMR (400 MHz, $CDCl_3$), ^{13}C NMR (100 MHz, $CDCl_3$) and HRMS.[280]

In parallel, chelidamic acid **92** was monoprotected using benzyl bromide (BnBr), as shown in Scheme 3.2. Firstly **92** was heated to 65 °C in DMF in the presence of $NaHCO_3$. 0.5 equiv. of BnBr was then added and the mixture stirred at 65 °C overnight. The reaction mixture was filtered by suction filtration and solvent removed under reduced pressure leaving an oily yellow residue which was dissolved in CH_3OH. To this residue H_2O was added, after which **93** precipitated from solution as an off white solid in 50% yield. Compound **93** was assessed by ^{1}H NMR (400 MHz, DMSO-d_6), ^{13}C NMR (100 MHz, DMSO-d_6), HRMS and IR analysis with the appearance of a singlet resonance at 5.38 ppm, representing the CH_2 protons, and the aromatic protons of the benzyl group appearing at 7.49 ppm and 7.44 – 7.37 ppm in the ^{1}H NMR spectrum, confirming monoprotection of **92**.

It is worth noting at this point that this project has been carried out in collaboration with Dr. Jonathan Kitchen and that all syntheses and measurements of the (*R,R*) enantiomer **88**

have been carried out by him. For the purpose of this chapter results obtained for the (*S,S*) enantiomer **87** will be discussed more with regular relevant referencing to the results obtained for **88**.

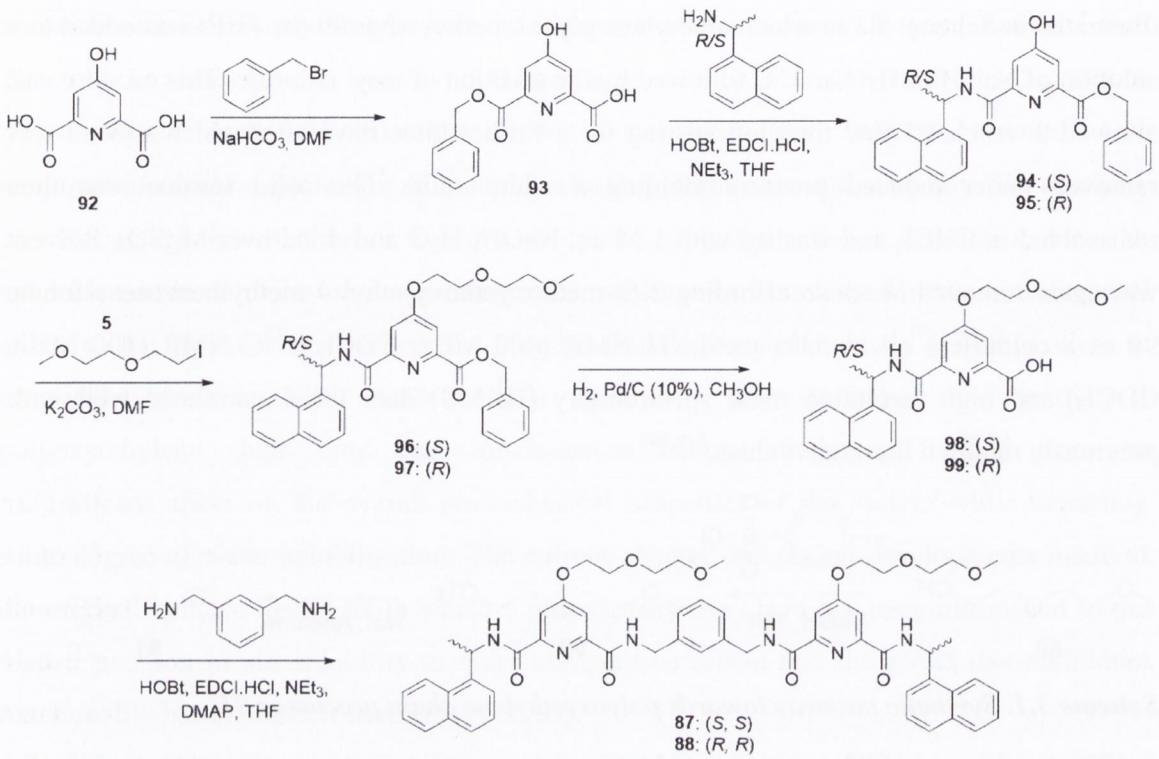

Scheme 3.2. *Synthetic pathway towards helicate ligands* ***87*** *and* ***88****.*

Introduction of the appropriate (*S* or *R*) 1-(1-naphthyl)-ethylamine antenna moiety was achieved *via* an EDCI·HCl peptide coupling reaction. A mixture of 6-(benzyloxycarbonyl)-4-hydroxypicolinic (**93**), HOBt, NEt_3 and 1 equiv. of (*S*)-(-)-1-(1-naphthyl)ethylamine in THF were placed under Ar and cooled to 0 °C. After 30 mins of stirring EDCI·HCl was added to the mixture and stirred at 0 °C for a further 30 mins. The reaction mixture was then allowed to reach RT and stirred for a further 48 hrs, leaving a yellow solution with a white solid residue. The solution was filtered and THF removed under reduced pressure to give an orange oil which was taken up into CH_2Cl_2. The solution was then washed with 2.0 M HCl, sat. aq. $NaHCO_3$, H_2O and brine and the organic phase dried over $MgSO_4$. The solvent was removed under reduced pressure, yielding **94** as an orange oil in 97% yield. The appearance of a doublet at 1.78 ppm and a multiplet at 6.06 ppm in the ^1H NMR spectrum (600 MHz, $CDCl_3$) of **94**, corresponding to the CH_3 and CH groups of the antenna moiety, respectively, clearly indicate peptide bond formation and the successful functionalisation of **93**. Compound **94** was also characterised by ^{13}C NMR (150 MHz, $CDCl_3$), HRMS and IR analysis and was shown to give identical results.

The polyoxyethylene chain **91** was grafted onto (*S*)-benzyl 4-hydroxy-6-(1-(naphthalen-1-yl)ethylcarbamoyl)picolinate (**94**) by means of another S_N2 substitution reaction. Ligand **94** and K_2CO_3 were stirred in anhydrous DMF for 30 mins at 25 °C before one equiv. of **91** was added and the reaction mixture stirred at 50 °C for a further 72 hrs. The solvent was removed under reduced pressure leaving a brown oily residue which was redissolved in CH_2Cl_2 and washed with 1% acetic acid, H_2O and dried over $MgSO_4$. The solvent was removed under reduced pressure yielding an orange oil which was purified by silica flash column chromatography under gradient elution conditions (Hexane/Ethyl Acetate) affording **96** in 40% yield. Successful product formation was indicated by resonances representing the CH_2 and CH_3 groups of the appended chain appearing at 3.28, 3.47, 3.57, 4.07 and 4.41 ppm in the ^1H NMR spectrum (600 MHz, $CDCl_3$) of **96**. Compound **96** was also verified by ^{13}C NMR (150 MHz, $CDCl_3$), HRMS and IR analysis.

Removal of the benzyl protecting group was achieved by hydrogenolysis using a Parr hydrogen shaker apparatus. Compound **96** was placed with a 10% Pd/C catalyst in CH_3OH under 3 atm of H_2 for 48 hrs. The reaction mixture was then filtered through celite and solvent removed *in vacuo* yielding the half helicate precursor **98** in 84% yield. The half helicate precursor **98** was identified by ^1H NMR (400 MHz, DMSO-d_6), ^{13}C NMR (100 MHz, DMSO-d_6), HRMS, elemental and IR analysis with the disappearance of the CH_2 and benzyl proton resonances representing deprotection of **96** giving **98**.

The desired compounds **87** and **88** were obtained in the final step *via* a second peptide coupling reaction similar to that discussed above for **94** and **95**. A mixture of (*S*)-4-(2-(2-methoxyethoxy)ethoxy)-6-(1-(naphthalen-1-yl)ethylcarbamoyl)picolinic acid (**98**), HOBt, DMAP, NEt_3, and 0.5 equiv. of *m*-xylylenediamine in THF were placed under Ar and cooled to 0 °C. After 30 mins of stirring EDCI·HCl was added to the mixture and the resulting mixture stirred at 0 °C for a further 30 mins. The reaction mixture was then allowed to reach RT and stirred for 48 hrs. The solution was then filtered and THF removed under reduced pressure to give an orange oil which was taken up in CH_2Cl_2. An acid-base extraction yielded a brown fluffy solid which was redisssolved in CH_2Cl_2 and precipitated out of diethyl ether giving **87** as a white solid in 45% yield while **88** was afforded in 40% yield. Both compounds **87** and **88** were characterised by ^1H NMR (600 MHz, CD_3CN), ^{13}C NMR (150 MHz, CD_3CN), HRMS, elemental and IR analyses. A detailed assignment of all the protons for **87** and **88** was performed by a combination of 1D and 2D NMR experiments (see Appendix Figures A3.1 – A3.5). As shown below in the ^1H NMR spectrum (600 MHz, CD_3CN) of **87**, Figure 3.1 (see Figure A3.6 for ^1H NMR spectrum of **88**), signals corresponding to the two CH_2 methylene group protons of the spacer group reside at 3.71 and 3.67 ppm, the triplet of

the two NH protons (adjacent to the CH_2 groups) appear at 8.99 ppm and the four phenyl proton resonances are located at 7.16 and 7.07 ppm evidencing the isolation of the desired product **87** (*S,S*).

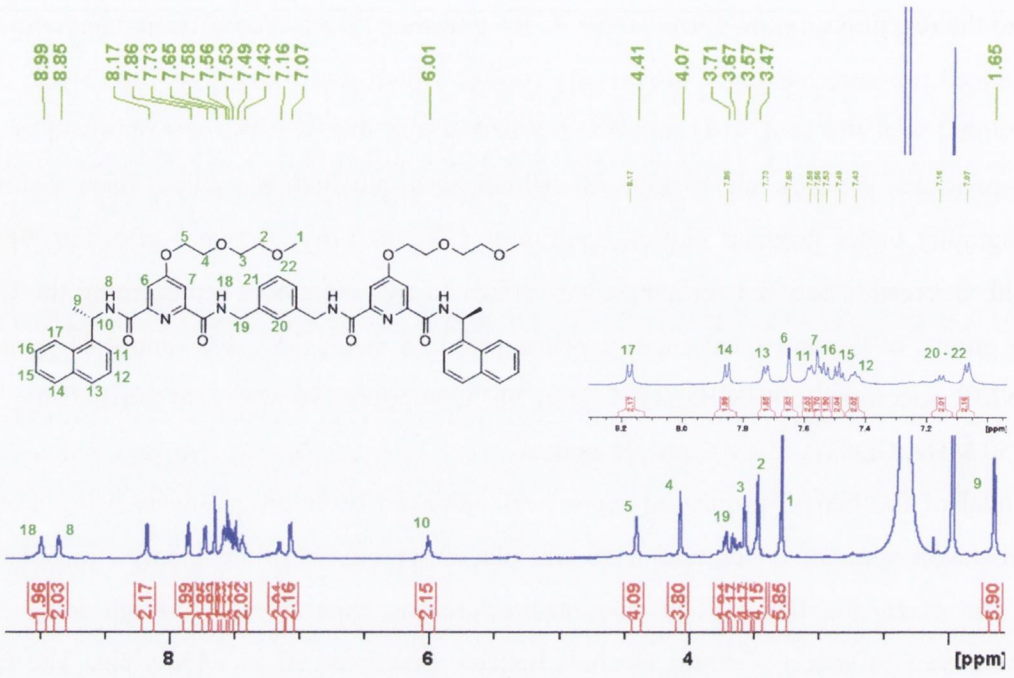

Figure 3.1. *^{1}H NMR spectrum (600 MHz, CD_3CN) of **87** (S,S).*

3.2 Formation of dimetallic triple stranded helicate complexes $Eu_2.87_3$ (*S,S*) and $Eu_2.88_3$ (*R,R*)

Following successful synthesis of **87** and **88** the dimetallic triple stranded helicate complexes, $Eu_2.87_3$ (*S,S*) and $Eu_2.88_3$ (*R,R*), were prepared by complexing the appropriate ligand with $Eu(CF_3SO_3)_3$ in a 2:3 stoichiometric M:L ratio in HPLC CH_3OH.

The synthetic procedure entailed application of microwave irradiation at 70 °C for 10 mins (see Scheme 3.3) followed by vapour diffusion of diethyl ether, affording the isolated complexes $Eu_2.87_3$ and $Eu_2.88_3$ as white solids in 78% and 71% yields respectively. Both $Eu_2.87_3$ and $Eu_2.88_3$ were characterised by ^{1}H NMR (see Figure 3.2 and Appendix Figure A3.7), but neither $Eu_2.87_3$ nor $Eu_2.88_3$ were detectable by HRMS in the range of solvents (CH_3OH, CH_2Cl_2, CH_3CN) investigated. To date, it has also not been possible to verify the formation of other similar 2:3 helicate systems studied within the Gunnlaugsson group by HRMS, despite many attempts.

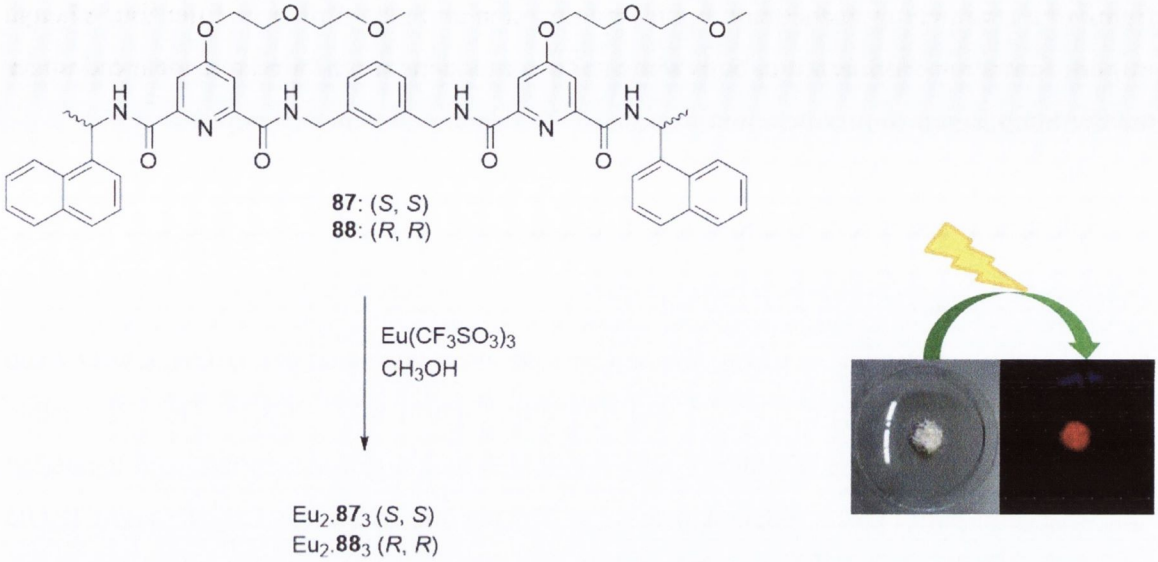

Scheme 3.3. *Preparation of Eu^{III} complexes $Eu_2.87_3$ and $Eu_2.88_3$ carried out under microwave irradiation at 70 °C.*

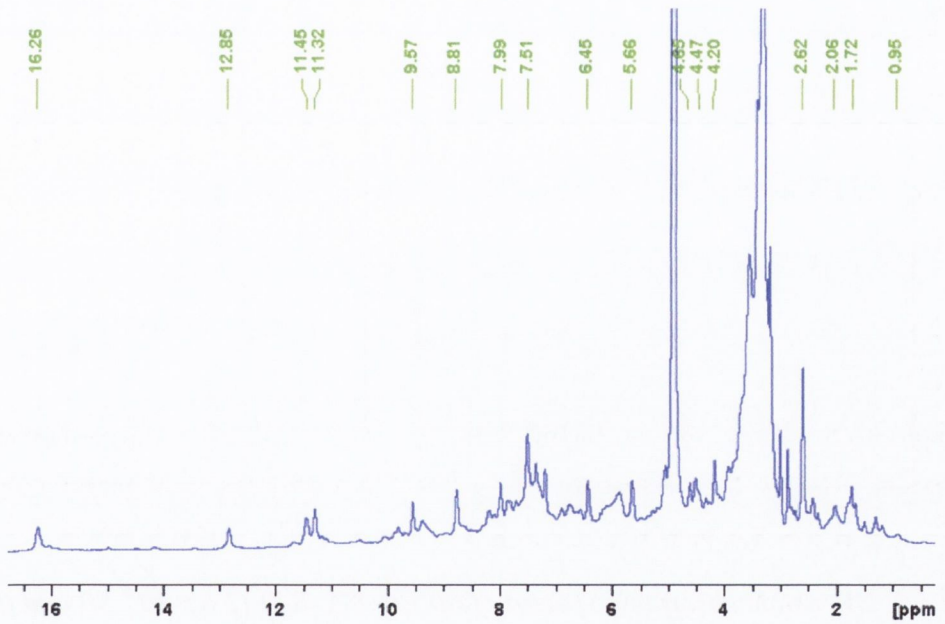

Figure 3.2. *^{1}H NMR spectrum (400 MHz, CD_3OD-d_4) of $Eu_2.87_3$ (S,S.).*

The paramagnetic nature of Eu^{III} induces large chemical shifting and broadening of signals in its ^{1}H NMR complex spectra (400 MHz, CD_3OD-d_4). As is evident from those shown for $Eu_2.87_3$ and $Eu_2.88_3$, which display identical ^{1}H NMR spectra, signals appear broadened and shifted, clearly signifying successful complexation. Elemental and IR analyses were also employed to verify successful formation of both complexes. Elemental analysis confirmed formation of the desired 2:3 species in both cases while IR was also representative of Eu^{III} complexation *via* a shift of the amide carbonyl group stretching frequency. A reduction in the IR stretching frequency of the amide carbonyl band (from 1657 cm^{-1} to 1629 cm^{-1} for $Eu_2.87_3$ and from 1655 cm^{-1} to 1623 cm^{-1} for $Eu_2.88_3$) in each case

signified a lengthening of the bond upon complexation and thus further justified $Eu_2.\mathbf{87}_3$ and $Eu_2.\mathbf{88}_3$ formation. Furthermore, both white solid compounds were found to appear red under the UV lamp, again signifying complexation of the ligand to the metal centre.

Once complexes $Eu_2.\mathbf{87}_3$ and $Eu_2.\mathbf{88}_3$ had been synthesised and characterised their photophysical properties in solution were then examined.

3.3 Photophysical characterisation of complexes $Eu_2.87_3$ and $Eu_2.88_3$

The photophysical properties of $Eu_2.\mathbf{87}_3$ and Eu2.$\mathbf{88}_3$ were evaluated in CH_3OH, CD_3OD and CH_3CN, as shown in Figure 3.3 – 3.6 and Appendix Figures A3.8 - A3.14. The UV–visible absorption spectra of these complexes were dominated by a major absorption band located at λ_{max} = 281 nm with two shoulders appearing at 270 nm and 293 nm in CH_3OH and CD_3OD but which were less pronounced in CH_3CN. This band is assigned to the naphthalene antenna $S_0 \rightarrow S_1$ $\pi \rightarrow \pi^*$ transition while the $S_0 \rightarrow S_2$ $\pi \rightarrow \pi^*$ transition was also evident at λ_{max} = 223 nm.

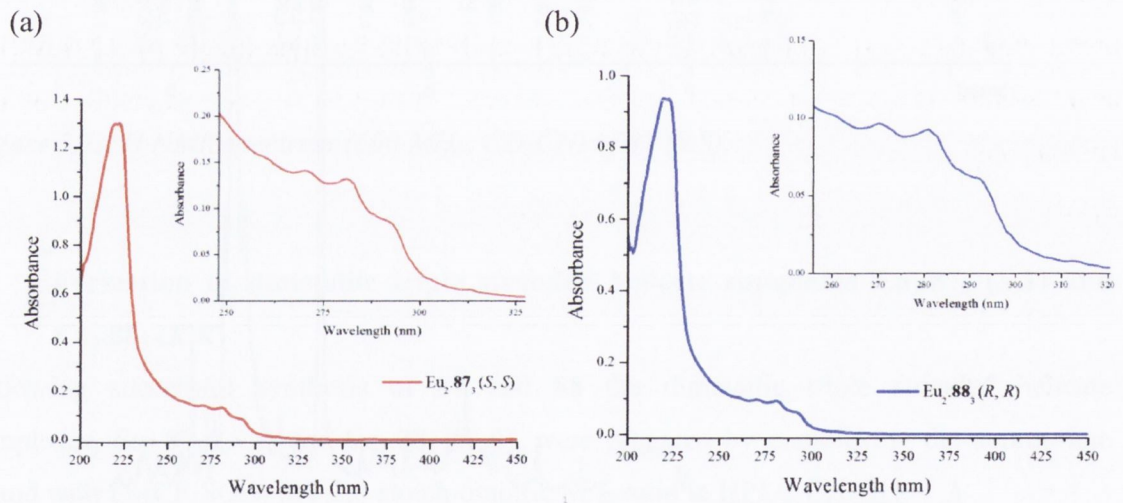

Figure 3.3. *UV-visible absorption spectra of (a) $Eu_2.\mathbf{87}_3$ (S,S) (2.6 x 10^{-6} M) and (b) $Eu_2.\mathbf{88}_3$ (R,R) (2 x 10^{-6} M) in CH_3OH.*

Excitation of the naphthalene chromophore at λ_{max} = 281 nm gave rise to Eu^{III}-centred luminescence from both complexes in all three solvent systems studied indicating effective population of the $^5D_0$ excited state and subsequent deactivation to the ^5F_J (J = 0 - 4) ground states with line-like emission bands appearing at 579 nm ($^5D_0 \rightarrow {}^7F_0$), 593 nm ($^5D_0 \rightarrow {}^7F_1$), 614 nm ($^5D_0 \rightarrow {}^7F_2$), 649 nm ($^5D_0 \rightarrow {}^7F_3$), and 695 nm ($^5D_0 \rightarrow {}^7F_4$), respectively, as shown in Figure 3.4 and Appendix Figures A3.10 - A3.11.

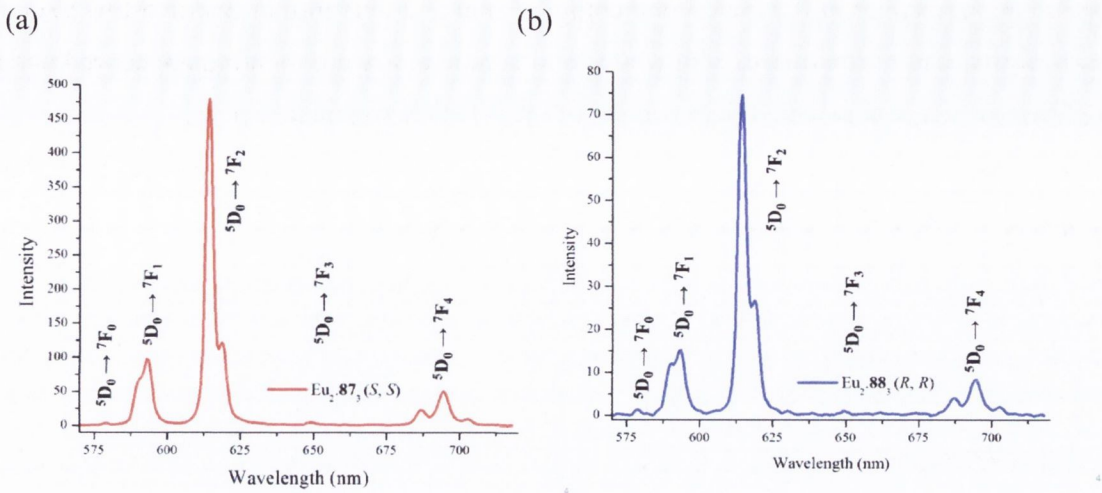

Figure 3.4. *Eu^{III}-centred luminescence emission spectra of (a) $Eu_2.\mathbf{87}_3$ (S,S) (2.6 x 10^{-6} M) and (b) $Eu_2.\mathbf{88}_3$ (R,R) (2 x 10^{-6} M) in CH_3OH.*

The excitation spectra of $Eu_2.\mathbf{87}_3$ and $Eu_2.\mathbf{88}_3$ were also recorded in CH_3OH, CH_3OD and CH_3CN and displayed maximum intensity (λ_{em}= 615 nm) at approximately 226 nm with a broad shoulder at 281 nm (shown below in Figure 3.5 and Appendix Figure A3.12 – A3.13) again signifying successful sensitisation of the Eu^{III} centre by indirect excitation of the antenna moiety.

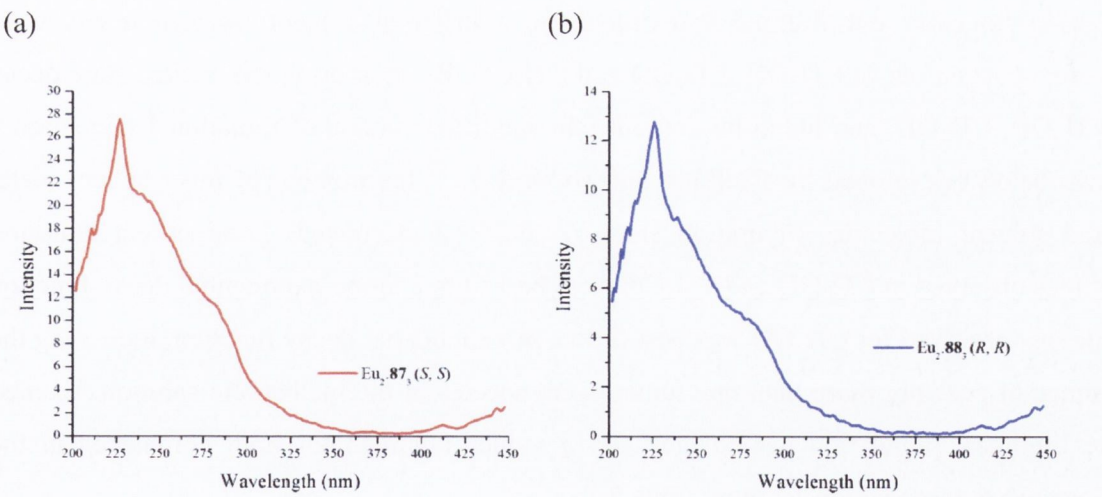

Figure 3.5. *Excitation spectra of (a) $Eu_2.\mathbf{87}_3$ (S,S) (2.6 x 10^{-6} M) and (b) $Eu_2.\mathbf{88}_3$ (R,R) (2 x 10^{-6} M) in CH_3OH (λ_{em} = 615 nm).*

Ligand centred emission was also recorded in both CH_3OH and CH_3CN, as shown in Figure 3.6 and Appendix Figure A3.14, with a band centred at λ_{max} = 400 nm. This band was shown to undergo a decrease in emission intensity following the formation of the 2:3 species *in situ*, confirming efficient energy transfer from the ligand to the metal centre upon complexation.

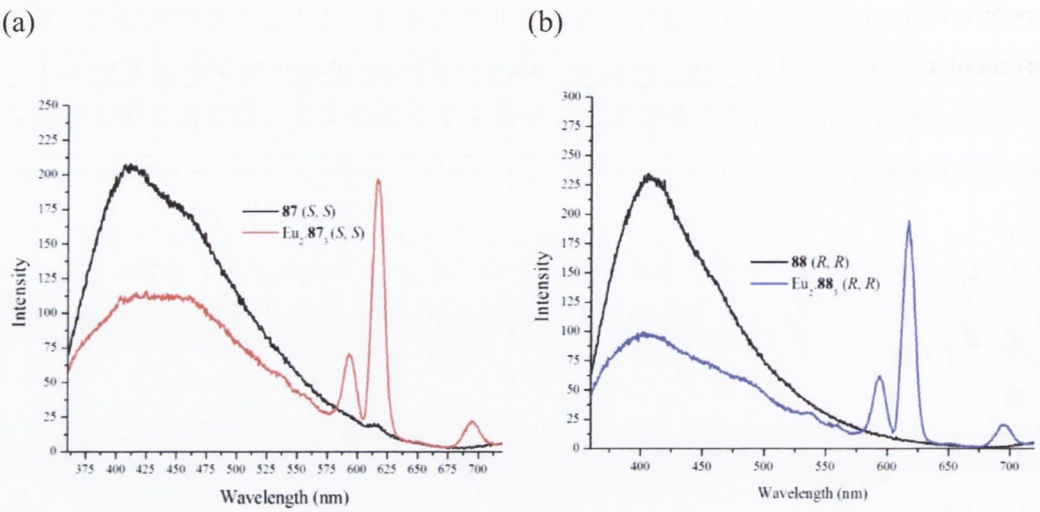

Figure 3.6. *Fluorescence spectra of (a) ligand* ***87*** *(S,S) (1 x 10^{-5} M) and (b)* ***88*** *(R,R) (1 x 10^{-5} M) recorded in CH_3OH before and after the addition of 0.65 equiv. $Eu(CF_3SO_3)_3$.*

According to previously studied helicate systems **62** – **66** it was expected that both Eu^{III} ions in $Eu_2.\mathbf{87}_3$ and $Eu_2.\mathbf{88}_3$ would reside in a fully saturated coordinative environment free from any binding solvent oscillators, expressing q values of 0. To investigate if this was in fact the case for $Eu_2.\mathbf{87}_3$ and $Eu_2.\mathbf{88}_3$ lifetime measurements for both complexes were recorded. However, since $Eu_2.\mathbf{87}_3$ and $Eu_2.\mathbf{88}_3$ were not readily soluble in H_2O it was necessary to carry out lifetime experiments in a different solvent. Measurements were therefore carried out in CH_3OH, CD_3OD and CH_3CN. By measuring the excited state decay in CH_3OH, CD_3OD, and inputting data into the modified version of Equation 1 (Equation 9 shown below) developed by Faulkner and co-workers,[87] the number of inner sphere metal bound solvent molecules (hydration state q) could be calculated. Luminescent emission lifetimes observed in CD_3OD and CH_3CN were best fit to a mono-exponential decay function while that observed for CH_3OH was best fit to a bi-exponential decay function, indicating the presence of possibly more than one luminescent species in the methanolic solution. Excited state lifetimes, population percentages and q values obtained for both complexes in the various solvents are summarised in Table 3.1.

Equation 9: $$q^{EuIII} = 2.4[(1/\tau_{CH3OH})-1/\tau_{CD3OD})-0.25]$$

Excited state lifetimes of 1.39 ms and 1.32 ms were exhibited by the major species in CH_3OH, which were present in 80% and 83% in solution for $Eu_2.\mathbf{87}_3$ and $Eu_2.\mathbf{88}_3$ respectively, correlating to q values of 0.2 in both cases. These values suggest that the dimetallic triple stranded helicate species $Eu_2.\mathbf{87}_3$ and $Eu_2.\mathbf{88}_3$ are the most predominant in solution, in which both Eu^{III} centres are coordinatively saturated within the helical structure

through coordination to three tridentate ligands. It is possible that the second shorter excited state lifetime observed in CH_3OH corresponds to a partially dissociated species in which one of the three ligand strands has disassembled, leaving a 2:2 species in solution, in which each Eu^{III} ion is free to coordinate to three solvent molecules, corresponding to the estimated q value of 3.

Table 3.1. *Eu^{III}-centred lifetimes (ms), species population percentages and calculated hydration state (q) values for Eu^{III} in $Eu_2.87_3$ and $Eu_2.88_3$ as measured in CH_3OH, CD_3OD and CH_3CN at RT.*

Complex	τ_{CH3OH} (ms) % population		τ_{CD3OD} (ms)	τ_{CH3CN} (ms)	q values	
					Major species	Minor species
$Eu_2.87_3$	1.39 80%	0.58 20%	2.49	1.52	0.2 ± 0.5	2.6 ± 0.5
$Eu_2.88_3$	1.32 83%	0.49 17%	2.36	1.49	0.2 ± 0.5	3.3 ± 0.5

A relative method was used to calculate the quantum yields and the efficiency of lanthanide sensitisation (η_{sens}) for both complexes in CH_3CN and CH_3OH solutions. This method compares both the absorbance and emission intensity of the unknown sample ($Eu_2.87_3$ or $Eu_2.88_3$) to a standard reference solution according to:[105,108,281]

Equation 10: $$Q_{rel}^{Eu,L} = \frac{Q_x}{Q_r} = \frac{E_x}{E_r} \times \frac{A_r(\lambda_r)}{A_x(\lambda_x)} \times \frac{I_r(\lambda_r)}{I_x(\lambda_x)} \times \frac{n_x^2}{n_r^2}$$

where subscript r represents the reference and x the sample under investigation; E is the integrated luminescence intensity, A is the absorbance at the excitation wavelength, I is the intensity of the excitation light at the same wavelength, and n is the refractive index of the solution. The standard solution employed is that of $Cs_3[Eu(dpa)_3]$ (7.5×10^{-5} M) in tris buffer 0.1M (absorbance = 0.20) for which the quantum yield is $\Phi_{tot} = 24 + 2.5\%$ (under excitation at 279 nm).[105,108] Since the magnetic dipole allowed (MD) transition ($^5D_0 \rightarrow {}^7F_1$) is independent of the environment surrounding the Ln^{III} it may be used therefore as an 'internal reference' for the calculation of the radiative lifetime (τ_R) given by: [105,108,187,281]

Equation 11: $$\frac{1}{\tau_R} = A_{MD,0} \cdot n^3 \cdot \left(\frac{I_{tot}}{I_{MD}}\right)$$

where $A_{MD,0}$ (= 14.65 s^{-1}) is the spontaneous emission probability of the $^5D_0 \rightarrow {}^7F_1$ transition, n is the refractive index of the medium, and I_{tot}/I_{MD} is the ratio of the integrated total emission from the $^5D_0 \rightarrow {}^7F_J$ transitions (where $J = 0 - 6$) to the area of the Eu($^5D_0 \rightarrow {}^7F_1$) transition. τ_{obs} (determined experimentally) and τ_R may then be used to evaluate the intrinsic quantum yield of the Eu^{III} (Φ_{Ln}^{Ln}) by implementing equation 12:[105,108,187,281]

Equation 12: $$\Phi_{Ln}^{Ln} = \frac{\tau_{obs}}{\tau_R}$$

The efficiency of lanthanide sensitisation (η_{sens}) is equal to the ratio between Φ_{tot} (determined experimentally) and Φ_{Ln}^{Ln} as given by equation 13:

Equation 13: $$\eta_{sens} = \frac{\Phi_{tot}}{\Phi_{Ln}^{Ln}}$$

Quantum yields (Φ_{tot}) were measured for the Eu^{III}-centred emission from $Eu_2.\mathbf{87}_3$ and $Eu_2.\mathbf{88}_3$ and were found to be 3.55 % and 3.19 % in CH_3OH and 4.14% and 4.41% in CH_3CN for $Eu_2.\mathbf{87}_3$ and $Eu_2.\mathbf{88}_3$ respectively, see Table 3.2 below. These quantum yield values, in particular for CH_3CN, were slightly lower than those estimated for the parent chiral mononuclear Eu^{III} 'Trinity sliotar' complexes recently reported in our laboratory (4.4% for Eu.$\mathbf{56}_3$ and Eu.$\mathbf{57}_3$ in CH_3OH and 7.3% and 7.6% for Eu.$\mathbf{56}_3$ and Eu.$\mathbf{57}_3$ in CH_3CN, respectively).[187] Lifetime values were relatively similar in both solvents for $Eu_2.\mathbf{87}_3$ and $Eu_2.\mathbf{88}_3$ (see Table 3.2) but slightly shorter in comparison to those calculated for the parent mononuclear structures Eu.$\mathbf{56}_3$ and Eu.$\mathbf{57}_3$ (1.76 ms and 1.75 ms in CH_3OH and 1.85 ms and 1.84 ms in CH_3CN for Eu.$\mathbf{56}_3$ and Eu.$\mathbf{57}_3$, respectively).[187] However, comparison of Φ_{Ln}^{Ln} values calculated for the helicate complexes $Eu_2.\mathbf{87}_3$ and $Eu_2.\mathbf{88}_3$ (see Table 3.2) and mononuclear complexes Eu.$\mathbf{56}_3$ and Eu.$\mathbf{57}_3$ (13.0 in CH_3OH and 14.8 and 15.0 in CH_3CN for Eu.$\mathbf{56}_3$ and Eu.$\mathbf{57}_3$, respectively) indicates that non-radiative deactivation *via* quenching (giving slightly lower lifetimes) does not play such a prominent role in reducing $\Phi_{tot.}$ It is in fact the efficiency of the sensitisation step (η_{sens}, ($\Phi_{tot} = \eta_{isc}.\eta_{et}\Phi_{Ln}^{Ln} = \eta_{sens}\Phi_{Ln}^{Ln}$ where η_{isc} is the efficiency of intersystem crossing and η_{et} the efficiency of energy transfer) which is responsible for these reduced quantum yield values for $Eu_2.\mathbf{87}_3$ and $Eu_2.\mathbf{88}_3$ in comparison to Eu.$\mathbf{56}_3$ and Eu.$\mathbf{57}_3$ (η_{sens} = 33.5% and 33.6% in CH_3OH and 49% and 51.3% in CH_3CN for Eu.$\mathbf{56}_3$ and Eu.$\mathbf{57}_3$, respectively) – quantum yield values which are still significantly high in comparison to values obtained by either Piguet[282] or Muller[130] for similar systems. This

observation reflects the major role played by the naphthalene groups in shielding the Eu^{III} ions from deactivating solvent oscillators in the local coordination sphere.

Table 3.2. *Lifetime values, quantum yield percentages and sensitisation efficiencies (η_{sens}) of Eu^{III} complexes measured in CH_3CN and CH_3OH at 25 °C calculated using equations 10 - 13 (upon excitation at λ = 279 nm) – note the estimated error for quantum yields is ±10%.*[130]

Complex	τ_{obs}, ms	Φ_{tot}, %	τ_R, ms	Φ	η_{sens}, %	Solvent
Eu_2.**87**$_3$	1.453 (± 0.001)	4.14 (± 0.10)	10	23.08	18.07	CH_3CN
Eu_2.**88**$_3$	1.424 (± 0.002)	4.41 (± 0.04)	10	25.25	17.47	CH_3CN
Eu_2.**87**$_3$	1.398 (± 0.004)	3.55 (± 0.04)	6.7	21.07	16.90	CH_3OH
Eu_2.**88**$_3$	1.413 (± 0.002)	3.19 (± 0.05)	6.3	22.34	14.32	CH_3OH

3.4 Chiro-Optical properties of 87 (*S*,*S*), 88 (*R*,*R*), Eu_2.**87**$_3$ (*S*,*S*) and Eu_2.**88**$_3$ (*R*,*R*) - CD and CPL measurements

For the purpose of ensuring that ligand chirality had been retained following synthesis and in order to probe whether the chirality of the ligand had been transferred to the metal centre upon complexation the chiro-optical properties of ligands **87** (*S*,*S*) and **88** (*R*,*R*) and their corresponding helicate complexes were evaluated by CD and CPL spectroscopy.

The CD spectra for ligands **87** (*S*,*S*) and **88** (*R*,*R*) and complexes Eu_2.**87**$_3$ (*S*,*S*) and Eu_2.**88**$_3$ (*R*,*R*) were recorded in CH_3CN, as shown in Figure 3.7, with the latter being formed in solution upon the addition of 0.67 equiv. of $Eu(CF_3SO_3)_3$. As shown, the enantiomeric relationship between stereoisomers **87** (*S*,*S*) and **88** (*R*,*R*) was clearly evident with both CD spectra displaying mirror images of one another. In the case of ligand **87** (*S*,*S*) a positive absorption band was centred at 230 nm, with two broad shoulders located at 250 nm and 270 nm, while a large negative band occurred at 214 nm.

An equal but opposite CD spectrum was exhibited by **88** (*R*,*R*). A disappearance of the two shoulders at 250 nm and 270 nm was observed upon the addition of 0.67 equiv. of Eu^{III} and subsequent formation of the triple stranded dimetallic helicates in solution. Concomitantly, in the CD spectra for the corresponding complexes, an equal but opposite

Cotton effect was observed. A dramatic increase in absorption was exhibited by the band at 214 nm while the band located at 230 nm experienced a slight shift to 227 nm and also a large enhancement in absorption. The changes observed in the CD spectra upon the formation of the helical assemblies reflect ligand conformational changes and induction of additional topological chirality as Eu_2.**87**$_3$ (*S,S*) and Eu_2.**88**$_3$ (*R,R*) are formed. Slight discrepancies in CD spectra can be attributed to minor differences in concentrations.

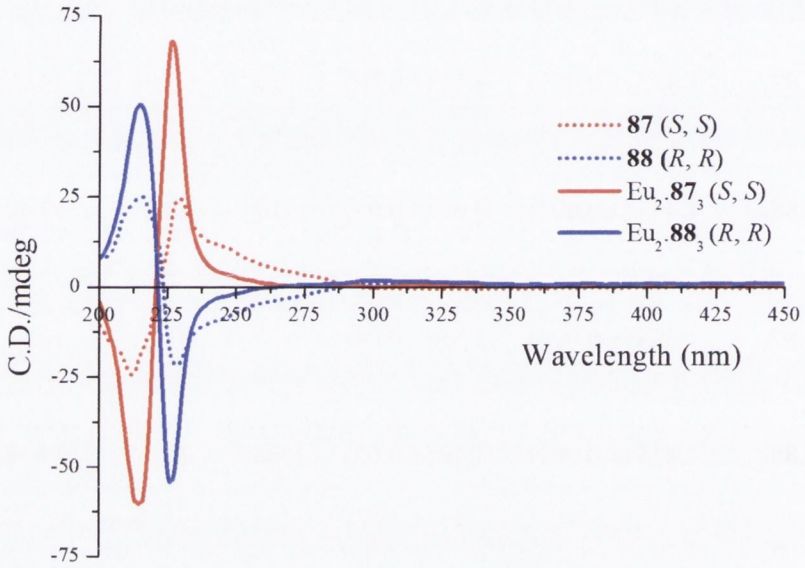

Figure 3.7. *Circular dichroism spectra of ligands* ***87*** *(S,S) and* ***88*** *(R,R) (1 x* 10^{-5} *M) recorded in* CH_3CN *at RT before and after the addition of 0.67 equiv.* $Eu(CF_3SO_3)_3$.

As discussed in chapter two CPL spectra can be employed as a spectroscopic tool to evaluate whether chirality has been transferred from the ligands to the Eu^{III} centre upon complexation and thus determine if the Ln^{III} is residing in a chiral environment. CPL spectra were recorded in CH_3CN, CH_3OH and a mixed CH_3OH:H_2O (75:25) solvent system as shown in Figure 3.8 and Appendix Figure A3.15. Excitation of the naphthalene antennae at λ = 281 nm gave rise, in all cases, to Eu^{III}-centred chiral emission with the $^5D_0 \rightarrow {}^7F_J$ (J = 1 – 4) transition bands of the complexes being of equal magnitude and opposite sign, demonstrating the chiral nature of the Eu^{III} excited states and again confirming the optical purity of enantiomers Eu_2.**87**$_3$ (*S,S*) and Eu_2.**88**$_3$ (*R,R*).

Positive bands were located at 598 nm and 653 nm, corresponding to the $^5D_0 \rightarrow {}^7F_J$ (J = 1, 3) transitions, in the CPL spectrum of the Eu_2.**87**$_3$ (*S,S*) complex. The $^5D_0 \rightarrow {}^7F_J$ (J = 2, 4) transition bands were split, in which the $^5D_0 \rightarrow {}^7F_2$ transition appeared as a negative signal at 618 nm and a positive signal at 624 nm. Similarly, the $^5D_0 \rightarrow {}^7F_4$ transition was depicted as a band split in two where a positive signal was observed at 707 nm and a negative signal located at 698 nm. Conversely, the CPL emission spectrum of Eu_2.**87**$_3$ (*R,R*) displayed a CPL

profile which was exactly the mirror image of the (*S,S*) enantiomer, possessing signals of the same amplitude but of opposite sign.

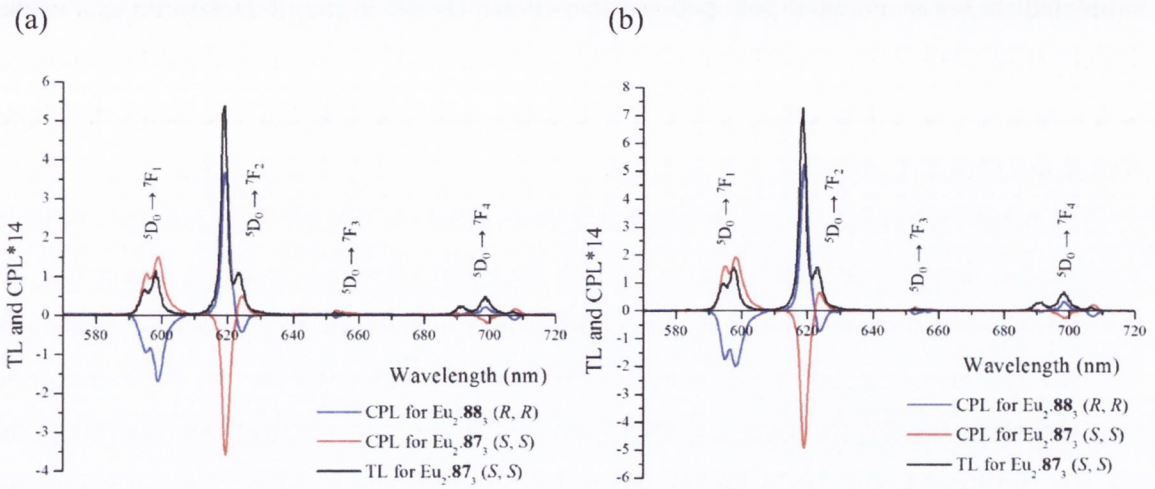

Figure 3.8. *Total Eu^{III}-centred emission and CPL spectra of complexes $Eu_2.87_3$ (S,S) and $Eu_2.88_3$ (R,R) recorded in (a) CH_3OH and (b) a $CH_3OH:H_2O$ (75:25) solvent system (excitation at λ = 281 nm).*

Table 3.3. *Summary of dissymmetry factors obtained for $Eu_2.87_3$ (S,S) and $Eu_2.88_3$ (R,R) in CH_3CN, CH_3OH and $CH_3OH:H_2O$ (75:25) solvent systems.*

Complex	CH_3CN		CH_3OH		$CH_3OH:H_2O$ (75:25)	
	(g_{lum}) 598 nm	(g_{lum}) 619 nm	(g_{lum}) 598 nm	(g_{lum}) 619 nm	(g_{lum}) 598 nm	(g_{lum}) 619 nm
$Eu_2.87_3$	0.17	-0.09	0.18	-0.09	0.20	-0.12
$Eu_2.88_3$	-0.19	0.10	-0.18	0.11	-0.21	0.13

Comparison of the CPL spectra of $Eu_2.87_3$ (*S,S*) and $Eu_2.88_3$ (*R,R*) to those of the analogous 'Trinity sliotar' complexes,[93,187] whose absolute configurations have been determined by X-ray crystallography, allows us to predict the absolute configurations of $Eu_2.87_3$ (*S,S*) and $Eu_2.88_3$ (*R,R*) as being $\Delta\Delta$ and $\Lambda\Lambda$, respectively. CPL data demonstrates the preferential formation of right or left handed helicate self-assembly *via* ligand asymmetric induction - similar to that observed for previously studied helicate ligands **62** - **66**.[64,69] Dissymmetry factor values for the $^5D_0 \rightarrow {}^7F_1$ and $^5D_0 \rightarrow {}^7F_2$ transitions obtained from measurements carried out in the three solvent systems were calculated and are summarised in Table 3.3.

As mentioned in chapter two, dissymmetry factors are a measure of the "degree of chirality" sensed by an electronic transition.[258] Particularly large dissymmetry factors were estimated for the magnetic dipole allowed transition ($^5D_0 \rightarrow {}^7F_1$) in all cases with g_{lum} values of 0.17 (CH_3CN), 0.18 (CH_3OH) and 0.20 (CH_3OH:H_2O, (75:25)) obtained for Eu_2.**87**$_3$ (*S*,*S*) and values of -0.19 (CH_3CN), -0.18 (CH_3OH) and -0.21 (CH_3OH:H_2O, (75:25)) calculated for the Eu_2.**88**$_3$ (*R*,*R*) complex.

The magnitudes of g_{lum} may be taken as a measure of the degree of optical activity in an electronic emissive transition which is determined by the detailed structural features of the local metal environment induced by the coordinating ligands. In comparison to previously reported g_{lum} values for helicate complexes of **63** – **66**, g_{lum} values for the $^5D_0 \rightarrow {}^7F_1$ transition (in CH_3OH) in Eu_2.**87**$_3$ (*S*,*S*) and Eu_2.**88**$_3$ (*R*,*R*) were found to be relatively similar (±0.23 for Eu_2.**63**$_3$ and Eu_2.**64**$_3$ and ±0.21 for Eu_2.**65**$_3$ and Eu_2.**66**$_3$). However, slightly larger values for g_{lum}($^5D_0 \rightarrow {}^7F_2$) were estimated for Eu_2.**87**$_3$ (*S*,*S*) and Eu_2.**88**$_3$ (*R*,*R*) (±0.05 for Eu_2.**63**$_3$ and Eu_2.**64**$_3$ and ±0.06 for Eu_2.**65**$_3$ and Eu_2.**66**$_3$).[64,69] These results suggest a comparable chiral arrangement of the ligands around the luminescent Eu^{III}-centres in Eu_2.**87**$_3$ (*S*,*S*) and Eu_2.**88**$_3$ (*R*,*R*) to those helicates of **63** – **66**.

Having examined the ground and excited state properties of the complexes and investigated their chiro-optical properties the next step was to evaluate the Eu^{III}-directed self-assembly behaviour of **87** (*S*,*S*) and **88** (*R*,*R*) *in situ* in order to establish their ability to form the desired 2:3 helicate species in solvents of varying competitiveness.

3.5 Studies of the formation of helicates Eu_2.**87**$_3$ and Eu_2.**88**$_3$ *in situ*

The Eu^{III}-directed self-assembly of Eu_2.**87**$_3$ and Eu_2.**88**$_3$ *in situ* was investigated by a series of spectroscopic measurements. This procedure entailed the titration of a 1 x 10^{-5} M solution of either **87** or **88** against increasing amounts of a $Eu(CF_3SO_3)_3$ stock solution and then analysing the changes in the UV-visible absorption, fluorescence and time-delayed Eu^{III}-centred emission of the resulting solution. Studies were performed in CH_3CN (to enable comparison to helicate studies previously reported), CH_3OH and CH_3OH:H_2O solvent systems (50:50 and 80:20 mixtures). The latter two were carried out to investigate the influence more competitive protic solvents have on the self-assembly process. Each titration experiment was repeated three times to ensure data reproducibility.

3.5.1 Spectroscopic solution studies carried out in CH_3CN

Prior to metal addition an initial UV-visible absorption spectrum of ligand **87** displayed two characteristic bands. One band was centred at λ_{max} = 223 nm, which is characteristic of an $S_0 \rightarrow S_2$ $\pi \rightarrow \pi^*$ transition within the chromoporic unit. The second band was located at λ_{max} =

281 nm (ε = 17100 M^{-1} cm^{-1}), which presented hyperfine structure with two shoulders located at 271 nm and 293 nm. This band is characteristic of a $S_0 \rightarrow S_1$ $\pi \rightarrow \pi^*$ transition of a 1-substituted naphthalene derivative.

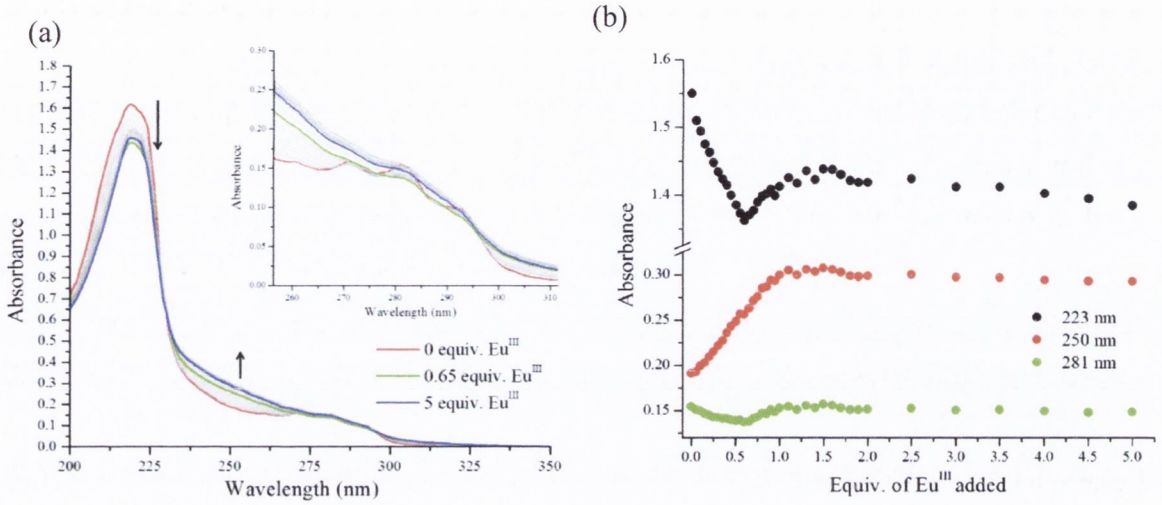

Figure 3.9. *(a) The overall changes in the UV-visible absorption spectra upon titrating* ***87*** *(1 x 10^{-5} M) against $Eu(CF_3SO_3)_3$ (0→5 equiv.) in CH_3CN at RT. (b) Corresponding experimental binding isotherm of absorbance at λ = 223, 250 and 281 nm.*

The overall changes in the UV-visible absorption spectrum of **87** as a function of added [Eu^{III}] are displayed in Figure 3.9 (a). As shown by the binding isotherm in Figure 3.9 (b), upon the addition of $Eu(CF_3SO_3)_3$ a hypochromic effect was experienced by the band located at λ_{max} = 223 nm up until the addition of approximately 0.6 equiv. of the metal salt. Subsequent additions of Eu^{III} then gave rise to a small absorption enhancement up until the addition of 1 equiv. of metal, after which the absorbance began to plateau. These changes suggest formation of an initial 2:3 M:L stoichiometric species in solution after which equilibrium is shifted towards a second 2:2 species. Loss in hyperfine structure was also evident for the band centred at λ_{max} = 281 nm upon additions between 0→1 equiv. of Eu^{III} after which no noticeable changes were observed. Concurrently, a sharp increase in absorption located at λ = 250 nm was displayed as the self-assembly process proceeded between aliquots of 0→1 equiv. of Eu^{III}. This was followed by a plateau at higher Eu^{III} concentrations. These changes in the UV-visible absorption spectrum of **87** with increasing concentrations of Eu^{III} are indicative of changes in ligand conformation as equilibrium is displaced and different stoichiometric species evolve in solution. Interestingly, in comparison to solution studies carried out on the mononuclear systems **56** and **57**, smaller changes in the band representing the naphthalene moiety (λ = 281 nm) were observed for the formation of the helicate structures in solution. This is due to π-π packing interactions being present in the

mononuclear systems, giving rise to more noticeable changes. These interactions are not expected to occur in the helical assemblies, and so less pronounced changes for this band are observed.

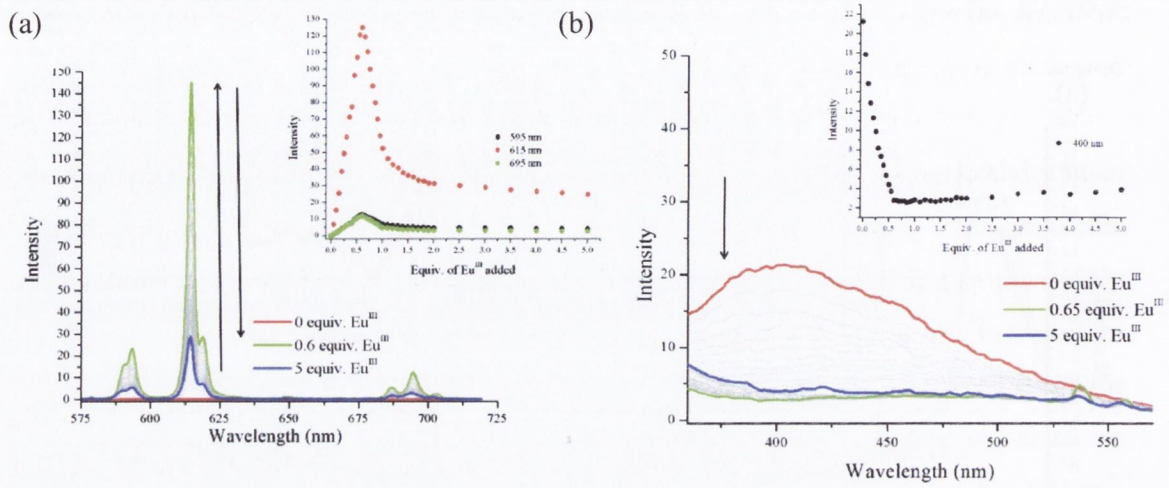

Figure 3.10. *The overall changes in the (a) Eu^{III}–centred phosphorescence spectra and (b) fluorescence emission spectra upon titrating* ***87*** *(1 x 10^{-5} M) against $Eu(CF_3SO_3)_3$ (0→5 equiv.) in CH_3CN at RT.* ***Inset****: corresponding experimental binding isotherm of (a) Eu^{III} phosphorescence emission intensity at λ = 595, 615 and 695 nm and (b) fluorescence intensity at λ = 400 nm (λ_{ex} = 281 nm).*

Upon excitation of the antenna at λ = 281 nm a gradual enhancement in a typical long wavelength Eu^{III}-centred luminescence emission spectrum was depicted as the titration progressed. The overall changes in the Eu^{III}-centred emission spectra, as shown in Figure 3.10 (a), were most significant between additions of 0→0.6 equiv. of Eu^{III}, during which a large enhancement in intensity for the bands located at 595 nm, 615 nm and 695 nm were observed, corresponding to electronic deactivation from the $^5D_0$ excited state to ^7F_J states (where J = 1, 2 and 4). This 'switching on' effect of the Eu^{III}-centred emission, *via* the antenna effect, up until the addition of approximately 0.6 equiv. of Eu^{III} suggests the formation of the desired 2:3 M:L luminescent helicate species in solution. As illustrated by the binding isotherm graph in Figure 3.10 (a) (inset) additional aliquots of the metal salt results in a sharp decrease in luminescence intensity until a plateau is reached at Eu^{III} concentrations greater than 1 equiv., suggesting a shift in equilibrium towards a lesser emissive species at higher Eu^{III} concentrations.

The fluorescence emission spectrum of **87** was very weak but was also affected by the Eu^{III}-directed self-assembly process. As shown in Figure 3.10 (b) above a large quenching effect was experienced by the band corresponding to the fluorescence emission of **87** (centred at λ_{max} = 400 nm) where quenching by 87% (and 74% for **88**, see Figure A3.16.) was evident after the addition of *ca.* 0.65 equiv. of Eu^{III}. This effect can be attributed to an energy

transfer process in which energy is transferred from the ligand excited state to the Eu^{III} metal centre in the 2:3 helicate species giving rise to characteristic Eu^{III}-centred luminescence emission *via* indirect excitation of ligand **87**. Simultaneously, the evolution of characteristic Eu^{III}-centred emission was evident in the fluorescence spectra as the complexation process took place *in situ*, as discussed above.

The overall changes in the UV-visible absorption, fluorescence emission and Eu^{III}-centred phosphorescence spectra following the titration of the corresponding enantiomer **88** with $Eu(CF_3SO_3)_3$ were identical to those observed above for **88**, as shown in Figure A3.16 - 17, confirming that both enantiomers display the same behaviour throughout the self-assembly process in CH_3CN solution.

3.5.1.1 Fitting of CH_3CN titration data and determination of complex stability constants

As shown for chapter one, the global changes in both the UV-visible absorption and Eu^{III}-centred emission spectroscopic data were fitted using the non-linear regression analysis program SPECFIT in order to gain a better understanding of the formation of the various self-assembly species in solution and also for the calculation of complex stability constants.

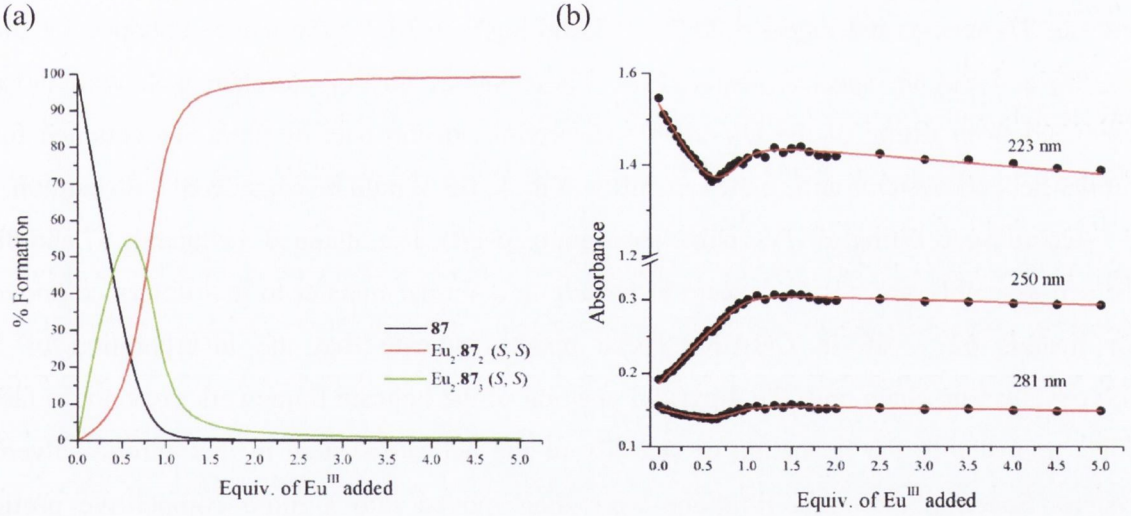

Figure 3.11. *The speciation distribution diagram obtained from the UV-visible absorption titration data fit (upon titrating ligand* ***87*** *(S,S) against* $Eu(CF_3SO_3)_3$ *in* CH_3CN*) and (b) the fit of the experimental binding isotherms using the non-linear regression analysis program SPECFIT.*

Results obtained from fitting of the UV-visible absorption titration data (as shown in Figure 3.11) point to the presence of three absorbing species in solution, namely the ligand itself **87**, the 2:2 (Eu_2.$\mathbf{87}_2$) and the 2:3 (Eu_2.$\mathbf{87}_3$) stoichiometric species. As shown from the fit of the experimental binding isotherms, in Figure 3.11 (b), a good fit was observed with analysis of the speciation distribution diagram indicating the predominant formation of the 2:3 helicate species with it being formed in *ca.* 55% after the addition of 0.6 equiv. of Eu^{III}.

Additional aliquots of Eu^{III} lead to an equilibrium displacement towards the 2:2 species with it being formed in *ca.* 78% following the addition of 1 equiv. of Eu^{III}.

Fitting of UV-visible absorption spectra data following titration of the corresponding enantiomeric ligand **88** with Eu^{III} in CH_3CN showed a similar behaviour (as shown in Figure A3.18) with the 2:3 helicate species being formed in *ca.* 68% upon the addition of 0.6 equiv. of Eu^{III} followed by a subsequent shift in equilibrium towards the 2:2 species, with it being formed in *ca.* 70% following the addition of 1 equiv. of Eu^{III}.

Binding constants were evaluated from these fits giving values of $\log\beta_{22} = 20.1 \pm 0.3$ and $\log\beta_{23} = 26.0 \pm 0.4$ for the $Eu_2.\mathbf{87}_2$ and $Eu_2.\mathbf{87}_3$ species and $\log\beta_{22} = 20.1 \pm 0.3$ and $\log\beta_{23} = 26.4 \pm 0.4$ for the $Eu_2.\mathbf{88}_2$ and $Eu_2.\mathbf{88}_3$ species, respectively (see Table 3.4). These values are in close agreement to those previously reported for Eu^{III}-directed self-assemblies of ligands **62** – **66** in CH_3CN. Analysis of the changes observed in the Eu^{III}-centred emission was also carried out (as shown in Figure A3.19 - A3.20) and indicates the presence of two luminescent species in solution, *i.e.* the 2:3 helicate species and the lesser emissive 2:2 species. Larger binding constants were obtained following fitting of phosphorescence titration data in both instances with values of $\log\beta_{22} = 22.2 \pm 0.3$ and $\log\beta_{23} = 29.2 \pm 0.4$ obtained for the $Eu_2.\mathbf{87}_2$ and $Eu_2.\mathbf{87}_3$ species and $\log\beta_{22} = 23.3 \pm 0.5$ and $\log\beta_{23} = 30.9 \pm 0.6$ values obtained for the $Eu_2.\mathbf{88}_2$ and $Eu_2.\mathbf{88}_3$ species, respectively. These values do not correlate well with those estimated from fitting of the UV-visible absorption spectra data or to values obtained for similar helicate systems and so the reliability of these fits should be considered with caution.

According to fitting of UV-visible absorption spectra data obtained for ligands **87** and **88** the self-assembly process does seem to behave in a similar manner to that described above for ligands **62** – **66** in CH_3CN. These results indicate that the incorporation of a polyoxyethylene chain onto the 4 pyridyl position of the helicate framework does not in fact affect appreciably the formation or stability of the helicate system in this aprotic solvent system. Spectrophotometric titrations were then moved into a more competitive protic methanolic solvent system in order to evaluate the effect this solvent may have on the self-assembly process.

3.5.2 Spectroscopic solution studies carried out in CH_3OH

Having analysed the self-assembly formation in CH_3CN we next moved solution studies to a more competitive medium using CH_3OH. The UV-visible absorption spectrum of ligand **87** was again first recorded in CH_3OH and shown to consist of two characteristic bands as was observed in CH_3CN, *i.e.* a high energy band centred at $\lambda_{max} = 226$ nm and a longer wavelength band located at $\lambda_{max} = 281$ nm ($\varepsilon = 17000\ M^{-1}\ cm^{-1}$), which presented less hyperfine structure (shoulders located at 271 nm and 293 nm) than was observed in CH_3CN.

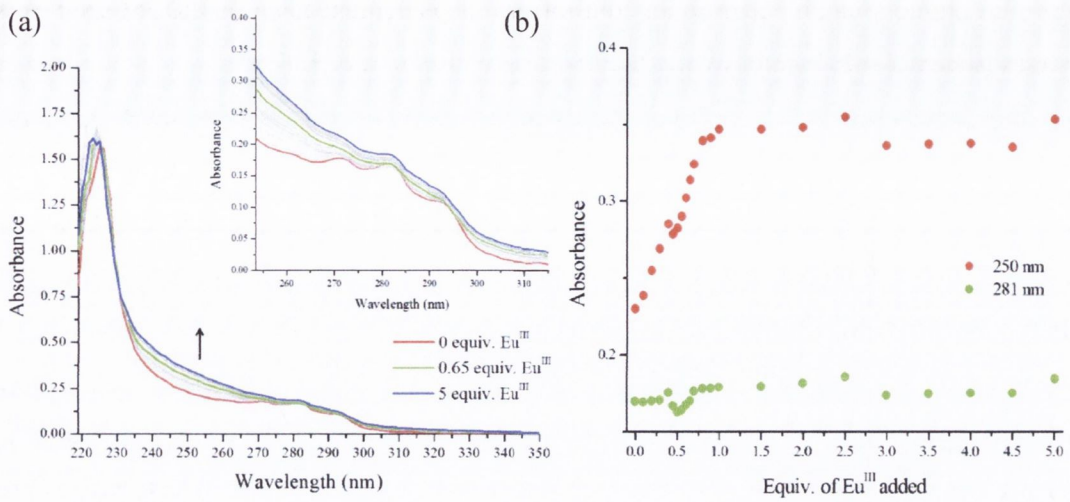

Figure 3.12. *(a) The overall changes in the UV-visible absorption spectra upon titrating* ***87*** *(1 x 10^{-5} M) against $Eu(CF_3SO_3)_3$ (0→5 equiv.) in CH_3OH at RT. (b) Corresponding experimental binding isotherm of absorbance at λ = 223, 250 and 281 nm.*

The overall changes observed in the UV-visible absorption spectrum of ligand **87** upon the addition of $Eu(CF_3SO_3)_3$ to a 1 x 10^{-5} M solution of **87** in CH_3OH are shown in Figure 3.12 (a). From Figure 3.12 (a) it is clear that a loss in the hyperfine structure of the band centred at λ = 281 nm is observed only, with no noticeable shift or evidence of an absorption increase/decrease. Again the band located at 226 nm experienced only a minor blue-shift (from λ = 226 nm to λ = 223 nm between additions 0→0.65 equiv. of Eu^{III}) with no noticeable increase/decrease in the ligand absorption. However, as shown by the binding isotherm in Figure 3.12 (b), upon the addition of $Eu(CF_3SO_3)_3$ an enhancement in absorption was observed at λ_{max} = 250 nm up until the addition of approximately 1 equiv. of the metal salt with subsequent additions resulting in an absorption plateau. As shown above for the solution studies carried out in CH_3CN, these changes in the UV-visible absorption spectrum of **87** are indicative of ligand perturbation as the self-assembly process proceeds and new species evolve in solution, particularly between the addition of 0→1 equiv. of Eu^{III}. The changes observed in the UV-visible absorption spectrum of **87** are much less pronounced in CH_3OH to that demonstrated in CH_3CN which could signify a self-assembly process which is less accessible due to the enhanced competitive nature of the surrounding environment.

In a similar manner to that described above, the evolution of the time-delayed Eu^{III}-centred luminescence emission was monitored upon excitation of the antenna group at λ = 281 nm as ligand **87** was titrated with increasing concentrations of Eu^{III}. As shown by the overall changes in the Eu^{III} luminescence spectra, illustrated in Figure 3.13 (a), a gradual enhancement in the characteristic line-like emission bands located at 595 nm, 615 nm and

695 nm is depicted which corresponds to electronic deactivation from the $^5D_0$ excited state to ^7F_J states (where $J = 1$, 2 and 4).

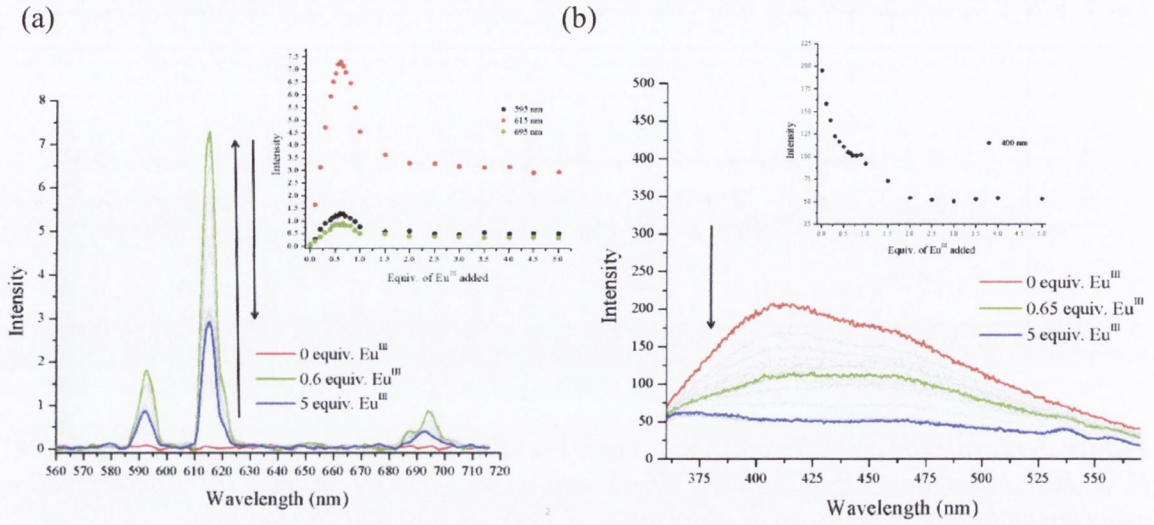

Figure 3.13. *The overall changes in the (b) Eu^{III}–centred phosphorescence spectra and (c) thr fluorescence emission spectra upon titrating* ***87*** *(1 x 10^{-5} M) against $Eu(CF_3SO_3)_3$ (0→5 equiv.) in CH_3OH at RT.* ***Inset****: corresponding experimental binding isotherm of (a) Eu^{III} phosphorescence emission intensity at λ = 592, 615 and 695 nm and (b) fluorescence intensity at λ = 400 nm (λ_{ex} = 281 nm).*

The binding isotherm graph, shown Figure 3.13 (a) (inset) demonstrates that upon the addition of 0→0.6 equiv. of Eu^{III} a rapid increase in the emission intensity was observed, similarly for that seen in CH_3CN, followed by a sharp decrease up until approximately 1 equiv. of Eu^{III}. Additional aliquots of Eu^{III} result in an eventual plateau in luminescence intensity. These changes suggest an initial formation of the desired $Eu_2.\mathbf{87}_3$ helical species, after which the 2:2 $Eu_2.\mathbf{87}_2$ becomes the dominant species in solution, as was previously observed in CH_3CN.

The fluorescence emission spectrum of **87** was also recorded in CH_3OH, as shown in Figure 3.13 (b), showing the band centred at λ_{max} = 400 nm experiencing a moderate quenching effect after the addition of *ca.* 0.65 equiv. of Eu^{III} (47% and 56% for **87** and **88** in CH_3OH, respectively (see Figure A3.22). As mentioned above, this band corresponds to the fluorescence emission band of the ligand and so this quenching effect can be attributed to an energy transfer process in which energy is transferred from the ligand excited state to the Eu^{III} metal centre giving rise to characteristic Eu^{III}-centred luminescence emission. These changes demonstrate effective sensitisation from the ligand to the metal centre *via* the 'antenna effect'.

The overall changes in the UV-visible absorption, fluorescence emission and Eu^{III}-centred phosphorescence spectra following the titration of **88** with $Eu(CF_3SO_3)_3$ in CH_3OH

were also investigated. Again an identical behaviour was displayed for **88** (see Figure A3.21 – A3.22) confirming that the self-assembly process proceeds in the same manner to that observed for **87** in CH_3OH solution.

3.5.2.1 Fitting of CH_3OH titration data and determination of complex stability constants

In order to investigate species stoichiometry and stability constants for the self-assembly process in CH_3OH the UV-visible absorption and luminescence titration data were analysed by fitting the global changes using the program SPECFIT (see Figure 3.14 - Figure 3.15 and Figure A23 – A3.24).

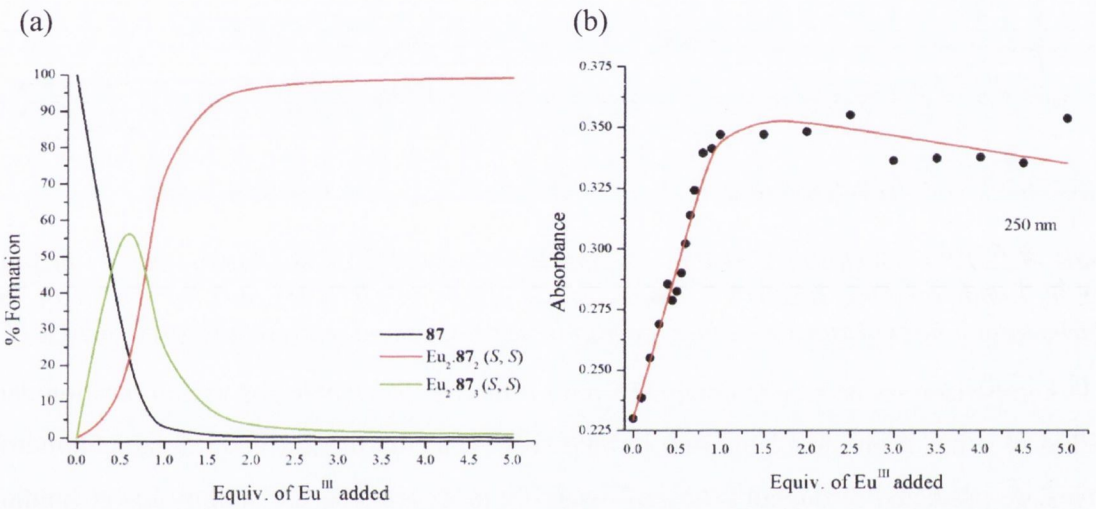

Figure 3.14. *The speciation distribution diagram obtained from the UV-visible absorption titration data fit (upon titrating ligand* ***87*** *against* $Eu(CF_3SO_3)_3$ *in* CH_3OH*) and (b) the fit of the experimental binding isotherm using the non-linear regression analysis program SPECFIT.*

The speciation distribution diagram obtained from fitting the UV-visible absorption spectra (see Figure 3.14 (a)) shows the presence of three absorbing species in solution including the ligand itself **87**, the 2:2 (Eu_2.**87**$_2$) and the 2:3 (Eu_2.**87**$_3$) helical species, and as shown from the fit of the experimental binding isotherms (Figure 3.14 (b)) an acceptable fit was observed. Between the addition of 0.4→0.8 equiv. of Eu^{III} the most predominant species in solution is the 2:3 Eu_2.**87**$_3$ dimetallic triple stranded helical species with it being formed in approximately 54% at 0.6 equiv. of Eu^{III}. At higher Eu^{III} concentrations a shift in equilibrium towards formation of the 2:2 complex is reflected by the sharp decrease in emission intensity as the titration proceeds. The Eu_2.**87**$_2$ species is formed in approximately 98% yield upon the addition of 3 equiv. of the metal salt. Similar results were displayed following fitting the changes in the UV-visible absorption spectra of ligand **88** in which the Eu_2.**88**$_3$ dimetallic triple stranded helical species is formed in approximately 76% at 0.6 equiv. of Eu^{III} and the

$Eu_2.\mathbf{88}_2$ species is formed in approximately 82% upon the addition of 3 equiv. of the metal salt. Stability constants were evaluated with values of $\log\beta_{22} = 19.8 \pm 0$ and $\log\beta_{23} = 25.7 \pm 0.3$ obtained for the $Eu_2.\mathbf{87}_2$ and $Eu_2.\mathbf{87}_3$ species and $\log\beta_{22} = 19.0 \pm 0$ and $\log\beta_{23} = 25.6 \pm 0.1$ obtained for the $Eu_2.\mathbf{88}_2$ and the $Eu_2.\mathbf{88}_3$ species, respectively.

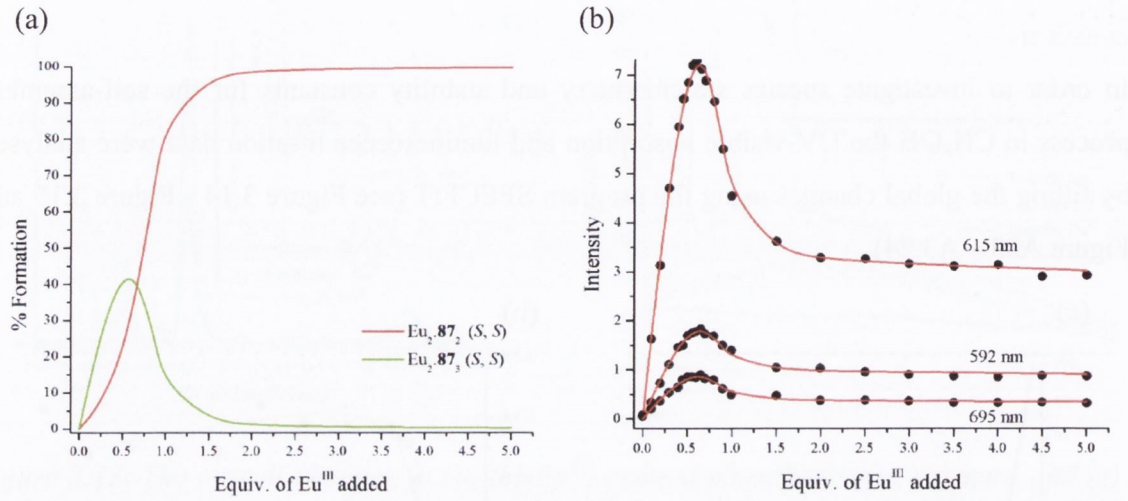

Figure 3.15. *The speciation distribution diagram obtained from the luminescence titration data fit (upon titrating ligand* ***87*** *against* $Eu(CF_3SO_3)_3$ *in* CH_3OH*) and (b) the fit of the experimental binding isotherms using the non-linear regression analysis program SPECFIT.*

In comparison to the results obtained from fitting the UV-visible absorption titration data in CH_3CN it has been elucidated that in both solvent media the 2:2 and 2:3 stoichiometric species are produced throughout the self-assembly process while the slightly lower binding constants evaluated from measurements carried out in CH_3OH illustrate that the competitive nature of the methanolic solvent system does have a minor effect on the stability of the complex species, see Table 3.4 for summary of binding constants. These minor stability differences are further exemplified by the small difference in quantum yields calculated in the two solvent systems, as discussed in previous sections.

Analysis of luminescence titration data from spectrophotometric measurements of ligands **87** and **88** in CH_3OH by means of fitting using SPECFIT were shown to correlate well with results reported for fitting of the UV-visible absorption titration data, as shown in Figure 3.15 and Figure A3.24. As shown by the speciation distribution diagram for **87** (Figure 3.15 (a)) the initial emission intensity increase corresponds to the evolution of the dimetallic triple stranded helicate *in situ* with it forming in 41% upon the addition of 0.6 equiv. of Eu^{III}. The rapid decrease in Eu^{III}-centred emission intensity at λ = 592, 615 and 695 nm is due to the 2:2 stoichiometric species becoming the predominant complex in solution at higher Eu^{III} concentrations with it being formed in over 99% at 3 equiv. of Eu^{III}. A similar trend was observed following fitting of the luminescence titration data of **88**, as shown in Figure A3.24,

with $Eu_2.\mathbf{88}_3$ being formed in 24% at 0.6 equiv. of Eu^{III} and the 2:2 species in 99% at 3 equiv. of Eu^{III}. Stability constants of $\log\beta_{22} = 20.0 \pm 0.2$ and $\log\beta_{23} = 25.5 \pm 0.2$ were evaluated for $Eu_2.\mathbf{87}_2$ and $Eu_2.\mathbf{87}_3$ while values of $\log\beta_{22} = 19.3 \pm 0.1$ and $\log\beta_{23} = 24.4 \pm 0.2$ were obtained for $Eu_2.\mathbf{88}_2$ and $Eu_2.\mathbf{88}_3$. These values are in good agreement with those determined from the changes in the UV-visible absorption spectra.

Table 3.4. *Binding constants obtained by fitting spectroscopic data.*Value fixed, otherwise convergence not reached.*

Ligand	UV-visible absorption		Luminescence		Solvent
	$\log\beta_{22}$	$\log\beta_{23}$	$\log\beta_{22}$	$\log\beta_{23}$	
87	20.1 ± 0.3	26.0 ± 0.4	22.2 ±0.3	29.2 ± 0.4	CH_3CN
	19.8*	25.7 ± 0.3	20.0 ± 0.2	25.5 ± 0.2	CH_3OH
88	20.1 ± 0.3	26.4 ± 0.4	23.3 ± 0.5	30.9 ± 0.6	CH_3CN
	19.0*	25.6 ± 0.1	19.3 ± 0.1	24.4 ± 0.2	CH_3OH

Only minor changes in the UV-visible absorption spectra of ligands **87** and **88** were observed for the Eu^{III}-directed self-assembly of helicates $Eu_2.\mathbf{L}_3$ (**L** = **87** and **88**) upon titrating in CH_3OH in comparison to values obtained from studies carried out in CH_3CN. This could be as a result of the enhanced competitive nature of the methanolic solvent medium in that the protic CH_3OH molecules may partake in inducing an effect which begins to restrict the self-assembly process to some degree *i.e.* conformational changes towards the formation of the helicate species may not be as attainable as was possible in organic CH_3CN solution - H-bonding interactions between the solvent molecules and ligand amine nitrogens for example. Nevertheless, it was possible to fit this data and confirm the formation of the desired dimetallic triple stranded species $Eu_2.\mathbf{87}_3$ and $Eu_2.\mathbf{88}_3$ leading us to believe that it was worthwhile taking these systems and investigating further their ability to self-assemble in an even more competitive mixed CH_3OH:H_2O solvent system. A 50:50 mixed CH_3OH:H_2O solvent system was initially chosen to conduct these studies.

3.5.3 Spectroscopic solution studies carried out in CH_3OH:H_2O solvent systems

As seen before, the UV-visible absorption spectrum of ligands **87** and **88**, as shown in Figure 3.16 (a) and Appendix Figure A3.25 (a), consisted of a short wavelength band centred at 224 nm and a longer wavelength band located at 281 nm which possessed two shoulders at 271 and 293 nm. Upon titrating a 1 x 10^{-5} M ligand CH_3OH:H_2O (50:50) solution against $Eu(CF_3SO_3)_3$ (0→6 equiv.) no obvious changes occurred to either the band located at 224 nm

nor the band located at 281 nm throughout the experiment, see binding isotherms graphs in Figure 3.16 and Appendix Figure A3.25 (a) inset. This lack of ligand perturbation suggests little, slow or no conformational changes in solution.

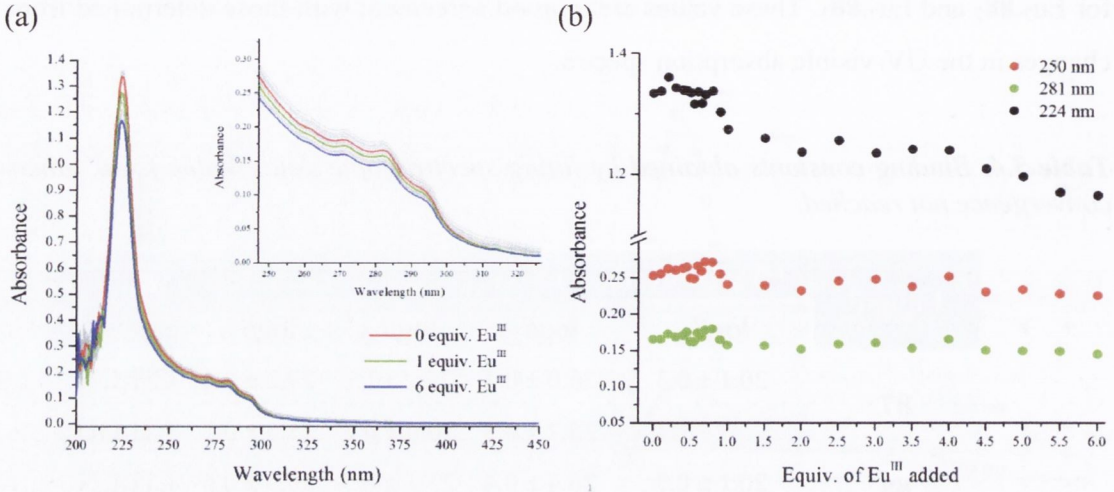

Figure 3.16. *(a) The overall changes in the UV-visible absorption spectra upon titrating* ***87*** *(1 x 10^{-5} M) against $Eu(CF_3SO_3)_3$ (0→6 equiv.) in CH_3OH:H_2O (50:50) at RT. (b) Corresponding experimental binding isotherm of absorbance at λ = 224, 250 and 281 nm.*

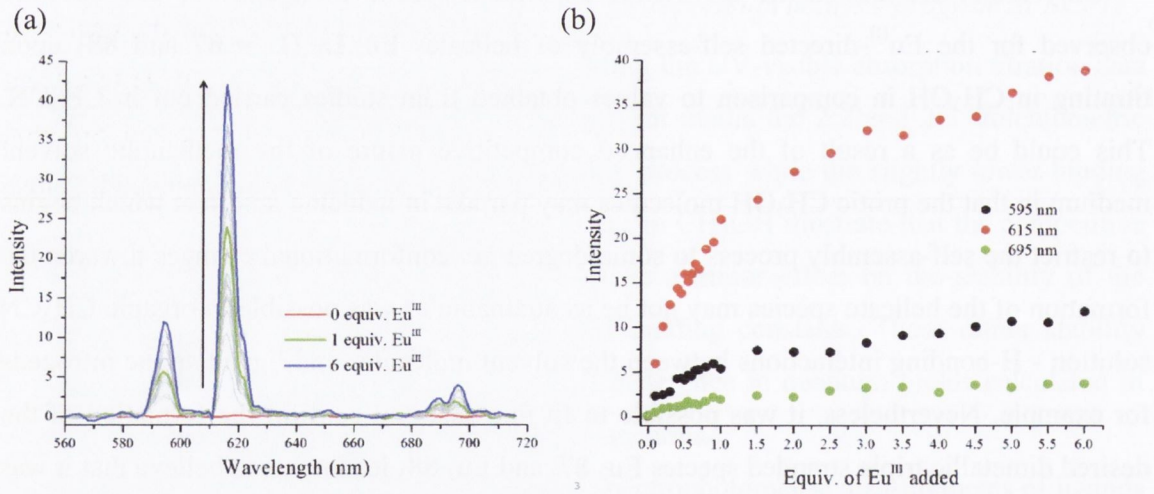

Figure 3.17. *(a) The overall changes in the Eu^{III}–centred phosphorescence spectra upon titrating* ***87*** *(1 x 10^{-5} M) against $Eu(CF_3SO_3)_3$ (0→6 equiv.) in CH_3OH:H_2O (50:50) at RT. (b) Corresponding experimental binding isotherm of Eu^{III} phosphorescence emission intensity at λ = 595, 615 and 695 nm (λ_{ex} = 281 nm).*

Concurrently, as shown in Figure 3.17 and Appendix Figure A3.25 (b), the overall changes in the Eu^{III}-centred luminescence (following excitation at λ = 281 nm as before) indicate ligand complexation and subsequent Eu^{III} sensitisation of the $^5D_0$ excited state. The characteristic narrow emission bands occurring at 595 615 and 695 nm, which correspond to the $^5D_0 \rightarrow {}^7F_J$ (where J = 1, 2 and 4) transitions, do not however follow the same trend as was demonstrated previously for studies carried out in CH_3CN or CH_3OH. A sharp increase

in intensity from 0→0.65 equiv of Eu^{III} was evident, followed by a less pronounced increase from 0.65→6 equiv.

Since changes occurring at this point in the titration usually point to the formation of the helical assembly this result was initially thought to reflect 2:3 species formation in solution. This was found not to be the case as fitting by non-linear regression analysis of this data was not possible – as speculated by analysing the lack of changes in the UV-visible absorption spectra. This continued emission increase is possibly due to the formation of a mixture of the 1:1 and 2:1 (M:L) species as more Eu^{III} is added to the system *i.e.* where no change in ligand conformation is observed or would result in a UV-visible absorption change. At higher Eu^{III} concentrations there may simply be higher concentrations of the 1:1 and 2:1 species *in situ* as the system equilibrium is 'pushed' towards complexation. This would account for the enhanced emission spectrum as the titration proceeds. Another possibility is simply that the stability of the helicate assemblies in this more competitive medium is much lower to the previously encountered systems therefore requiring the addition of a large excess of metal to form the helicate. This unusual behaviour may also be as a result of poor solubility of the ligand in the presence of H_2O. The large hydrophobic aromatic functional groups of the ligand may cause exclusion of H_2O and/or cause stacking between ligand molecules in solution preventing facile assembly. By reducing the H_2O content of the CH_3OH:H_2O solvent system to an 80:20 mixture an attempt to address these postulations was undertaken. Solution studies discussed in the remaining sections of this chapter were carried out on ligand **87** only.

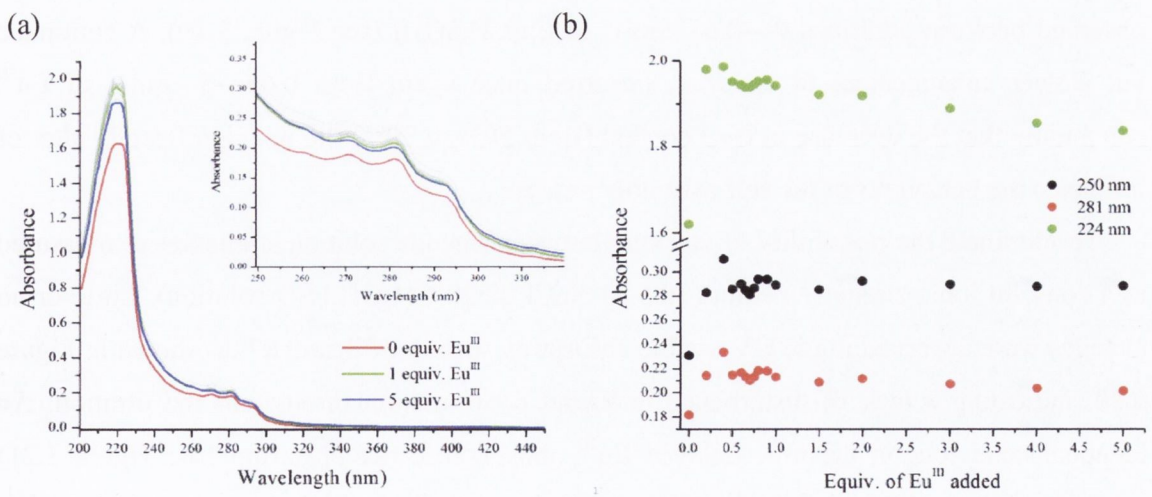

Figure 3.18. *(a) The overall changes in the UV-visible absorption spectra upon titrating* ***87*** *(1 x 10^{-5} M) against $Eu(CF_3SO_3)_3$ (0→6 equiv.) in CH_3OH:H_2O (80:20) at RT. (b) Corresponding experimental binding isotherm of absorbance at λ = 224, 250 and 281 nm.*

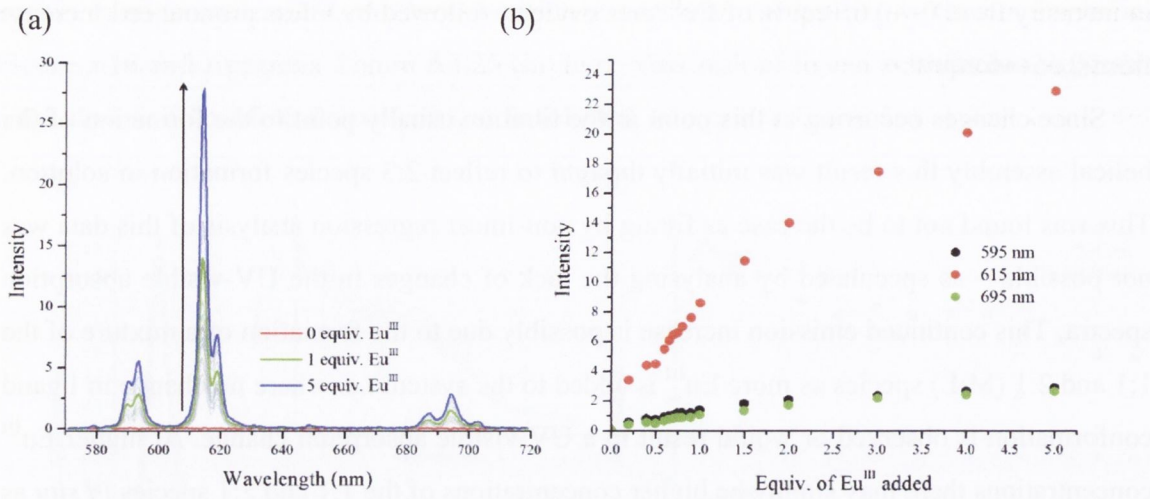

Figure 3.19. *(a) The overall changes in the Eu^{III}–centred phosphorescence spectra upon titrating* ***87*** *(1 x 10^{-5} M) against $Eu(CF_3SO_3)_3$ (0→6 equiv.) in $CH_3OH:H_2O$ (80:20) at RT. (b) Corresponding experimental binding isotherm of Eu^{III} phosphorescence emission intensity at λ = 595, 615 and 695 nm (λ_{ex} = 281 nm).*

The overall changes in the UV-visible absorption spectrum of ligand **87** for solution studies carried out in an 80:20 $CH_3OH:H_2O$ solvent system are shown in Figure 3.18. Minor changes were observed for the high energy absorption band but no noticeable trend was obvious while for the band located at λ = 281 nm only a slight increase in absorption was observed. Again, no significant changes could be followed in this region of the spectrum.

As seen before for studies conducted in the 50:50 $CH_3OH:H_2O$ mixed system a rapid enhancement in the Eu^{III}-centred emission bands centred at 595, 615 and 695 nm was observed between additions 0→0.65 equiv. of $Eu(CF_3SO_3)_3$ (see Figure 3.19). A continued but slower enhancement in emission occurred once again from 0.65→5 equiv. of Eu^{III} concluding that the decrease in H_2O content (from 50% to 20%) did not significantly alter or influence the behaviour of the self-assembly process.

To eliminate the possibility of stacking between ligands solution studies were measured in a constant ionic strength medium (0.5 M NaCl 80:20 $CH_3OH:H_2O$ solution). Little or no changes were observed in the UV-visible absorption spectra of ligand **87**, as shown in Figure 3.20, indicating a lack of disturbance in ligand conformation throughout the titration. An identical behaviour in the time delayed Eu^{III} phosphorescence spectrum (see Figure 3.21) pointed again to either an increased concentration of the 1:1 and 2:1 species as additional aliquots of Eu^{III} are added to the system or to low binding constants of the helicate systems in this aqueous environment. This theory would coincide with the fact that there are very few changes in the UV-visible absorption spectrum.

To prevent the possibility of amine protonation in an aqueous environment and subsequent influence on complexation the Eu^{III}-directed self-assembly process was next

evaluated in a 0.1 M HEPES/0.1 M NaCl $CH_3OH:H_2O$ (80:20) solution, as shown in Figure A3.26. An identical behaviour was displayed in this buffered medium to that demonstrated in previous solution studies containing a $CH_3OH:H_2O$ medium.

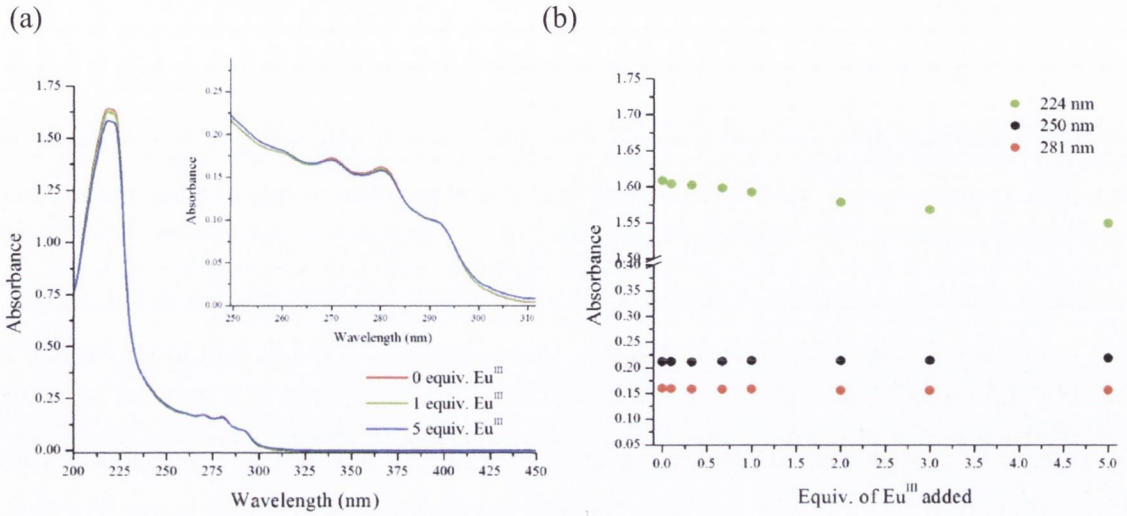

Figure 3.20. *(a) The overall changes in the UV-visible absorption spectra upon titrating* ***87*** *(1 x 10^{-5} M) against $Eu(CF_3SO_3)_3$ (0→5 equiv.) in a 0.5 M NaCl $CH_3OH:H_2O$ (80:20) solution at RT. (b) Corresponding experimental binding isotherm of absorbance at λ = 224, 250 and 281 nm.*

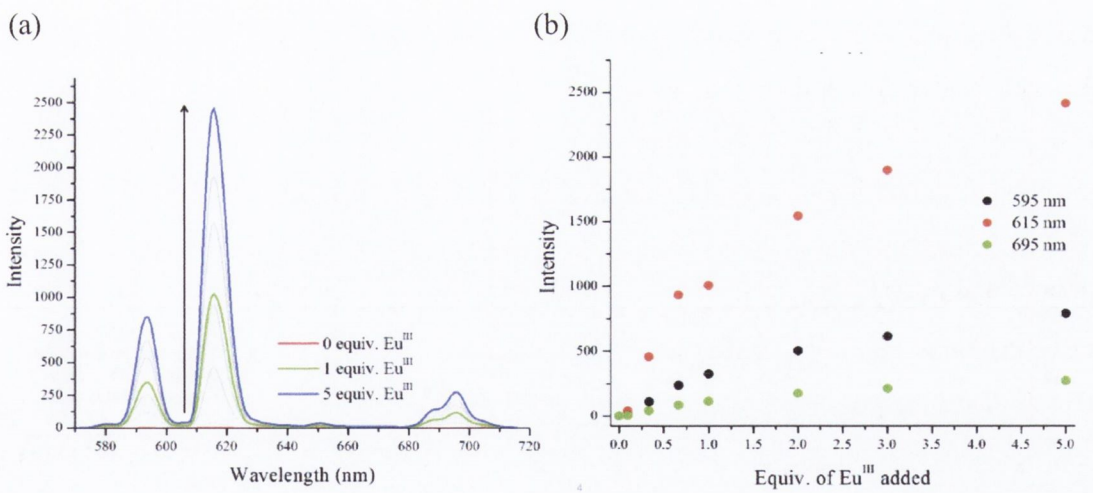

Figure 3.21. *(a) The overall changes in the Eu^{III}-centred emission spectra upon titrating* ***87*** *(1 x 10^{-5} M) against $Eu(CF_3SO_3)_3$ (0→5 equiv.) in a 0.5 M NaCl $CH_3OH:H_2O$ (80:20) solution at RT. (b) Corresponding experimental binding isotherm of phosphorescence at λ = 595, 615 and 695 nm.*

Although studies conducted in a constant ionic strength and buffered media eliminated the possibility of ligand stacking and/or amine protonation it is still possible that the ligand itself and/or resulting complexes are not fully soluble within this heightened polar solvent system. It is additionally plausible to conclude that the self-assembly of the desired dimetallic triple stranded helicate occurs at a much slower rate in an aqueous environment. A number of

kinetic measurements were therefore conducted to investigate if the spectroscopic trend would remain the same after allowing the system to reach a state of stable equilibrium *i.e.* by carrying out the same titration as above over a longer period of time may result in the identification of different species in solution.

3.6 Stability measurements *in situ*

Stability measurements *in situ* involved the addition of increasing concentrations of $Eu(CF_3SO_3)_3$ to a 1 x 10^{-5} M 80:20 $CH_3OH:H_2O$ mixed solution of ligand **87** as before, but, a time period of 19 hrs was left between the addition of metal. An initial 0.2 equiv. of Eu^{III} was added and the emergence of time delayed Eu^{III}-centred emission was measured every hr from 0→19 hrs. The emission intensity of the $^5D_0 \rightarrow {}^7F_J$ (J = 1, 2 and 4) transitions located at 595, 615 and 695 nm after each phosphorescence scan was plotted against time, as shown in Figure 3.22 (a). After this, 0.4 equiv. of Eu^{III} were added and the Eu^{III} phosphorescence measured every hr from 0→19 hrs, the results being shown in Appendix Figure A3.27 (a). The same procedure was repeated after the addition of 0.6, 0.8, 1.0 and 5 equiv. of $Eu(CF_3SO_3)_3$.(see Appendix Figure A3.27 (b) – (e)).

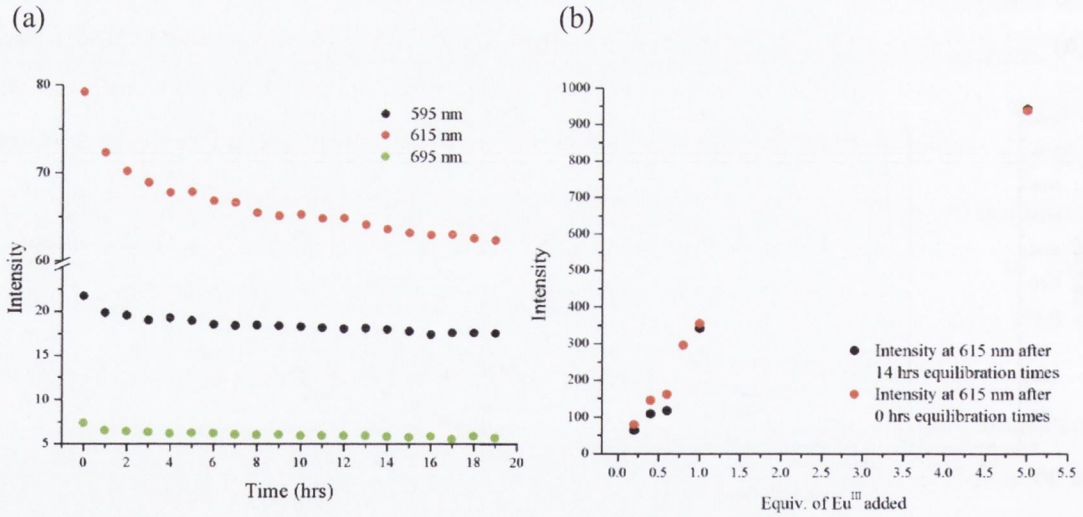

Figure 3.22. *(a) Eu^{III}-centred emission intensity at λ = 595, 615 and 695 nm following the addition of 0.2 equiv. of $Eu(CF_3SO_3)_3$ to ligand **87** in a $CH_3OH:H_2O$ (80:20) solution from 0 – 19 hrs at RT (upon excitation at λ = 281 nm) and (b) emission intensity at λ = 615 nm following the addition of 0.2, 0.4, 0.6, 0.8, 1.0 and 5.0 equiv. of $Eu(CF_3SO_3)_3$ after 14 hrs.*

Since it was definite that equilibrium of the system had been reached after a period of 14 hrs the intensity (after 14 hrs) at 615 nm following the addition of 0.2, 0.4, 0.6, 1.0 and 5.0 equiv. was plotted, as shown in Figure 3.22 (b). As shown, an identical trend was observed in the overall changes of the characteristic Eu^{III} luminescence spectra after 14 hrs compared to

measurements carried in the usual manner, *i.e.* where an additional metal salt aliquot is made immediately after one full spectroscopic measurement. These findings suggest that either the kinetics of the system are even slower than first anticipated (requiring up to weeks for the self-assembly process to take place) or that a kinetic effect is not responsible for the trend observed.

Lifetime measurements were also conducted for the self-assembly system of ligand **87** in the CH_3OH:H_2O (80:20) solvent medium for comparison. The Eu_2.**87**$_3$ self-assembly was formed *in situ* by adding 0.67 equiv. of $Eu(CF_3SO_3)_3$ to a $1x10^{-5}$ M solution of **87**. Luminescent emission lifetimes observed in this solvent were best fit to a bi-exponential decay, indicating the presence of more than one luminescent species in solution, as was shown in above sections for CH_3OH. Excited state lifetimes of 1.47 ms and 0.37 ms were exhibited with the longer lived excited state species present in 89%. These lifetimes are similar to those observed in CH_3OH and so would suggest formation of the dimetallic triple stranded helicate species Eu_2.**87**$_3$ in the partial aqueous solution. A further 10 equiv. of Eu^{III} were then added and luminescent emission lifetimes evaluated with values of 1.37ms (87%) and 0.37 ms elucidated, again indicating the presence of the 2:3 species in solution.

It was established from these stability and lifetime measurements that formation of the desired dimetallic triple stranded helicates in an aqueous environment was not hindered by slow kinetics but is due to a thermodynamic issue in which the stability constants associated with the formation of the 2:3 species in this medium are so low that a huge excess of metal concentration is necessary to reach helicate formation. It was speculated that the stability of the solid complex Eu_2.**87**$_3$ in such a competitive solvent system should also be investigated.

3.7 Stability measurements on complex Eu_2.**87**$_3$

Following synthesis of the solid complex under microwave irradiation, as discussed in section 3.2, the stability of the complex was measured by monitoring the Eu^{III}-centred emission spectrum exhibited from the solid dissolved in the 80:20 mixed CH_3OH:H_2O solution.

As shown below, no significant decrease in emission, which would conclude dissociation of the helicate in the mixed solution, was obvious. This confirms that in an 80:20 CH_3OH:H_2O medium the Eu_2.**87**$_3$ complex (which is synthesised by microwave irradiation) remains intact and stable. A similar observation was made for the corresponding (*R*,*R*) Eu_2.**87**$_3$ complex (see Appendix Figure A3.28). These results prove promising for future developments in this area for these systems. Addition of the Eu_2.**87**$_3$ complex to a 50:50 CH_3OH:H_2O solvent system gave rise to the formation of a precipitate however, providing the limit to this helicate system in a partial H_2O environment.

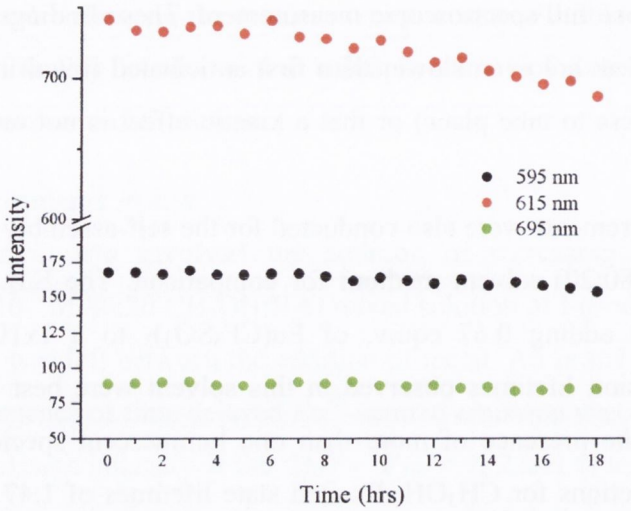

Figure 3.23. *Eu^{III}-centred emission intensity at λ = 595, 615 and 695 nm from $Eu_2.87_3$ complex in a $CH_3OH:H_2O$ (80:20) solution from 0 – 18 hrs at RT (excitation at λ = 281 nm).*

3.8 Conclusion

Ligands **87** and **88** were designed with the aim of meeting certain criteria for the formation of enantiomerically pure dimetallic triple stranded helicates in more competitive solvent media. Four different requirements were set out – the incorporation of a tridentate dpa binding unit for Ln^{III} encapsulation, a chiral naphthalene antenna moiety for Eu^{III} sensitisation and an *m*-xylylenediamine linking spacer group to attain a ditopic ligand capable of self-assembling in a 2:3 M:L stoichiometric manner, as was demonstrated by previously studied systems involving compounds **63** – **66**. An additional polyoxyethylene functionality grafted onto the 4 pyridyl position was intended to induce enhanced solubility in more competitive media. Synthesis of chiral ligands **87** and **88** was achieved by a relatively short synthetic pathway and their formation verified by ^{1}H NMR, ^{13}C NMR, IR, ESMS and elemental analysis. Complexation of **87** and **88** with $Eu(CF_3SO_3)_3$ in a 2:3 M:L ratio under microwave irradiation yielded the desired dimetallic triple stranded helicates $Eu_2.87_3$ and $Eu_2.88_3$ which were characterised by ^{1}H NMR, IR and elemental analysis.

Photophysical studies were carried out on both complexes in CH_3CN and CH_3OH illustrating UV-visible absorption bands characteristic of the central pyridine unit and naphthalene chromophore while luminescence and excitation emission spectra confirmed successful sensitisation of the Eu^{III} excited $^5D_0$ state in both complexes. Lifetime measurements conducted in CH_3CN, CD_3OD and CH_3OH revealed the presence of one luminescent species in CH_3CN and CD_3OD while two luminescent species were apparent in CH_3OH with the major species possessing a *q* value of 0. This confirmed a Eu^{III} environment in which three tridentate binding units are coordinated to the Eu^{III} centre giving a fully

saturated coordination sphere where Eu^{III} is nine-coordinate and free from any solvent bound oscillators. Quantum yield calculations were also performed in both CH_3CN and CH_3OH with Φ_{tot} values slightly lower than those observed for Eu.**56**$_3$ and Eu.**57**$_3$ measured in the same solvent systems. Calculation of η_{sens} did indicate that the sensitisation pathway for helicate complexes Eu_2.**87**$_3$ and Eu_2.**88**$_3$ was less efficient than for Eu.**56**$_3$ and Eu.**57**$_3$.

Chiro-Optical CD and CPL measurements confirmed that chirality of the ligands had been transferred to the metal centre *via* asymmetric induction. CPL spectra were mirror images of one another confirming the enantiomeric nature between the ligands and their corresponding complexes. Dissymmetry factors for the $^5D_0 \rightarrow {}^7F_1$ and $^5D_0 \rightarrow {}^7F_2$ transitions were calculated and found to be in close agreement to those previously reported within our group suggesting a comparable chiral arrangement of the ligands around the Eu^{III}-centres in Eu_2.**87**$_3$ and Eu_2.**88**$_3$ to those helicate ligand systems of **63** – **66**. Comparison of CPL spectra of Eu_2.**87**$_3$ and Eu_2.**88**$_3$ to those of the analogous mononuclear complexes, whose absolute configurations have been determined by X-ray crystallography, also allowed the prediction of the stereochemistry of Eu_2.**87**$_3$ and Eu_2.**88**$_3$ in which the absolute configurations were estimated as being $\Delta\Delta$ and $\Lambda\Lambda$, respectively.

Studies on the formation of helicates Eu_2.**87**$_3$ and Eu_2.**88**$_3$ *in situ* were conducted in an organic medium (CH_3CN) and the more competitive protic methanolic solvent system. The overall changes in the spectroscopic properties upon titrating **87** and **88** against $Eu(CF_3SO_3)_3$ in both solvents were fit using SPECFIT and confirm formation of the 2:2 Eu_2.**L**$_2$ (**L** = **87**, **88**) and the desired Eu_2.**L**$_3$ (**L** = **87**, **88**) helical species with binding constants obtained comparable to those calculated for **63** – **66**. Lower binding constants and smaller percentage yields were evaluated upon moving from CH_3CN to CH_3OH however, reflecting the enhanced competitive nature of CH_3OH.

An unusual behaviour was displayed in the spectroscopic data following measurements carried out in CH_3OH:H_2O solvent systems (for both 50:50 and 80:20 CH_3OH:H_2O mixtures) where no significant changes were observed in the UV-visible absorption spectra of ligand **87** and a continued enhancement in Eu^{III}-centred emission was demonstrated from between 0 – 5 equiv. of Eu^{III}. Conducting titrations in a constant ionic strength and buffered medium had no effect on this unusual self-assembly behaviour in the partial aqueous environment.

Stability measurements *in situ* gave identical results confirming that it was not a kinetic effect of the system. This was further verified by implementing lifetime measurements which gave similar lifetime values in the mixed solvent system (CH_3OH:H_2O, 80:20) to those calculated in CH_3OH, indicating the presence of the long lived 2:3 helicate species upon the addition of 0.67 Eu^{III} (89%) and similarly at 10 equiv. (87%). These results suggest that

thermodynamic binding constants are lower in this enhanced competitive medium. Luminescence stability measurements carried out on the $Eu_2.\mathbf{87}_3$ complex itself in an 80:20 $CH_3OH:H_2O$ environment evidenced the stability of $Eu_2.\mathbf{87}_3$ but once the H_2O content was increased to 50% a precipitate was instantly formed, marking the limit of these systems in an aqueous environment of such constitution. In order to fully solubilise these chiral supramolecular systems in a 100% water environment and develop them into functional materials groups showing a substantial enhancement in water solubilisation is required.

Future studies may include the synthesis of the target helicate ligand below which is derivatised with a sulfonate functional group in the 4-*para* pyridyl position. This moiety is currently under investigation within our group and has proven successful at aiding water solubilising of the related mononuclear systems.

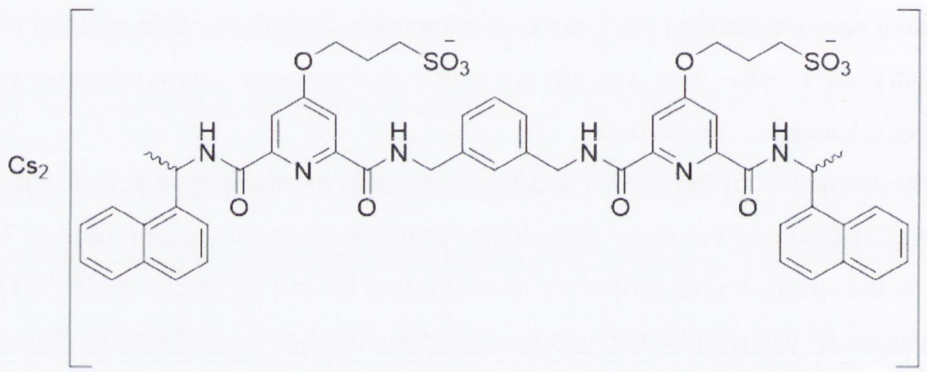

Chapter Four

Functionalisation of half-helicate precursors for potential biological activity

4. Introduction

As illustrated in chapter two, the simple half-helicate precursors **79** (*S*) and **80** (*R*) offer a relatively facile synthetic route towards the formation of novel Ln^{III} luminescent frameworks. By exploiting this synthetic route the suitability of monometallic Ln^{III}-directed self-assemblies of this nature can therefore be modified and tuned to suit various disciplines of application, as was previously observed upon the incorporation of an aliphatic alkyl chain for solid-state fabrication using the Langmuir-Blodgett technique. By furnishing the Ln^{III} assembly such that the photophysical properties of the system may be applied to other areas of research, self-assembled systems of this type can be promoted for use as chiral luminescent responsive probes. For example, these monometallic Ln^{III}-directed self-assemblies can be implemented as optical reporters of a particular target analyte. Furthermore, if functionalised appropriately, they can be utilised as biologically active targeting agents. The acidic side group functionality of **79** (*S*) and **80** (*R*) presents a handle by which these systems can easily be modified and so it was envisaged, for this project, that grafting of substituents to this moiety may facilitate accessibility and enhancement of properties such as water solubility; in concert with the possibility of expressing biological activity.

Much emphasis has been placed on the development of small molecules capable of binding DNA for imaging/sensing and/or for the potential exhibition of anticancer activity.[283-286] Most notably, Ru^{II}-polypyridyl and 1,8-naphthalimide based derivatives are both important classes of DNA binders that show significant anti-cancer activity, receiving a great deal of attention within our laboratory.[287-291] Recently, the quarternisation of a (pyrazino[2,3-h]dipyrido[3,2-a:2'3'-c]phenazine (pdppz) ligand has been shown to be an effective way of increasing its DNA binding affinity while its cationic nature proved successful at inducing favourable solubility properties, enabling studies to be carried out in biological media.[283] Moreover, a series of *N*-pyridinium 4-amino-1,8-naphthalimide derivatives have been developed within the Gunnlaugsson group and shown to intercalate *st*-DNA with significantly high affinity (ca 10^5 M^{-1}).[287,288] The pyridinium side chain incorporated undeniably influences the overall water solubility of the naphthalimide system and it is postulated that it also favours electrostatic interactions with the negatively charge phosphate backbone of DNA.[287,288] Inspired by these studies and the current interest in moving supramolecular chiral Ln^{III}-directed self-assembled systems into an aqueous environment it was our intention to append a positively charged pyridine side chain to the

chiral Ln^{III} chelating sensitising precursors **79** (*S*) and **80** (*R*). This led to the design of the positively charged chiral ligands **100** (*S*) and **101** (*R*).

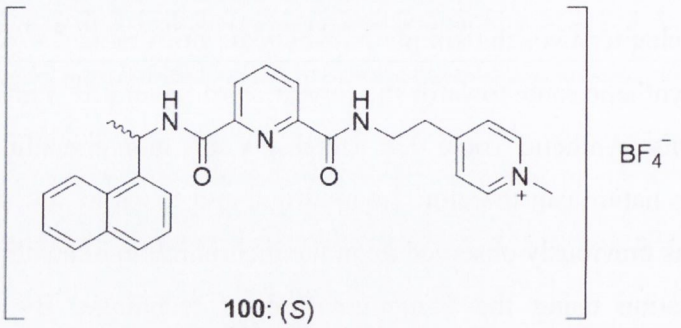

100: (*S*)
101: (*R*)

Another well-established class of compounds currently under investigation within our laboratory are Pt-containing compounds exhibiting anticancer activity.[289] The most widely recognised Pt-containing chemotherapeutic drug is known as cisplatin **102**.[292] Its structure was first described by Peyrone in 1844 however its biological activity wasn't observed until 1967 by Rosenberg and co-workers.[293,294] The key reaction step in its mode of action appears to be its binding to and crosslinking of DNA at two neighbouring guanine bases, triggering cell apoptosis. Cisplatin **102** is commonly used to treat testicular and ovarian cancers but unfortunately severe toxic side effects (such as nausea, ear damage, vomiting and kidney toxicity) are associated with its administration. Drug resistance is also commonly encountered, which has led to the development of new second generation derivatives carboplatin **103** and oxaliplatin **104** which possess slightly lower toxic side effects.[292] Toxicity and drug resistance are the two main factors governing the evolution of new groups of Pt-containing compounds displaying anticancer behaviour such as Pt^{II} complexes containing 2,2':6,2"-terpyridine.

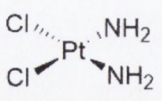

102

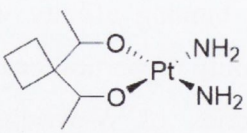

103

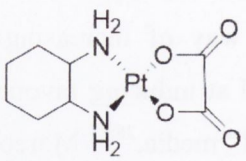

104

$[Pt(terpy)X]^{n+}$ (where X represents ligands occupying the fourth coordination site and "n" is the charge of the complex) is a square planar Pt^{II} complex which has undergone intense investigation since it was first discovered, by Lipppard and co-workers, to intercalate DNA.[295] In this initial study chloroterpyridineplatinum(II) ($[Pt(terpy)Cl]^+$) **105** and 2-hydroxyethanethiolatoterpyridineplatinum(II) ($[Pt(terpy)HET]^+$) **106** were investigated with

studies suggesting intercalation in both cases. UV-visible absorption spectral changes were displayed following the addition of calf thymus DNA (*ct*-DNA) to a solution of **106**. A Scatchard plot of the data depicted behaviour typical of that for binding *via* DNA intercalation. Fluorescence spectroscopy indicated that **106** inhibits competitively, binding of the intercalating dye ethidium bromide to *ct*-DNA and was also shown to increase the viscosity of *ct*-DNA. Complex **106** caused the melting temperature of *ct*-DNA to increase by up to 5 °C and induced circular dichroism spectra upon binding. Furthermore, it was demonstrated that circular viral DNA, from bacteriophage PM2, was unwound by **106** in a similar manner to that observed for the well-known intercalator ethidium bromide. These finding were conclusive of DNA binding *via* intercalation of the planar Pt^{II} terpy moiety.

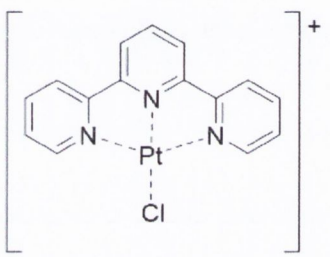

105

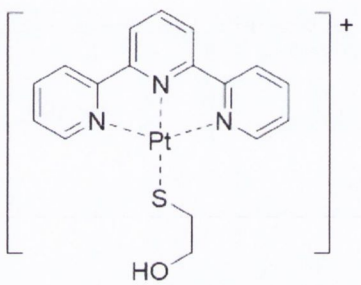

106

These studies, together with later studies conducted by Lippard and co-workers on related analogues of **105** and **106**[296,297] initiated research in this field with a wide range of Pt^{II} terpyridine-based systems being developed for use as DNA targeting agents.[292,298-301]

Mixed *d-f* supramolecular complexes possessing a luminescent Ln^{III} unit linked to a DNA intercalating Pt^{II} terpy moiety, on the other hand, are rare. Combining these two building blocks may expose novel dual functioning systems in the generation of new luminescent bioprobes. One such example, which has been developed by Pikramenou and co-workers,[302] is the hairpin-shaped heterotrimetallic Ln^{III} luminescent complex Nd.**107**. The diethylenetriaminepentaacetic acid ligand derivative provides five oxygen and three nitrogen donor atoms for Nd^{III} encapsulation, two thiophenol chromophoric Ln^{III} sensitising components and two sulphur donor atoms for Pt^{II}-terpy binding. Excitation into the visible absorption band located at 515 nm gave rise to Nd^{III}-centred luminescence with emission bands centred at λ_{max} = 1060 and 1340 nm. These bands are characteristic of deactivation from the Nd^{III} $^4F_{3/2}$ excited state to ground states $^4I_{11/2}$ and $^4I_{13/2}$. No change in relative quantum yield was observed upon interaction of Nd.**107** with *ct*-DNA demonstrating that the Ln^{III} portion of the structure is not involved in DNA binding. Bisintercalation of the two Pt^{II}-terpy units was however, evident from linear dichroism studies and confirmed by molecular

modelling data. The Nd^{III}-centred luminescence can therefore be used as a "reporter" of DNA bisintercalation.[302]

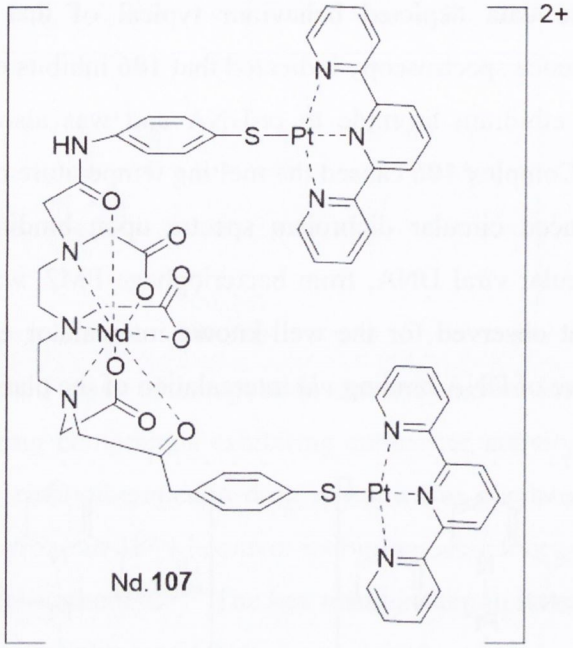

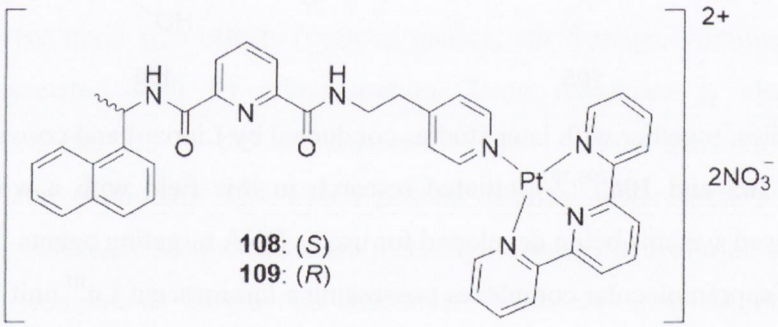

As discussed in previous chapters, Ln^{III}-complexes exhibit unique photophysical properties (line-line emission spectra, long-lifetimes of emission *etc.*) while Pt^{II}-terpy complexes, as described above, are capable of binding to DNA. These observations influenced us to combine the luminescent characteristics of the monometallic Ln^{III}-directed self-assemblies with the DNA binding ability of the Pt^{II}-terpy centre. Since the basic half-helicate framework (**79** (*S*) and **80** (*R*)) is equipped with a tridentate Ln^{III} chelating cavity, a chiral naphthalene sensitising group and an acidic side group available for substitution it was anticipated that attachment of an ethyl pyridine side group to **79** (*S*) and **80** (*R*) would provide a terminal donor nitrogen atom capable of Pt^{II}-terpy coordination. Chiral compounds **108** (*S*) and **109** (*R*) were designed to meet such criteria.

This chapter focuses on the modification of simple half helicate systems **79** (*S*) and **80** (*R*). The intention was to furnish mononuclear chiral Ln^{III}-templated self-assemblies with complete water solubility in concert with perhaps biologically active functionality.

The general aim of this chapter was to develop ligand systems which:

1) Were synthetically straightforward and easily attainable.

2) Formed stable self-assembled complexes in solution (in competitive media in particular).

3) In the case of Ln^{III} complexes of **108** and **109**, exhibited DNA interaction/reporting.

The following sections detail the synthesis and characterisation of compounds **100**, **101**, and the photophysical measurements carried out on the investigation of their ability to assemble *in situ*. Quaternisation of the pyridine side chain was expected to encourage full water solubilisation of compounds **100** and **101** allowing studies to be carried out in an aqueous environment. The remainder of the chapter focuses on the synthesis and characterisation of complexes **108** and **109** and the photophysical measurements implemented to establish their behaviour in solution.

4.1 Synthesis and characterisation of compounds 100 (*S*) and 101 (*R*)

Compounds **100** (*S*) and **101** (*R*) were synthesised in two steps, as shown below in Scheme 4.1, starting with the previously reported half-helicate precursors **79** (*S*) and **80** (*R*). The 4-(2-aminoethyl)pyridine functionality was appended *via* an EDCI·HCl peptide coupling reaction, similar to that described for previous chapters.

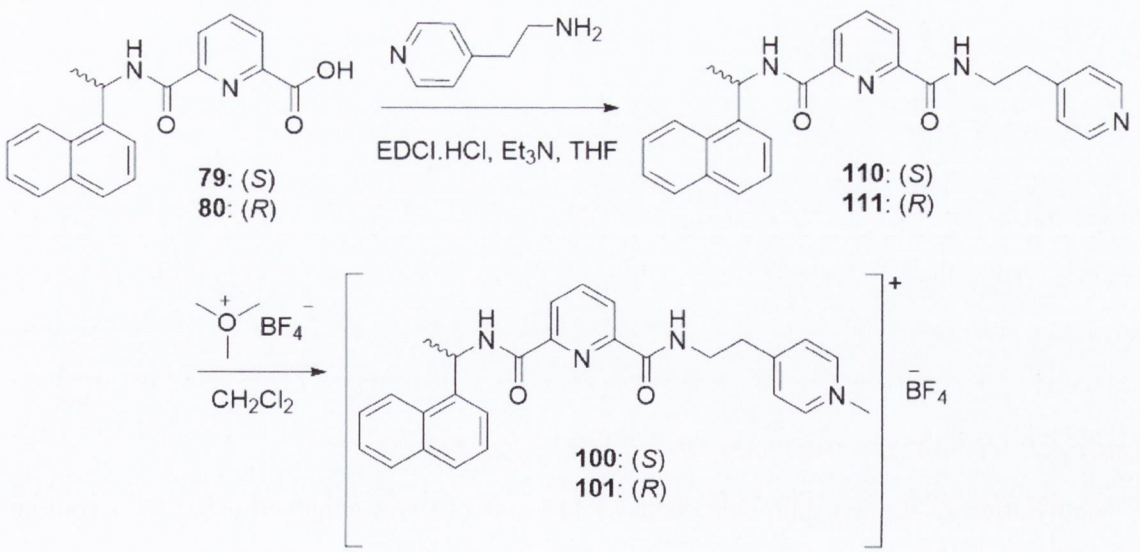

Scheme 4.1. *Synthetic pathway for tridentate pyridine functionalised ligands* ***110*** *(S) and* ***111*** *(R) and methylated pyridinium ligands* ***100*** *(S) and* ***101*** *(R).*

A mixture of (*S*)-6-(1-(naphthalen-1-yl)ethylcarbamoyl)picolinic acid (**79**) or (*R*)-6-(1-(naphthalen-1-yl)ethylcarbamoyl)picolinic acid (**80**), NEt_3, and 1 equiv. of 4-(2-aminoethyl)pyridine in THF were placed under Ar and cooled to 0 °C. After 30 mins of stirring EDCI·HCl was added to the mixture and stirred at 0 °C for a further 30 mins. The

reaction mixture was then allowed to reach RT and stirred for another 72 hrs. The solution was filtered and THF removed under reduced pressure to give a brown oil which was taken up in CH_2Cl_2. The solution was then washed with 0.05 M HCl, sat. aq. $NaHCO_3$, H_2O and brine and the organic phase dried over $MgSO_4$. Solvent was removed under reduced pressure affording a yellow oil which was purified by flash chromatography (CH_2Cl_2:CH_3OH), yielding a white solid in yields of 33% and 43% for **110** (*S*) and **111** (*R*), respectively. Compounds **110** (*S*) and **111** (*R*) were characterised by ^1H NMR (600 MHz, DMSO-d_6), ^{13}C NMR (150 MHz, DMSO-d_6), HRMS, elemental and IR analyses. A detailed assignment of all the protons for **110** and **111** was performed using both 1D and 2D NMR experiments (Appendix Figures A4.1 – A4.3). As shown below for the ^1H NMR spectrum (600 MHz, DMSO-d_6) of **110**, see Figure 4.1 (see Appendix Figure A4.4 for ^1H NMR spectrum (600 MHz, DMSO-d_6) of **111**), signals resonating at 9.47 ppm, 3.66 ppm and 2.95 ppm represent the protons associated with the amine group (next to the CH_2 group) and the two CH_2 group protons of the amino pyridine side chain, respectively. Peaks corresponding to the aromatic protons of the pyridine side chain are located at 8.44 and 7.29 ppm.

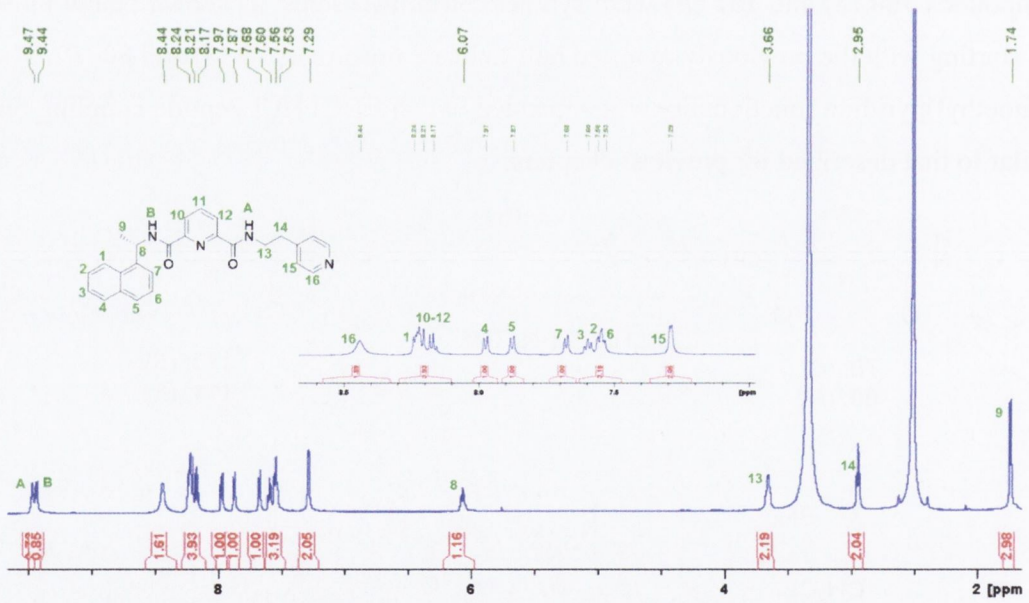

Figure 4.1. *^1H NMR spectrum (600 MHz, DMSO-d_6) of **110** (S).*

Methylation of the pyridine side chain of **110** and **111** was achieved using the oxonium alkylating agent trimethyloxonium tetrafluoroborate. A solution of (*S*)-*N*2-(1-(naphthalen-1-yl)ethyl)-*N*6-(2-(pyridin-4-yl)ethyl)pyridine-2,6-dicarboxamide (**110**) or (*R*)-*N*2-(1-(naphthalen-1-yl)ethyl)-*N*6-(2-(pyridin-4-yl)ethyl)pyridine-2,6-dicarboxamide (**111**) in dry CH_2Cl_2 was placed under Ar. 1.3 equiv. of trimethyloxonium tetrafluoroborate was then added and the reaction mixture stirred at RT for 72 hours after which CH_3OH was used to quench the reaction. Methylated compounds **100** and **101** were isolated as off white solids

via diffusion of diethyl ether into the reaction mixture solution and obtained in yields of 79% and 85% for **100** and **101**, respectively. Formation of the desired compounds **100** and **101** was verified by ^{1}H NMR (600 MHz, DMSO-d_6), ^{13}C NMR (150 MHz, DMSO-d_6), HRMS, elemental and IR analyses while a detailed assignment of all the protons for **100** and **101** was again achieved using a combination of 1D and 2D NMR experiments (Appendix Figures A4.5 – A4.9). As shown below for the ^{1}H NMR spectrum (600 MHz, DMSO-d_6) of **100**, see Figure 4.2 (see Appendix Figure A4.5 for ^{1}H NMR spectrum (600 MHz, DMSO-d_6) of **101**), proton signals, corresponding to the CH_3 of the alkylated pyridine moiety resonate at 4.27 ppm. Aromatic peaks associated with the CH protons next to the alkylated pyridine were also shifted downfield from 8.44 to 8.82 ppm, indicative of the change in the local environment experienced by these protons following methylation.

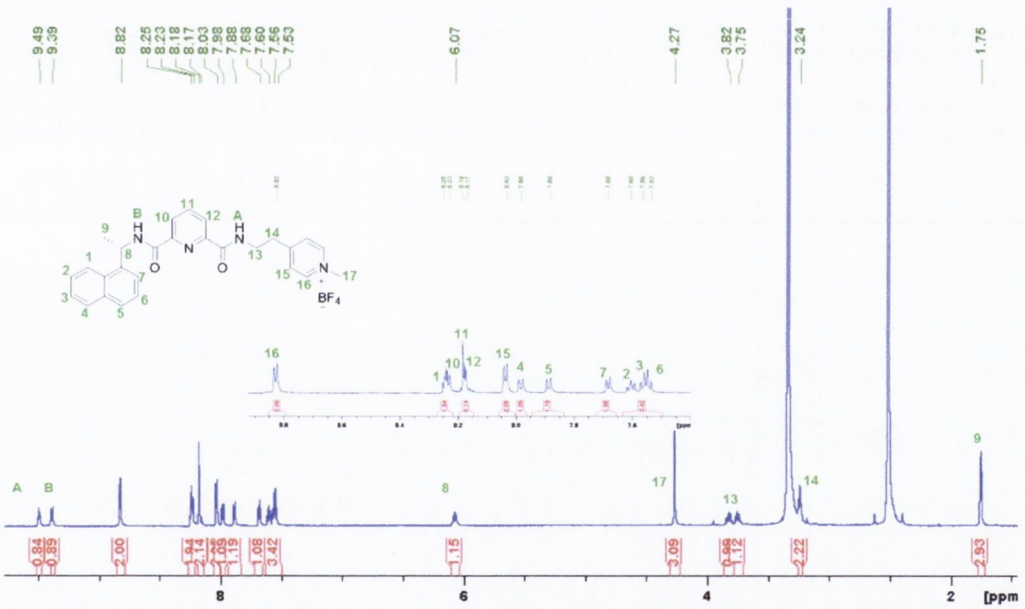

Figure 4.2. *^{1}H NMR spectrum (600 MHz, DMSO-d_6) of **100** (S).*

Although it was anticipated that the positively charged nitrogen would aid the solubilisation of compounds **100** (*S*) and **101** (*R*) in water this was found not to be the case. These compounds were therefore photophysically evaluated in less polar solvents. Ligands **110** (*S*) and **111** (*R*) also represented new chemical motifs suitable for Ln^{III} binding and sensitisation, and so all four compounds were analysed by circular dichroism measurements and their Ln^{III}-directed self-assembly formation was investigated *in situ*.

Furthermore, it should be stated that formation of the 1:3 Eu.$\mathbf{L}_3$ (**L** = **110** and **111**) complexes was also attempted, however, characterisation of these compounds proved challenging. Elemental analysis and lifetime measurements of the isolated solid complexes did not evidence the formation of the fully saturated 1:3 Eu.$\mathbf{L}_3$ (**L** = **110** and **111**) complexes as expected. By reacting compounds **110** and **111** with Eu^{III} under microwave irradiation

(kinetic control) the coordination of the more accessible pyridine nitrogen of the side chain may have given rise to a more complicated, unpredictable structured complex network. Nonetheless, the formation of the thermodynamic products *in situ* was investigated, and is discussed in the following section.

4.2 Chiro-Optical properties of pyridine ligands 110 (*S*) and 111 (*R*), their corresponding complexes and ligands 100 (*S*) and 101 (*R*)

CD spectra were recorded for ligands **110** (*S*) and **111** (*R*) in CH_3CN at RT, as shown below in Figure 4.3. CD spectra were also recorded for the self-assembly species following the addition of 0.33 equiv. of $Eu(CF_3SO_3)_3$ in CH_3CN at RT. CD spectra obtained for the ligands were mirror images of one another demonstrating the enantiomeric purity of compounds **110** (*S*) and **111** (*R*). Positive CD signals were located at 206, 229 and 285 nm while a negative band was located at 220 nm for ligand **110** (*S*). A CD spectrum of equal amplitude but opposite sign was evident for the corresponding *R* enantiomer **111** (*R*).

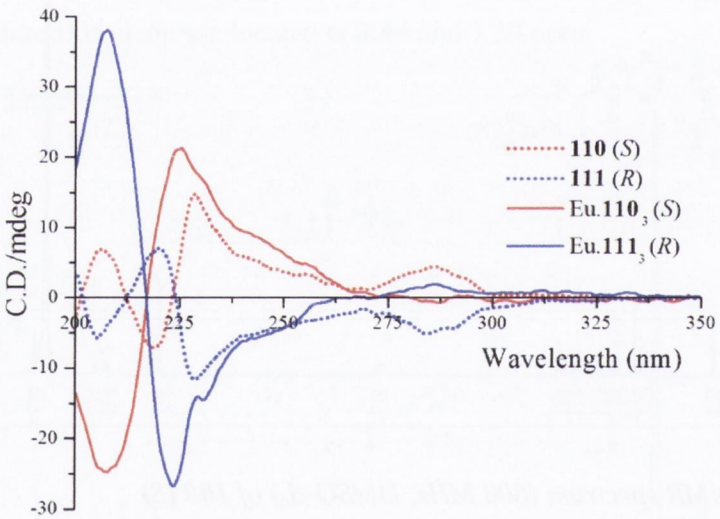

Figure 4.3. *Circular dichroism spectra of ligands* ***110*** *(S) and* ***111*** *(R) (2 x 10^{-5} M) recorded in CH_3CN at RT before and after the addition of 0.33 equiv. of $Eu(CF_3SO_3)_3$ - note that slight discrepancies in intensities can be derived from differences in concentrations.*

Upon the addition of 0.33 equiv. of $Eu(CF_3SO_3)_3$ a significant enhancement was experienced by the band located at 229 nm for **110** (*S*). Concurrently, a slight shift to 226 nm was also evident, while simultaneously, the band located at 206 nm disappeared and the band centred at 220 nm also increased in relative absorption intensity, in addition to a shift to 208 nm. The opposite CD trend was observed for compound **111** (*R*) upon the addition of 0.33 equiv. Eu^{III}, indicating an identical CD behaviour, and thus conformational changes for both systems as different species evolve in solution.

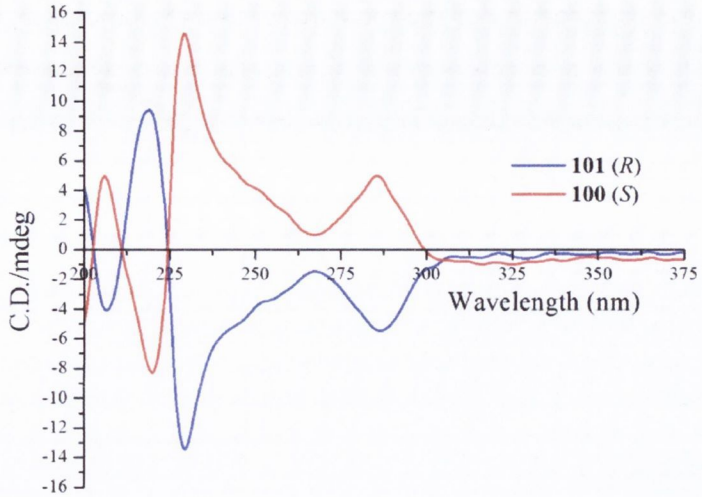

Figure 4.4. *Circular dichroism spectra of ligands* ***100*** *(S) and* ***101*** *(R) (2 x 10^{-5} M) recorded in CH_3CN at RT - note that slight discrepancies in intensities can be derived from differences in concentrations.*

The CD spectra were recorded for **100** (*S*) and **101** (*R*) in CH_3CN (see Figure 4.4) and since it was anticipated that these systems could be moved into more competitive media the CD spectra were also recorded in CH_3OH (see Appendix Figure A4.10). Similarly to that above, the enantiomeric relationship between compounds **100** (*S*) and **101** (*R*) was clearly evident in both cases with opposite CD spectra obtained for each chiral ligand in both solvents. The CD spectra exhibited by **100** (*S*) and **101** (*R*) were almost indistinguishable to those obtained for **110** (*S*) and **111** (*R*) above with positive CD bands again located at 206, 229 and 285 nm and a negative peak centred at 220 nm for the *S* enantiomer **100**. CD spectra measured in CH_3OH were very similar to those described for **100** (*S*) and **101** (*R*) in CH_3CN suggesting that, as expected, methylation of the pyridine moiety does not affect the chirality of the system in anyway. Furthermore, CD spectra recorded in CH_3OH confirm that species conformation is unchanged in both solvent systems.

4.3 Eu^{III}-directed self-assembly of 110 (*S*) and 111 (*R*) in CH_3CN

The Eu^{III}-directed self-assembly of Eu.**110**$_3$ and Eu.**111**$_3$ *in situ* was investigated by a series of spectroscopic measurements which involved the titration of a 1 x 10^{-5} M solution of either **110** or **111** against increasing amounts of a $Eu(CF_3SO_3)_3$ stock solution. Changes in the UV-visible absorption, fluorescence and time-delayed Eu^{III}-centred emission spectra of the solution were then analysed. Studies were performed in CH_3CN (to enable comparison to half-helicate amphiphilic ligands **81** (*S*) and **82** (*R*)). In addition, monitoring the self-assembly process of ligands **110** and **111** should give an insight into the species stoichiometry expected for the self-assembly of related compounds **100** (*S*) and **101** (*R*).

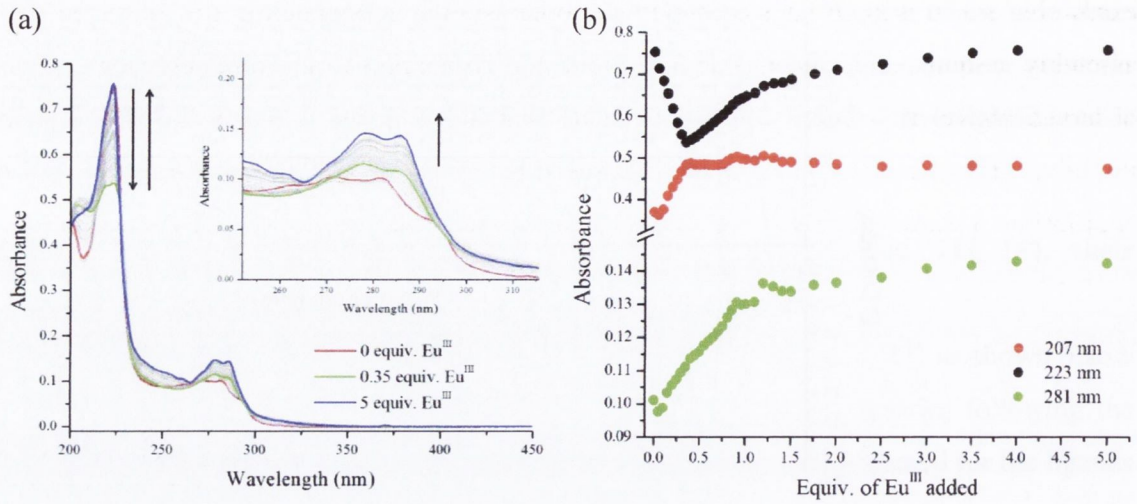

Figure 4.5. *(a) The overall changes in the UV-visible absorption spectra and (b) corresponding experimental binding isotherm of absorbance at λ = 207, 223 and 281 nm upon titrating* ***110*** *(1 x 10^{-5} M) against $Eu(CF_3SO_3)_3$ (0→5 equiv.) in CH_3CN at RT.*

The overall changes observed in the UV-visible absorption spectra of **110** upon titrating against $Eu(CF_3SO_3)_3$ in CH_3CN are displayed Figure 4.5. The UV-visible absorption spectrum of ligand **110** is structurally identical to that observed for the previously studied amphiphilic pair **81** (*S*) and **82** (*R*), consisting of a long wavelength absorption band located at λ_{max} = 281 nm and a higher energy absorption band centred at λ_{max} = 223 nm. These UV-visible absorption peaks represent the $S_0 \rightarrow S_1$ $\pi \rightarrow \pi^*$ transition and the $S_0 \rightarrow S_2$ $\pi \rightarrow \pi^*$ transition, respectively. Upon the addition of 0→0.35 equiv. of $Eu(CF_3SO_3)_3$ the absorption band located at λ_{max} = 223 nm experienced a hypochromic shift, as shown in the binding isotherm graph in Figure 4.5 (b). Additional aliquots of the metal salt caused this peak to increase in relative absorption intensity up until 1 equiv. of Eu^{III} after which a plateau in absorption was reached at higher Eu^{III} concentrations. Concomitantly, the absorption band centred at λ_{max} = 281 nm displayed a gradual enhancement in absorption upon the addition of 0→1 equiv. of $Eu(CF_3SO_3)_3$, after which a gradual plateau in absorption was again observed. Changes in the UV-visible absorption spectra in this manner, as the Eu^{III}-templated self-assembly process proceeded, suggested a displacement in the equilibrium of the system as different stoichiometric species evolved in solution.

As shown in Figure 4.6 (a), a gradual enhancement in a typical Eu^{III}-centred emission spectrum was exhibited upon the addition of 0→0.35 equiv. of $Eu(CF_3SO_3)$ with characteristic bands located at 595 nm, 615 nm and 695 nm. These luminescence transitions represent deactivation from the Eu^{III} excited state $^5D_0 \rightarrow {}^7F_J$ ground states (where J = 1, 2 and 4). Subsequent aliquots of metal gave rise to a sharp decrease in luminescence intensity up until approximately 1.5 equiv. of Eu^{III}, after which a plateau in emission was reached. By

examining spectroscopic data compiled for other similar mononuclear Ln^{III}-directed self-assembly systems evaluated in our laboratory and comparing to the luminescence changes observed above, it is acceptable to speculate that these changes signify the evolution of initially, a 1:3 (M:L) (Eu.**110**$_3$) species followed by, at higher Eu^{III} concentrations, a shift in equilibrium towards the lesser emissive 1:2 (Eu.**110**$_2$) and then the 1:1 (Eu.**110**) species.

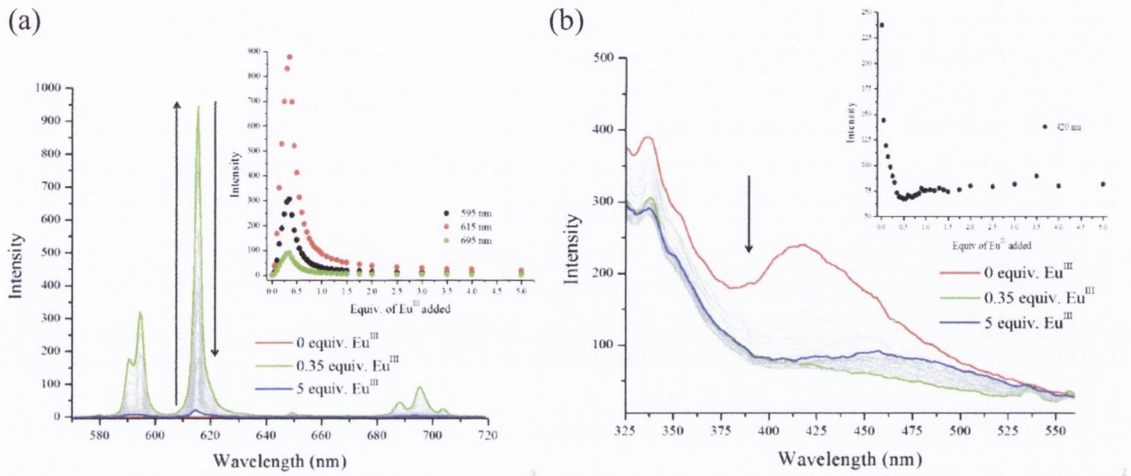

Figure 4.6. *The overall changes in the (a) Eu^{III}–centred phosphorescence spectra and (b) fluorescence spectra upon titrating* ***110*** *(1 x 10^{-5} M) against $Eu(CF_3SO_3)_3$ (0→5 equiv.) in CH_3CN at RT.* ***Inset****: corresponding experimental binding isotherm of (aEu^{III} phosphorescence emission intensity at λ = 595, 615 and 695 nm and (b) fluorescence intensity at λ =420 nm (λ_{ex} = 281 nm).*

The fluorescence emission spectrum of **110** was also affected as the Eu^{III}-directed self-assembly process led to the formation of different species in solution, see Figure 4.6 (b), where a large quenching effect was experienced by the band which corresponds to the fluorescence emission band of **110** (centred at λ_{max} = 420 nm) where quenching by 69% (and 42% for **111**, see Appendix Figure A4.11) was evident after the addition of *ca.* 0.35 equiv. of Eu^{III}. This effect can be attributed to an energy transfer process in which energy is transferred from the ligand excited state *via* the antenna effect to the Eu^{III} metal centre as the 1:3 tris chelate complex is formed *in situ.*

Concurrently, the changes in the UV-visible absorption, fluorescence and Eu^{III}-centred emission spectra following the titration of a 1 x 10^{-5} M solution of ligand **111** against increasing concentrations of $Eu(CF_3SO_3)_3$ in CH_3CN were identical to that shown for **110** (see Appendix Figure A4.11).

In order to confirm the above speculations and elucidate the stoichiometry and binding constants associated with the various species formed in solution this data was further examined by non-linear regression analysis using the program SPECFIT, and this shall be discussed in the next section.

4.4 Fitting of titration data and determination of complex stability constants

The global changes observed in the UV-visible absorption spectra following the titration of **110** and **111** with $Eu(CF_3SO_3)_3$ were fit using non-linear regression analysis in order to gain a better understanding of the self-assembly process in solution.

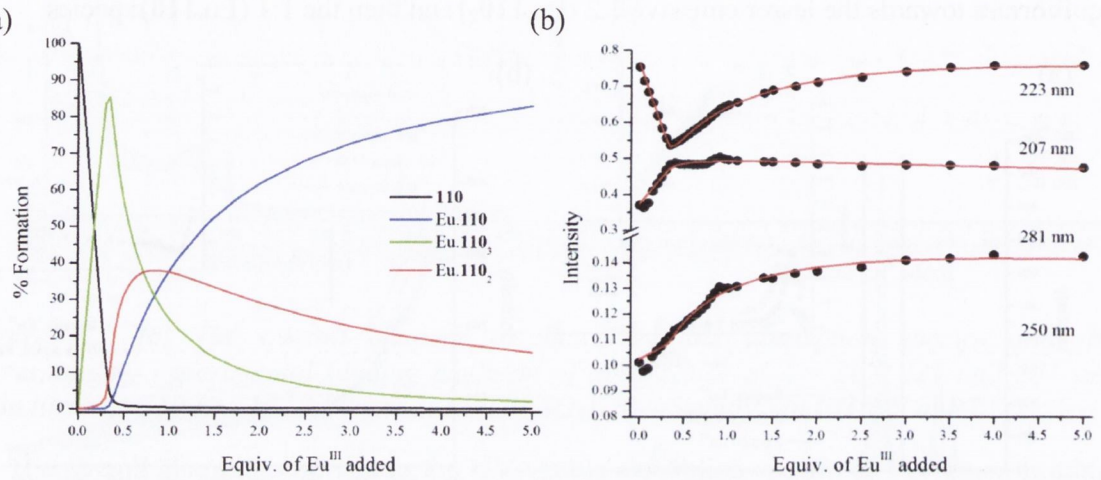

Figure 4.7. *(a) The speciation distribution diagram obtained from the UV-visible absorption titration data fit (upon titrating ligand **110** against $Eu(CF_3SO_3)_3$ in CH_3CN) and (b) the fit of the experimental binding isotherms using the non-linear regression analysis program SPECFIT.*

Analysis of the data for the titration of ligand **110**, as shown in Figure 4.7, indicated the presence of four absorbing species in solution - the ligand itself (**110**), the 1:3 (Eu.**110**$_3$), the 1:2 (Eu.**110**$_2$) and the 1:1 (Eu.**110**) species. As shown in the speciation distribution graph in Figure 4.7 (a), it was evident that after the addition of 0.33 equiv. of $Eu(CF_3SO_3)_3$ the 1:3 (Eu.**110**$_3$) species was the most dominant species formed in solution, present in 85% yield. A binding constant of $\log\beta_{13} = 21.9 \pm 0.4$ was calculated for the tris chelate complex (Eu.**110**$_3$) while the 1:2 (Eu.**110**$_2$) species was formed with a binding constant of $\log\beta_{12} = 14.7 \pm 0.6$. At higher concentrations of the metal salt the 1:1 (Eu.**110**) species evolved, with it being formed in 82% yield following the addition of 5 equiv. of Eu^{III} with a binding constant of $\log\beta_{11} = 7.5 \pm 0.4$. Fitting of the overall changes observed in the UV-visible absorption spectra data following the titration of ligand **111** with $Eu(CF_3SO_3)_3$ in CH_3CN demonstrated an identical self-assembly behaviour in solution for the corresponding *R* enantiomer with binding constants of $\log\beta_{11} = 7.5 \pm 0.3$, $\log\beta_{12} = 14.8 \pm 0.5$ and $\log\beta_{13} = 22.1 \pm 0.6$ calculated for the 1:1 (Eu.**111**), the 1:2 (Eu.**111**$_2$) and the 1:3 (Eu.**111**$_3$) species, respectively (see Appendix Figure A4.12).

It was not possible to fit the luminescence titration data following the titration of either ligand **110** or **111** with $Eu(CF_3SO_3)_3$ in CH_3CN. Although the binding constants calculated from fitting of the UV-visible absorption data above were slightly larger to those observed

for the similar mononuclear systems of **56** and **57** ($\log\beta_{11}$ = 6.8 ± 0.1 , $\log\beta_{11}$ = 6.4 ± 0.3, $\log\beta_{13}$ = 20.0 ± 0.3 and $\log\beta_{13}$ = 20.3 ± 0.5 for Eu.**56**, Eu.**57**, Eu.**56**$_3$ and Eu.**57**$_3$, respectively)[187] it was acceptable to assume that the Eu^{III}-directed self-assembly behaviour of **110** and **111** *in situ* remained relatively unchanged.

From these measurements it was expected that the Eu^{III}-directed self-assembly process of the related methylated pyridinium analogues **100** (*S*) and **101** (*R*) should proceed in a similar manner to that described above.

4.5 Formation of self-assembled species *in situ* – 101 (*R*)

The main goal for compounds **100** (*S*) and **101** (*R*) was to bring solution studies, and the formation of the corresponding Ln^{III} complexes, from organic media towards more competitive protic media, such as CH_3OH and H_2O. Methylation of compounds **110** (*S*) and **111** (*R*) afforded positively charged compounds **100** (*S*) and **101** (*R*) which did not exhibit full water solubilisation but did allow for studies to be carried out in the more competitive protic methanol medium.

Compound **101** (*R*) was therefore initially titrated against $Eu(CF_3SO_3)_3$ in CH_3OH and the overall changes in the UV-visible absorption, Eu^{III}-centred emission and fluorescence spectra monitored. An unusual behaviour was exhibited by this system in which no noticeable changes were observed in the UV-visible absorption spectra upon increasing concentrations of Eu^{III}. Furthermore, fluorescence spectra was shown to continuously increase in intensity, as did Eu^{III}-centred emission. The Eu^{III}-centred luminescence binding isotherms displayed by the system showed a sharp increase in luminescence intensity from 0→1 equiv. of the metal salt added with subsequent additions giving rise to a less steep increase at higher Eu^{III} concentrations. These results do suggest sensitisation and thus self-assembly between the ligand and the Eu^{III} ion in solution, however, it was not possible to explain this trend or fit this data which signifies that a more complicated process may be occurring. Since methanol is a protic solvent it may be preventing/hindering the self-assembly process through H-bonding interactions with the ligand molecules. The extra positive charge on the ligand structure in the presence of methanol may induce a particular ligand conformational network in solution, interfering with the self-assembly process in solution.[282]

Studies were therefore carried out in an organic CH_3CN medium to investigate if the self-assembly process occurred with the formation of the 1:3 Eu^{III} complex in a less competitive solvent medium. The overall changes observed in the UV-visible absorption, Eu^{III}-centred emission and fluorescence spectra upon the titration of ligand **101** against $Eu(CF_3SO_3)_3$ in CH_3CN are depicted in Figure 4.8. The UV-visible absorption spectra did undergo changes at λ = 223 and 281 nm but it was clear that the process was not as

straightforward as was encountered for related structures.[70] Again an unusual behaviour was evident, in particular from the Eu^{III}-centred emission spectra, where the shape of each emission band dramatically changed as the titration proceeded, suggesting a rearrangement of the various species in solution. This titration data was also not found to be reproducible, *i.e.* a different phosphorescence binding isotherm was demonstrated depending on the amount of time allowed between each metal addition. It was anticipated that the expected stoichiometric species were initially evolving in solution but were undergoing instant disassembly due to electrostatic repulsion between adjacent positively charged ligands. No obvious changes were observed in the weak ligand centred fluorescence emission spectrum (see Appendix Figure A4.13).

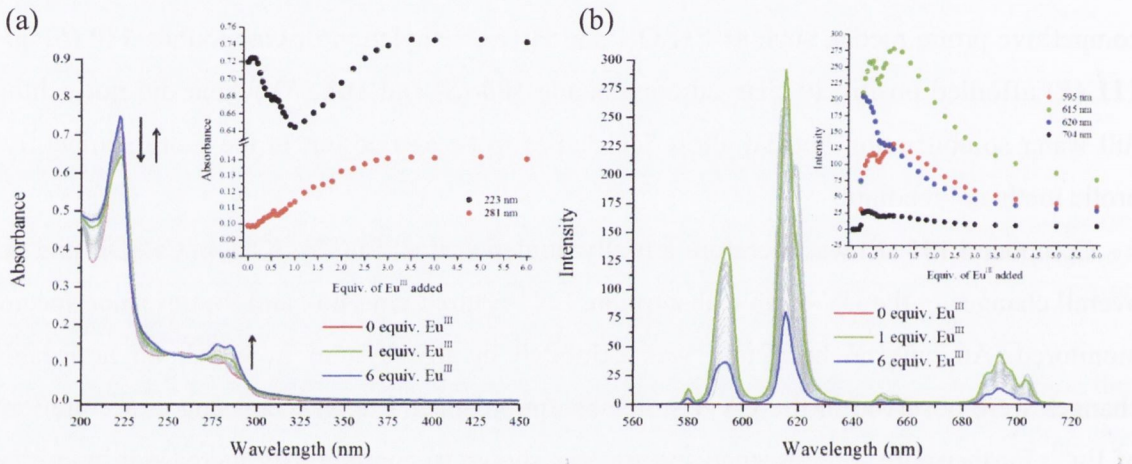

Figure 4.8. *The overall changes in the (a) UV-visible absorption spectra and (b) Eu^{III}–centred phosphorescence spectra upon titrating* ***101*** *(1 x 10^{-5} M) against $Eu(CF_3SO_3)_3$ (0→6 equiv.) in CH_3CN at RT.* ***Inset****: corresponding experimental binding isotherm of (a) absorbance at λ = 223 and 281 nm and (b) Eu^{III} phosphorescence emission intensity at λ = 595, 615, 620 and 704 nm (λ_{ex} = 281 nm).*

These unpredictable results instigated us to evaluate the kinetics of the self-assembly process by monitoring changes which may occur over time due to an unstable system. These results are discussed in the following section.

4.6 Kinetics studies on a solution of compound 101 (*R*) in the presence of 0.33 equiv. of $Eu(CF_3SO_3)_3$ in CH_3CN

A 1:3 (Eu:$\mathbf{101}_3$) solution was prepared by adding 0.33 equiv. of $Eu(CF_3SO_3)_3$ to a 1 x 10^{-5} M solution of compound **101** in CH_3CN. As shown in Figure 4.9 (a), the UV-visible absorption spectrum of the solution was recorded after 0 mins and again after 14 hrs 30 mins, after which only minor changes were observed. The Eu^{III}-centred emission was also monitored every 30 mins from 0 – 14 hrs 30 mins, the results of which are displayed in Figure 4.9 (b) and (c). Initially Eu^{III}-centred emission was exhibited from the solution, upon excitation of

the naphthalene antenna at λ = 281 nm, with characteristic bands located at λ = 580, 593, 614, 650 and 695 nm. These emission peaks correspond to deactivation from the Eu^{III} excited state $^5D_0$ to ^7F_J ground states where J = 0 – 4. From these results it is clear that the Eu^{III} centre does coordinate the tridentate chelating unit of the ligand, enabling sensitisation of the Eu^{III} metal centre *via* excitation into the naphthalene chromophore. However, possibly due to electrostatic repulsion between neighbouring positively charged pyridinium moieties, the complex almost instantaneously disassembles. Furthermore, the positive charge located on the pyridinium side chain may also repel the positively charged Eu^{III}, as there is little evidence of any Eu^{III}-centred luminescence, which would be expected even from the lesser emissive 1:1 (Eu.**101**) species.

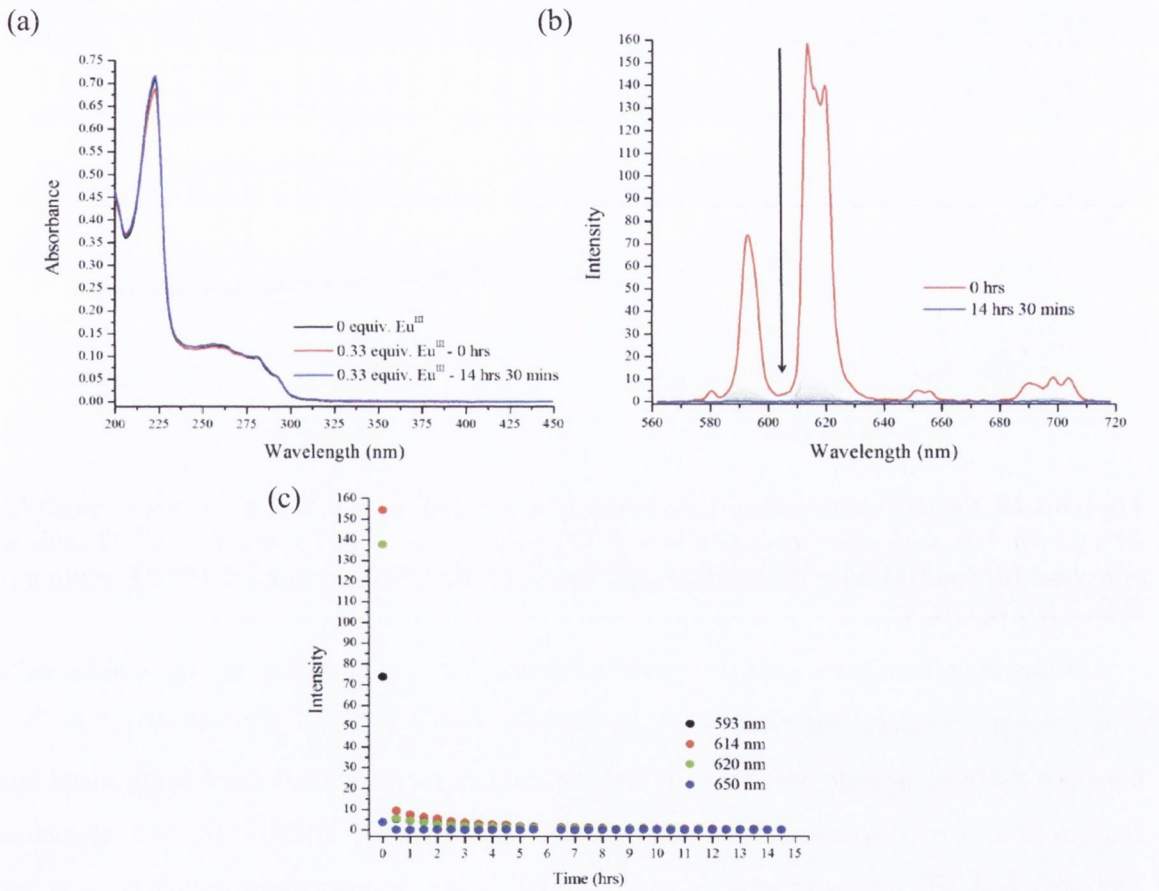

Figure 4.9. *(a) UV-visible absorption spectrum of ligand* ***101*** *(1 x 10^{-5} M) recorded in CH_3CN at RT before the addition of $Eu(CF_3SO_3)_3$ and at 0 hrs and 14hrs 30 mins after the addition of 0.33 equiv. $Eu(CF_3SO_3)_3$. (b) Eu^{III}–centred phosphorescence spectra recorded from 0⟶14 hrs 30 mins following the addition of 0.33 equiv. of $Eu(CF_3SO_3)_3$ to* ***101*** *in CH_3CN at RT. (c) Corresponding experimental binding isotherm of Eu^{III}-centred emission intensity at λ = 593, 614, 620 and 650 nm after each scan (recorded every 30 mins).*

These results were further confirmed following a more detailed kinetic measurement of the Eu^{III}-centred emission at λ = 595, 615, 620 and 704 nm after every 0.2 seconds on a 1 x

10^{-5} M solution of ligand **101** in the presence of 0.33 equiv. of $Eu(CF_3SO_3)_3$, as shown in Figure 4.10 (a). After approximately 50 mins luminescence intensity was almost completely quenched, indicating complete dissociation of the complex in solution. This measurement was also carried out on a 1 x 10^{-5} M solution of ligand **101** in the presence of 1 equiv. of $Eu(CF_3SO_3)_3$, as shown in Figure 4.10 (b). It has been established from this data that initially, the 1:3 complex is assembled in solution, followed almost immediately by dissociation. However at higher Eu^{III} concentrations, equilibrium is pushed towards the formation of the 1:1 (Eu.**101**) species in solution.

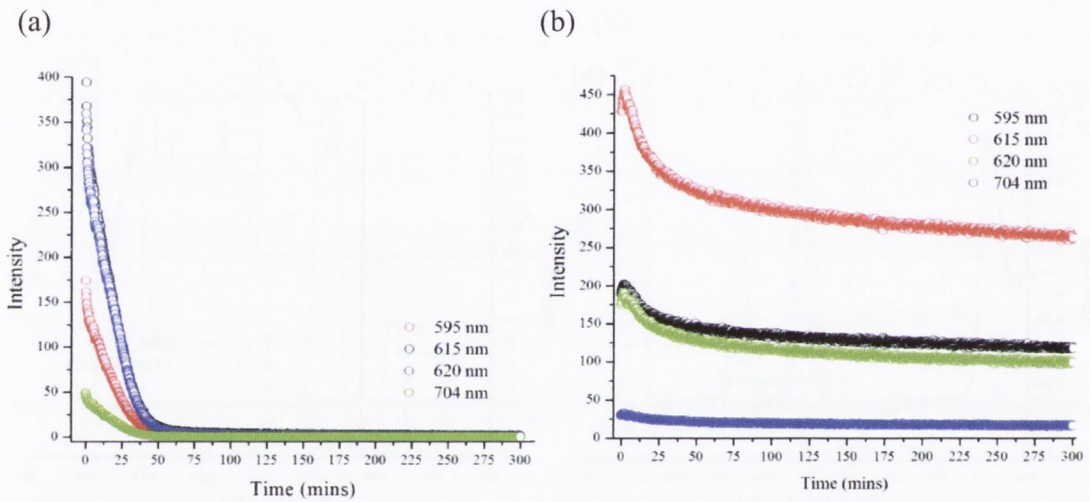

Figure 4.10. *(a) Eu^{III}-centred emission intensity at λ = 595, 615, 620 and 704 nm recorded at RT every 0.2 seconds after the addition of 0.33 equiv. of $Eu(CF_3SO_3)_3$ to a 1 x 10^{-5} M solution of ligand **101** and (b) after the addition of 1 equiv. of $Eu(CF_3SO_3)_3$ to a 1 x 10^{-5} M solution of ligand **101** (CH_3CN).*

4.7 Summary of the synthesis and Eu^{III}-directed self-assembly of the pyridinium ligands 100 (*S*) and 101 (*R*)

Four novel chiral ligands based on the half-helicate framework have been synthesised and characterised by conventional methods (NMR spectroscopy, HRMS, IR and elemental analyses) and CD spectroscopy. *In situ* solution study investigations indicated that the uncharged aminopyridine functionalised ligands **110** (*S*) and **111** (*R*) were suitable for Eu^{III}-directed self-assembly in CH_3CN forming three expected species in solution, *i.e.* the 1:1 (Eu.**L**), 1:2 (Eu:$\mathbf{L}_2$) and 1:3 (Eu:$\mathbf{L}_3$) (**L** = **110** and **111**) species with binding constants comparable to those previously reported for analogue systems. However, the chiral positively charged pyridinium compounds **100** (*S*) and **101** (*R*) were found to be insoluble in H_2O and displayed an unstable behaviour in solution. From the above studies it can be deduced that

the proximity of the positive charge to the Ln^{III} chelating core renders it unsuitable for the assembly of the various species in solution.

To address these issues it would be necessary to firstly incorporate a more influential water solubilising group to aid full water solubility, and also, if a positively charged moiety is being integrated at the acidic side chain six position, it should ideally be incorporated using a longer spacer functional group in order to ensure the prevention of electrostatic repulsions.

In parallel to these studies Pt^{II}-terpy complexes **108** (*S*) and **109** (*R*) were synthesised and their ability to self-assemble in solution *via* Eu^{III}-templated self-assembly probed.

4.8 Synthesis and characterisation of compounds 108 (*S*) and 109 (*R*)

As discussed above, chiral Pt^{II}-terpy complexes **108** (*S*) and **109** (*R*) were designed with the intention of furnishing chiral Ln^{III}-directed self-assemblies with water solubilisation in concert with the potential capability of interacting with biomolecules, such as DNA.

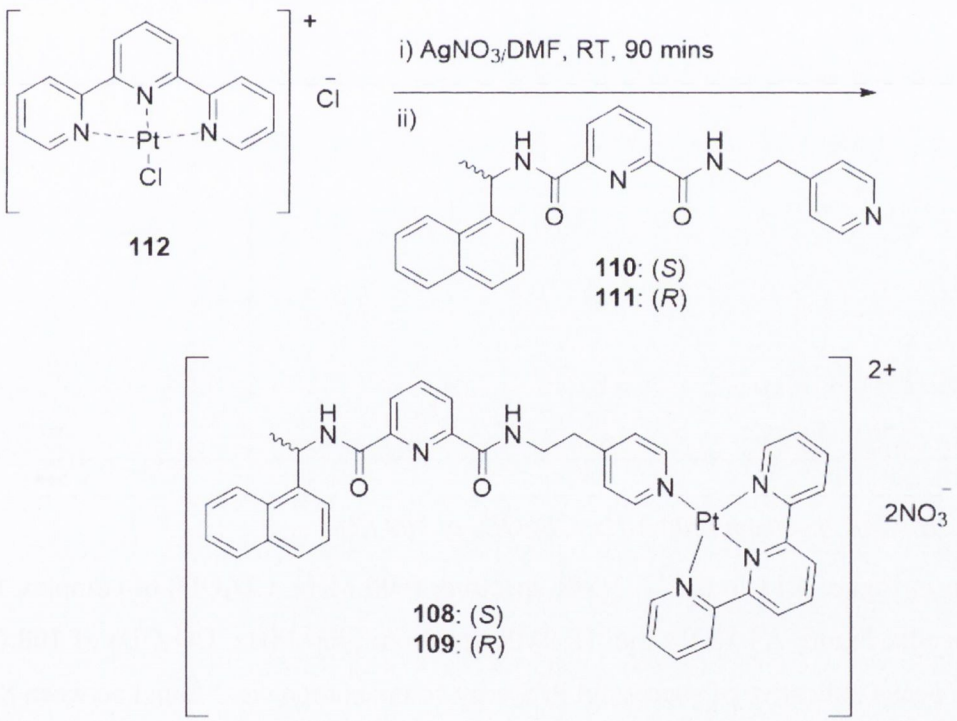

Scheme 4.2. *Synthetic pathway for Pt^{II}-terpy functionalised ligands **108** (S) and **109** (R).*

Compounds **108** (*S*) and **109** (*R*) were synthesised in two steps using the previously synthesised precursors **110** (*S*) and **111** (*R*) and the [Pt(terpy)Cl]Cl complex **112**, as shown in Scheme 4.2. The [Pt(terpy)Cl]Cl complex **112** was synthesised by Dr. Swagata Banerjee according to a previously described literature procedure.[303] The final step towards the formation of the desired complexes **108** and **109** also involved following a previously reported literature procedure[299] and first entailed the stirring of a suspension of the

(2,2';6'2''-terpyridine)platinum^{II} chloride complex **112** with 2 equiv. of $AgNO_3$ in DMF under darkness for 90 mins. The resulting mixture was then filtered to remove the white AgCl precipitate. 1.2 equiv. of (*S*)-N2-(1-(naphthalen-1-yl)ethyl)-N6-(2-(pyridin-4-yl)ethyl)pyridine-2,6-dicarboxamide **110** or (*R*)-N2-(1-(naphthalen-1-yl)ethyl)-N6-(2-(pyridin-4-yl)ethyl)pyridine-2,6-dicarboxamide **111** was then added dropwise to the filtrate over a period of 2 hrs. The reaction mixture was then filtered and the solution slowly added to diethyl ether. Complex products **108** and **109** were collected as orange solids by suction filtration in yields of 78% and 71%, respectively.

Formation of the desired complexes **108** and **109** was verified using ^{1}H NMR, ^{13}C NMR HRMS, IR and elemental analyses. A combination of 1D and 2D NMR experiments were also employed in order to assign each proton resonance in the ^{1}H NMR spectrum (Appendix Figures A4.14 – A4.17).

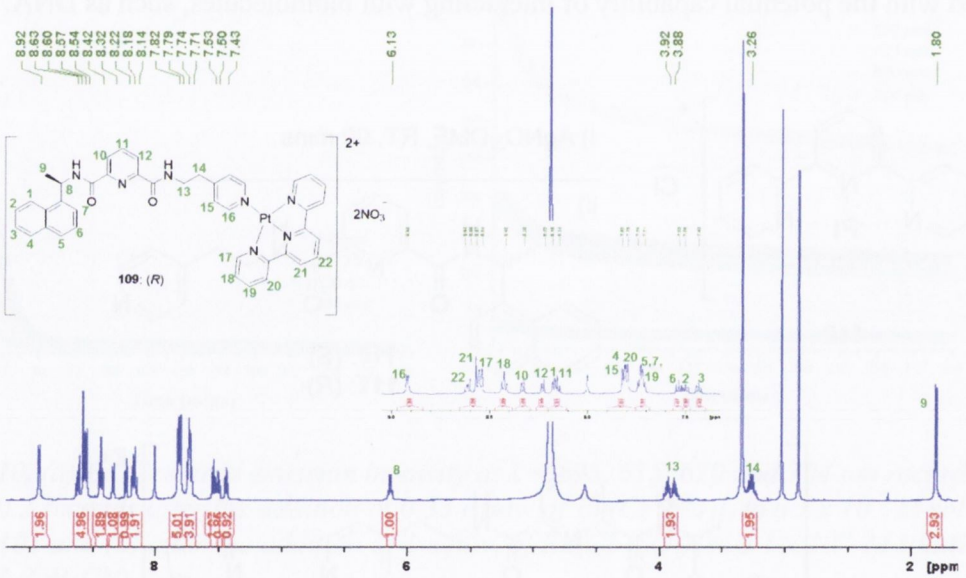

Figure 4.11. *^{1}H NMR spectrum (600 MHz, CD_3OD) of* ***109*** *(R).*

As shown in Figure 4.11 in the ^{1}H NMR spectrum (600 MHz, CD_3OD) of complex **109** (*R*) (see Appendix Figure A4.18 for the ^{1}H NMR spectrum (400 MHz, CD_3OD) of **108** (*S*)) characteristic peaks indicative of successful Pt^{II}-terpy complexation were found between 8.63 – 8.60 ppm, 8.57 – 8.54 ppm, at 8.42 ppm, between 8.18 – 8.14 ppm and 7.74 – 7.71 ppm. These signals correspond to the eleven aromatic protons of the terpy moiety. In addition to the above analyses, crystals of both chiral Pt^{II}-terpy complexes **108** (*S*) and **109** (*R*) were grown *via* diethyl ether diffusion into the reaction mixture. These crystals were suitable for solid state X-ray crystallographic analysis which was carried out by Dr. Jonathan A. Kitchen.

4.9 X-ray crystal structure analysis of Pt^{II} complexes 108 (*S*) and 109 (*R*)

Single crystals of complexes **108** (*S*) and **109** (*R*) were grown by the diffusion of diethyl ether into a DMF solution of either **108** (*S*) or **109** (*R*). The solid state structure of both **108** (*S*) and **109** (*R*) were determined at 100 K and were shown to crystallise in the chiral orthorhombic space group P_{212121} with one DMF solvent molecule and two nitrate anions in the asymmetric unit in each case (see Figure 4.12 and Appendix Tables A4.1 and A4.2).

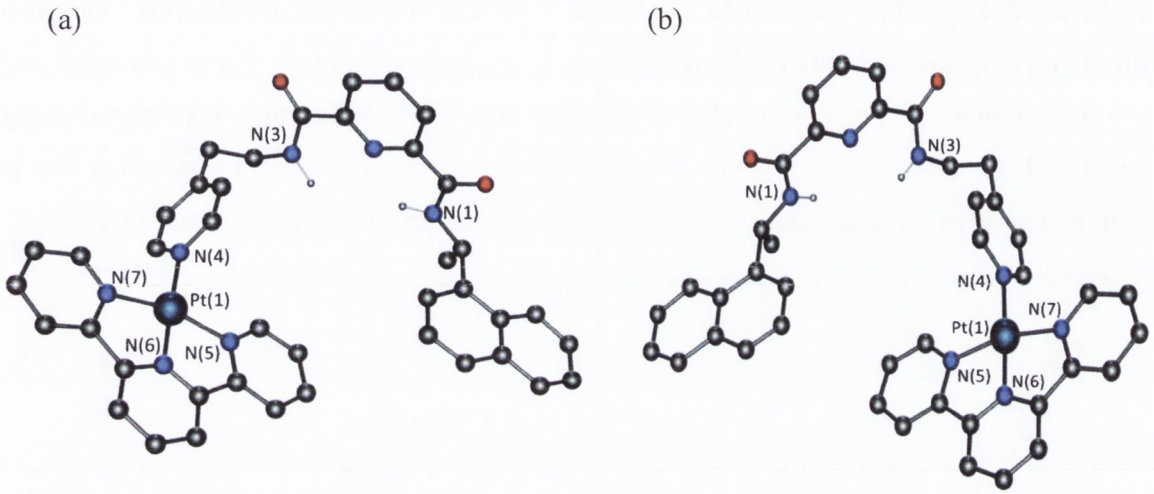

Figure 4.12. *Crystal structures of ligands (a)* ***109*** *(R) and (b)* ***108*** *(S) with thermal ellipsoids shown at 50% probability.*

Table 4.1. *Selected bond lengths (Å) and angles (°) for* ***109*** *(R).*

Bond lengths (Å)/angles (°)	
Pt(1)-N(6)	1.955(5)
Pt(1)-N(7)	2.026(4)
Pt(1)-N(4)	2.030(4)
Pt(1)-N(5)	2.038(4)
N(6)-Pt(1)-N(7)	81.50(17)
N(6)-Pt(1)-N(4)	177.96(17)
N(7)-Pt(1)-N(4)	100.13(16)
N(6)-Pt(1)-N(5)	81.11(17)
N(7)-Pt(1)-N(5)	162.57(16)
N(4)-Pt(1)-N(5)	97.27(16)

The Pt^{II} metal ion was shown to be in the expected square planar geometry with the *cis* N-Pt-N angles in the range 81.1° – 100.1° for **109** (*R*), see Table 4.1 and Appendix Table A4.3 for **108** (*S*). For **109** (*R*) the Pt…N bond lengths ranged from 2.0 – 2.04 Å, consistent with

literature values (see Appendix Table A4.3 for **108** (*S*)).[289] π-π stacking interactions existed between the terpyridine moiety of one molecule and the pyridine unit of an adjacent molecule with a centroid....centroid distance of 3.459 Å for **109** (*R*) and 3.449 Å for **108** (*S*).

Up to six H-bonding interactions were evident between one of the nitrate anions and the Pt^{II}-terpy complex **109** where two of the amide NH protons H-bonded with the central pyridine nitrogen atom and two of the nitrate oxygen atoms, see Table 4.2 and Appendix Table A4.4 for bond lengths and angles of classical H-bonding interactions. The two remaining non-classical H-bonding interactions were observed between the nitrate anion and two CH protons belonging to the terpyridine unit. This H-bonding network strongly influenced the overall packing nature of the complex structure in which the complex **109** is slightly bent in order to accommodate these H-bonding interactions (see Figure 4.13).

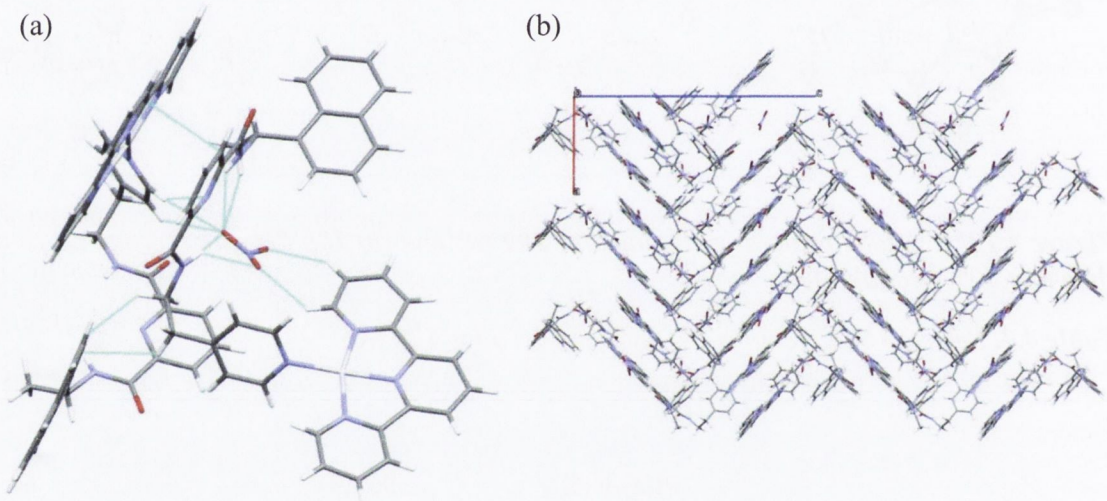

Figure 4.13. *(a) The X-ray crystal structure of **109** (R) showing H-bonding interactions. (b) X-ray packing diagram of **109** (R) viewed down the b-axis.*

Table 4.2. *Hydrogen bonds lengths and angles for ligand **109** (R) (Å and °). Symmetry transformations used to generate equivalent atoms: [a] x+1/2,-y+1/2,-z+1.*

D-H...A	d(D-H)	d(H...A)	d(D...A)	<(DHA)
N(1)-H(1X)...O(200)[a]	0.82	2.38	3.072(6)	142.9
N(3)-H(3X)...O(200)[a]	0.88	2.17	2.965(7)	150.8

4.10 Chiro-Optical properties of Pt^{II}-terpy complexes 108 (*S*) and 109 (*R*)

CD spectra were recorded for complexes **108** (*S*) and **109** (*R*) in CH_3OH at RT as shown below in Figure 4.14. Although there was a slight disturbance in the baseline at shorter

wavelengths for both measurements it is clear that the complexes were formed as a pair of enantiomers, displaying CD spectra which were mirror images of one another.

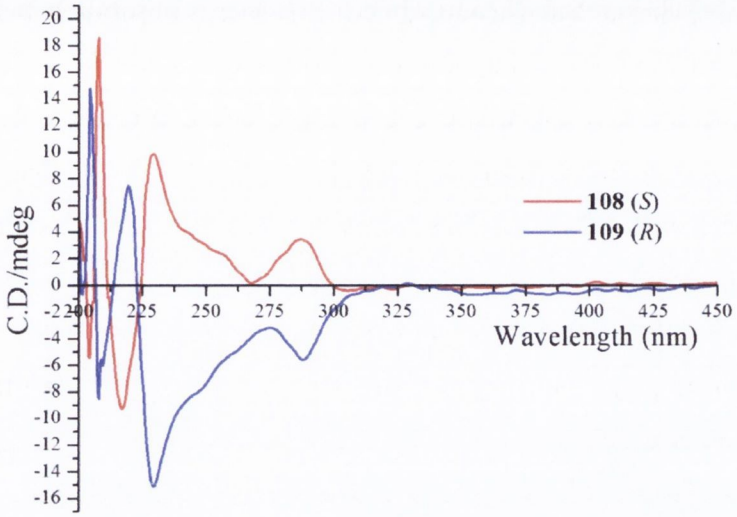

Figure 4.14. *Circular dichroism spectra of ligands* ***108*** *(S) and* ***109*** *(R) (2 x 10^{-5} M) recorded in CH_3OH at RT - note that slight discrepancies in intensities can be derived from differences in concentrations.*

A similar CD profile was exhibited for the chiral complexes **108** (*S*) and **109** (*R*) as was encountered in previous sections. The CD spectrum corresponding to the *S* enantiomer **108** displayed positive signals located at λ = 287, 229 and 208 nm with a negative peak centred at λ =217 nm. The CD spectrum for **109** (*R*) was composed of bands located at equal wavelengths and magnitude but opposite in sign, indicating the chiral relationship between the two complexes.

4.11 Self-assembly studies between 109 (*R*) and Eu^{III} in protic and aprotic media

Considering the objective of this project was to develop Ln^{III}-directed mononuclear systems in a more competitive environment solution studies were initially carried out in CH_3OH. In addition to this, since the counter anion of the synthesised Pt^{II}-terpy complexes was a nitrate anion studies were conducted by titrating a solution of **109** (*R*) against increasing concentrations of $Eu(NO_3)_3.5H_2O$ (for consistency) in CH_3OH and the changes in the UV-visible absorption and Eu^{III}-centred emission spectra monitored.

As shown in Figure 4.15 (a) the UV-visible absorption spectrum of ligand **109** (*R*) consisted of absorption bands corresponding to both the transitions within the pyridyl and naphthalene groups as before and those representative of terpyridyl and ^{1}MLCT transitions of the incorporated Pt^{II}-terpy complex. The long wavelength low energy absorption band centred at λ = 340 nm, which displayed a small shoulder at λ =326 nm, was attributed to the intraligand π-π^* transitions of the terpyridyl moiety by comparison to the previously studied $[Pt(terpy)Cl]^+$ complex.[289,304,305] Weak absorption bands were also observed at even lower

energy wavelengths located at λ = 370 and 390 nm which can be presumably assigned to the ^{1}MLCT transition from Pt(*d*) → terpy(π*).[289,304,305] Shorter wavelength absorption shoulders were found at λ = 283 nm and 272 nm while a high energy absorption band was centred at λ = 224 nm. These UV-visible absorption peaks correspond to the $S_0 \rightarrow S_1$ and $S_0 \rightarrow S_2$ π → π* transitions within the naphthalene and pyridyl functionalities as observed in previous sections.[305]

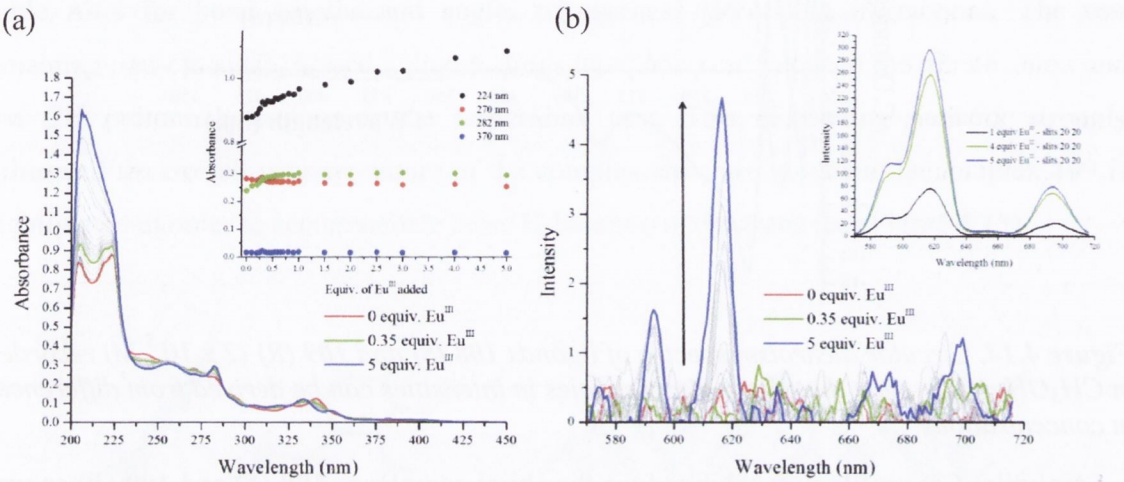

Figure 4.15. *The overall changes in the (a) UV-visible absorption and (b) Eu^{III}-centred emission spectra upon titrating ligand* ***109*** *(R) (1 x 10^{-5} M) against $Eu(NO_3)_3.5H_2O$ in CH_3OH at RT.* ***Inset****: (a) corresponding experimental binding isotherm of absorbance at λ = 224, 270, 282 and 370 nm and (b) Eu^{III}-centred phosphorescence emission upon the addition of 1, 4 and 5 equiv. of Eu^{III} after changing the emission slit settings from 5 to 20 nm.*

As mentioned, Pt^{II}-terpy complexes usually possess square planar geometry and exhibit an oxidation state of +2 giving rise to a d^8 electronic configuration. The ligand field splitting diagram associated with Pt^{II} in this geometry reveals a single unoccupied high energy antibonding dx^2-y^2 orbital.[305] Upon UV-visible absorption population of this orbital and subsequent generation of the excited state complex displays significant distortion and a large increase in the Pt-L bond lengths. The *d-d* excited state potential energy surface possesses an energy minimum which is markedly displaced from that of the ground state. Population of the dx^2-y^2 orbital and thus generation of the Pt^{II} excited state is therefore unfavourable and so luminescence emission is greatly affected. Furthermore, the excited molecules can revert back to the ground state through a thermally accessible isoenergetic crossing point of the ground state and excited state potential energy surfaces by non-radiative internal conversion or intersystem crossing. In addition to this, luminescence radiative decay constants are small for Laporte forbidden *d-d* transitions meaning Pt^{II} complexes are usually only weakly luminescent or non-luminescent in solution at RT. Introduction of conjugated aromatic ligands around the Pt^{II} metal results in lower energy ligand-centred (LC) (π-π* or n-π*) and

charge-transfer (CT) transitions (from the Pt^{II} *d* orbital to the π^* orbital on the ligand) however the close proximity of the thermally accessible *d-d* states can still provide a pathway for non-radiative deactivation to occur and reduce the luminescence quantum yield of the Pt^{II} complex.[305] It is for this reason that no Pt^{II} centred emission was observed for the **109** (*R*) complex in solution.

Minor UV-visible absorption changes were observed upon titrating ligand **109** (*R*) against increasing concentration of $Eu(NO_3)_3.5H_2O$ in CH_3OH, with a number of isosbestic points appearing at 348, 337, 287 and 277 nm, respectively. These changes do suggest a conformational change as the complex coordinates the Eu^{III} centre, however, only very weak Eu^{III}-centred emission was observed at high metal concentrations. It is possible that the metal centre is not fully encapsulated (steric bulk) and shielded from deactivating solvent molecules, *i.e.* minor changes in the UV-visible absorption spectra indicate conformational changes, which may be due to the formation of the 1:1 or the 1:2 species in solution. However, the large bulky Pt^{II}-terpy unit may hinder the assembly of a third molecule, therefore leaving the Eu^{III} free to coordinate deactivating solvent molecules. Furthermore, as was discussed in section 4.9, the nitrate group has been shown to strongly interact with the molecule *via* H-bonding interactions which may prevent the Eu^{III} metal from binding to the tridentate binding cavity.

Because the self-assembly of complex **109** (*R*) with $Eu(NO_3)_3.5H_2O$ in CH_3OH did not behave as expected studies were again moved back to the less competitive aprotic CH_3CN medium. Upon preparation of the 1×10^{-5} M solution of complex **109** (*R*) for the titration against $Eu(CF_3SO_3)_3$ in CH_3CN the UV-visible absorption spectrum of complex **109** (*R*) alone was found to slowly change over time. The UV-visible absorption spectrum of complex **109** (*R*) in CH_3CN was therefore monitored and recorded every 10 mins, as shown in Figure 4.16.

A change in the UV-visible absorption spectrum of complex **109** (*R*) in the presence of CH_3CN was observed over time. In particular, changes were most significant in the UV-visible absorption region at longer wavelengths which are associated with the terpyridine moiety. These results suggest the displacement of the Pt^{II}-terpy unit from **109** (*R*) as CH_3CN preferentially coordinates to the Pt^{II} centre and causes the removal of the pyridine side chain of the ligand. These findings were further supported by ^1H NMR spectroscopy evidence and are discussed in the next section.

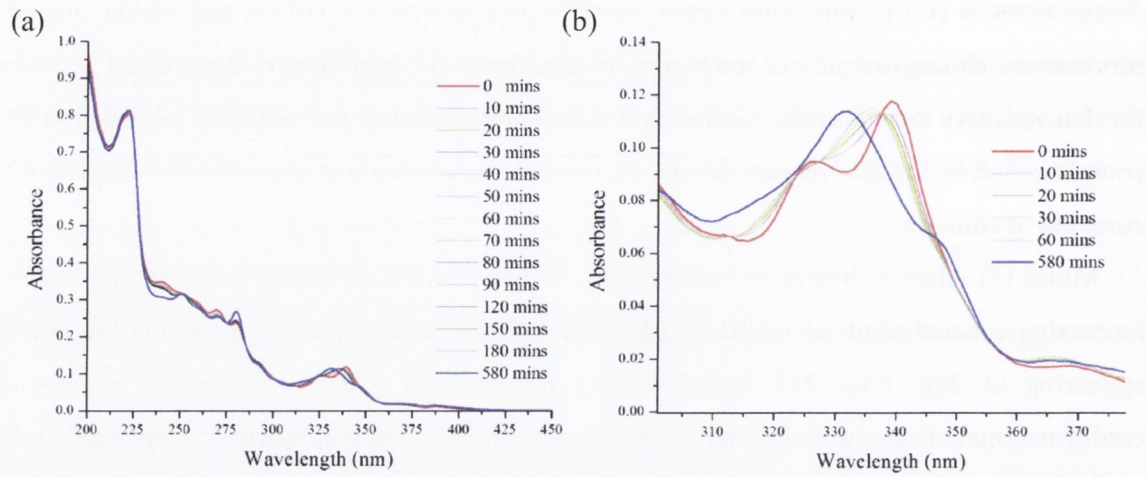

Figure 4.16. *UV-visible absorption spectrum of complex* ***109*** *(R) (1 x 10^{-5} M) in CH_3CN recorded every 10 mins from 0→580 mins at RT.*

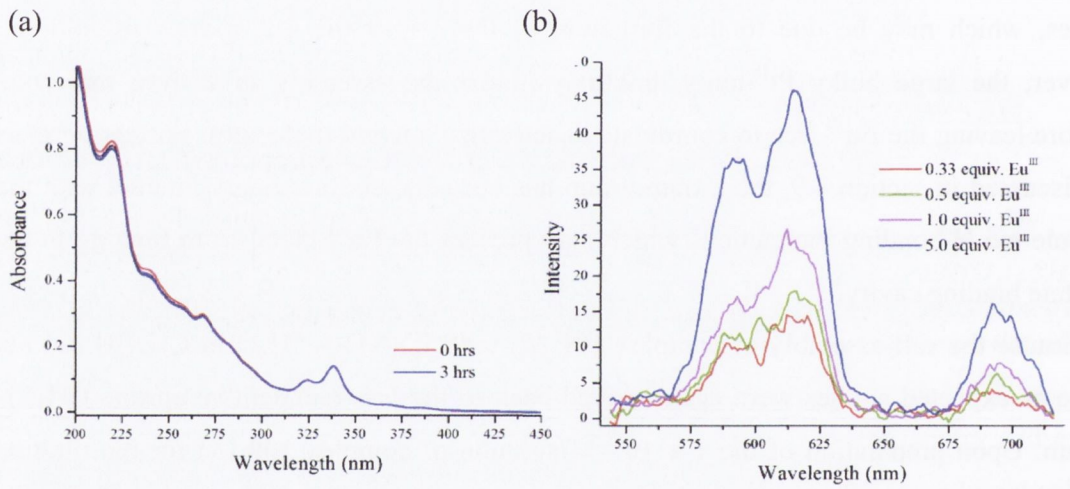

Figure 4.17. *(a) UV-visible absorption spectrum of ligand* ***109*** *(R) (1 x 10^{-5} M) recorded every 15 mins from 0→3 hrs in H_2O at RT. (b) Eu^{III}-centred emission recorded following the addition of 0.33, 0.5, 1 and 5 equiv. of $Eu(CF_3SO_3)_3$ to the ligand* ***109*** *(R) (1 x 10^{-5} M) solution in H_2O at RT.*

Since complex **109** (*R*) was water soluble preliminary solution studies were conducted in which the stability of complex **109** was first evaluated in H_2O over time. As shown in Figure 4.17 (a) no noticeable change in the UV-visible absorption spectrum was observed, confirming that the complex does remain intact in H_2O. To this, 0.33 equiv. of $Eu(CF_3SO_3)_3$ was added and the Eu^{III}-centred emission monitored. As shown in Figure 4.17 (b) the system was only weakly luminescent upon this metal equiv. addition and upon additional aliquots (0.5, 1.0 and 5.0 equiv. of $Eu(CF_3SO_3)_3$) gave rise to only a very small enhancement in Eu^{III}-centred luminescence. These results again signify incomplete coordination of the Eu^{III}, possibly due to the inability of three tridentate **109** (*R*) complexes to fully coordinate the metal centre, allowing deactivation *via* non-radiative decay.

Poor Eu^{III}-centred luminescence in both protic solvents, CH_3OH and H_2O, and the conclusion that the **109** (*R*) complex was dissociating in CH_3CN led to the realisation that a number of Pt^{II}-terpy complex structural characteristics should be re-evaluated. In order to obtain Ln^{III}-directed self-assemblies involving the Pt^{II}-terpy moiety perhaps two structural changes should be made. The distance between the Pt^{II}-terpy centre and the Ln^{III} tridentate dpa coordinating unit should be increased to avoid steric hindrance between ligands as they assemble around the metal centre. In addition to this, incorporation of the Pt^{II}-terpy unit should be achieved by covalently attaching the Pt^{II} metal to the Ln^{III} coordinating unit, to ensure complex stability in different solvent media. To confirm that the Pt^{II}-terpy unit was becoming displaced in CH_3CN a number of ^1H NMR measurements were conducted and shall be discussed below.

4.12 ^1H NMR studies on complex 109 (*R*) in CH_3OH and CH_3CN

In order to confirm that complex **109** (*R*) was unstable in the presence of CH_3CN a number of ^1H NMR measurements were carried out. A CD_3OD and a CD_3OD:CD_3CN (50:50) solution of complex **109** (*R*) were prepared and the ^1H NMR spectrum (600 MHz) of each sample analysed every day for six days. As shown in Figure 4.18 and Appendix Figures A4.19 and A4.20, no noticeable change was observed for the complex **109** (*R*) CD_3OD solution after 6 days, confirming complex stability in the methanol environment.

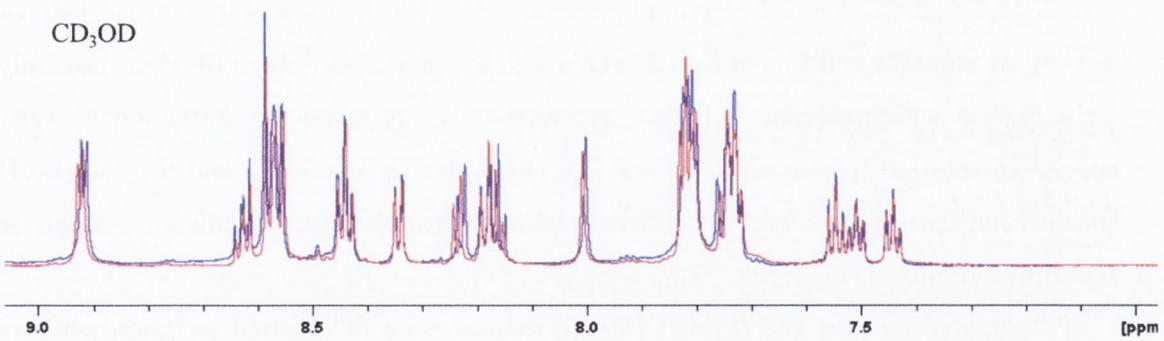

Figure 4.18. *An overlay of the aromatic region of the ^1H NMR spectrum (600 MHz, CD_3OD) of* ***109*** *(R) after 0 hrs and 6 days.*

As shown in Appendix Figure A4.21, an initial measurement of the complex **109** (*R*) ^1H NMR spectrum (600 MHz, CD_3OD:CD_3CN (50:50)) in a CH_3OH:CD_3CN (50:50) mixture showed a loss in peak resolution as the structure instantly began to disassemble. Continued monitoring of this mixed solution over a period of six days illustrated a dynamic system which slowly changed over time. As shown in Figure 4.19 and Appendix Figure A4.22 the ^1H NMR spectrum (600 MHz, CD_3OD:CD_3CN (50:50) recorded after six days was

significantly structurally different to that observed initially, confirming a change in the structure of the complex in the presence of CD_3CN over time.

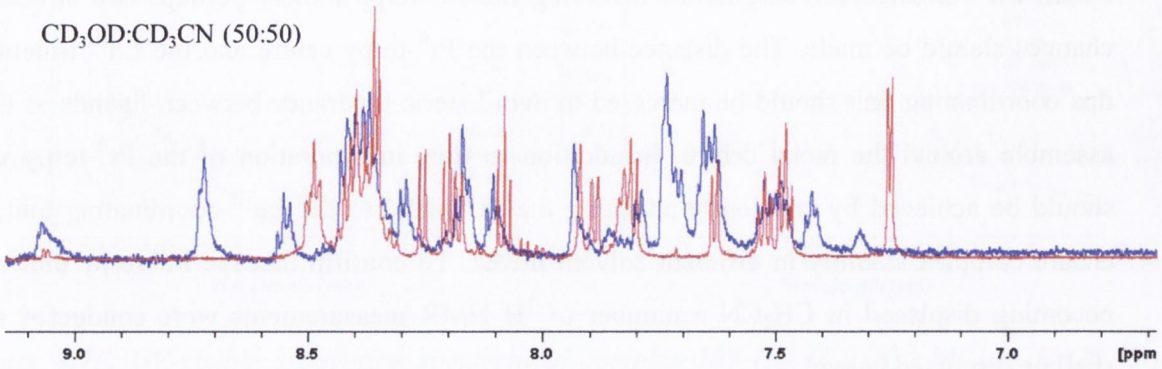

Figure 4.19. *An overlay of the aromatic region of the ^1H NMR spectrum (600 MHz, $CD_3OD:CD_3CN$ (50:50)) of* ***109*** *(R) after 0 hrs and 6 days.*

4.13 Conclusion and future work

This chapter focused on the synthesis and characterisation of six novel chiral compounds for the development of water soluble and biologically relevant Ln^{III}-directed self-assembly systems. X-ray crystal structures of Pt^{II}-terpy complexes **108** (*S*) and **109** (*R*) were grown and analysed confirming the square planar geometry of the metal centre. Self-assembly was only conclusively evident for the two uncharged ligands **110** and **111** in which the 1:1 (Eu:**L**), the 1:2 (Eu:$\mathbf{L}_2$) and the 1:3 (Eu:$\mathbf{L}_3$) (**L** = **110** and **111**) species were present upon Eu^{III}-directed self-assembly in solution. The pyridinium compound **101** (*R*) showed an unusual behaviour in CH_3OH upon the addition of $Eu(CF_3SO_3)_3$ which was not possible to fit while assembly in CH_3CN was unreproducible. Kinetics measurements suggested the formation of various species in solution (presumably the 1:3 (Eu.$\mathbf{101}_3$), the 1:2 (Eu.$\mathbf{101}_2$) and the 1:1 (Eu.**101**) species) but due to electrostatic repulsions between neighbouring ligands an unstable self-assembly system was observed.

Pt^{II}-terpy complexes **108** (*S*) and **109** (*R*) displayed no Pt^{II}-centred emission while only very weak Eu^{III}-centred emission was exhibited in CH_3OH and H_2O upon the addition of Eu^{III}. Steric hindrance was proposed as being a plausible reason as to why such low intensity luminescence was observed. Furthermore, considering that a counter nitrate anion is shown to participate in multiple H-bonding interactions in the solid state it cannot be neglected that the presence of the nitrate anion can have an effect on the system and may also prevent Eu^{III}-directed self-assembly. In CH_3CN solution UV-visible absorption analysis and ^1H NMR spectroscopy gave evidence of an unstable complex; where the pyridine side chain of the

ligand is more than likely replaced by an CH_3CN molecule in the coordination of the Pt^{II}-terpy unit.

While results for these Eu^{III}-directed self-assembly studies, for both the pyridinium and Pt-terpy functionalised ligands, were not expected, a greater understanding of these systems was attained, highlighting the importance in undertaking such a study. In order to develop Ln^{III}-directed self-assemblies incorporating the Pt^{II}-terpy unit it is more likely that the incorporation of a longer linking unit would enable Ln^{III}-directed self-assembly in solution in which steric hindrance is avoided and the various Ln^{III}-directed self-assemblies are accessible. Another consideration would be to attach the Pt^{II}-terpy centre covalently, to ensure greater stability. One such idea would be the synthesis of the chiral Ln^{III} coordinating complexes:

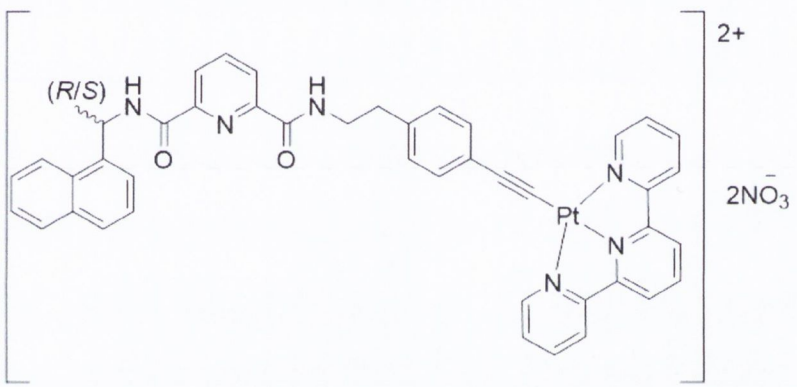

Chapter Five

Self-assembly of a thiol H_2dpa unit for AuNP surface attachment

5. Introduction

As was discussed in chapter one, the H_2dpa tridentate coordinating ligand **1** is a well-known ligand commonly employed for Ln^{III} coordination and sensitisation due to its ability to form highly stable fully saturated water soluble luminescent complexes. The photophysical properties of Eu^{III} and Tb^{III} tris chelate complexes of **1**, $Cs_3[Eu(dpa)_3]$ and $Cs_3[Tb(dpa)_3]$ in particular, have received substantial attention, owing to their high quantum yields in Tris buffered solution (0.1 M) (24% ± 2.5% and 22% ± 2.5% for $Cs_3[Eu(dpa)_3]$ and $Cs_3[Tb(dpa)_3]$, respectively) and as a result are often employed as secondary standards for quantum yield determination.[105]

Furthermore, these relatively simple $Ln(\mathbf{1})_3^{3-}$ complexes are shaped like a three bladed propeller, giving rise to two enantiomeric forms, either Δ- or Λ- chirality. Meskers and co-workers have carried out in depth studies on these chiral Ln^{III} complexes for their use in chiral molecular recognition.[306-308] Upon the addition of small quantities of an enantiomerically resolved quencher species to racemic solutions of $Ln(\mathbf{1})_3^{3-}$ (which initially display no CPL activity) enantioselective quenching of Ln^{III} luminescence can be observed. In this manner $Ln(\mathbf{1})_3^{3-}$ complexes have found use in the chiral discrimination of biomolecules, such as cytochrome-c and vitamin B_{12} derivatives, in which the chiral biomolecule preferentially quenches one $Ln(\mathbf{1})_3^{3-}$ enantiomeric form and is less reactive towards the other form. An excited state Ln^{III}-centred CPL signal is therefore induced, reflecting molecular recognition of one chiral compound over the other.[306-308] Such valuable applicability of these mononuclear Ln^{III}-directed self-assembled systems provokes further functionalisation of the H_2dpa unit for the development of more versatile, highly sensitive and selective Ln^{III} luminescent probes.

As is evidenced by the multitude of examples described in chapter one, derivatives of **1** have received tremendous attention for the formation of both mononuclear and multinuclear Ln^{III}-directed self-assemblies. Specifically, the research conducted by Bünzli and co-workers,[106] in which four novel derivatives of **1** were synthesised **5** – **8** and were shown to form tris chelate complexes with Eu^{III} and Tb^{III}. Solution studies on **5** – **8** revealed that modification of the 4-*para* position of **1** did allow the tuning of, but more importantly, did not bare a detrimental effect on the photophysical properties of the resulting complex. This study showed that modification of such systems in this manner may pave the way towards the manifestation of solid surface attachment and/or biomolecule conjugation without significant loss of the unique Ln^{III} luminescent characteristics.

In recent times, gold nanoparticles (AuNPs) have been responsible for many of the significant advances made in the field of biomedical research, including drug delivery, biodiagnostics and cancer research.[309-311] This is down to their many fascinating attributes, including their tuneable size and shape dependent optoelectronic properties and their biocompatibility. Moreover, AuNPs can be easily synthesised and readily functionalised using thiol linkages (in view of the soft nature of both sulphur and gold) allowing the facile adsorption and high loading of probes/sensors/imaging agents onto the surface of the AuNPs. Since AuNPs display high surface areas this feature can subsequently improve the selectivity and sensitivity of biomedical diagnostic and therapeutic techniques.[195,312]

Despite the unique advantages AuNPs have to offer, and the aforementioned distinctive photophysical properties of the Ln^{III} metals, only very few examples of Ln^{III} luminescent complexes which have been attached to AuNPs have been explored.[313-315]

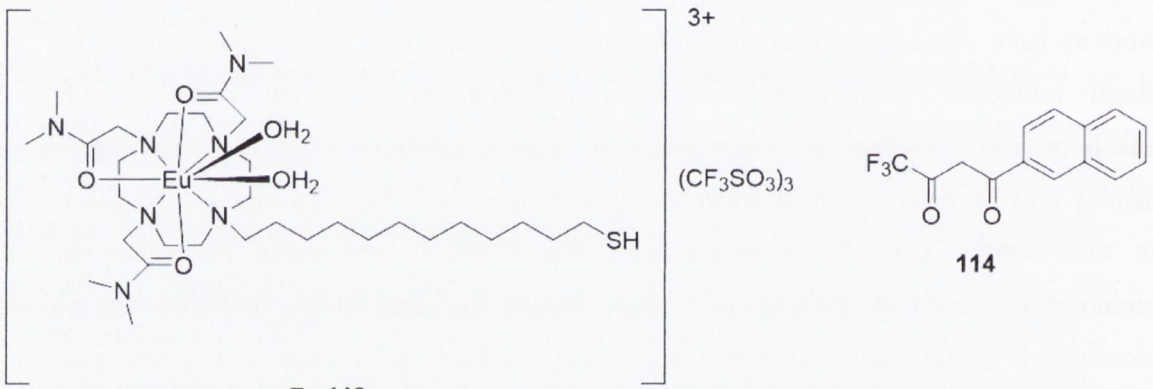

Eu.**113** **114**

Research carried out within the Gunnlaugsson group in this area has involved the development of heptadentate macrocyclic cyclen based Ln^{III} complexes of **113**.[194-196,198] Complexes of compound **113**, possessing three acetamide arms and a C_{12} alkyl thiol chain, have been conjugated to AuNPs by means of tethering through the terminal alkyl thiol group. Adsorption of Eu.**113** onto the surface of the AuNPs yielded the conjugate AuNP-Eu.**113**, which was found to be non-luminescent in HEPES buffer solution (0.1 M, pH 7.4) due to the absence of a sensitising antenna moiety and the presence of two metal-bound water molecules which gave rise to additional quenching. However, following formation of a ternary complex, by the displacement of the two H_2O molecules by the β-diketone **114**, and upon excitation at λ_{ex} = 336 nm (λ_{ex} of the antenna **114**), a highly luminescent AuNP-Eu.**113**.**114** conjugate was evident in solution. Sensing of biologically relevant phosphates, such as flavin monophosphate, was also achieved through the displacement of **114** by flavin monophosphate which resulted in the formation of a new ternary complex that was not luminescent. This was reflected by an almost complete quenching of the Eu^{III}-centred emission upon the addition of the analyte to a solution of AuNP-Eu.**113**.**114**.[196] The

luminescent properties of the AuNP-Eu.**113**.**114** conjugate were further analysed by investigating, as a function of pH, the spectroscopic properties of the self-assembly. It was found that, within the physiological pH range, the Eu^{III}-centred emission of the AuNP-Eu.**113**.**114** conjugate was 'switched on'. In addition, a correlation was made between the spectroscopic changes observed and the quenching of the antenna as a function of pH. The changes observed were primarily assigned to the deprotonation of **114** at basic pH values.[194]

Studies on the AuNP-Eu.**113**.**114** conjugate system were further extended to evaluate its interaction with proteins, focusing on bovine serum albumin (BSA).[195] Changes in the photophysical properties of the self-assembly were monitored, at physiological pH, as a function of BSA concentration. It was demonstrated that the Eu^{III}-centred emission arising from the Eu.**113**.**114** self-assembly attached to the AuNP surface was almost completely quenched upon increasing concentrations of BSA. Binding constant calculations indicated that emission quenching was not due to the displacement of **114** by BSA, as was observed above, but rather as a result of a strong interaction between the naphthalene antenna **114** and BSA. Competitive titrations using ibuprofen and warfarin were conducted to investigate the ability of the AuNP-Eu.**113**.**114** conjugate to act as a luminescent sensing tool for BSA-drug binding interactions. Ibuprofen was shown to partially displace BSA from the antenna **114**, resulting in a 75% enhancement in the metal centred emission. Consequently the AuNP-Eu.**113**.**114** system can be referred to as a reporter for the ibuprofen-BSA binding interaction. Titrations conducted with warfarin, on the other hand, revealed that it did not share a common binding site with **114**.[195]

More recently, AuNP surface functionalisation with the Yb.**113** complex has been achieved, which, following ternary complex formation with a xylenol orange (XO) antenna (λ_{ex} = 580 nm), has led to the development of the first NIR Ln^{III} emitting AuNP systems of this type – AuNP-Yb.**113**.XO.[198] Furthermore, it was demonstrated that the NIR emission arising from the AuNP-Yb.**113**.XO conjugate can be switched "on–off" in a reversible manner over several cycles as a function of pH enabling the AuNP-Yb.**113**.XO conjugate to function as a supramolecular NIR switch.

Evidently much emphasis is currently being placed in our group on the functionalisation of AuNPs with Ln^{III} luminescent centres for bioimaging and sensing purposes. Notably, the H_2dpa unit has not undergone much derivatisation at the 4-*para* position to accomplish such objectives. Few examples exist in which the H_2dpa framework has been modified at the 4-*para* position for nanoparticle attachment.

On such example is the diaminopyridine structure **116**, which has been developed for the non-covalent self-assembly of silver nanocrystal aggregates in solution.[316] In this study silver

nanocrystals were stabilised by the chemisorption of the long alkane chain dodecane thiol **115** and *N*,*N*-2,6-pyridinediylbis[undecamide]-4-oxy-[12-mercapto dodecanyl] **116**. Compound **116** incorporated a receptor site which accommodated the recognition and selective binding of the long alkane diuracil chain substrate **117**, which possessed two complimentary binding sites. When dispersed in a suitable solvent these nanocrystals were found to aggregate due to the non-covalent binding between **116** and **117**. Both ^{1}H NMR and IR spectroscopy were implemented to confirm aggregation was due to the formation of a 2:1 species in which one molecule of **117** was bound to two molecules of **116**, which were adsorbed onto different silver nanocrystal surfaces, *via* two triple arrays of complimentary H-bonds. It was also demonstrated from these studies that the number of reaction sites present on the surface can be used to control the aggregation kinetics.[316]

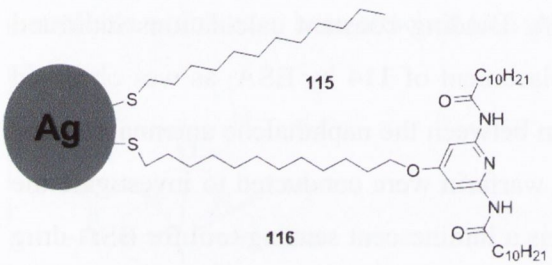

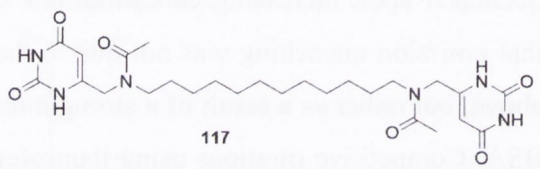

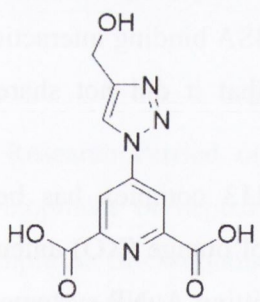

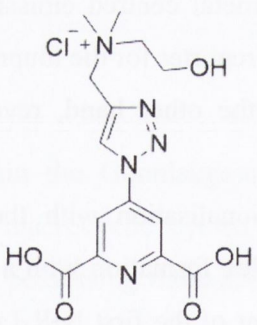

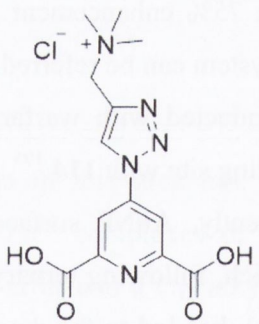

A series of Ln^{III} complexes based on the 4-triazoyl dipicolinic acid derivatives **118–120** have recently been modified for the formation of luminescent hybrid silica nanoparticles (Silica-NPs).[317] Silica-NPs were doped with 1:3 (Ln:L) complexes Na_3.Ln.**118**$_3$, Ln.**119**$_3$ and Ln.**120**$_3$ (Ln = Eu^{III} and Tb^{III}) by directly entrapping them into the silica matrix during NP formation. The luminescent properties of the functionalised nanoparticles were then analysed in a water suspension and the results were compared to those obtained for their corresponding complexes in a 0.1 M Tris-HCl buffer (pH = 7.45) solution. Silica-NPs doped with the hydroxy terminated complexes Na_3.Ln.**118**$_3$ (Ln = Eu^{III} and Tb^{III}) were found to be non-emissive but the luminescent properties of silica-NPs embedded with complexes Ln.**119**$_3$ and Ln.**120**$_3$ (Ln = Eu^{III} and Tb^{III}), silica-NP-Ln.**119**$_3$ and silica-NP-Ln.**120**$_3$,

compared well to luminescent studies performed on the complexes alone. The luminescent excited state lifetimes were relatively unaltered, however, quantum yield values were shown to decrease upon doping, which is possibly due to dissociation of some of the complex molecules upon silica-NP formation. From these results, it was deduced that complexes bearing the ammonium moieties were more easily embedded; which can be explained by their higher capability to interact with the silica network. These hybrid silica-NPs were also further functionalised with alkoxysilane precursors, with the objective being to further graft these to biomolecules, and their cytotoxicity assessed indicating that functionalisation with a terminal alkyne group did not impact the survival of LNCaP prostate tumour cells.[317]

Although the authors from the above study used silica-NPs (while we use AuNPs), and the method employed for NP fabrication is quite different to that practiced within the Gunnlaugsson group, involving NP entrapment of the Ln^{III} complex (as opposed to adsorbing Ln^{III} coordinating units/complexes to the AuNP surface through terminal thiol moieties), this study does provide an important proof of principle as it demonstrates the possibility of obtaining Ln^{III} luminescent nanoparticles using 1:3 (M:L) dpa-based chelating complexes while also emphasising the importance in the choice of the functional group appended to the 4-*para* position for subsequent solid state attachment.

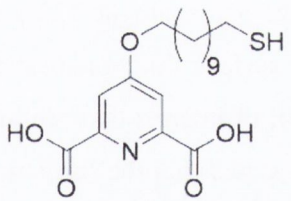

121

The dipicolinic acid C_{11} substituted analogue **121** was developed by McGimpsey and co-workers for the assembly of Cu^{II} containing photocurrent-generating systems on flat gold surfaces.[318] Since such success was acquired in our laboratory utilising a thiol terminated C_{12} long alkyl chain appended to a Ln^{III} cyclen based system it was envisaged, for this project, that by grafting this same type of alkyl chain to the 4-*para* position of the pyridine-2,6-dicarboxylic acid framework, in a similar manner to that described in the latter literature example, it would be possible to develop a fully water soluble Ln^{III} coordinating unit. Furthermore, opportunities to adsorb such systems onto the surface of AuNPs may be explored for the formation of luminescent hybrid 1:3 (M:L) Ln^{III}-directed self-assembly-AuNP conjugates, which exhibit, in tandem, the properties of the Ln^{III} metals and AuNPs. Compound **122** was therefore proposed as a target molecule to meet such criteria, displaying four important features:

1) A tridentate chelating unit for Ln^{III} coordination and formation of 1:3 complexes.

2) A pyridine chromophoric unit which has been shown to be an effective Ln^{III} sensitiser.
3) Two carboxylic acid functional groups to aid water solubilisation.
4) A C_{12} thiol terminated alkyl chain for AuNP attachment.

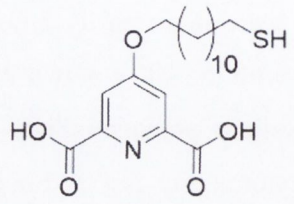

122

In addition to offering the potential to fabricate AuNPs another avenue which may be explored for compound **122** is its use as a protein tag. Many efforts have been directed toward the development of tags for site-specific attachment of Ln^{III} to proteins using chemical derivatisation of protein cysteine residues with lanthanide-chelating reagents.[319-321] The presence of a terminal thiol functionality in **122** may also allow its attachment to such amino acid residues through a disulphide bridge connection. The paramagnetic nature of the Ln^{III} metal centre can then be utilised, by NMR spectroscopy, to assist in long-range protein structure elucidation.[319-321]

The applications available to the dpa analogue **122** are limitless; but since the expertise of the Gunnlaugsson group is in the surface functionalisation of AuNPs with Ln^{III} luminescent complexes it was within this realm of interest that preliminary measurements for ligand **122** were first conducted. It should be stated that the formation of aggregates through H-bonding interactions and/or S-S bonds was anticipated for this system and so this possibility was also taken into account when carrying out studies with compound **122**. The following section describes the synthesis of compound **122**, followed by sections which detail the Ln^{III}-directed self-assembly of ligand **122** with Eu^{III} and Tb^{III} in aqueous solution. The Ln^{III} luminescent properties of the self-assembled 1:3 Ln.$\mathbf{122}_3$ (Ln = Eu^{III} and Tb^{III}) complexes, such as excited state lifetimes, quantum yield determination and hydration state q values were also evaluated. The chapter concludes with preliminary results obtained for the synthesis and characterisation of AuNPs functionalised with compound **122**.

5.1 Synthesis of compound 122

Preparation of compound 4-(12-mercaptododecyloxy)pyridine-2,6-dicarboxylic acid **122** was achieved by following the two part parallel synthetic procedure shown in Scheme 5.1.

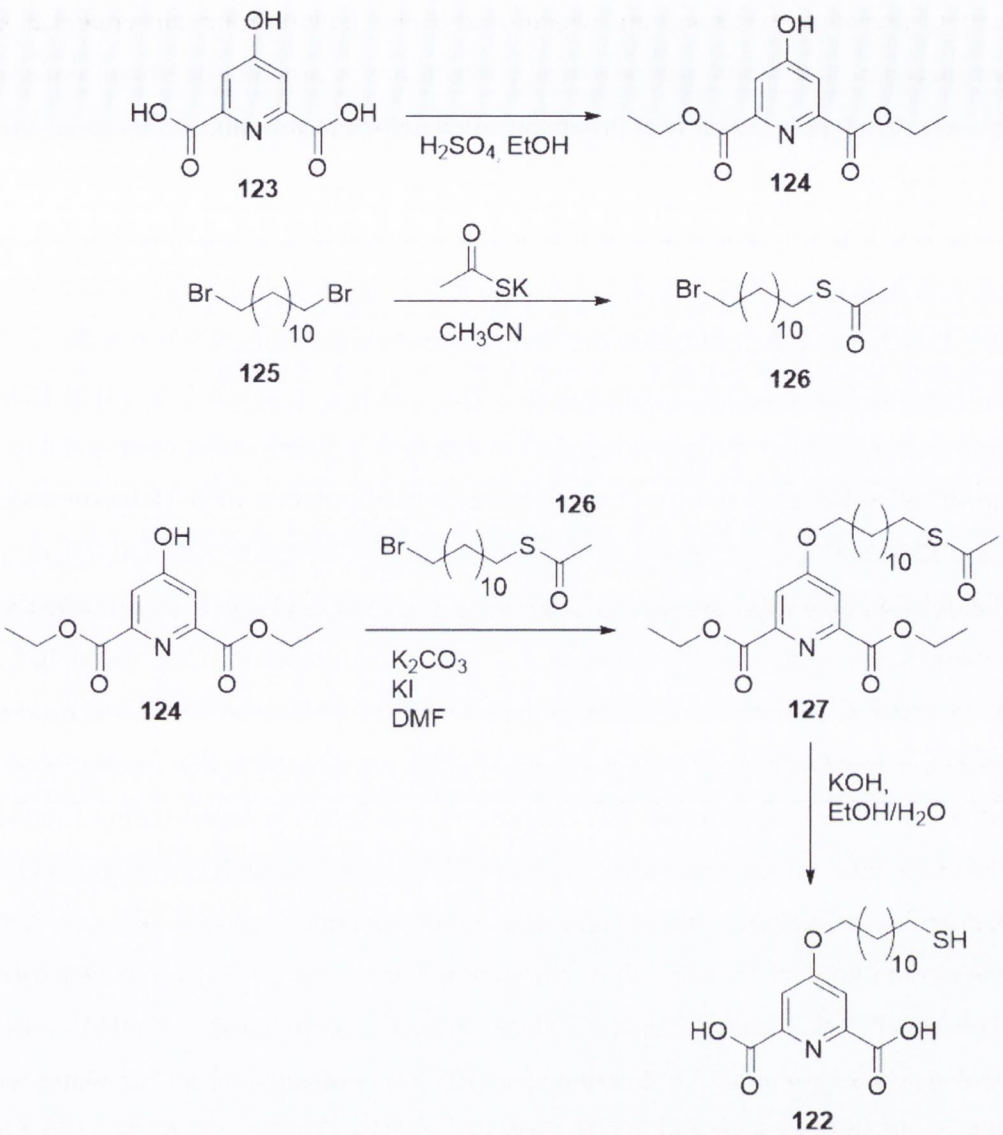

Scheme 5.1. *Synthetic pathway towards the formation of ligand* ***122****.*

The commercially available reagent chelidamic acid **123** was converted to the corresponding diethyl ester compound, diethyl 4-hydroxypyridine-2,6-dicarboxylate **124**, using a previously reported literature procedure.[176] An excess of concentrated H_2SO_4 was added to a stirring solution of **123** in EtOH and refluxed for 4 hrs, after which the solvent was removed under reduced pressure yielding an oily residue. This residue was then dissolved in H_2O and neutralised using $NaHCO_3$. The diester product **124** was extracted into CH_2Cl_2 and then dried over $MgSO_4$. The solvent was again removed under reduced pressure yielding the pure product **124** as a white solid in 62% yield. ^{1}H NMR spectrum (400 MHz, $CDCl_3$), ^{13}C NMR spectrum (100 MHz, $CDCl_3$) and HRMS were employed to verify formation of the desired compound with characteristic resonances appearing at 4.43 ppm and 1.39 ppm in the ^{1}H NMR spectrum (400 MHz, $CDCl_3$) of **124**. These signals can be attributed to the two CH_2 and two CH_3 group protons, respectively.

In parallel, monosubstitution of the dibromo precursor 1,12-dibromododecane **125** was carried out according to a previously reported procedure.[322] Compound **125** and potassium thioacetate, in a 3.3:1 ratio, were first dissolved in CH_3CN and the mixture refluxed for 48 hrs. The reaction mixture was then poured into H_2O and the crude compound extracted into diethyl ether. The organic layers were combined, washed with H_2O, dried over $MgSO_4$, and then evaporated to dryness. Silica flash chromatography using a hexane/ethyl acetate solvent system (0 – 3%) as the eluant afforded the desired compound as an off white solid in 32% yield which was characterised by ^{1}H NMR (400 MHz, $CDCl_3$), ^{13}C NMR (100 MHz, $CDCl_3$) and IR spectroscopy. Proton resonance signals located at 2.30 ppm, which correspond to the CH_3 group of the substituted thiol moiety, evidenced the formation of *S*-12-bromododecyl ethanethioate **126**.

The diethyl 4-hydroxypyridine-2,6-dicarboxylate compound **124** was then reacted with the C_{12} thiolated alky chain moiety **126** in an S_N2 substitution reaction. Compound **124** and two equiv. of dry K_2CO_3 were stirred in anhydrous DMF for 30 mins at 25 °C. An excess of 1.8 equiv. of compound **126** and a catalytic amount of KI were added to this reaction mixture and heated at 80 °C for 6 days under Ar. The solvent was removed under reduced pressure yielding a brown solid which was redissolved in CH_2Cl_2, washed with 1% acetic acid and H_2O and dried over $MgSO_4$. The solvent was removed under reduced pressure before purifying the crude product by silica flash chromatography using a CH_2Cl_2/CH_3OH solvent system (0–10%) as the eluent. The desired compound diethyl 4-(12-(acetylthio)dodecyloxy)pyridine-2,6-dicarboxylate **127** was collected as an off white waxy solid in 87% yield and characterised by ^{1}H NMR (600 MHz, $CDCl_3$), ^{13}C NMR (150 MHz, $CDCl_3$), HRMS, IR and elemental analysis. Signals corresponding to both the alkyl chain proton resonances and the two ethyl ester group protons were observed, clearly denoting successful grafting of the chain onto the H_2dpa unit.

Hydrolysis of the two ester functionalities and removal of the thioacetate moiety were achieved simultaneously. Compound **127** was dissolved in EtOH and then an aq. KOH solution (3.2 equiv.) was added to this solution. The reaction mixture was stirred at RT for 5 hrs. After this time the reaction had reached completion (as confirmed by monitoring the reaction by TLC (CH_2Cl_2:CH_3OH, 96:4)). The mixture was then filtered, washed with diethyl ether and acidified to pH 1 using concentrated HCl. Compound **122** was extracted into ethyl acetate, after which the solvent was removed under reduced pressure affording **122** as a white powder in 54% yield. Deprotection was evidenced by the disappearance of the CH_3 proton resonances assigned to the thioacetate group. The absence of signals associated with the ethyl ester also confirmed product formation, as shown in the ^{1}H NMR spectrum (600 MHz,

$CDCl_3$) of **122** in Figure 5.1. Compound **122** was also confirmed by ^{13}C NMR (150 MHz, $CDCl_3$), IR and elemental analysis.

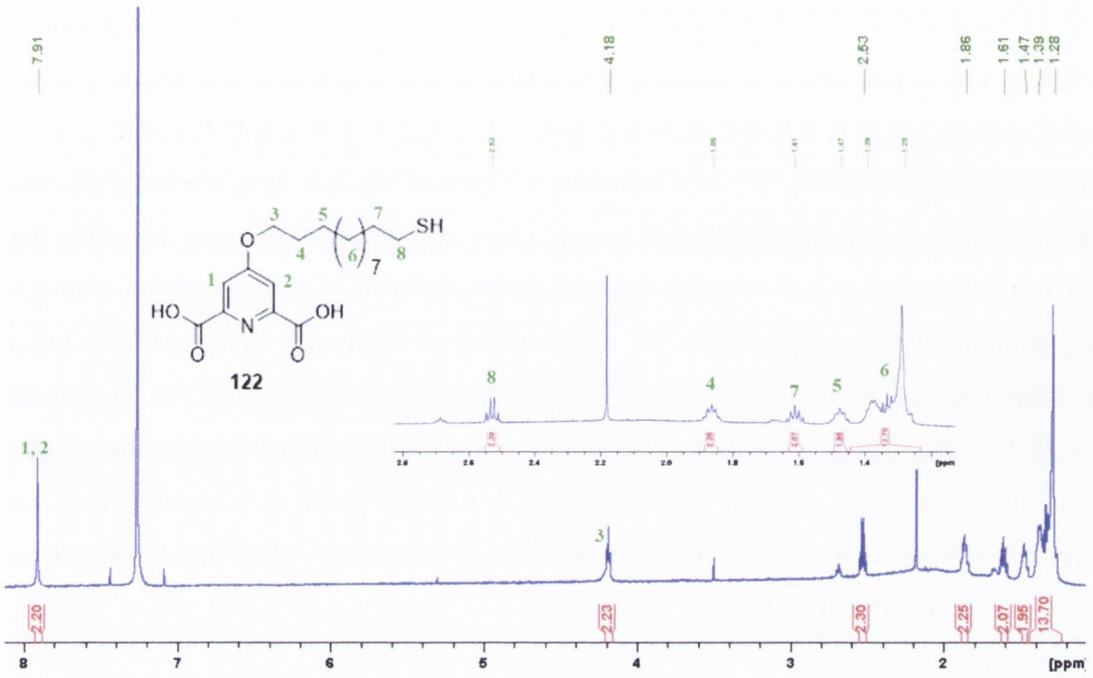

Figure 5.1. *^1H NMR (600 MHz, $CDCl_3$) of compound **122**.*

Before investigating the potential applications of compound **122** in an aqueous medium (*i.e.* AuNP attachment and/or biomolecule interaction/conjugation) it was first necessary to evaluate the interaction of compound **122** with $Eu(CF_3SO_3)_3$ and $Tb(CF_3SO_3)_3$ in an aqueous environment and to establish the self-assembly behaviour of the various luminescent complex species in solution. The two acidic functional groups of **122** were anticipated to induce full water solubility of this compound. However, upon the preparation of stock solutions for the spectroscopic studies described below, it was found that both the concentration of the ligand and the number of equiv. of the base (KOH) added were important factors in determining whether the ligand would remain dissolved in H_2O. Ligand **122** stock solutions of 4.8×10^{-4} M and 6.4×10^{-4} M in H_2O were prepared by adding 4.2 equiv. of KOH to a suspension of **122** in H_2O and heated under microwave irradiation at 115 ^oC for 15 mins.

5.2 Studies of the formation of Eu^{III}- and Tb^{III}-directed self-assemblies of 122 *in situ*

In order to investigate the Ln-directed self-assembly of compound **122** in an aqueous solution a number of spectroscopic titrations were carried out. Titrations were conducted in a similar manner to that described by Bünzli and co-workers[106] for those spectroscopic studies carried out on the analogous compounds **5** – **8** (described above and in chapter one). Therefore, the

conditions employed involved preparing a ligand solution in the concentration range of 10^{-4} M in a 0.1 M Tris-HCl (I = 0.1 M) buffered solution (pH = 7.45) for subsequent titration against increasing concentrations of $Ln(CF_3SO_3)_3$ (Ln = Eu^{III} and Tb^{III}). This ligand concentration range was also chosen due to the relatively low UV-visible absorption intensity of the ligand itself. In addition, it was estimated that a ligand concentration in this range (10^{-4} M) should encourage the formation of the 1:3 species (Ln.**122**$_3$) in almost 100% yield.

Compound **122** (2.25 x 10^{-4} M) was initially titrated against $Eu(CF_3SO_3)_3$ and the spectroscopic changes closely monitored. Excited state lifetime measurements following the addition of 0.33 equiv. of Eu^{III} were best fit to a mono-exponential decay function giving a lifetime value of 1.63 ms which evidenced the formation of solely the 1:3 species (Eu.**112**$_3$) at this metal concentration. Unfortunately further additions of $Eu(CF_3SO_3)_3$ to the ligand solution (2.25 x 10^{-4} M) gave rise to the formation of a cloudy precipitate and so the sample was diluted to a ligand concentration of 1 x 10^{-4} M. This did not result in full solubility of the self-assembly system and so it was therefore decided to reduce the ligand concentration to the lower concentration of 1 x 10^{-5} M.

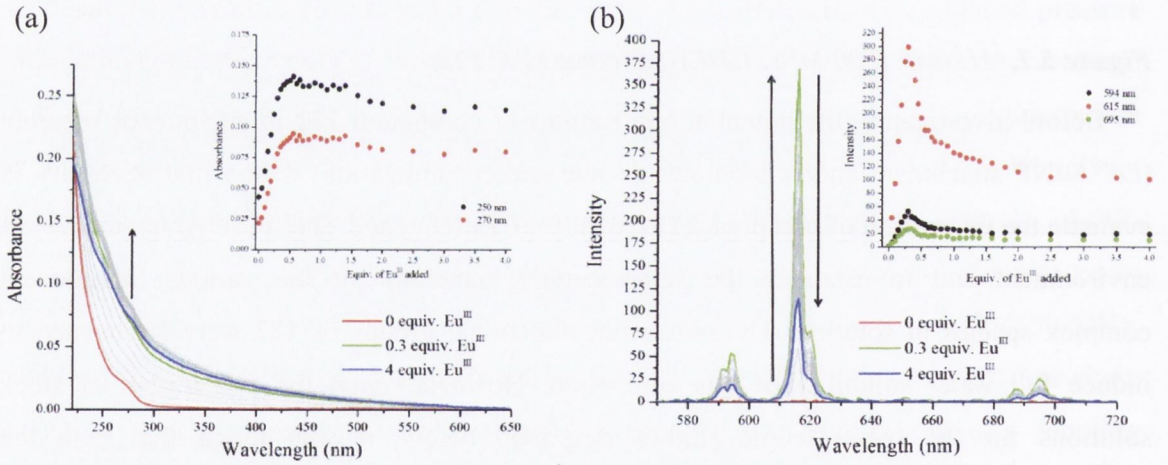

Figure 5.2. *The overall changes in the (a) UV-visible absorption spectra and (b) Eu^{III}–centred phosphorescence spectra upon titrating* ***122*** *(1 x 10^{-5} M) against $Eu(CF_3SO_3)_3$ (0→4 equiv.) in a 0.1 M Tris-HCl buffered solution at RT.* ***Inset****: corresponding experimental binding isotherm of (a) absorbance at λ = 250 and 270 nm and (b) Eu^{III} phosphorescence emission intensity at λ = 594, 615 and 695 nm (λ_{ex} = 270 nm).*

As shown in Figure 5.2 the changes observed in the UV-visible absorption spectra were then monitored as ligand **122** (1 x 10^{-5} M) was titrated against a stock solution of $Eu(CF_3SO_3)_3$. The ligand **122** itself was not fluorescent and as such only the Eu^{III}-centred emission was analysed. The ligand UV-visible absorption spectrum was weak with a band centred at λ_{max} = 270 nm (ε = 2118 M^{-1} cm^{-1}) which can be characterised by overlapping broad peaks assigned to both the n – π^* and π – π^* transitions.[106] As shown in Figure 5.2 (a)

only minor changes were observed in the overall shape of this band upon increasing concentrations of Eu^{III}, however, a sharp enhancement in the relative UV-visible absorption intensity was experienced by this band located at λ = 270 nm between additions of 0→0.35 equiv. of Eu^{III}. Additional aliquots of the metal salt resulted in a plateau in the UV-visible absorption spectra (see Figure 5.2 (a) inset). These changes can be attributed to the evolution of the different stoichiometric species in solution as the self-assembly process proceeds.

The evolution of a characteristic Eu^{III}-centred emission spectrum was displayed upon the addition of $Eu(CF_3SO_3)_3$ to ligand **122** with bands centred at λ = 594, 615 and 695 nm. These emission bands represent the radiative deactivation of the energy from the Eu^{III} $^5D_0$ excited state to ground states ^7F_J, where J = 1, 2 and 4. The Eu^{III}-centred emission spectra initially experienced an enhancement in luminescence intensity with the most intense luminescence observed following the addition of 0.3 equiv. of Eu^{III}. Subsequent additions of the metal gave rise to a sharp decrease in luminescence intensity (see Figure 5.2 (b) inset) followed by an eventual plateau. By comparing these changes to those previously reported for similar systems developed within our group and to the work of Bünzli and co-workers[106] it can be assumed that these changes are associated with the predominant formation of the most luminescent 1:3 Eu.$\mathbf{122}_3$ species at lower metal concentrations followed by the evolution of the lesser emissive 1:2 Eu.$\mathbf{122}_2$ and 1:1 Eu.**122** species. The fitting of this data and calculation of species binding constants by non-linear regression analysis is discussed in the following section. A highly luminescent red solution was observed under the UV lamp after the addition of four equiv. of $Eu(CF_3SO_3)_3$, as shown in Figure 5.3 (a).

Compound **122** (1 x 10^{-5} M) was also titrated against increasing concentrations of $Tb(CF_3SO_3)_3$ in a 0.1 M Tris-HCl (I = 0.1 M) buffered solution (pH = 7.45). An almost identical trend to that described above was observed for the changes in the UV-visible absorption spectra where the band centred at λ = 270 nm again experienced minor changes in its overall shape but did undergo a large hyperchromic effect upon increasing concentrations of Tb^{III} (see Figure 5.4 (a)). A sharp enhancement in this band was displayed upon the addition of 0→0.35 equiv. of Tb^{III} followed by a plateau in absorbance at higher Tb^{III} concentrations.

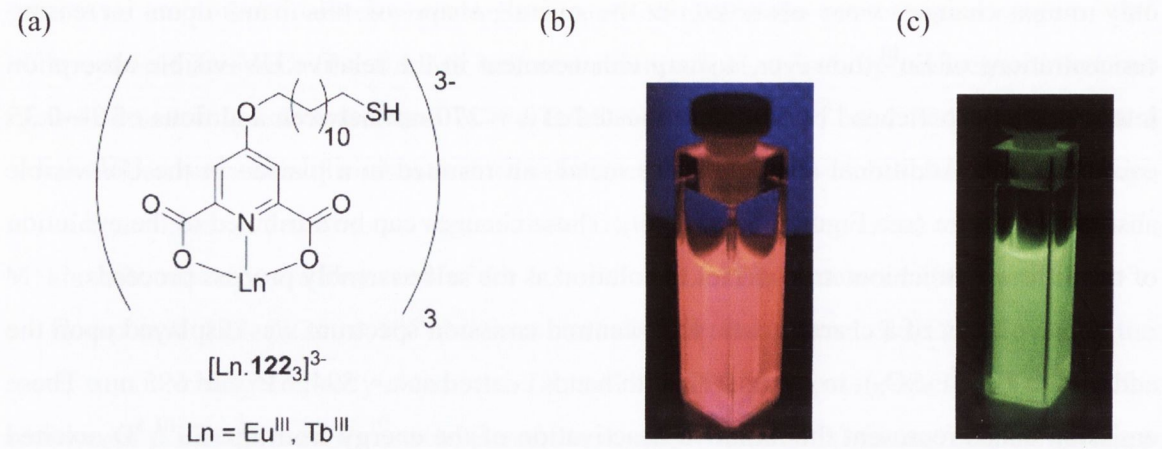

Figure 5.3. *(a) The highly emissive 1:3 M:L [Ln.**122**$_3$]$^{3-}$ complex formed in 0.1 M Tris-HCl buffered solution. (b) red and (c) green emission observed under the UV lamp from solution studies samples following the addition of four equiv. of Eu(CF$_3$SO$_3$)$_3$ and Tb(CF$_3$SO$_3$)$_3$ to ligand **122** (1 x 10^{-5} M) in a 0.1 M Tris-HCl buffered solution, respectively.*

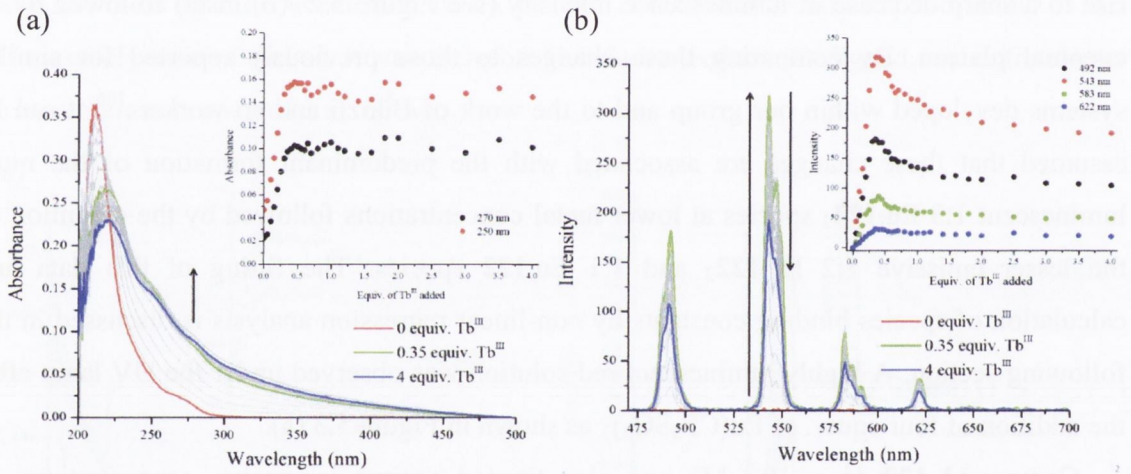

Figure 5.4. *The overall changes in the (a) UV-visible absorption spectra and (b) Tb^{III}–centred phosphorescence spectra upon titrating **122** (1 x 10^{-5} M) against Tb(CF$_3$SO$_3$)$_3$ (0→4 equiv.) in 0.1 M Tris-HCl buffered solution at RT. **Inset**: corresponding experimental binding isotherm of (a) absorbance at λ = 250 and 270 nm and (b) Tb^{III} phosphorescence emission intensity at λ = 492, 543, 583 and 622 nm (λ$_{ex}$ = 270 nm).*

The overall changes observed in the luminescence spectrum are shown in Figure 5.4 (b). As shown, an enhancement in the characteristic Tb^{III}-centred emission spectrum was evident upon the addition of 0→0.35 equiv. of Tb(CF$_3$SO$_3$)$_3$, with bands representative of deactivation from the Tb^{III} ^{5}D$_4$ excited state to ground states ^{7}F$_J$ (where J = 6, 5, 4 and 3) located at 492, 543, 583 and 622 nm. A slight decrease in the emission spectrum was then displayed up until the addition of 1 equiv. of metal which was then followed by a plateau at higher Tb^{III} concentrations. Again, these changes in the overall luminescence upon titrating compound **122** with increasing concentrations of Tb(CF$_3$SO$_3$)$_3$ can be attributed to the evolution of different stoichiometric species in solution with the predominant formation of

the most luminescent 1:3 species Tb.**122**$_3$ evident after the addition of 0.35 equiv. of Tb^{III}. These global changes in the UV-visible absorption and luminescence spectra were also fit by non-linear regression analysis and shall also be discussed in the next section. A picture of the sample under the UV lamp following the addition of four equiv. of $Tb(CF_3SO_3)_3$ is displayed in Figure 5.3 (b), showing clearly that the system is highly luminescent in H_2O. As mentioned in chapter three each titration experiment was repeated three times to ensure data reproducibility.

5.2.1 Fitting of titration data and determination of complex stability constants

Fitting of the global changes in the spectroscopic data using the non-linear regression analysis program SPECFIT was implemented in order to gain a better understanding of the self-assembly process and to calculate the binding constants associated with the various self-assembled species in solution.

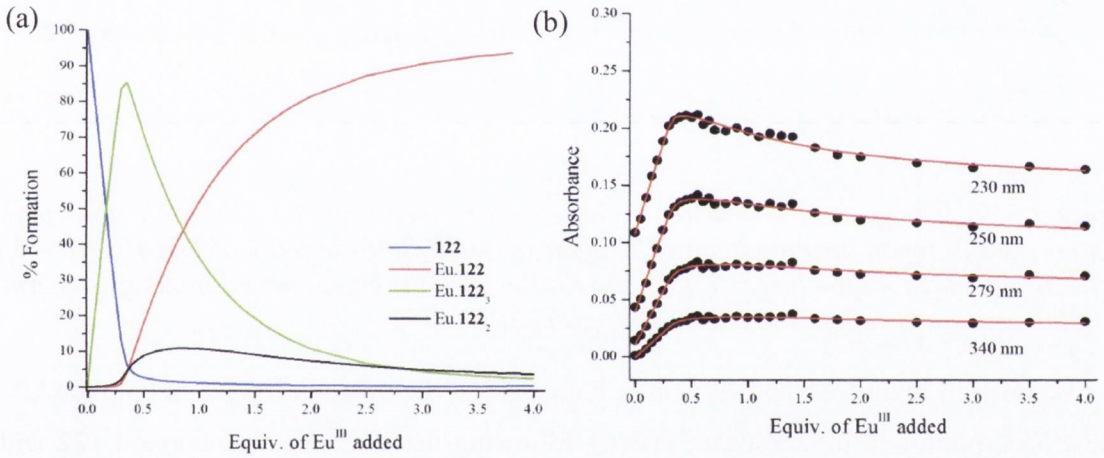

Figure 5.5. *(a) The speciation distribution diagram obtained from the UV-visible absorption titration data fit (upon titrating ligand* ***122*** *against $Eu(CF_3SO_3)_3$ in a 0.1 M Tris-HCl buffered solution) and (b) the fit of the experimental binding isotherms using the non-linear regression analysis program SPECFIT.*

The speciation distribution diagram obtained following the fitting of the overall changes in the UV-visible absorption spectra upon the titration of ligand **122** with $Eu(CF_3SO_3)_3$ is displayed in Figure 5.5 (a) while the binding isotherm from the fit is depicted in Figure 5.5 (b). It was estimated from this data that there were four absorbing species in solution - the ligand **122** itself, the 1:3 Eu.**122**$_3$, the 1:2 Eu.**122**$_2$ and the 1:1 Eu.**122** species. Upon the addition of 0.35 equiv. of Eu^{III} the predominant formation of the 1:3 Eu.**122**$_3$ species is evident with it being formed in 85% yield with a binding constant of $\log\beta_{13} = 20.4$. Further additions cause a shift in the equilibrium distribution towards the formation of the 1:2 Eu.**122**$_2$ and the 1:1 Eu.**122** species which were formed with binding constants of $\log\beta_{12} = 13.1$ and $\log\beta_{11} = 7.2$, respectively.

These values correlate well to the results obtained following the fitting of the corresponding luminescence titration data. As shown in the speciation distribution diagram in Appendix Figure A5.1 the most luminescent 1:3 tris chelate complex Eu.**122**$_3$ is formed in 73% yield following the addition of 0.3 equiv. of Eu^{III}. A binding constant of $\log\beta_{13} = 21.4$ was calculated for this species while binding constant values of $\log\beta_{12} = 14.9$ and $\log\beta_{11} = 7.2$ were calculated for the lesser emissive 1:2 Eu.**122**$_2$ and the 1:1 Eu.**122** species, respectively.

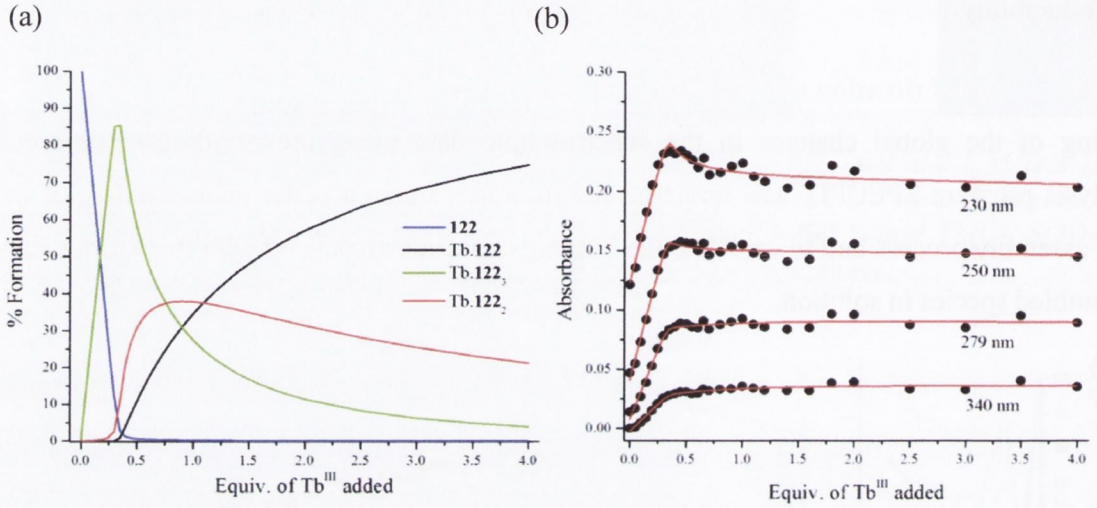

Figure 5.6. *(a) The speciation distribution diagram obtained from the UV-visible absorption titration data fit (upon titrating ligand* ***122*** *against $Tb(CF_3SO_3)_3$ in a 0.1 M Tris-HCl (I = 0.1 M NaCl) buffered solution (pH = 7.45)) and (b) the fit of the experimental binding isotherms using the non-linear regression analysis program SPECFIT.*

As shown in Figure 5.6 and Appendix Figure A5.2, the overall changes in both the UV-visible absorption and luminescence spectra following the titration of compound **122** with $Tb(CF_3SO_3)_3$ were also fit using SPECFIT. Analysis of the UV-visible absorption titration data using evolving factor analysis revealed the presence of four absorbing species in solution– the ligand itself **122**, the 1:3 Tb.**122**$_3$, the 1:2 Tb.**122**$_2$ and the 1:1 Tb.**122** species. From the speciation distribution diagram in Figure 5.6 (a) it is clear that the 1:3 Tb.**122**$_3$ self-assembly is preferentially formed in solution after the addition of 0.35 equiv. of $Tb(CF_3SO_3)_3$ with it being formed in 85% at this point in the titration. Binding constants of $\log\beta_{13} = 22.1$, $\log\beta_{12} = 14.8$ and $\log\beta_{11} = 7.5$ were calculated from this fit for the Tb.**122**$_3$, the 1:2 Tb.**122**$_2$ and the 1:1 Tb.**122** species, respectively.

Table 5.1. *Binding constants obtained by fitting spectroscopic data. *Value fixed, otherwise convergence not reached.*

Complex		UV-visible absorption	Luminescence
Eu^{III}	$\log\beta_{11}$	7.2 ± 0.2	7.2 *
	$\log\beta_{12}$	13.1*	14.9 ± 0.1
	$\log\beta_{13}$	20.4 ± 0.4	21.4 ±0.2
Tb^{III}	$\log\beta_{11}$	7.5 ±0.3	7.5 *
	$\log\beta_{12}$	14.8*	14.7 ± 0.2
	$\log\beta_{13}$	22.1 ± 0.5	21.7 ± 0.2

The global changes in the luminescence data for this titration were also fit with results confirming those obtained above (see Appendix Figure A5.2). As the Tb^{III} metal salt is added the most predominant species in solution becomes the highly emissive 1:3 Tb.**122**$_3$ complex, which is formed with a binding constant of $\log\beta_{13}$ = 21.7. It can be seen from the speciation distribution diagram obtained from this fit (see Appendix Figure A5.2 (a)) that upon the addition of 0.3 equiv. of Tb^{III} it is formed in 82%. Additional aliquots of Tb^{III} then gives rise to a sharp decrease in luminescence which corresponds to a rapid decrease in the concentration of the 1:3 species, with the simultaneous evolution of the 1:2 Tb.**122**$_2$ and the 1:1 Tb.**122** species which were formed with binding constants of $\log\beta_{12}$ = 14.7 and $\log\beta_{11}$ = 7.5, respectively. A summary of the binding constants calculated from the fits are given in Table 5.1. Binding constant values correlate well to those calculated for the related analogue systems developed by Bünzli and co-workers (see Section 1.3).[106]

5.3 Excited state lifetimes and quantum yield determination

Excited state lifetimes for Eu^{III} and Tb^{III} were measured for both 1:3 complexes (Eu.**122**$_3$ and Tb.**122**$_3$) in a 0.1 M Tris-HCl buffered solution and D_2O in order to investigate if the Ln^{III} was residing in a fully saturated coordination sphere, as expected. A ligand concentration of 2.25 x 10^{-4} M was used for this measurement for the purpose of ensuring 100% formation of the 1:3 complex in solution. Luminescent emission lifetimes observed in the 0.1 M Tris-HCl buffered solution and D_2O were best fit to a mono-exponential decay function confirming the presence of only one luminescent species in solution for both solvents. Values of 1.58 ms and 1.87 ms for Eu.**122**$_3$ and 1.41 ms and 1.38 ms for Tb.**122**$_3$ were determined in the 0.1 M Tris-HCl (I = 0.1 M NaCl) buffered solution (pH = 7.45) and D_2O, respectively. By inputting this data into Equation 1, as described in previous sections, the number of Ln^{III} solvent bound molecules (q value) could be estimated, and, in both cases, q values of 0 were determined,

indicating that the Eu^{III} and Tb^{III} ions were residing within a fully saturated nine-coordinate sphere of three ligands.

Table 5.2. *Eu^{III}- and Tb^{III}-centred excited state lifetimes (ms), absorbance at λ = 279 nm, species population percentages, calculated hydration state (q) values and quantum yield % for Eu^{III}- and Tb^{III}-directed self-assembled species of ligand **122** as measured at RT in a 0.1 M Tris-HCl buffered solution and D_2O at various concentrations – note the estimated error for quantum yields is ±10%.*[130]

Complex	Ligand concentration (M)	τ_{H2O} (ms)		τ_{D2O} (ms)	*q* value	Φ_{tot}, %
Eu^{III}	2.25×10^{-4}	1.58		1.87	0.2	10.62 (± 0.43)
	1×10^{-4}	1.52 (96%)	0.44 (4%)	-	-	13.13 (± 0.35)
	5×10^{-5}	1.51 (95%)	0.41 (5%)	-	-	13.66 (±1.01)
Tb^{III}	2.25×10^{-4}	1.41		1.38	0.4	21.91 (±2.72)
	1×10^{-4}	1.47 (95%)	0.46 (5%)	-	-	25.93 (±0.41)
	5×10^{-5}	1.44 (93%)	0.44 (7%)	-	-	23.66 (±1.83)

A relative method was then employed to calculate the emission quantum yields for both complexes in a 0.1 M Tris-HCl (I = 0.1 M) buffered solution (pH = 7.45). This method compares both the UV-visible absorbance and emission intensity of the unknown sample (Eu.**122**$_3$ or Tb.**122**$_3$) to the standard reference (Cs_3[Eu(dpa)$_3$] and Cs_3[Tb(dpa)$_3$]) solution, as was described in chapter three.[105,281] Quantum yields (Φ_{tot}) were measured for the Eu^{III}-and the Tb^{III}-centred emission from Eu.**122**$_3$ and Tb.**122**$_3$ using the solutions above (ligand concentration = 2.25×10^{-4} M). However, as the quantum yield experiment requires six measurements of both the UV-visible absorption and the emission spectra the appearance of a white precipitate (which was luminescent under the UV lamp) was evident from the solution after this time, rendering the quantum yield values unreliable. Quantum yield measurements were therefore repeated at the lower ligand concentrations of 1×10^{-4} M and 5×10^{-5} M in order to avoid this solubility issue.

The stability of the parent tris dpa $[Ln(\mathbf{1})_3]^{2-}$ complexes in water has been widely studied by ^{1}H NMR in the 10^{-3} M concentration range and by spectroscopic measurements in more dilute solutions (10^{-5} M) with all studies indicating that a dissociation equilibrium occurs in solution. The extent of dissociation was shown to increase with increased dilution of the solution.[105,281,323,324] Similarly, for 1:3 tris complexes of compound **122**, this was found to be the case. Although self-assembled solutions (where ligand concentrations of 1×10^{-4} M and 5

x 10^{-5} M were implemented) remained clear, without the formation of a precipitate, lifetime measurements concluded the presence of two luminescent species in solution for both Eu^{III} and Tb^{III} systems at these two ligand concentrations. The quantum yield values were taken as being 13.66% and 23.66% for the Eu.**112**$_3$ and Tb.**122**$_3$ self-assembled systems, respectively. It is important to note however, that the 1:3 Eu.**112**$_3$ and Tb.**122**$_3$ species are present in 95% and 93% at this concentration, respectively (see Table 5.2). These quantum yield values are in close agreement with those calculated for the related structures **5** – **8**, in which the 4-*para* position of the parent H_2dpa framework has been substituted with a polyethylene chain bearing either a -OMe, -NH_2, -OH or –Phta terminal moiety.[106]

Having established that it was possible to form highly luminescent Eu^{III} and Tb^{III} 1:3 systems in a 0.1 M Tris-HCl buffered solution the functionalisation of AuNPs with compound **122** was then attempted.

5.4 Surface functionalisation of AuNPs with compound 122

There exist, a number of methods for the synthesis of AuNPs, with most of the standard procedures starting from the commercially available hydrogen tetrachloroaurate ($HAuCl_4$).[325] Two of the most common methods used are the citrate method, developed by Turkevitch *et al.* in 1951,[326] and the Brust-Schiffrin method.[327] The citrate method involves the reduction of Au^{III} to Au^0 in H_2O by citrate, allowing for the subsequent replacement of the citrate ligand by another appropriate functional ligand. The Brust-Schiffrin method consists of a water–toluene biphasic synthesis using $HAuCl_4$, tetraoctylammonium bromide (TOAB), $NaBH_4$ and a thiol ligand for functionalisation/stabilisation. This method is by far the most commonly employed method.

The Gunnlaugsson group have found that a modified version of the Brust-Schiffrin method has been the most successful when functionalising the surface of AuNPs with cyclen based Ln^{III} luminescent complexes bearing a terminal thiol moiety.[198] This two-phase method involves firstly mixing an aqueous solution of $HAuCl_4$ with a solution of the phase transfer agent TOAB in toluene with vigorous stirring. The Au^{III} is then transferred, facilitated by TOAB, into the organic layer where it is reduced to Au^0 by the addition of the reducing agent $NaBH_4$. A rapid change in the colour of the organic layer from orange to purple confirms reduction and formation of the gold nanoparticles in solution. The water layer is then removed by separation and the organic layer washed with H_2O, 0.1 M HCl and then finally 0.1 M NaOH. The surface plasmon resonance (SPR) band in the UV-visible absorption spectrum of this solution is characteristic of the collective oscillations of electrons at the surface of the AuNPs in response to optical excitation. The presence of this band therefore confirms formation of colloidal gold in solution. This band is very sensitive to the

composition, size, shape, interparticle distance and environment of the AuNPs but is usually located at 520 nm in EtOH for AuNPs possessing a diameter of 5 nm.[325] Functionalisation of the surface of the AuNPs is then usually achieved by exchanging the TOAB stabilising molecules with the thiol terminated ligand by stirring a H_2O solution of the compound with the AuNPs toluene solution overnight. Confirmation of successful adsorption of the ligand onto the AuNPs surface and transfer of the AuNPs into the H_2O phase is signified by a colour change in which the deep purple colour is transferred from the organic toluene layer to the aqueous phase.[198]

This synthetic route was initially attempted for the functionalisation of AuNPs with compound **122**, however, difficulties were encountered as no transfer of the AuNPs into the aqueous layer was observed, indicating that the compound had not been adsorbed onto the surface of the AuNPs. This could be due to, as was discussed above, the difficulty in fully solublising compound **122** in H_2O at higher concentration ranges.

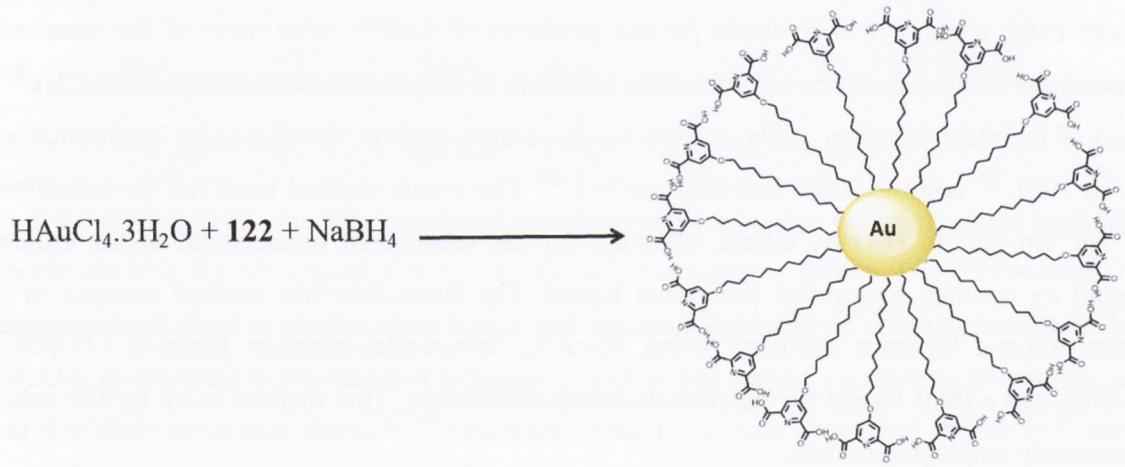

Figure 5.7. *Formation and functionalisation of AuNPs with compound* ***122****.*

Another literature procedure, which avoids the use of a second phase or a phase transfer stabilising agent, was then employed (see Figure 5.7).[328] In an effort to directly functionalise the surface of the AuNPs a solution of compound **122,** in a 60:40 CH_3OH:EtOH mixture (4.82×10^{-5} M), was added dropwise to a solution of $HAuCl_4.3H_2O$ in 5 mL of CH_3OH, (2.4×10^{-5} M), giving rise to a yellow cloudy solution. After 20 mins of stirring a solution of $NaBH_4$ in H_2O (2.4×10^{-4} M) was added dropwise to the reaction mixture. A black suspension almost immediately precipitated from solution. This black deposit was then separated from the reaction mixture by centrifugation. The organic phase was removed and the black deposit had H_2O added to it with stirring. Centrifugation was again implemented in order to separate the black deposit from the aqueous solution which appeared pink in colour.

This pink aqueous solution was removed and H_2O was again added to the black deposit. The pink coloured aqueous layer was again separated and removed by centrifugation. This process was repeated four times until the H_2O solution showed no colour.

(a) (b) (c)

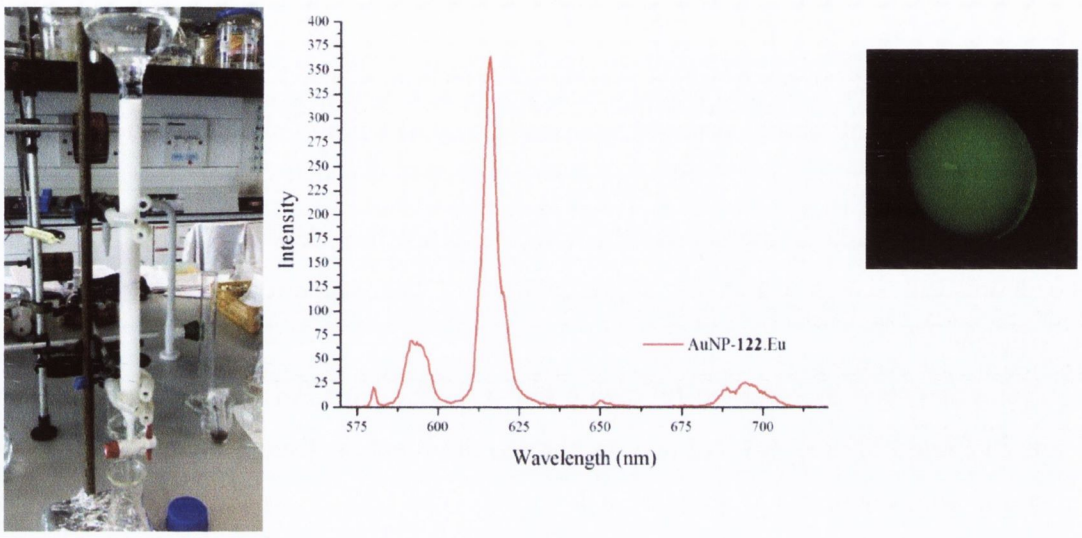

Figure 5.8. *(a) Sephadex G15 column used to purify AuNP-**122** solution, (b) Eu^{III}-centred emission observed following the addition of excess $Eu(CF_3SO_3)_3$ to a solution of AuNP-**122**, and (c) green colour observed under the UV lamp following the addition of excess $Tb(CF_3SO_3)_3$ to a solution of AuNP-**122** (λ_{ex} = 279 nm).*

A UV-visible absorption spectrum of the pink aqueous solution showed the presence of bands located at λ = 279 nm and 515 nm (see Appendix Figure A5.3). These two absorption bands correspond to those of compound **122** and to the SPR band associated with the AuNPs, respectively, pointing to the successful functionalisation of the surface of the AuNPs with ligand **122**. The functionalised AuNPs (AuNP-**122**) were then purified by size exclusion chromatography using a sephadex G15 column with 0.1 M NaCl as the eluent. The functionalised AuNPs were seen as a faint pink/purple band as they moved down the column (see Figure 5.8 (a)). To further confirm successful tethering of the compound to the solid surface *via* the thiol linkage an excess of both $Eu(CF_3SO_3)_3$ and $Tb(CF_3SO_3)_3$ were added to the pink aqueous solution. As shown in Figure 5.8 (b) Eu^{III}-centred emission was exhibited by the solution to which Eu^{III} was added, following excitation at λ = 279 nm. Under the UV lamp green emission was also clearly evident from the solution when excess $Tb(CF_3SO_3)_3$ had been added (see Figure 5.8 (c)). Both results demonstrate that compound **122** is in solution, bound to the AuNPs by means of the thiol functionality, permitting access to the Ln^{III} coordinating tridentate unit for Ln^{III} sensitisation. Although these results evidence the successful functionalisation of the AuNPs with compound **122**, its poor solubility in polar solvents, as was encountered in previous sections, may have prevented facile

functionalisation, which in turn led to conflicting characterisation results which are discussed in the following section.

The purified AuNP-**122** were characterised by dynamic light scattering (DLS) and transmission electron microscopy (TEM) which are described in the following section.

5.5 Characterisation of functionalised AuNPs – TEM and DLS

Transmission electron microscopy (TEM) is a technique used to obtain high resolution images of very small particle samples, as small as up to 1 nm.[329] An ultra-thin sample of the material under investigation is illuminated with a beam of electrons which either interacts with or passes through (transmits) the sample, generating dark and bright regions on a phosphorescent screen which are representative of the structure and size of the sample constituents.[329]

Preliminary results obtained following the analysis of the AuNP-**122** sample are shown below in Figure 5.9 (a), (b) and (c). As shown, the functionalised AuNPs were spherically structured with diameters ranging from 1 – 7 nm. The particle size distribution (see Figure 5.9 (c)) was calculated by measuring the diameter of *ca.* 961 particles and indicated that the AuNP-**122** possessed an average core diameter of 2.21 nm. It was difficult to distinguish the AuNPs from background noise when processing the data using the programme Image J. This was due to their small size and consequently, the quality of the images produced, meaning it was possible that the actual average core diameter value was slightly larger. However, the AuNPs would need to be re-synthesised and re-examined to confirm this. Furthermore, upon magnification, (Figure 5.9 (c)), the functionalised AuNPs appeared less well defined in the TEM images due to the melting of the organic material coating the AuNPs.

Dynamic light scattering (DLS) was also used to characterise the functionalised AuNPs-**122**. DLS is a technique used to measure the size distribution of small particles suspended in solution which are undergoing Brownian motion.[330] Brownian motion is the random motion of particles suspended in solution resulting from their collision with each other and their bombardment with surrounding solvent molecules and can be defined by a property known as the translational diffusion coefficient, d(H). The translational diffusion coefficient depends on the size of the particles, with larger particles moving slower in solution in comparison to smaller molecules. DLS measures the translation diffusion coefficient by measuring the rate at which the intensity of the illuminating light source fluctuates, with smaller particles causing the intensity of the scattered light to fluctuate more rapidly than larger particles. The translational diffusion coefficient can then be related to the size of the particles according to the Stokes-Einstein equation:

Equation 14: $$d(H) = \frac{kT}{3\pi\eta D}$$

where d(H) is the hydrodynamic diameter, D is the translational diffusion coefficient, k is Boltzmanns constant, T is the absolute temperature and η is the viscosity of the solution.[330]

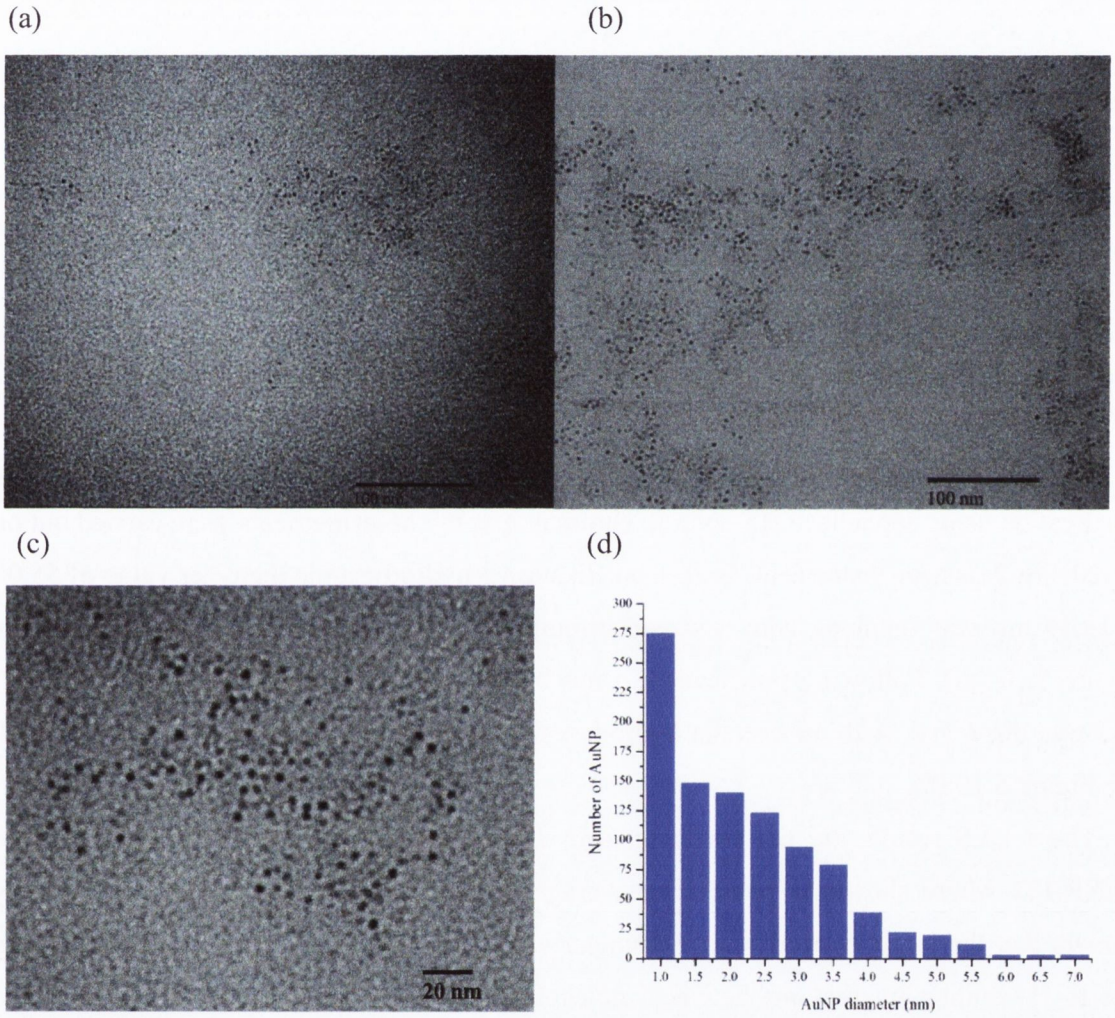

Figure 5.9. *(a), (b), (c) TEM images of AuNP-**122** after deposition onto copper grids and (d) particle size distribution graph calculated from the TEM data.*

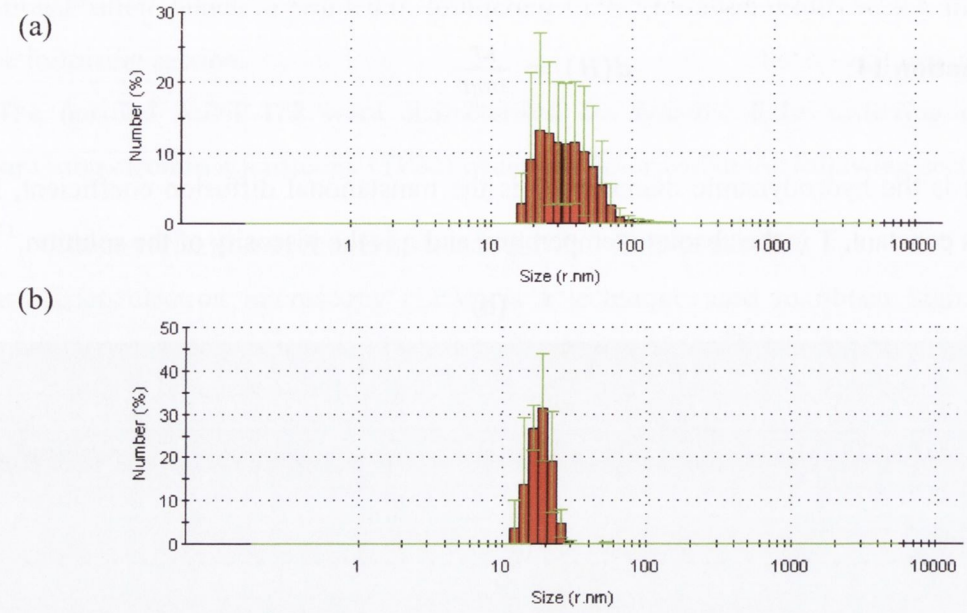

Figure 5.10. *Particle size distribution plots as determined from DLS analysis for AuNP-**122** (a) before and (b) after purification using sephadex G15.*

DLS analysis was used to characterise the AuNP-**122** once before and once after purification using sephadex G15 column chromatography. Measurements were carried out on a Malvern Zetasizer Instrument. Before purification a hydrodynamic diameter value of 55.08 ± 19.19 nm was obtained with a size distribution ranging from 16.34 – 198.00 nm, (see Figure 5.10 (a)). Following purification, a much narrower size distribution range of AuNP-**122** was displayed, with an average hydrodynamic diameter value of 19.42 ± 3.0 obtained, see Figure 5.10 (b).

These DLS results did not correlate well with those evidenced by TEM above where AuNP-**122** where shown to possess an average core diameter of 2.2 nm. It was initially thought that the larger hydrodynamic diameter value obtained from DLS measurements was due to H-bonding interactions between molecules of **122** on adjacent AuNPs, causing the accumulation of AuNPs and consequently giving rise to larger hydrodynamic diameter values. By again examining the TEM images above it can be observed that it is possible that agglomerates were formed, which would coincide with this speculation. Excess NaOH was added to this DLS sample, in an effort to remove potential H-bonding interactions and gain a better insight into the system. However, the system formed much larger particles almost immediately (417 nm). The addition of excess HCl was also attempted in an effort to reduce the number of potential H-bonding interactions but gave a similar result where much larger particles were instantly observed (278 nm). It is possible that the functionalised AuNP-**122** may have undergone agglomeration due to an instability of the system, appearing as larger particles from DLS measurements. These preliminary results and theories require more

ttention to fully elucidate the stability and behaviour of the AuNP-**122** conjugate in order to extend the use of this system.

5.6 Conclusion

This chapter focused on the development of a modified H_2dpa structure for potential use as a Ln^{III} luminescent centre in biologically relevant applications such as AuNP attachment or protein interaction/structure elucidation. The target compound **122** possessed a number of features suitable for these objectives such as a tridentate Ln^{III} chelating unit; two carboxylic acid side groups for water solubilisation and a C_{12} thiol terminated alkyl chain in the 4-*para* position for AuNP or cysteine residue grafting. Compound **122** was synthesised in four steps before its Ln^{III}-directed self-assembly behaviour (Ln^{III} = Eu and Tb) in aqueous solution was evaluated. It was found that upon the addition of 0.33 equiv. of $Eu(CF_3SO_3)_3$ in a 0.1 M Tris-HCl buffered solution the 1:3 Eu.$\mathbf{122}_3$ highly luminescent species was formed predominantly in solution with high binding constants of $\log\beta_{13}$ = 20.4 and $\log\beta_{13}$ = 21.4. A similar behaviour was evidenced for the Tb^{III} system in which the 1:3 Tb.$\mathbf{122}_3$ was formed in a 0.1 M Tris-HCl buffered solution with comparable binding constants of $\log\beta_{13}$ = 22.1 and $\log\beta_{13}$ = 21.7 (from fitting of the UV-visible absorption and luminescence titration data, respectively). Excited state lifetime measurements were then implemented in order to calculate hydration state q values. Lifetimes measurements were best fit to a mono-exponential decay function, when a ligand concentration of 2.25 x 10^{-4} M was used, giving values of 1.58 and 1.41 ms for the 1:3 complexes Eu.$\mathbf{122}_3$ and Tb.$\mathbf{122}_3$, respectively,. Hydration state q values of 0 were calculated in both cases confirming a fully saturated coordination sphere for both Eu.$\mathbf{122}_3$ and Tb.$\mathbf{122}_3$. Both complexes were unstable at this concentration resulting in their precipitation at the end of the experiment. Lower ligand concentrations were therefore used (1 x 10^{-4} M and 5 x 10^{-5} M) for excited state lifetimes measurements and quantum yield determination. Both complexes Eu.$\mathbf{122}_3$ and Tb.$\mathbf{122}_3$ were shown to dissociate at these concentrations but remained present in relatively high yields, as was evidenced by percentage population values (see Table 5.2). Quantum yield calculations were determined at these ligand concentrations with values of 13.66% and 23.66% appearing to be the most reliable (in relation to the solubility of the system at a ligand concentration of 5 x 10^{-5} M) which were obtained for the Eu.$\mathbf{112}_3$ and Tb.$\mathbf{122}_3$ self-assembled systems, respectively. From these photophysical measurements it can be deduced that highly luminescent 1:3 Eu^{III} and Tb^{III} complexes can be assembled in a 0.1 M Tris-HCl buffered solution (pH = 7.45). Most notably, from these measurements, it was observed that the solubility range of the ligand must be carefully considered when carrying out further studies on this system.

The functionalisation of AuNPs with compound **122** was attempted using the modified Brust-Schiffrin method previously reported within our laboratory. No transfer of functionalised AuNPs into the aqueous phase was observed using this biphasic synthetic route. Another synthetic strategy was therefore undertaken which involved the simultaneous formation and functionalisation of AuNPs with compound **122** in solution, generating AuNP-**122**. AuNP-**122** were preliminary investigated and characterised following purification using sephadex G15 column chromatography. The addition of excess $Eu(CF_3SO_3)_3$ and $Tb(CF_3SO_3)_3$ to an aqueous solution of AuNP-**122**, following excitation of the sensitising unit at λ_{ex} = 279 nm, gave rise to Ln^{III}-centred emission. Both TEM and DLS analysis were implemented in order to investigate the size of the diameter of the functionalised AuNP-**122** giving conflicting results which may possibly be due to the formation of AuNP agglomerates in solution. More work in this area is required however. It would be necessary to fine tune the synthesis of the functionalised AuNPs and to develop a method which best suits these systems.

From the above results it can be concluded that a solid platform of knowledge for this system has been developed. Following substitution at the 4-*para* position 1:3 $Ln(\mathbf{122})_3$ mononuclear complexes can be formed in an aqueous environment retaining the high luminescent properties of the H_2dpa system. Preliminary experiments on the functionalisation of AuNPs with **122** were promising with UV-visible and Ln^{III}-centred emission spectra indicating the fabrication of the AuNPs with compound **122** through the thiol linkage. TEM and DLS measurements did give conflicting results but this could be as a result of the formation of agglomerates in solution, which would not be as obvious from TEM images. A more in depth study of the functionalisation of the AuNPs with compound **122** is required in order to adjust the synthetic procedure and ensure exact characterisation and behaviour. Once this synthetic route has been improved a limitless number of avenues can be examined for AuNP-**122**, such as drug delivery agents, imaging and/or sensing probes.[331]

Chapter Six

Experimental

6. General experimental details

All starting materials were purchased from commercial sources and used as received. Solvents were of HPLC grade and were used without further purification. Dry solvents were prepared in accordance with standard procedures described by Vogel, with distillation prior to each use.[332] Chromatographic columns were performed manually using silica gel 60 (230-240 mesh ASTM) or were run on an automatic Teldyne Isco Combiflash Companion machine using pre-packed silica columns. Thin-layer chromatography (TLC) was conducted using both Merck Kiesegel 60 F_{254} silica plates and observed under UV light. Melting points were determined using an Electrochemical IA900 digital melting point apparatus. Electro mass spectra were determined using a Mass Lynx NT V 3.4 on a Waters 600 controller connected to a 996 photodiode array detector with HPLC-grade carrier solvents. A peak-matching method was used to determine accurate molecular weights using leucine enkephaline (H-Tyr-Gly-Gly-Phe-Leu-OH) as the standard reference (m/z = 556.2771); all accurate mass were reported within ± 5 ppm of the expected mass. Elemental analyses were carried out at the Microanalytical Laboratory, School of Chemistry and Chemical Biology, University College Dublin. Infrared spectra were recorded on a Perkin Elmer Spectrum One FT-IR spectrometer equipped with a Universal ATR sampling accessory. Solid samples were recorded directly as neat samples in cm^{-1}. NMR data were recorded in commercially available deuterated solvents on either a Bruker Spectrospin DPX-400 spectrometer which operates at 400.13 MHz for ^{1}H NMR and 100.6 MHz for ^{13}C NMR or a Bruker-AV-600 spectrometer which operates at 600.13 MHz for ^{1}H NMR and 150.2 MHz for ^{13}C NMR. Tetramethylsilane (TMS) was used as an internal standard and shifts were referenced relative to the internal solvent signals with chemical shifts expressed in parts per million (ppm / δ).

6.1 UV-visible absorption and luminescence spectroscopy

Using a 1.0 cm path length quartz cell, UV-visible absorption and luminescence spectra were recorded at RT using a Varian CARY 50 spectrophotometer. The solvents employed were of HPLC or spectrophotometric grade. For UV-visible absorption measurements the wavelength range was set from 450 nm to 200 nm with a scan rate of 600 nm min^{-1}. The blank used was a sample of the solvent system in which the titration was undertaken. All luminescence scans were measured in arbitrary units unless otherwise stated. The luminescence data was collected between 470 and 700 nm for the Tb^{III} emission, 570 and 720 nm for the Eu^{III} emission and 540 and 730 nm for the Sm^{III} emission.

6.2 Luminescence lifetime measurements

The luminescence lifetime measurements for the Eu^{III} complexes in chapters 2, 3 and 5 were carried out on a Varian Carey Eclipse Fluorimeter in time-resolved mode at 298 K. All lifetime measurements were obtained from an average of six independent measurements, each recorded with a different gate time in the range 0.020 – 0.045 ms.

6.3 Quantum yield determination

As was described in Section 3.3 a relative method was employed to calculate the quantum yield values (Φ_{tot}) for Ln^{III} complexes in chapters 3 and 5. This method compares both the UV-visible absorbance and emission intensity of the unknown sample to standard reference solutions of $Cs_3[Eu(dpa)_3]$ or $Cs_3[Tb(dpa)_3]$ in a 0.1 M Tris-HCl (I = 0.1 M) buffered solution (pH = 7.45) (Φ_{tot} = 24.0 ± 2.5% and Φ_{tot} = 22.0 ± 2.5% for $Cs_3[Eu(dpa)_3]$ and $Cs_3[Tb(dpa)_3]$, respectively)[105,187,281] The estimated error for the quantum yield values is ± 10%.

6.4 NIR emission spectroscopy

Luminescence spectra in the near-IR region were recorded on a Fluorolog FL 3-22 spectrophotometer from Horiba Jobin Yvon with double grating emission and excitation monochromators, and a R5509-73 photomultiplier. Light intensity was measured by using a C9940-22 detector with a range from 800 – 1700 nm from Hamamatsu, cooled to 77 K and coupled to a Jobin Yvon SpectrAcq v5.20 data acquisition system. All measurements were performed at 298 K, with this temperature being kept constant using a thermostated unit block.

For the measurement of the Nd^{III} luminescence lifetimes, the samples were excited using a pulsed nitrogen laser (PTI- 3301, 337 nm) operating at 10 Hz. Light emitted at right angles to the excitation beam was focused onto the slits of a monochromator (PTI120), which was used to select the appropriate wavelength. The growth and decay of the luminescence at selected wavelengths were detected using a germanium photodiode (Edinburgh instruments, EI- P) and recorded using a digital oscilloscope (Tektronix TDS220) before being transferred to a PC for analysis. Time-resolved emission spectra were obtained by measuring the growth and decay of the luminescence at each of a series of wavelengths. Luminescence lifetimes were obtained by iterative reconvulution of the detector response (obtained using a scatterer) with exponential components for growth and decay of the metal centered luminescence, using a spreadsheet running in Microsoft Excel. The details of this approach have already bee*n discussed.[264]

6.5 Circular Dichroism and circularly polarized luminescence measurements

CD spectra were recorded on a Jasco J-810-150S spectropolarimeter in a 1.2 mL cell. Each CD trace represents an average of three scans. All CD are represented as mdeg *vs* λ (nm). CPL spectra were recorded by Dr. R. Peacock at the University of Glasgow. Calibration of the emission monochromator was accomplished by passing scattered light from a low power He-Ne laser through the detection system. The optical detection system consisted of a photoelastic modulator (PEM, Hinds Int.) operating at 50 kHz and a linear polariser, which together act as a circular analyser, followed by a long pass filter, focusing lens and a 0.22 m double monochromator. The emitted light was detected by a cooled EM1-9558QB photomultiplier tube operating in photon counting mode. The 50 kHz reference signal from the photoelastic modulator was used to direct the incoming pulses into two separated counters. An up counter, which counts every photon pulse and thus is a measure of the total luminescence signal $I = I_{left} + I_{right}$, and an up/down counter, which adds pulses when the analyser is transmitting to the left circularly polarised light and subtracts pulses when the analyser is transmitting right circularly polarised light. The second counter provides a measure of the differential emission intensity $\Delta I = I_{left} - I_{right}$.

6.6 Complexation microwave reactions

Complexation reactions were carried out in 2-5 mL Biotage Microwave Vials in a Biotage Initiator Eight EXP microwave reactor. Reactions were performed at 70 °C for 10 mins in HPLC grade CH_3OH.

6.7 Langmuir film measurements

Surface pressure–area isotherms and time stability measurements were carried out at 25 °C on a KSV MiniMicro Langmuir-Blodgett trough (KSV, Finland) with a surface area between 1700 and 8700 mm^2. Water was purified with a Milli-Q® Integral system (Millipore), and its resistivity was measured to be higher than 18 MΩ cm. Chloroform (puriss. p.a. ≥ 99.8%, Sigma-Aldrich) was used as a spreading solvent for ligands **81** and **82**; a 9:1 mixture of chloroform/CH_3OH mixture was used for complexes Ln.**81**$_3$ and Ln.**82**$_3$. Typically drops (20 μl) of the surfactant solution (*ca.* 0.25 mM) were deposited using a microsyringe on the water subphase. After leaving the solvent to evaporate for 20 min, the barriers were compressed at 6 mm min^{-1} and the surface pressure was monitored using a platinum Wilhelmy plate.

6.8 X-ray crystallographic characterisation

Single crystal X-ray diffraction data for **81** was collected using graphite monochromated Cu-Kα radiation (λ = 1.54184 Å) on an Oxford Diffraction SuperNova diffractometer. The diffractometer was equipped with a Cryostream N_2 open-flow cooling device,[333] and the data was collected at 150(2) K. A series of ω-scans were performed in such a way as to collect all unique reflections to a maximum of 0.80 Å. Cell parameters and intensity data (including interframe scaling) were processed using CrysAlis Pro.30.[334] X-ray data for **82** was collected on a Rigaku Saturn 724 CCD diffractometer using graphite-monochromated Mo-Kα radiation (λ = 0.71073 Å). The data was collected using Crystalclear-SM 1.4.0 software. Data integration, reduction and correction for absorption and polarization effects were all performed using Crystalclear-SM 1.4.0 software. Space group determination was obtained using Crystal structure ver. 3.8. X-ray data for **108** and **109** was collected on a Bruker APEX II CCD diffractometer using graphite monochromated Cu-Kα radiation (λ = 1.54178 Å). The data sets were collected using APEX2 software; with data integration, reduction, and correction for absorption and polarization effects, as well as space group determinations, all performed using APEX2. All structures were solved by direct methods (SHELXS-97) and refined against all F^2 data (SHELXL-97).[335] Hydrogen atoms, except for N–H protons, were positioned geometrically and refined using a riding model with d(CH_{aro}) = 0.95 Å, *U*iso =1.2*U*eq (C) for aromatic protons, d(CH) =1.0 Å, *U*iso =1.2*U*eq (C) for CH, 0.99 Å, *U*iso =1.2*U*eq (C) for CH_2 and 0.98 Å, *U*iso =1.2*U*eq (C) for CH_3. Amide N–H protons were found from the difference map and fixed to the attached atoms. All data collection and analysis was performed by Dr. Jonathan A. Kitchen.

6.9 Characterisation of the surface-modified AuNPs

The size of the functionalised AuNP and their distribution in aqueous solution were analysed by Transmission Electron Microscopy (TEM) and Dynamic Light Scattering (DLS), respectively. TEM measurements were carried out at the Centre for Microscopy and Analysis (CMA, Trinity College Dublin) using a JEOL 2100 microscope. DLS measurements were conducted on a Zetasizer Nano Series (Malvern Instrument).

6.10 Experimental details for Chapter Two

6-(Benzyloxycarbonyl)picolinic acid (84)[254]

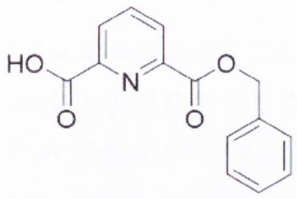

2,6-Pyridinedicarboxylic acid **83** (2.00 g, 12 mmol, 1.00 equiv.) and $NaHCO_3$ (1.21 g, 14 mmol, 1.20 equiv.) were added to DMF (40 mL) and allowed to stir at 65 °C. To this, benzyl bromide (1.71 mL, 14 mmol, 1.20 equiv.) was added and the resulting suspension stirred under argon for 5 hrs. After cooling to RT the reaction mixture was diluted with H_2O (40 mL), neutralised with saturated aq. $NaHCO_3$ and extracted with AcOEt to remove the diester side product. The aq. layer was acidified to pH 3 with 1 M HCl and extracted with AcOEt. The organic extracts were combined, washed with H_2O and brine, dried over $MgSO_4$ and volatiles were removed under reduced pressure yielding the crude product as a white solid. The solid was redissolved in CH_2Cl_2, washed with H_2O and brine and then dried over $MgSO_4$. The solvent was then removed under reduced pressure yielding **84** as a white crystalline solid in 52% yield (402 mg). HRMS (*m/z*) (ES^+) Calculated for $C_{14}H_{11}NO_4Na^+$ *m/z* = 280.0586 $[M + Na]^+$. Found *m/z* = 280.0579; ^1H NMR (400 MHz, $CDCl_3$) δ_H: 8.44 (1H, d, *J* = 7.9 Hz, pyridine-H), 8.40 (1H, d, *J* = 7.9 Hz, pyridine-H), 8.14 (1H, t, *J* = 7.9 Hz, pyridine-H), 7.50 (2H, d, *J* = 7.3 Hz, Ar-H), 7.44 (3H, m, Ar-H), 5.48 (2H, s, CH_2); ^{13}C NMR (100 MHz , $CDCl_3$) δ_C: 163.43, 163.36, 146.76, 146.48, 139.64, 134.99, 128.87, 128.77, 128.76, 128.58, 126.81, 68.05.

(S)-Benzyl 6-(1-(naphthalen-1-yl)ethylcarbamoyl)picolinate (85)[69]

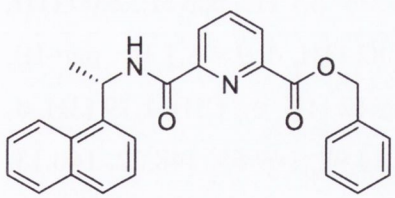

HOBt (0.37 g, 2.70 mmol, 1.00 equiv.), (*S*)-(-)-1-(1-naphthyl)ethylamine (0.44 mL, 2.70 mmol, 1.00 equiv.) and NEt_3 (0.40 mL, 2.90 mmol, 1.05 equiv.) were added to a solution of 6-(benzyloxycarbonyl)picolinic acid **84** (0.70 g, 2.70 mmol, 1.00 equiv.) in dry THF (25 mL) and placed under argon. The reaction mixture was cooled to 0 °C with stirring for 30 mins. To this, EDCI·HCl (0.55 g, 2.90 mmol, 1.05 equiv.) was then added and the resulting suspension was left stirring at 0 °C for a further 30 mins. The reaction mixture was then allowed to reach RT and then stirring was continued for a further 48 hrs, leaving a yellow solution with a white solid residue. The insoluble residue was removed by suction filtration and THF was removed under reduced pressure to give the crude product as an orange oil. The impure product was taken up in CH_2Cl_2 and washed with 1.0 M HCl, sat. aq. $NaHCO_3$, H_2O and brine. The

organic layer was then dried over $MgSO_4$ and the solvent was removed under reduced pressure yielding the pure product as an orange oil in 84% yield (1.04 g). HRMS (*m/z*) (ES^+) Calculated for $C_{14}H_{11}NO_4Na^+$ *m/z* = 433.1528 $[M + Na]^+$. Found *m/z* = 433.1521; ^1H NMR (400 MHz, $CDCl_3$) δ_H: 8.50 (1H, d, *J* = 8.4 Hz, NH), 8.44 (1H, d, *J* = 7.6 Hz, pyridine-H), 8.23 (2H, m, nap-H), 8.0 (1H, t, *J* = 7.7 Hz, pyridine-H), 7.90 (1H, d, *J* = 7.8 Hz, pyridine-H), 7.84 (1H, d, *J* = 7.9 Hz, nap-H), 7.64 (1H, d, *J* = 7.3 Hz, nap-H), 7.57 – 7.38 (8H, m, 3 nap-H, 5 Ar-H), 6.19 (1H, m, CH), 5.42 (2H, s, CH_2), 1.82 (3H, d, *J* = 7.0 Hz, CH_3) ; ^{13}C NMR (100 MHz, $CDCl_3$) δ_C: 163.73, 161.94, 149.69, 146.04, 138.05, 137.94, 134.94, 133.49, 130.60, 128.38, 128.22, 128.04, 127.83, 127.76, 126.87, 126.04, 125.31, 125.11, 124.93, 122.86, 122.21, 67.05, 44.46, 20.95.

(S)-6-(1-(Naphthalen-1-yl)ethylcarbamoyl)picolinic acid (79)[69]

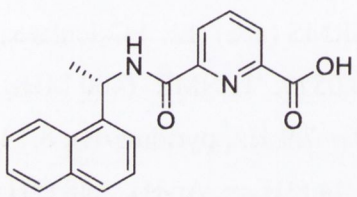

Pd/C (10%) (0.02 g, 0.20 mmol, 0.10 equiv.) was added to a solution of (*S*)-benzyl 6-(1-(naphthalen-1-yl)ethylcarbamoyl)picolinate **80** (0.93 g, 2.10 mmol, 1.00 equiv.) in CH_3OH (60 mL) and placed on a Parr hydrogen shaker apparatus under 3 atm of hydrogen gas for 24 hrs. The reaction mixture was then filtered through a plug of celite and the solvent was removed under reduced pressure to give the product as a dark yellow oil in 76% yield (562 mg). HRMS (*m/z*) (ES^-) Calculated for $C_{19}H_{15}N_2O_3^-$ *m/z* = 319.1083 $[M - H]^-$. Found *m/z* = 319.1091; ^1H NMR (400 MHz, DMSO-d_6) δ_H: 8.55 (1H, d, *J* = 8.3 Hz, NH), 8.43 (1H, d, *J* = 7.7 Hz, pyridine-H), 8.23 (1H, d, *J* = 7.6 Hz, pyridine-H), 8.17 (1H, d, *J* = 8.1 Hz, nap-H), 8.00 (1H, t, *J* = 8.1 Hz, pyridine-H), 7.88 (1H, d, *J* = 7.7 Hz, nap-H), 7.82 (1H, d, *J* = 8.1 Hz, nap-H), 7.63 (1H, d, *J* = 7.2 Hz, nap-H), 7.53 – 7.45 (3H, m, nap-H), 6.12 (1H, m, CH), 1.79 (3H, d, *J* = 6.8 Hz, CH_3); ^{13}C NMR (100 MHz, $CDCl_3$) δ_C: 167.04, 163.98, 149.65, 148.22, 140.13, 139.33, 133.82, 130.79, 129.18, 127.92, 126.88, 126.80, 126.37, 126.10, 125.99, 123.49, 123.18.

N_2-[1-Hexadecyl]-N_6-[(S)-1-(naphthalen-1-yl)ethyl]pyridine-2,6-dicarboxamide (81)

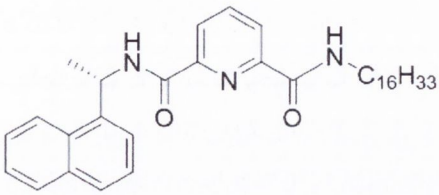

HOBt (0.14 g, 1.05 mmol, 1.00 equiv.), hexadecylamine (0.25 g, 1.05 mmol, 1.00 equiv.) and Et_3N (0.15 mL, 1.10 mmol, 1.05 equiv.) were added to a solution of compound **79** (0.37 g, 1.05 mmol, 1.00 equiv.) in dry THF (20 mL) and placed under argon. The reaction mixture was cooled to 0 °C with stirring for 30 mins. To this, EDCI·HCl (0.21 g, 1.10 mmol, 1.05 equiv.) was added and the resulting suspension was left stirring at 0 °C for a further 30 mins. The reaction mixture was then allowed to reach RT, and then stirring was continued for a further 48 hrs, leaving a yellow solution with a white solid residue. The insoluble residue was removed by suction filtration and THF was removed under reduced pressure to give the crude product as an orange oil. The impure product was taken up in CH_2Cl_2 and washed with 1.0 M HCl, sat. aq. $NaHCO_3$, H_2O and brine. The organic layer was then dried over $MgSO_4$ and the solvent was removed under reduced pressure yielding N_2-[1-hexadecyl]-N_6-[(1*S*)-1-(naphthalen-1-yl)ethyl]pyridine-2,6-dicarboxamide **81** as a pale yellow oil (322 mg, 51%). HRMS (*m/z*) (ES^+) Calculated for $C_{35}H_{49}N_3O_2Na^+$ *m/z* = 566.3722 $[M + Na]^+$. Found *m/z* = 566.3721. ^{1}H-NMR (600 MHz, $CDCl_3$) δ_H: δ 8.37 (1H, m, NH), 8.35 (1H, d, *J* = 8.6 Hz, pyridine-H), 8.25 (1H, d, *J* = 7.9 Hz, pyridine-H), 8.15 (1H, d, *J* = 8.5 Hz, nap-H), 7.92 (1H, t, *J* = 7.8 Hz, pyridine-H), 7.88 (1H, t, *J* = 5.9 Hz, NH), 7.80 (1H, d, *J* = 8.0 Hz, nap-H), 7.71 (1H, d, *J* = 8.2 Hz, nap-H), 7.52 (1H, m, nap-H), 7.51 (1H, m, nap-H), 7.46 (1H, t, *J* = 7.2 Hz, nap-H), 7.34 (1H, t, *J* = 7.7 Hz, nap-H), 6.08 (1H, m, CH), 3.31 (1H, m, CH_2), 3.19 (1H, m, CH_2), 1.75 (3H, d, *J* = 6.8 Hz, CH_3), 1.44 (2H, t, *J* = 6.3 Hz, CH_2), 1.27 – 1.21 (26H, m, 13CH_2), 0.9 (3H, t, *J* = 7.0 Hz, CH_3); ^{13}C-NMR (150 MHz, $CDCl_3$) δ_C: 163.3, 162.7, 148.8, 148.6, 138.7, 138.0, 133.8, 131.0, 128.8, 128.3, 126.5, 125.8, 125.0, 124.9, 124.8, 123.2, 122.7, 45.1, 39.5, 31.8, 29.6-29.2 (11xCH_2), 26.9, 22.6, 20.8, 14.0. IR(neat): 3309, 2921, 2852, 1654, 1524, 1443, 1375, 1237, 1074, 999, 844, 798, 776, 722, 677 cm^{-1}.

N_2-[1-Hexadecyl]-N_6-[(R)-1-(naphthalen-1-yl)ethyl]pyridine-2,6-dicarboxamide (82)

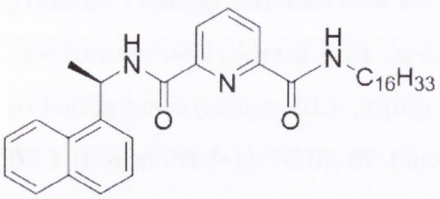

Compound **80** (0.50 g, 1.50 mmol, 1.00 equiv.) and HOBt (0.21 g, 1.50 mmol, 1.00 equiv.) were added to a 100 mL RBF and placed under argon. THF (20 mL), hexadecylamine (0.38 g, 1.50 mmol, 1.00 equiv.) and Et_3N (0.23 mL, 1.60 mmol, 1.05 equiv.) were added and the resulting orange solution was cooled to 0 °C. After 30 mins EDCI·HCl (0.32 g, 1.60 mmol, 1.05 equiv.) was added and the mixture stirred at 0 °C for a further 30 mins. The reaction mixture was allowed to reach RT and stirred for a further 48 hrs. The organic solvent was removed *in vacuo* to give an orange oil that was subsequently taken up in CH_2Cl_2, washed with 1 M HCl, sat. aq. $NaHCO_3$, H_2O and brine. The organic layer was dried over $MgSO_4$ and solvent removed under reduced pressure affording the product N_2-[1-hexadecyl]-N_6-[(1*S*)-1-(naphthalen-1-yl)ethyl]pyridine-2,6-dicarboxamide (**77**) as a pale yellow oil (606 mg, 71%). HRMS (*m/z*) (ES^+) Calculated for $C_{35}H_{49}N_3O_2Na^+$ *m/z* = 566.3722 $[M + Na]^+$. Found *m/z* = 566.3720. ^{1}H-NMR (400 MHz, $CDCl_3$, δ_H): δ 8.37 (1H, d, *J* = 7.5 Hz, pyridine-H), 8.28 (1H, d, *J* = 7.8 Hz, pyridine-H), 8.25 (1H, d, *J* = 8.5 Hz, NH), 8.17 (1H, d, *J* = 8.5 Hz, nap-H), 7.95 (1H, t, *J* = 7.8 Hz, pyridine-H), 7.83 (1H, m, nap-H), 7.73 – 7.78 (2H, m, 1 x nap-H, 1 x NH), 7.46 – 7.57 (3H, m, nap-H), 7.38 (1H, t, *J* = 7.7 Hz nap-H), 6.10 (1H, m, CH), 3.34 (1H, m, CH_2), 3.25 (1H, m, CH_2), 1.78 (3H, d, *J* = 6.8 Hz, CH_3), 1.47 (2H, t, *J* = 6.6 Hz, CH_2), 1.29 – 1.22 (26H, s, $13CH_2$), 0.9 (3H, t, *J* = 6.8 Hz, CH_3); ^{13}C-NMR (150 MHz, $CDCl_3$) δ_C: 163.3, 162.7, 148.9, 148.6, 138.8, 138.0, 133.9, 131.1, 128.9, 128.4, 126.6, 125.9, 125.1, 125.0, 125.0, 123.4, 122.8, 45.3, 39.6, 31.9, 29.7-29.3 ($11xCH_2$), 26.9, 22.7, 20.9, 14.1. IR(neat): 3303, 2922, 2852, 1650, 1523, 1443, 1375, 1310, 1075, 999, 845, 799, 776, 721, 676 cm^{-1}.

*Synthesis of Ln^{III} complexes Ln.**81**$_3$:*

*Synthesis of Eu.**81**$_3$:*

Ligand **81** (0.026 g, 0.05 mmol, 3 equiv.) in 5 mL CH_3OH had solid $Ln(CF_3SO_3)_3$ (0.010 g, 0.02 mmol, 1 equiv.) added and was heated at 70 °C under microwave irradiation for 10 minutes. The resulting clear yellow solution was subjected to vapour diffusion of diethyl ether affording Eu.**81**$_3$ as a white solid in 56% yield. HRMS (*m/z*) (MS-LD^+) Calculated for $C_{72}H_{98}F_6N_6O_{10}S_2Eu^+$ *m/z* = 1537.5902. Found *m/z* = 1537.5862; Elemental analysis for $C_{108}H_{147}N_9O_{15}F_9S_3Eu$ (2229.92 $gmol^{-1}$) Calculated: C 58.15, H 6.64, N 5.65. Found C 57.99,

H 6.50, N 5.58%. IR(neat): 3284, 2920, 2852, 1633, 1594, 1560, 1459, 1242, 1187, 1165, 1029, 839, 801, 779, 753, 720 cm^{-1}.

*Synthesis of Nd.**81**$_3$:*

Ligand **81** (0.032 g, 0.06 mmol, 3 equiv.) in 5 mL CH_3OH had solid $Nd(CF_3SO_3)_3$ (0.012 g, 0.02 mmol, 1 equiv.) added and was heated at 70 °C under microwave irradiation for 10 minutes. The resulting clear yellow solution was subjected to vapour diffusion of diethyl ether affording Nd.**81**$_3$ as a white solid in 50% yield. HRMS (*m/z*) (MS-LD$^+$) Calculated for $C_{72}H_{98}F_6N_6O_{10}S_2Nd^+$ *m/z* = 1526.5767. Found *m/z* = 1526.5824; Elemental analysis for $C_{108}H_{147}N_9O_{15}F_9S_3Nd.3H_2O$ Calculated: C 56.97, H 6.77, N 5.54; Found C 56.57, H 6.25, N 5.66%. IR(neat): 3290, 2920, 2853, 1631, 1594, 1560, 1458, 1238, 1164, 1030, 800, 779, 753 cm^{-1}.

*Synthesis of Tb.**81**$_3$:*

Ligand **81** (0.021 g, 0.04 mmol, 3 equiv.) in 5 mL CH_3OH had solid $Tb(CF_3SO_3)_3$ (0.008 g, 0.01 mmol, 1 equiv.) added and was heated at 70 °C under microwave irradiation for 10 minutes. The resulting clear yellow solution was subjected to vapour diffusion of diethyl ether affording Tb.**81**$_3$ as a white solid in 52% yield. HRMS (*m/z*) (MS-LD$^+$) Calculated for $C_{72}H_{98}F_6N_6O_{10}S_2Tb^+$ *m/z* = 1543.5944. Found *m/z* = 1543.5908; Elemental analysis for $C_{108}H_{147}N_9O_{15}F_9S_3Tb.5H_2O$ (2327.56 $gmol^{-1}$) Calculated: C 55.73, H 6.80, N 5.42. Found C 55.73, H 6.80, N 5.42%. IR(neat): 3282, 2925, 2854, 1634, 1596, 1558, 1457, 1240, 1197, 1164, 1030, 839, 801, 779, 752, 721 cm^{-1}.

*Synthesis of Sm.**81**$_3$:*

Ligand **81** (0.030 g, 0.05 mmol, 3 equiv.) in 5 mL CH_3OH had solid $Sm(CF_3SO_3)_3$ (0.011 g, 0.02 mmol, 1 equiv.) added and was heated at 70 °C under microwave irradiation for 10 minutes. The resulting clear yellow solution was subjected to vapour diffusion of diethyl ether affording Sm.**81**$_3$ as a white solid in 46% yield. HRMS (*m/z*) (MS-LD$^+$) Calculated for $C_{72}H_{98}F_6N_6O_{10}S_2Sm^+$ *m/z* = 1536.5887. Found *m/z* = 1536.5863; Elemental analysis for $C_{108}H_{147}N_9O_{15}F_9S_3Sm.H_2O$ (2246.95 $gmol^{-1}$) Calculated: C 57.73, H 6.68, N 5.61. Found C 57.45, H 6.40, N 5.83%. IR(neat): 3282, 2925, 2854, 1633, 1595, 1558, 1457, 1238, 1163, 1030, 838, 801, 779, 750 cm^{-1}.

*Synthesis of Lu.**81**$_3$:*

Ligand **81** (0.034 g, 0.06 mmol, 3 equiv.) in 5 mL CH_3OH had solid $Lu(CF_3SO_3)_3$ (0.013 g, 0.02 mmol, 1 equiv.) added and was heated at 70 °C under microwave irradiation for 10 minutes. The resulting clear yellow solution was subjected to vapour diffusion of diethyl ether affording Lu.**81**$_3$ as a white solid in 53% yield. HRMS (*m/z*) (MS-LD$^+$) Calculated for $C_{72}H_{98}F_6N_6O_{10}S_2Lu^+$ *m/z* = 1559.6098. Found *m/z* = 1559.6055; Elemental analysis for $C_{108}H_{147}N_9O_{15}F_9S_3Lu.3H_2O$ (2307.59 gmol^{-1}) Calculated: C 56.21, H 6.68, N 5.58. Found C 56.21, H 5.94, N 5.83%. IR(neat): 3277, 2925, 2854, 1638, 1598, 1561, 1461, 1240, 1199, 1163, 1030, 839, 801, 779, 757, 722 cm^{-1}.

*Synthesis of Dy.**81**$_3$:*

Ligand **81** (0.032 g, 0.06 mmol, 3 equiv.) in 5 mL CH_3OH had solid $Dy(CF_3SO_3)_3$ (0.018 g, 0.03 mmol, 1 equiv.) added and was heated at 70 °C under microwave irradiation for 10 minutes. The resulting clear yellow solutions was subjected to vapour diffusion of diethyl ether affording Dy.**81**$_3$ as a white solid in 36 % yield. HRMS (*m/z*) (MS-LD$^+$) Calculated for $C_{72}H_{98}F_6N_6O_{10}S_2Dy^+$ *m/z* = 1548.5982. Found *m/z* = 1548.5920; Elemental analysis for $C_{108}H_{147}N_9O_{15}F_9S_3Dy.5H_2O$ (2331.13 gmol^{-1}) Calculated: C 55.64, H 6.79, N 5.41. Found C 55.68, H 6.26, N 5.27%. IR(neat): 3277, 2925, 2854, 1635, 1596, 1562, 1460, 1240, 1164, 1030, 840, 800, 778, 755 cm^{-1}.

*Synthesis of Ln^{III} complexes Ln.**82**$_3$:*

*Synthesis of Eu.**82**$_3$:*

Ligand **82** (0.028 g, 0.05 mmol, 3 equiv.) in 5 mL CH_3OH had solid $Eu(CF_3SO_3)_3$ (0.010 g, 0.02 mmol, 1 equiv.) added and was heated at 70 °C under microwave irradiation for 10 minutes. The resulting clear yellow solution was subjected to vapour diffusion of diethyl ether affording Eu.**82**$_3$ as a white solid in 42% yield. HRMS (*m/z*) (MS-LD$^+$) Calculated for $C_{72}H_{98}F_6N_6O_{10}S_2Eu^+$ *m/z* = 1537.5903. Found *m/z* = 1537.5897; Elemental analysis for $C_{108}H_{147}N_9O_{15}F_9S_3Eu$ (2229.92 gmol^{-1}) Calculated: C 58.15, H 6.64, N 5.65. Found C 57.16, H 6.31, N 5.55%. IR(neat): 3274, 2924, 2854, 1634, 1595, 1558, 1457, 1241, 1197, 1163, 1030, 839, 801, 779, 752, 721 cm^{-1}.

*Synthesis of Nd.**82**$_3$:*

Ligand **82** (0.030 g, 0.06 mmol, 3 equiv.) in 5 mL CH_3OH had solid $Nd(CF_3SO_3)_3$ (0.011 g, 0.02 mmol, 1 equiv.) added and was heated at 70 °C under microwave irradiation for 10 minutes. The resulting clear yellow solution was subjected to vapour diffusion of diethyl ether affording Nd.**82**$_3$ as a white solid in 59% yield. HRMS (*m/z*) (MS-LD$^+$) Calculated for $C_{72}H_{98}F_6N_6O_{10}S_2Nd^+$ *m/z* = 1526.5767. Found *m/z* = 1526.5822; Elemental analysis for $C_{108}H_{147}N_9O_{15}F_9S_3Nd$ Calculated: C 58.41, H 6.68, N 5.68; Found C 58.94, H 6.67, N 5.74%. IR(neat): 3292, 2925, 2854, 1633, 1594, 1559, 1457, 1237, 1165, 1030, 800, 778, 752 cm^{-1}.

*Synthesis of Tb.**82**$_3$:*

Ligand **82** (0.028 g, 0.05 mmol, 3 equiv.) in 5 mL CH_3OH had solid $Tb(CF_3SO_3)_3$ (0.01 g, 0.02 mmol, 1 equiv.) added and was heated at 70 °C under microwave irradiation for 10 minutes. The resulting clear yellow solution was subjected to vapour diffusion of diethyl ether affording Tb.**82**$_3$ as a white solid in 71% yield. HRMS (*m/z*) (MS-LD$^+$) Calculated for $C_{72}H_{98}F_6N_6O_{10}S_2Tb^+$ *m/z* = 1543.5944. Found *m/z* = 1543.5914; Elemental analysis for $C_{108}H_{147}N_9O_{15}F_9S_3Tb.3H_2O$ (2291.55 $gmol^{-1}$) Calculated: C 56.61, H 6.73, N 5.50. Found C 56.47, H 6.23, N 5.39%. IR(neat): 3276, 2925, 2854, 1634, 1596, 1558, 1460, 1276, 1198, 1163, 1030, 839, 801, 779, 721 cm^{-1}.

*Synthesis of Sm.**82**$_3$:*

Ligand **82** (0.025 g, 0.05 mmol, 3 equiv.) in 5 mL CH_3OH had solid $Sm(CF_3SO_3)_3$ (0.009 g, 0.02 mmol, 1 equiv.) added and was heated at 70 °C under microwave irradiation for 10 minutes. The resulting clear yellow solution was subjected to vapour diffusion of diethyl ether affording Sm.**82**$_3$ as a white solid in 50% yield. HRMS (*m/z*) (MS-LD$^+$) Calculated for $C_{72}H_{98}F_6N_6O_{10}S_2Sm^+$ *m/z* = 1536.5887. Found *m/z* = 1536.5853; Elemental analysis for $C_{108}H_{147}N_9O_{15}F_9S_3Sm.$ (2228.925 $gmol^{-1}$) Calculated: C 58.14, H 6.65, N 5.65. Found C 58.79, H 6.95, N 5.55%. IR(neat): 3283, 2925, 2854, 1633, 1595, 1559, 1458, 1238, 1225, 1165, 1030, 839, 800, 778, 722 cm^{-1}.

*Synthesis of Lu.**82**$_3$:*

Ligand **82** (0.027 g, 0.05 mmol, 3 equiv.) in 5 mL CH_3OH had solid $Lu(CF_3SO_3)_3$ (0.009 g, 0.02 mmol, 1 equiv.) added and was heated at 70 °C under microwave irradiation for 10 minutes. The resulting clear yellow solution was subjected to vapour diffusion of diethyl

ether affording Lu.**82**$_3$ as a white solid in 52% yield. HRMS (*m/z*) (MS-LD$^+$) Calculated for $C_{72}H_{98}F_6N_6O_{10}S_2Lu^+$ *m/z* = 1559.6098. Found *m/z* = 1559.5941; Elemental analysis for $C_{108}H_{147}N_9O_{15}F_9S_3Lu.2H_2O$ (2251.94 gmol^{-1}) Calculated: C 56.64, H 6.65, N 5.50. Found C 56.38, H 6.21, N 5.41%. IR(neat): 3270, 2926, 2854, 1635, 1598, 1562, 1461, 1240, 1161, 1029, 917, 841, 800, 777, 723 cm^{-1}.

*Synthesis of Dy.**82**$_3$:*

Ligand **82** (0.025 g, 0.05 mmol, 3 equiv.) in 5 mL CH_3OH had solid $Dy(CF_3SO_3)_3$ (0.009 g, 0.02 mmol, 1 equiv.) added and was heated at 70 °C under microwave irradiation for 10 minutes. The resulting clear yellow solution was subjected to vapour diffusion of diethyl ether affording Dy.**82**$_3$ as a white solid in 50 % yield. HRMS (*m/z*) (MS-LD$^+$) Calculated for $C_{72}H_{98}F_6N_6O_{10}S_2Dy^+$ *m/z* = 1548.5982. Found *m/z* = 1548.6006; Elemental analysis for $C_{108}H_{147}N_9O_{15}F_9S_3Dy.3H_2O$ (2240.93 gmol^{-1}) Calculated: C 56.47, H 6.71, N 5.49. Found C 56.08, H 6.53, N 5.35%. IR(neat): 3275, 2925, 2854, 1634, 1596, 1562, 1460, 1240, 1163, 1030, 840, 800, 778, 755, 722 cm^{-1}.

6.11 Experimental details for Chapter Three

***2-(2-Methoxyethoxy)ethyl 4-methylbenzenesulfonate (90)*[280]**

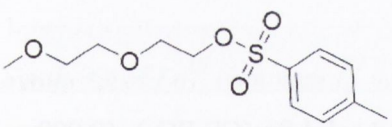

Diethylene glycol monomethyl ether (**89**) (10 g, 9.8 mL, 83.2 mmol, 1 equiv.) in THF (30 mL) was added to a solution of NaOH (4.9 g, 122.5 mmol, 1.5 equiv.) in H_2O (50 mL) at 0 °C. 4-toluenesulfonyl chloride (17.4 g, 9.3 mmol, 1.1 equiv.) was added to the solution and the mixture was allowed to reach RT. The solution was then left stirring for a further 72 hrs. The solvent was removed under reduced pressure yielding a white solid which was then redissolved in $CHCl_3$. The solution was washed with 1 M aq. NaOH and H_2O and then dried over $MgSO_4$. The solvent was removed under reduced pressure affording a colourless oil in 53% yield (12.26 g). HRMS (*m/z*) (ES$^+$) Calculated for $C_{12}H_{19}O_5S$ *m/z* = 275.0953 [M + H]$^+$. Found *m/z* = 275.0953. ^{1}H-NMR (400 MHz, $CDCl_3$) : δ_H 7.72 (2H, d, *J* = 8.2 Hz, Ar-H), 7.28 (2H, d, *J* = 8.0 Hz, Ar-H), 4.10 (2H, m, CH_2), 3.61 (2H, m, CH_2), 3.50 (2H, m, CH_2), 3.40 (2H, m, CH_2), 3.27 (3H, m, OCH_3) 2.37 (3H, s, CH_3); ^{13}C NMR (100 MHz, $CDCl_3$) δ_C: 144.38, 132.43, 129.37, 127.50, 71.31, 70.17, 68.79, 68.20, 58.56, 21.16.

***1-Iodo-2-(2-methoxyethoxy)ethane (91)*[280]**

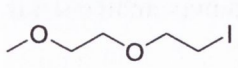

Compound **90** (9.47 g, 34.5 mmol, 1 equiv.) and NaI (7.24 g, 48.3 mmol, 1.4 equiv.) were refluxed in acetone (100 mL) for 16 hrs. The white precipitate which formed was removed by suction filtration and the solvent was removed under reduced pressure. The residue was redissolved in $CHCl_3$, washed with H_2O and brine and then dried over $MgSO_4$. The solvent was removed under reduced pressure yielding the pure product as a brown oil in 85% yield (6.75 g). HRMS (*m/z*) (ES^+) Calculated for $C_5H_{11}O_2INa$ *m/z* = 252.9702 $[M + Na]^+$. Found *m/z* = 252.9710. ^{1}H-NMR (400 MHz, $CDCl_3$) δ_H: 3.77 (2H, t, *J* = 6.8 Hz, C<u>H</u>$_2$,CH_2I), 3.67 (2H, m, CH_2), 3.57 (2H, m, C<u>H</u>$_2$$OCH_3$), 3.40 (3H, s, OCH_3) 3.28 (2H, t, *J* = 7.1 Hz, CH_2I); ^{13}C NMR (100 MHz, $CDCl_3$) δ_C: 71.56, 71.40, 69.63, 58.68, 2.31.

6-(Benzyloxycarbonyl)-4-hydroxypicolinic acid (93)

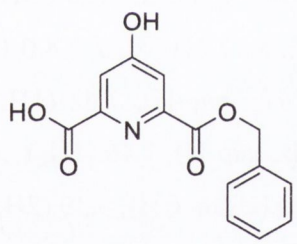

Chelidamic acid **92** (1 g, 5.46 mmol, 2 equiv.), $NaHCO_3$ (0.229 g, 2.73 mmol, 1 equiv.) and DMF (320 mL) were placed, with molecular sieves, under argon. To this, benzyl bromide (0.324 mL, 2.73 mmol, 1 equiv.) was added and the reaction mixture was stirred at 65 °C overnight. The reaction mixture was filtered through a plug of celite and the solvent was removed under reduced pressure. The yellow oil was dissolved in CH_3OH and had H_2O added, yielding a brown solid in 50% yield (746 mg). HRMS (*m/z*) (ES^+) Calculated for $C_{14}H_{11}NO_5Na$ *m/z* = 296.0535 $[M + Na]^+$. Found *m/z* = 296.0525. ^{1}H-NMR (400 MHz, DMSO-d_6) δ_H: 11.52 (1H, brs, OH), 7.59 (1H, d, *J* = 2.1 Hz, pyridine-H), 7.57 (1H, d, *J* = 2.1 Hz, pyridine-H), 7.49 (2H, d, *J* = 6.8 Hz, Ar-H), 7.44 – 7.37 (3H, m, Ar-H), 5.38 (2H, s, CH_2); ^{13}C NMR (100 MHz, DMSO-d_6) δ_C: 165.85, 165.68, 164.16, 150.47, 149.15, 135.78, 128.54, 128.37, 128.30, 115.20, 115.12, 66.80. IR(neat): 3319, 3032, 2687, 1719, 1611, 1575, 1497, 1454, 1381, 1341, 1237, 1160, 1140, 1105, 1028, 1000, 970, 949, 930, 888, 876, 824, 785, 750, 697 cm^{-1}.

(S)-Benzyl 4-hydroxy-6-(1-(naphthalen-1-yl)ethylcarbamoyl)picolinate (94)

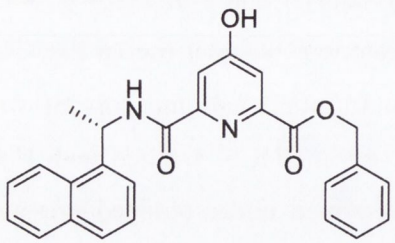

HOBt (0.24 g, 1.76 mmol, 1.00 equiv.) (*S*)-(-)-1-(1-naphthyl)ethylamine (0.28 mL, 1.76 mmol, 1.00 equiv.) and NEt_3 (0.26 mL, 1.85 mmol, 1.05 equiv.) were added to a solution of compound **93** (0.48 g, 1.76 mmol, 1.00 equiv.) in dry THF (30 mL) and placed under argon. The reaction mixture was cooled to 0 °C with stirring for 30 mins. EDCI·HCl (0.35 g, 1.85 mmol, 1.05 equiv.) was then added and the suspension was left stirring at 0 °C for a further 30 mins. The reaction mixture was then allowed to reach RT. Stirring was continued for another 48 hrs, leaving a yellow solution with a white solid residue. The insoluble residue was removed by suction filtration and THF was removed under reduced pressure to give the crude product as an orange oil. The impure product was taken up in CH_2Cl_2 and washed with 2.0 M HCl, sat. aq. $NaHCO_3$, H_2O and brine. The organic layer was then dried over $MgSO_4$ and the solvent was removed under reduced pressure yielding an orange oil in 97% yield (782 mg). HRMS (*m/z*) (ES^+) Calculated for $C_{26}H_{22}N_2O_4Na^+$ *m/z* = 449.1477 $[M + Na]^+$. Found *m/z* = 449.1476; ^1H NMR (600 MHz, $CDCl_3$) δ_H: 8.74 (1H, d, *J* = 8.0 Hz, NH), 8.13 (1H, s, pyridine-H), 8.12 (1H, d, *J* = 8.0 Hz, nap-H), 7.83 (1H, d, *J* = 8.0 Hz, nap-H), 7.75, (1H, d, *J* = 8.2 Hz, nap-H), 7.62 (1H, s, pyridine-H), 7.59 (1H, d, *J* = 7.2 Hz, nap-H), 7.51 (1h, t, *J* = 7.6 Hz, nap-H), 7.46 (1H, t, *J* = 7.5 Hz, nap-H), 7.44 – 7.36 (6H, m, benzyl-H x 5, nap-H x 1), 6.06 (1H, m, CH), 5.39 (2H, s, CH_2), 1.78 (3H, d, *J* = 6.8 Hz, CH_3); ^{13}C-NMR (150 MHz, $CDCl_3$) δ_C: 164.05, 162.87, 150.15, 148.93, 148.65, 137.86, 135.18, 133.87, 130.78, 128.85, 128.63, 128.50, 128.32, 128.23, 126.49, 125.72, 125.36, 122.92, 122.70, 116.12, 113.76, 67.68, 45.58, 21.33. IR(neat): 3062, 2928, 1720, 1655, 1599, 1574, 1524, 1438, 1381, 1349, 1228, 1180, 1157, 1111, 995, 887, 860, 799, 776, 736, 695 cm^{-1}.

(S)-Benzyl4-(2-(2-methoxyethoxy)ethoxy)-6-(1-(naphthalen-1-yl)ethylcarbamoyl) picolinate (96)

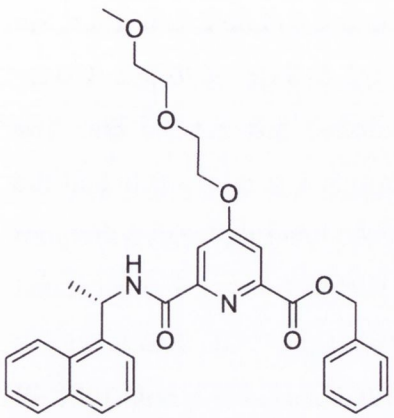

Compound **94** (0.5 g, 1.17 mmol, 1.1 equiv.) and K_2CO_3 (0.162 g, 1.17 mmol, 1.1 equiv.) were stirred in anhydrous DMF for 30 mins at 25 °C. 1-iodo-2-(2-methoxyethoxy)ethane (0.245 g, 1.07 mmol, 1 equiv.) was added and the reaction was stirred at 60 °C for 72 hrs. The solvent was removed under reduced pressure affording a brown oil which was redissolved in CH_2Cl_2 (60 mL) and washed with 1% acetic acid and H_2O and then dried over $MgSO_4$. The solvent was evaporated to dryness giving rise to an orange oil which was purified by silica column chromatography under gradient elution conditions (hexane/ethyl acetate) (40% yield, 248 mg). HRMS (*m/z*) (ES^+) Calculated for $C_{31}H_{32}N_2O6Na^+$ *m/z* = 551.2158 $[M + Na]^+$. Found *m/z* = 551.2164. ^{1}H-NMR (600 MHz, $CDCl_3$) δ_H: 8.62 (1H, d, *J* = 7.2 Hz, NH), 8.23 (1H, d, *J* = 8.5 Hz, nap-H), 7.94 (1H, d, *J* = 2.4 Hz, pyridine-H), 7.87 (1H, d, *J* = 8.1 Hz, nap-H), 7.80 (1H, d, *J* = 8.2 Hz, nap-H), 7.74 (1H, s, pyridine-H), 7.61 (1H, d, *J* = 7.1 Hz, nap-H), 7.54 (1H, t, *J* = 3.7 Hz, nap-H), 7.50 (1H, m, nap-H), 7.47 (1H, m, nap-H), 7.42 (2H, m, benzyl-H), 7.37 – 7.36 (3H, m, benzyl-H), 6.61 (1H, m, CH), 5.37 (2H, s, CH_2), 4.27 (2H, m, polyethyoxy-CH_2), 3.87 (2H, m, polyethyoxy-CH_2), 3.70 (2H, m, polyethyoxy-CH_2), 3.57 (2H, m, polyethyoxy-CH_2), 3.39 (2H, s, polyethyoxy-CH_3), 1.79 (3H, d, *J* = 6.8 Hz, CH_3); ^{13}C-NMR (150 MHz, $CDCl_3$) δ_C: 166.92, 163.99, 162.26, 151.92, 147.80, 138.28, 135.20, 133.74, 130.83, 128.64, 128.44, 128.41, 128.30, 128.25, 128.02, 128.00, 126.25, 125.54, 125.20, 123.10, 122.47, 114.88, 110.53, 71.70, 70.63, 68.91, 68.04, 67.27, 58.87, 44.82, 21.22. IR(neat): 3371, 3063, 2927, 2878, 1727, 1668, 1596, 1519, 1561, 1440, 1387, 1343, 1308, 1235, 1108, 1054, 1028, 996, 801, 779, 741, 698 cm^{-1}.

(S)-4-(2-(2-Methoxyethoxy)ethoxy)-6-(1-(naphthalen-1-yl)ethylcarbamoyl)picolinic acid (98)

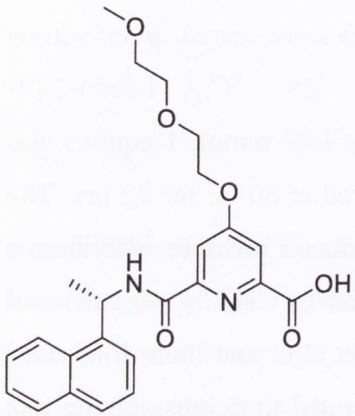

Pd/C (10%) (0.002 g, 0.01 mmol, 0.10 equiv.) was added to a solution of compound **96** (0.058 g, 0.11 mmol, 1.00 equiv.) in CH_3OH (30 mL) and placed on a Parr hydrogen shaker apparatus under 3 atm of hydrogen gas for 48 hrs. The reaction mixture was filtered through a plug of celite and the solvent was removed under reduced pressure to give the pure product in 84 % yield (41 mg). HRMS (*m/z*) (ES^-) Calculated for $C_{24}H26N_2O6^-$ *m/z* = 461.1689 $[M - Na]^-$. Found *m/z* = 461.1699; Elemental analysis for $C_{24}H_{26}N_2O_6.H_2O$ (456.49 $gmol^{-1}$) calc: C 63.15, H 6.18, N 6.14; found C 63.54, H 5.83, N 6.12%. ^1H NMR (400 MHz, DMSO-d_6) δ_H: 8.77 (1H, d, *J* = 8.5 Hz, NH), 8.19 (1H, d, *J* = 8.2 Hz nap-H), 7.96 (1H, d, *J* = 7.9 Hz, nap-H), 7.86 (1H, d, *J* = 8.0 Hz, nap-H), 7.67 (2H, m, nap-H, pyridine-H), 7.58 (1H, t, *J* = 6.8 Hz, nap-H), 7.56 – 7.51 (2H, m, nap-H, pyridine-H), 6.06 (1H, m, CH), 4.35 (2H, b, CH_2), 3.78 (2H, t, *J* = 3.8 Hz, CH_2) 3.59 (2H, t, *J* = 4.4 Hz, CH_2), 3.45 (2H, t, *J* = 4.7 Hz, CH_2), 3.23 (3H, s, CH_3), 1.70 (3H, d, *J* = 6.7 Hz, CH_3); ^{13}C NMR (100 MHz , DMSO-d_6) δ_C: 167.16, 166.73, 162.14, 152.07, 148.39, 139.41, 133.37, 130.39, 128.71, 127.56, 126.34, 125.66, 125.48, 123.01, 122.67, 111.10, 113.85, 71.22, 69.71, 68.44, 68.24, 58.03, 21.24. IR(neat): 3286, 2926, 1751, 1645, 1595, 1523, 1443, 1348, 1240, 1179, 1107, 1053, 997, 938, 878, 801, 777, 737, 697 cm^{-1}.

N2,N2'-(1,3-Phenylenebis(methylene))bis(4-(2-(2-methoxyethoxy)ethoxy)-N6-((S)-1-(naphthalen-1-yl)ethyl)pyridine-2,6-dicarboxamide) (87)

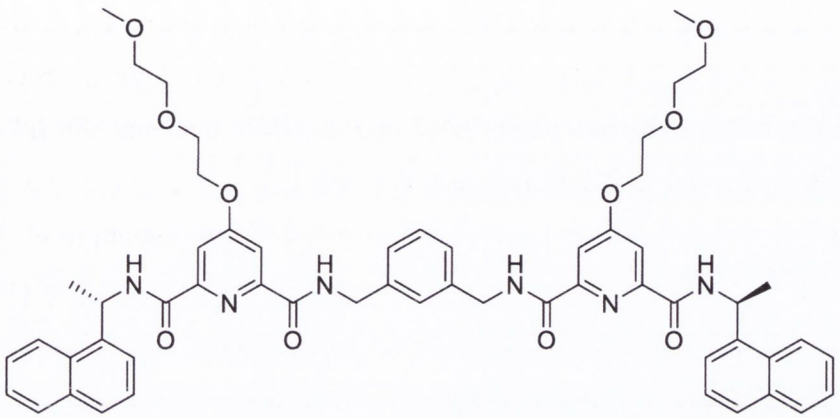

HOBt (0.055 g, 0.41 mmol, 2.10 equiv.), 1,3-phenylene dimethanamine (0.025 mL, 0.19 mmol, 1.00 equiv.), DMAP (0.025 g, 0.20 mmol, 1.05 equiv.) and NEt_3 (0.057 mL, 0.41 mmol, 2.1 equiv.) were added to a solution of compound **96** (0.17 g, 0.39 mmol, 2.00 equiv.) in dry THF (30 mL) and placed under argon. The reaction mixture was cooled to 0 °C with stirring for 30 mins. EDCI·HCl (0.117 g, 0.61 mmol, 3.1 equiv.) was then added and the suspension was left stirring at 0 °C for a further 30 mins. The reaction mixture was then allowed to reach RT. Stirring was continued for another 48 hrs. The insoluble residue was removed by suction filtration and THF was removed under reduced pressure to give the crude product as an orange oil. The impure product was taken up in CH_2Cl_2 and washed with 2.0 M HCl, sat. aq. $NaHCO_3$, H_2O and brine. The organic layer was then dried over $MgSO_4$ and the solvent was removed under reduced pressure yielding a brown fluffy solid. The solid was redisssolved in CH_2Cl_2 and precipitated out of diethyl ether which was then filtered, giving **87** as a white solid in 45% yield (171 mg). m.p. 135 – 138 °C HRMS (*m/z*) (ES^+) Calculated for $C_{56}H_{60}N_6O_{10}Na^+$ *m/z* = 999.4269 $[M + Na]^+$. Found *m/z* = 999.4273; Elemental analysis for $C_{56}H_{60}N_6O_{10}$.NaCl (1034.40 $gmol^{-1}$) calc: C 64.95, H 5.84, N 8.12; found C 64.83, H 5.78, N 7.81%. ^1H NMR (600 MHz, CD_3CN) δ_H: 8.98 (2H, t, J = 6.2 Hz, NH), 8.85 (2H, d, J = 8.3 Hz, NH), 8.17 (2H, d, J = 8.5 Hz, nap-H), 7.85 (2H, d, J = 8.0 Hz, nap-H), 7.72 (2H, d, J = 7.8 Hz, nap-H), 7.65 (2H, d, J = 2.5 Hz, pyridine-H), 7.58 (2H, d, J = 6.5 Hz nap-H) 7.55 (2H, d, J = 2.4 Hz, pyridine-H), 7.54 (2H, t, J = 7.3 Hz, nap-H), 7.49 (2H, t, J = 7.7 Hz, nap-H), 7.43 (2H, t, J = 7.7 Hz, nap-H), 7.16 (1H, t, J = 7.5 Hz, phenyl-H), 7.07 (3H, m, phenyl-H), 6.01 (2H, m, CH), 4.41 (4H, d, J = 5.8 Hz, N-CH_2), 4.07 (4H, t, J = 4.2 Hz, CH_2), 3.71 (2H, m, CH_2), 3.66 (2H, m, CH_2), 3.57 (4H, m, CH_2), 3.46 (4H, t, J = 4.8 Hz, CH_2), 3.28 (6H, s, CH_3), 1.64 (6H, d, J = 6.8 Hz, CH_3); ^{13}C NMR (150 MHz , CD_3CN, δ_C) 168.31,

164.63, 163.47, 151.78, 151.70, 140.24, 134.68, 131.84, 129.68, 129.42, 128.67, 127.25, 126.64, 126.39, 126.03, 124.10, 123.97, 111.76, 111.62, 72.47, 71.13, 69.59, 69.14, 58.87, 45.96, 43.22, 21.38. IR(neat): 3300, 2932, 1657, 1599, 1519, 1439, 1398, 1344, 1309, 1239, 1109, 882, 801, 778, 693 cm^{-1}.

N2,N2'-(1,3-Phenylenebis(methylene))bis(4-(2-(2-methoxyethoxy)ethoxy)-N6-((R)-1-(naphthalen-1-yl)ethyl)pyridine-2,6-dicarboxamide) (88)

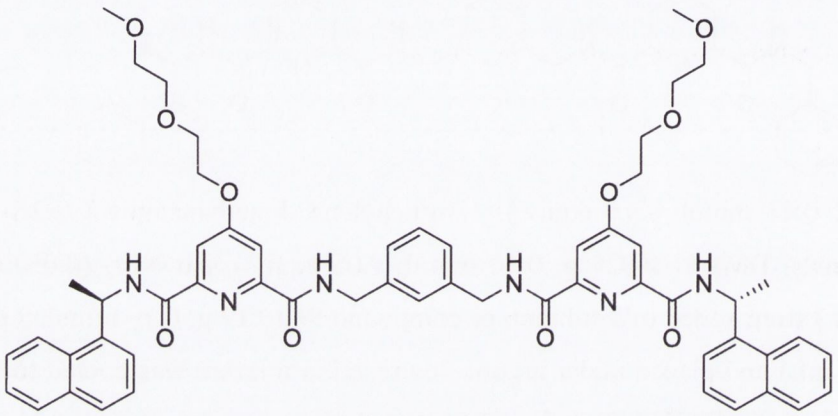

HOBt (0.055 g, 0.41 mmol, 2.10 equiv.), 1,3-phenylene dimethanamine (0.025 mL, 0.19 mmol, 1.00 equiv.), DMAP (0.025 g, 0.20 mmol, 1.05 equiv.) and NEt_3 (0.057 mL, 0.41 mmol, 2.1 equiv.) were added to a solution of compound **99** (0.17 g, 0.39 mmol, 2.00 equiv.) in dry THF (30 mL) and placed under argon. The reaction mixture was cooled to 0 °C with stirring for 30 mins. EDCI·HCl (0.117 g, 0.61 mmol, 3.1 equiv.) was then added and the suspension was left stirring at 0 °C for a further 30 mins. The reaction mixture was then allowed to reach RT. Stirring was continued for another 48 hrs. The insoluble residue was removed by suction filtration and THF was removed under reduced pressure to give the crude product as an orange oil. The impure product was taken up in CH_2Cl_2 and washed with 2.0 M HCl, sat. aq. $NaHCO_3$, H_2O and brine. The organic layer was then dried over $MgSO_4$ and the solvent was removed under reduced pressure yielding a brown fluffy solid. The solid was redisssolved in CH_2Cl_2 and precipitated out of diethyl ether which was then filtered, giving **88** as a white solid in 30% yield (114 mg). m.p. 136 – 142 °C. HRMS (*m/z*) (ES^+) Calculated for $C_{56}H_{60}N_6O_{10}Na^+$ *m/z* = 999.4269 $[M + Na]^+$. Found *m/z* = 999.4296; Elemental analysis for $C_{56}H_{60}N_6O_{10}.H_2O$ (995.13 $gmol^{-1}$) calc: C 67.59, H 6.28, N 8.45; found C 67.42, H 5.98, N 8.36%. ^1H NMR (600 MHz, DMSO-d_6) δ_H: 9.84 (2H, t, *J* = 6.3 Hz, NH), 9.43 (2H, d, *J* = 8.6 Hz, NH), 8.21 (2H, d, *J* = 8.5 Hz, nap-H), 7.94 (2H, d, *J* = 8.0 Hz, nap-H), 7.83 (2H, d, *J* = 8.1 Hz, nap-H), 7.65 – 7.51 (12H, m, 4 x pyridine-H, 8 x nap-H), 7.33 (1H, t, *J* = 7.6 Hz,

phenyl-H), 7.24 (3H, m, phenyl-H), 6.03 (2H, m, CH), 4.62 (4H, d, J = 6.3 Hz, N-CH_2), 4.22 (4H, m, CH_2), 3.73 (2H, m, CH_2), 3.67 (2H, m, CH_2), 3.54 (4H, m, CH_2), 3.42 (4H, t, J = 4.7 Hz, CH_2), 3.21 (6H, s, CH_3), 1.68 (6H, d, J = 6.9 Hz, CH_3); ^{13}C NMR (100 MHz , DMSO-d_6) δ_C: 167.19, 163.63, 162.41, 151.20, 151.05, 140.08, 139.78, 133.70, 130.68, 129.03, 128.81, 127.82, 126.63, 125.97, 125.73, 125.70, 125.23, 123.42, 123.06, 110.93, 110.86, 71.60, 70.09, 68.79, 68.24, 58.39, 45.06, 42.46, 21.88. IR(neat): 3305, 2878, 1655, 1599, 1517, 1438, 1398, 1343, 1308, 1238, 1108, 882, 800, 777, 693 cm^{-1}.

Synthesis of Eu^{III} complexes $Eu_2.\mathbf{L}_3$:

Synthesis of $Eu_2.\mathbf{87}_3$

Ligand **87** (0.026 g, 0.03 mmol, 3 equiv.) in 5 mL CH_3OH had solid $Eu(CF_3SO_3)_3$ (0.011 g, 0.02 mmol, 2 equiv.) added and was heated at 70 °C under microwave irradiation for 10 minutes. The resulting clear yellow solution was subjected to vapour diffusion of diethyl ether affording $Eu_2.\mathbf{87}_3$ as a white solid in 78% yield. Elemental analysis for $C_{174}H_{180}N_{18}O_{48}F_{18}S_6Eu_2.\ 3H_2O$ (4183.72 $gmol^{-1}$) Calculated: C 49.95, H 4.48, N 6.03. Found C 49.88, H 4.38, N 6.01%. IR(neat): 3267, 1629, 1598, 1555, 1446, 1282, 1240, 1157, 1056, 1029, 780 cm^{-1}.

Synthesis of $Eu_2.\mathbf{88}_3$

Ligand **88** (0.020 g, 0.021 mmol, 3 equiv.) in 4 mL CH_3OH had solid $Eu(CF_3SO_3)_3$ (0.008 g, 0.014 mmol, 2 equiv.) added and was heated at 70 °C under microwave irradiation for 10 minutes. The resulting clear yellow solution was subjected to vapour diffusion of diethyl ether affording $Eu_2.\mathbf{88}_3$ as a white solid in 71% yield. Elemental analysis for $C_{174}H_{180}N_{18}O_{48}F_{18}S_6Eu_2.$ (4129.67 $gmol^{-1}$) Calculated: C 50.61, H 4.39, N 6.11. Found C 50.31, H 4.29, N 6.05%. IR(neat): 3276, 1623, 1598, 1555, 1447, 1279, 1240, 1156, 1056, 1028, 779 cm^{-1}.

6.12 Experimental details for Chapter Four

(S)-N2-(1-(Naphthalen-1-yl)ethyl)-N6-(2-(pyridin-4-yl)ethyl)pyridine-2,6-dicarboxamide (110)

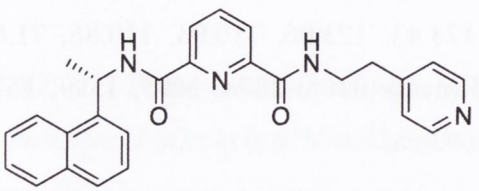

4-(2-Aminoethyl)pyridine (0.09 mL, 0.78 mmol, 1 equiv.) and NEt_3 (0.11 mL, 0.8 mmol, 1.05 equiv.) were added to a solution of compound **79** (0.25 g, 0.78 mmol, 1 equiv.) in dry THF (20 mL) and placed under argon. The reaction mixture was cooled to 0 °C with stirring for 30 mins. EDCI·HCl (0.22 g, 1.2 mmol, 1.5 equiv.) was then added and the suspension was left stirring at 0 °C for a further 30 mins. The reaction mixture was then allowed to reach RT. Stirring was continued for another 72 hrs. THF was removed under reduced pressure yielding the crude product as a brown oil. The impure product was taken up in CH_2Cl_2 and washed with 0.05 M HCl, sat. aq. $NaHCO_3$, H_2O and brine. The organic layer was then dried over $MgSO_4$ and the solvent was removed under reduced pressure affording a yellow oil which was purified by silica chromatography (CH_2Cl_2:CH_3OH), yielding **110** as a white solid in 33% yield (109 mg). m.p. 88 – 89 °C HRMS (*m/z*) (ES^+) Calculated for $C_{26}H_{25}N_4O_2$ *m/z* = 425.1978 $[M + H]^+$. Found *m/z* = 425.1973. Elemental analysis for $C_{26}H_{24}N_4O_2.0.5NaHCO_3$ (466.50 $gmol^{-1}$) calc: C 68.23, H 5.29, N 12.01; found C 68.19, H 5.57, N 11.91%. ^{1}H-NMR (600 MHz, DMSO-d_6) δ_H: 9.47 (1H, t, *J* = 7.7 Hz, NH), 9.44 (1H, d, *J* = 8.2 Hz, NH), 8.44 (2H, s, pyridine-H), 8.24 - 8.21 (3H, m, pyridine-H (x2), nap-H), 8.17 (1H, t, *J* = 7.6 Hz, pyridine-H), 7.97 (1H, d, *J* = 8.0 Hz, nap-H), 7.87 (1H, d, *J* = 8.3 Hz), 7.68 (1H, d, *J* = 7.0 Hz, nap-H), 7.60 (1H, t, *J* = 8.2 Hz, nap-H), 7.56 – 7.53 (2H, m, nap-H), 7.29 (2H, d, *J* = 4.0 Hz, pyridine-H), 6.07 (1H, m, CH), 3.66 (2H, m, CH_2), 2.95 (2H, t, *J* = 8.3 Hz, CH_2), 1.74 (3H, d, *J* = 6.6 Hz); ^{13}C NMR (150 MHz, DMSO-d_6) δ_C: 163.31 , 162.38, 149.46, 148.89, 148.15, 139.62, 139.43, 133.41, 130.42, 128.72, 127.54, 126.32, 125.66, 125.43, 124.68, 124.48, 124.25, 123.11, 122.69, 44.70, 39.5, 34.32, 21.47. IR(neat): 3299, 3053, 2933, 1655, 1601, 1523, 1444, 1417, 1370, 1312, 1237, 1172, 1118, 1073, 999, 845, 801, 778, 747, 679 cm^{-1}.

(R)-N2-(1-(Naphthalen-1-yl)ethyl)-N6-(2-(pyridin-4-yl)ethyl)pyridine-2,6-dicarboxamide (111)

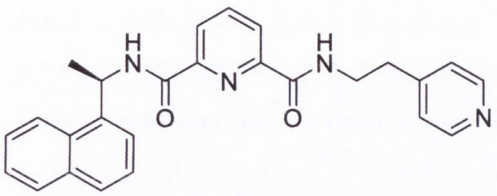

4-(2-Aminoethyl)pyridine (0.1 mL, 0.81 mmol, 1 equiv.) and NEt_3 (0.12 mL, 0.85 mmol, 1.05 equiv.) were added to a solution of compound **80** (0.26 g, 0.81 mmol, 1 equiv.) in dry THF (20 mL) and placed under argon. The reaction mixture was cooled to 0 °C with stirring for 30 mins. EDCI·HCl (0.23 g, 1.2 mmol, 1.5 equiv.) was then added and the suspension was left stirring at 0 °C for a further 30 mins. The reaction mixture was then allowed to reach RT. Stirring was continued for another 72 hrs. THF was removed under reduced pressure yielding the crude product as a brown oil. The impure product was redissolved in CH_2Cl_2 and washed with 0.05 M HCl, sat. aq. $NaHCO_3$, H_2O and brine. The organic layer was then dried over $MgSO_4$ and the solvent was removed under reduced pressure affording a yellow oil which was purified by silica chromatography (CH_2Cl_2:CH_3OH), yielding **111** as a white solid in 43% yield (148 mg). m.p. 88 – 89 °C. HRMS (*m/z*) (ES^+) Calculated for $C_{26}H_{25}N_4O_2$ *m/z* = 423.1821 $[M - H]^+$. Found *m/z* = 423.1829. Elemental analysis for $C_{26}H_{24}N_4O_2.CH_2Cl_2$ ($509.43 gmol^{-1}$)) calc: C 63.66, H 5.14, N 11.00; found C 63.95, H 5.18, N 11.02%. ^{1}H-NMR (600 MHz, DMSO-d_6, 298 K): δ_H 9.47 (1H, t, *J* = 7.6 Hz, NH), 9.44 (1H, d, *J* = 8.4 Hz, NH), 8.44 (2H, s, pyridine-H), 8.24 - 8.16 (4H, m, pyridine-H (x3), nap-H), 7.97 (1H, d, *J* = 8.0 Hz, nap-H), 7.87 (1H, d, *J* = 8.0 Hz), 7.67 (1H, d, *J* = 7.0 Hz, nap-H), 7.60 (1H, t, *J* = 8.4 Hz, nap-H), 7.56 – 7.53 (2H, m, nap-H), 7.28 (2H, d, *J* = 4.8 Hz, pyridine-H), 6.07 (1H, m, CH), 3.66 (2H, m, CH_2), 2.95 (2H, t, *J* = 8.4 Hz, CH_2), 1.74 (3H, d, *J* = 7.0 Hz); ^{13}C NMR (150 MHz, DMSO-d_6) 163.65, 162.71, 149.79, 149.18, 149.03, 148.47, 139.95, 139.77, 133.74, 130.75, 129.06, 127.87, 126.66, 126.00, 125.77, 125.02, 124.81, 124.54, 123.44, 123.02, 45.04, 39.82, 34.65, 21.80. IR(neat): 3295, 3053, 2931, 1654, 1601, 1522, 1443, 1416, 1371, 1312, 1237, 1172, 1118, 1073, 999, 844, 801, 777, 747, 676 cm^{-1}.

(S)-1-Methyl-4-(2-(6-(1-(naphthalen-1-yl)ethylcarbamoyl)picolinamido)ethyl)pyridinium tetrafluoroborate (100)

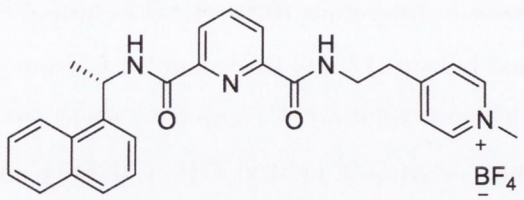

Compound **110** (0.1 g, 0.2 mmol, 1 equiv.) in dry CH_2Cl_2 (30 mL) was placed under argon. Trimethyloxonium tetrafluoroborate (0.04 g, 1.3 equiv.) was added and the reaction mixture was stirred at RT for 72 hrs. The reaction mixture was then quenched using CH_3OH (5 mL) and subjected to diethyl ether diffusion, after which the pure product **100** precipitated from solution as an off white solid in 79% yield (83 mg). m.p. 127 – 128 °C HRMS (*m/z*) (ES^+) Calculated for $C_{27}H_{27}N_4O_2$ *m/z* = 439.2134 $[M]^+$. Found *m/z* = 439.2138. Elemental analysis for $C_{27}H_{27}BF_4N_4O_2.0.5CH_2Cl_2$ (568.80 $gmol^{-1}$) calc: C 58.07, H 4.96, N 9.85; found C 58.42, H 5.01, N 10.02%. ^{1}H-NMR (600 MHz, DMSO-d_6) δ_H: 9.49 (1H, t, *J* = 7.4 Hz, NH), 9.39 (1H, d, *J* = 8.4 Hz, NH), 8.82 (2H, d, *J* = 6.5 pyridine-H), 8.25 – 8.23 (2H, m, pyridine-H (x1), nap-H (x1)), 8.18 – 8.17 (2H, m, pyridine-H (x2)), 8.03 (2H, d, *J* = 6.5 Hz, pyridine-H (x2)), 7.98 (1H, d, *J* = 8.1 Hz, nap-H), 7.88 (1H, d, *J* = 8.1 Hz, nap-H), 7.68 (1H, d, *J* = 7.1 Hz nap-H), 7.60 (1H, t, *J* = 8.1 Hz, nap-H), 7.57 (1H, m, nap-H), 7.53 (1H, m, nap-H), 6.07 (1H, m, CH), 4.27 (3H, s, CH_3), 3.82 (1H, m, CH_2), 3.75 (1H, m, CH_2), 3.24 (2H, t, *J* = 7.8 Hz, CH_2), 1.75 (3H, d, *J* = 7.1 Hz, CH_3); ^{13}C NMR (100 MHz, DMSO-d_6) δ_C: 163.54, 162.36, 159.09, 148.73, 148.63, 144.68, 139.50, 139.45, 133.42, 130.45, 128.74, 127.69, 127.60, 126.37, 125.71, 125.42, 124.84, 124.54, 123.12, 122.66, 47.20, 44.71, 38.35, 34.86, 21.40; IR(neat): 3367, 3061, 1648, 1522, 1444, 1377, 1310, 1239, 1187, 1050, 999, 844, 804, 781, 755, 670 cm^{-1}.

(R)-1-Methyl-4-(2-(6-(1-(naphthalen-1-yl)ethylcarbamoyl)picolinamido)ethyl)pyridinium tetrafluoroborate (101)

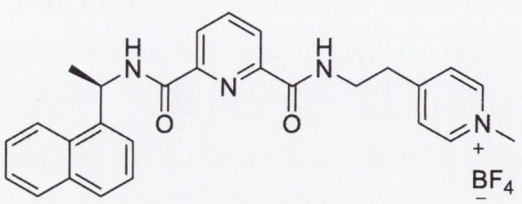

Compound **111** (0.08 g, 0.2 mmol, 1 equiv.) in dry CH_2Cl_2 (25 mL) was placed under argon. Trimethyloxonium tetrafluoroborate (0.04 g, 1.3 equiv.) was added and the reaction stirred at RT for 72 hrs. The reaction mixture was then quenched using CH_3OH (5 mL) and subjected to diethyl ether diffusion, after which the pure product **101** precipitated from solution as an off white solid in 85% yield (90 mg). m.p. 127 – 128 °C HRMS (*m/z*) (ES^+) Calculated for $C_{27}H_{27}N_4O_2$ *m/z* = 439.2134 $[M]^+$. Found *m/z* = 439.2132. Elemental analysis for $C_{27}H_{27}BF_4N_4O_2.0.5CH_2Cl_2$ (568.80 $gmol^{-1}$) calc: C 58.07,

H 4.96, N 9.85; found C 58.35, H 4.90, N 9.88%. ^{1}H-NMR (600 MHz, DMSO-d_6) δ_H: 9.50 (1H, t, J = 7.2 Hz, NH), 9.40 (1H, d, J = 8.3 Hz, NH), 8.82 (2H, d, J = 6.3, pyridine-H), 8.25 – 8.23 (2H, m, pyridine-H (x1), nap-H (x1)), 8.18 – 8.17 (2H, m, pyridine-H (x2)), 8.03 (2H, d, J = 6.5 Hz, pyridine-H (x2)), 7.98 (1H, d, J = 8.1 Hz, nap-H), 7.88 (1H, d, J = 8.1 Hz, nap-H), 7.68 (1H, d, J = 7.2 Hz nap-H), 7.60 (1H, t, J = 8.3 Hz, nap-H), 7.56 (1H, m, nap-H), 7.54 (1H, m, nap-H), 6.07 (1H, m, CH), 4.27 (3H, s, CH_3), 3.82 (1H, m, CH_2), 3.75 (1H, m, CH_2), 3.24 (2H, t, J = 7.9 Hz, CH_2), 1.74 (3H, d, J = 7.0 Hz, CH_3); ^{13}C NMR (100 MHz, DMSO-d_6) δ_C: 163.92, 162.74, 159.45, 149.09, 148.97, 145.04, 139.84, 139.82, 133.75, 130.78, 129.07, 128.02, 127.92, 126.70, 126.04, 125.76, 125.18, 124.88, 123.45, 123.00, 47.54, 45.06, 38.71, 35.23, 21.71; IR(neat): 3365, 3061, 1648, 1521, 1444, 1377, 1310, 1239, 1187, 1050, 999, 842, 805, 781, 754, 669 cm^{-1}.

2,2';6',2''-Terpyridine((S)-N2-(1-(naphthalen-1-yl)ethyl)-N6-(2-(pyridin-4-yl)ethyl) pyridine-2,6-dicarboxamide)platinum(II) nitrate complex (108)[299,303]

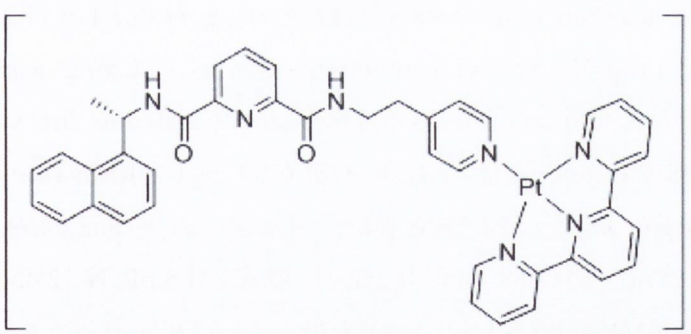

Compound **112** (0.06 g, 0.14 mmol, 1 equiv.) and $AgNO_3$ (0.04 g, 0.2 mmol, 2 equiv.) were stirred under darkness in DMF (20 mL) for 90 mins. A white AgCl precipitate formed, which was removed by suction filtration. A solution of compound **110** (0.06 g, 0.14 mmol, 1.2 equiv.) in DMF (5 mL) was added dropwise to the reaction mixture and stirring was continued at RT for 2 hrs. The reaction mixture was filtered and then slowly added to diethyl ether affording the pure product **108** as a yellow solid in 78% yield (107 mg). HRMS (*m/z*) (MALDI+) Calculated for $C_{41}H_{35}N_7O_2Pt$ *m/z* = 852.2500 $[M]^{2+}$. Found *m/z* = 852.2483. Elemental analysis for $C_{41}H_{35}N_9O_8Pt.2H_2O$ (1012.88 gmol^{-1}) calc: C 48.62, H 3.88, N 12.45; found C 48.53, H 3.82, N 12.78%. ^{1}H NMR (400 MHz, CD_3OD-d_4) δ_H: 8.91 (2H, d, J = 6.1 Hz, pyridine-H), 8.64 – 8.56 (5H, m, terpy-H), 8.45 (2H, t, J = 7.2 Hz, terpy-H), 8.35 (1H, d, J = 7.8 Hz, pyridine-H), 8.23 – 8.14 (3H, m, pyridine-H (x2), nap-H (x1)), 7.82 – 7.73 (9H, m, nap-H (x3), pyridine-H (x2), terpy-H (x4)), 7.57 – 7.49 (2H, m, nap-H (x2)), 7.44 (1H, t, J = 7.6 Hz, nap-H), 6.15 (1H, m, CH), 3.89 (2H, m, CH_2), 3.25 (2H, m, CH_2), 1.81 (3H, d, J = 6.5 Hz, CH_3); ^{13}C NMR (100 MHz, CD_3OD-d_4) δ_C: 166.24, 164.86, 159.66, 157.52, 156.84,

152.98, 152.58, 150.44, 150.30, 144.94, 144.30, 140.60, 140.11, 135.35, 132.35, 130.50, 130.24, 129.92, 129.11, 127.42, 127.09, 126.83, 126.67, 126.34, 125.90, 125.40, 124.26, 123.93, 46.48, 40.63, 36.59, 21.30. IR(neat): 3293, 3083, 1662, 1625, 1535, 1479, 1369, 1327, 1256, 1187, 1092, 1078, 1060, 1034, 998, 848, 824, 811, 776, 724, 676 cm^{-1}.

2,2';6',2''-Terpyridine((R)-N2-(1-(naphthalen-1-yl)ethyl)-N6-(2-(pyridin-4-yl)ethyl) pyridine-2,6-dicarboxamide)platinum(II) nitrate complex (109)[299,303]

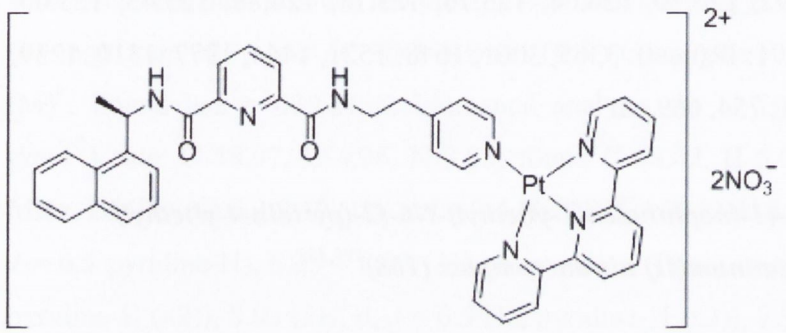

Compound **112** (0.09 g, 0.2 mmol, 1 equiv.) and $AgNO_3$ (0.06 g, 0.3 mmol, 2 equiv.) were stirred under darkness in DMF (20 mL) for 90 mins. A white AgCl precipitate formed, which was removed by suction filtration. A solution of compound **111** (0.06 g, 0.2 mmol, 1.2 equiv.) in DMF (5 mL) was added dropwise to the reaction mixture and stirring was continued at RT for 2 hrs. The reaction mixture was filtered and then slowly added to diethyl ether affording thepure product **109** as a yellow solid in 71% yield (139 mg). HRMS (*m/z*) (MALDI+) Calculated for $C_{41}H_{35}N_7O_2Pt$ *m/z* = 852.2500 $[M]^{2+}$. Found *m/z* = 852.2469. Elemental analysis for $C_{41}H_{35}N_9O_8Pt.2H_2O$ (1012.88 $gmol^{-1}$) calc: C 48.62, H 3.88, N 12.45; found C 48.66, H 3.97, N 12.83%. ^1H NMR (600 MHz, CD_3OD-d_4) δ_H: 8.92 (2H, d, J = 6.5 Hz, pyridine-H), 8.63 – 8.60 (1H, m, terpy-H), 8.57 – 8.54 (4H, m, terpy-H), 8.42 (2H, t, J = 8.1 Hz, terpy-H), 8.32 (1H, d, J = 8.1 Hz, pyridine-H), 8.22 (1H, d, J = 6.9 Hz, pyridine-H), 8.18 – 8.14 (2H, m, nap-H (x1), pyridine (x1), 7.82 – 7.79 (5H, m, nap-H (x1), terpy-H (x2), pyridine-H (x2)), 7.74 – 7.71 (4H, m, nap-H (x2), terpy-H (x2)), 7.53 (1H, t, J = 8.3 Hz, nap-H), 7.50 (1H, t, J = 8.1 Hz, nap-H), 7.43 (1H, t, J = 8.0 Hz, nap-H), 6.13 (1H, m, CH), 3.92 (1H, m, CH_2), 3.88 (1H, m, CH_2), 3.26 (2H, m, CH_2), 1.80 (3H, d, J = 7.0 Hz, CH_3); ^{13}C NMR (150 MHz, CD_3OD-d_4) δ_C: 164.70, 163.31, 158.07, 156.00, 1555.24, 151.42, 151.02, 148.90, 148.76, 143.37, 142.73, 139.01, 138.61, 133.79, 130.77, 128.95, 128.68, 128.36, 127.52, 125.84, 125.53, 125.26, 125.13, 124.76, 124.34, 123.84, 122.70, 122.39, 44.95, 39.06, 35.00, 19.78; IR(neat): 3292, 3083, 1662, 1626, 1536, 1479, 1370, 1327, 1257, 1187, 1092, 1079, 1060, 1034, 998, 848, 824, 811, 777, 724, 677 cm^{-1}.

6.13 Experimental details for Chapter Five

S-12-Bromododecyl ethanethioate / Thioacetic Acid S-(12-bromododecyl) Ester (126)[322]

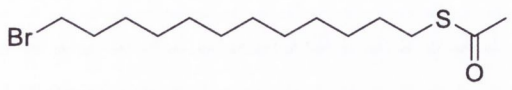

1,12-dibromododecane **125** (8 g, 24.4 mmol) and potassium thioacetate (0.93g, 8.1 mmol) were dissolved in CH_3CN (120 mL) and the mixture was heated under reflux for 48 hrs. The reaction mixture was poured into H_2O (150 mL) and extracted with diethyl ether. The organic layers were combined and washed with H_2O, dried over $MgSO_4$, and evaporated to dryness. Silica flash chromatography using hexane/ethyl acetate (0 – 3%) as the eluant yielded the desired compound **126** as an off white solid (32%, 2.52 g). ^{1}H-NMR (400 MHz, $CDCl_3$, 298 K): δ_H 3.38 (2H, t, J = 7.7 Hz, CH_2Br), 2.84 (2H, t, J = 7.7 Hz, CH_2S), 2.30 (3H, s, $COCH_3$), 1.83 (2H, q, J = 7.7 Hz, $\underline{CH_2}CH_2Br$), 1.57 – 1.24 (18H, m, 9 x CH_2); ^{13}C NMR (100 MHz, $CDCl_3$) δ_C: 34.02, 32.80, 30.61, 29.46, 29.44, 29.40, 29.37, 29.12, 29.06, 28.77, 28.72, 28.14. IR(neat): 2914, 2849, 1683, 1467, 1112, 958, 717 cm^{-1}.

Diethyl 4-hydroxypyridine-2,6-dicarboxylate (124)[176]

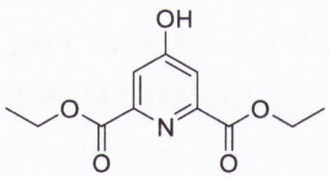

H_2SO_4 (30%) (6.25 mL, 75.20 mmol) was added to chelidamic acid **124** (3 g, 16.39 mmol) in EtOH (60 mL) and refluxed for 4 hrs. The solvent was removed under reduced pressure yielding an oily residue which was then placed in H_2O. The reaction mixture was neutralised using $NaHCO_3$ and the diester extracted into CH_2Cl_2. The organic layer was dried over $MgSO_4$ and the solvent was removed *in vacuo* yielding the pure product as a white solid in 62% yield. HRMS (*m/z*) (ES^+) Calculated for $C_{11}H_{14}NO5$ *m/z* = 240.0872 $[M + H]^+$. Found *m/z* = 240.0872. ^{1}H-NMR (400 MHz, $CDCl_3$) δ_H: 7.31 (2H, s, 2 x pyridine-H), 4.43 (4H, q, J = 7.8 Hz, 2 x CH_2), 1.39 (6H, t, J = 7.5 Hz, 2 x CH_3); ^{13}C NMR (100 MHz, $CDCl_3$,) δ_C: 162.37, 119.05, 63.16, 14.04.

Diethyl 4-(12-(acetylthio)dodecyloxy)pyridine-2,6-dicarboxylate (127)

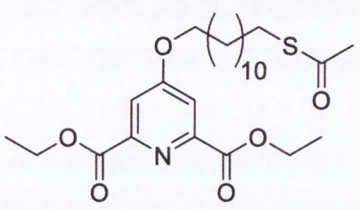

Compound **124** (0.30 g, 1.3 mmol, 1 equiv.) and dry K_2CO_3 (0.35 g, 2.5 mmol, 2 equiv.) were stirred in dry DMF (30 mL) for 30 mins at 25 °C. Compound **126** (0.61 g, 1.8 mmol) and KI (0.03 g) were added and the reaction was heated at 60 °C for 6 days under argon. The solvent was removed under reduced pressure yielding a brown solid which was redissolved in CH_2Cl_2, washed with 1% acetic acid and H_2O and then dried over $MgSO_4$. Silica flash chromatography using CH_2Cl_2/CH_3OH (0 – 10%) as the eluant yielded the desired compound **127** as an off white waxy solid (87% yield, 545 mg). HRMS (*m/z*) (ES^+) Calculated for $C_{25}H_{39}NO_6SNa$ *m/z* = 504.2396 $[M + Na]^+$. Found *m/z* = 504.2401. Elemental analysis for $C_{25}H_{39}NO_6S$ (481.65 $gmol^{-1}$) calc: C 62.34, H 8.16, N 2.91; found C 62.36, H 8.38, N 2.80%. ^1H NMR (600 MHz, $CDCl_3$) δ_H: 7.76 (2H, s, pyridine-H), 4.47 (4H, q, J = 7.1 Hz, 2 x ethyl-CH_2), 4.12 (2H, t, J = 6.5 Hz, OCH_2), 2.86 (2H, t, J = 7.4 Hz, CH_2S), 2.31 (3H, s, $SCOCH_3$), 1.83 (2H, m, $OCH_2\underline{CH_2}$), 1.56 (2H, m, $\underline{CH_2}CH_2S$), 1.45 (8H, m, 2 x ethyl-CH_3, 1 x CH_2), 1.31 – 1.27 (14H, m, 7 x CH_2); ^{13}C NMR (150 MHz, $CDCl_3$) δ_C: 195.90, 166.91, 164.67, 149.99, 114.19, 68.89, 62.21, 30.48, 29.36, 29.34, 29.32, 29.28, 29.09, 29.00, 28.94, 28.66, 28.60, 25.69, 14.05. IR(neat): 3087, 2979, 2916, 2852, 1716, 1685, 1598, 1565, 1472, 1448, 1415, 1395, 1371, 1342, 1282, 1251, 1151, 1118, 1102, 1037, 1029, 989, 969, 949, 934, 891, 868, 823, 807, 787, 733, 718, 702, 676 cm^{-1}.

4-(12-Mercaptododecyloxy)pyridine-2,6-dicarboxylic acid (122)[318]

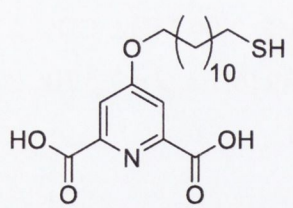

0.12 g (0.25 mmol) of compound **127** was dissolved in EtOH (5 mL) and 20 mL of an aq. KOH solution (0.83 g, 15 mmol, 3.2 equiv.) was added. The reaction was stirred at RT for 5 hrs and followed by TLC (CH_2Cl_2:CH_3OH, 96:4). Once the reaction had reached completion the mixture was filtered by suction filtration and washed with diethyl ether. The aq. phase was acidified to pH 1 using conc. HCl and the pure product **122** was then extracted into AcOEt. The solvent was removed under reduced pressure affording the desired product **122** as a white powder in 54% yield (52 mg). m.p. 223 – 227 °C Elemental analysis for $C_{19}H_{29}NO_5S$ (383.50 $gmol^{-1}$) calc: C 59.51, H 7.62, N 3.65; found C 59.23, H 7.52, N 3.65%. ^1H-NMR (600 MHz, $CDCl_3$) δ_H: 7.91(2H, s, pyridine-H), 4.18 (2H, t, J = 6.4 Hz, OCH_2), 2.52 (2H, q, J = 7.3 Hz, CH_2S), 1.86 (2H, m, $OCH_2\underline{CH_2}$), 1.61 (2H, m, $\underline{CH_2}CH_2S$), 1.47 (2H, m, CH_2), 1.39 – 1.28 (14H, m, 7 x CH_2); ^{13}C NMR (150

MHz, $CDCl_3$) δ_C: 168.70, 163.37, 147.45, 114.43, 69.81, 34.01, 30.91, 29.51, 29.47, 29.43, 29.17, 29.05, 28.58, 28.35, 25.73, 24.64; IR(neat) 3229, 2918, 2850, 2573, 1749, 1724, 1605, 1562, 1464, 1445, 1417, 1403, 1360, 1300, 1279, 1191, 1159, 1108, 1058, 1019, 1008, 902, 877, 829, 803, 756, 695, 681 cm^{-1}.

References

References

1. Steed, J. W.; Atwood, J. L. Concepts. In *Supramolecular Chemistry*, John Wiley & Sons, Ltd: 2009; pp 1-48.
2. Lehn, J.-M. *Angew. Chem. , Int. Ed.* **1988**, *27*, 89-122.
3. Lehn, J.-M. *Proc. Natl. Acad. Sci. U. S. A.* **2002**, *99* , 4763-4768.
4. Lehn, J.-M. *Science* **2002**, *295*, 2400-2403.
5. Lehn, J. M. *Angew. Chem. Int. Ed.* **2013**, *52*, 2836-2850.
6. Pedersen, C. J. *J. Am. Chem. Soc.* **1967**, *89*, 7017-7036.
7. Dietrich, B.; Lehn, J. M.; Sauvage, J. P. *Tetrahedron Lett.* **1969**, *10*, 2889-2892.
8. Gokel, G. W.; Dishong, D. M.; Diamond, C. J. *J. Chem. Soc. , Chem. Commun.* **1980**, 1053-1054.
9. Weber, E.; Vogtle, F. *Inorg. Chim. Acta* **1980**, *45*, L65-L67.
10. Vickers, M. S.; Beer, P. D. *Chem. Soc. Rev.* **2007**, *36*, 211-225.
11. Kilah, N. L.; Wise, M. D.; Serpell, C. J.; Thompson, A. L.; White, N. G.; Christensen, K. E.; Beer, P. D. *J. Am. Chem. Soc.* **2010**, *132*, 11893-11895.
12. Evans, N. H.; Serpell, C. J.; Beer, P. D. *Angew. Chem. Int. Ed.* **2011**, *50*, 2507-2510.
13. Dietrich-Buchecker, C. O.; Sauvage, J. P. *Chem. Rev.* **1987**, *87*, 795-810.
14. Chichak, K. S.; Cantrill, S. J.; Pease, A. R.; Chiu, S.-H.; Cave, G. W. V.; Atwood, J. L.; Stoddart, J. F. *Science* **2004**, *304*, 1308-1312.
15. Amabilino, D. B.; Stoddart, J. F. *Chem. Rev.* **1995**, *95*, 2725-2828.
16. Chauvin, A.-S.; Comby, S.; Song, B.; Vandevyver, C. D. B.; Bünzli, J.-C. G. *Chem. Eur. J.* **2007**, *13*, 9515-9526.
17. Piguet, C.; Bernardinelli, G.; Hopfgartner, G. *Chem. Rev.* **1997**, *97*, 2005-2062.
18. Piguet, C.; Borkovec, M.; Hamacek, J.; Zeckert, K. *Coord. Chem. Rev.* **2005**, *249*, 705-729.
19. Bünzli, J.-C. G.; Chauvin, A.-S.; Vandevyver, C. D. B.; Song, B.; Comby, S. *Ann. N. Y. Acad. Sci.* **2008**, *1130*, 97-105.
20. Bünzli, J.-C. G.; Petoud, S.; Piguet, C.; Renaud, F. *J. Alloys Comp.* **1997**, *249*, 14-24.
21. Comby, S.; Stomeo, F.; McCoy, C. P.; Gunnlaugsson, T. *Helv. Chim. Acta* **2009**, *92*, 2461-2473.
22. Chauvin, A. S.; Comby, S.; Baud, M.; De Piano, C.; Duhot, C.; Bünzli, J.-C. G. *Inorg. Chem.* **2009**, *48*, 10687-10696.
23. Piguet, C.; Bünzli, J.-C. G. Self-assembled lanthanide helicates: from basic thermodynamics to applications. In *Handbook on the Physics and Chemistry of Rare Earths*, Elsevier Science B.V.: Amsterdam, 2010; pp 301-581.
24. Williams, A. F.; Piguet, C.; Bernardinelli, G. *Angew. Chem. , Int. Ed.* **1991**, *30*, 1490-1492.
25. Lehn, J. M.; Rigault, A. *Angew. Chem. Int. Ed. Engl.* **1988**, *27*, 1095-1097.
26. Lehn, J. M.; Rigault, A.; Siegel, J.; Harrowfield, J.; Chevrier, B.; Moras, D. *Proc. Natl. Acad. Sci. U. S. A.* **1987**, *84*, 2565-2569.
27. Constable, E. C. *Nature* **1990**, *346*, 314-315.
28. Constable, E. C.; Ward, M. D.; Tocher, D. A. *J. Chem. Soc. , Dalton Trans.* **1991**, 1675-1683.
29. Piguet, C.; Bernardinelli, G.; Williams, A. F. *Inorg. Chem.* **1989**, *28*, 2920-2925.
30. Rowsell, J. L. C.; Millward, A. R.; Park, K. S.; Yaghi, O. M. *J. Am. Chem. Soc.* **2004**, *126*, 5666-5667.
31. Rowsell, J. L. C.; Yaghi, O. M. *J. Am. Chem. Soc.* **2006**, *128*, 1304-1315.

32. Tranchemontagne, D. J.; Mendoza-Cortes, J. L.; O'Keeffe, M.; Yaghi, O. M. *Chem. Soc. Rev.* **2009**, *38*, 1257-1283.
33. Murray, L. J.; Dinca, M.; Long, J. R. *Chem. Soc. Rev.* **2009**, *38*, 1294-1314.
34. Ma, L.; Abney, C.; Lin, W. *Chem. Soc. Rev.* **2009**, *38*, 1248-1256.
35. Allendorf, M. D.; Bauer, C. A.; Bhakta, R. K.; Houk, R. J. T. *Chem. Soc. Rev.* **2009**, *38*, 1330-1352.
36. de Silva, A. P.; Moody, T. S.; Wright, G. D. *Analyst* **2009**, *134*, 2385-2393.
37. Bünzli, J.-C. *Chem. Lett.* **2009**, *38*, 104-109.
38. Bünzli, J. C. *Chem. Rev.* **2010**, *110*, 2729-2755.
39. Gunnlaugsson, T.; Leonard, J. P. *Chem. Commun.* **2005**, 3114-3131.
40. Gunnlaugsson, T.; Harte, A. J.; Leonard, J. P.; Nieuwenhuyzen, M. *Chem. Commun.* **2002**, 2134-2135.
41. McMahon, B.; Mauer, P.; McCoy, C. P.; Lee, T. C.; Gunnlaugsson, T. *J. Am. Chem. Soc.* **2009**, *131*, 17542-17543.
42. McMahon, B. K.; Gunnlaugsson, T. *Tetrahedron Lett.* **2010**, *51*, 5406-5410.
43. McMahon, B. K.; Gunnlaugsson, T. *J. Am. Chem. Soc.* **2012**, doi: 10.1021/ja300887k.
44. McMahon, B. K.; Pal, R.; Parker, D. *Chem. Commun.* **2013**, *49*, 5363-5365.
45. Parker, D. *Coord. Chem. Rev.* **2000**, *205*, 109-130.
46. Parker, D.; Dickins, R. S.; Puschmann, H.; Crossland, C.; Howard, J. A. K. *Chem. Rev.* **2002**, *102*, 1977-2010.
47. Binnemans, K. *Chem. Rev.* **2009**, *109*, 4283-4374.
48. de Bettencourt-Dias, A. *Dalton Trans.* **2007**, 2229-2241.
49. Bünzli, J.-C. G.; Comby, S.; Chauvin, A.-S.; Vandevyver, C. D. B. *J. Rare Earths* **2007**, *25*, 257-274.
50. Barin, G.; Frasconi, M.; Dyar, S. M.; Iehl, J.; Buyukcakir, O.; Sarjeant, A. A.; Carmieli, R.; Coskun, A.; Wasielewski, M. R.; Stoddart, J. F. *J. Am. Chem. Soc.* **2013**, *135*, 2466-2469.
51. Fahrenbach, A. C.; Warren, S. C.; Incorvati, J. T.; Avestro, A. J.; Barnes, J. C.; Stoddart, J. F.; Grzybowski, B. A. *Adv. Mater.* **2013**, *25*, 331-348.
52. Stoddart, J. F. *Chem. Soc. Rev.* **2009**, *38*, 1802-1820.
53. Klajn, R.; Fang, L.; Coskun, A.; Olson, M. A.; Wesson, P. J.; Stoddart, J. F.; Grzybowski, B. A. *J. Am. Chem. Soc.* **2009**, *131*, 4233-4235.
54. de Silva, A. P.; Gunaratne, H. Q. N.; Gunnlaugsson, T.; Huxley, A. J. M.; McCoy, C. P.; Rademacher, J. T.; Rice, T. E. *Chem. Rev.* **1997**, *97*, 1515.
55. de Silva, A. P.; Dixon, I. M.; Gunaratne, H. Q. N.; Gunnlaugsson, T.; Maxwell, P. R. S.; Rice, T. E. *J. Am. Chem. Soc.* **1999**, *121*, 1393-1394.
56. Goldup, S. M.; Leigh, D. A.; Lusby, P. J.; McBurney, R. T.; Slawin, A. M. Z. *Angew. Chem. Int. Ed.* **2008**, *47*, 6999-7003.
57. Prikhod'ko, A. I.; Durola, F.; Sauvage, J. P. *J. Am. Chem. Soc.* **2007**, *130*, 448-449.
58. Gunnlaugsson, T.; Stomeo, F. *Org. Biomol. Chem.* **2007**, *5*, 1999-2009.
59. Eliseeva, S. V.; Bünzli, J. C. *Chem. Soc. Rev.* **2010**, *39*, 189-227.
60. Eliseeva, S. V.; Bünzli, J. C. *New J. Chem.* **2011**, *35*, 1165-1176.
61. Bünzli, J.-C. G.; André, N.; Elhabiri, M.; Muller, G.; Piguet, C. *J. Alloys Comp.* **2000**, *303/304*, 66-74.
62. Bünzli, J.-C. G.; Piguet, C. *Chem. Rev.* **2002**, *102*, 1897-1928.
63. Bünzli, J.-C. G.; Piguet, C. *Chem. Soc. Rev.* **2005**, *34*, 1048-1077.
64. Lincheneau, C.; Peacock, R. D.; Gunnlaugsson, T. *Chem. Asian J.* **2010**, *5*, 500-504.
65. Lincheneau, C.; Leonard, J. P.; McCabe, T.; Gunnlaugsson, T. *Chem. Commun.* **2011**, *47*, 7119-7121.
66. Lincheneau, C.; Destribats, C.; Barry, D. E.; Kitchen, J. A.; Peacock, R. D.; Gunnlaugsson, T. *Dalton Trans.* **2011**, *40*, 12056-12059.

67. Lincheneau, C.; Stomeo, F.; Comby, S.; Gunnlaugsson, T. *Aust. J. Chem.* **2011**, *64*, 1315-1326.
68. Lincheneau, C.; Duke, R. M.; Gunnlaugsson, T. *Org. Biomol. Chem.* **2012**, *10*, 6069-6073.
69. Stomeo, F.; Lincheneau, C.; Leonard, J. P.; O'Brien, J. E.; Peacock, R. D.; McCoy, C. P.; Gunnlaugsson, T. *J. Am. Chem. Soc.* **2009**, *131*, 9636-9637.
70. Kitchen, J. A.; Barry, D. E.; Mercs, L.; Albrecht, M.; Peacock, R. D.; Gunnlaugsson, T. *Angew. Chem. Int. Ed.* **2012**, *51*, 704-708.
71. Kotova, O.; Daly, R.; dos Santos, C. M. G.; Boese, M.; Kruger, P. E.; Boland, J. J.; Gunnlaugsson, T. *Angew. Chem. Int. Ed.* **2012**, *51*, 7208-7212.
72. Cotton, S. Introduction to the Lanthanides. In *Lanthanide and Actinide Chemistry*, John Wiley & Sons, Ltd: 2006; pp 1-7.
73. Bünzli, J.-C. G. *Acc. Chem. Res.* **2006**, *39*, 53-61.
74. Mayo, B. C. *J. Am. Chem. Soc.* **1969**, *91*, 5160.
75. Huang, C.; Bian, Z. Introduction. In *Rare Earth Coordination Chemistry*, John Wiley & Sons, Ltd: 2010; pp 1-39.
76. Bünzli, J.-C. G. Rare Earth Luminescent Centers in Organic and Biochemical compounds. In *Spectroscopic Properties of Rare Earths in Optical Materials*, Liu, G. K., Jacquier, B., Eds.; Springer Verlag: Berlin, 2005; pp 462-499.
77. Parker, D.; Williams, J. A. G. *J. Chem. Soc. , Dalton Trans.* **1996**, 3613-3628.
78. Shinoda, S.; Tsukube, H. *Analyst (Cambridge, U. K.)* **2011**, *136*, 431-435.
79. Thibon, A.; Pierre, V. r. *Anal Bioanal Chem* **2009**, *394*, 107-120.
80. Hagan, A. K.; Zuchner, T. *Anal. Bioanal. Chem.* **2011**, *400*, 2847-2864.
81. dos Santos, C. M. G.; Harte, A. J.; Quinn, S. J.; Gunnlaugsson, T. *Coord. Chem. Rev.* **2008**, *252*, 2512-2527.
82. Faulkner, S.; Natrajan, L. S.; Perry, W. S.; Sykes, D. *Dalton Trans.* **2009**, 3890-3899.
83. dos Santos, C. M. G.; Harte, A. J.; Quinn, S. J.; Gunnlaugsson, T. *Coord. Chem. Rev.* **2008**, *252*, 2512-2527.
84. Bünzli, J. C. G.; Eliseeva, S. V. Basics of Lanthanide Photophysics. In *Lanthanide Luminescence*, Springer Berlin Heidelberg: Berlin, 2010; pp 1-45.
85. Bünzli, J. C. G. Rare Earth Luminescent Centers in Organic and Biochemical Compounds. In *Spectroscopic Properties of Rare Earths in Optical Materials*, 83 ed.; Hull, R., Parisi, J., Osgood, R. M., Jr., Warlimont, H., Liu, G., Jacquier, B., Eds.; Springer Berlin Heidelberg: 2005; pp 462-499.
86. Supkowski, R. M.; Horrocks, W. d. Jr. *Inorg. Chim. Acta* **2002**, *340*, 44-48.
87. Beeby, A.; Clarkson, I. M.; Dickins, R. S.; Faulkner, S.; Parker, D.; Royle, L.; de Sousa, A. S.; Williams, J. A. G.; Woods, M. *J. Chem. Soc. , Perkin Trans. 2* **1999**, 493-503.
88. Comby, S.; Imbert, D.; Chauvin, A.-S.; Bünzli, J.-C. G. *Inorg. Chem.* **2006**, *45*, 732-743.
89. Charbonniere, L. J.; Ziessel, R. *Helv. Chim. Acta* **2003**, *86*, 3402.
90. Tallec, G.; Imbert, D.; Fries, P. H.; Mazzanti, M. *Dalton Trans.* **2010**, *39*, 9490-9492.
91. Marcos, P. M.; Ascenso, J. R.; Segurado, M. A. P.; Cragg, P. J.; Michel, S.; Hubscher-Bruder, V.; Arnaud-Neu, F. *Supramolecular Chemistry* **2011**, *23*, 93-101.
92. Sun, W.-Y.; Yoshizawa, M.; Kusukawa, T.; Fujita, M. *Curr. Opin. Chem. Biol.* **2002**, *6*, 757-764.
93. Leonard, J. P.; Jensen, P.; McCabe, T.; O'Brien, J. E.; Peacock, R. D.; Kruger, P. E.; Gunnlaugsson, T. *J. Am. Chem. Soc.* **2007**, *129*, 10986-10987.
94. Albrecht, M.; Osetska, O.; Bünzli, J.-C. G.; Gumy, F.; Fröhlich, R. *Chem. Eur. J.* **2009**, *15*, 8791-8799.

95. Albrecht, M. *Z. Anorg. Allg. Chem.* **2010**, *636*, 2198-2204.
96. Fernandez-Moreira, V.; Song, B.; Sivagnanam, V.; Chauvin, A. S.; Vandevyver, C. D. B.; Gijs, M.; Hemmila, I.; Lehr, H. A.; Bünzli, J. C. *Analyst* **2010**, *135*, 42-52.
97. Terazzi, E.; Guénée, L.; Varin, J.; Bocquet, B.; Lemonnier, J.-F.; Emery, D.; Mareda, J.; Piguet, C. *Chem. Eur. J.* **2011**, *17*, 184-195.
98. Bozoklu, G.; Marchal, C.; Gateau, C.; Pcaut, J.; Imbert, D.; Mazzanti, M. *Chem. Eur. J.* **2010**, *16*, 6159-6163.
99. Tang, X.-L.; Wang, W.-H.; Dou, W.; Jiang, J.; Liu, W.-S.; Qin, W.-W.; Zhang, G.-L.; Zhang, H.-R.; Yu, K.-B.; Zheng, L.-M. *Angew. Chem. Int. Ed.* **2009**, *48*, 3499-3502.
100. de Lill, D. T.; de Bettencourt-Dias, A.; Cahill, C. L. *Inorg. Chem.* **2007**, *46*, 3960-3965.
101. Tang, Q.; Liu, S.; Liu, Y.; Miao, J.; Li, S.; Zhang, L.; Shi, Z.; Zhen, Z. *Inorg. Chem.* **2013**, 2799-2801.
102. Grenthe, I. *J. Am. Chem. Soc.* **1961**, *83*, 360-364.
103. Brayshaw, P. A.; Bünzli, J.-C. G.; Froidevaux, P.; Harrowfield, J. M.; Kim, Y.; Sobolev, A. N. *Inorg. Chem.* **1995**, *34*, 2068-2076.
104. Mondry, A.; Starynowicz, P. *J. Alloys Compd.* **1995**, *225*, 367-371.
105. Chauvin, A.-S.; Gumy, F.; Imbert, D.; Bünzli, J.-C. G. *Spectrosc. Lett.* **2004**, *37*, 517-532; erratum, **2006**, *40(1)*, 193.
106. Gassner, A. L.; Duhot, C.; Bünzli, J. C. G.; Chauvin, A.-S. *Inorg. Chem.* **2008**, *47*, 7802-7812.
107. George, M. R.; Golden, C. A.; Grossel, M. C.; Curry, R. J. *Inorg. Chem.* **2006**, *45*, 1739-1744.
108. *Spectrosc. Lett.* **2007**, *40*, 193.
109. Lamture, J. B.; Zhou, Z. H.; Kumar, A. S.; Wensel, T. G. *Inorg. Chem.* **1995**, *34*, 864-869.
110. Andres, J.; Chauvin, A. S. *Inorg. Chem.* **2011**, *50*, 10082-10090.
111. Tanase, S.; Gallego, P. M.; de Gelder, R.; Fu, W. T. *Inorg. Chim. Acta* **2007**, *360*, 102-108.
112. de Bettencourt-Dias, A.; Viswanathan, S.; Rollett, A. *J. Am. Chem. Soc.* **2007**, *129*, 15436-15437.
113. de Bettencourt-Dias, A.; Barber, P. S.; Viswanathan, S.; de Lill, D. T.; Rollett, A.; Ling, G.; Altun, S. *Inorg. Chem.* **2010**, *49*, 8848-8861.
114. de Bettencourt-Dias, A.; Barber, P. S.; Bauer, S. *J. Am. Chem. Soc.* **2012**, *134*, 6987-6994.
115. Comby, S.; Imbert, D.; Chauvin, A.-S.; Bünzli, J.-C. G.; Charbonnière, L. J.; Ziessel, R. F. *Inorg. Chem.* **2004**, *43*, 7369-7379.
116. Dossing, A. *Eur. J. Inorg. Chem.* **2005**, 1425-1434.
117. Mukkala, V. M.; Kwiatkowski, M.; Kankare, J.; Takalo, H. *Helv. Chim. Acta* **1993**, *76*, 893-899.
118. de Silva, A. P.; Gunaratne, H. Q. N.; Rice, T. E. *Angew. Chem. Int. Ed. Engl.* **1996**, *35*, 2116-2118.
119. Andreiadis, E. S.; Demadrill, R.; Imbert, D.; Pecaut, J.; Mazzanti, M. *Chem. Eur. J.* **2009**, *15*, 9458-9476.
120. Giraud, M.; Andreiadis, E. S.; Fisyuk, A. S.; Demadrille, R.; Pecaut, J.; Imbert, D.; Mazzanti, M. *Inorg. Chem.* **2008**, *47*, 3952-3954.
121. Andreiadis, E. S.; Imbert, D.; Pecaut, J.; Demadrill, R.; Mazzanti, M. *Dalton Trans.* **2012**, *41*, 1268.
122. Petoud, S.; Bünzli, J.-C. G.; Schenk, K. J.; Piguet, C. *Inorg. Chem.* **1997**, *36*, 1345-1353.
123. Piguet, C.; Williams, A. F.; Bernardinelli, G.; Bünzli, J.-C. G. *Inorg. Chem.* **1993**, *32*, 4139-4149.

124. Piguet, C.; Williams, A. F.; Bernardinelli, G.; Moret, E.; Bünzli, J.-C. G. *Helv. Chim. Acta* **1992**, *75*, 1697-1717.
125. Piguet, C.; Bünzli, J. C. G.; Bernardinelli, G.; Bochet, C. G.; Froidevaux, P. *J. Chem. Soc. , Dalton Trans.* **1995**, 83-97.
126. Muller, G.; Bünzli, J.-C. G.; Schenk, K. J.; Piguet, C.; Hopfgartner, G. *Inorg. Chem.* **2001**, *40*, 2642-2651.
127. Escande, A.; Guene, L.; Buchwalder, K.-L.; Piguet, C. *Inorg. Chem.* **2009**, 1132-1147.
128. Shavaleev, N. M.; Scopelliti, R.; Gumy, F.; Bünzli, J.-C. G. *Inorg. Chem.* **2009**, *48*, 6178-6191.
129. Shavaleev, N. M.; Gumy, F.; Scopelliti, R.; Bünzli, J.-C. G. *Inorg. Chem.* **2009**, *48*, 5611-5613.
130. Hua, K. T.; Xu, J.; Quiroz, E. E.; Lopez, S.; Ingram, A. J.; Johnson, V. A.; Tisch, A. R.; de Bettencourt-Dias, A.; Straus, D. A.; Muller, G. *Inorg. Chem.* **2012**, *51*, 647-660.
131. Moussa, A.; Pham, C.; Bommireddy, S.; Muller, G. *Chirality* **2009**, *21*, 497-506.
132. Brittain, H. G. *Inorg. Chem.* **1981**, *20*, 3007-3013.
133. Muller, G.; Schmidt, B.; Jiricek, J.; Hopfgartner, G.; Riehl, J. P.; Bünzli, J.-C. G.; Piguet, C. *J. Chem. Soc. , Dalton Trans.* **2001**, 2655-2662.
134. Bonsall, S. D.; Houcheime, M.; Straus, D. A.; Muller, G. *Chem. Commun.* **2007**, *3676*.
135. Yuasa, J.; Ohno, T.; Miyata, K.; Tsumatori, H.; Hasegawa, Y.; Kawai, T. *J. Am. Chem. Soc.* **2011**, *133*, 9892-9902.
136. Do, K.; Muller, F. C.; Muller, G. *J. Phys. Chem. Lett.* **2008**, *112*, 6789-6793.
137. Petoud, S.; Muller, G.; Moore, E. G.; Xu, J.; Sokolnicki, J.; Riehl, J. P.; Le, U. N.; Cohen, S. M.; Raymond, K. N. *J. Am. Chem. Soc.* **2007**, *129*, 77-83.
138. Seitz, M.; Moore, E. G.; Ingram, A. J.; Muller, G.; Raymond, K. N. *J. Am. Chem. Soc.* **2007**, *129*, 15468-15470.
139. Hoffart, D. J.; Loeb, S. J. *Angew. Chem. , Int. Ed.* **2005**, *44*, 901-904.
140. Floquet, S.; Ouali, N.; Bocquet, B.; Bernardinelli, G.; Imbert, D.; Bünzli, J.-C. G.; Hopfgartner, G.; Piguet, C. *Chem. --Eur. J.* **2003**, 1860-1875.
141. Piguet, C.; Rivara-Minten, E.; Hopfgartner, G.; Bünzli, J.-C. G. *Helv. Chim. Acta* **1995**, *78*, 1541-66.
142. Ronson, T. K.; Adams, H.; Harding, L. P.; Pope, S. J. A.; Sykes, D.; Faulkner, S.; Ward, M. D. *Dalton Trans.* **2007**, 1006-1022.
143. Song, B.; Sivagnanam, V.; Vandevyver, C. D. B.; Hemmila, I.; Lehr, H. A.; Gijs, M. A. M.; Bünzli, J. C. G. *Analyst* **2009**, *134*, 1991-1993.
144. Song, B.; Vandevyver, C. D. B.; Deiters, E.; Chauvin, A. S.; Hemmila, I.; Bünzli, J.-C. G. *Analyst* **2008**, *133*.
145. Lessmann, J. J.; Horrocks, W. d. Jr. *Inorg. Chem.* **2000**, *39*, 3114-3124.
146. Marchal, C.; Filinchuk, Y.; Imbert, D.; Bünzli, J.-C. G.; Mazzanti, M. *Inorg. Chem.* **2007**, *46*, 6242-6244.
147. de Bettencourt-Dias, A. *Inorg. Chem.* **2005**, *44*, 2734-2741.
148. Chen, X.-Y.; Marchal, C.; Filinchuk, Y.; Imhof, A.; Mazzanti, M. *Chem. Commun.* **2008**, 3378-3380.
149. Bretonniere, Y.; Mazzanti, M.; Pecaut, J.; Olmstead, M. M. *J. Am. Chem. Soc.* **2002**, *124*, 9012-9013.
150. Chen, X.-Y.; Bretonniere, Y.; Pecaut, J.; Imbert, D.; Mazzanti, M. *Inorg. Chem.* **2007**, *46*, 625-637.
151. Bozoklu, G.; Gateau, C.; Imbert, D.; Pécaut, J.; Robeyns, K.; Filinchuk, Y.; Memon, F.; Muller, G.; Mazzanti, M. *J. Am. Chem. Soc.* **2012**, *134*, 8372-8375.

152. Mamula, O.; Lama, M.; Telfer, S. G.; Nakamura, A.; Kuroda, R.; Stoeckli-Evans, H.; Scopelliti, R. *Angew. Chem. , Int. Ed.* **2005**, *44*, 2527-2531.
153. Mamula, O.; Lama, M.; Stoeckli-Evans, H.; Shova, S. *Angew. Chem. , Int. Ed.* **2006**, *45*, 4940-4944.
154. Lama, M.; Mamula, O.; Kottas, G. S.; Rizzo, F.; De Cola, L.; Nakamura, A.; Kuroda, R.; Stoeckli-Evans, H. *Chem. Eur. J.* **2007**, *13*, 7358-7373.
155. Zebret, S.; Torres, E.; Terreno, E.; Guenee, L.; Senatore, C.; Hamacek, J. *Dalton Trans.* **2011**, *40*, 4284-4290.
156. Zebret, S.; Dupont, N.; Besnard, C.; Bernardinelli, G.; Hamacek, J. *Dalton Trans.* **2012**, *41*, 4817-4823.
157. Zebret, S.; Dupont, N.; Bernardinelli, G.; Hamacek, J. *Chem. --Eur. J.* **2009**, *15*, 3355-3358.
158. Aroussi, B. E.; Zebret, S.; Besnard, C.; Perrotter, P.; Hamacek, J. *J. Am. Chem. Soc.* **2011**, *133*, 10764-10767.
159. Hamacek, J.; Besnard, C.; Penhouet, T.; Morgantini, P. Y. *Chem. --Eur. J.* **2011**, *17*, 6753-6764.
160. Hamacek, J.; Bernardinelli, G.; Filinchuk, Y. *Eur. J. Inorg. Chem.* **2008**, 3419-3422.
161. Eliseeva, S. V.; Auböck, G.; van Mourik, F.; Cannizzo, A.; Song, B.; Deiters, E.; Chauvin, A. S.; Chergui, M.; Bünzli, J.-C. *J. Phys. Chem. B* **2010**, *114*, 2932-2937.
162. Piguet, C.; Bünzli, J.-C. G.; Bernardinelli, G.; Hopfgartner, G.; Williams, A. F. *J. Am. Chem. Soc.* **1993**, *115*, 8197-8206.
163. Piguet, C.; Bünzli, J. C. G.; Bernardinelli, G.; Hopfgartner, G.; Williams, A. F. *J. Am. Chem. Soc.* **1993**, *115*, 8197-8206.
164. Piguet, C.; Hopfgartner, G.; Williams, A. F.; Bünzli, J.-C. G. *J. Chem. Soc. ,Chem. Commun.* **1995**, 491-493.
165. Piguet, C.; Bernardinelli, G.; Bünzli, J.-C. G.; Petoud, S.; Hopfgartner, G. *J. Chem. Soc. , Chem. Commun.* **1995**, 2575-2577.
166. Bernardinelli, G.; Piguet, C.; Williams, A. F. *Angew. Chem. Int. Ed.* **1992**, *31*, 1622-1624.
167. Williams, A. F.; Piguet, C.; Bernardinelli, G. *Angew. Chem. , Int. Ed.* **1991**, *30*, 1490-1492.
168. Hamacek, J.; Blanc, S.; Elhabiri, M.; Leize, E.; Van Dorsselaer, A.; Piguet, C.; Albrecht-Gary, A.-M. *J. Am. Chem. Soc.* **2003**, *125*, 1541-1550.
169. André, N.; Scopelliti, R.; Hopfgartner, G.; Piguet, C.; Bünzli, J.-C. G. *Chem. Commun.* **2002**, 214-215.
170. André, N.; Jensen, T. B.; Scopelliti, R.; Imbert, D.; Elhabiri, M.; Hopfgartner, G.; Piguet, C.; Bünzli, J.-C. G. *Inorg. Chem.* **2004**, *43*, 515-529.
171. Floquet, S.; Borkovec, M.; Bernardinelli, G.; Pinto, A.; Leuthold, L. A.; Hopfgartner, G.; Imbert, D.; Bünzli, J.-C. G. *Chem. --Eur. J.* **2004**, *10*, 1091-1105.
172. Cantuel, M.; Gumy, F.; Bünzli, J.-C. G.; Piguet, C. *Dalton Trans.* **2006**, 2647-2660.
173. Riis-Johannessen, T.; Bernardinelli, G.; Filinchuk, Y.; Clifford, S.; Favera, N. D.; Piguet, C. *Inorg. Chem.* **2009**, *48*, 5512-5525.
174. Deiters, E.; Song, B.; Chauvin, A. S.; Vandevyver, C. D. B.; Gumy, F.; Bünzli, J.-C. G. *Chem. Eur. J.* **2009**, *15*, 885-900.
175. Eliseeva, S. V.; Song, B.; Vandevyver, C. D. B.; Chauvin, A. S.; Wacker, J. B.; Bünzli, J.-C. G. *New J. Chem.* **2010**, *34*, 2915-2921.
176. Vandevyver, C. D. B.; Chauvin, A.-S.; Comby, S.; Bünzli, J.-C. G. *Chem. Commun.* **2007**, 1716-1718.
177. Martin, N.; Bünzli, J.-C. G.; McKee, V.; Piguet, C.; Hopfgartner, G. *Inorg. Chem.* **1998**, *37*, 577-589.
178. Elhabiri, M.; Scopelliti, R.; Bünzli, J.-C. G.; Piguet, C. *Chem. Commun.* **1998**, 2347-2349.

179. Elhabiri, M.; Scopelliti, R.; Bünzli, J.-C. G.; Piguet, C. *J. Am. Chem. Soc.* **1999**, *121*, 10747-10762.
180. Elhabiri, M.; Hamacek, J.; Bünzli, J.-C. G.; Albrecht-Gary, A.-M. *Eur. J. Inorg. Chem.* **2004**, 51-62.
181. Song, B.; Vandevyver, C. D. B.; Chauvin, A. S.; Bünzli, J.-C. G. *Org. Biomol. Chem.* **2008**, *6*, 4125-4133.
182. Bassett, A. P.; Magennis, S. W.; Glover, P. B.; Lewis, D. J.; Spencer, N.; Parsons, S.; Williams, R. M.; De Cola, L.; Pikramenou, Z. *J. Am. Chem. Soc.* **2004**, *126*, 9413-9424.
183. Albrecht, M.; Fröhlich, R.; Bünzli, J.-C. G.; Aebischer, A.; Gumy, F.; Hamacek, J. *J. Am. Chem. Soc.* **2007**, 14178-14179.
184. Albrecht, M.; Osetska, O. *Eur. J. Inorg. Chem.* **2010**, *2010*, 4678-4682.
185. Wang, B.; Zang, Z.; Wang, H.; Dou, W.; Tang, X.; Liu, W.; Shao, Y.; Ma, J.; Li, Y.; Zhou, J. *Angew. Chem. Int. Ed.* **2013**, *52*, 3756-3759.
186. Zapata, F.; Blackburn, O. A.; Langton, M. J.; Faulkner, S.; Beer, P. D. *Chem. Commun.* **2013**, *49*, 8157-8159.
187. Kotova, O.; Kitchen, J. A.; Lincheneau, C.; Peacock, R. D.; Gunnlaugsson, T. *Chem. Eur. J.* **2013**, *19*, 16181-16186.
188. Castellano, B. M.; Eggers, D. K. *J. Phys. Chem. B* **2013**, *117*, 8180-8188.
189. Cantuel, M.; Bernardinelli, G.; Muller, G.; Riehl, J. P.; Piguet, C. *Inorg. Chem.* **2004**, *43*, 1840-1849.
190. Albrecht, M.; Schmid, S.; Dehn, S.; Wickleder, C.; Zhang, S.; Bassett, A. P.; Pikramenou, Z.; Frohlichd, R. *New J. Chem.* **2007**, *31*, 1755-1762.
191. McMahon, B. K.; Gunnlaugsson, T. *J. Am. Chem. Soc.* **2012**, *134*, 10725-10728.
192. Gunnlaugsson, T.; McCoy, C. P.; Stomeo, F. *Tetrahedron Lett.* **2004**, *45*, 8403-8407.
193. Stomeo, F.; Plush, S. E.; Gunnlaugsson, T. *Chem. Mater.* **2006**, *18*, 4336-4343.
194. Bonnet, C. S.; Massue, J.; Quinn, S. J.; Gunnlaugsson, T. *Org. Biomol. Chem.* **2009**, *7*, 3074-3078.
195. Comby, S.; Gunnlaugsson, T. *ACS Nano* **2011**, *5*, 7184-7197.
196. Massue, J.; Quinn, S. J.; Gunnlaugsson, T. *J. Am. Chem. Soc.* **2008**, *130*, 6900-6901.
197. Murray, N. S.; Jarvis, S. P.; Gunnlaugsson, T. *Chem. Commun.* **2009**, 4959-4961.
198. Truman, L. K.; Comby, S.; Gunnlaugsson, T. *Angew. Chem. Int. Ed.* **2012**, *51*, 9624-9627.
199. Langmuir, I. *J. Am. Chem. Soc.* **1917**, *39*, 1848-1906.
200. Blodgett, K. B. *J. Am. Chem. Soc.* **1934**, *56*, 495.
201. Blodgett, K. B.; Langmuir, I. *Phys. Rev.* . **1937**, *51*, 964-982.
202. Blodgett, K. B. *J. Am. Chem. Soc.* **1935**, *57*, 1007-1022.
203. Langmuir, I.; Schaefer, V. J. *J. Am. Chem. Soc.* **1938**, *60*, 1351-1360.
204. Kuhn, H. *Pure Appl. Chem.* **1971**, *27*, 421-438.
205. Kuhn, H. *Pure Appl. Chem.* **1979**, *51*, 341-352.
206. Kuhn, H. *Pure Appl. Chem.* **1981**, *53*, 2105-2122.
207. Petty, M. C. *Langmuir-Blodgett films: An Introduction;* Cambridge University Press: 1996.
208. Talham, D. R. *Chem. Rev.* **2004**, *104*, 5479-5501.
209. Barraud, A.; Lesieur, P.; Richard, J.; Ruaudel-Teixier, A.; Vandevyver, M. *Thin Sol. Films* **1988**, *160*, 81-85.
210. Barraud, A.; Lesieur, P.; Ruaudel-Teixier, A.; Vandevyver, M. *Thin Sol. Films* **1985**, *134*, 195-199.
211. Huang, Y.; Gan, L.; Huang, C.-H.; Meng, F. *Supramolecular Science* **1998**, *5*, 457-460.
212. Nakamura, T.; Tanaka, M.; Sekiguchi, T.; Kawabata, Y. *J. Am. Chem. Soc.* **1986**, *108*, 1302-1303.

213. Bryce, M. R.; Petty, M. C. *Nature* **1995**, *374*, 771-776.
214. Ward, R. J.; Dhindsa, A. S.; Bryce, M. R.; Munro, H. S.; Petty, M. C. *Thin Sol. Films* **1991**, *198*, 363-367.
215. Mendes, P. M.; Flood, A. M.; Stoddart, J. F. *Appl. Phys. A.* **2005**, *80*, 1197-1209.
216. White, N. G.; Feltham, H. L. C.; Gandolfi, C.; Albrecht, M.; Brooker, S. *Dalton Trans.* **2010**, *39*, 3751-3758.
217. Kitchen, J. A.; White, N. G.; Albrecht, M.; Jameson, G. N. L.; Tallon, J. L.; Brooker, S. *Chem. Commun.* **2010**, *46*, 6464-6466.
218. Gandolfi, C.; Cotting, T.; Martinho, P. N.; Sereda, O.; Neels, A.; Morgan, G. G.; Albrecht, M. *Dalton Trans.* **2011**, *40*, 1855.
219. Gandolfi, C.; Moitzi, C.; Schurtenberger, P.; Morgan, G. G.; Albrecht, M. *J. Am. Chem. Soc.* **2008**, *130*, 14434-14435.
220. Armand, F.; Badoux, C.; Bonville, P.; Ruaudel-Teixier, A.; Kahn, O. *Langmuir* **1995**, *11*, 3467-3472.
221. Coronel, P.; Barraud, A.; Claude, R.; Kahn, O.; Ruaudel-Teixier, A.; Zarembowitch, J. *J. Chem. Soc. , Chem. Commun.* **1989**, 193-194.
222. Ruaudel-Teixier, A.; Barraud, A.; Coronel, P. *Thin Sol. Films* **1988**, 107-115.
223. Bodenthin, Y.; Pietsch, U.; Mohwald, H.; Kurth, D. G. *J. Am. Chem. Soc.* **2005**, *127*, 3110-3115.
224. Soyer, H. M. C.; Boillot, M.-L.; Delhaes, P. *Langmuir* **1998**, *14*, 5890-5895.
225. Brooker, S.; Kitchen, J. A. *Dalton Trans.* **2009**, 7340.
226. Roubeau, O.; Agricole, B.; Clerac, R.; Ravaine, S. *J. Phys. Chem. B* **2004**, *108*, 15110-15116.
227. Soyer, H.; Mingotaud, C.; Boillot, M.-L.; Delhaes, P. *Langmuir* **1998**, *14*, 5890-5895.
228. Davis, F.; Higson, P. J. *Biosens. Bioelectron.* **2005**, *21*, 1-20.
229. Gidalevitz, D.; Huang, Z.; Rice, S. A. *Biophys. J.* **1999**, *76*, 2797-2802.
230. Singhal, R.; Gambhir, A.; Pandey, M. K.; Annapoorni, S.; Malhotra, B. D. *Biosens. Bioelectron.* **2002**, *17*, 697-703.
231. Singhal, R.; Takashima, W.; Kanteo, K.; Samanta, S. B.; Annapoorni, S.; Malhotra, B. D. *Sens. Actuators, B* **2002**, *86*, 42-48.
232. Soloducho, J.; Cabaj, J.; Swist, A. *Sensors* **2009**, *9*, 7733-7752.
233. Qian, D.-J.; Nakahara, H.; Fukuda, K.; Yang, K.-Z. *Langmuir* **1995**, *11*, 4491-4494.
234. Qian, D.-J.; Yang, K.-Z.; Nakahara, H.; Fukuda, K. *Langmuir* **1997**, *13*, 5925-5932.
235. Zhang, R.-J.; Liu, H.-G.; Yang, K.-Z.; Si, Z.-K.; Zhu, G.-Y.; Zhang, H.-W. *Thin Sol. Films* **1997**, *295*, 228-233.
236. Zhang, R.-J.; Yang, K.-Z.; Yub, A.-C.; Zhao, X.-S. *Thin Sol. Films* **2000**, *363*, 275-278.
237. Gomes, L. F.; de Oliveira, K. T.; Neri, C. R.; de Sousa Filho, P. C.; Dal Banco, M. J.; Ramos, A. P.; Zaniquelli, M. E. D.; Serra, O. A. *J. Lumin.* **2008**, *128*, 1339-1347.
238. Adati, R. D.; Pavinatto, F. J.; Monteiro, J. H. S. K.; Davolos, M. R.; Jafelicci, M.; Oliveira Jr., O. N. *New J. Chem.* **2012**, *36*, 1978-1984.
239. Bian, Z.; Wang, K.; Jin, L.; Huang, C. *Colloids and Surfaces A, Physicochem. Eng. Aspects* **2005**, *257-258*, 67-70.
240. Ito, T.; Yashiro, H.; Yamase, T. *J. Cluster Sci.* **2006**, *17*, 375-387.
241. Ito, T.; Yamase, T. *J. Alloys Comp.* **2006**, *408-412*, 813-815.
242. Sousa, F. L.; Frreira, A. S.; Sa Ferreira, R. A.; Cavaleiro, A. M. V.; Carlos, L. D.; Nogueira, H. I. S.; Trindade, T. *J. Alloys Comp.* **2004**, *374*, 371-376.
243. Dutton, P. J.; Conte, L. *Langmuir* **1999**, *15*, 613-617.
244. Lemmetyinen, H.; Vuorimaa, E.; Jutila, A.; Mukkala, V. M.; Takalo, H.; Kankare, J. *Luminescence* **2000**, *15*, 341-350.

245. Zhou, D. J.; Huang, C. H.; Wang, K. Z.; Xu, G. X.; Zhao, X. S.; Xie, X.; Xu, L. G.; Li, T. K. *Langmuir* **1994**, *10*, 1910-1912.
246. Souto, J.; Tomilova, L.; Aroca, R.; De Saja, J. A. *Langmuir* **1992**, *8*, 942-946.
247. Souto, J.; Aroca, R.; De Saja, J. A. *J. Phys. Chem.* **1994**, *98*, 8998-9001.
248. Gorbunova, Y.; Rodriguez-Mendez, M. L.; Souto, J.; Tomilova, L.; De Saja, J. A. *Chem. Mater.* **1995**, *7*, 1443-1447.
249. Rodriguez-Mendez, M. L.; Gobernado-Mitre, M. I.; Souto, J.; De Saja-Gonzalez, J.; De Saja, J. A. *Sensors and Actuators B: Chemical* **1995**, *24-25*, 643-646.
250. Alvarez, J.; Souto, J.; Rodriguez-Mendez, M. L.; De Saja, J. A. *Sensors and Actuators B: Chemical* **1998**, *48*, 339-343.
251. Rodriguez-Mendez, M. L.; Gorbunova, Y.; De Saja, J. A. *Langmuir* **2002**, *18*, 9560-9565.
252. Yan, B.; Xu, B. *J. Fluoresc.* **2009**, *19*, 663-671.
253. Datta, A.; Raymond, K. N. *Acc. Chem. Res.* **2009**, *42*, 938-947.
254. Gardiner, J.; Thomae, A. V.; Mathada, R. I.; Seebach, D.; Kramer, S. D. *Chem. Biodivers.* **2006**, *3*, 1181-1201.
255. Telfer, S. G.; McLean, T. M.; Waterland, M. R. *Dalton* **2011**, 3097-3108.
256. Dickens, R. S.; Howard, J. A. K.; Maupin, C. L.; Moloney, J. M.; Parker, D.; Peacock, R. D.; Riehl, J. P.; Siligardi, G. *New J. Chem.* **1998**, 891-899.
257. Field, J. E.; Muller, G.; Riehl, J. P.; Venkataraman, D. *J. Am. Chem. Soc.* **2003**, *125*, 11808-11809.
258. Richardson, F. S. *Inorg. Chem.* **1980**, *19*, 2806-2812.
259. Seitz, M.; Do, K.; Ingram, A. J.; Moore, E. G.; Muller, G.; Raymond, K. N. *Inorg. Chem.* **2009**, *48*, 8469-8479.
260. Gampp, H.; Maeder, M.; Meyer, C. J.; Zuberbühler, A. D. *Talanta* **1985**, *32*, 95-101.
261. Gampp, H.; Maeder, M.; Meyer, C. J.; Zuberbühler, A. D. *Talanta* **1986**, *33*, 943-951.
262. Truman, L. K. PhD thesis. Trinity College Dublin, 2012.
263. Aboshyan-Sorgho, L.; Besnard, C.; Pattison, P.; Kittilstved, K. R.; Aebischer, A.; Bünzli, J.-C. G.; Hauser, A.; Piguet, C. *Angew. Chem. , Int. Ed.* **2011**, *50*, 4108-4112.
264. Beeby, A.; Burton-Pye, B. P.; Faulkner, S.; Motson, G. R.; Jeffery, J. C.; McCleverty, J. A.; Ward, M. D. *J. Chem. Soc. , Dalton Trans.* **2002**, 1923-1928.
265. Torelli, S.; Imbert, D.; Cantuel, M.; Bernardinelli, G.; Delahaye, S.; Hauser, A.; Bünzli, J.-C. G.; Piguet, C. *Chem. Eur. J.* **2005**, *11*, 3228-3242.
266. Wada, Y.; Okubo, T.; Ryo, M.; Nakazawa, T.; Hasegawa, Y.; Yanagida, S. *J. Am. Chem. Soc.* **2000**, *122*, 8583-8584.
267. Yanagida, S.; Hasegawa, Y.; Murakoshi, K.; Wada, Y.; Nakashima, N.; Yamanaka, T. *Coord. Chem. Rev.* **1998**, *171*, 461-480.
268. Nonat, A. M.; Quinn, S. J.; Gunnlaugsson, T. *Inorg. Chem.* **2009**, *48*, 4646-4648.
269. Pope, S. J. A.; Coe, B. J.; Faulkner, S.; Bichenkova, E. V.; Yu, X.; Douglas, K. T. *J. Am. Chem. Soc.* **2004**, *126*, 9490-9491.
270. Lehr, J.; Bennett, J.; Tropiano, M.; Sorensen, T. J.; Faulkner, S.; Beer, P. D.; Davis, J. J. *Langmuir* **2013**, *29*, 1475.
271. Albrecht, M. *Chem. Rev.* **2001**, *101*, 3457-3497.
272. Constable, E. C.; Elder, S. M.; Raithby, P. R.; Ward, M. D. *Polyhedron* **1991**, *10*, 1395-1400.
273. Fu, Y.; Sun, J.; Li, Q.; Chen, Y.; Dai, W.; Wang, D.; Mak, T. C. W.; Tang, W.; Hu, H. *J. Chem. Soc. , Dalton Trans.* **1996**, 2309-2313.
274. Ruettimann, S.; Piguet, C.; Bernardinelli, G.; Bocquet, B.; Williams, A. F. *J. Am. Chem. Soc.* **1992**, *114*, 4230-4237.
275. Potts, K. T.; Keshavarz, K.; Tham, F. S.; Abruna, H. D.; Arana, C. *Inorg. Chem.* **1993**, *32*, 4450-4456.

276. Deiters, E.; Song, B.; Chauvin, A. S.; Vandevyver, C. D. B.; Bünzli, J. C. *New J. Chem.* **2008**, *32*.
277. Oshovsky, G. V.; Reinhoudt, D. N.; Verboom, W. *Angew. Chem. , Int. Ed.* **2007**, *46*, 2366-2393.
278. Lindstrom, U. M. *Chem. Rev.* **2002**, *102*, 2751-2772.
279. Collie, L.; Denness, J. E.; Parker, D.; O'Carroll, F.; Tachon, C. *J. Chem. Soc. , Perkin Trans. 2* **1993**, 1747-1758.
280. Arnaud, A.; Belleney, J.; Boue, F.; Bouteiller, L.; Carrot, G.; Wintgens, V. *Angew. Chem. Int. Ed.* **2004**, *43*, 1718-1721.
281. Werts, M. H. V.; Jukes, R. T. F.; Verhoeven, J. W. *Phys. Chem. Chem. Phys.* **2002**, *4*, 1542-1548.
282. Le Borgne, T.; Benech, J.-M.; Floquet, S.; Bernardinelli, G.; Aliprandini, C.; Bettensa, P.; Piguet, C. *Dalton Trans.* **2003**, 3856-3868.
283. Elmes, R. B. P.; Erby, M.; Cloonan, S. M.; Quinn, S. J.; Williams, D. C.; Gunnlaugsson, T. *Chem. Commun.* **2011**, *47*, 686-688.
284. Neidle, S.; Thurston, D. E. *Nat. Rev. Cancer* **2005**, *5*, 285.
285. Griffith, D.; Morgan, M. P.; Marmion, C. J. *Chem. Commun.* **2009**, 6735-6737.
286. Vos, J. G.; Kelly, J. M. *Dalton Trans.* **2006**, 4869-4883.
287. Banerjee, S.; Kitchen, J. A.; Gunnlaugsson, T.; Kelly, J. M. *Org. Biomol. Chem.* **2012**, *10*, 3033.
288. Banerjee, S.; Kitchen, J. A.; Gunnlaugsson, T.; Kelly, J. M. *Org. Biomol. Chem.* **2013**, *11*, 5642-56655.
289. Banerjee, S.; Kitchen, J. A.; Bright, S. A.; O'Brien, J. E.; Williams, D. C.; Kelly, J. M.; Gunnlaugsson, T. *Chem. Commun.* **2013**, *49*, 8522-8524.
290. Elmes, R. B. P.; Orange, K. N.; Cloonan, S. M.; Williams, D. C.; Gunnlaugsson, T. *J. Am. Chem. Soc.* **2011**, *133*, 15862-15865.
291. Elmes, R. B. P.; Kitchen, J. A.; Williams, D. C.; Gunnlaugsson, T. *Dalton Trans.* **2012**, *41*, 6607-6610.
292. Reedijk, J. *Eur. J. Inorg. Chem.* **2009**, 1303-1312.
293. Peyrone, M. *Ann. Chem. Pharm.* **1844**, *51*, 1-29.
294. Rosenberg, B.; Van Camp, L.; Grimley, E. B.; Thomson, A. J. *J. Biol. Chem.* **1967**, *242*, 1347-1352.
295. Jennette, K. W.; Lippard, S. J.; VAssiliades, G. A.; Baueri, W. R. *Proc Natl Acad Sci U S A* **2013**, *71*, 3839-3843.
296. Howe-Grant, M.; Wu, K. C.; Bauer, W. R.; Lippard, S. J. *Biochemistry* **1976**, *15*, 4339.
297. Howe-Grant, M.; Lippard, S. J. *Biochemistry* **1979**, *18*, 5762.
298. Peyratout, C. S.; Aldridge, T. K.; Crites, D. K.; McMIllin, D. R. *Inorg. Chem.* **1995**, *34*, 4484-4489.
299. Hosseini, S. S.; Bhadbhade, M.; Clarke, R. J.; Rutledge, P. J.; Rendina, L. M. *Dalton Trans.* **2011**, *40*, 506.
300. Clark, M. L.; Green, R. L.; Johnson, O. E.; Fanwick, P. E.; McMIllin, D. R. *Inorg. Chem.* **2008**, *47*, 9410-9418.
301. McFadyen, W. D.; Wakelin, L. P. G.; Roos, I. A. G.; Hillcoat, B. L. *Biochem J* **1987**, *242*, 177-183.
302. Glover, P. B.; Ashton, P. R.; Childs, L. J.; Rodger, A.; Kercher, M.; Williams, R. M.; De Cola, L.; Pikramenou, Z. *J. Am. Chem. Soc.* **2003**, *125*, 9918-9919.
303. Lo, Y.-C.; Ko, T.-P.; Su, W.-C.; Su, T.-L.; Wang, A. H. J. *J. Inorg. Biochem.* **2009**, *103*, 1082-1092.
304. Aldridge, T. K.; Stacy, E. M.; McMIllin, D. R. *Inorg. Chem.* **1994**, *33*, 722.
305. Williams, J. Platinum. In *Photochemistry and Photophysics of Coordination Compounds*, Springer Berlin / Heidelberg, Ed.; 2007; Vol. 281, p 205.

306. Meskers, S. C. J.; Dekkers, P. J. M. *J. Phys. Chem. A* **2001**, *105*, 4589-4599.
307. Meskers, S. C. J.; Ubbink, M.; Canters, G. W.; Dekkers, P. J. M. *Journal of Physical Chemistry* **1996**, *100*, 17957-17969.
308. Meskers, S. C. J.; Dekkers, P. J. M. *J. Am. Chem. Soc.* **1998**, *120*, 6413-6414.
309. Ghosh, P.; Han, G.; De, M.; Kim, C. K.; Rotello, V. M. *Adv. Drug Del. Rev.* **2008**, *60*, 1307-1315.
310. Gil, P. R.; Parak, W. J. *ACS Nano* **2008**, *2*, 2200-2205.
311. Rosi, N. L.; Mirkin, C. A. *Chem. Rev.* **2005**, *105*, 1547-1562.
312. Daniel, M. C.; Astruc, D. *Chem. Rev.* **2004**, *104*, 293-346.
313. Ipe, B. I.; Yoosaf, K.; Thomas, K. G. *J. Am. Chem. Soc.* **2006**, *128*, 1907-1913.
314. Lewis, D. J.; Day, T. M.; MacPherson, J. V.; Pikramenou, Z. *Chem. Commun.* **2006**, 1433-1435.
315. Davies, A.; Lewis, D. J.; Watson, S. P.; Thomas, S. G.; Pikramenou, Z. *Proc. Ntl. Acad. Sci. USA* **2012**, *109*, 1862-1867.
316. Fulham, S.; Rao, S. N.; Fitzmaurice, D. *J. Phys. Chem. B* **2000**, *104*, 6164-6173.
317. Gaillard, C.; Adumeau, P.; Canet, J.-L.; Gautier, A.; Boyer, D.; Beaudoin, C.; Hesling, C.; Morel, L.; Mahiou, R. *J. Mater. Chem. B* **2013**, *1*, 4306.
318. Soto, E.; MacDonald, J. C.; Cooper, C. G. F.; McGimpsey, W. G. *J. Am. Chem. Soc.* **2003**, *125*, 2838-2839.
319. Su, X.-C.; Man, B.; Beeren, S.; Liang, H.; Simonsen, S.; Schmitz, C.; Huber, T.; Messerle, B. A.; Otting, G. *J. Am. Chem. Soc.* **2013**, *130*, 10486-10487.
320. Potapov, A.; Yagi, H.; Huber, T.; Jergic, S.; Dixon, N. E.; Otting, G.; Goldfarb, D. *J. Am. Chem. Soc.* **2010**, *132*, 9040-9048.
321. Li, J.; Pilla, K. B.; Li, Q.; Zhang, Z.; Su, X.; Huber, T.; Yang, J. *J. Am. Chem. Soc.* **2013**, *135*, 8294-8303.
322. Yokokawa, S.; Tamaki, K.; Ito, E.; Hara, M. *J. Phys. Chem. B* **2003**, *107*, 3544-35551.
323. Ouali, N.; Bocquet, B.; Rigault, S.; Morgantini, P. Y.; Weber, J.; Piguet, C. *Inorg. Chem.* **2002**, *41*, 1436-1445.
324. Picot, A.; D'Aleo, A.; Baldeck, P. L.; Grichine, A.; Duperray, A.; Andraud, C.; Maury, O. *J. Am. Chem. Soc.* **2008**, *130*, 1532-1533.
325. Boisselier, E.; Astruc, D. *Chem. Soc. Rev.* **2009**, *38*, 1759-1782.
326. Turkevich, J.; Stevenson, P. C.; Hillier, J. *Discuss. Faraday Soc.* **1951**, *11*, 55-75.
327. Brust, M.; Walker, M.; Bethell, D.; Schiffrin, D. J.; Whyman, R. *J. Chem. Soc. ,Chem. Commun.* **1994**, 801-802.
328. Moriggi, L.; Cannizzo, C.; Dumas, E.; Mayer, C. R.; Ulianov, A.; Helm, L. *J. Am. Chem. Soc.* **2009**, *131*, 10828.
329. Smith, D. J. Chapter 1 Characterisation of Nanomaterials Using Transmission Electron Microscopy. In *Nanocharacterisation*, The Royal Society of Chemistry: 2007; pp 1-27.
330. Berne, B. J.; Pecora, R. *Dynamic Light Scattering: with applications to chemistry, biology and physics;* Dover Publications: Mineola, N. Y., 2000.
331. Dreaden, E. C.; Alkilany, A. M.; Huang, X.; Murphy, C. J.; El-Sayed, M. A. *Chem. Soc. Rev.* **2012**, *41*, 2740-2779.
332. Vogel, A. I.; Tatchell, A. R.; Furnis, B. S.; Hannaford, A. J.; Smith, P. W. G. *Vogel's Textbook of Practical Organic Chemistry;* 5 ed.; Prentice Hall: New York: 1996.
333. Cosier, J.; Glazer, A. M. *J. Appl. Crystalogr.* **1986**, *19*, 105-107.
334. Otwinowski, Z.; Minor, W. *Methods Enzymol* **1997**, *276*, 307-326.
335. Sheldrick, G. M. *Acta Crystallogr. Sect. A* **2008**, *A64*, 112-122.

Appendices

Appendix Two

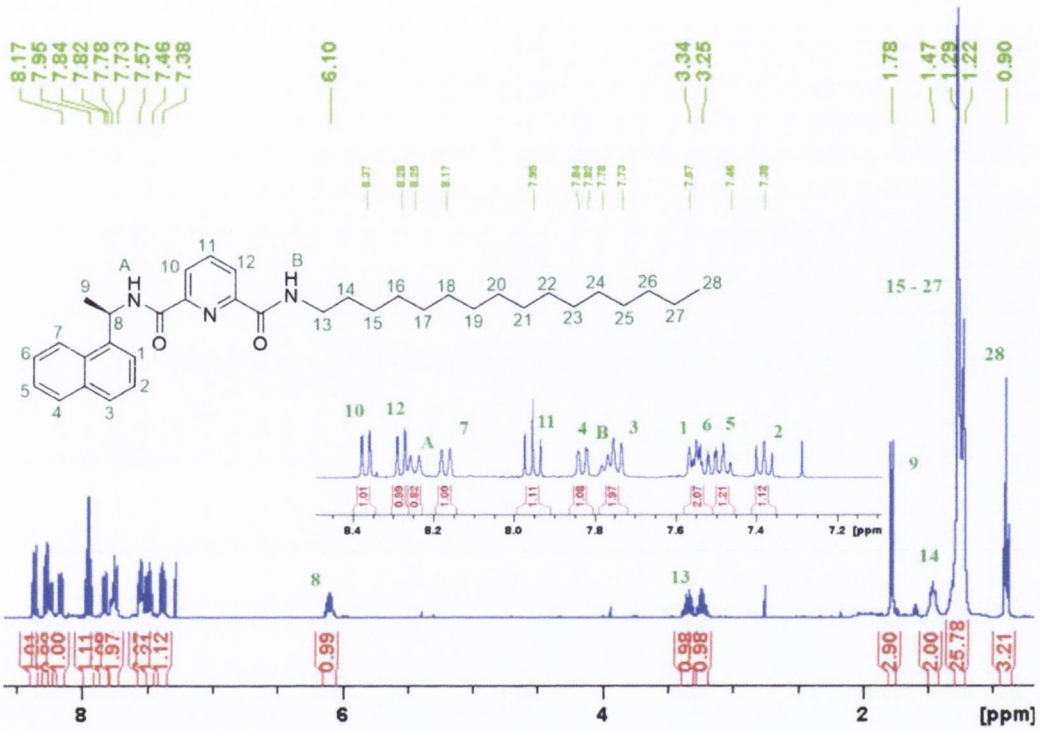

Figure A2.1. *^{1}H NMR spectrum (400 MHz, $CDCl_3$) of* ***82*** *(R).*

Table A2.1: *Crystal data and structure refinement for* ***81****.*

Identification code	**81**	
Empirical formula	$C_{35}\ H_{49}\ N_3\ O_2$	
Formula weight	543.77	
Temperature	150(2) K	
Wavelength	1.54180 Å	
Crystal system	Monoclinic	
Space group	P(2)1	
Unit cell dimensions	a = 11.259(2) Å	a = 90°.
	b = 17.782(4) Å	β = 95.09(3)°.
	c = 15.950(3) Å	γ = 90°.
Volume	3180.7(11) $Å^3$	
Z	4	
Density (calculated)	1.136 Mg/m^3	
Absorption coefficient	0.541 mm^{-1}	
F(000)	184	
Crystal size	0.46 x 0.09 x 0.02 mm^3	
Theta range for data collection	3.73 to 76.89°.	
Index ranges	-14<=h<=14, -22<=k<=22, -19<=l<=20	
Reflections collected	66087	
Independent reflections	13245 [R(int) = 0.0609]	
Completeness to theta = 76.89°	99.4 %	
Absorption correction	Semi-empirical from equivalents	
Max. and min. transmission	1.00000 and 0.61634	
Refinement method	Full-matrix least-squares on F^2	
Data / restraints / parameters	13245 / 1 / 725	
Goodness-of-fit on F^2	1.029	
Final R indices [I>2sigma(I)]	R1 = 0.0421, wR2 = 0.1102	
R indices (all data)	R1 = 0.0468, wR2 = 0.1151	
Absolute structure parameter	-0.14(13)	
Largest diff. peak and hole	0.190 and -0.144 $e.Å^{-3}$	

Table A2.2: *Crystal data and structure refinement for* ***82****.*

Identification code	**82**	
Empirical formula	$C_{35}H_{49}N_3O_2$	
Formula weight	543.77	
Temperature	108(2) K	
Wavelength	0.71073 Å	
Crystal system	Monoclinic	
Space group	P2(1)	
Unit cell dimensions	a = 11.246(2) Å	a = 90°.
	b = 17.766(4) Å	β = 95.11(3)°.
	c = 16.042(3) Å	γ = 90°.
Volume	3192.4(11) $Å^3$	
Z	4	
Density (calculated)	1.131 Mg/m^3	
Absorption coefficient	0.070 mm^{-1}	
F(000)	1184	
Crystal size	0.60 x 0.20 x 0.20 mm^3	
Theta range for data collection	1.71 to 24.50°.	
Index ranges	-13<=h<=13, -17<=k<=20, -18<=l<=18	
Reflections collected	24917	
Independent reflections	5505 [R(int) = 0.1072]	
Completeness to theta = 24.50°	99.9 %	
Absorption correction	Semi-empirical from equivalents	
Max. and min. transmission	0.9862 and 0.9593	
Refinement method	Full-matrix least-squares on F^2	
Data / restraints / parameters	5505 / 1 / 725	
Goodness-of-fit on F^2	1.209	
Final R indices [I>2sigma(I)]	R1 = 0.0899, wR2 = 0.1995	
R indices (all data)	R1 = 0.1077, wR2 = 0.2174	
Largest diff. peak and hole	0.247 and -0.317 $e.Å^{-3}$	

Table A2.3. *Hydrogen bonds lengths and angles for ligand* ***82*** *(Å and °). Symmetry transformations used to generate equivalent atoms:* [a] *-x+1,y+1/2,-z+2* [b] *x+1,y,z*

D-H...A	d(D-H)	d(H...A)	d(D...A)	<(DHA)
N(1)-H(1X)...O(102)[a]	0.86	2.26	3.051 (7)	152.6
N(3)-H(3X)...O(102)[a]	0.86	2.09	2.935 (7)	168.6
N(103)-H(10X)...O(2)[b]	0.86	2.30	2.998(7)	154.9
N(101)-H(10Y)...O(2)[b]	0.86	2.19	3.011(7)	159.1

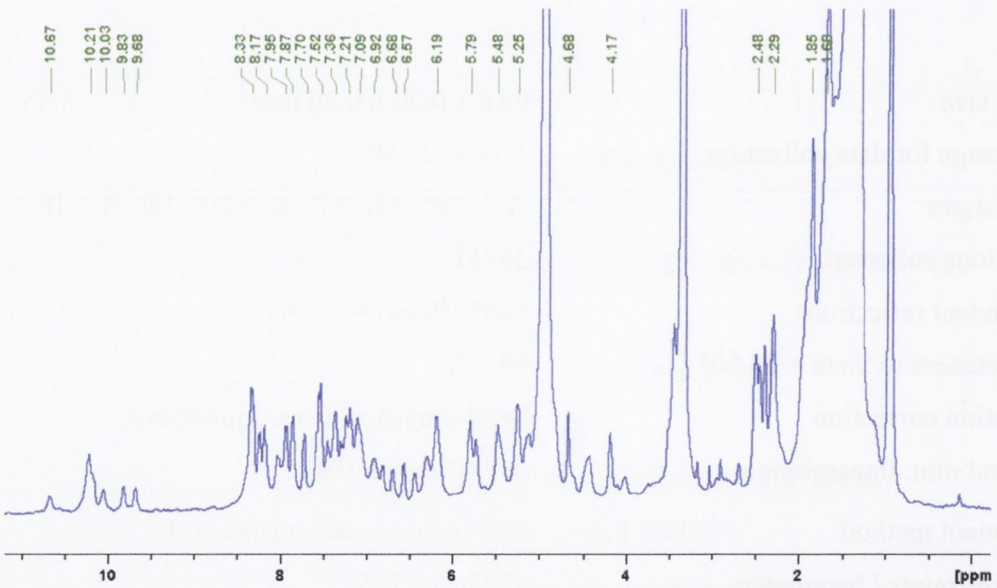

Figure A2.2. *[1]H NMR spectrum (400 MHz, CD_3OD-d_4) of Eu.**82**$_3$.*

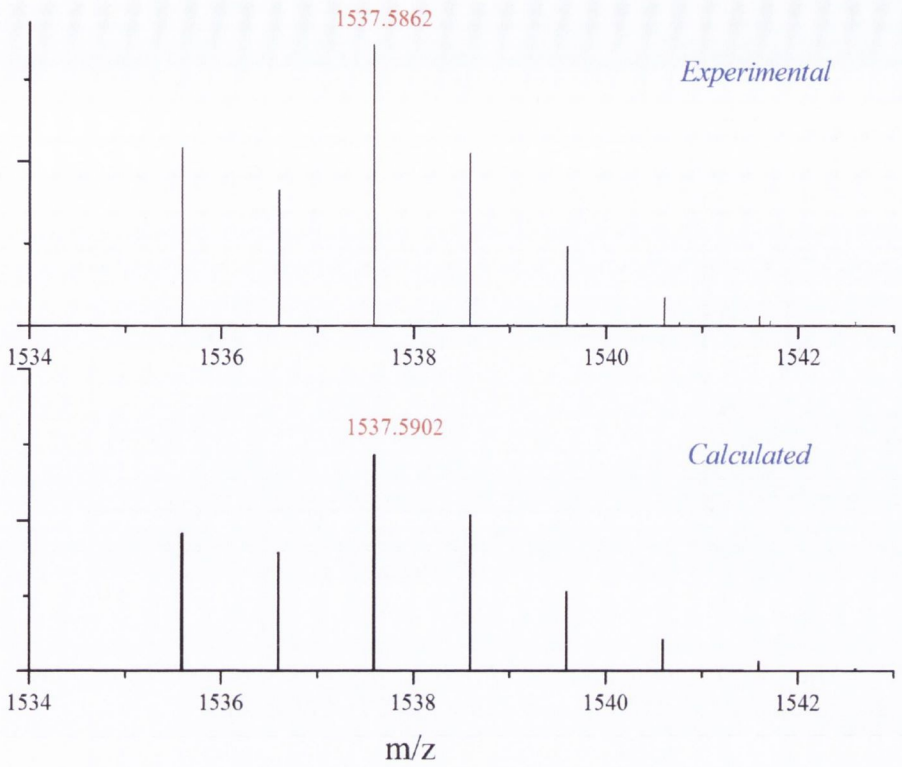

Figure A2.3. *The calculated and experimental isotopic distribution patterns for Eu.**81**$_2$ showing the 1:2 (M:L) stoichiometric pattern for a molecular species formula $[M - 2CF_3SO_3]^+$.*

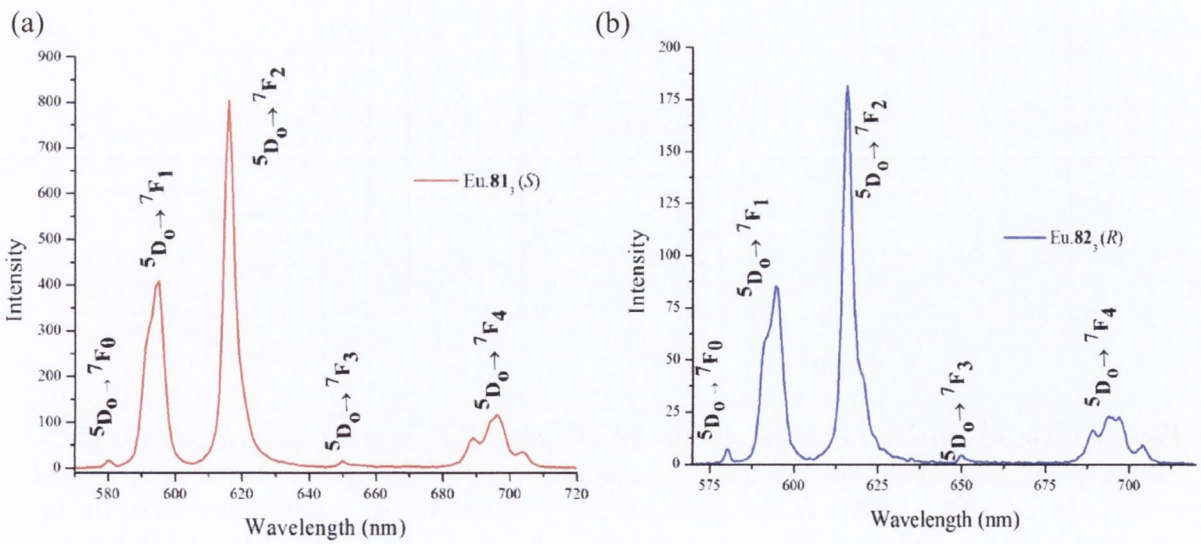

Figure A2.4. *Eu^{III}-centred luminescence emission spectra of (a) Eu.**81**$_3$ (S) and (b) Eu.**82**$_3$ (R) in CH_3OH.*

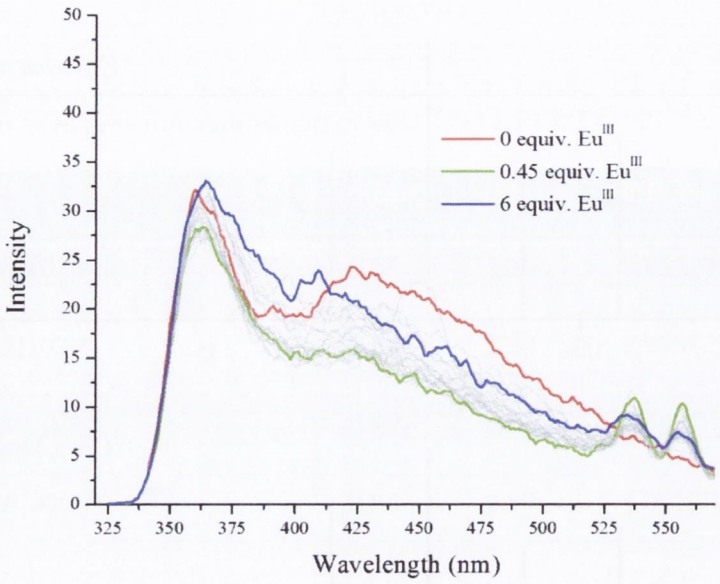

Figure A2.5. *The overall changes in the fluorescence emission spectra upon titrating* ***81*** *(S) (1 x 10^{-5} M) against Eu(CF$_3$SO$_3$)$_3$ (0→6 equiv.) in CH$_3$CN at RT.*

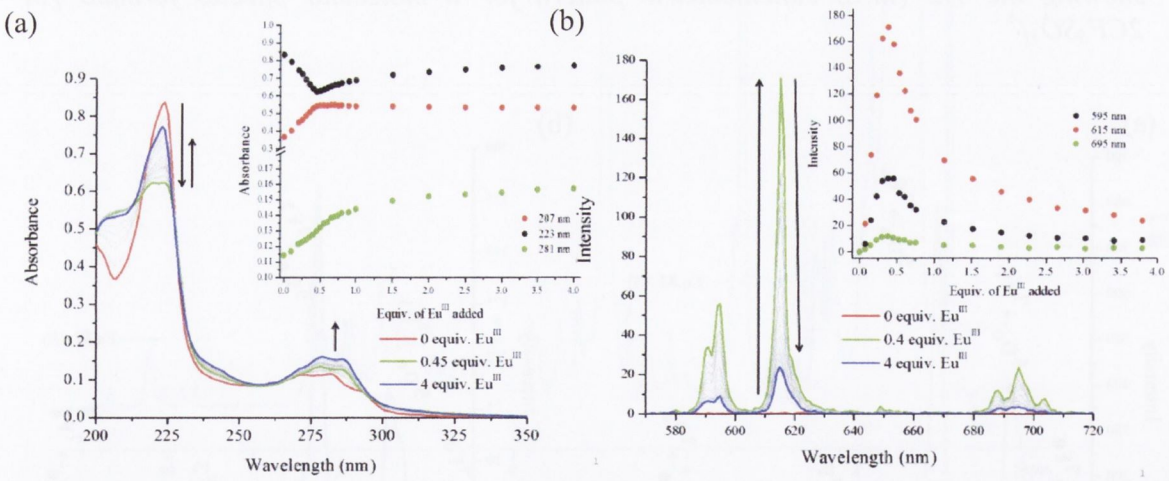

Figure A2.6. *The overall changes in the (a) UV-visible absorption spectra and (b) Eu^{III}–centred phosphorescence spectra upon titrating* ***82*** *(1 x 10^{-5} M) against Eu(CF$_3$SO$_3$)$_3$ (0→4 equiv.) in CH$_3$CN at RT.* ***Inset****: corresponding experimental binding isotherm of (a) absorbance at λ = 223 and 281 nm and (b) Eu^{III} phosphorescence emission intensity at λ = 595, 615 and 695 nm.*

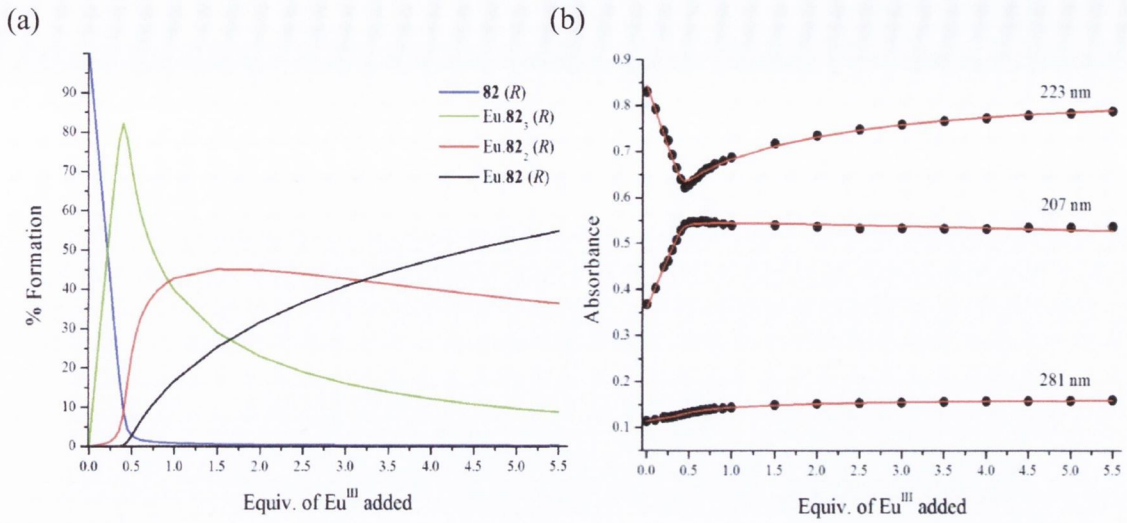

Figure A2.7. *(a) The speciation distribution diagram obtained from the UV-visible absorption titration data fit (upon titrating ligand* ***82*** *against $Eu(CF_3SO_3)_3$ in CH_3CN) and (b) the fit of the experimental binding isotherms using the non-linear regression analysis program SPECFIT.*

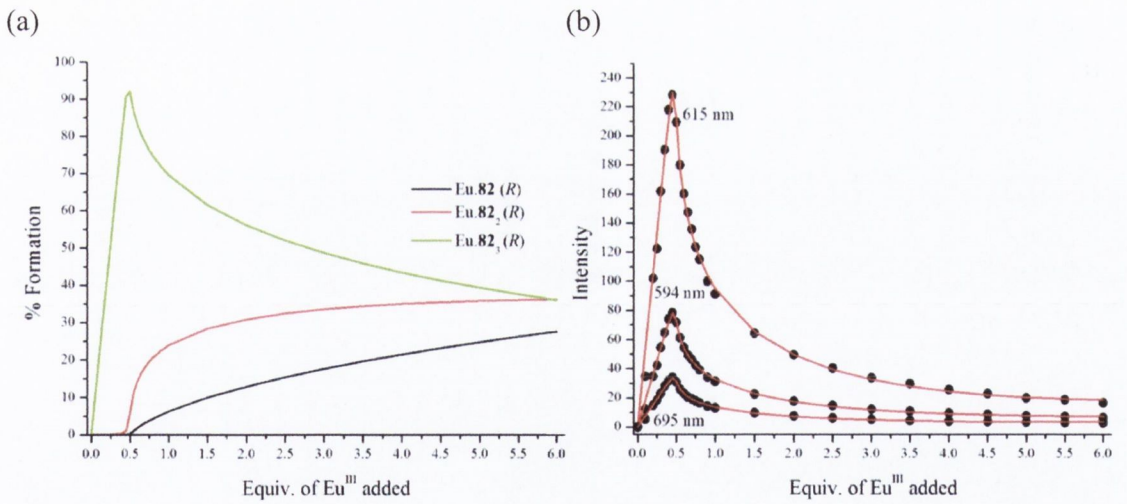

Figure A2.8. *(a) The speciation distribution diagram obtained from the luminescence titration data fit (upon titrating ligand* ***82*** *against $Eu(CF_3SO_3)_3$ in CH_3CN) and (b) the fit of the experimental binding isotherms using the non-linear regression analysis program SPECFIT.*

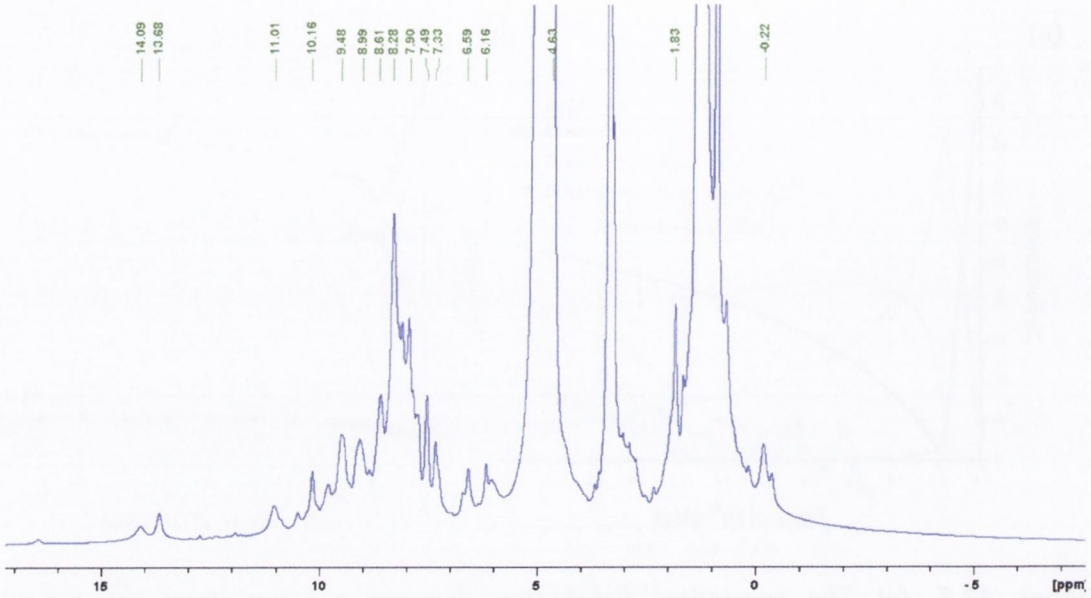

Figure A2.9. *^{1}H NMR spectrum (400 MHz, CD_3OD-d_4) of Nd.**81**$_3$.*

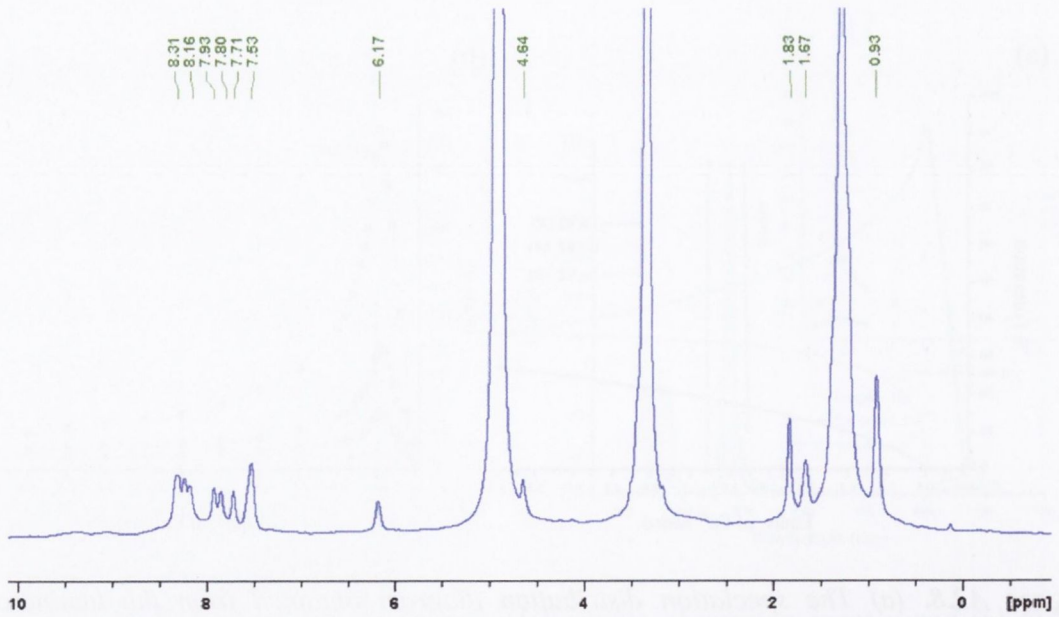

Figure A2.10. *^{1}H NMR spectrum (400 MHz, CD_3OD-d_4) of Nd.**82**$_3$.*

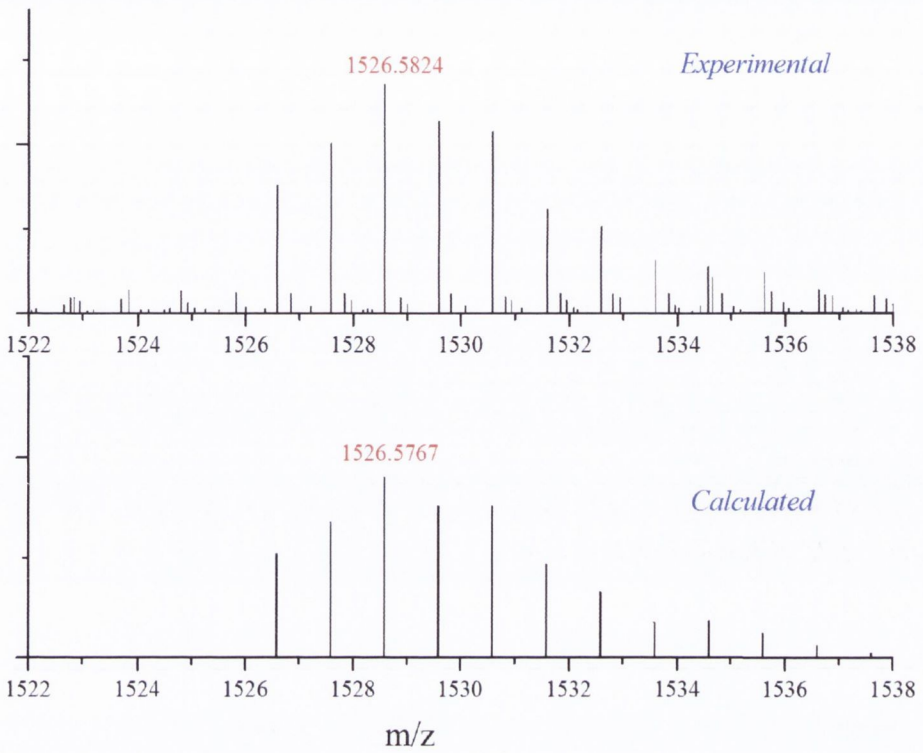

Figure A2.11. *The calculated and experimental isotopic distribution patterns for Nd.**81**$_2$ showing the 1:2 (M:L) stoichiometric pattern for a molecular species formula [M – 2CF$_3$SO$_3$]$^+$.*

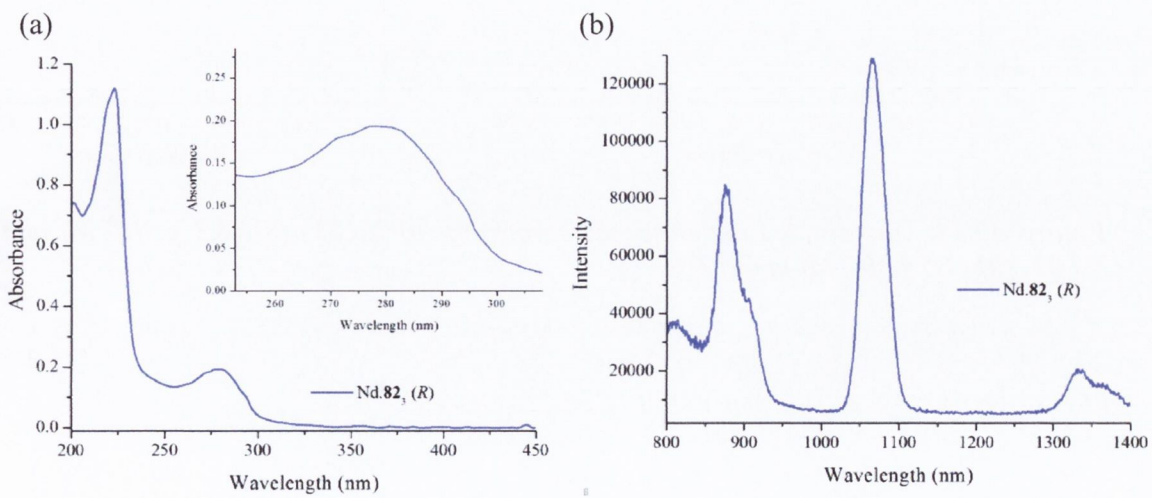

Figure A2.12. *(a) UV-visible absorption spectra and (b) corrected luminescence spectra of Nd.**82**$_3$ (R) (4.5 x 10^{-6} M) in CH$_3$CN.*

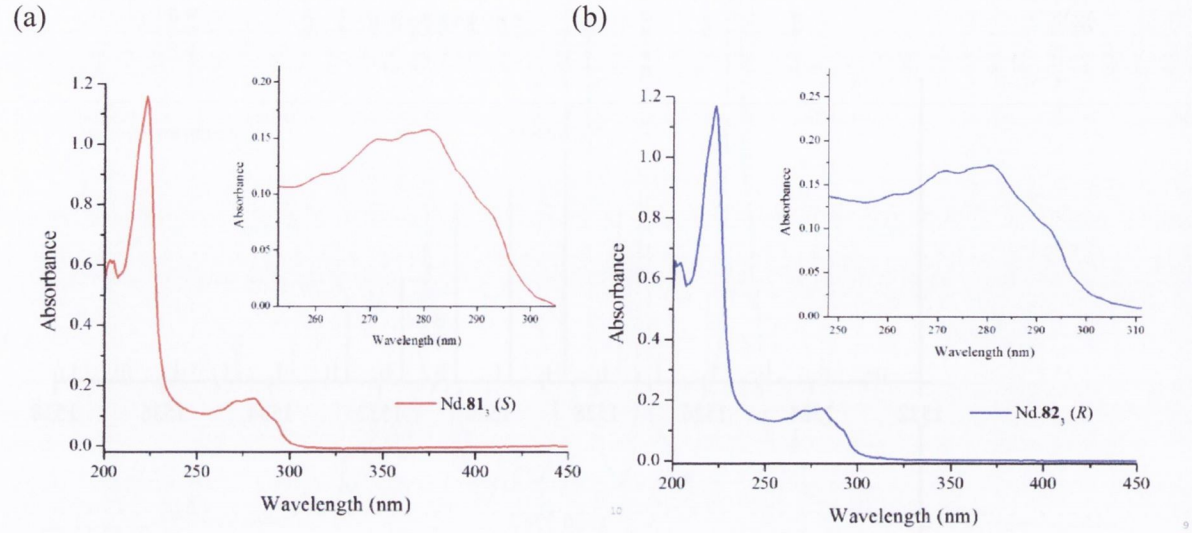

Figure A2.13. *UV-visible absorption spectra of (a) Nd.**81**$_3$ (S) (4.6 x 10^{-6} M) and (b) Nd.**82**$_3$ (R) (3.8 x 10^{-6} M) in CH_3OH.*

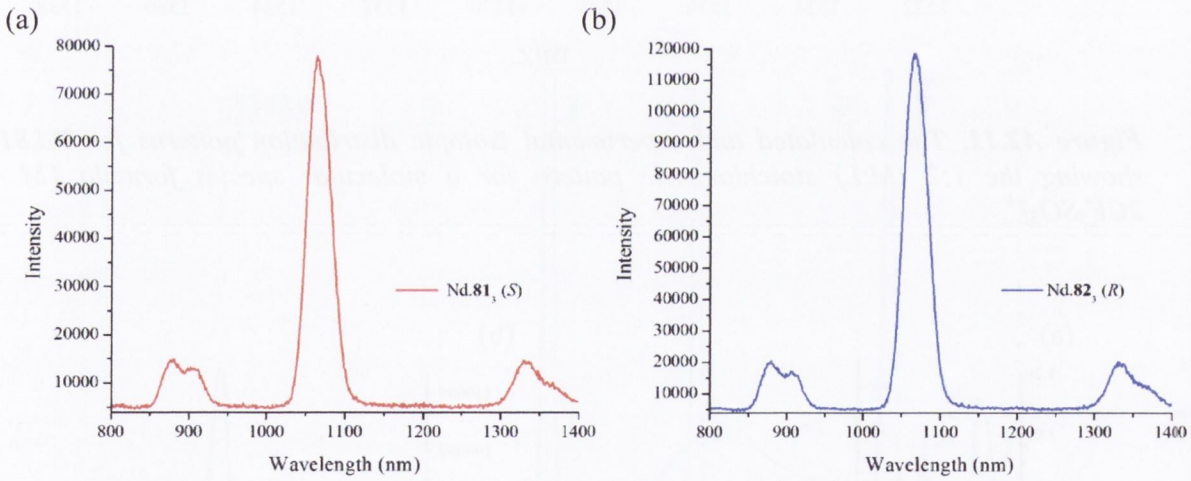

Figure A2.14. *Uncorrected luminescence spectra of (a) Nd.**81**$_3$ (S) (6.3 x 10^{-6} M) and (b) Nd.**82**$_3$ (R) (4.5 x 10^{-6} M) in CH_3CN.*

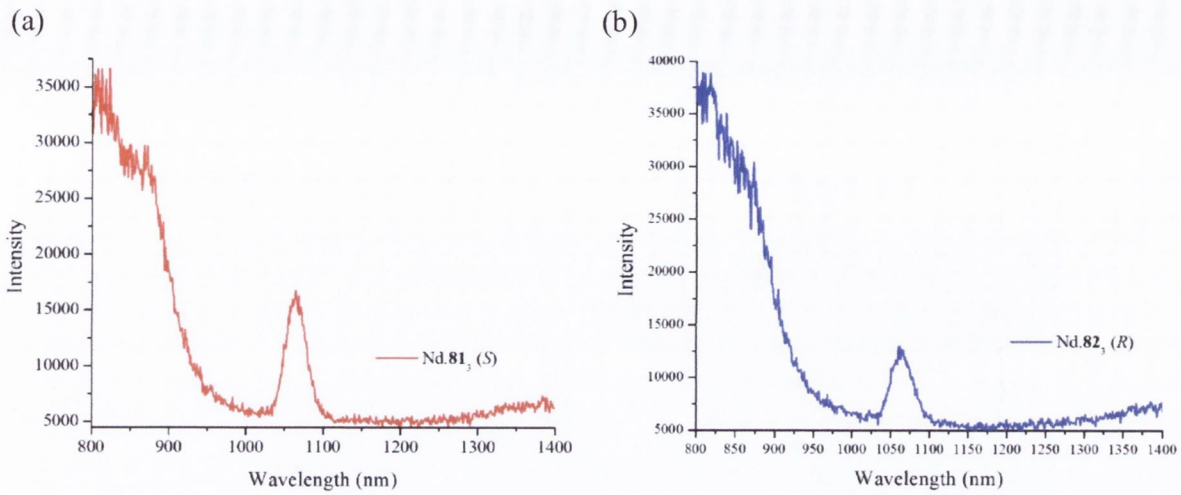

Figure A2.15. *Corrected luminescence spectra of (a) Nd.**81**$_3$ (S) (4.6 x 10^{-6} M) and (b) Nd.**82**$_3$ (R) (3.8 x 10^{-6} M) in CH_3OH.*

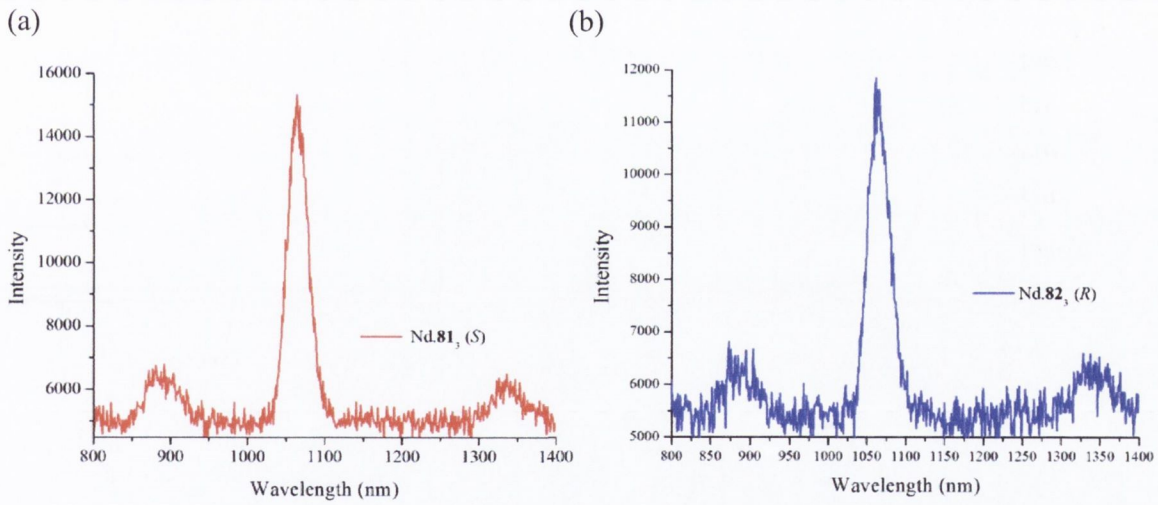

Figure A2.16. *Uncorrected luminescence spectra of (a) Nd.**81**$_3$ (S) (4.6 x 10^{-6} M) and (b) Nd.**82**$_3$ (R) (3.8 x 10^{-6} M) in CH_3OH.*

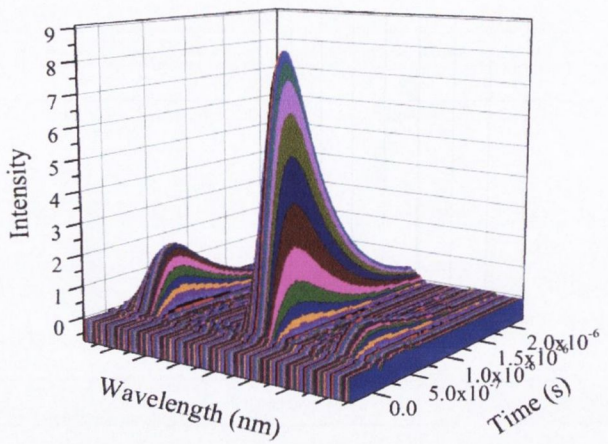

Figure A2.17. *Time-resolved emission spectrum of Nd.**82**$_3$ after excitation at 337 nm, showing sensitised Ln^{III}-based luminescence.*

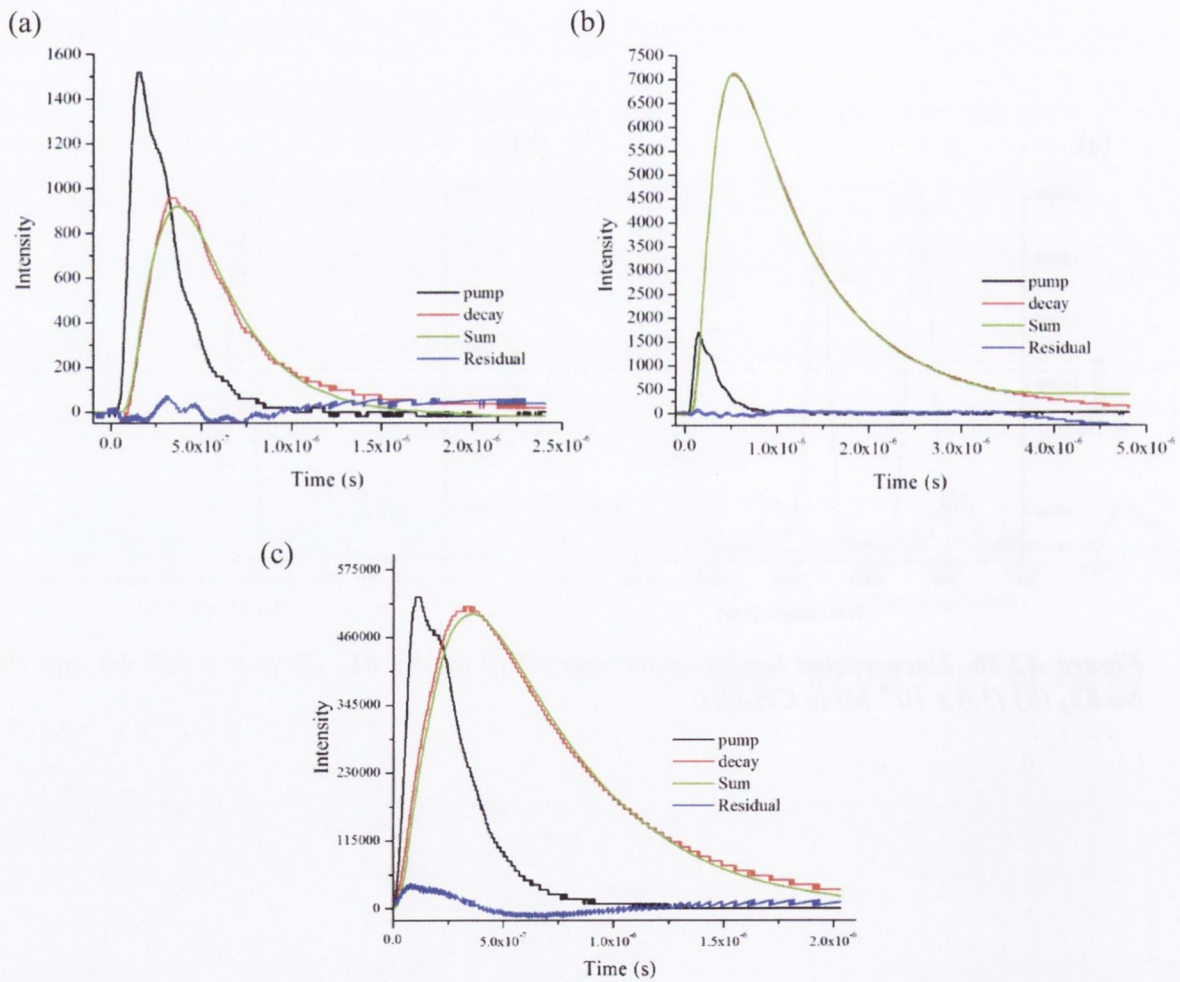

Figure A2.18. *Decay curves obtained from Nd.**82**$_3$ in (a) CH_3OH, (b) CD_3OD and (c) CH_3CN at 1064 nm and residuals for fitted curve generated by deconvulution of the instrument response function with a single exponential function.*

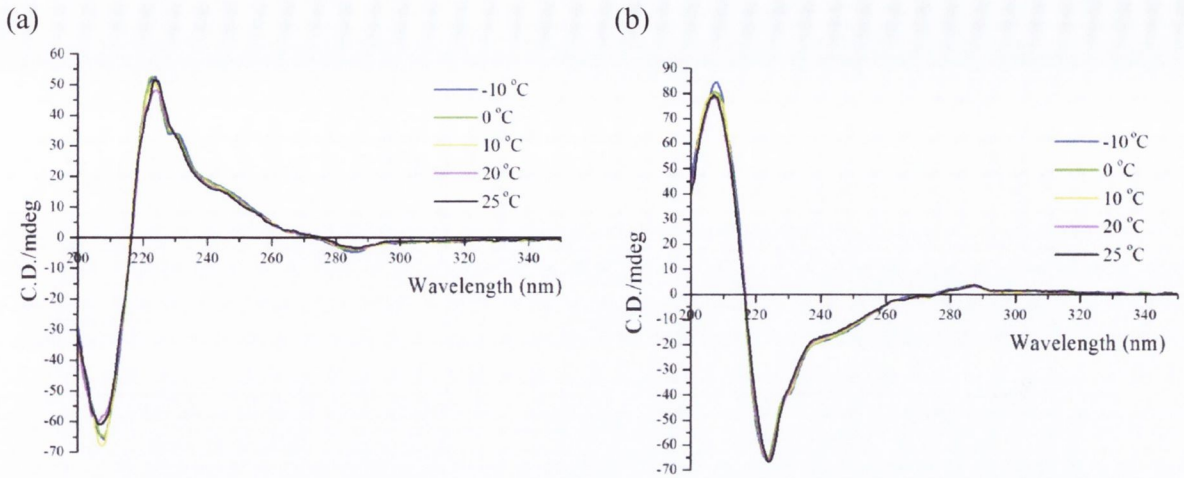

Figure A2.19. *CD spectra of (a) Nd.**81**$_3$ (S) and (b) Nd.**82**$_3$ (R) recorded at -10, 0 +10, +20 and +25 °C in CH_3CN.*

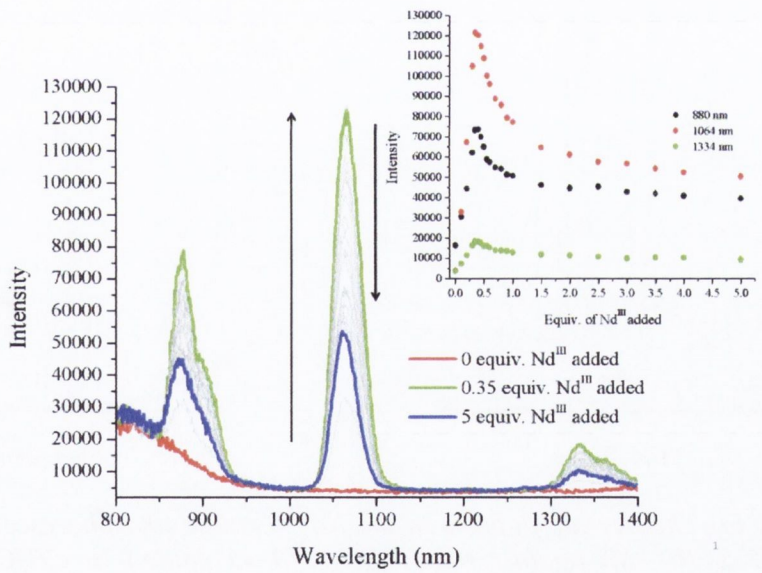

Figure A2.20. *Corrected luminescence spectra upon titrating ligand **81** (S) against specific known volumes of $Nd(CF_3SO_3)_3$.*

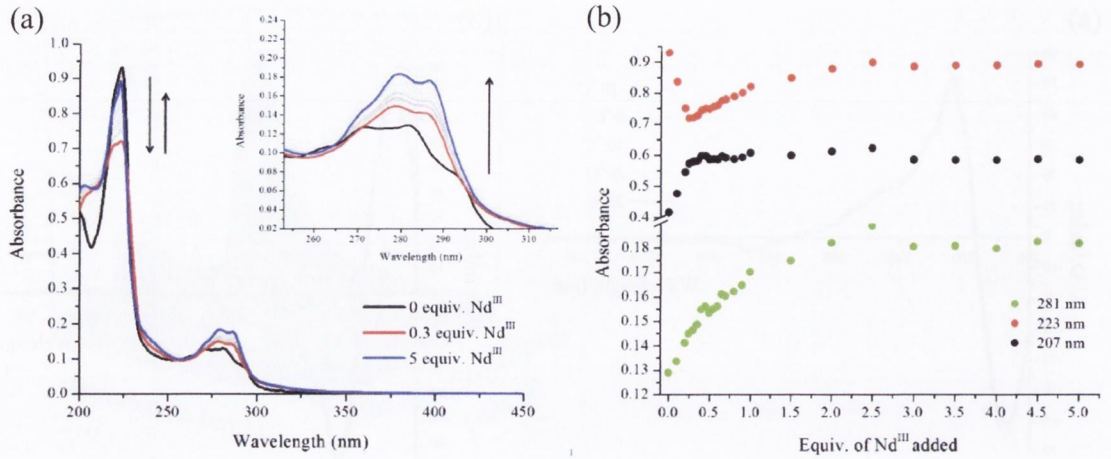

Figure A2.21. *The overall changes in (a) UV-visible absorption spectra upon titrating* ***82*** *(1 x 10^{-5} M) against $Nd(CF_3SO_3)_3$ (0→5 equiv.) in CH_3CN at RT. (b) corresponding experimental binding isotherm of absorbance at λ = 207, 223 and 281 nm.*

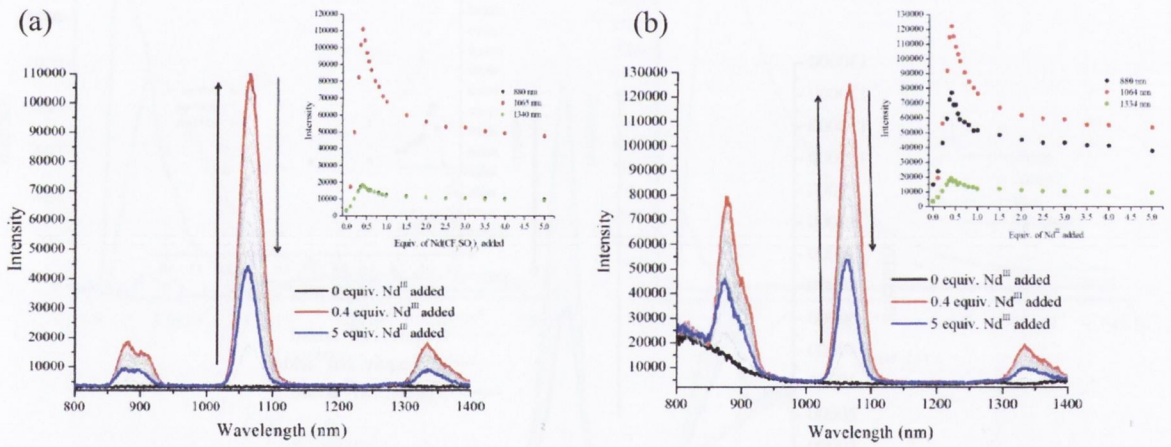

Figure A2.22. *(a) The overall changes in the Nd^{III}–centred phosphorescence spectra upon titrating* ***82*** *(1 x 10^{-5} M) against $Nd(CF_3SO_3)_3$ (0→5 equiv.) in CH_3CN at RT.* ***Inset****: corresponding experimental binding isotherm of (a) absorbance at λ = 207, 223 and 281 nm. (b) The corrected luminescence spectra upon titrating ligand* ***82*** *(R) against specific known volumes of $Nd(CF_3SO_3)_3$.*

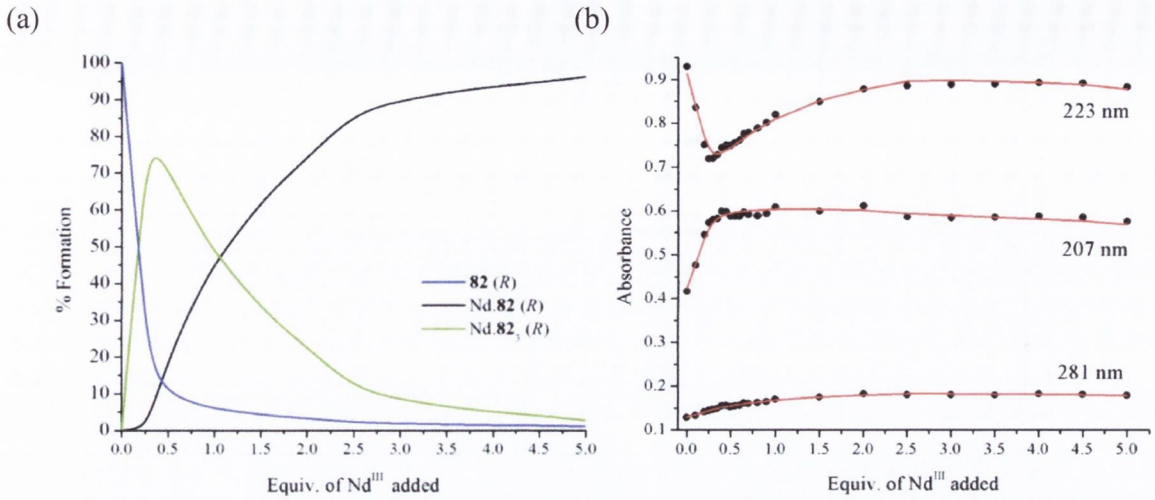

Figure A2.23. *(a) The speciation distribution diagram obtained from the UV-visible absorption titration data fit (upon titrating ligand* ***82*** *against $Nd(CF_3SO_3)_3$ in CH_3CN) and (b) the fit of the experimental binding isotherms using the non-linear regression analysis program SPECFIT.*

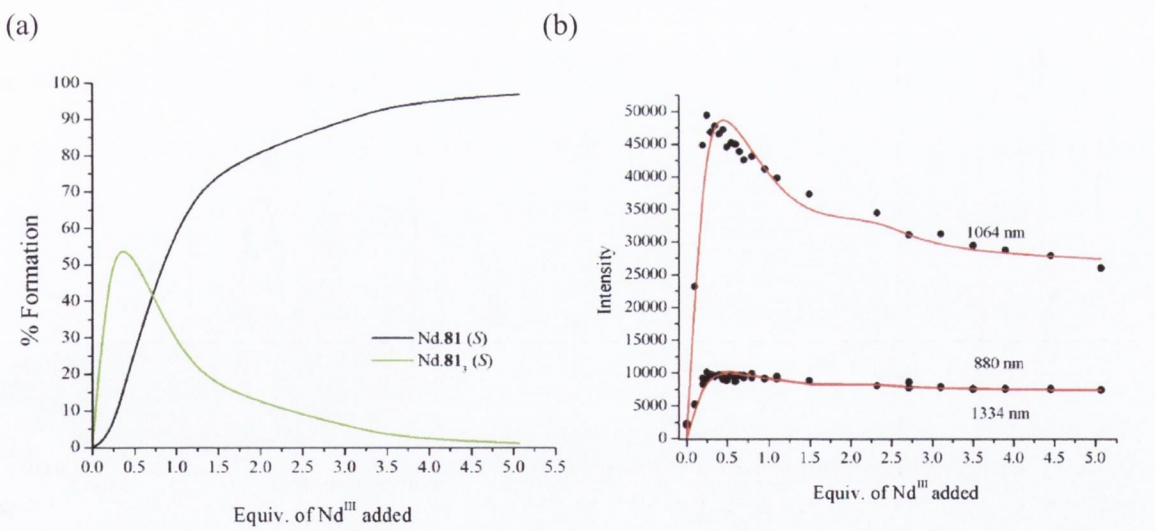

Figure A2.24. *(a) The speciation distribution diagram obtained from the luminescence titration data fit (upon titrating ligand* ***81*** *against $Nd(CF_3SO_3)_3$ in CH_3CN) and (b) the fit of the experimental binding isotherms using the non-linear regression analysis program SPECFIT.*

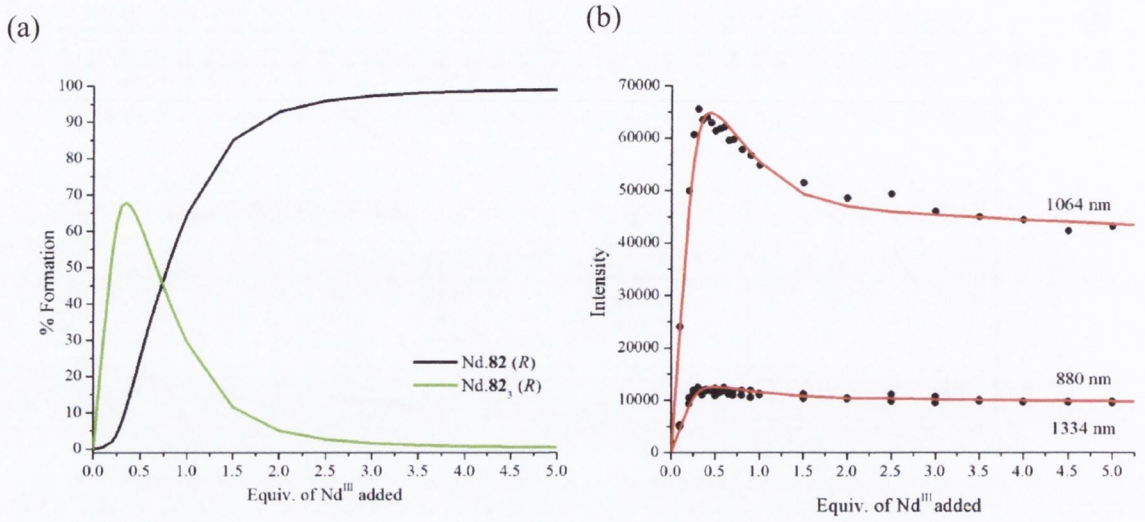

Figure A2.25. *(a) The speciation distribution diagram obtained from the luminescence titration data fit (upon titrating ligand* ***82*** *against $Nd(CF_3SO_3)_3$ in CH_3CN) and (b) the fit of the experimental binding isotherms using the non-linear regression analysis program SPECFIT.*

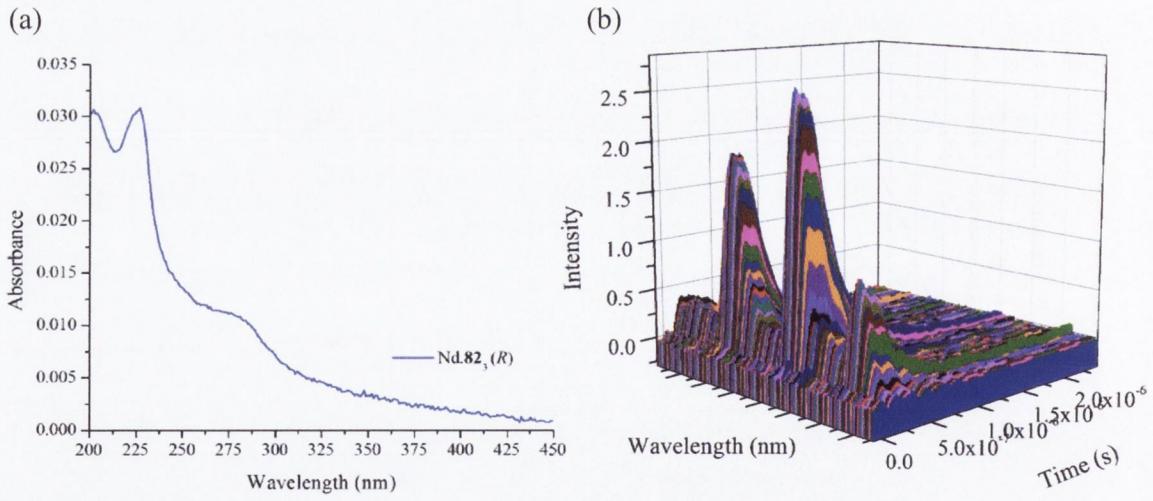

Figure A2.26. *(a) UV-visible absorption spectrum of Langmuir-Blodgett Nd.**82**$_3$ (S) monolayer and (b) time-resolved emission spectrum of Nd.**82**$_3$ (S) monolayer after excitation at 337 nm, showing sensitised Nd^{III}-based luminescence.*

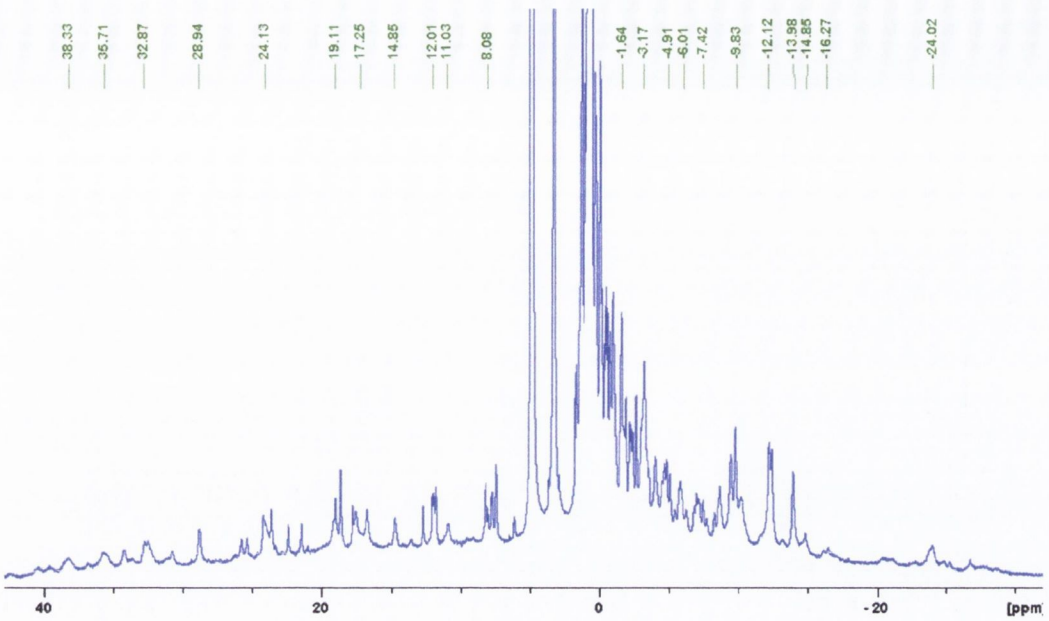

Figure A2.27. *^{1}H NMR spectrum (400 MHz, CD_3OD-d_4) of Tb.**81**$_3$.*

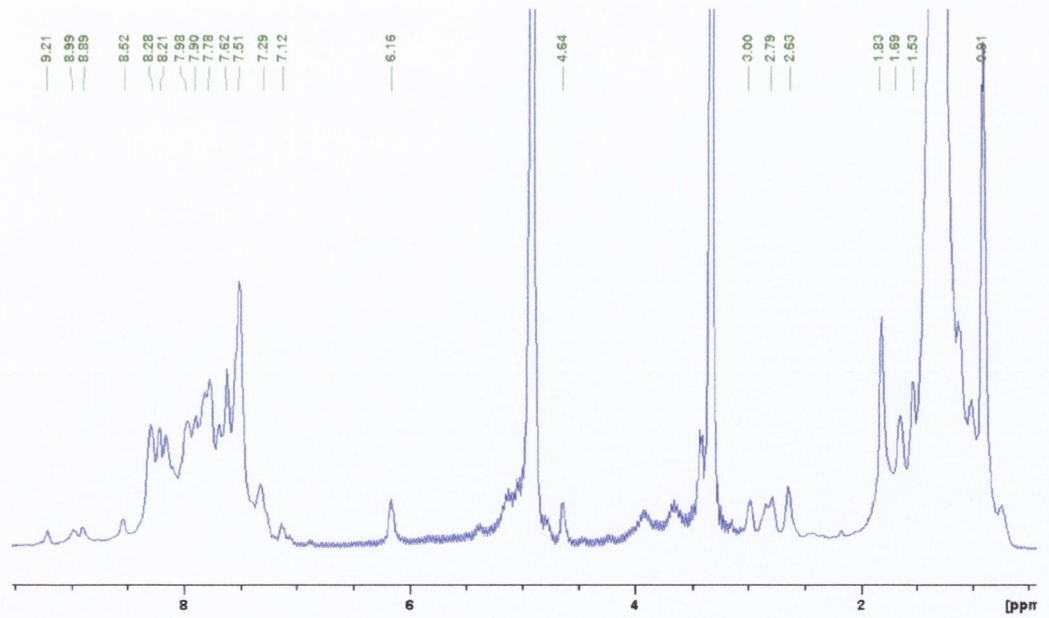

Figure A2.28. *^{1}H NMR spectrum (400 MHz, CD_3OD-d_4) of Sm.**81**$_3$.*

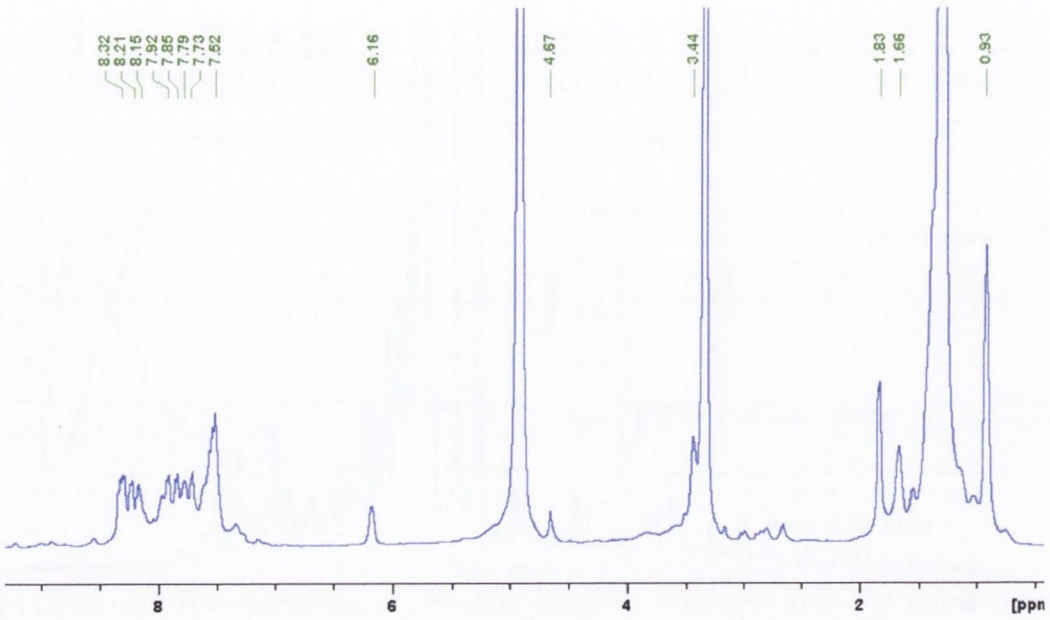

Figure A2.29. *^{1}H NMR spectrum (400 MHz, CD_3OD-d_4) of Sm.**82**$_3$.*

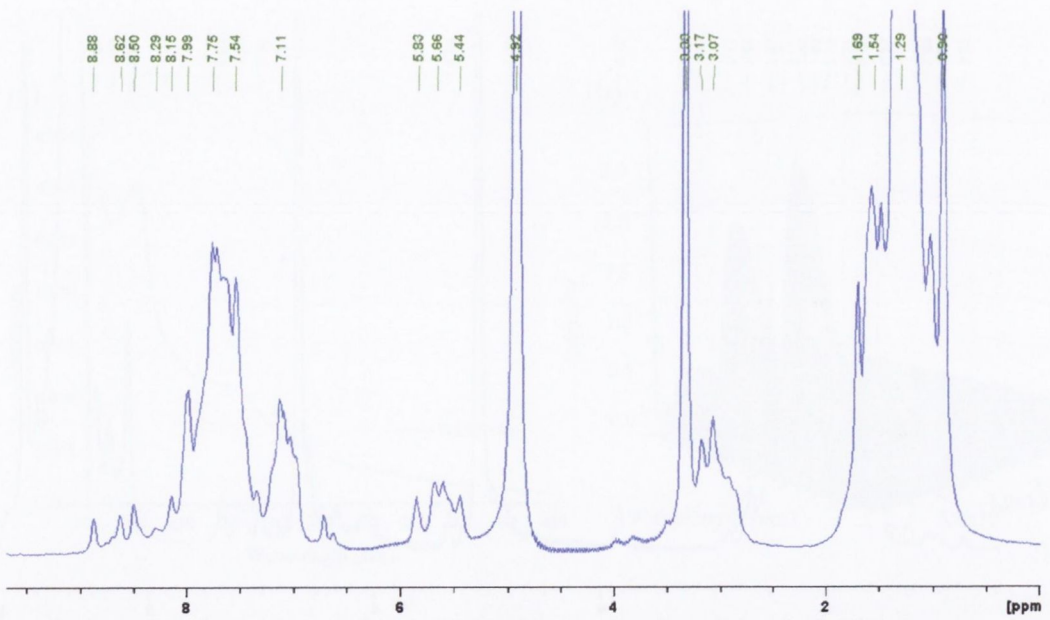

Figure A2.30. *^{1}H NMR spectrum (400 MHz, CD_3OD-d_4) of Lu.**81**$_3$.*

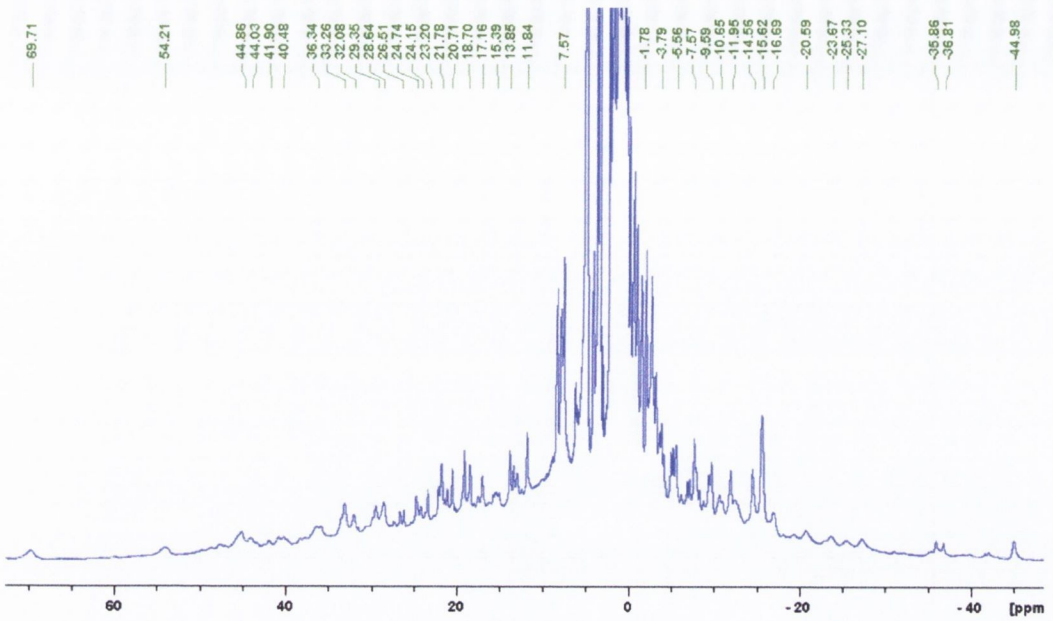

Figure A2.31. *^{1}H NMR spectrum (400 MHz, CD_3OD-d_4) of Dy.**81**$_3$.*

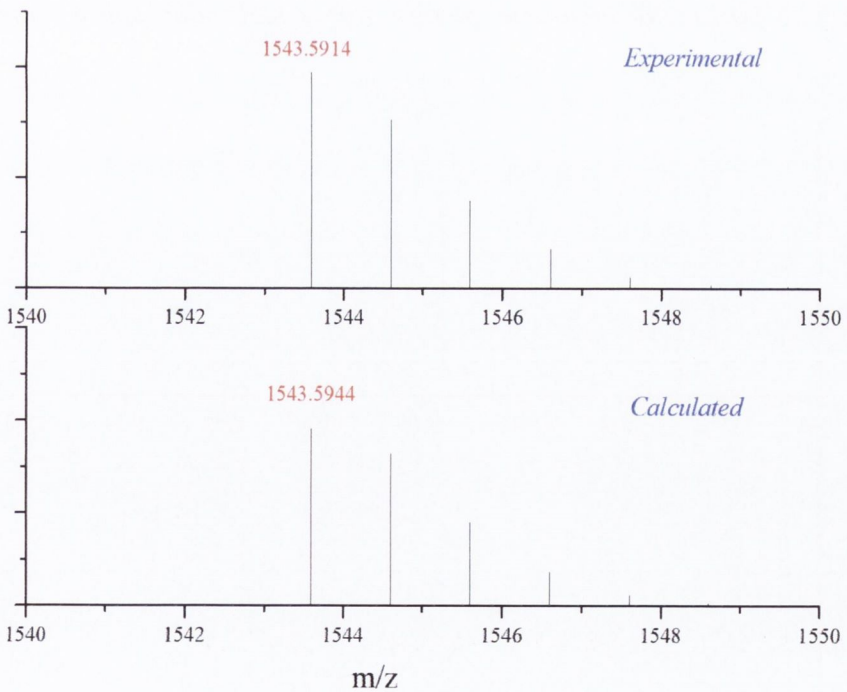

Figure A2.32. *The calculated and experimental isotopic distribution patterns for Tb.**81**$_2$ showing the 1:2 (M:L) stoichiometric pattern for a molecular species formula $[M - 2CF_3SO_3]^+$.*

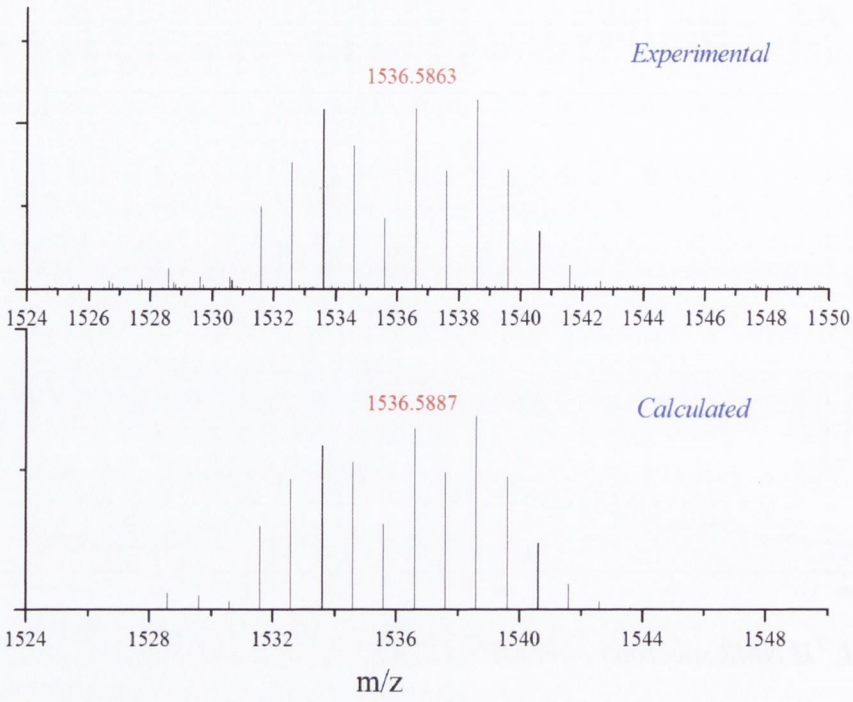

Figure A2.33. *The calculated and experimental isotopic distribution patterns for Sm.**81**$_2$ showing the 1:2 (M:L) stoichiometric pattern for a molecular species formula $[M - 2CF_3SO_3]^+$.*

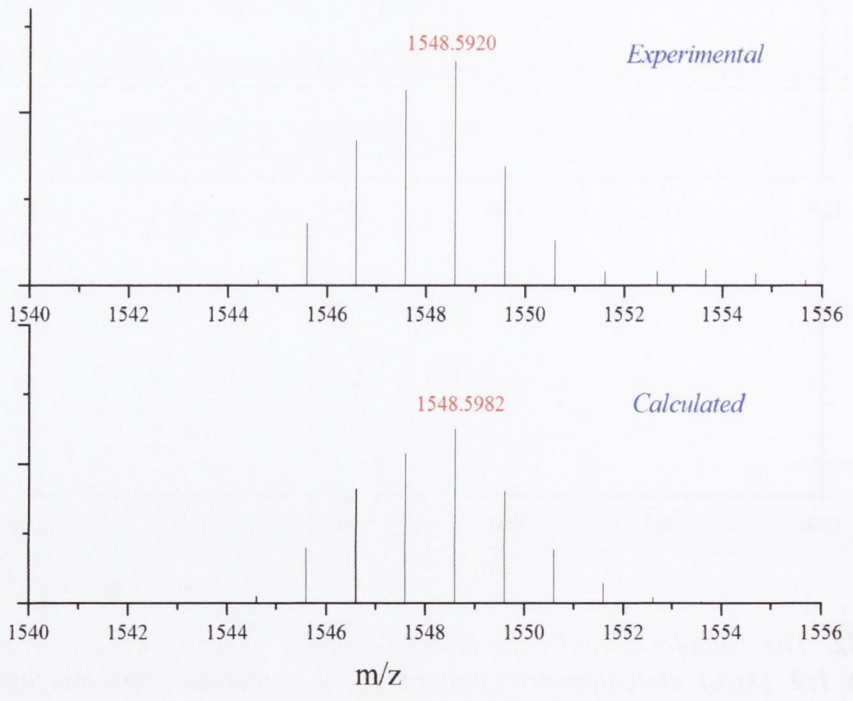

Figure A2.34. *The calculated and experimental isotopic distribution patterns for Dy.**81**$_2$ showing the 1:2 (M:L) stoichiometric pattern for a molecular species formula $[M - 2CF_3SO_3]^+$.*

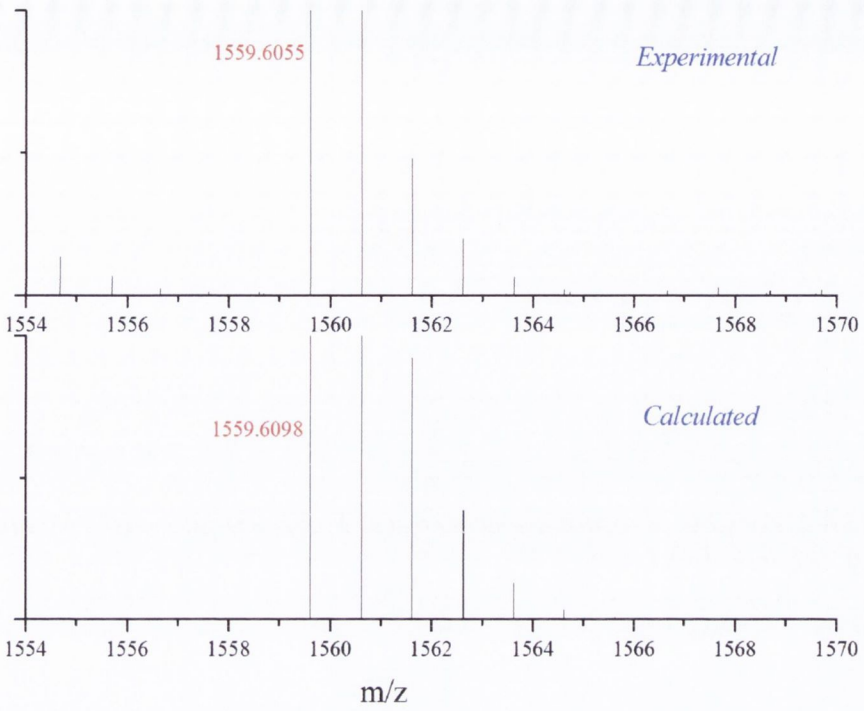

Figure A2.35. *The calculated and experimental isotopic distribution patterns for Lu.**81**$_2$ showing the 1:2 (M:L) stoichiometric pattern for a molecular species formula [M – 2CF$_3$SO$_3$]$^+$.*

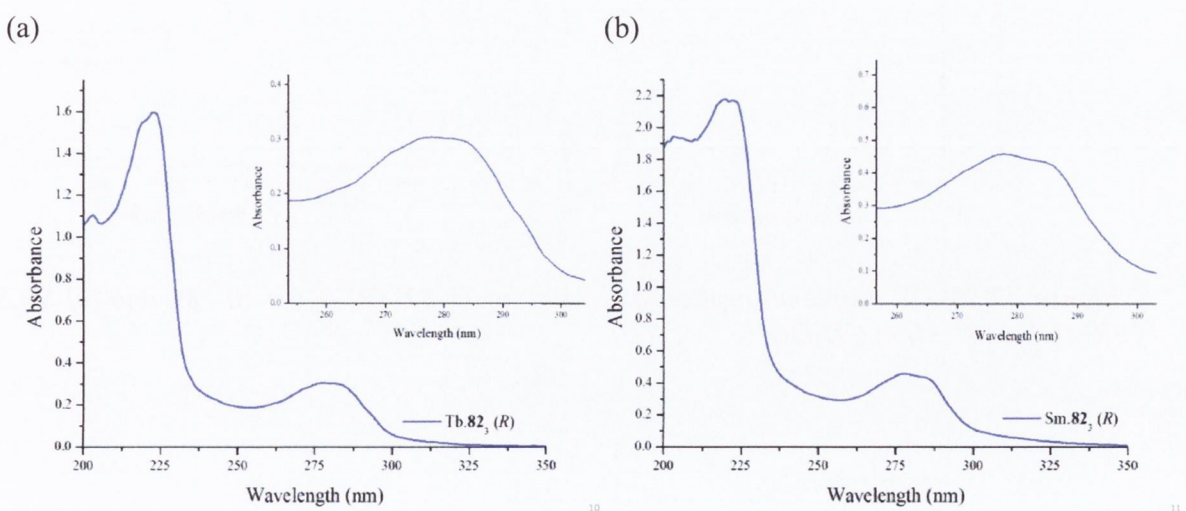

Figure A2.36. *UV-visible absorption spectra of (a) Tb.**82**$_3$ (R) (8.7 x 10^{-6} M) and (b) Sm.**82**$_3$ (R) (1.2 x 10^{-5} M) in CH$_3$CN.*

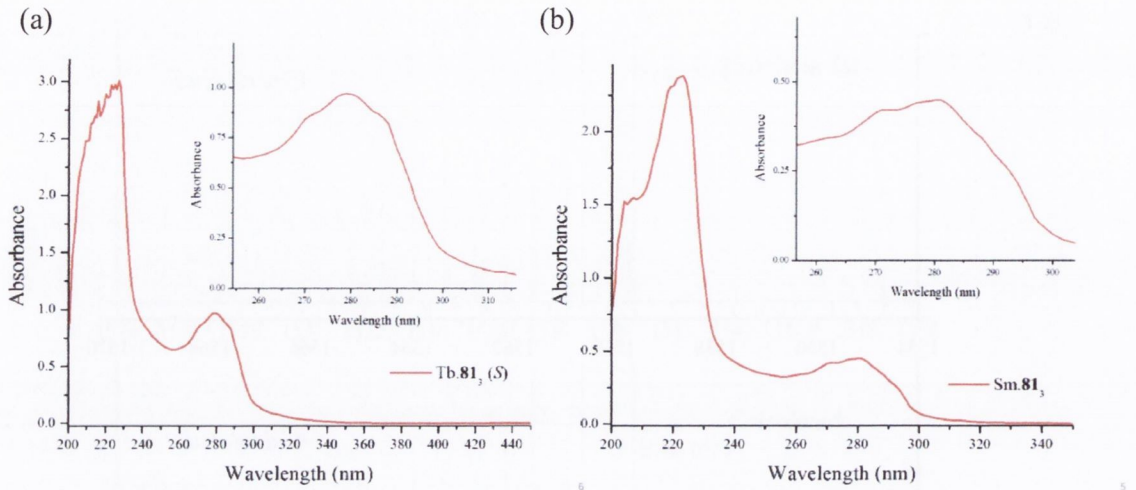

Figure A2.37. *UV-visible absorption spectra of (a) Tb.**81**$_3$ (S) (2.3 x 10^{-5} M) and (b) Sm.**82**$_3$ (S) (1.2 x 10^{-5} M) in CH$_3$OH.*

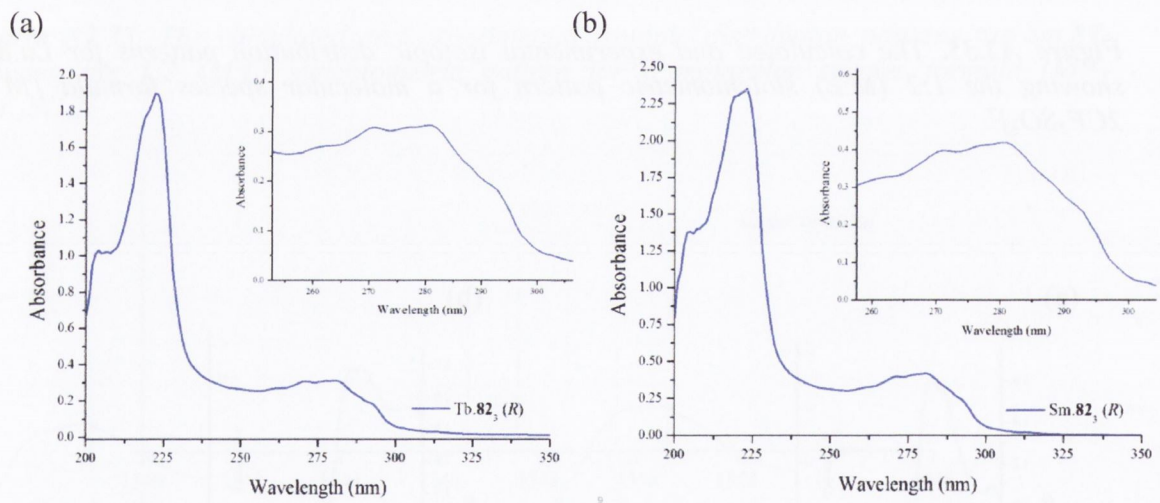

Figure A2.38. *UV-visible absorption spectra of (a) Tb.**82**$_3$ (R) (7.6 x 10^{-6} M) and (b) Sm.**82**$_3$ (R) (1.1 x 10^{-5} M) in CH$_3$OH.*

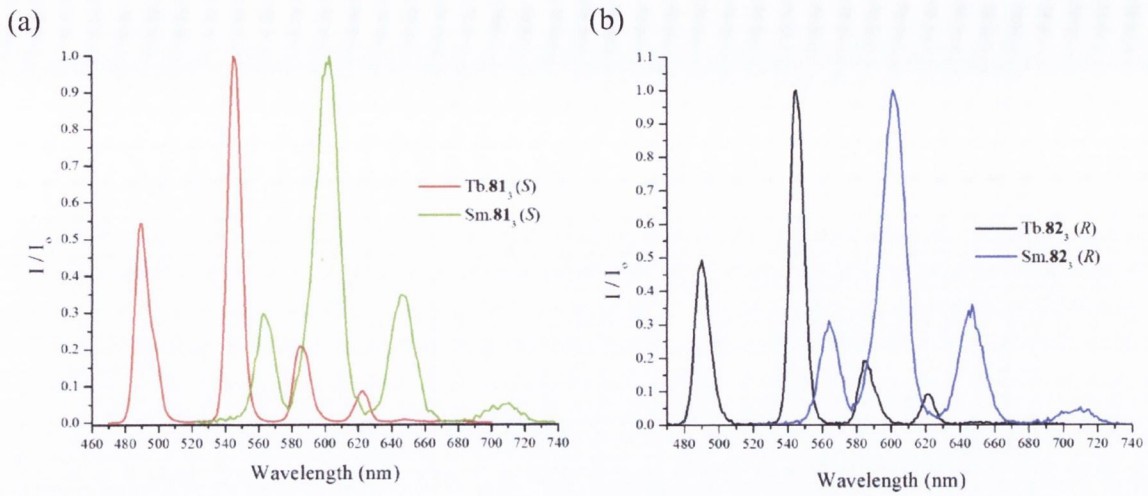

Figure A2.39. *Phosphorescence spectra of (a) Tb.**81**$_3$ (S) and Sm.**81**$_3$ (S) and (b) Tb.**82**$_3$ (R) and Sm.**82**$_3$ (R) recorded in CH_3OH.*

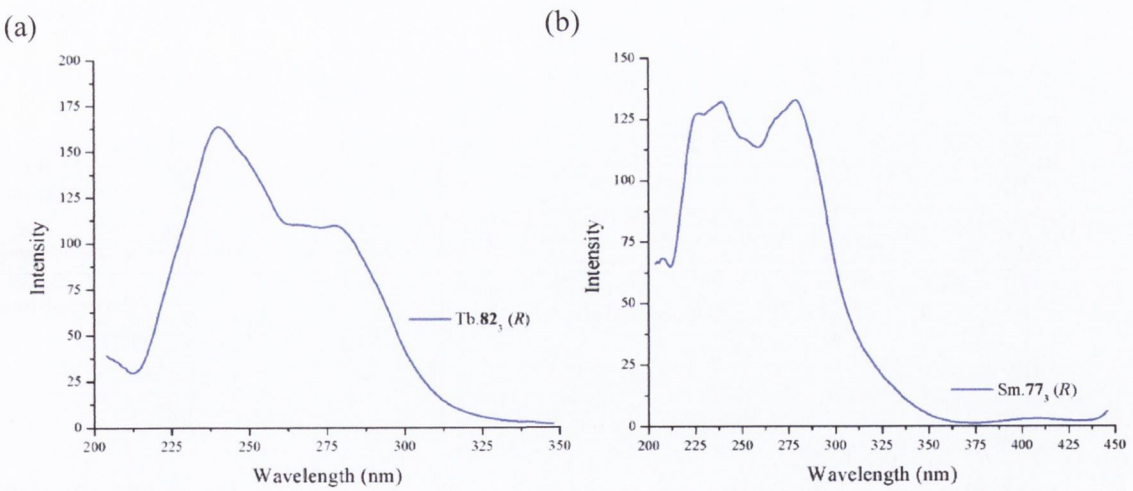

Figure A2.40. *Excitation spectra of (a) Tb.**82**$_3$ (R) (8.7 x 10^{-6} M) (λ_{em} = 545 nm) and (b) Sm.**82**$_3$ (R) (1.2 x 10^{-5} M) (λ_{em} = 645 nm) in CH_3CN.*

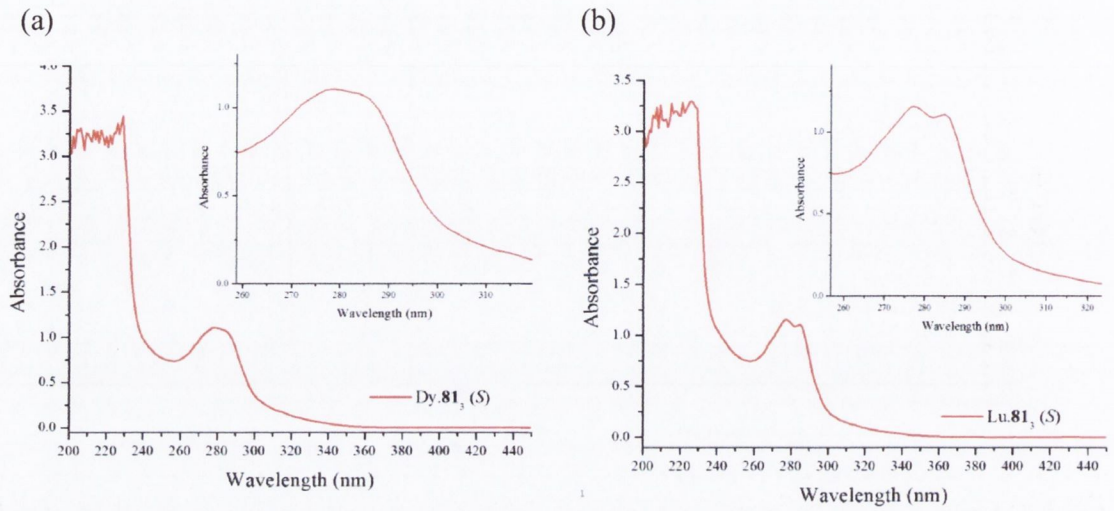

Figure A2.41. *UV-visible absorption spectra of (a) Dy.**81**$_3$ (S) (3.1 x 10^{-5} M) and (b) Lu.**81**$_3$ (S) (2.9 x 10^{-5} M) in CH_3CN.*

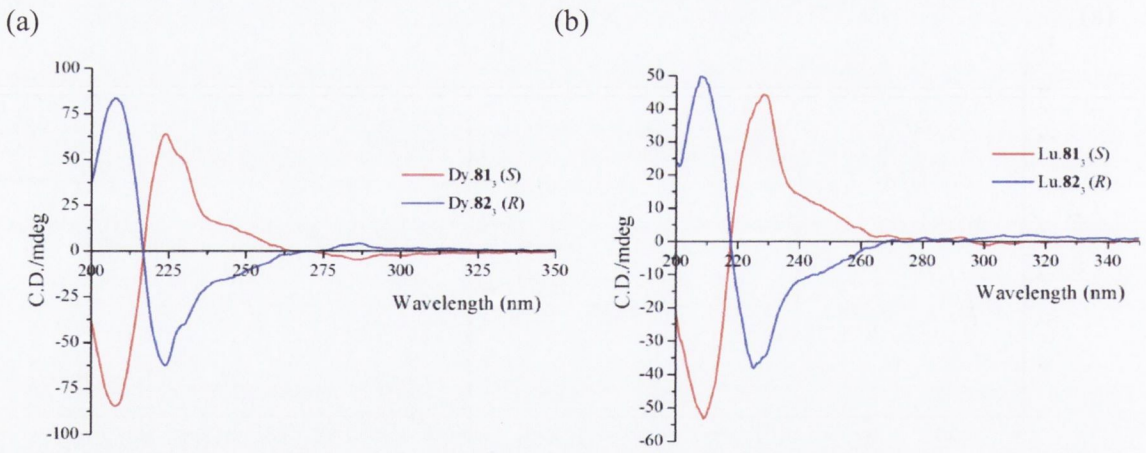

Figure A2.42. *Circular dichroism spectra of ligands **81** (S) (3.3 x 10^{-5} M) and **82** (R) (3.9 x 10^{-5} M for (a) and 3.3 x 10^{-5} M for (b)) recorded in CH_3CN at RT after the addition of 0.33 equiv. of (a) $Dy(CF_3SO_3)_3$ and (b) $Lu(CF_3SO_3)_3$ - note that slight discrepancies in intensities can be derived from differences in concentrations.*

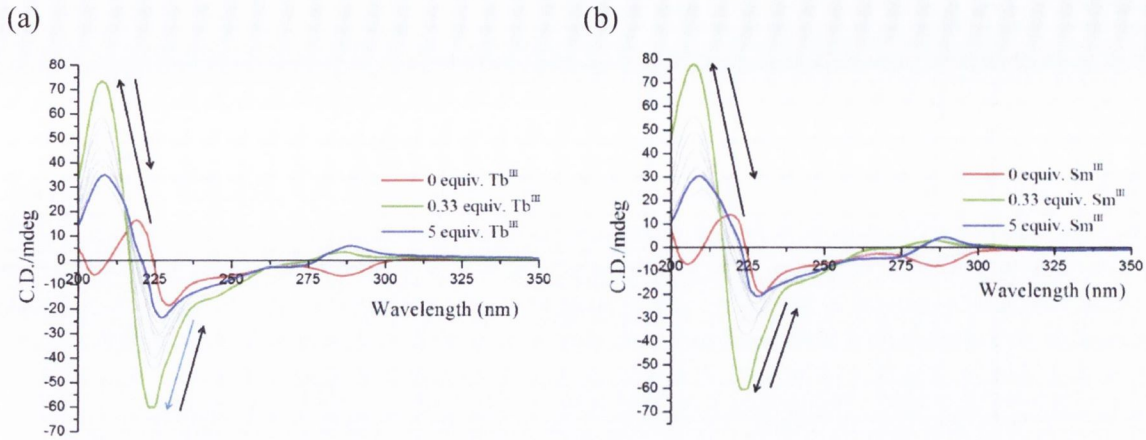

Figure A2.43. *The overall changes in the CD spectra of* ***82*** *(R) (3.5 x 10^{-5} M for (a) and (3.4 x 10^{-5} M) for (b)) upon titrating against increasing concentrations of (a) $Tb(CF_3SO_3)_3$ (0→5 equiv.) and (b) $Sm(CF_3SO_3)_3$ (0→5 equiv.) at RT in CH_3CN.*

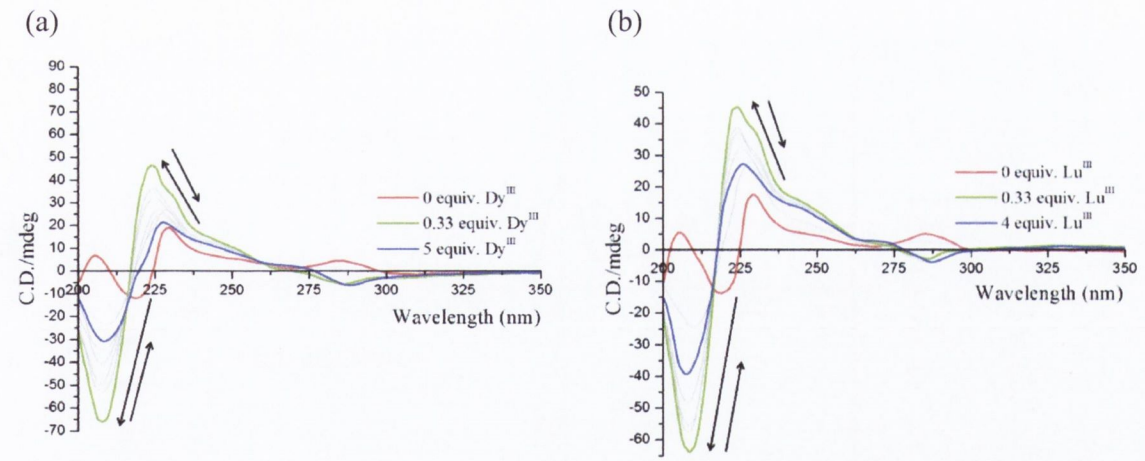

Figure A2.44. *The overall changes in the CD spectra of* ***81*** *(S) (3.4 x 10^{-5} M for (a) and 3.4 x 10^{-5} M for (b)) upon titrating against increasing concentrations of (a) $Dy(CF_3SO_3)_3$ (0→5 equiv.) and (b) $Lu(CF_3SO_3)_3$ (0→4 equiv.) at RT in CH_3CN.*

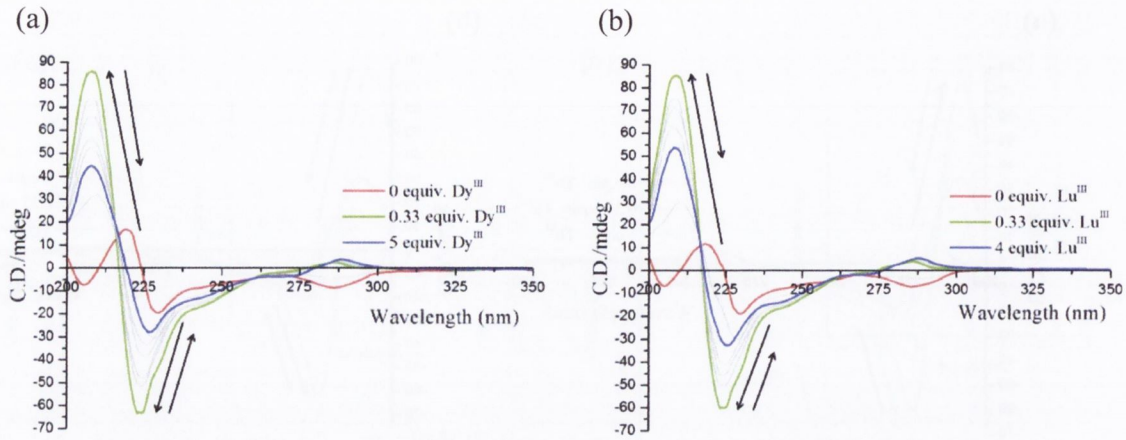

Figure A2.45. *The overall changes in the CD spectra of* ***82*** *(R) (3.6 x 10^{-5} M for (a) and 3.5 x 10^{-5} M for (b)) upon titrating against increasing concentrations of (a) $Dy(CF_3SO_3)_3$ (0→5 equiv.) and (b) $Lu(CF_3SO_3)_3$ (0→4 equiv.) at RT in CH_3CN.*

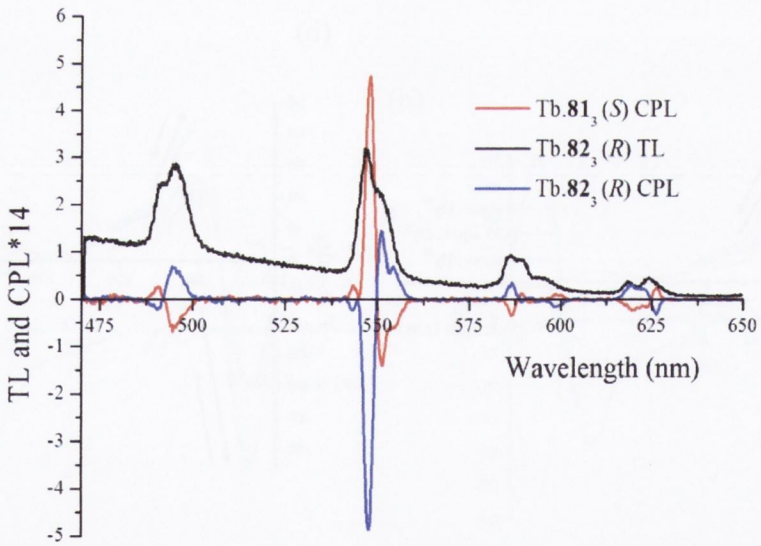

Figure A2.46. *Total Tb^{III}-centred emission and CPL spectra of complexes Tb.**81**$_3$ (S) and Tb.**82**$_3$ (R) recorded in CH_3CN (excitation at λ = 281nm).*

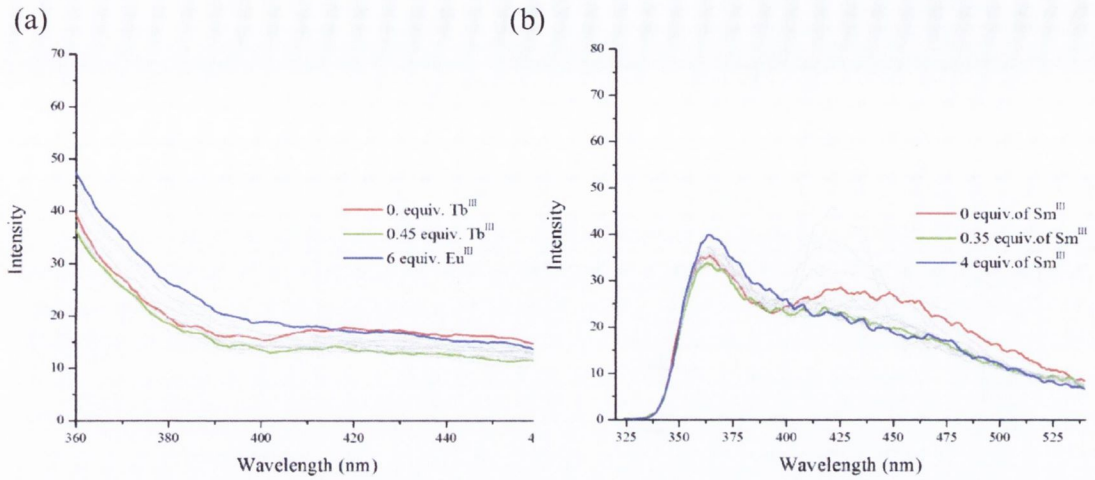

Figure A2.47. *The overall changes in the fluorescence emission spectra upon titrating* ***81*** *(S) (1 x 10^{-5} M) against (a) $Tb(CF_3SO_3)_3$ (0→6 equiv.) and (b) $Sm(CF_3SO_3)_3$ (0→4 equiv.) in CH_3CN at RT.*

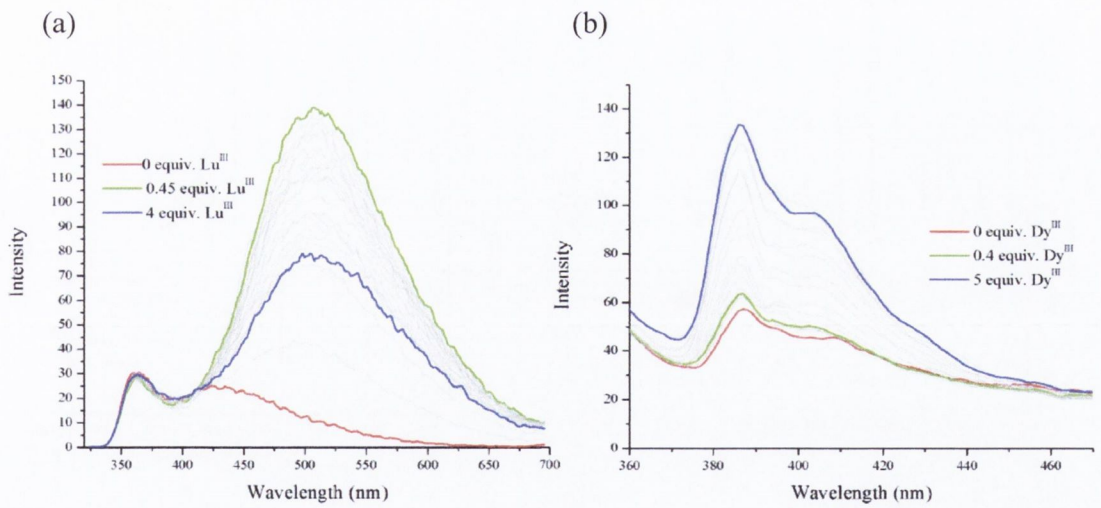

Figure A2.48. *The overall changes in the fluorescence emission spectra upon titrating* ***81*** *(S) (1 x 10^{-5} M) against (a) $Lu(CF_3SO_3)_3$ (0→4 equiv.) and (b) Dy $(CF_3SO_3)_3$ (0→5 equiv.) in CH_3CN at RT.*

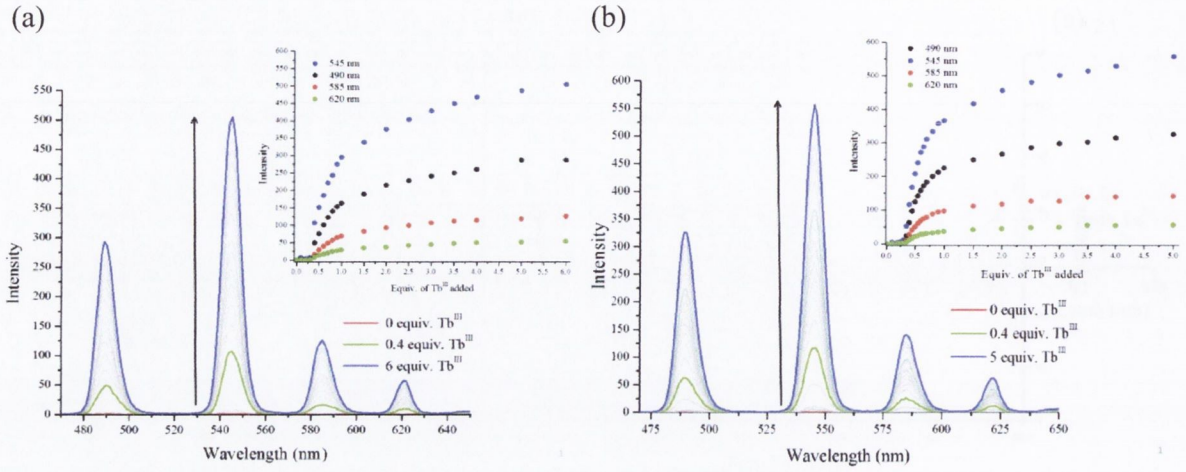

Figure A2.49. *The overall changes in the luminescence spectra upon titrating (a)* ***81*** *(0→6 equiv.) and (b)* ***82*** *(0→5 equiv.) (1 x 10^{-5} M) against $Tb(CF_3SO_3)_3$ in CH_3CN at RT.* ***Inset****: corresponding experimental binding isotherm of luminescence at λ = 490, 545, 585 and 620 nm.*

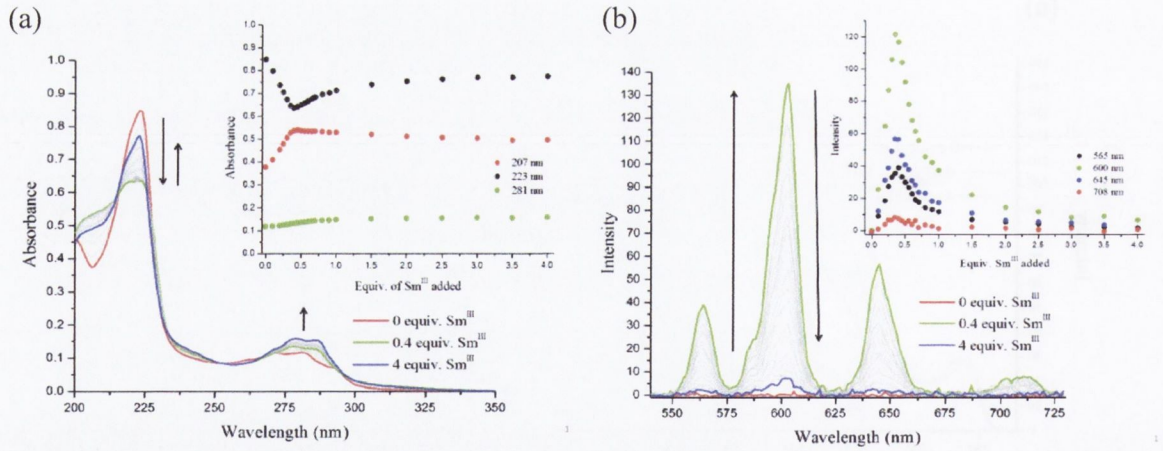

Figure A2.50. *The overall changes in the (a) UV-visible absorption spectra and (b) Sm^{III}–centred phosphorescence spectra upon titrating* ***82*** *(1 x 10^{-5} M) against $Sm(CF_3SO_3)_3$ (0→4 equiv.) in CH_3CN at RT.* ***Inset****: corresponding experimental binding isotherm of (a) absorbance at λ = 207, 223 and 281 nm and (b) Sm^{III} phosphorescence emission intensity at λ = 565, 600, 645 and 708 nm.*

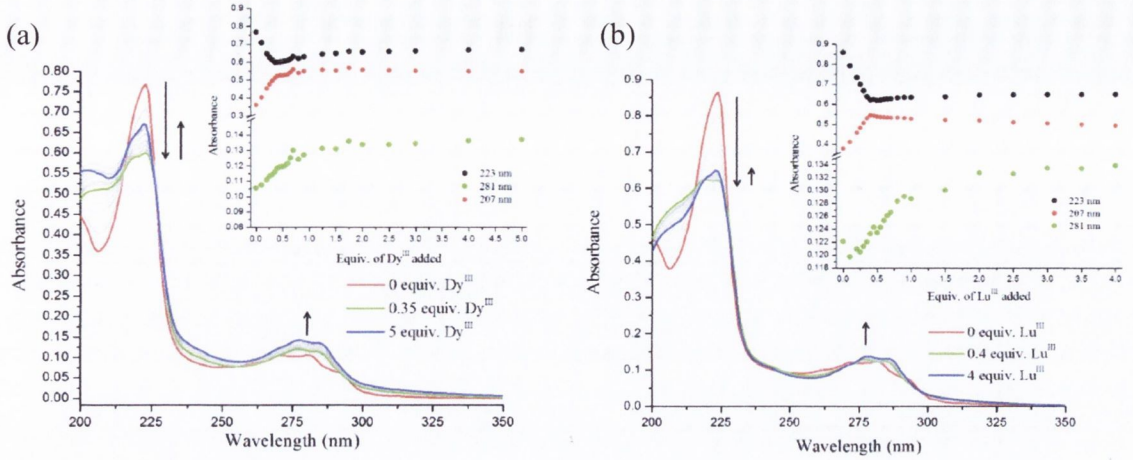

Figure A2.51. *The overall changes in the UV-visible absorption spectra upon titrating* ***81*** *(1 x 10^{-5} M) against (a) $Dy(CF_3SO_3)_3$ (0→5 equiv.) and (b) $Lu(CF_3SO_3)_3$ (0→4 equiv.) in CH_3CN at RT.* ***Inset****: corresponding experimental binding isotherm of absorbance at λ = 207, 223 and 281 nm.*

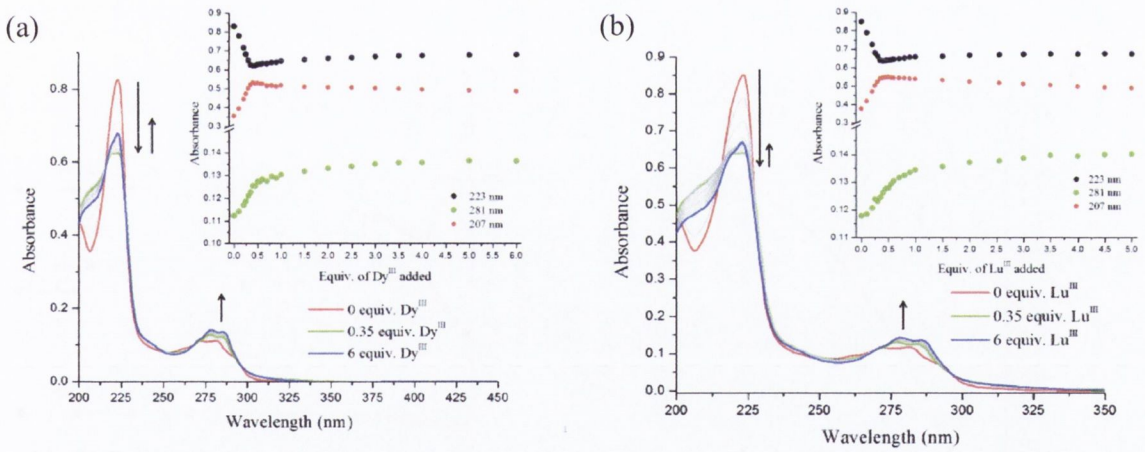

Figure A2.52. *The overall changes in the UV-visible absorption spectra upon titrating* ***82*** *(1 x 10^{-5} M) against (a) $Dy(CF_3SO_3)_3$ (0→6 equiv.) and (b) $Lu(CF_3SO_3)_3$ (0→6 equiv.) in CH_3CN at RT.* ***Inset****: corresponding experimental binding isotherm of absorbance at λ = 207, 223 and 281 nm.*

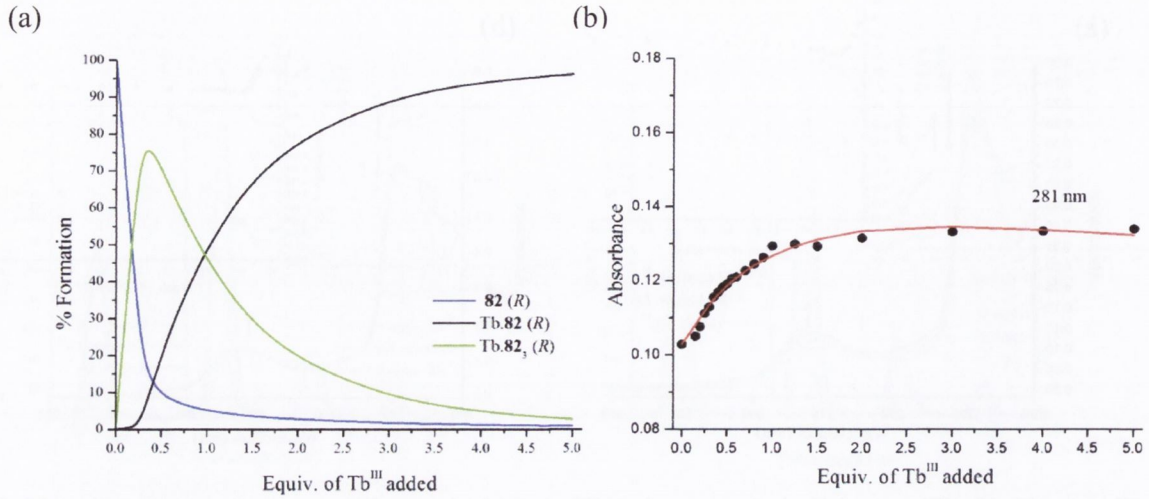

Figure A2.53. *(a) The speciation distribution diagram obtained from the UV-visible absorption titration data fit (upon titrating ligand* ***82*** *against $Tb(CF_3SO_3)_3$ in CH_3CN) and (b) the fit of the experimental binding isotherms using the non-linear regression analysis program SPECFIT.*

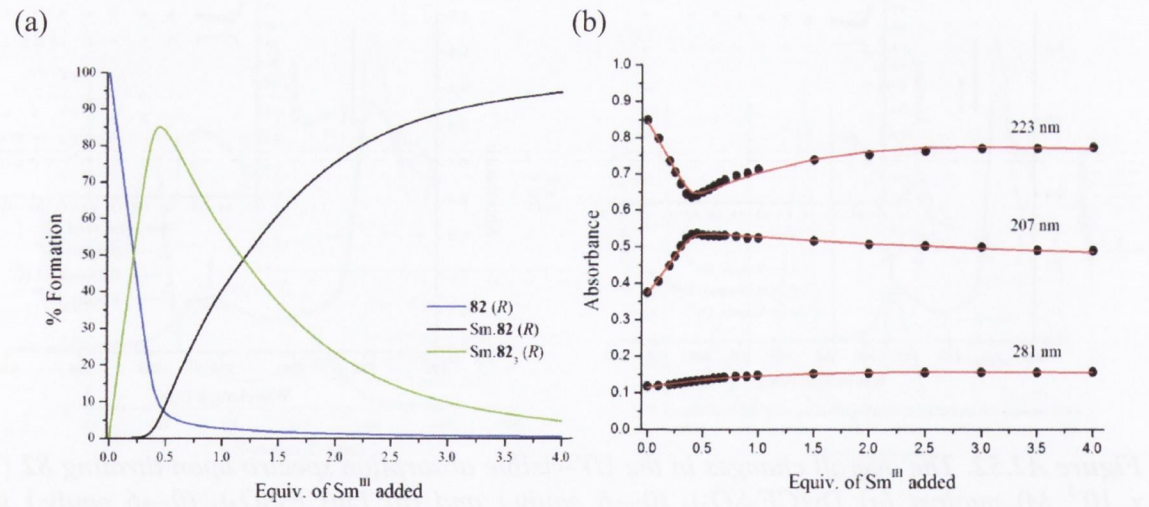

Figure A2.54. *(a) The speciation distribution diagram obtained from the UV-visible absorption titration data fit (upon titrating ligand* ***82*** *against $Sm(CF_3SO_3)_3$ in CH_3CN) and (b) the fit of the experimental binding isotherms using the non-linear regression analysis program SPECFIT.*

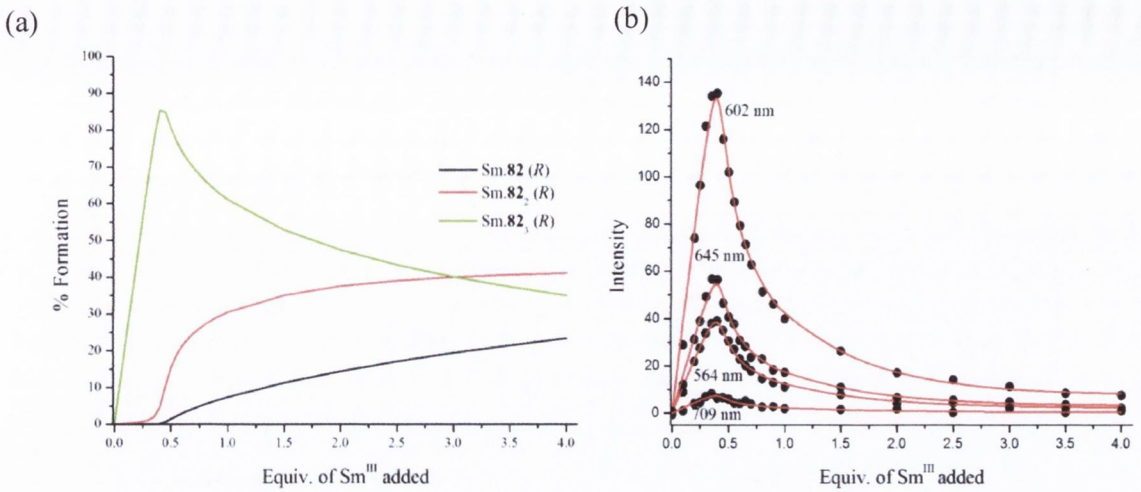

Figure A2.55. *(a) The speciation distribution diagram obtained from the luminescence titration data fit (upon titrating ligand* ***82*** *against $Sm(CF_3SO_3)_3$ in CH_3CN) and (b) the fit of the experimental binding isotherms using the non-linear regression analysis program SPECFIT.*

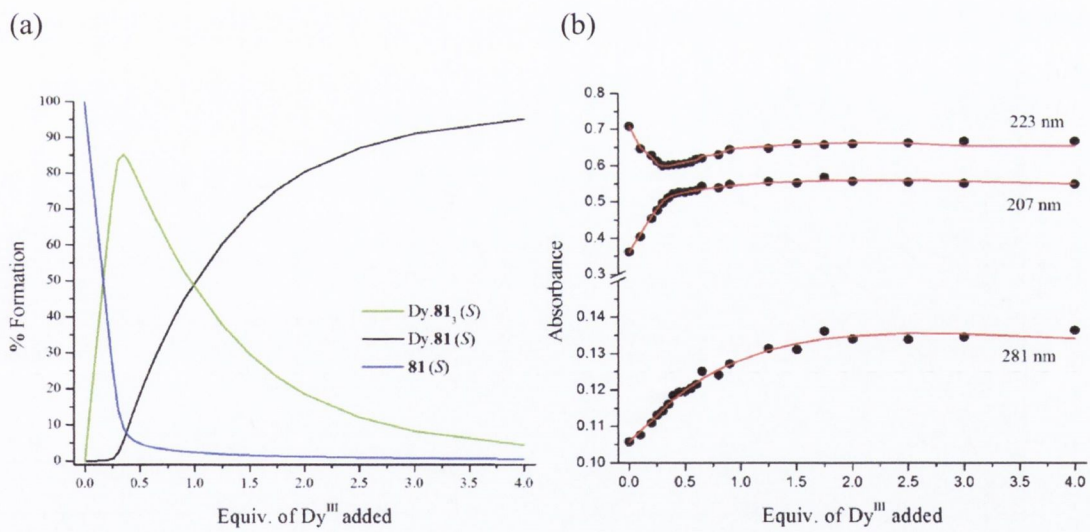

Figure A2.56. *(a) The speciation distribution diagram obtained from the UV-visible absorption titration data fit (upon titrating ligand* ***81*** *against $Dy(CF_3SO_3)_3$ in CH_3CN) and (b) the fit of the experimental binding isotherms using the non-linear regression analysis program SPECFIT.*

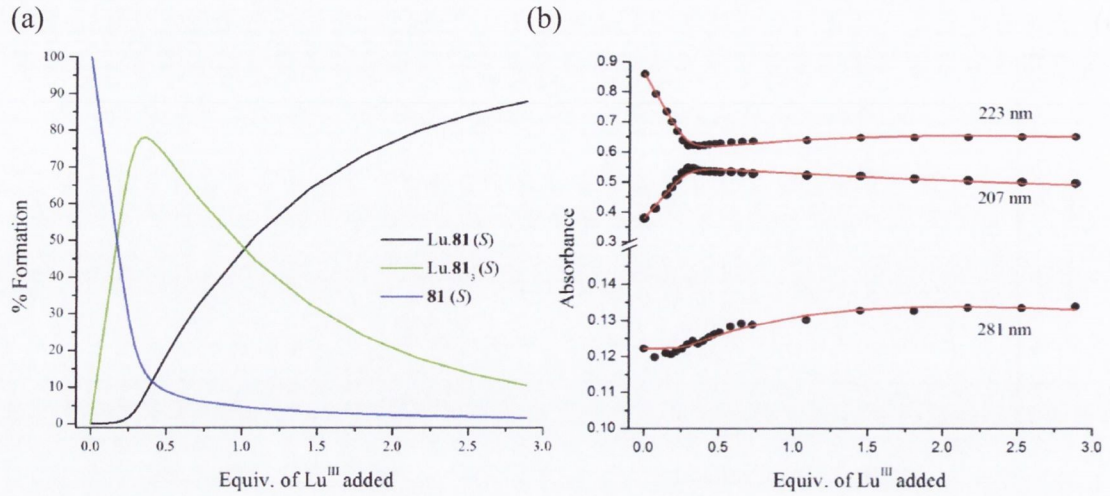

Figure A2.57. *(a) The speciation distribution diagram obtained from the UV-visible absorption titration data fit (upon titrating ligand* ***81*** *against $Lu(CF_3SO_3)_3$ in CH_3CN) and (b) the fit of the experimental binding isotherms using the non-linear regression analysis program SPECFIT.*

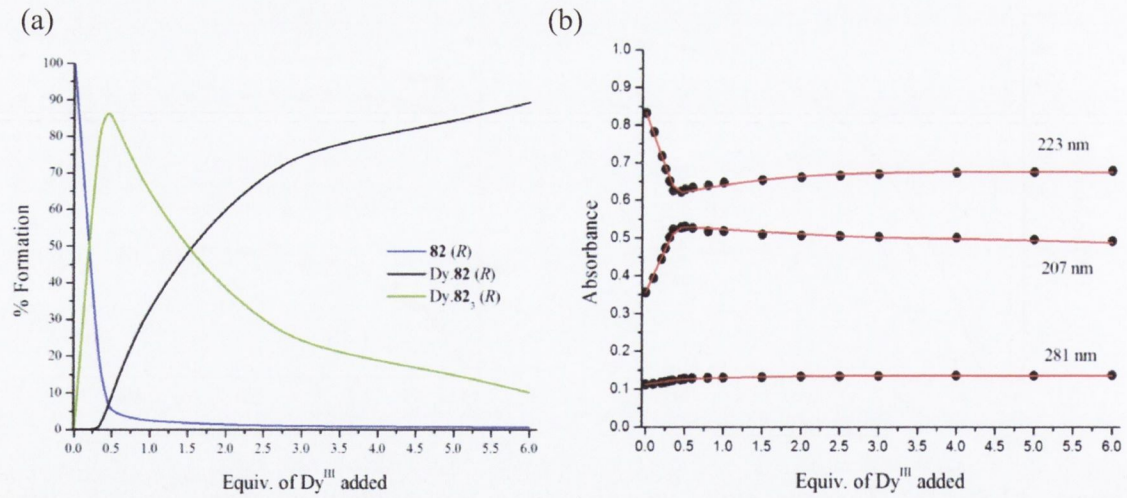

Figure A2.58. *(a) The speciation distribution diagram obtained from the UV-visible absorption titration data fit (upon titrating ligand* ***82*** *against $Dy(CF_3SO_3)_3$ in CH_3CN) and (b) the fit of the experimental binding isotherms using the non-linear regression analysis program SPECFIT.*

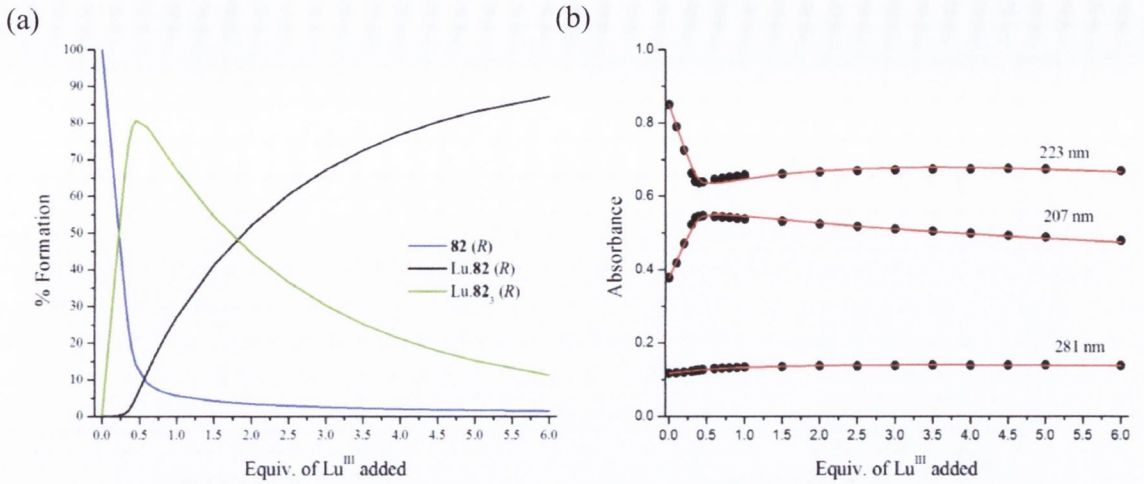

Figure A2.59. *(a) The speciation distribution diagram obtained from the UV-visible absorption titration data fit (upon titrating ligand* ***82*** *against $Lu(CF_3SO_3)_3$ in CH_3CN) and (b) the fit of the experimental binding isotherms using the non-linear regression analysis program SPECFIT.*

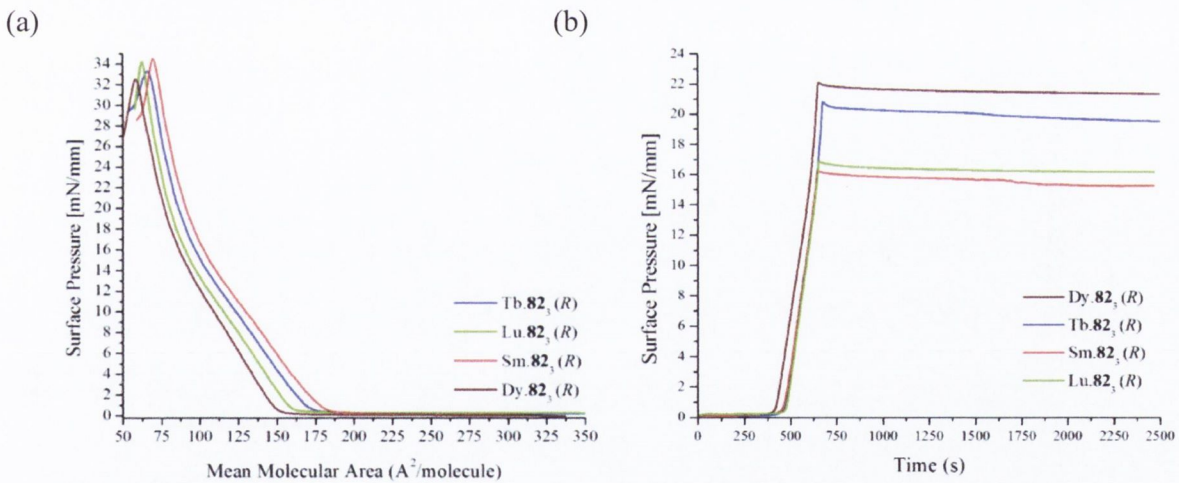

Figure A2.60. *(a) Surface pressure-area isotherms of Ln.**82**$_3$ (R). (b) Surface pressure-time profiles for Langmuir monolayers of Ln.**82**$_3$ (R), Ln = Tb^{III}, Sm^{III}, Lu^{III}, Dy^{III}.*

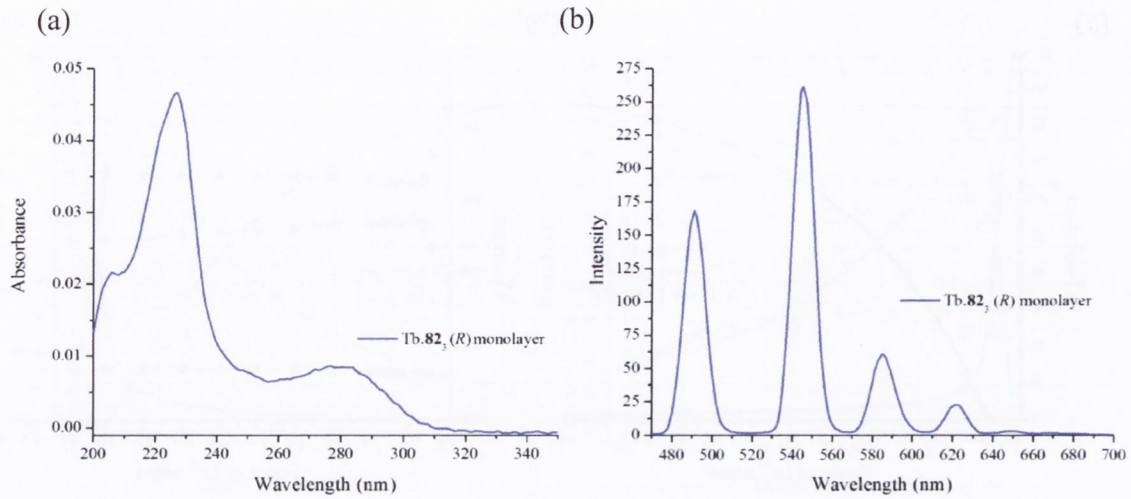

Figure A2.61. *(a) UV-visible absorption spectra and (b) Tb^{III}-centred phosphorescence spectra of Tb.**82**$_3$ (R) immobilised on quartz slide (excitation at λ_{ex} = 281 nm).*

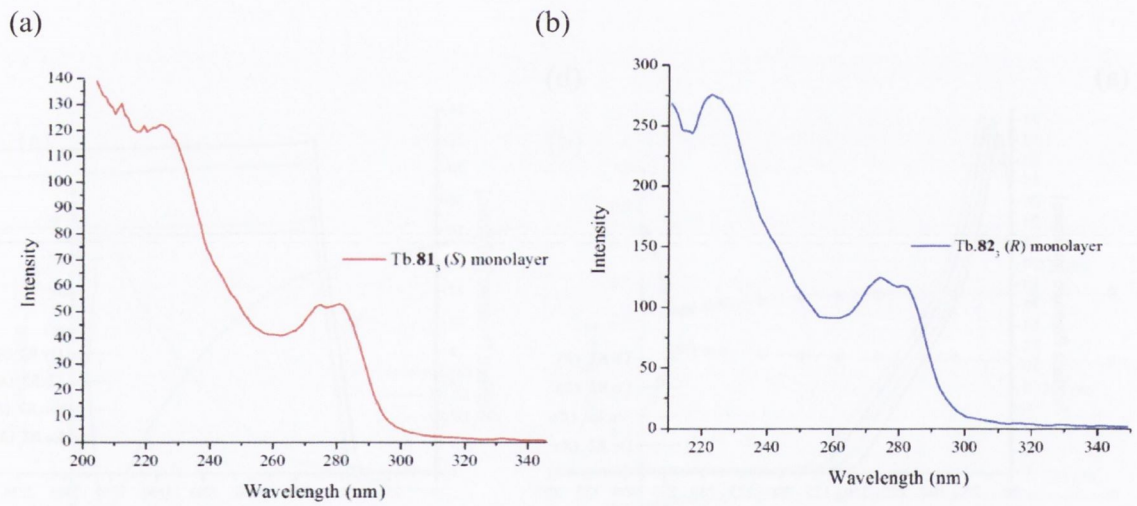

Figure A2.62. *Excitation spectra exhibited by (a) Tb.**81**$_3$ (S) monolayer and (b) Tb.**82**$_3$ (R) monolayer (λ_{em} = 545 nm).*

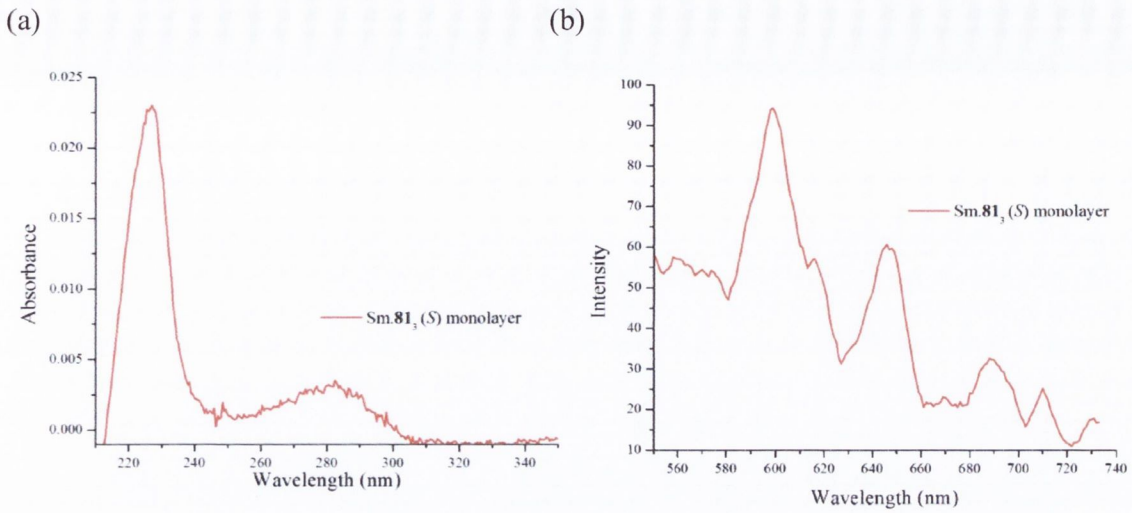

Figure A2.63. *(a) UV-visible absorption spectra and (b) Sm^{III}-centred phosphorescence spectra of Sm.**81**$_3$ (S) immobilised on quartz slide (excitation at λ_{ex} = 281 nm).*

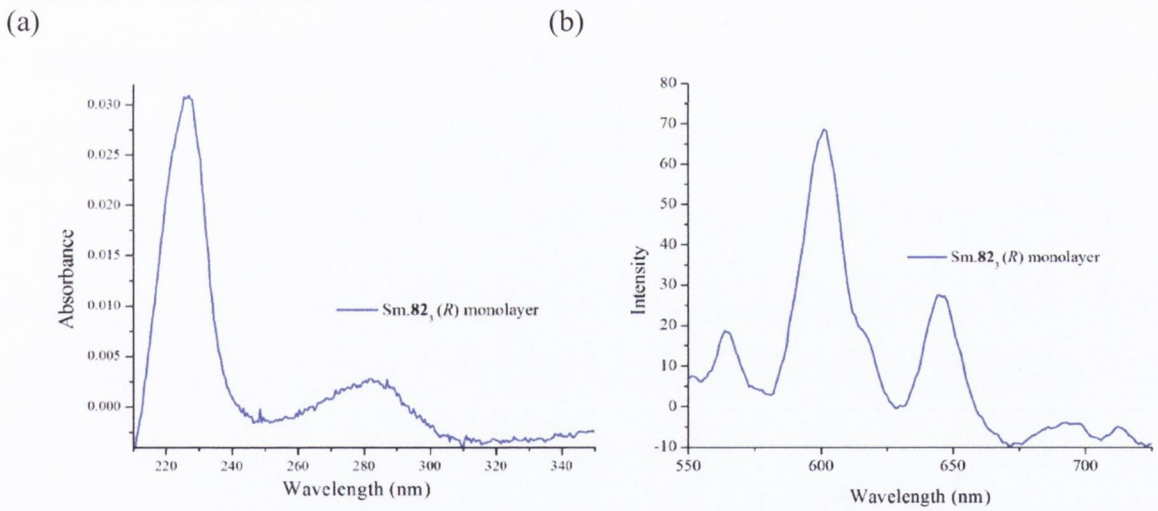

Figure A2.64. *(a) UV-visible absorption spectra and (b) Sm^{III}-centred phosphorescence spectra of Sm.**82**$_3$ (R) immobilised on quartz slide (excitation at λ_{ex} = 281 nm).*

Appendix Three

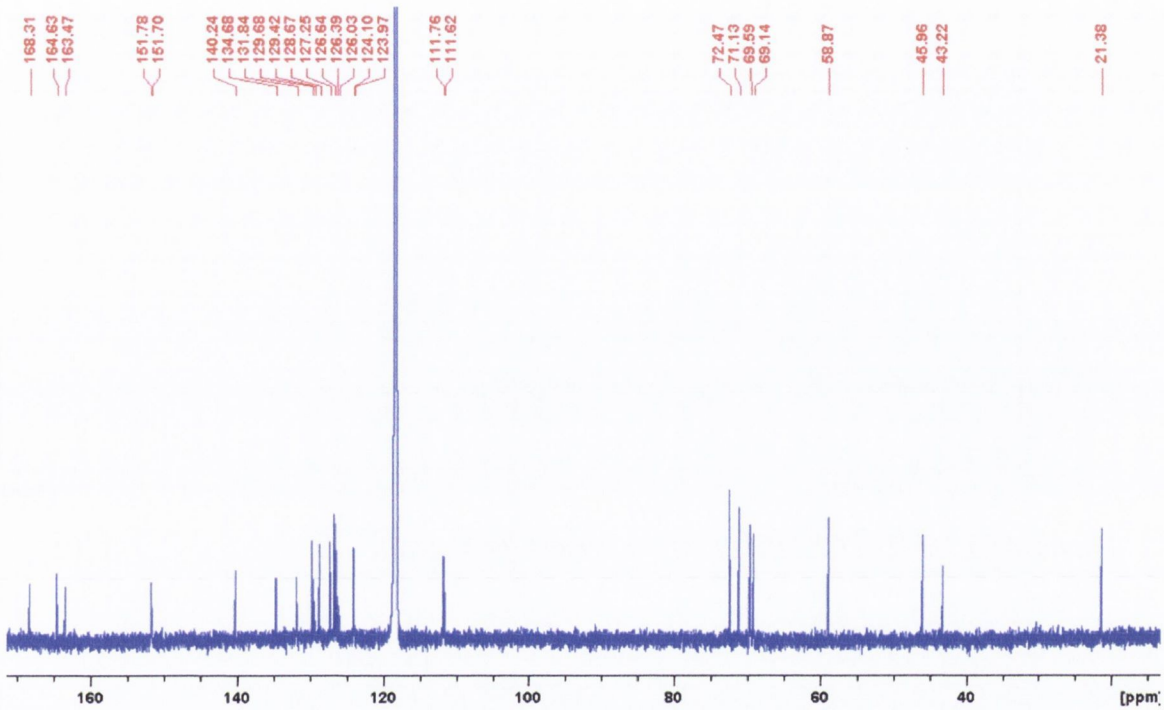

Figure A3.1. *^{13}C NMR spectrum (150 MHz, CD_3CN) of* ***87*** *(S,S).*

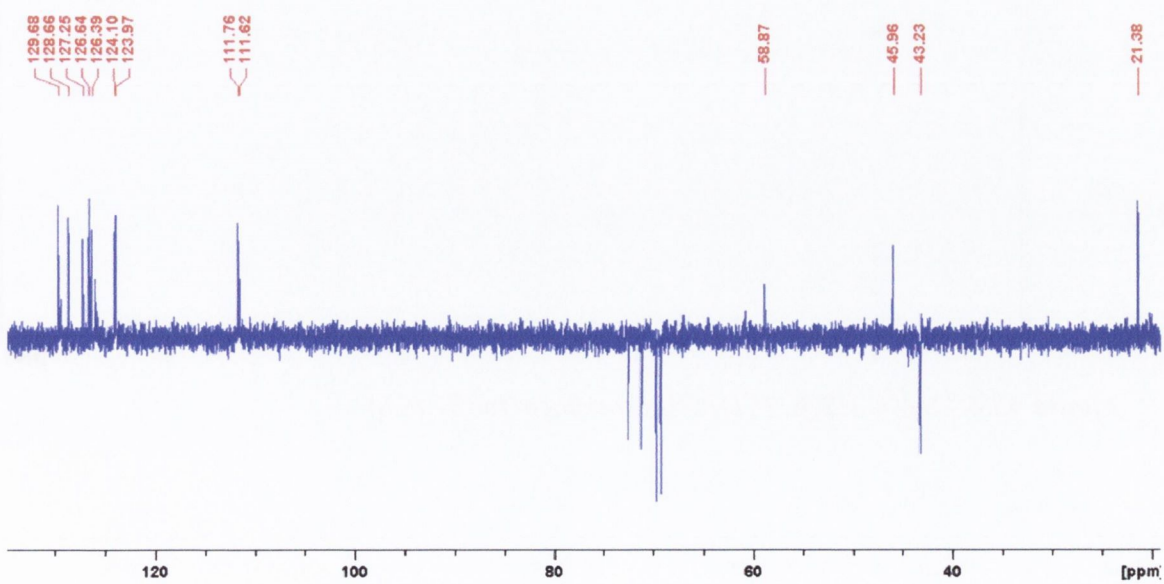

Figure A3.2. *^{13}C DEPT-135 spectrum (150 MHz, CD_3CN) of* ***87*** *(S,S).*

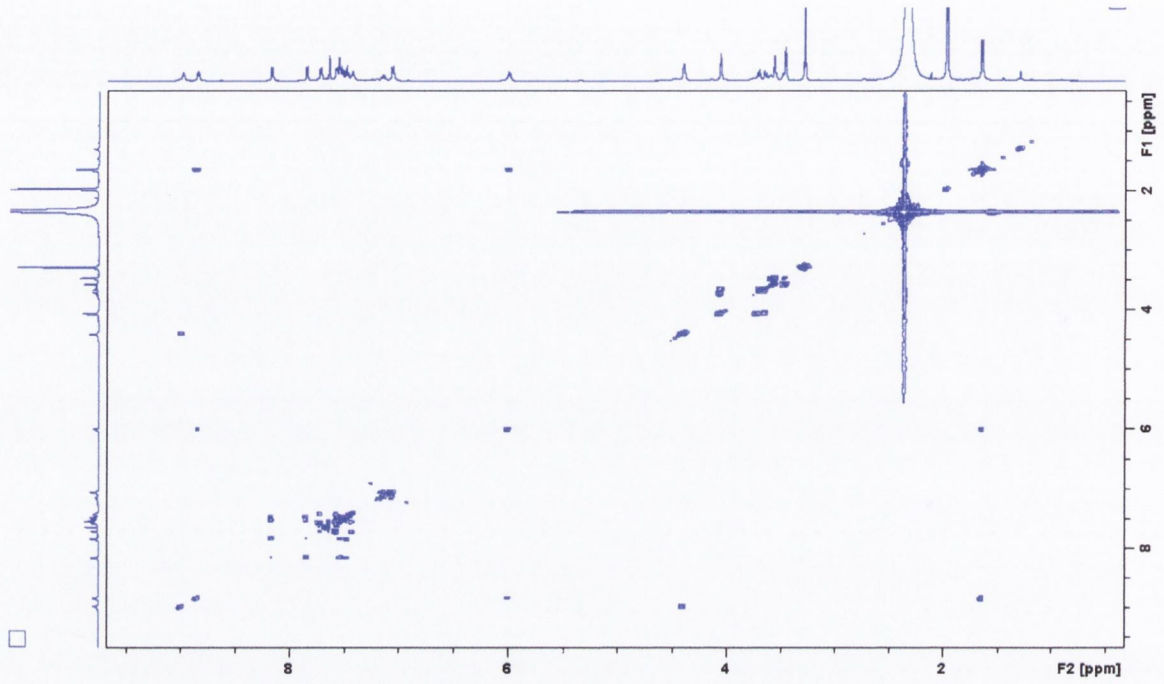

Figure A3.3. *^{1}H-^{1}H COSY (CD_3CN) experiment for* ***87*** *(S,S).*

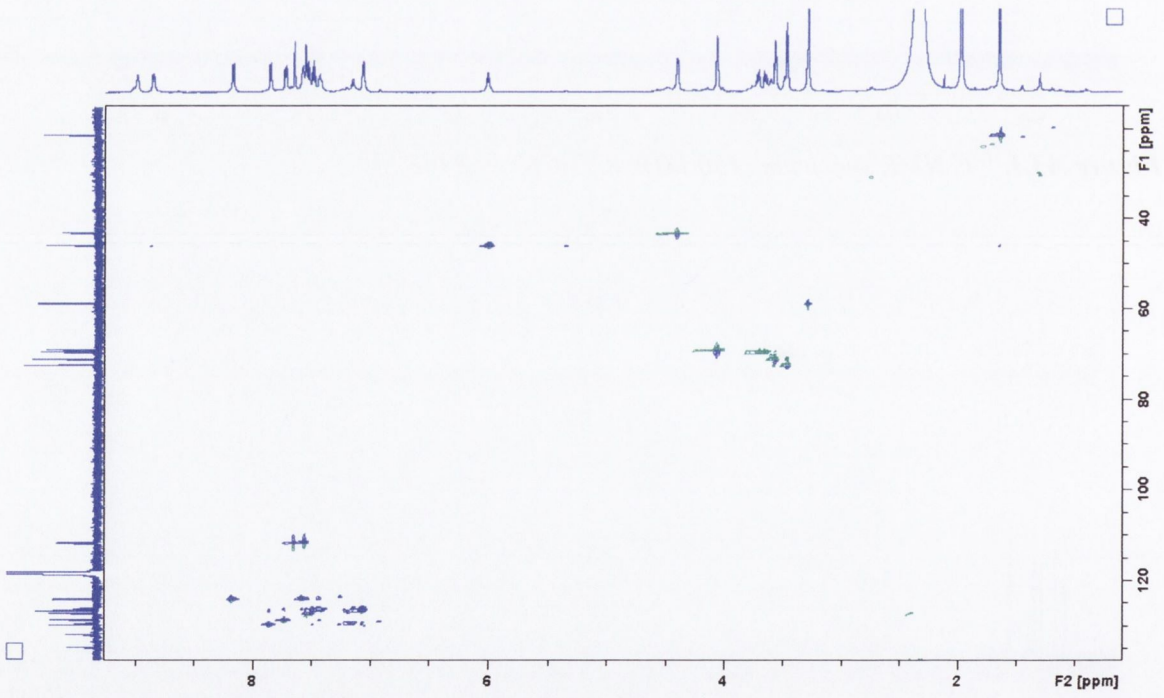

Figure A3.4. *^{1}H-^{13}C HSQC (CD_3CN) experiment for* ***87*** *(S,S).*

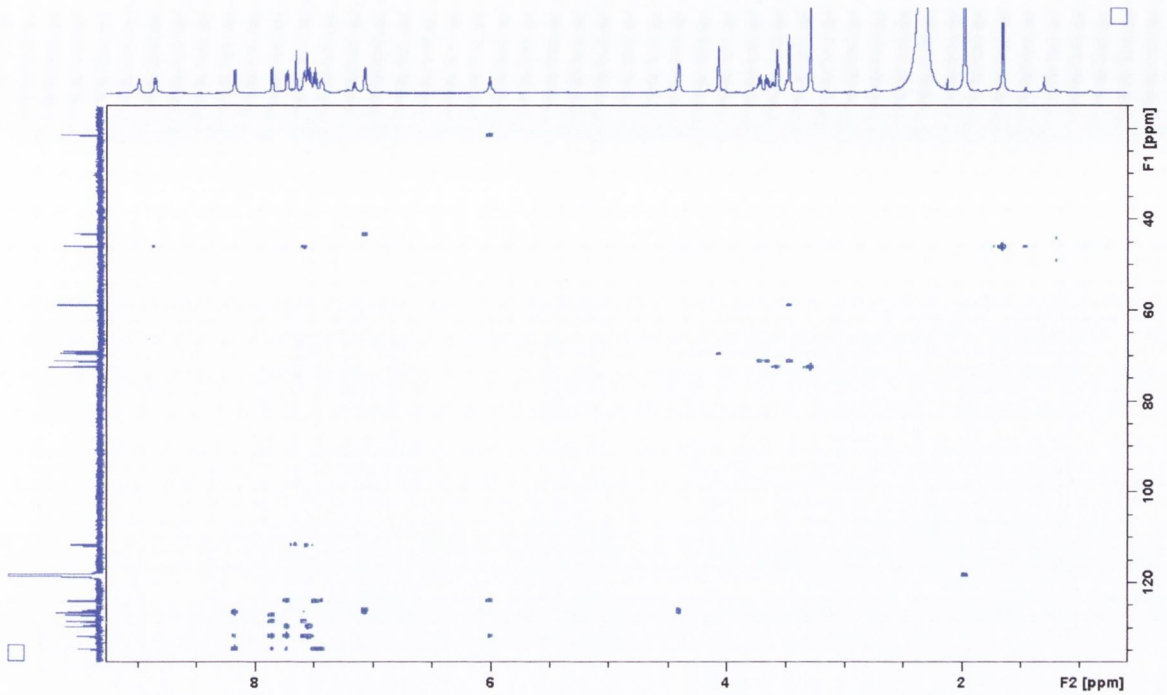

Figure A3.5. *HMBC (CD_3CN) experiment for* ***87*** *(S,S).*

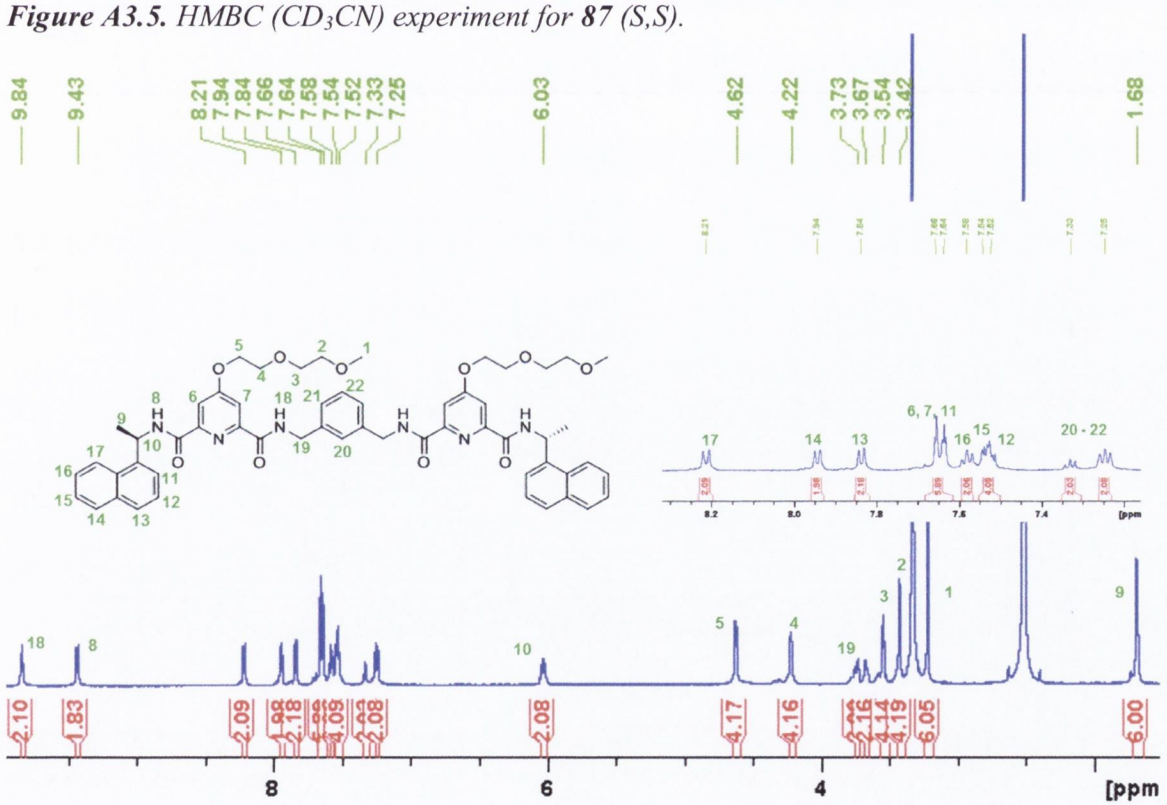

Figure A3.6. *^{1}H NMR spectrum (600 MHz, DMSO-d_6) of* ***88*** *(R,R).*

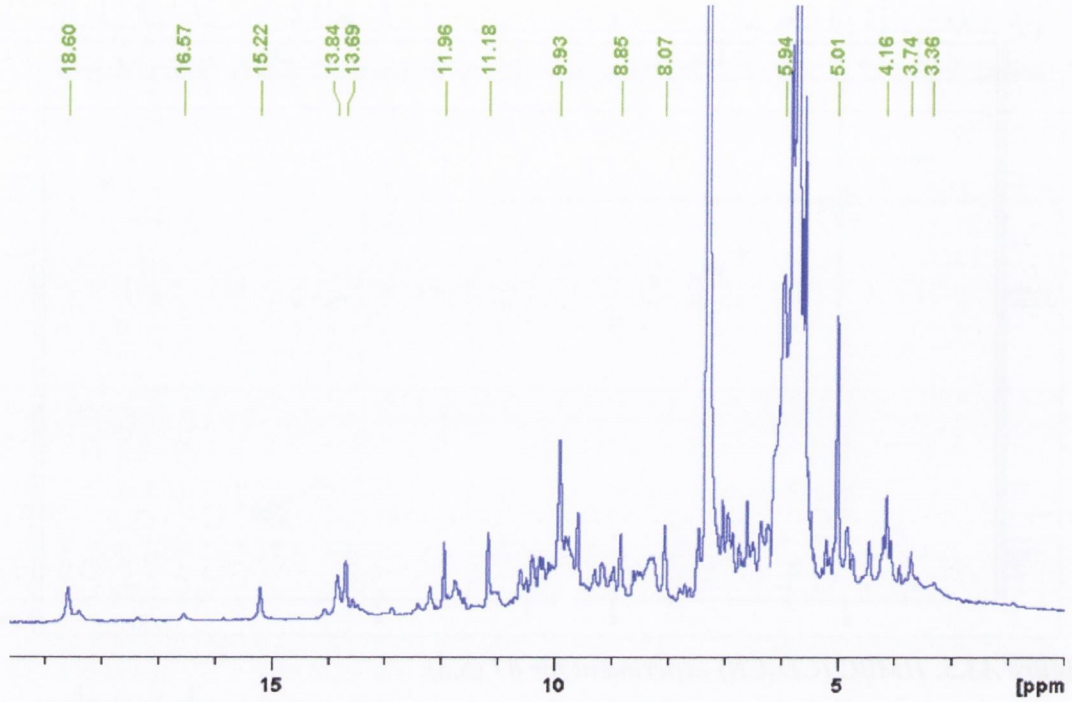

Figure A3.7. *^{1}H NMR spectrum (400 MHz, CD_3OD-d_4) of Eu_2.**88**$_3$ (R,R).*

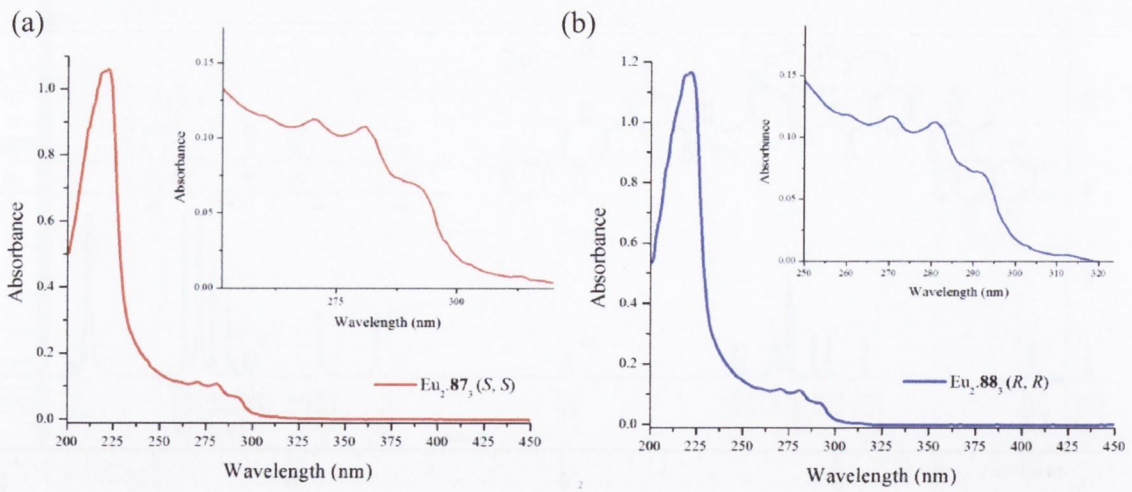

Figure A3.8. *UV-visible absorption spectra of (a) Eu_2.**87**$_3$ (S,S) (2.1 x 10^{-6} M) and (b) Eu_2.**88**$_3$ (R,R) (2 x 10^{-6} M) in CD_3OD.*

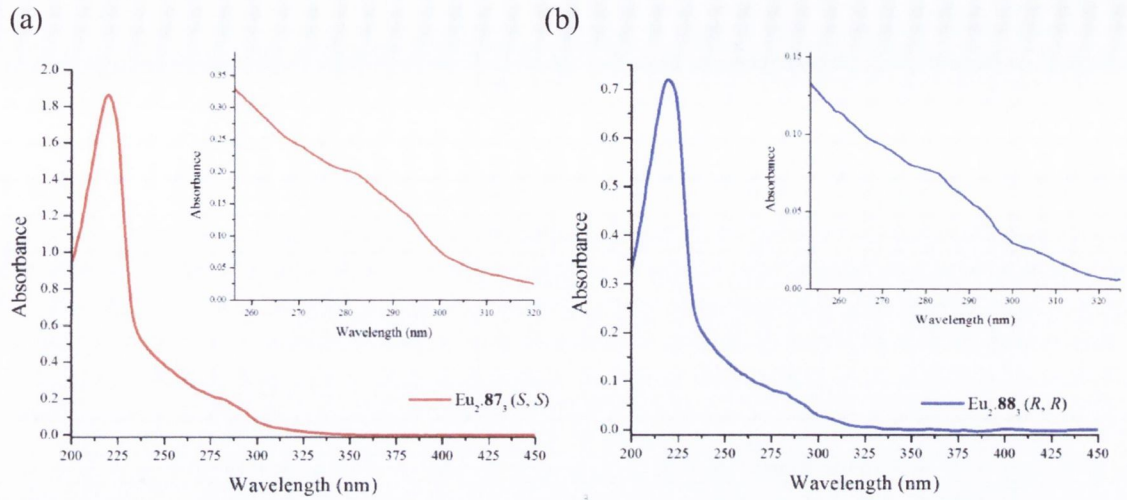

Figure A3.9. *UV-visible absorption spectra of (a) Eu_2.**87**$_3$ (S,S) (4.8 x 10^{-6} M) and (b) Eu_2.**88**$_3$ (R,R) (2 x 10^{-6} M) in CH_3CN.*

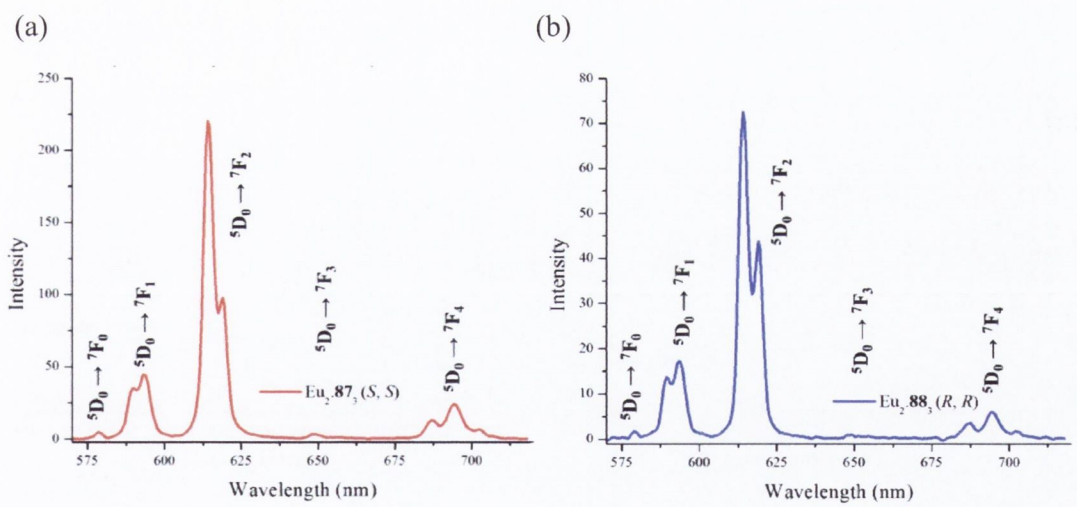

Figure A3.10. *Eu^{III} centred luminescence emission spectra of (a) Eu_2.**87**$_3$ (S,S) (2.1 x 10^{-6} M) and (b) Eu_2.**88**$_3$ (R,R) (2 x 10^{-6} M) in CD_3OD.*

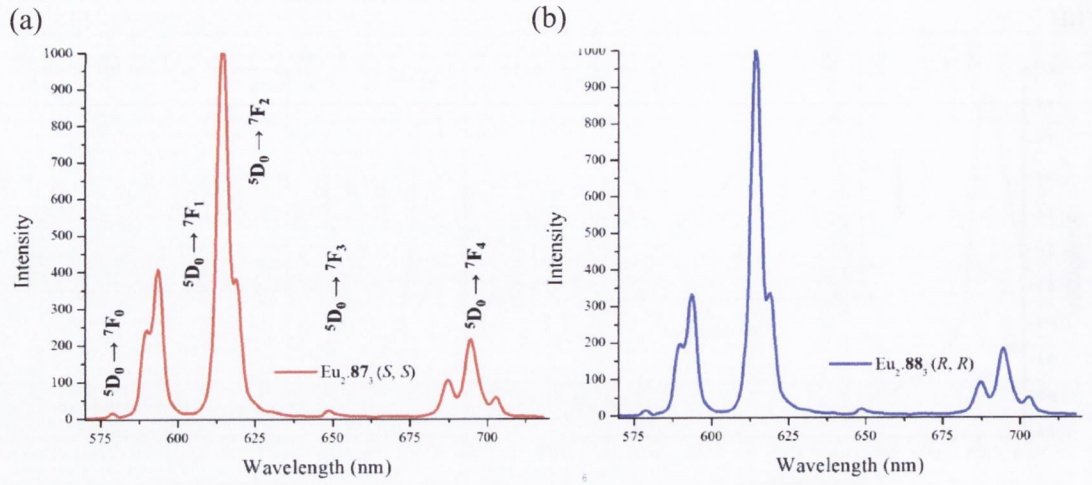

Figure A3.11. *Eu^{III}-centred luminescence emission spectra of (a) $Eu_2.87_3$ (S,S) (4.8×10^{-6} M) and (b) $Eu_2.88_3$ (R,R) (2×10^{-6} M) in CH_3CN.*

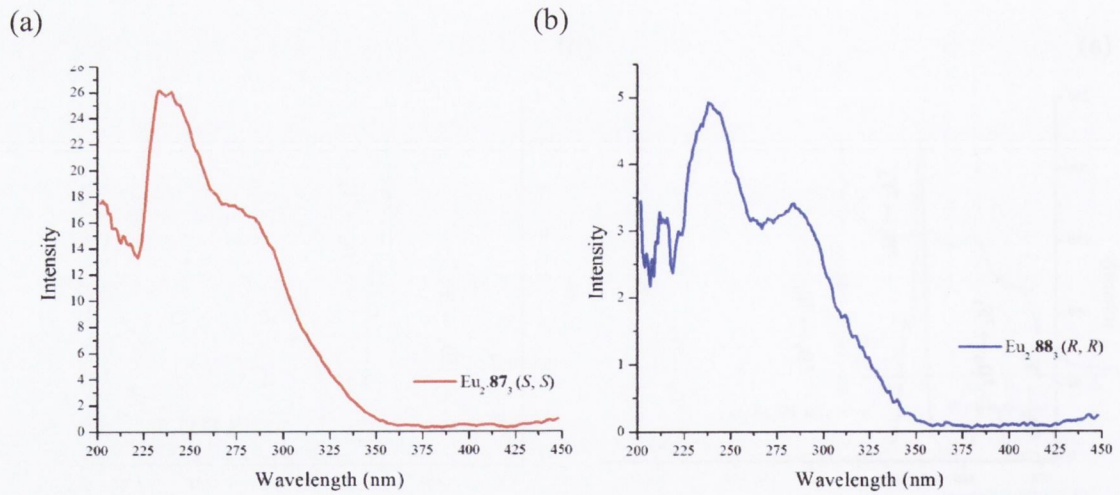

Figure A3.12. *Excitation spectra of (a) $Eu_2.87_3$ (S,S) (2.1×10^{-6} M) and (b) $Eu_2.88_3$ (R,R) (2×10^{-6} M) in CD_3OD (λ_{em} = 615 nm).*

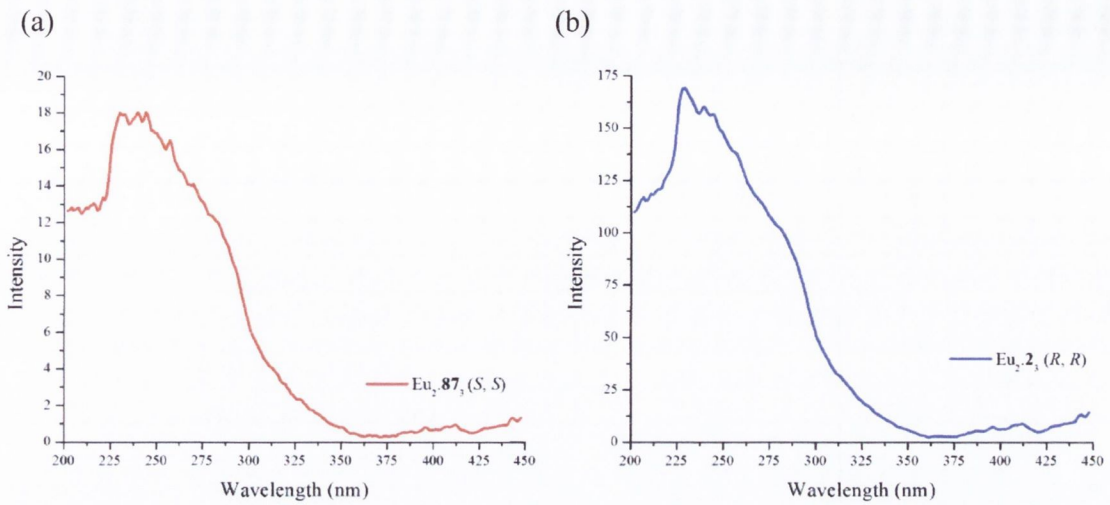

Figure A3.13. *Excitation spectra of (a) $Eu_2.87_3$ (S,S) (4.8×10^{-6} M) and (b) $Eu_2.88_3$ (R,R) (2×10^{-6} M) in CH_3CN (λ_{em} = 615 nm).*

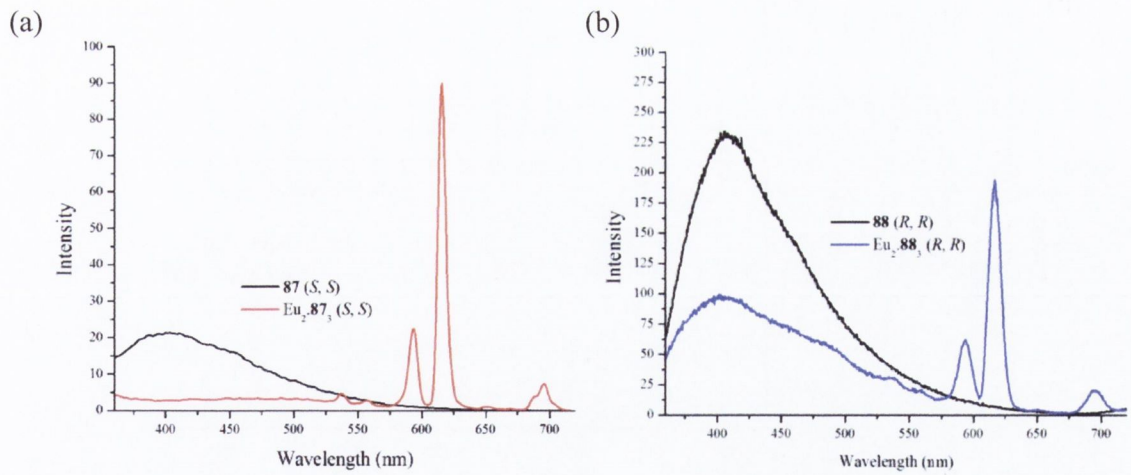

Figure A3.14. *Fluorescence spectra of (a) ligand **87** (S, S) (1×10^{-5} M) and (b) **88** (R, R) (1×10^{-5} M) recorded in CH_3CN before and after the addition of 0.65 equiv. $Eu(CF_3SO_3)_3$.*

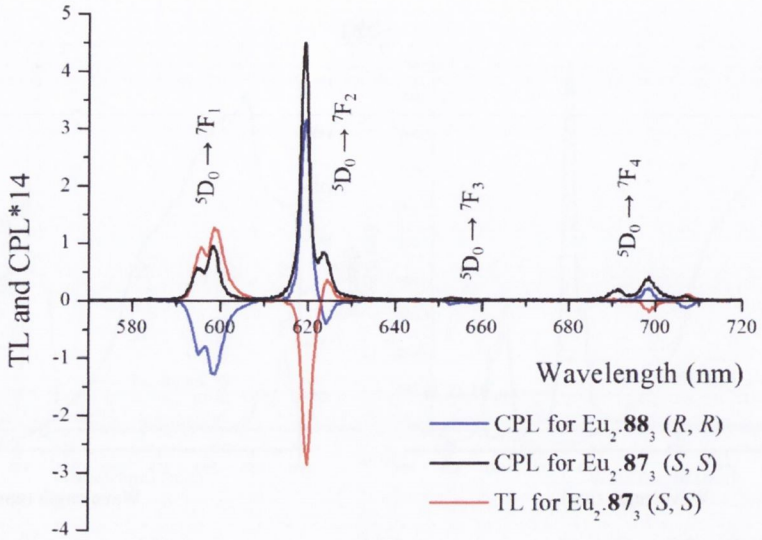

Figure A3.15. *Total Eu^{III}-centred emission and CPL spectra of complexes $Eu_2.\mathbf{87}_3$ (S,S) and $Eu_2.\mathbf{88}_3$ (R,R) recorded in CH_3CN.*

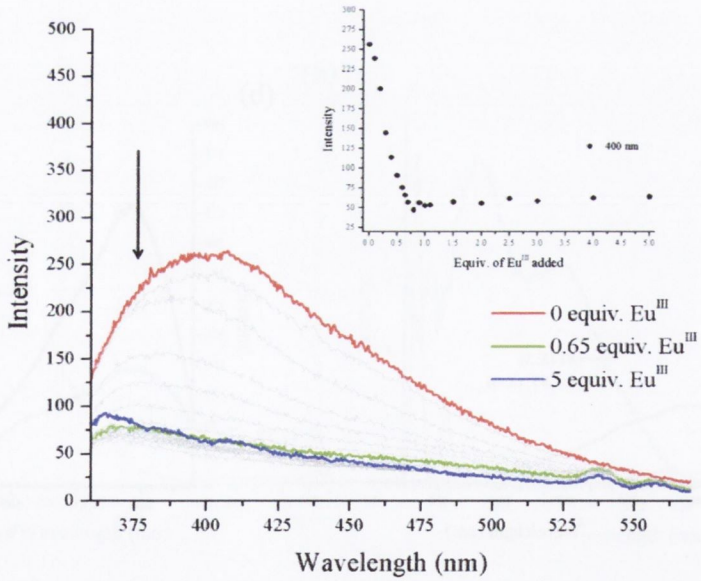

Figure A3.16. *The overall changes in the fluorescence emission spectra upon titrating* ***88*** *(R,R) (1 x 10^{-5} M) against $Eu(CF_3SO_3)_3$ (0→5 equiv.) in CH_3CN at RT.* ***Inset****: corresponding experimental binding isotherm of fluorescence intensity at λ = 400 nm.*

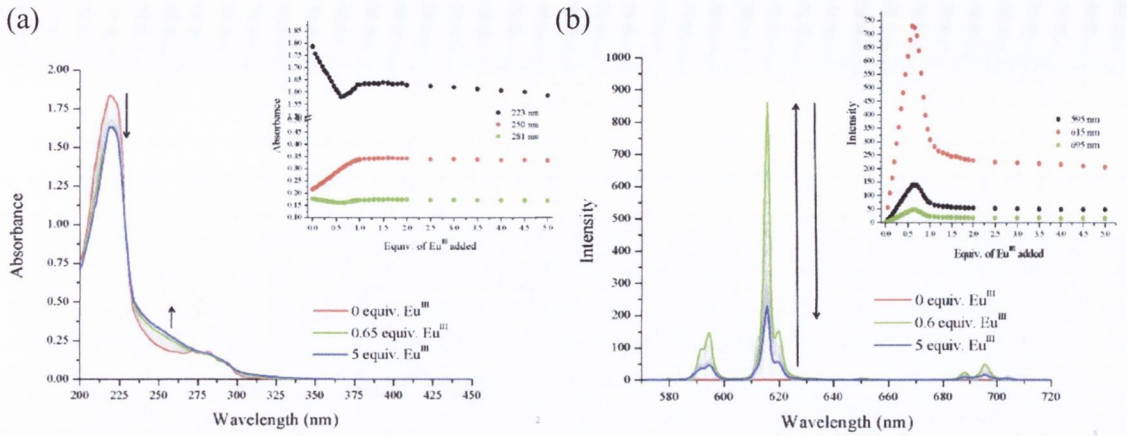

Figure A3.17. *The overall changes in the (a) UV-visible absorption spectra and (b) Eu^{III}–centred phosphorescence spectra upon titrating* ***88*** *(R,R) (1 x 10^{-5} M) against $Eu(CF_3SO_3)_3$ (0→5 equiv.) in CH_3CN at RT.* ***Inset****: corresponding experimental binding isotherm of (a) absorbance at λ = 223, 250 & 281 nm and (b) Eu^{III} phosphorescence emission intensity at λ = 595, 615 and 695 nm.*

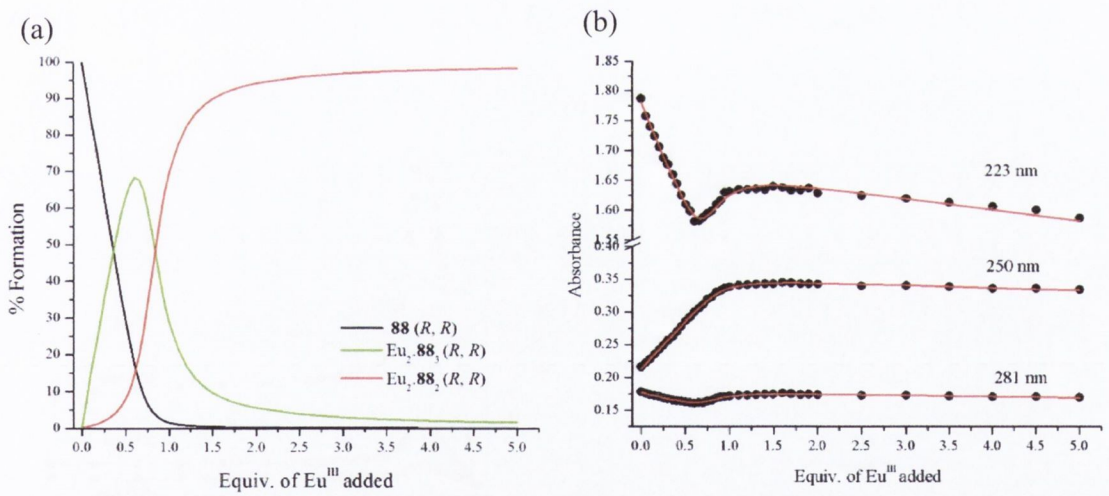

Figure A3.18. *The speciation distribution diagram obtained from the UV-visible absorption titration data fit (upon titrating ligand* ***88*** *(R,R) against $Eu(CF_3SO_3)_3$ in CH_3CN) and (b) the fit of the experimental binding isotherms using the non-linear regression analysis program SPECFIT.*

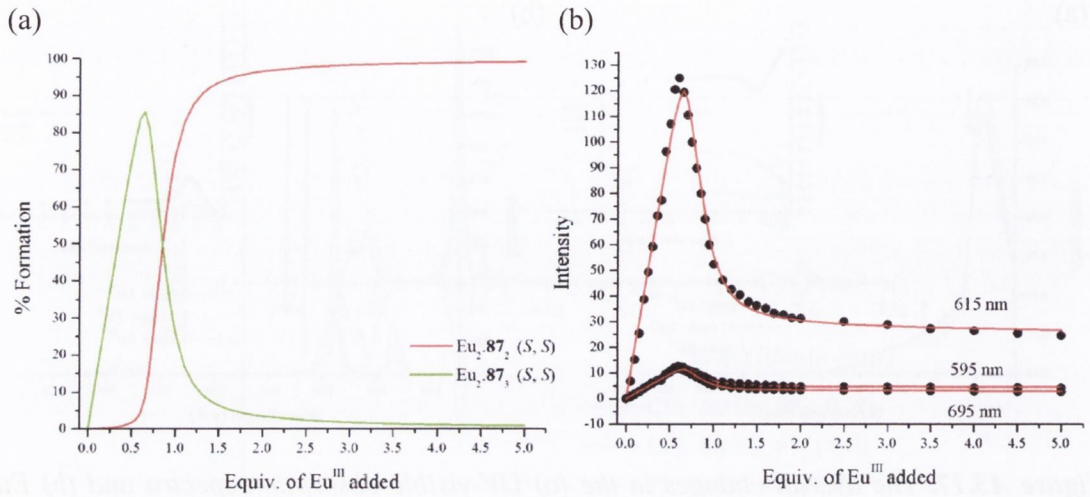

Figure A3.19. *The speciation distribution diagram obtained from the luminescence titration data fit (upon titrating ligand* ***87*** *(S,S) against Eu(CF$_3$SO$_3$)$_3$ in CH$_3$CN) and (b) the fit of the experimental binding isotherms using the non-linear regression analysis program SPECFIT.*

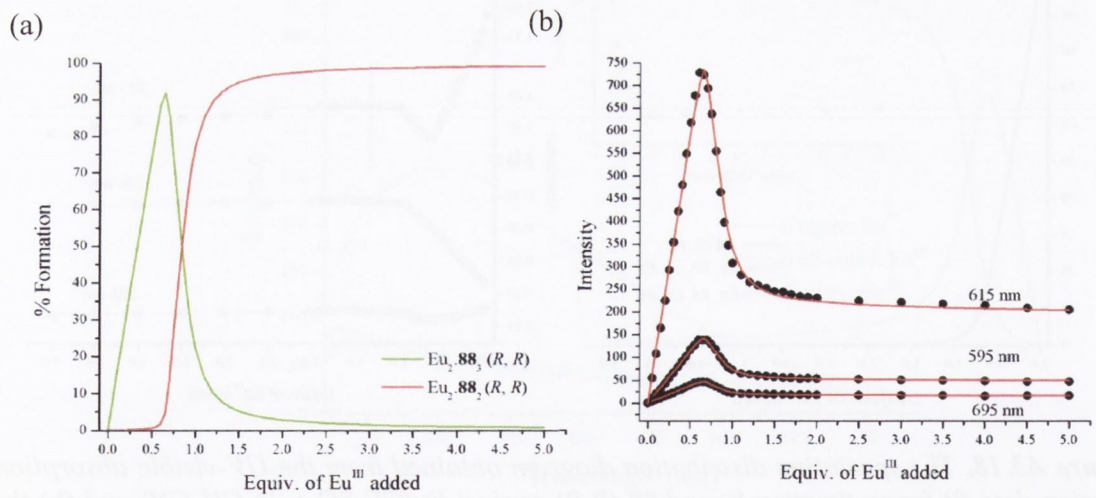

Figure A3.20. *The speciation distribution diagram obtained from the luminescence titration data fit (upon titrating ligand* ***88*** *(R,R) against Eu(CF$_3$SO$_3$)$_3$ in CH$_3$CN) and (b) the fit of the experimental binding isotherms using the non-linear regression analysis program SPECFIT.*

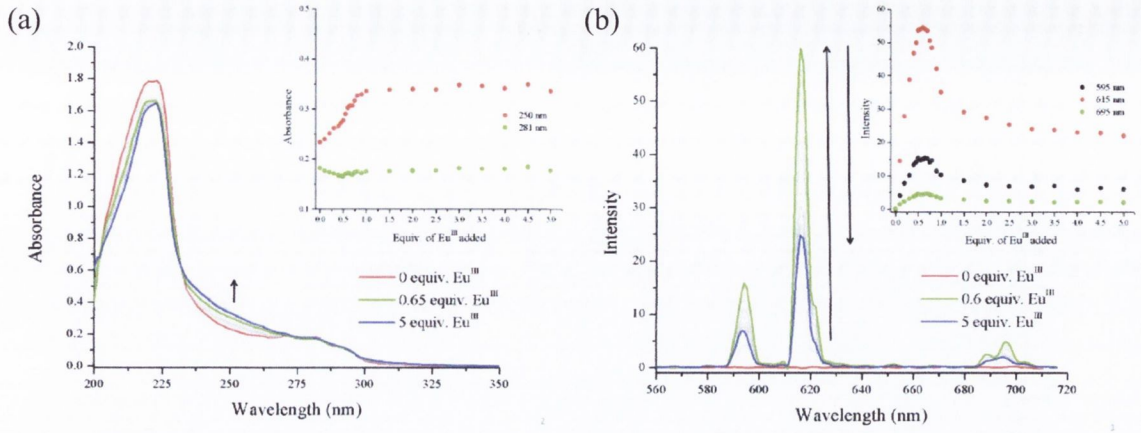

Figure A3.21. *The overall changes in the (a) UV-visible absorption spectra and (b) Eu^{III}–centred phosphorescence spectra upon titrating* ***88*** *(R,R) (1 x 10^{-5} M) against $Eu(CF_3SO_3)_3$ (0→5 equiv.) in CH_3OH at RT.* ***Inset****: corresponding experimental binding isotherm of (a) absorbance at λ = 223, 250 & 281 nm and (b) Eu^{III} phosphorescence emission intensity at λ = 595, 615 and 695 nm.*

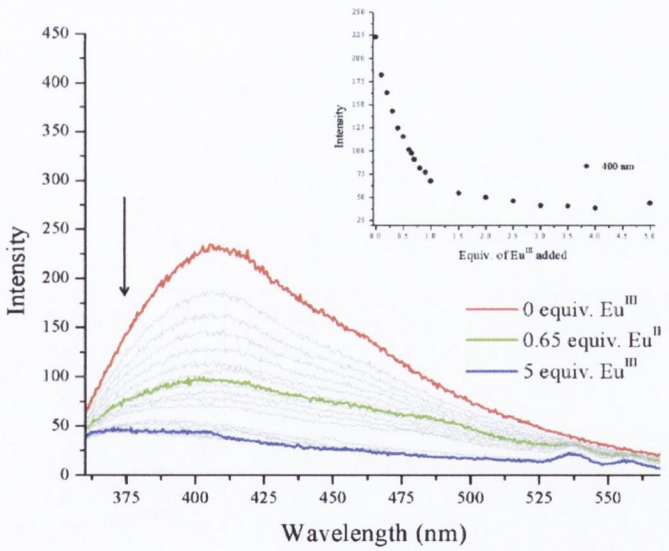

Figure A3.22. *The overall changes in the fluorescence emission spectra upon titrating* ***88*** *(R,R) (1 x 10^{-5} M) against $Eu(CF_3SO_3)_3$ (0→5 equiv.) in CH_3OH at RT.* ***Inset****: corresponding experimental binding isotherm of fluorescence intensity at λ = 400 nm.*

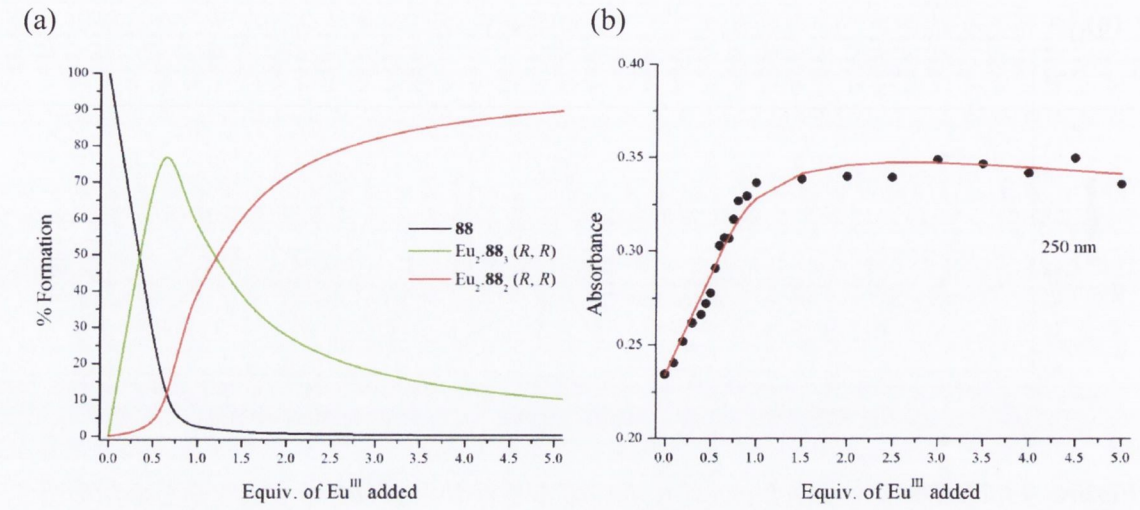

Figure A3.23. *The speciation distribution diagram obtained from the UV-visible absorption titration data fit (upon titrating ligand* ***88*** *(R,R) against $Eu(CF_3SO_3)_3$ in CH_3OH) and (b) the fit of the experimental binding isotherm using the non-linear regression analysis program SPECFIT.*

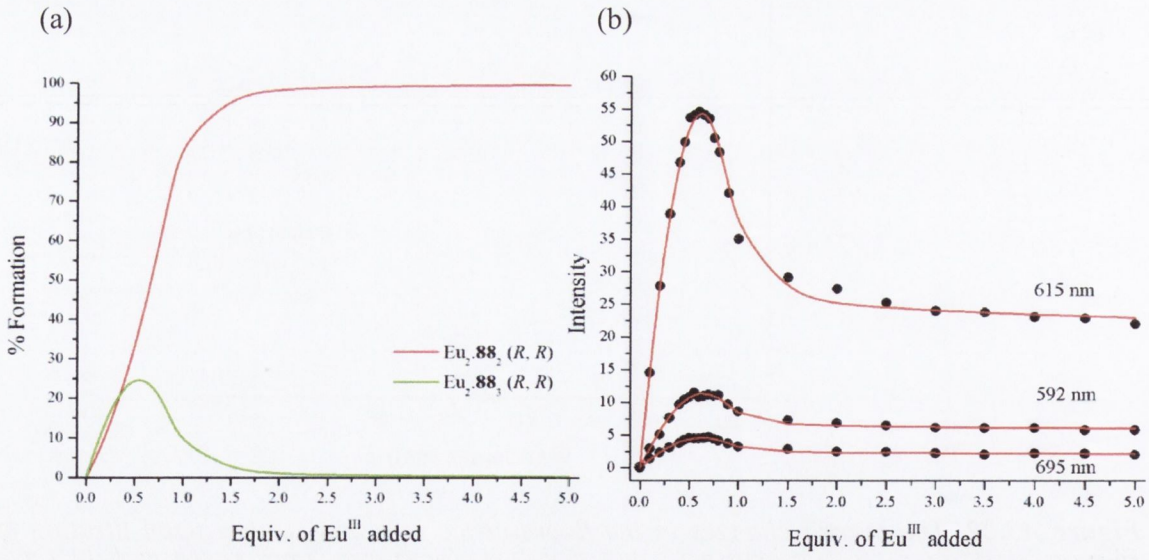

Figure A3.24. *The speciation distribution diagram obtained from the luminescence titration data fit (upon titrating ligand* ***88*** *(R,R) against $Eu(CF_3SO_3)_3$ in CH_3OH) and (b) the fit of the experimental binding isotherms using the non-linear regression analysis program SPECFIT.*

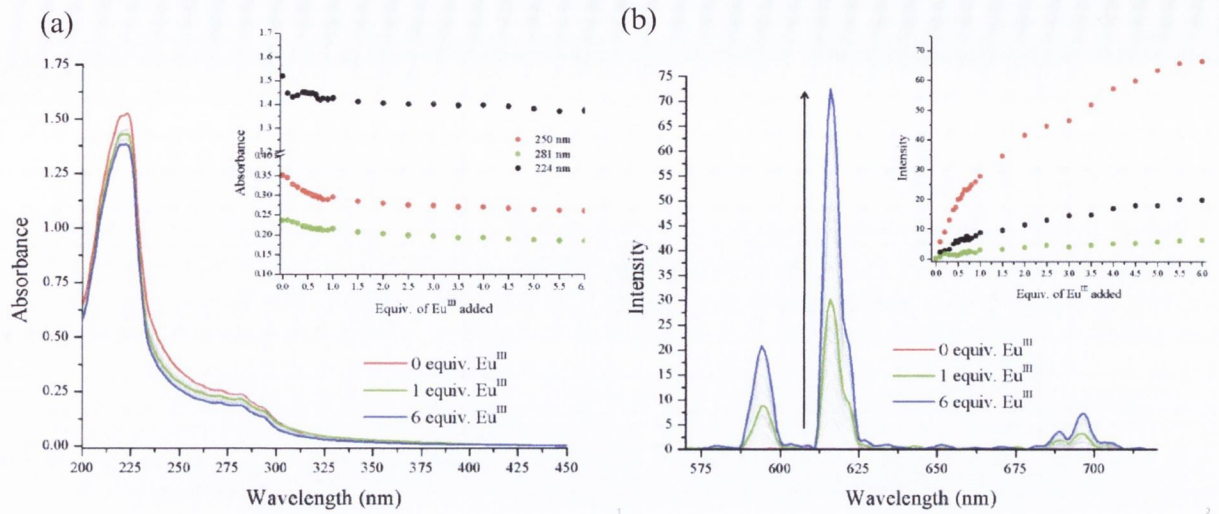

Figure A3.25. *The overall changes in the (a) UV-visible absorption spectra and (b) Eu^{III}–centred phosphorescence spectra upon titrating* ***88*** *(1 x 10^{-5} M) against $Eu(CF_3SO_3)_3$ (0→6 equiv.) in CH_3OH:H_2O (50:50) at RT.* ***Inset****: corresponding experimental binding isotherm of (a) absorbance at λ = 224, 250 & 281 nm and (b) Eu^{III} phosphorescence emission intensity at λ = 595, 615 and 695 nm.*

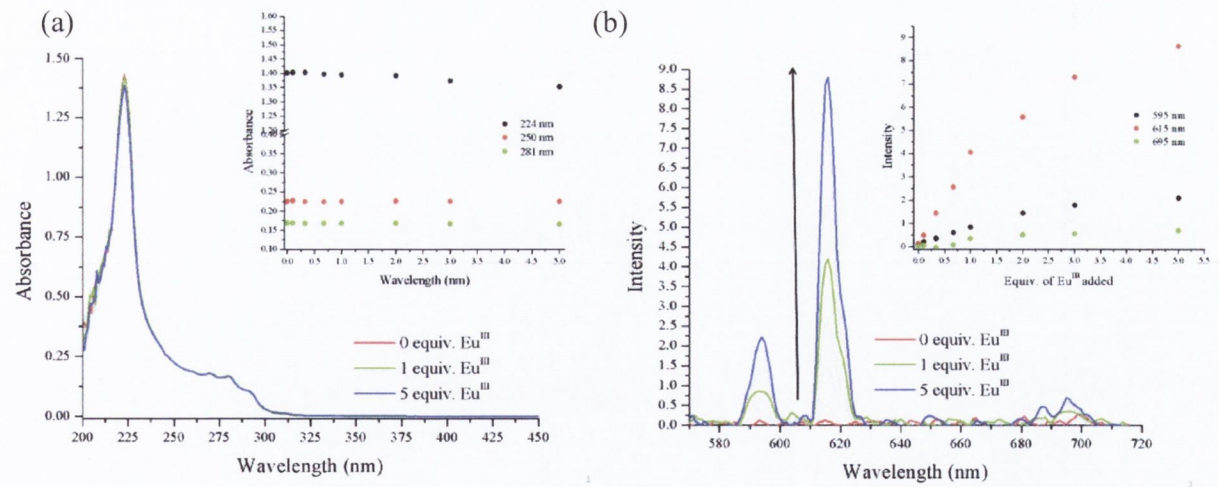

Figure A3.26. *The overall changes in the (a) UV-visible absorption spectra and (b) Eu^{III}–centred phosphorescence spectra upon titrating* ***87*** *(1 x 10^{-5} M) against $Eu(CF_3SO_3)_3$ (0→5 equiv.) in a 0.1M HEPES/0.1M NaCl CH_3OH:H_2O (80:20) solution at RT.* ***Inset****: corresponding experimental binding isotherm of (a) absorbance at λ = 224, 250 & 281 nm and (b) Eu^{III} phosphorescence emission intensity at λ = 595, 615 and 695 nm.*

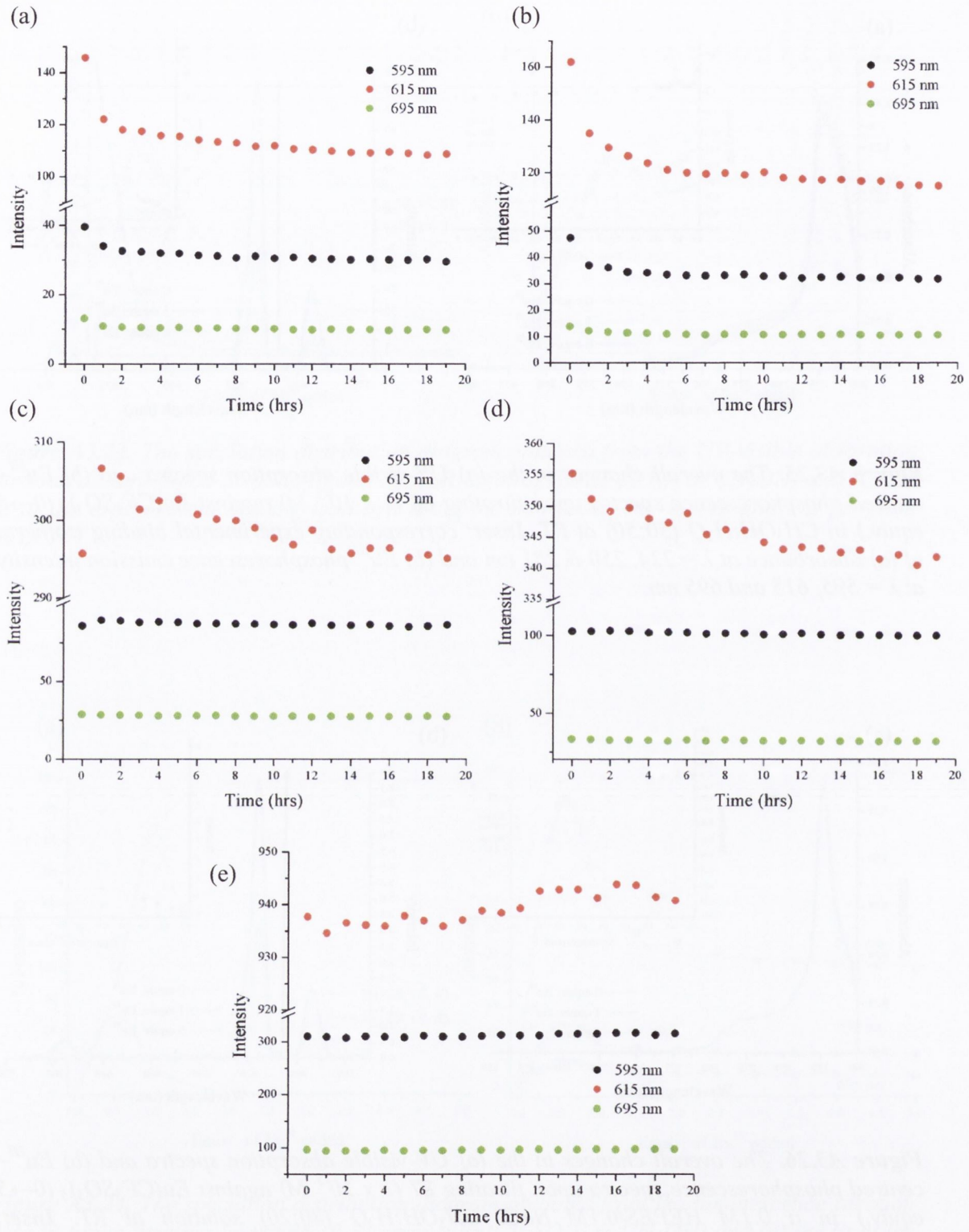

Figure A3.27. *Eu^{III}-centred emission intensity at λ = 595, 615 and 695 nm following the addition of (a) 0.4, (b) 0.6, (c) 0.8, (d) 1.0 and (e) 5.0 equivalents of $Eu(CF_3SO_3)_3$ to ligand **87** in a CH_3OH:H_2O (80:20) solution from 0→19 hrs at RT (excitation at λ = 281 nm).*

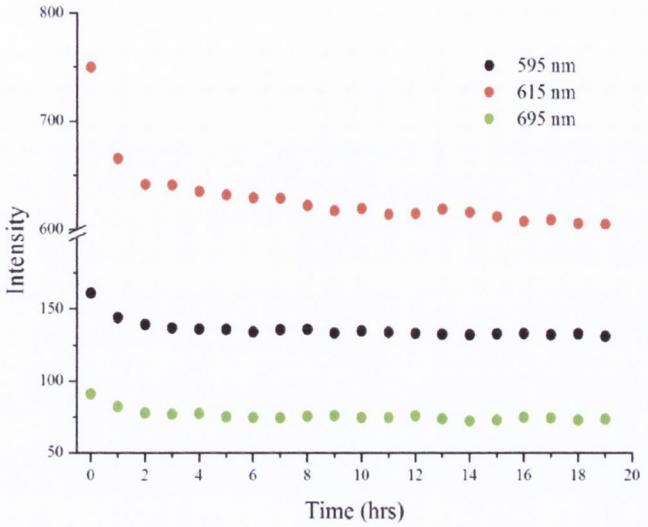

Figure A3.28. *Eu^{III}-centred emission intensity at λ = 595, 615 and 695 nm from $Eu_2.\mathbf{88}_3$ complex in a $CH_3OH:H_2O$ (80:20) solution from 0→18 hrs at RT (excitation at λ = 281 nm).*

Appendix Four

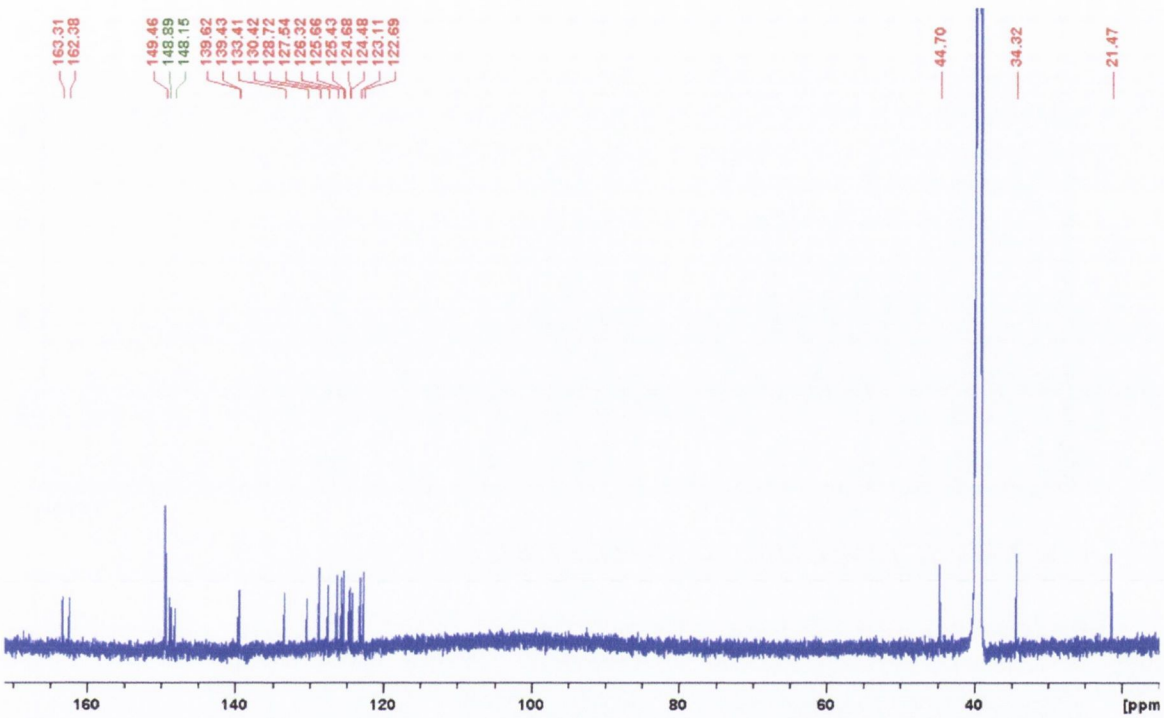

Figure A4.1. *^{13}C NMR spectrum (150 MHz, DMSO-d_6) of* ***110*** *(S).*

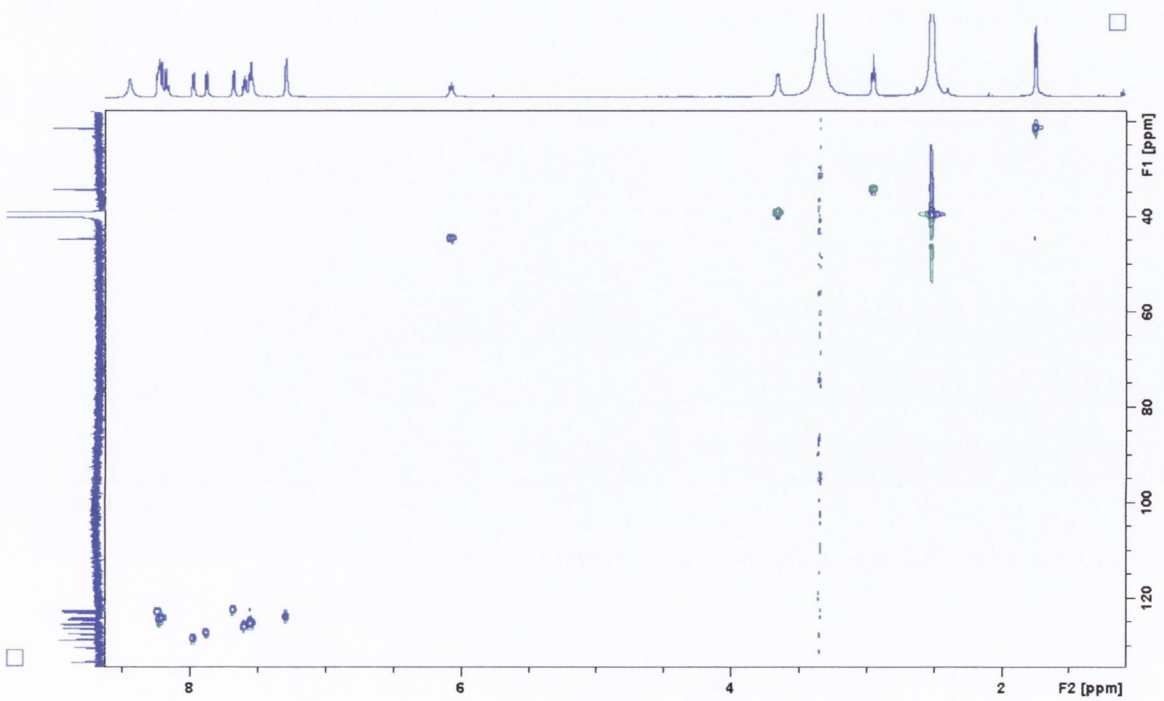

Figure A4.2. *^{1}H-^{13}C HSQC (DMSO-d_6) experiment for* ***110*** *(S).*

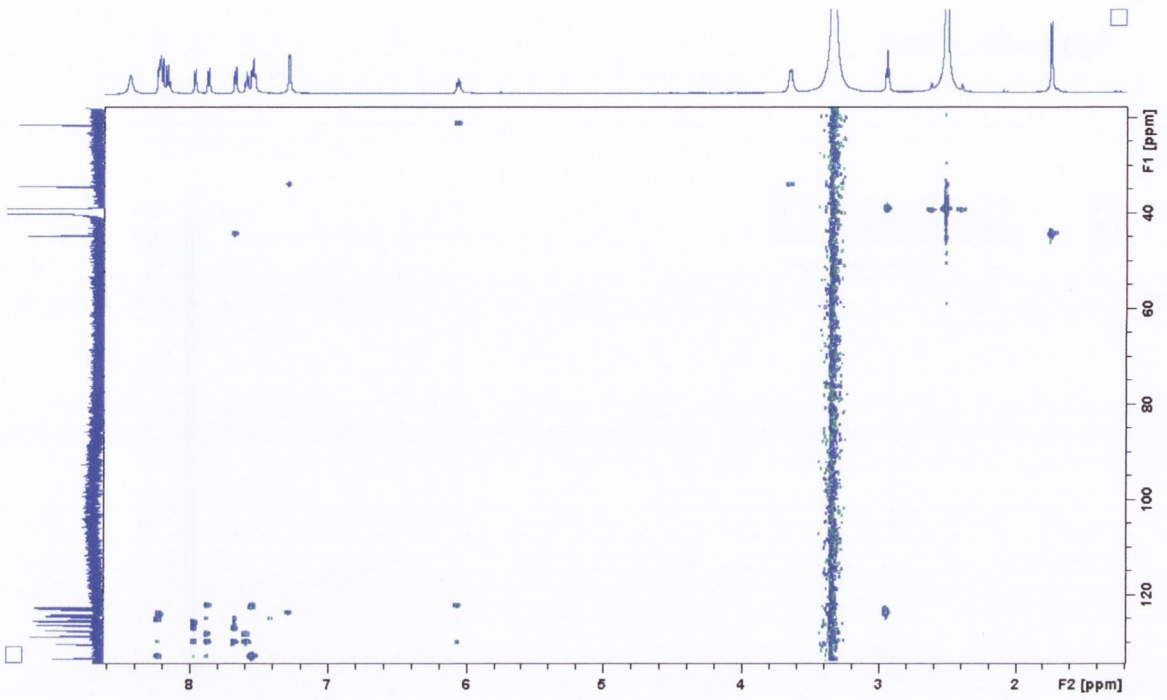

Figure A4.3. *HMBC (DMSO-d_6) experiment for* ***110*** *(S).*

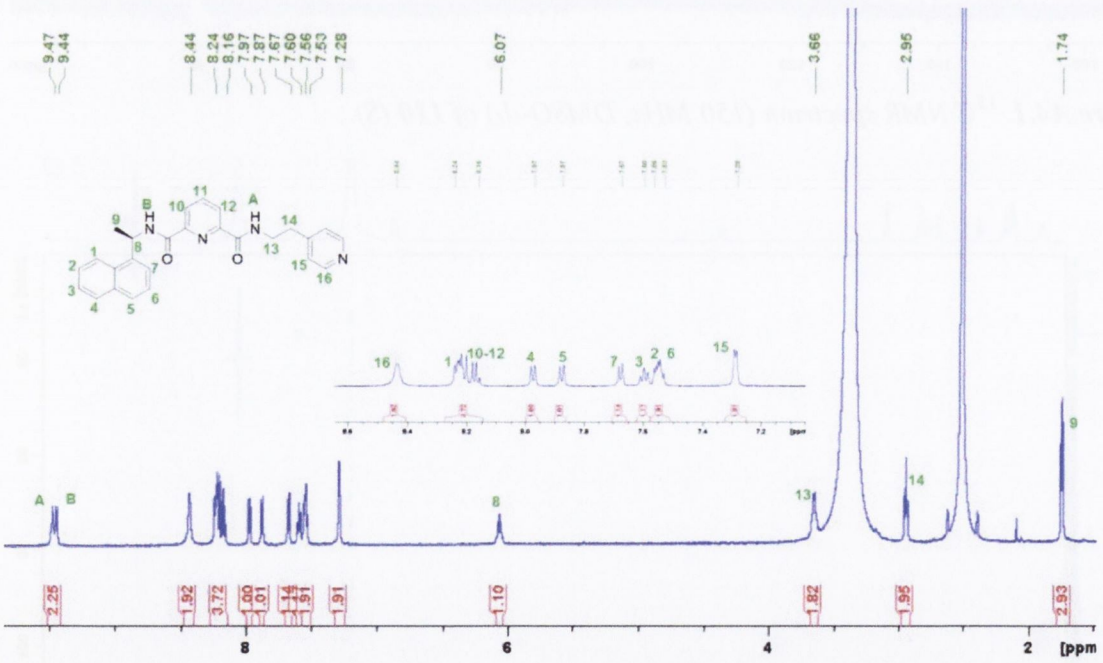

Figure A4.4. *^{1}H NMR spectrum (600 MHz, DMSO-d_6) of* ***111*** *(R).*

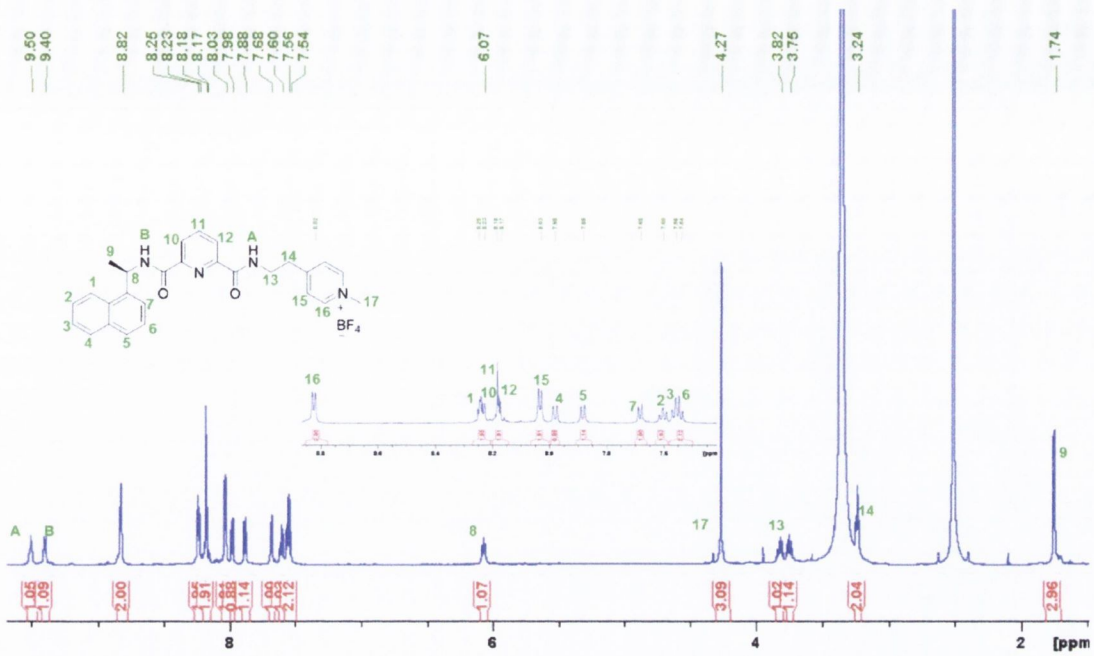

Figure A4.5. *^{1}H NMR spectrum (600 MHz, DMSO-d_6) of* ***101*** *(R).*

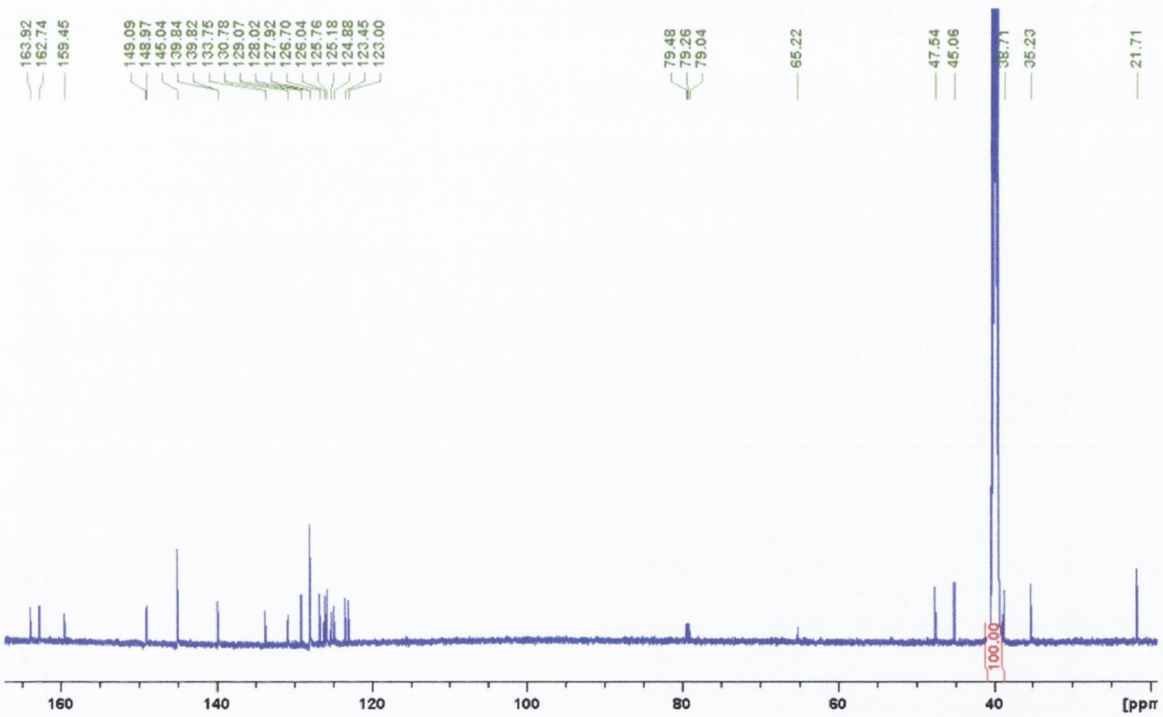

Figure A4.6. *^{13}C NMR spectrum (150 MHz, DMSO-d_6) of* ***101*** *(R).*

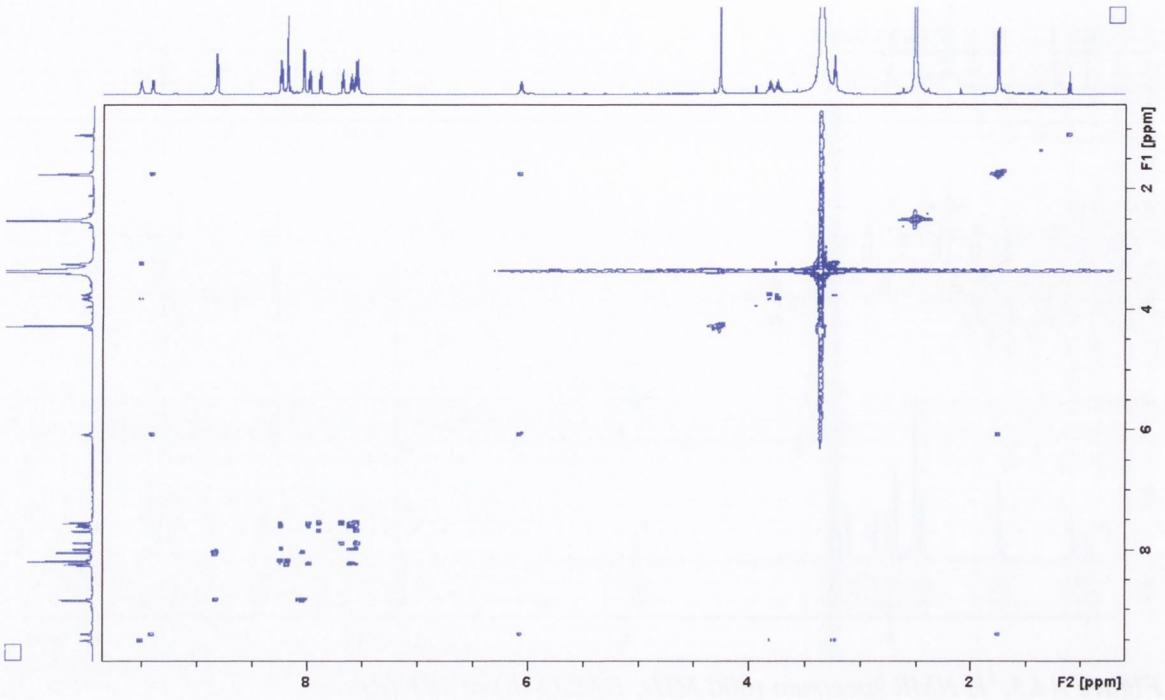

Figure A4.7. *^{1}H-^{1}H COSY (DMSO-d_6) experiment for* ***101*** *(R).*

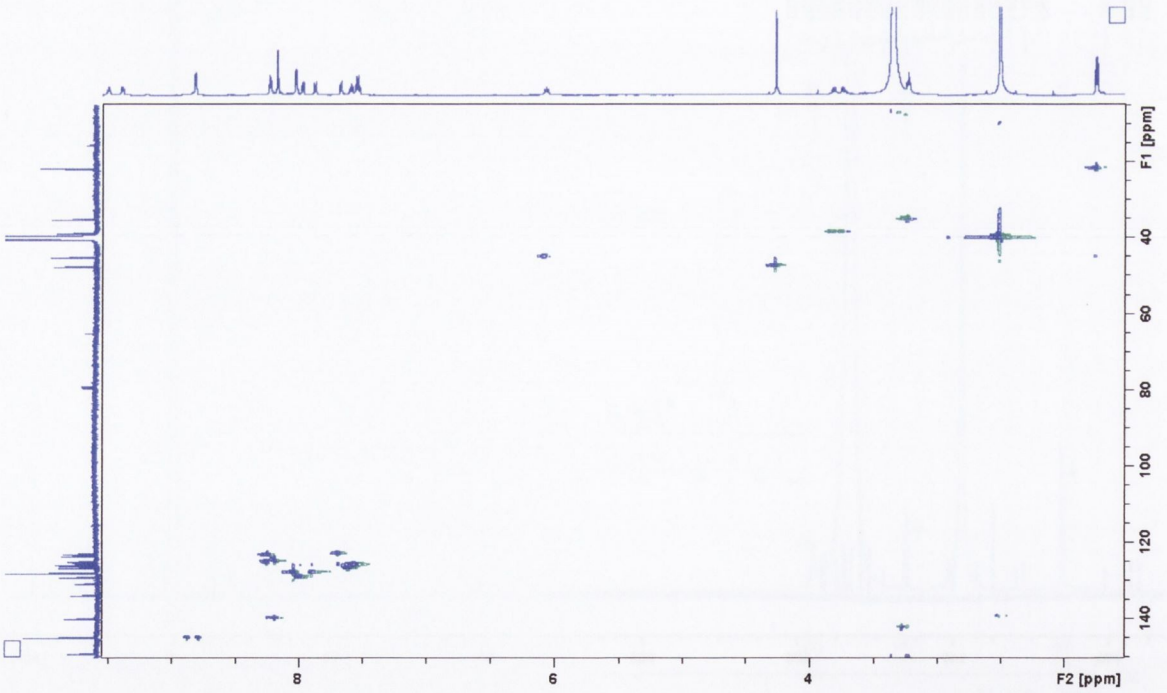

Figure A4.8. *^{1}H-^{13}C HSQC (DMSO-d_6) experiment for* ***101*** *(R).*

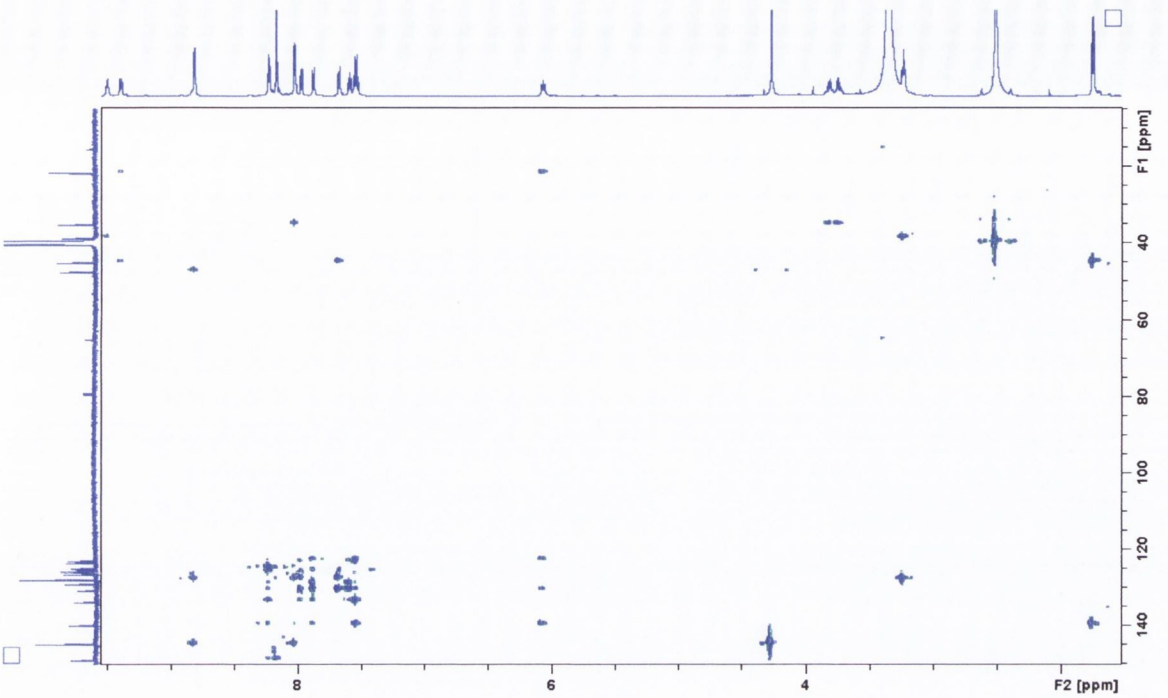

Figure A4.9. *HMBC (DMSO-d_6) experiment for* ***101*** *(R).*

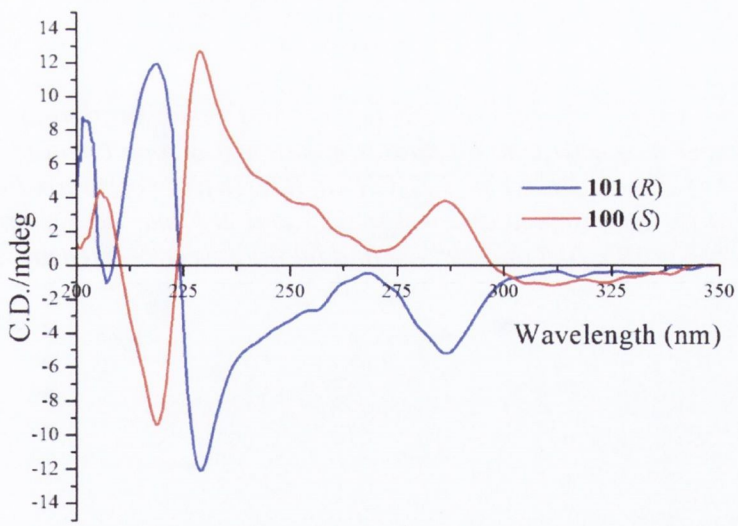

Figure A4.10. *Circular dichroism spectra of ligands* ***100*** *(S) and* ***101*** *(R) (2 x 10^{-5} M) recorded in CH_3OH at RT - note that slight discrepancies in intensities can be derived from differences in concentrations.*

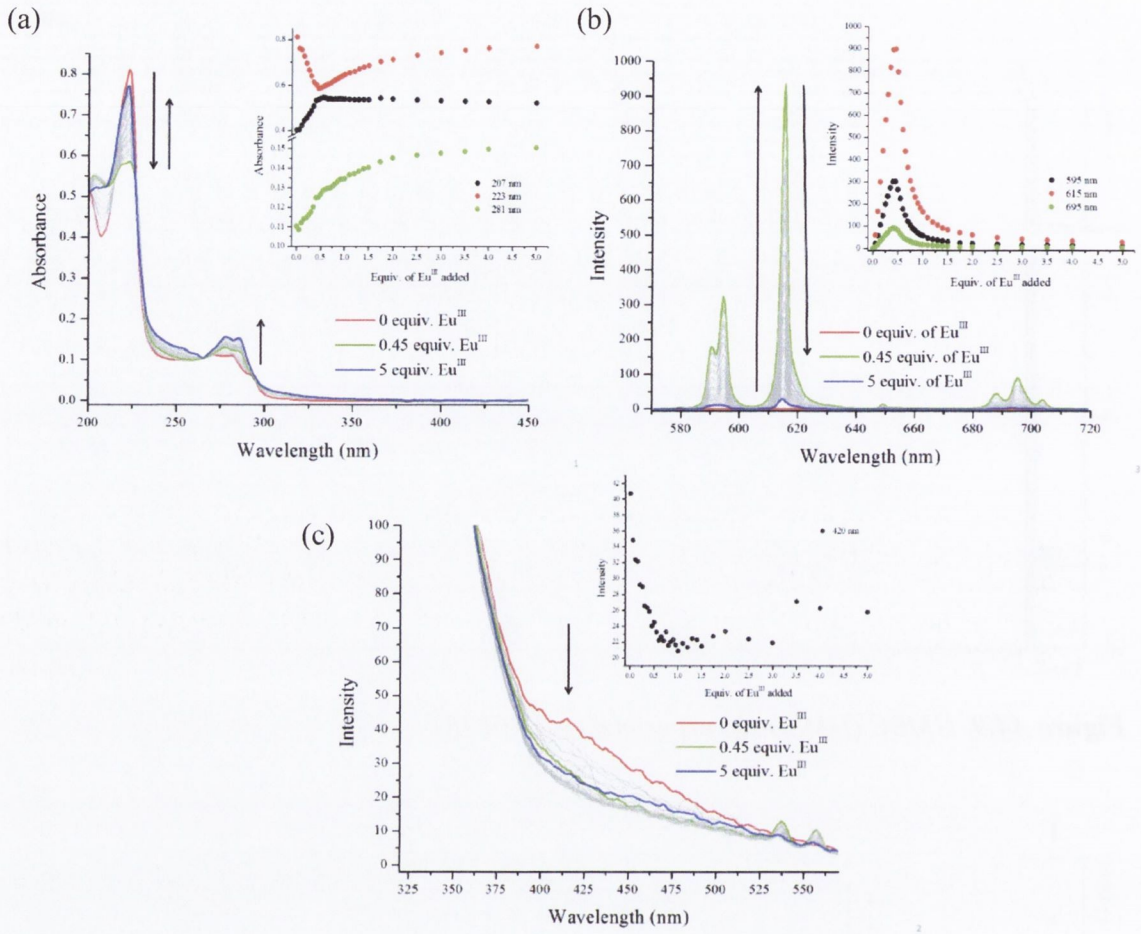

Figure A4.11. *The overall changes in the (a) UV-visible absorption spectra, (b) Eu^{III}–centred phosphorescence spectra and (c) fluorescence spectra upon titrating* ***111*** *(1 x 10^{-5} M) against $Eu(CF_3SO_3)_3$ (0→5 equiv.) in CH_3CN at RT.* ***Inset****: corresponding experimental binding isotherm of (a) absorbance at λ = 207, 223 and 281 nm, (b) Eu^{III} phosphorescence emission intensity at λ = 595, 615 and 695 nm and (c) fluorescence intensity at 420 nm .*

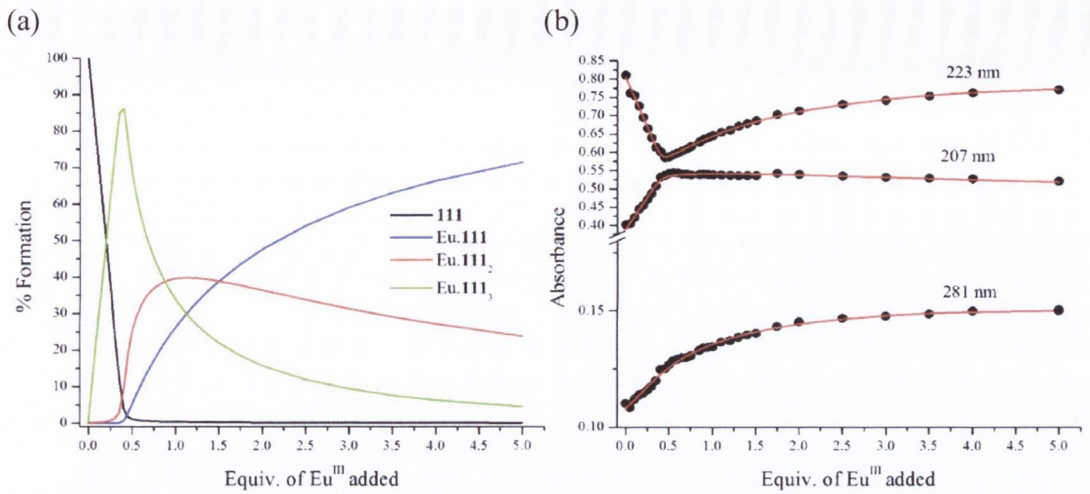

Figure A4.12. *(a) The speciation distribution diagram obtained from the UV-visible absorption titration data fit (upon titrating ligand* ***111*** *against $Eu(CF_3SO_3)_3$ in CH_3CN) and (b) the fit of the experimental binding isotherms using the non-linear regression analysis program SPECFIT.*

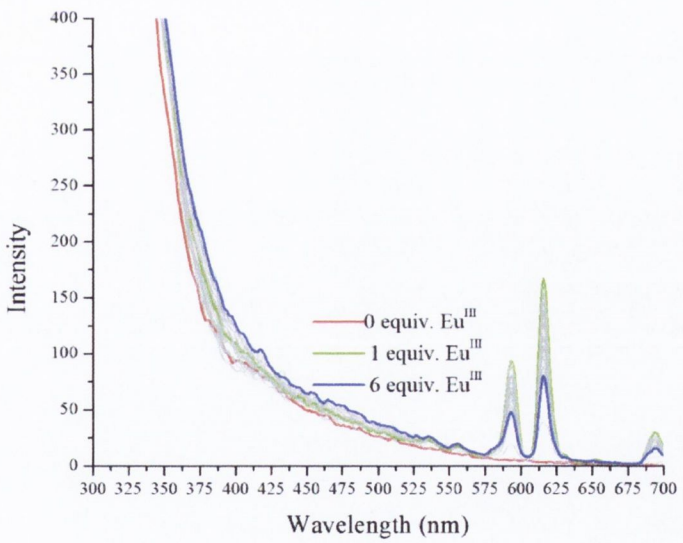

Figure A4.13. *The overall changes in the fluorescence spectra upon titrating* ***101*** *(1×10^{-5} M) against $Eu(CF_3SO_3)_3$ (0→6 equiv.) in CH_3CN at RT.*

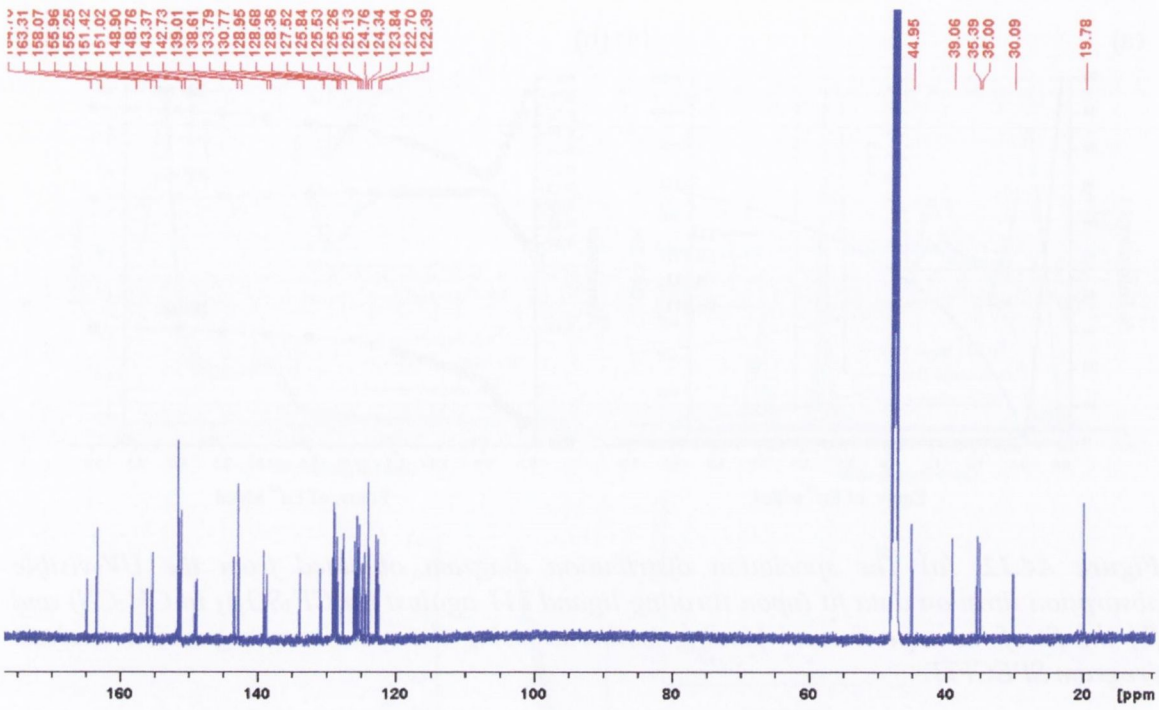

Figure A4.14. *^{13}C NMR spectrum (150 MHz, CD_3OD-d_4) of* ***109*** *(R).*

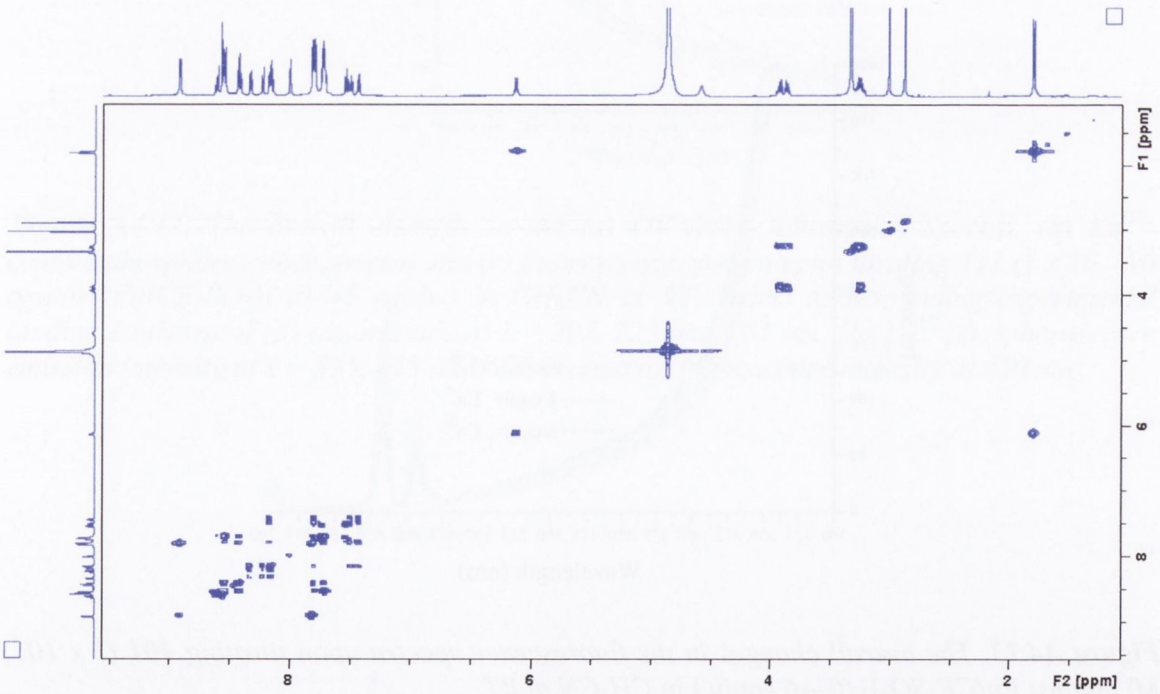

Figure A4.15. *^1H-^1H COSY (CD_3OD-d_4) experiment for* ***109*** *(R).*

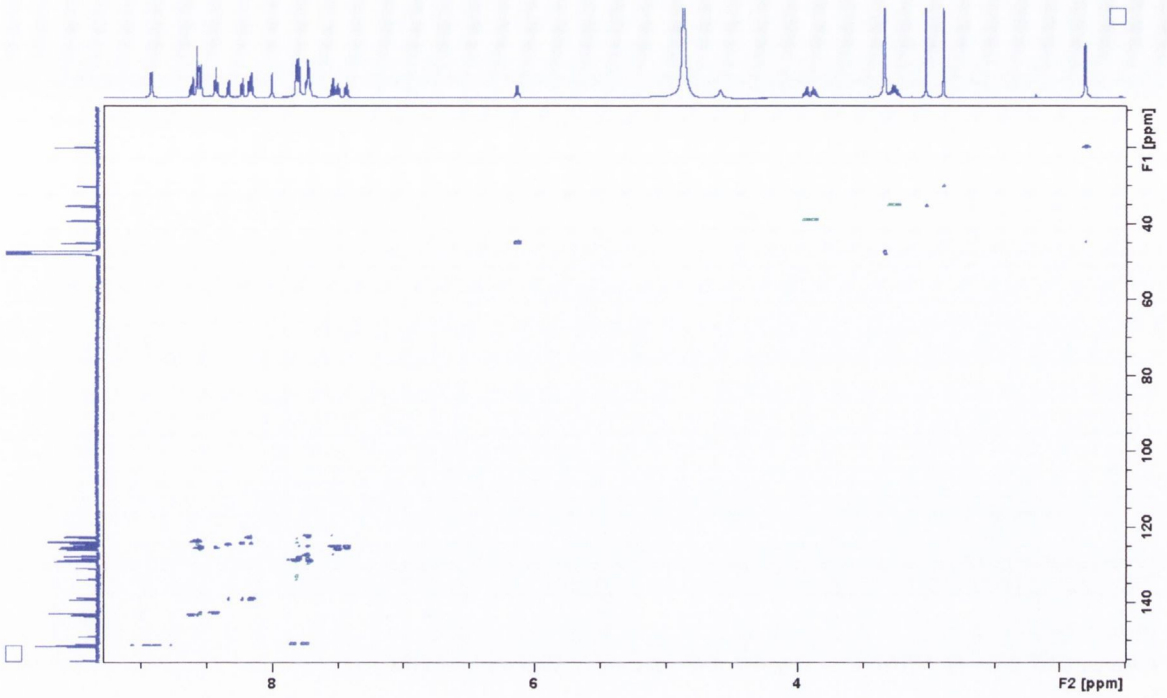

Figure A4.16. *^{1}H-^{13}C HSQC (CD_3OD-d_4) experiment for* ***109*** *(R).*

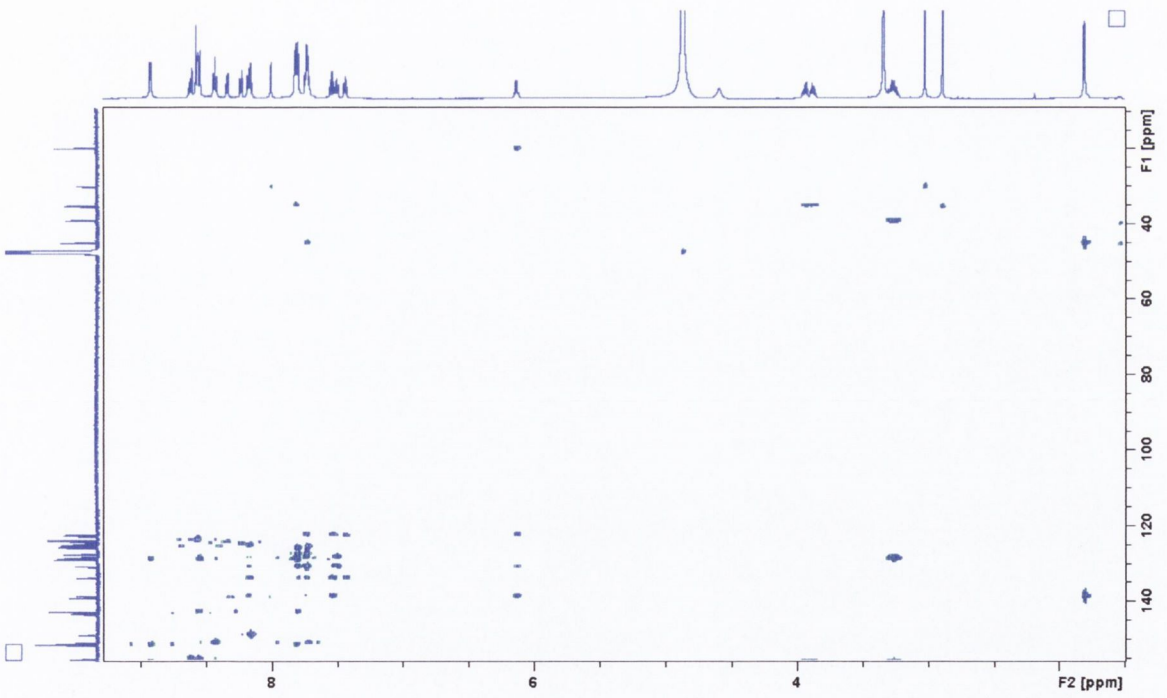

Figure A4.17. *HMBC (CD_3OD-d_4) experiment for* ***109*** *(R).*

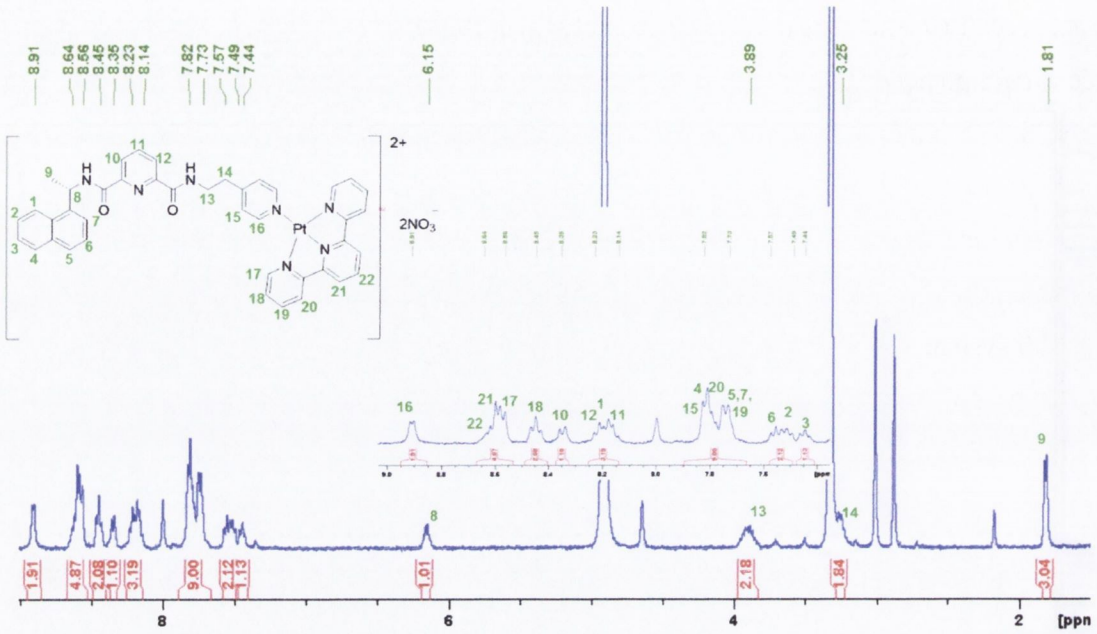

Figure A4.18. *^{1}H NMR spectrum (600 MHz, DMSO-d_6) of* ***108*** *(S).*

Table A4.1. *Crystal data and structure refinement for* ***108****.*

Identification code	**108**	
Empirical formula	C44 H42 N10 O9 Pt	
Formula weight	1049.97	
Temperature	100(2) K	
Wavelength	1.54178 Å	
Crystal system	Orthorhombic	
Space group	P2(1)2(1)2(1)	
Unit cell dimensions	a = 10.4349(2) Å	a= 90°.
	b = 15.6332(4) Å	b= 90°.
	c = 25.4007(6) Å	g = 90°.
Volume	4143.64(16) $Å^3$	
Z	4	
Density (calculated)	1.683 Mg/m^3	
Absorption coefficient	6.936 mm^{-1}	
F(000)	2104	
Crystal size	0.53 x 0.10 x 0.08 mm^3	
Theta range for data collection	3.32 to 64.80°.	
Index ranges	-12<=h<=11, -17<=k<=15, -28<=l<=29	
Reflections collected	18448	
Independent reflections	6462 [R(int) = 0.0364]	
Completeness to theta = 64.80°	95.4 %	
Absorption correction	Semi-empirical from equivalents	
Max. and min. transmission	0.7525 and 0.4374	
Refinement method	Full-matrix least-squares on F^2	
Data / restraints / parameters	6462 / 0 / 591	
Goodness-of-fit on F^2	1.058	
Final R indices [I>2sigma(I)]	R1 = 0.0334, wR2 = 0.0806	
R indices (all data)	R1 = 0.0353, wR2 = 0.0824	
Absolute structure parameter	0.006(8)	
Largest diff. peak and hole	1.849 and -0.802 $e.Å^{-3}$	

Table A4.2. *Crystal data and structure refinement for* ***109****.*

Identification code	**109**	
Empirical formula	C44 H42 N10 O9 Pt	
Formula weight	1049.97	
Temperature	100(2) K	
Wavelength	1.54178 Å	
Crystal system	Orthorhombic	
Space group	P2(1)2(1)2(1)	
Unit cell dimensions	a = 10.3900(5) Å	a= 90°.
	b = 15.6690(7) Å	b= 90°.
	c = 25.4718(13) Å	g = 90°.
Volume	4146.8(3) $Å^3$	
Z	4	
Density (calculated)	1.682 Mg/m^3	
Absorption coefficient	6.931 mm^{-1}	
F(000)	2104	
Crystal size	0.53 x 0.10 x 0.08 mm^3	
Theta range for data collection	11.31 to 64.98°.	
Index ranges	-12<=h<=12, -17<=k<=18, -19<=l<=29	
Reflections collected	13137	
Independent reflections	5991 [R(int) = 0.0340]	
Completeness to theta = 64.98°	89.1 %	
Absorption correction	Semi-empirical from equivalents	
Max. and min. transmission	0.7528 and 0.3254	
Refinement method	Full-matrix least-squares on F^2	
Data / restraints / parameters	5991 / 0 / 591	
Goodness-of-fit on F^2	1.026	
Final R indices [I>2sigma(I)]	R1 = 0.0309, wR2 = 0.0806	
R indices (all data)	R1 = 0.0318, wR2 = 0.0815	
Absolute structure parameter	0.018(8)	
Largest diff. peak and hole	1.514 and -1.085 $e.Å^{-3}$	

Table A4.3. *Selected bond lengths (Å) and angles (°) for* ***108*** *(S).*

Bond lengths (Å)/angles (°)	
Pt(1)-N(6)	1.962(4)
Pt(1)-N(5)	2.032(5)
Pt(1)-N(7)	2.033(5)
Pt(1)-N(4)	2.047(4)
N(6)-Pt(1)-N(5)	81.49(17)
N(6)-Pt(1)-N(7)	81.60(18)
N(5)-Pt(1)-N(7)	163.06(18)
N(6)-Pt(1)-N(4)	178.03(17)
N(5)-Pt(1)-N(4)	96.98(17)
N(7)-Pt(1)-N(54	99.94(18)

Table A4.4. *Hydrogen bonds lengths and angles for ligand* ***108*** *(S) (Å and °). Symmetry transformations used to generate equivalent atoms:* [a] *x-1,y,z.*

D-H...A	d(D-H)	d(H...A)	d(D...A)	<(DHA)
N(1)-H(1X)...O(200)[a]	0.83	2.38	3.081(6)	142.6
N(3)-H(3X)...O(200)[a]	0.88	2.18	2.985(7)	151.2

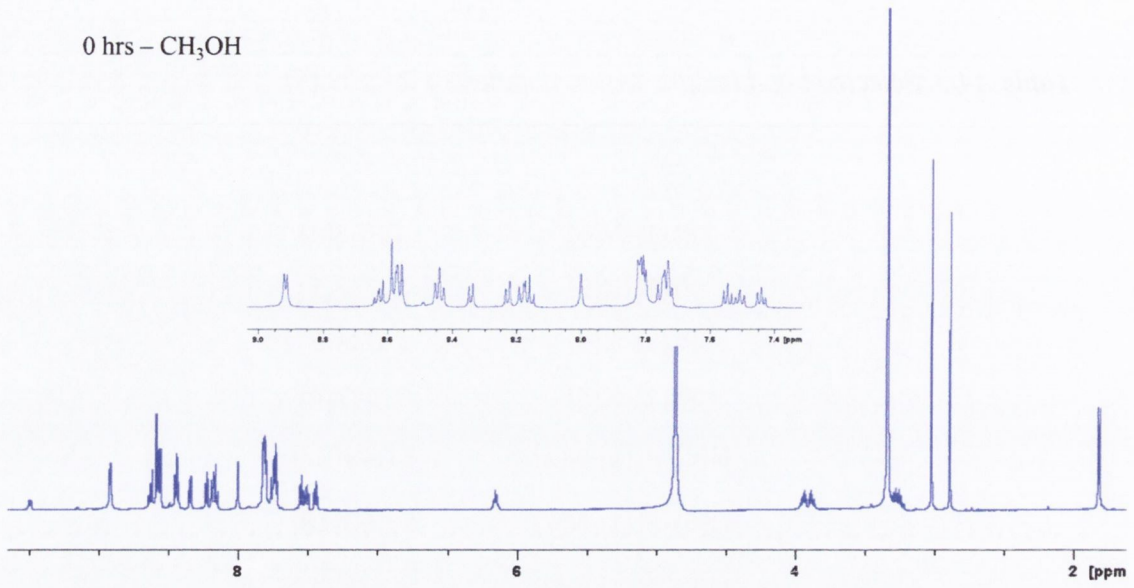

Figure A4.19 *.^{1}H NMR spectrum (600 MHz, CD_3OD-d_4) of complex* ***109*** *(R) after 0 hrs.*

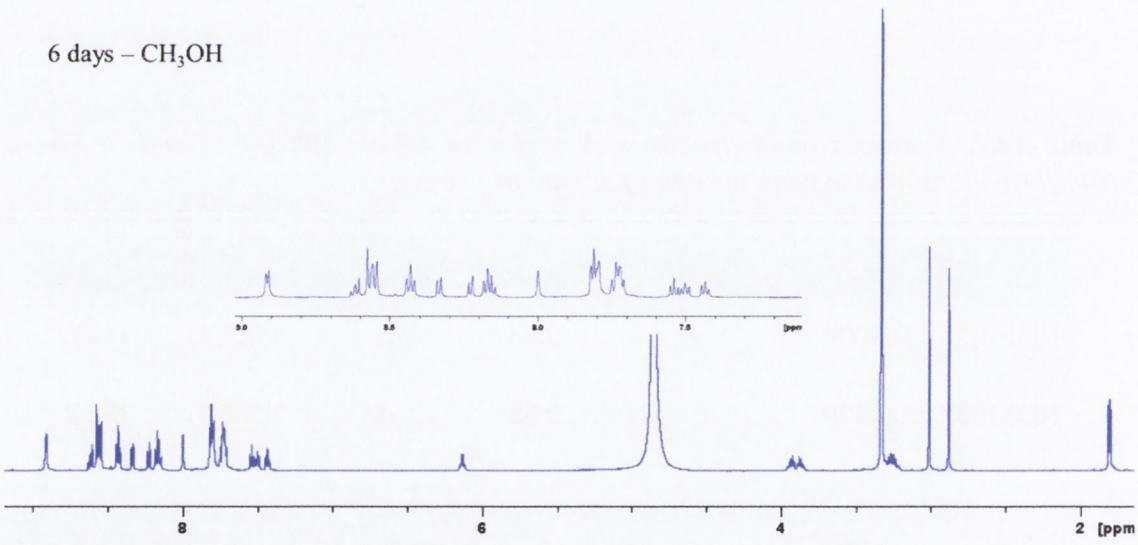

Figure A4.20. *^{1}H NMR spectrum (600 MHz, CD_3OD-d_4) of complex* ***109*** *(R) after 6 days.*

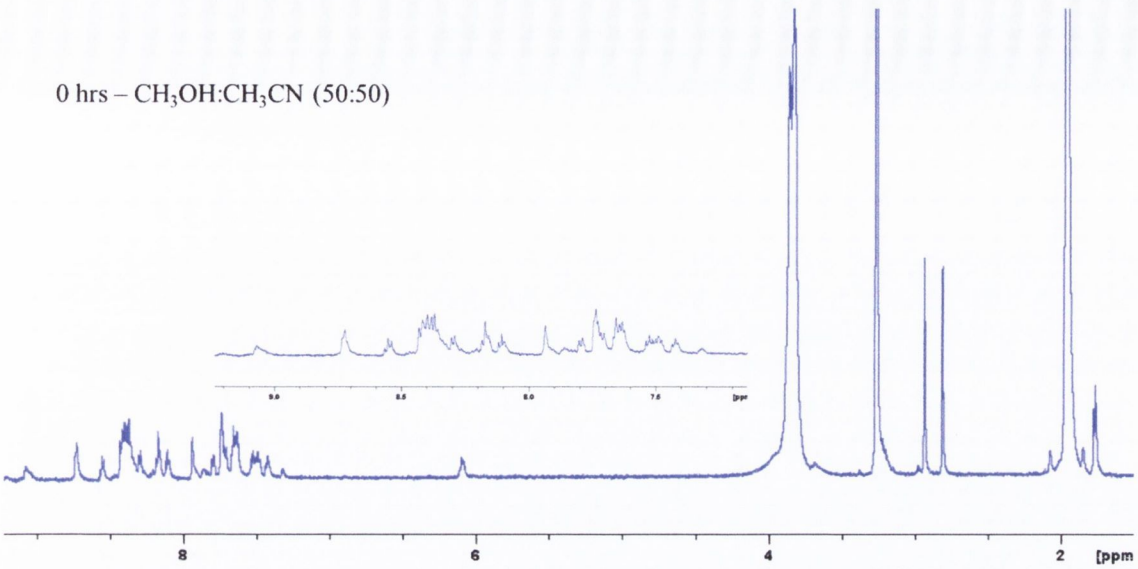

Figure A4.21. *^{1}H NMR spectrum (600 MHz, CD_3OD:CD_3CN (50:50)) of complex* ***109*** *(R) after 0 hrs.*

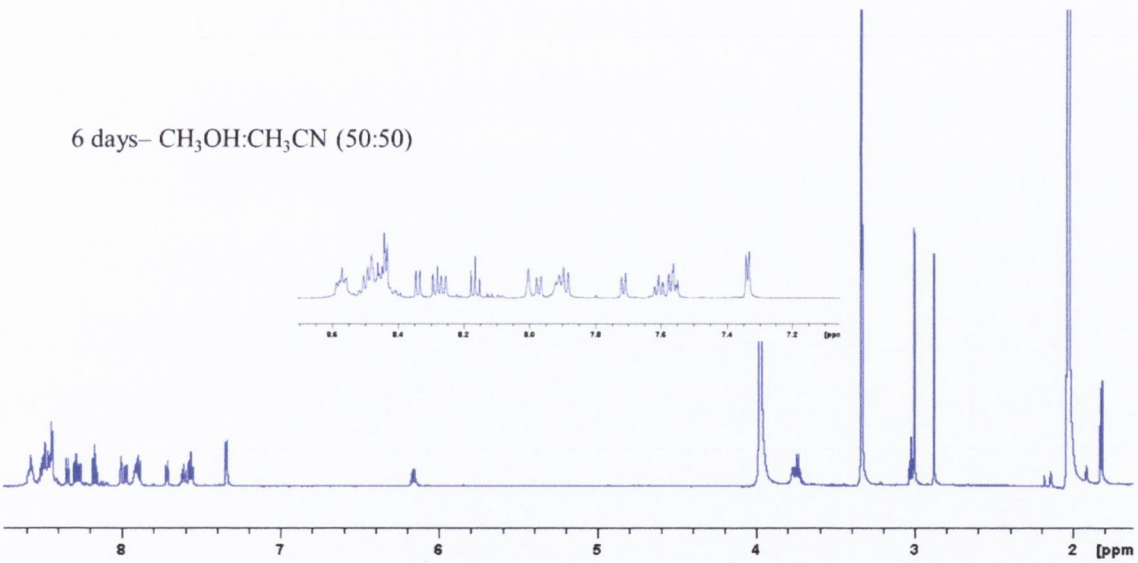

Figure A4.22. *^{1}H NMR spectrum (600 MHz, CD_3OD:CD_3CN (50:50)) of complex* ***109*** *(R)* after 6 days.

Appendix Five

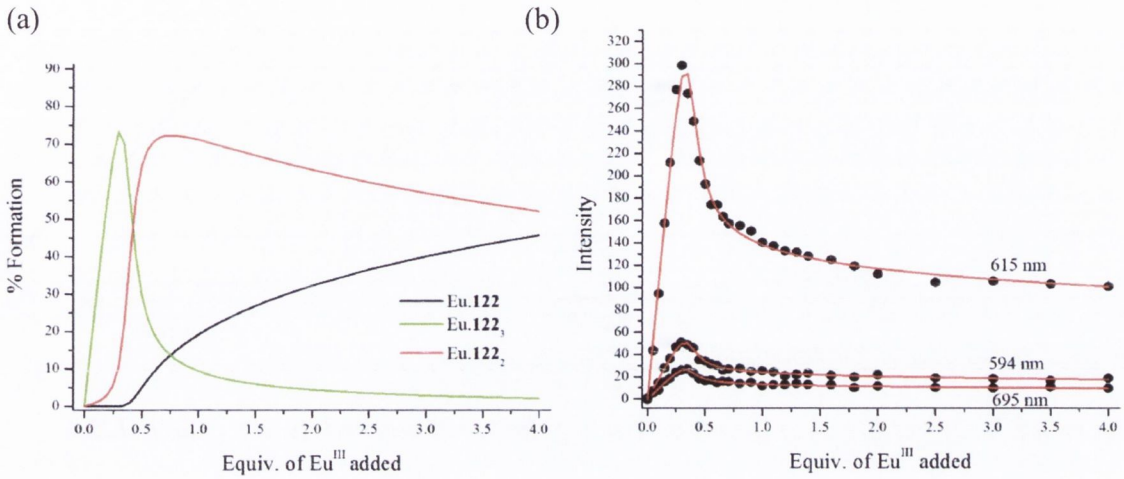

Figure A5.1. *(a) The speciation distribution diagram obtained from the luminescence titration data fit (upon titrating ligand* ***122*** *against $Eu(CF_3SO_3)_3$ 0.1 M Tris-HCl (I = 0.1 M NaCl) buffer solution (pH = 7.45)) and (b) the fit of the experimental binding isotherms using the non-linear regression analysis program SPECFIT.*

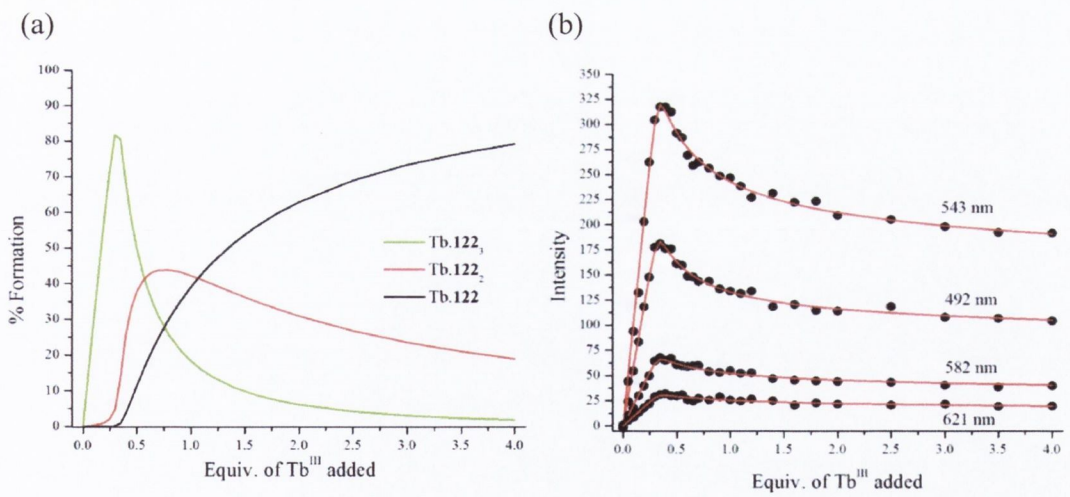

Figure A5.2. *(a) The speciation distribution diagram obtained from the luminescence titration data fit (upon titrating ligand* ***122*** *against $Tb(CF_3SO_3)_3$ 0.1 M Tris-HCl (I = 0.1 M NaCl) buffer solution (pH = 7.45)) and (b) the fit of the experimental binding isotherms using the non-linear regression analysis program SPECFIT.*

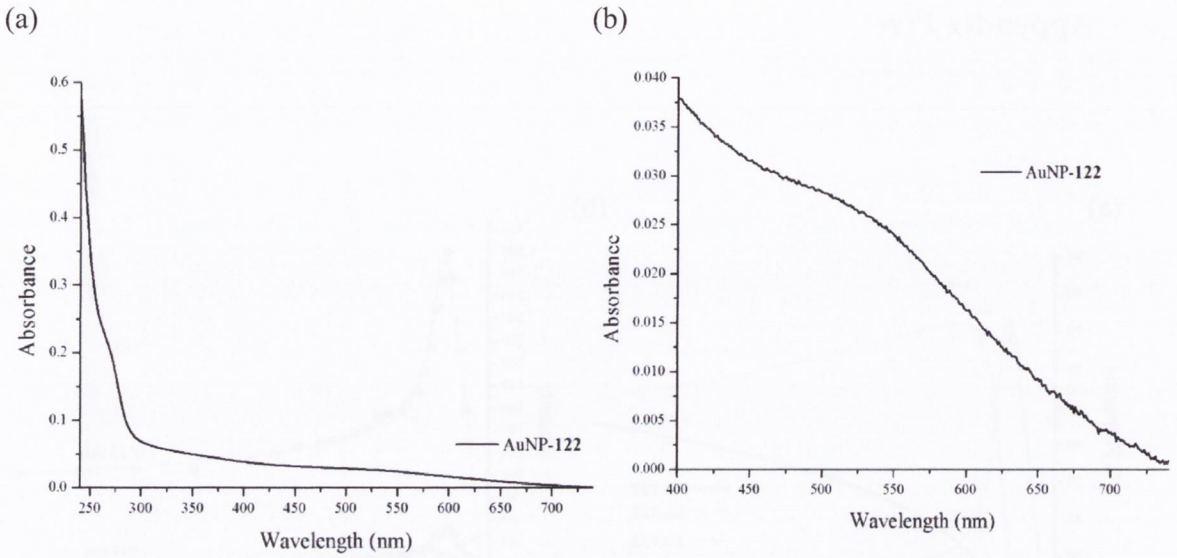

Figure A5.3. *UV-visible absorption spectrum of the functionalised AuNPs (AuNP-**122**).*

Publications

Dalton Transactions

Dynamic Article Links

Cite this: *Dalton Trans.*, 2011, **40**, 12056

www.rsc.org/dalton

COMMUNICATION

Lanthanide directed self-assembly synthesis and photophysical evaluation of chiral Eu(III) luminescent "half-helicates"†

Christophe Lincheneau,[a] Carole Destribats,[a] Dawn E. Barry,[a] Jonathan A. Kitchen,[a] Robert D. Peacock[b] and Thorfinnur Gunnlaugsson*[a]

Received 27th June 2011, Accepted 18th August 2011
DOI: 10.1039/c1dt11225b

The reaction between the asymmetrical pyridyl ligands 3 (*R*) and 4 (*S*) and Eu(III) in CH_3CN give rise to the formation of lanthanide luminescent 'half-helicates' in 1 : 3 (Ln:ligand) stoichiometry; the formation of which was observed by monitoring the changes in the ground and the excited state properties of the ligands, and in the time-resolved Eu-centred and the CPL emission.

The formation of metal directed self-assemblies from structurally defined ligands has become a major area of research within the field of supramolecular and nano-chemistry.[1-3] The majority of such examples has been based on the use of *d*-metal ions; which, due to their various coordination requirements, can give rise to complex and beautiful discrete structures.[4-6] Many of such systems, can also give rise to the formation of larger networks such as MOFs[7-8] and coordination polymers,[9-10] which can add function and unique properties to such architectures. In contrast to this, the use of lanthanide ions to direct the synthesis of functional supramolecular architectures,[11-12] or large networks,[13] has been explored to lesser degree. Recently we have developed both triple stranded helicates[14-16] and molecular bundles[17-18] by using C_2 symmetric pyridyl amides, possessing chiral antennae, *e.g.* **1** and **2**, by using lanthanide directed synthesis (Fig. 1). Using X-ray crystal structure analysis and a variety of spectroscopic techniques, we have determined their structure in the solid-state and in solution, where for the latter we show that these (and related self-assembly structures) are formed as stable homo-chiral species, that are formed with high binding constants.[19-21] Furthermore, through modification of the pyridyl ligands, we been able to access control over the ligand:metal ($\mathbf{L_n}\cdot\mathbf{Ln_m}$) stoichiometry and hence, the structural nature of the self-assembly products, which are usually also formed with significant intra-ligand contributions from hydrogen bonding and π–π stacking interactions. With the view of further elucidating the nature of the self-assembly formation, we decided to investigate the complex formation between **3** and **4** and Eu(III), but these ligands represent "half the ligands" employed in the synthesis of numerous enantiomerically pure di-metal triple stranded helicates, such as those formed from **1** and Eu(III). Herein, we demonstrate that despite the possibilities of forming various stoichiometries and numerous geometrical isomers of $\mathbf{3_n}\cdot\mathbf{Eu_m}$ and $\mathbf{4_n}\cdot\mathbf{Eu_m}$, then our results strong indicates that these are preferably formed in a 3 : 1 stoichiometry ($\mathbf{L_3}\cdot\mathbf{Ln_1}$) and as single chiral geometrical isomers in solution.

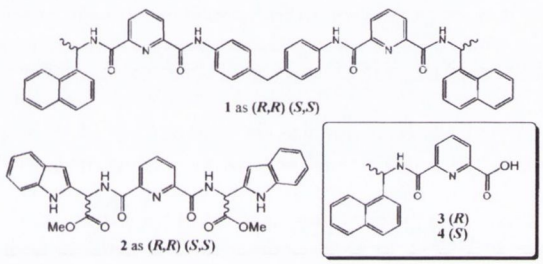

Fig. 1 Ligands **1** and **2** previously used in the formation of chiral self-assemblies and **3** and **4**, employed in the current study.

The synthesis of the $\mathbf{L_3}\cdot\mathbf{Eu_1}$ (see ESI†) stoichiometry was first undertaken by reacting $Eu(CF_3SO_3)_3$ with **3** or **4** in a 3 : 1 ligand to metal molar ratio in CH_3CN under microwave irradiation at 90 °C for 10 min. Compounds **3** and **4** were originally designed and synthesised for use in the development of **1**[14] and other analogues,[15,16] and the resulting complexes, $\mathbf{3_3}\cdot\mathbf{Eu_1}$ and $\mathbf{4_3}\cdot\mathbf{Eu_1}$, were isolated as off-white solids in good yields of 72% and 82%, respectively, from the diffusion of diethyl ether into the reaction solutions. HRMS-MALDI analysis confirmed the identity of the desired complexes with peaks at 1133.2395 *m/z* for $\mathbf{3_3}\cdot\mathbf{Eu_1}$ and 1133.2393 *m/z* for $\mathbf{4_3}\cdot\mathbf{Eu_1}$, demonstrating the formation of both as overall charge neutral species. On both occasions the observed isotopic distribution patterns matched that of the calculated one (see ESI†). The ^{1}H NMR (400 MHz, CD_3CN) of both $\mathbf{3_3}\cdot\mathbf{Eu_1}$ and $\mathbf{4_3}\cdot\mathbf{Eu_1}$, were significantly sifted and broadened in comparison to that seen for **3** and **4**; and the changes in the proton resonances of the two aryl groups were effected in the same way as was observed for the formation of the di-metalic triple stranded helicates of **1**.[16] The photophysical properties of both complexes were investigated in CH_3CN, H_2O and D_2O. In H_2O, the UV-vis absorption spectra of both was dominated by naphthalene π–π* transition at 281 nm and, with a higher *n*–π* pyridyl transition at 223 nm; and excitation

[a]*School of Chemistry, Centre for Synthesis and Chemical Biology, Trinity College Dublin, Dublin, 2, Ireland*
[b]*School of Chemistry, Joseph Black Building, University of Glasgow, Glasgow, G12 8QQ, U.K. E-mail: gunnlaut@tcd.ie; Fax: +353 1671 2826; Tel: +353 1 896 3459*

† Electronic supplementary information (ESI) available: Characterisation and 11 figures. See DOI: 10.1039/c1dt11225b

of 281 nm gave rise to a broad fluorescence with λ_{max} centred at *ca.* 450 nm (see ESI†); which was very much reduced in intensity in comparison to the free ligands. Moreover, the metal centred Eu(III) emission was also clearly observed, with strong contributions from the ($^5D_0 \rightarrow {}^7F_J$; $J = 0$–4) $\Delta J = 1, 2$ and 4, transitions upon excitation of the antenna, and weaker contributions from for the $\Delta J = 0$ and 3 transitions (see ESI†). Moreover, the excitation spectra of both complexes (using λ_{em} = 615 nm, ΔJ = 2) was structurally similar to that observed in the absorption spectra, confirming the sensitisation of Eu(III) emission by the antennae for both $\mathbf{3}_3\cdot\mathbf{Eu}_1$ and $\mathbf{4}_3\cdot\mathbf{Eu}_1$ (see ESI†). The Eu(III) excited stated lifetimes were recorded in both H_2O and D_2O, and were best fitted to bi-exponential decay, giving τ_1 = 1.70 ms (major) and τ_2 = 0.3 ms (minor) when recorded in H_2O and to a mono-exponential decay in D_2O with τ_1 = 3.91 ms for in $\mathbf{3}_3\cdot\mathbf{Eu}_1$. From these, the hydration state q, was determined as ~0; which confirms that the Eu(III) is coordinative saturated. For $\mathbf{4}_3\cdot\mathbf{Eu}_1$ similar results were observed, with a $q \sim 0$ (see ESI Table 1†). This suggests that the Eu(III) ion would be coordinated to the three pyridyl nitrogens, and the three amides and carboxylates, giving an overall coordination number of 9. When the Eu(III) emission was recorded in CH_3CN, the relative intensities were larger to that in H_2O, but the spectral structure remained the same (see ESI†). We also recorded the CD-spectra of **3** and **4** as well as the corresponding Eu(III) complexes $\mathbf{3}_3\cdot\mathbf{Eu}_1$ and $\mathbf{4}_3\cdot\mathbf{Eu}_1$ in CH_3CN (see ESI†), which demonstrated that both the ligands and the complexes were formed as pairs of enantiomers, and that significant differences were observed between the ligands and the complexes, particularly at long wavelengths (see later).

Having formed both $\mathbf{3}_3\cdot\mathbf{Eu}_1$ and $\mathbf{4}_3\cdot\mathbf{Eu}_1$ above, we next embarked on studying their self-assembly formation *in situ* using many of the same spectroscopic techniques discussed above. We first attempted to form both by stirring **3** and **4** (1×10^{-5} M) with 0.33 equivalents of $Eu(CF_3SO_3)_3$ for 5 min at room temperature, after which the UV-vis absorption and fluorescence emission spectra were recorded in CH_3CN. The results are shown in Fig. 2 for **3** and $\mathbf{3}_3\cdot\mathbf{Eu}_1$ (see ESI† for **4** and $\mathbf{4}_3\cdot\mathbf{Eu}_1$), and demonstrates that in the presence of Eu(III) the absorption band centred at λ_{max} = 224 nm and 210 nm experienced *ca.* 22%, hypochromic effect upon formation of $\mathbf{3}_3\cdot\mathbf{Eu}_1$. The excitation of the naphthyl antenna in **3** gave rise to a broad fluorescence emission,‡ however, upon binding to Eu(III) this emission band was significantly quenched. Moreover, the concomitant appearance of the Eu(III) emission was also clear in the fluorescence emission spectra, confirming the successful population of the Eu(III) $^5D_0$ excited state, which is thought to occur *via* the T_1 of the antenna after the population of S_1. Moreover, the excitation spectrum of the lanthanide centred emission, matched the transitions observed in the absorption spectrum as before. The excited state lifetimes of the $^5D_0$ excited state were also recorded in H_2O and D_2O, and matched well with those recorded above (See Table 1 ESI†). As before, when recorded in CH_3CN and D_2O, these were fitted best to a mono-exponential decay, suggesting the presence of a single luminescent species in solution. As discussed above, then significant changes were observed in the CD spectra **3** and **4** upon formation of $\mathbf{3}_3\cdot\mathbf{Eu}_1$ and $\mathbf{4}_3\cdot\mathbf{Eu}_1$; again, the *in situ* self-assembly formation matched that seen above (see ESI†) with two excitons of equal intensity but with opposite signs, being negative and positive for **3** and **4**, respectively (see ESI†). However, the self-assembly of the three ligands around the lanthanide ion resulted in significant changes in the optical activity of the resulting complexes, being most notable for the long wavelength absorption, which 'switched' signs as shown in Fig. 3 as an inset. The circular polarised luminescence (CPL) of both $\mathbf{3}_3\cdot\mathbf{Eu}_1$ and $\mathbf{4}_3\cdot\mathbf{Eu}_1$ were also recorded and are also shown in Fig. 3, where $\mathbf{3}_3\cdot\mathbf{Eu}_1$ displayed a negative band for the $^5D_0 \rightarrow {}^7F_1$ transition and a positive band at 617 nm for the $^5D_0 \rightarrow {}^7F_2$ transition with a weak negative shoulder at 620 nm. The emission band at 693 nm ($^5D_0 \rightarrow {}^7F_4$ transitions) showed a positive contribution at 692 nm followed by a negative one at 702 nm. Conversely, $\mathbf{4}_3\cdot\mathbf{Eu}_1$ exhibited the same bands with similar intensities but opposite sign indicating that the luminescence emission was chiral for both complexes. The dissymmetry factor g ($g = 2\Delta I/I$) was determined for both from the CPL luminescent spectra and were found to be high, which in the case of $\mathbf{3}_3\cdot\mathbf{Eu}_1$ gave g_{em} = −0.15 and 0.06 for the 600 nm and the 619 nm emission, respectively; while being g_{em} = 0.13 and −0.05 for $\mathbf{4}_3\cdot\mathbf{Eu}_1$. Reported g values tend to be weak when the CPL properties result predominantly from the chirality of the ligand.[22] However, the relatively high values obtained here suggested that each helical isomer $\mathbf{L}_3\cdot\mathbf{Eu}_1$ was formed as enantiomerically pure and most likely remain homochiral in solution.§ Moreover, the CPL spectra in Fig. 3, were structurally similar to that observed for the di-Eu(III) triple-stranded helicates of **1** (see ESI†), indicating that the symmetry of the "half-helicates" $\mathbf{3}_3\cdot\mathbf{Eu}_1$ and $\mathbf{4}_3\cdot\mathbf{Eu}_1$ were closely related to these, being either being C_3, or D_3[17] To shed some light on their geometry, we carried out MM2 calculations on $\mathbf{3}_3\cdot\mathbf{Eu}_1$ and $\mathbf{4}_3\cdot\mathbf{Eu}_1$ using different geometries around the Eu(III) ion. Of these, the most stable structures were determined to have the three antennae on the same side, directed towards the inside of a "half-helicate" (see ESI† and Scheme 1), and as such placing the methyl groups outside the coordination sphere of the ion. This geometry also allowed for π–π interaction between the antenna

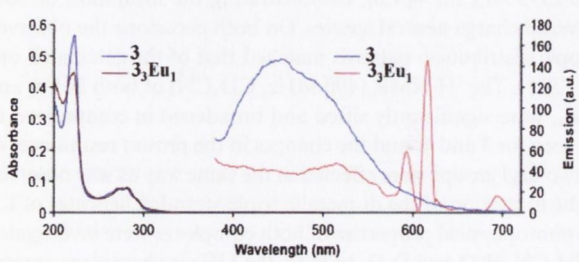

Fig. 2 The UV-vis absorption and fluorescence emission spectra (λ_{ex} = 281 nm) of **3** (blue) and $\mathbf{3}_3\cdot\mathbf{Eu}_1$ (red) in CH_3CN $C_L = 1 \times 10^{-5}$M.

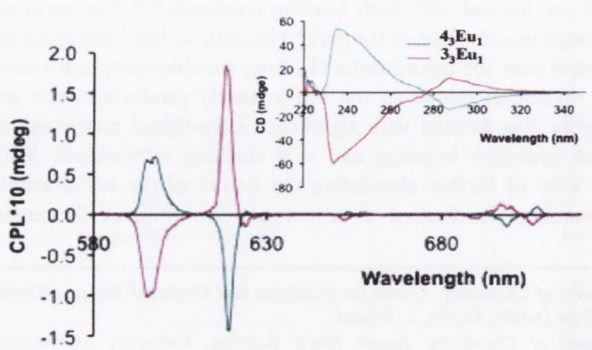

Fig. 3 The Eu(III) circular polarised emission spectra arising from $\mathbf{3}_3\cdot\mathbf{Eu}_1$(red) and $\mathbf{4}_3\cdot\mathbf{Eu}_1$ (blue) in CH_3OH λ_{ex} = 281 nm. Inset: The CD spectra of both complexes in CH_3CN.

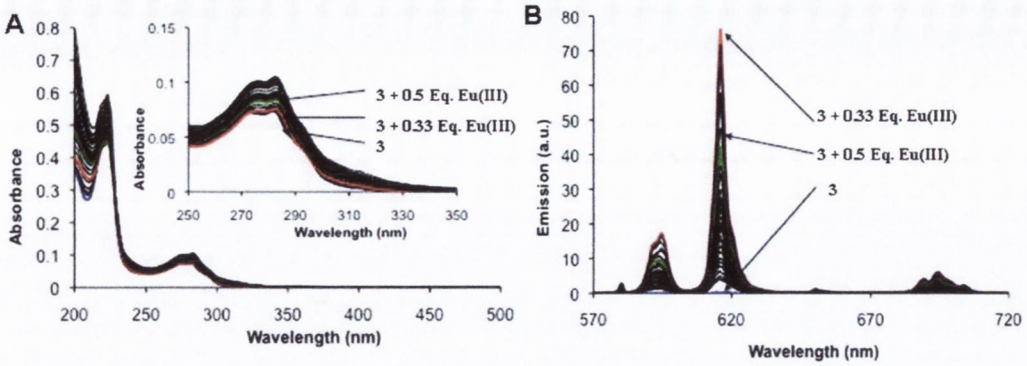

Fig. 4 The changes in the UV-visible absorption (**A**, and expanded as an inset) and the delayed Eu(III) emission (**B**) upon titrating **3** with $Eu(CF_3SO_3)_3$ in CH_3CN.

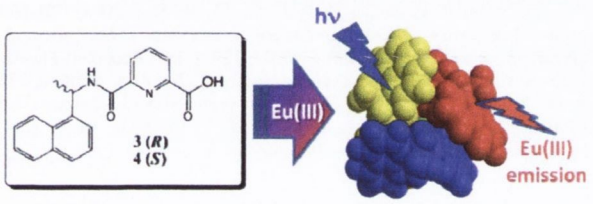

Scheme 1 Eu(III) and chiral pyridyl assymetrical carboxylate ligands $\mathbf{3}_1\cdot\mathbf{Eu}_1$ and $\mathbf{4}_1\cdot\mathbf{Eu}_1$ interact to form half-helicates.

and the pyridyl moieties to take place; similar to that seen in the X-ray crystal structures of the related molecular bundles previously developed by us.[17]

Having established that the Eu(III) directed self-assembly of **3** and **4** led to the formation of complexes in 3 : 1 stoichiometry, we carried out spectroscopic titrations on these ligands (1×10^{-5} M) using $Eu(CF_3SO_3)_3$ in CH_3CN. The changes obtained in the UV-vis absorption spectrum are shown in Fig. 4A, and demonstrated that a hyperchromic effect occurred within the addition of 0.33 equivalents of Eu(III); indicative of the formation of the desired 1 : 3 stoichiometric species. Upon further additions, no major changes occurred, except between 0.5–1 equivalents of Eu(III), where the above changes were partially reversed; suggesting that the equilibrium was shifted towards other stoichiometries as we had seen previously for **1**[17] and **2**.[18] The changes in the fluorescence and the Eu(III) emission were also concomitantly monitored and the changes in the Eu(III) emission are shown in Fig. 4B. These show the appearance of all the $^5D_0 \rightarrow {}^7F_J$ transitions (J = 0–4), mirroring that seen above, with intense contributions from the ΔJ = 1 and 2 transitions upon addition of Eu(III). Again, these results suggested the stable formation of the $\mathbf{L}_3\cdot\mathbf{Eu}_1$ self-assemblies in solution. Furthermore, as had been seen for the ground state, the Eu(III) emission was also effected above 0.33 equivalents; significant of the aforementioned displacement of the complexation equilibrium. To determine these and binding affinity of **3** and **4**, the changes observed in the above UV-vis titrations were fitted by using non-linear regression analysis. These showed that both $\mathbf{3}_3\cdot\mathbf{Eu}_1$ and $\mathbf{4}_3\cdot\mathbf{Eu}_1$, were formed in high yields of 87% and 91% (see ESI† for the speciation distribution diagrams) at 0.33 equivalents of Eu(III), and with high binding constant of log $\beta_{3:1}$ = 19.8 and 19.7, for $\mathbf{3}_3\cdot\mathbf{Eu}_1$ and $\mathbf{4}_3\cdot\mathbf{Eu}_1$, respectively. These analysis also confirmed that at higher Eu(III) concentrations the formation of the 1 : 1 species ($\mathbf{3}_1\cdot\mathbf{Eu}_1$ and $\mathbf{4}_1\cdot\mathbf{Eu}_1$) come dominant with a log $\beta_{1:1} \approx 6.5$–7. However, the 1 : 2 stoichiometries ($\mathbf{3}_2\cdot\mathbf{Eu}_1$ and $\mathbf{4}_2\cdot\mathbf{Eu}_1$) could not be accounted for in the fitting of the titration data.

In summary, we have developed ligands **3** and **4** and studied the self-assembly formation between these ligands and Eu(III) using various spectroscopic techniques. We have shown that this gives, rise to the formation of $\mathbf{3}_3\cdot\mathbf{Eu}_1$ and $\mathbf{4}_3\cdot\mathbf{Eu}_1$ in high yields, structures which are best described as adopting "half-helicate" geometry.

Acknowledgements

We thank Science Foundation Ireland (SFI PI Award 2010, and SFI RFP Awards 2008 and 2009), TCD (Postgraduate Award to CL) and The Irish Research Council for Science, Engineering & Technology (IRCSET) (Postdoctoral Fellowship to JAK) for financial support, and Dr John E. O'Brian and Dr Martin Feeney for helping out with NMR and MS, respectively.

Notes and references

‡ This might suggest some degree of aggregation or stacking in solution.
§ Attempts to grow crystals of high enough qualities for X-ray crystal structure analysis have been unsuccessful, and hence, we have not been able to assign the absolute configuration of $\mathbf{3}_3\cdot\mathbf{Eu}_1$ and $\mathbf{4}_3\cdot\mathbf{Eu}_1$. However, the comparison of their CD and CPL results with lanthanide bundles, 17 for which the absolute configuration has been solved using X-ray crystallography, can allow for the handedness of these "half helicates" to be predicted as being Λ and Δ for $\mathbf{3}_3\cdot\mathbf{Eu}_1$ and $\mathbf{4}_3\cdot\mathbf{Eu}_1$, respectively.

1 (*a*) J. C. B. Bünzli, *Chem. Rev.*, 2010, **110**, 2729; (*b*) S. V. Eliseeva and J. C. G. Bünzli, *Chem. Soc. Rev.*, 2010, **39**, 189; (*c*) C. P. Montgomery, B. S. Murray, E. J. New, R. Pal and D. Parker, *Acc. Chem. Res.*, 2009, **47**, 925; (*d*) J.-C. G. Bünzli, *Chem. Lett.*, 2009, **38**, 104; (*e*) J. C. G. Bünzli, *Acc. Chem. Res.*, 2006, **39**, 53; (*f*) J. C. G. Bünzli and C. Piguet, *Chem. Soc. Rev.*, 2005, **34**, 1048.
2 (*a*) C. M. G. dos Santos, A. J. Harte, S. J. Quinn and T. Gunnlaugsson, *Coord. Chem. Rev.*, 2008, **252**, 2512; (*b*) J. P. Leonard, C. B. Nolan, F. Stomeo and T. Gunnlaugsson, *Top. Curr. Chem.*, 2007, **281**, 1; (*c*) Gunnlaugsson and F. Stomeo, *Org. Biomol. Chem.*, 2007, **5**, 1999.
3 (*a*) S. Shinoda and H. Tsukube, *Analyst*, 2011, **136**, 431; (*b*) Faulkner, L. S. Natrajan, W. S. Perry and D. Sykes, *Dalton Trans.*, 2009, 3890; (*c*) A. Datta and K. N. Raymond, *Acc. Chem. Res.*, 2009, **42**, 938.
4 S. M. Goldup, D. A. Leigh, P. J. Lusby, R. T. McBurney and A. M. Z. Slawin, *Angew. Chem., Int. Ed.*, 2008, **47**, 6999.
5 A. J. Prikhod'ko, F. Durola and J. P. Sauvage, *J. Am. Chem. Soc.*, 2008, **130**, 448.
6 K. S. Chichak, S. J. Cantrill, A. R. Pease, S.-H. Chui, G. W. V. Cave, J. L. Atwood and J. F. Stoddart, *Science*, 2004, **304**, 1308.

7 L. MacGillivray (Ed.) *Metal–Organic Frameworks: Design and Application*, John Wiley & Sons, 2010.
8 (*a*) S. L. James, *Chem. Soc. Rev.*, 2003, **32**, 276; (*b*) M. Schroder; (Ed.) *Functional metal–organic frameworks: Gas storage separation and catalysis Top. Curr. Chem.*, 2010, **293**, 1–262.
9 (*a*) C. Janiak and J. K. Vieth, *New J. Chem.*, 2010, **34**, 2366; (*b*) T. Uemura, N. Yanai and S. Kitagawa, *Chem. Soc. Rev.*, 2009, **38**, 1228.
10 (*a*) S. V. Eliseeva and J. C. G. Bünzli, *Chem. Soc. Rev.*, 2010, **39**, 1; (*b*) R. J. Hill, D. L. Long, N. R. Champness, P. Hubberstey and M. Schroder, *Acc. Chem. Res.*, 2005, **38**, 335.
11 R. J. Hill, D.-L. Long, N. R. Champness, P. Hubberstey and M. Schröder, *Acc. Chem. Res.*, 2005, **38**, 337.
12 (*a*) M. Albrecht, O. Osetska, R. Frohlich, J.-C. G. Bünzli, A. Aebischer, F. Gumy and J. Hamacek, *J. Am. Chem. Soc.*, 2007, **129**, 14178; (*b*) N. S. Murray, S. P. Jarvis and T. Gunnlaugsson, *Chem. Commun.*, 2009, 4959; (*c*) S. J. A. Pope and R. H. Laye, *Dalton Trans.*, 2006, 3108; (*d*) S. J. A. Pope, B. P. Burton-Pye, R. Berridge, T. Khan, P. J. Skabara and S. Faulkner, *Dalton Trans.*, 2006, 2907.
13 (*a*) T. Riis-Johannessen, G. Bernardinelli, Y. Filinchuk, S. Clifford, N. D. Favera and C. Piguet, *Inorg. Chem.*, 2009, **48**, 5512; (*b*) E. Deiters, B. Song, A. S. Chauvin, C. D. B. Vandevyver, F. Gumy and J. C. G. Bünzli, *Chem. Eur. J.*, 2009, **15**, 885; (*c*) J. C. G. Bünzli, S. Comby, A. S. Chauvin and C. D. B. Vandevyver, *J. Rare Earths*, 2007, **25**, 257; (*d*) A. S. Chauvin, S. Comby, B. Song, C. D. B. Vandevyver, F. Thomas and J. C. G. Bünzli, *Chem. Eur. J.*, 2007, **13**(34), 9515; S. E. Plush and T. Gunnlaugsson, *Dalton Trans.*, 2008, 3801.
14 C. Lincheneau, R. D. Peacock and T. Gunnlaugsson, *Chem. Asian J.*, 2010, **5**, 500.
15 S. Comby, F. Stomeo, C. P. McCoy and T. Gunnlaugsson, *Helv. Chim. Acta*, 2009, **92**, 2461.
16 F. Stomeo, C. Lincheneau, J. P. Leonard, J. E. O'Brien, R. D. Peacock, C. P. McCoy and T. Gunnlaugsson, *J. Am. Chem. Soc.*, 2009, **131**, 9636.
17 J. P. Leonard, P Jensen, T. McCabe, J. E. O'Brien, R. D. Peacock, P. E. Kruger and T. Gunnlaugsson, *J. Am. Chem. Soc.*, 2007, **129**, 10986.
18 C. Lincheneau, J. P. Leonard, T. McCabe and T. Gunnlaugsson, *Chem. Commun.*, 2011, **47**, 7119.
19 (*a*) A. M. Nonat, C. Allain, S. Faulkner and T. Gunnlaugsson, *Inorg. Chem.*, 2010, **49**, 8449; (*b*) A. M. Nonat, A. J. Harte, K. Senechal-David, J. P. Leonard and T. Gunnlaugsson, *Dalton Trans.*, 2009, 4703; (*c*) K. Sénéchal-David, S. J. A. Pope, S. Quinn, S. Faulkner and T. Gunnlaugsson, *Inorg. Chem.*, 2006, **45**, 10040.
20 C. Butler, S. Goetz, C. M. Fitchett, P. E. Kruger and T. Gunnlaugsson, *Inorg. Chem.*, 2011, **50**, 2723.
21 (*a*) M. Cantuel, C. Lincheneau, T. Buffeteau, L. Jonusauskaite, T. Gunnlaugsson, G. Jonusauskas and N. D. McClenaghan, *Chem. Commun.*, 2010, **46**, 2486; (*b*) C. S. Bonnet, J. Massue, S. J. Quinn and T Gunnlaugsson, *Org. Biomol. Chem.*, 2009, **7**, 3074; (*c*) J. Massue, S. J. Quinn and T. Gunnlaugsson, *J. Am. Chem. Soc.*, 2008, **130**, 6900; (*d*) J. P. Leonard, C. M. G. Dos Santos, S. E. Plush, T. McCabe and T. Gunnlaugsson, *Chem. Commun.*, 2007, 129; (*e*) K. Sénéchal-David, J. P. Leonard, S. E. Plush and T. Gunnlaugsson, *Org. Lett.*, 2006, **8**, 2727.
22 S. D. Bonsall, M. Houcheime, D. A. Straus and G Muller, *Chem. Commun.*, 2007, 3676.

DOI: 10.1002/anie.201106863

Lanthanides

Circularly Polarized Lanthanide Luminescence from Langmuir–Blodgett Films Formed from Optically Active and Amphiphilic Eu^{III}-Based Self-Assembly Complexes**

Jonathan A. Kitchen, Dawn E. Barry, Laszlo Mercs, Martin Albrecht, Robert D. Peacock, and Thorfinnur Gunnlaugsson**

The development of functional nanomaterials and supramolecular systems is an active area of research, particularly for molecular recognition/sensing, catalysis, optical devices, and magnetically active compounds for switching and data storage.[1–9] While much attention has been focused on transition-metal-based supramolecular systems,[10,11] there has been a recent insurgence of lanthanide-based systems.[12–14] These ions possess rich coordination environments and unique physical properties, such as long-lived and long-wavelength emission in the visible or the NIR regions, as well as magnetic properties, which have been exploited for use in the developments of MRI contrast agents. Hence, these properties make them ideal and highly desirable candidates for the formation of functional supramolecular systems.[15,16] The development of supramolecular assemblies that can be further organized into functional devices is also of great current interest. These assemblies can be achieved by covalently attaching appropriate ligands and complexes to nanoparticles or flat surfaces, through the formation of polymers, or by forming thin films using Langmuir–Blodgett (LB) techniques.[17]

Herein we describe our efforts in bridging these two areas of research by employing lanthanide-directed synthesis (using ligands **1** and **2**) in the formation of chiral luminescent lanthanide amphiphilic complexes, and their use in the formation of LB films, the properties of which can be probed by using circularly polarized luminescence (CPL). The ligands were designed to include a terdentate coordination pocket with a closely associated sensitizing antenna (i.e. the *R*- or *S*-naphthylamine moieties) for the lanthanide ions such as Eu^{III} and Tb^{III}—an approach that has been extremely successful for the development of luminescent supramolecular self-assembly structures, such as chiral "bundles"[18] and dilanthanide triple-stranded helicates.[19–21] Additionally, a long hydrophobic hexadecyl chain was included to allow the formation of Langmuir–Blodgett films. Ligands **1** and **2** were prepared in yields of 74% and 82%, respectively, by employing EDCI·HCl peptide coupling reactions (EDCI·HCl = 1-(3-dimethylaminopropyl)-3-ethylcarbodiimide hydrochloride) between the *R* and the *S* isomers of precursors **3** and **4**, respectively,[18–20] and *N*-hexadecylamine (Figure 1).

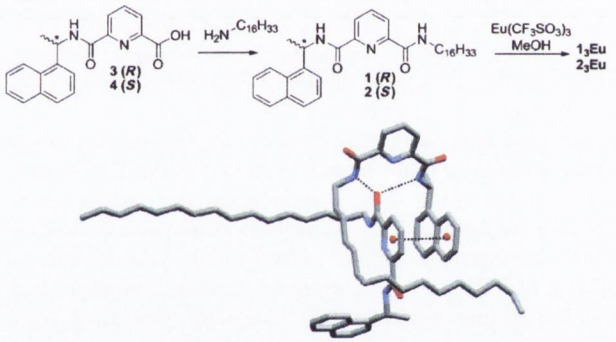

Figure 1. Synthesis of **1** (*R*), **2** (*S*), and their corresponding Eu^{III} complexes $\mathbf{1}_3Eu$ and $\mathbf{2}_3Eu$. a) EDCI·HCl, 1-hydroxybenzotriazole, THF, triethylamine, room temperature. Perspective view of the crystal structure of **1**. Dashed lines indicate intermolecular interactions (N–H···O hydrogen bonding, and π···π stacking). Hydrogen atoms are omitted for clarity.

The ligands were characterized using conventional methods (see the Supporting Information), as well as by using circular dichroism (CD) spectroscopy, which confirmed that the compounds were isolated as a pair of enantiomers (see Figure S1 in the Supporting Information). Moreover, rod-shaped single crystals were obtained by the slow evaporation of a solution of the two ligands in CH_2Cl_2/CH_3CN, allowing solid-state crystal structure analysis of both. The resulting X-ray structure of **1** was determined at 108 K and is shown in Figure 1 (see also the Supporting Information). The ligand crystallized in the chiral monoclinic space group $P2_1$ and contained two crystallographically independent molecules in the asymmetric unit. One molecule has a relatively *trans*

[*] Dr. J. A. Kitchen, D. E. Barry, Prof. T. Gunnlaugsson
School of Chemistry, Centre for Synthesis and Chemical Biology
Trinity College Dublin, College Green, Dublin 2 (Ireland)
E-mail: gunnlaut@tcd.ie
jkitchen@tcd.ie
Dr. L. Mercs, Prof. M. Albrecht
School of Chemistry and Chemical Biology
University College Dublin, Belfield, Dublin 4 (Ireland)
Prof. R. D. Peacock
School of Chemistry, Joseph Black Building
University of Glasgow, Glasgow, G12 8QQ (UK)

[**] We thank the Science Foundation Ireland (SFI PI Award 2010 (TG), SFI RFP Awards 2008 and 2009 (TG), the Irish Research Council for Science, Engineering & Technology (IRCSET, Postdoctoral Fellowship to J.A.K.), and the European Research Council (StG 208561, M.A.) for financial support. We would like to thank particularly Dr. Tom McCabe for assistance in collecting X-ray data.

Supporting information for this article is available on the WWW under http://dx.doi.org/10.1002/anie.201106863.

coplanar chain configuration (straight chain), while the other forms somewhat of a square through "kinks" in the chain. The two independent molecules pack into dimers through classical NH···O hydrogen bonding and offset face to face π···π stacking (Figure 1), whereby the pyridyl group of the straight chain compound sits inside the square adopted by the bent chain compound. Complexes of **1** and **2** with Nd^{III}, Sm^{III}, Eu^{III}, Tb^{III}, Dy^{III}, Yb^{III}, and Lu^{III} were formed and studied. However, this Communication focuses only on the Eu^{III} complexes $\mathbf{1}_3$Eu and $\mathbf{2}_3$Eu ($[Eu(\mathbf{L})_3](CF_3SO_3)_3$), prepared from **1** and **2**, respectively, by reaction with $Eu(CF_3SO_3)_3$ in 3:1 stoichiometry in methanol for 10 min under microwave irradiation. The pale yellow solutions were then subjected to vapor diffusion of diethyl ether to yield white solids, which under a UV lamp gave rise to typical red emission from the Eu^{III} center. Elemental analysis confirmed the formation of the desired products $\mathbf{1}_3$Eu and $\mathbf{2}_3$Eu, whereas electrospray ionization mass spectrometry gave dominantly the *m/z* peaks for the formation of $\mathbf{1}_2$Eu and $\mathbf{2}_2$Eu.

The photophysical properties of $\mathbf{1}_3$Eu and $\mathbf{2}_3$Eu were evaluated in CH_3CN, MeOH, H_2O, and D_2O solutions (see the Supporting Information). The UV/Vis absorption spectra of these complexes were dominated by an absorption assigned to the naphthalene $\pi\rightarrow\pi^*$ antenna with $\lambda_{max} = 281$ nm, and by the $n\rightarrow\pi^*$ transition of the central pyridyl unit. Excitation of the naphthalene antennae at 281 nm gave rise on both occasions to Eu^{III}-centered luminescence, indicating effective sensitization of the $^5D_0$ excited state and subsequent deactivation to the ^7F_J states with linelike emission bands observed at 580 nm ($^5D_0\rightarrow{}^7F_0$), 595 nm ($^5D_0\rightarrow{}^7F_1$), 615 nm ($^5D_0\rightarrow{}^7F_2$), 650 nm ($^5D_0\rightarrow{}^7F_3$), and 695 nm ($^5D_0\rightarrow{}^7F_4$). The coordination numbers of $\mathbf{1}_3$Eu and $\mathbf{2}_3$Eu were evaluated by determination of the number of water molecules bound to the Eu^{III} center, the hydration state (q), by monitoring their excited-state decay in H_2O and D_2O, respectively, in which these complexes were only sparingly soluble. From these measurements, a q value of around 0 was determined for these complexes (see the Supporting Information), indicating that they were coordinatively saturated in aqueous solutions.

The formation of $\mathbf{1}_3$Eu and $\mathbf{2}_3$Eu was next observed in solution by monitoring the changes in the absorption spectra of **1** and **2** and in the evolution of the Eu^{III}-centered luminescence upon titration with $Eu(CF_3SO_3)_3$ in CH_3CN at room temperature. The latter method is an ideal way of observing the formation of these desired self-assemblies, as the population of the Eu^{III} $^5D_0$ excited state would only be observed upon sensitization from the ligands, that is, through the antenna effect. The overall changes observed in the Eu^{III} emission for **2** are shown in Figure 2A, where all of the characteristic $^5D_0\rightarrow{}^7F_{1-4}$ Eu^{III} emission bands are observed upon formation of the self-assembly complex in solution. Analyzing the emission intensities of $^5D_0\rightarrow{}^7F_{1-4}$ as a function of added Eu^{III} equivalents reveals that the emission rapidly increases to a maximum at approximately 0.35 equivalents, after which it decreases and begins to plateau after the addition of 1 equivalent of Eu^{III} (see the Supporting Information). To gain a better understanding of the formation of these species in solution, these changes were further analyzed by fitting the global luminescence changes using nonlinear

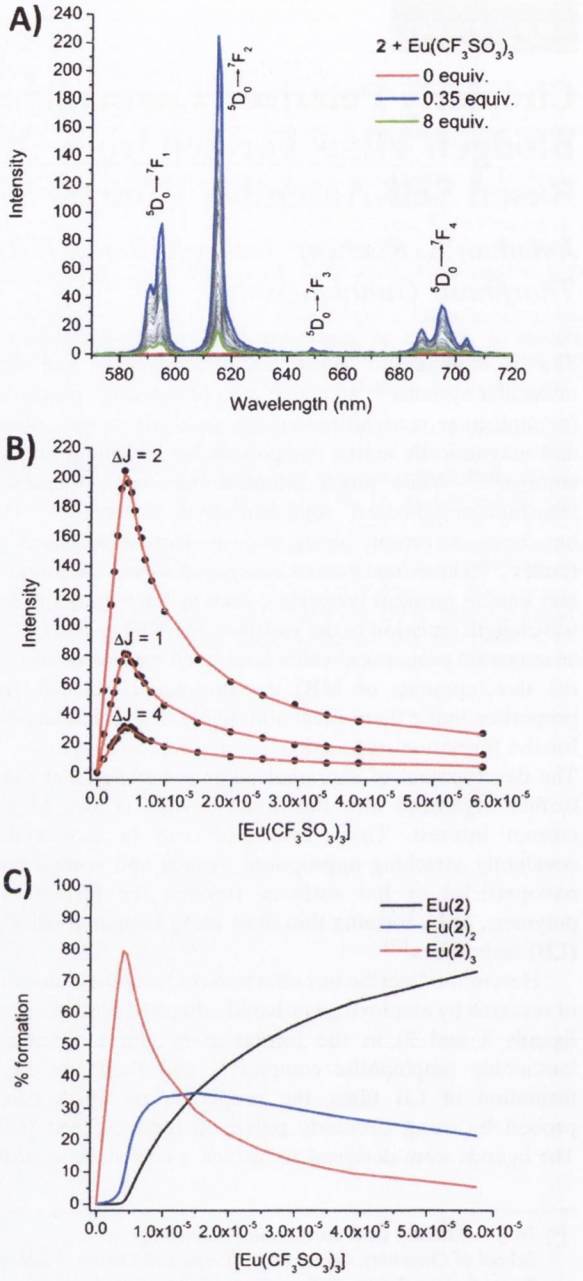

Figure 2. A) The overall changes in the Eu^{III} phosphorescence spectra upon titrating **2** with $Eu(CF_3SO_3)_3$ (0 to 10 equivalents) in MeCN at room temperature. B) Experimental binding isotherms for the changes in the Eu^{III} luminescence spectra upon titrating **2** with $Eu(CF_3SO_3)_3$ in MeCN at room temperature, and their corresponding fit by SPECFIT (——). C) Speciation-distribution diagram obtained from the fit.

regression analysis (using the software SPECFIT) to various L:Eu stoichiometries. The fitting of the changes observed in Figure 2A is shown in Figure 2B (see the Supporting Information for the fitting and the binding constants obtained for the analysis of **1**). On both occasions good fits were observed as demonstrated for the analysis of **2** in Figure 2B, for the changes in $\Delta J = 1$, 2, and 4, from which the formation of $\mathbf{2}_3$Eu in 80% yield was confirmed after addition of

0.3 equivalents Eu^{III}, with binding constants of $\log\beta = 19.9$-(± 0.2). Concurrently, the analysis for **1** showed similar luminescent behavior, and the self-assembly $\mathbf{1_3Eu}$ was formed with a comparable binding constant $\log\beta$ of 20.4-(± 0.2). On further addition of Eu^{III}, the equilibrium for both systems was displaced towards that of a species with the stoichiometry $[Eu(\mathbf{L})_2]$, which, after the addition of around 0.5 equivalents of Eu^{III}, were formed in 35 and 45% yields, respectively, and with binding constants of $\log\beta = 13.3$ (± 0.2) and 14.1 (± 0.2). On yet further addition of Eu^{III}, these equilibriums were displaced towards a new species, $[Eu(\mathbf{L})]$, which became the predominant species after the addition of 1.5 equivalents of Eu^{III}.

The solution formation of $\mathbf{1_3Eu}$ and $\mathbf{2_3Eu}$ was also observed by monitoring the changes in the absorption spectra, and by fitting the resulting global changes using nonlinear regression analysis. In particular, the changes in the absorbance bands at 207, 223, and 281 nm were analyzed (see the Supporting Information). These changes gave rise to similar results as those obtained from the analysis of the changes in the Eu^{III} emission: the formation of the $[Eu(\mathbf{L})_3]$ was confirmed after addition of 0.3 equivalents of Eu^{III} in around 85% yield with a binding constant of $\log\beta = 20.9$-(± 0.3). Similarly, analysis of the changes observed for **1** gave a $\log\beta$ value of 20.5(± 0.3). Moreover, the formation of the $[Eu(\mathbf{L})_2]$ species at around 0.5 equivalents of Eu^{III} was also confirmed in 45 and 35% yields for **1** and **2**, respectively, with $\log\beta$ value of 13.8, while upon further addition of Eu^{III} resulted in the formation of the 1:1 stoichiometry $[Eu(\mathbf{L})]$.

CD and CPL analysis of $\mathbf{1_3Eu}$ and $\mathbf{2_3Eu}$ in CH_3CN confirmed the enantiomeric nature of these complexes (see the Supporting Information). The CD spectra of $\mathbf{1_3Eu}$ and $\mathbf{2_3Eu}$ were significantly different to those of **1** and **2**, respectively, particularly for the naphthalene transitions. Importantly, both systems gave rise to Eu^{III}-centered CPL spectra upon excitation of the naphthalene antennae; all $^5D_0 \rightarrow {}^7F_{1-4}$ transitions were observed, clearly demonstrating that the Eu^{III} ion was sitting within a chiral environment, where the handedness of the ligand dictated the handedness of the chiral emission (CPL) from the metal ion. This is evident from Figure S15 (Supporting Information), which shows a negative band for the $\Delta J = 1$ transition and a positive band for $\Delta J = 2$ nm for $\mathbf{1_3Eu}$; however, these bands were found to be of opposite signs for $\mathbf{2_3Eu}$, confirming their formation as an enantiomeric pair. Comparison of these CPL spectra with those obtained previously in our laboratory using the symmetrical and chiral dinaphthalene amide analogue of **3** and **4**, for which the crystal structures of the 3:1 complexes are known,[18] allowed us to assign the absolute stereochemistry of these self-assemblies as Δ and Λ using **1** and **2**, respectively. Moreover, from these spectra, the luminescence dissymmetric factor g_{lum} was determined,[22a] which for $\mathbf{1_3Eu}$ gave $g_{lum} = -0.177$ and 0.106 for the $\Delta J = 1$ and 2 transitions, respectively (being $g_{lum} = 0.176$ and -0.102 for $\mathbf{2_3Eu}$). The former transition is close to that determined for the Eu^{III} complex of the aforementioned symmetric analogue of **3** ($g_{lum} = 0.28$),[18] while, for the $\Delta J = 2$ transition, g_{lum} was almost five times smaller ($g_{lum} = 0.50$).[18] This result might reflect the unsymmetical nature of $\mathbf{1_3Eu}$, as the $\Delta J = 2$ transition is highly sensitive to the change in the local coordination environment of Eu^{III} ion.[22]

Having formed $\mathbf{1_3Eu}$ and $\mathbf{2_3Eu}$ and analyzed their luminescent properties in solution, we investigated the self-assembling properties of $\mathbf{1_3Eu}$ and $\mathbf{2_3Eu}$ at the air–water interface by forming Langmuir films. Only a small number of examples of Langmuir–Blodgett films made from kinetically and thermodynamically stable lanthanide complexes have been reported.[23–38] Furthermore, only a few examples of CPL Langmuir–Blodgett films have been made,[28] and, to the best of our knowledge, no examples of CPL lanthanide emitting Langmuir–Blodgett films have been reported. The Langmuir films of $\mathbf{1_3Eu}$ and $\mathbf{2_3Eu}$ were identified by monitoring the pressure–area isotherms, where the exponential increase in surface pressure indicated transition from liquid-expanded phases to liquid-condensed and solid phases (Figure 3).[39]

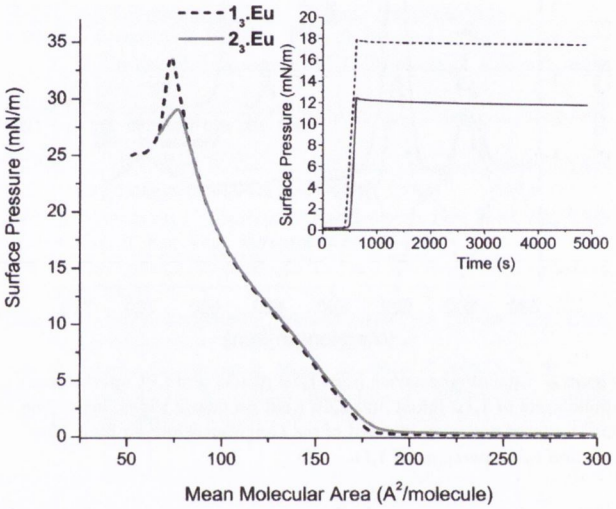

Figure 3. Pressure–area isotherms; inset shows pressure–time profiles for Langmuir films of $\mathbf{1_3Eu}$ (-----) and $\mathbf{2_3Eu}$ (——).

These films were seen to collapse at 34 $mN\,m^{-1}$ for $\mathbf{1_3Eu}$ and at 29 $mN\,m^{-1}$ for $\mathbf{2_3Eu}$, corresponding to areas of 75 ± 5 $Å^2$. These areas are approximately those expected for three alkyl chains (ca. 66 $Å^2$ per molecule),[40,41] and are in agreement with the complexes remaining intact at the air–water interface with supramolecular organization of $\mathbf{1_3Eu}$ and $\mathbf{2_3Eu}$ as monolayers. Excellent stability properties were exhibited by films of both complexes with no pressure decrease observed on keeping the films at the liquid-condensed phase for an extended period of time (>1 hour; Figure 3 inset). The $\mathbf{1_3Eu}$ and $\mathbf{2_3Eu}$ films were transferred onto quartz slides, and the formation of Langmuir–Blodgett monolayers was confirmed. The monolayers were transferred with high transfer ratios ($TR \approx 1$) on the emersion of the quartz support. The exact structural nature of these films is currently under investigation; however, we can assume that the polar Eu^{III} coordination sphere is orientated towards the water phase and the hexadecyl chains pointing out, as attempts to transfer these films by immersion was unsuccessful.

Communications

Lanthanides

J. A. Kitchen,* D. E. Barry, L. Mercs, M. Albrecht, R. D. Peacock, T. Gunnlaugsson* ——— ■■■■–■■■■

Circularly Polarized Lanthanide Luminescence from Langmuir–Blodgett Films Formed from Optically Active and Amphiphilic Eu^{III}-Based Self-Assembly Complexes

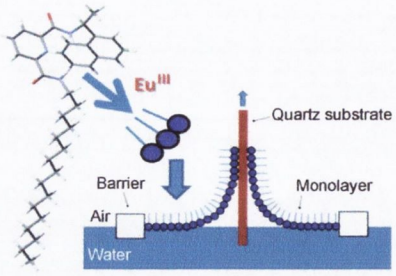

Europium union: The development of chiral amphiphilic self-assembled complexes by europium(III)-directed synthesis is described. These systems form stable Langmuir–Blodgett (LB) films on quartz slides to give stable monolayers that exhibit the first example of time-delayed Eu^{III}-centered emission and circularly polarized luminescence (CPL) from an LB film.

Langmuir

Article

pubs.acs.org/Langmuir

Near Infrared (NIR) Lanthanide Emissive Langmuir–Blodgett Monolayers Formed Using Nd(III) Directed Self-Assembly Synthesis of Chiral Amphiphilic Ligands

Dawn E. Barry,[†] Jonathan A. Kitchen,*[,†,#] Martin Albrecht,[‡] Stephen Faulkner,[§] and Thorfinnur Gunnlaugsson*[,†]

[†]School of Chemistry and Trinity Biomedical Sciences Institute, Trinity College Dublin, Dublin 2, Ireland

[‡]School of Chemistry and Chemical Biology, University College Dublin, Belfield, Dublin 4, Ireland

[§]Chemistry Research Laboratories, University of Oxford, 12 Mansfield Road, Oxford OX1 3TA, United Kingdom

Supporting Information

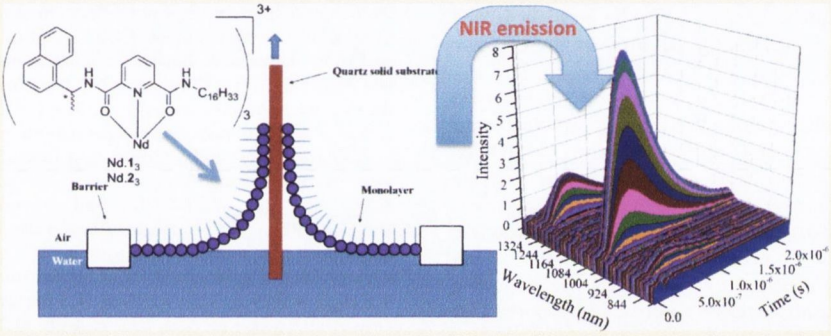

ABSTRACT: The incorporation of chiral amphiphilic lanthanide-directed self-assembled Nd(III) complexes ($\mathbf{Nd.1_3}$ and $\mathbf{Nd.2_3}$) into stable Langmuir monolayers, and the subsequent Langmuir–Blodgett film formation of these, is described. The photophysical properties of the enantiomeric pair of ligands **1** and **2** in the presence of $Nd(CF_3SO_3)_3$ were also investigated in CH_3CN solutions using UV–vis, fluorescence, and lanthanide luminescence spectroscopies. Analysis of the resulting self-assembly processes revealed that two main species were formed in solution,1:1 and 1:3 **Nd:L** self-assembly complexes, with the latter being the dominant species upon the addition of 0.33 equivalents of Nd(III). Excited state lifetime measurements of $\mathbf{Nd.1_3}$ and $\mathbf{Nd.2_3}$ in CH_3OH and CD_3OD and CH_3CN were also evaluated. The formation of the self-assembly in solution was also monitored by observing the changes in the circular dichroism (CD) spectra; and large differences were observed between the 1:3 and other stoichiometries in the spectra, allowing for correlation to be made with that seen in the emission studies of these systems. Surface pressure–area and surface pressure–time isotherms evidenced the formation of stable Langmuir monolayers of $\mathbf{Nd.1_3}$ and $\mathbf{Nd.2_3}$ at an air–water interface, and the deposition of these monolayers onto a quartz solid substrate (Langmuir–Blodgett films) gave rise to immobilized chiral monomolecular films which exhibited Nd(III) NIR luminescence upon excitation of the ligand chromophore, demonstrating efficient energy transfer to the Nd(III) excited state (sensitized) with concomitant emission centered at 800 and 1334 nm.

INTRODUCTION

The development of functional nanostructures using lanthanide-directed self-assembly has been a growing area of interest in recent times, as such systems have potential applications in molecular recognition/sensing and imaging and for use in optical devices.[1−6] The lanthanides, both visibly emitting (e.g., Eu(III), Tb(III) and Sm(III)) and NIR emitting (e.g., Nd(III) and Yb(III)), are ideal candidates for such applications, as they possess long-lived excited states and well-defined narrow-line-like emission bands.[3,7−9] However, the transitions are spin forbidden and generation of the excited states is best achieved through the use of a sensitizing chromophore (the antenna effect).[9] The NIR emitting lanthanides, such as Pr(III) Yb(III), Er(III), and Nd(III), offer major advantages over other visibly emitting lanthanides for applications in biology,[10] such as in the development of luminescent imaging agents and bioprobes, as the NIR emission (800−1000 nm) is transparent to biological tissue, therefore allowing imaging through relatively thick tissue samples. Moreover, from an optical devices point of view, the NIR emissive lanthanides can be employed in telecommunications optical networks, again owing to their emission in the transparent window of silica fibers (1000−1600 nm).[11] Of the

Received: June 25, 2013
Revised: August 12, 2013
Published: August 13, 2013

NIR emitting lanthanides, Nd(III) and Er(III) are particularly interesting as the luminescent behavior is highly sensitive to the external environment.[12−15] In particular, the high density of states in the excited state manifolds of Nd(III) and Er(III) ensures that nonradiative quenching of the lanthanide emissive state by associated C−H and O−H oscillators is more important in complexes with these ions than any other lanthanides, as they are quenched to a greater extent through closely associated C−H oscillators (in addition to N−H and O−H oscillators).[2,12,15−17] As well as introducing a strong dependence of luminescence quantum yield and lifetime upon structure, this phenomenon also means that ternary assemblies, involving guests such as biomolecules and complexes, will change the luminescence quantum yields of such species.[18−20] Such assemblies have already been widely exploited in systems where inner sphere solvation is changed when the assembly is formed;[21,22] however, there is also clear potential to exploit the more subtle effects inherent to the presence of local oscillators in lifetime resolved imaging. For practical application, Nd(III) complexes are ideal as luminescence quantum yields from Er(III) complexes in aqueous media tend to be very low indeed as a consequence of the small energy gap between the emissive state and ground state.

Often practical applications for luminescent lanthanide complexes/self-assemblies require their immobilization onto solid supports. However, not only must the Ln(III) be incorporated into/onto the solid support, but the desirable features of the Ln(III) system must be retained, i.e. surface attachment should not significantly alter the attractive luminescent properties observed in the bulk solid or in solution. To this end, significant research has been ongoing to incorporate luminescent complexes into solid supports. Our own efforts have resulted in the development of luminescent lanthanide systems within hydrogels[23,24] or conjugated to the surface of gold nanoparticles,[25−27] where in all cases there is retention of Ln(III) luminescent characteristics on transfer from solution to solid.[28] Recently we have also shown that chiral Eu(III) based complexes can be transferred to the surface of quartz solid substrates by utilizing the Langmuir−Blodgett technique, and the retention of photophysical properties is again observed, including retention of circularly polarized luminescence (CPL).[28] With the view of extending our interest in the development of functional lanthanide luminescent structures, we set out to form highly organized Langmuir monolayers formed by using lanthanide directed self-assembly from NIR emitting lanthanides. The ligands employed herein possess pyridnium dicarboxylic amide moieties, which we have employed in many of our self-assembly structures, as the formation of 3:1 of these with lanthanide ions gives rise to highly stable and robust supramolecular structures.[4] Our main objective was to then transfer these monolayers onto solid supports, giving rise to new surface bound materials with additional advantages over other solid matrix immobilization techniques currently being employed such as deposition precision, order, and control. Herein we detail the results from this study, carried out using the chiral ligands **1** and **2** (Scheme 1) and Nd(III). Investigation into the ability of these complexes to form luminescent self-assemblies as well as their ability to give stable Langmuir monolayers at an air−water interface was undertaken. Following deposition and subsequent Langmuir−Blodgett film formation, the photophysical properties of the immobilized monolayers of **Nd.1$_3$** and **Nd.2$_3$** were also investigated in detail, and to the best of our knowledge, these are the first examples of such lanthanide NIR emitting self-assembled monolayers to be developed to date.

EXPERIMENTAL SECTION

General. All starting materials were purchased from commercial sources and used as received. Solvents were of HPLC grade and used without purification. Electromass spectra were acquired using a Mass Lynx NT V 3.4 instrument on a Waters 600 controller connected to a 996 photodiode array detector with HPLC-grade CH_3CN, CH_2Cl_2, or CH_3OH as carrier solvent. A peak-matching method was used to determine accurate molecular weights using leucine enkephaline (H-Tyr-Gly-Gly-Phe-Leu-OH) as the standard reference (m/z = 556.2771); all accurate masses were reported within ±5 ppm of the expected mass. Elemental analyses were carried out at the Microanalytical Laboratory, School of Chemistry and Chemical Biology, University College Dublin. Infrared spectra were recorded on a Perkin-Elmer Spectrum One FT-IR spectrometer equipped with a Universal ATR sampling accessory. Solid samples were recorded directly as neat samples in cm^{-1}. Complexation reactions were carried out in 2−5 mL Biotage microwave vials in a Biotage Initiator Eight EXP microwave reactor. Reactions were performed at 70 °C for 10 min in HPLC grade methanol. Single crystal X-ray diffraction data for **1** were collected using graphite monochromated Cu Kα radiation (λ = 1.54184 Å) on an Oxford Diffraction SuperNova diffractometer. The diffractometer was equipped with a Cryostream N_2 open-flow cooling device,[29] and the data were collected at 150(2) K. Series of ω-scans were performed in such a way as to collect all unique reflections to a maximum of 0.80 Å. Cell parameters and intensity data (including interframe scaling) were processed using CrysAlis Pro.[30] The structure was solved by direct methods (SHELXS-97) and refined against all F^2 data (SHELXL-97).[31] Non-hydrogen atoms were refined with anisotropic displacement parameters. Hydrogen atoms, except for N−H protons, were positioned geometrically and refined using a riding model with d(CH_{aro}) = 0.95 Å, Uiso =1.2Ueq (C) for aromatic, d(CH) =1.0 Å, Uiso =1.2Ueq (C) for CH, 0.99 Å, Uiso =1.2Ueq (C) for CH_2 and 0.98 Å, Uiso =1.2Ueq (C) for CH_3. Amide N−H protons were found from the difference map and fixed to the attached atoms.

Synthesis. Complexes **Nd.1$_3$** and **Nd.2$_3$** were prepared by the reaction of **1** or **2** (30 mg, 0.06 mmol) in 5 mL of CH_3OH which had solid $Nd(CF_3SO_3)_3$ (18 mg, 0.03 mmol) added and was heated at 70 °C under microwave irradiation for 10 min. The resulting clear yellow solutions were subjected to vapor diffusion of diethyl ether, resulting in the formation of solids.

[Nd(1)$_3$](CF$_3$SO$_3$)$_3$ (Nd.1$_3$). Formed as white solid, 22 mg (50%). Elemental analysis for $C_{108}H_{147}N_9O_{15}F_9S_3Nd.3H_2O$ calcd: C 56.97, H 6.77, N 5.54; found C 56.57, H 6.25, N 5.66%. IR (neat): 3290, 2920, 2853, 1631 (C=O), 1594, 1560, 1458, 1238, 1164, 1030, 800, 779, 753 cm^{-1}. HR-MALDI-MS: 1526.5824 ([M-L-CF_3SO_3]$^+$, $C_{72}H_{98}N_6O_{10}F_6S_2Nd^+$; calcd, 1526.5767).

[Nd(2)$_3$](CF$_3$SO$_3$)$_3$ (Nd.2$_3$). Formed as white solid, 26 mg (59%). Elemental analysis for $C_{108}H_{147}N_9O_{15}F_9S_3Nd$ (2218.91 g mol^{-1}) calc: C 58.41, H 6.68, N 5.68; found C 58.94, H 6.67, N 5.74%. IR (neat): 3292, 2925, 2854, 1633 (C=O), 1594, 1559, 1457, 1237, 1165, 1030, 800, 778, 752 cm^{-1}. HR-MALDI-MS: 1526.5822 ([M-L-CF_3SO_3]$^+$, $C_{72}H_{98}N_6O_{10}F_6S_2Nd^+$; calcd, 1526.5767).

Photophysical Studies. The UV−visible absorption spectra were recorded at RT using a Varian Cary 50-spectrophotometer. The solvent employed was of HPLC grade. The wavelength range was set from 450 to 200 nm with a scan rate of 600 nm min^{-1}. Circular dichroism (CD) spectra were recorded on a Jasco J-810-150S spectropolarimeter. Luminescence spectra in the near-IR region was recorded on a Fluorolog FL 3-22 spectrophotometer from Horiba-Jobin-Yvon with double grating emission and excitation monochromators, and a R5509-73 photomultiplier. Light intensity was measured by using a C9940-22 detector from Hamamatsu (range 800−1700 nm) cooled to 77 K and coupled to a Jobin Yvon SpectrAcq v5.20 data acquisition system. For the measurement of the Nd(III) luminescence lifetimes, the samples were excited using a pulsed nitrogen laser (PTI-3301, 337 nm) operating at 10 Hz. Light emitted at right angles to the

dx.doi.org/10.1021/la402274s | Langmuir 2013, 29, 11506−11515

Scheme 1. Complexation of Ligands 1 and 2 with $Nd(CF_3SO_3)_3$ Affording the Desired $Nd.1_3$ and $Nd.2_3$ Complexes

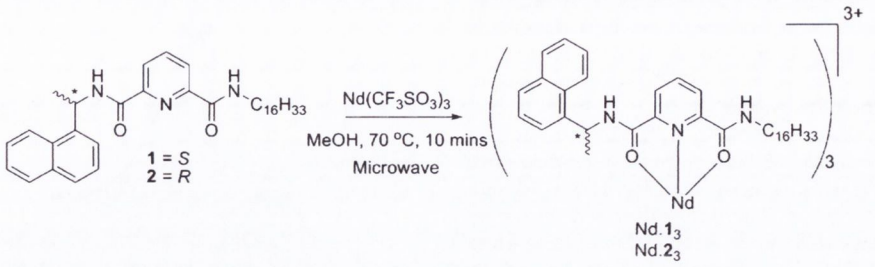

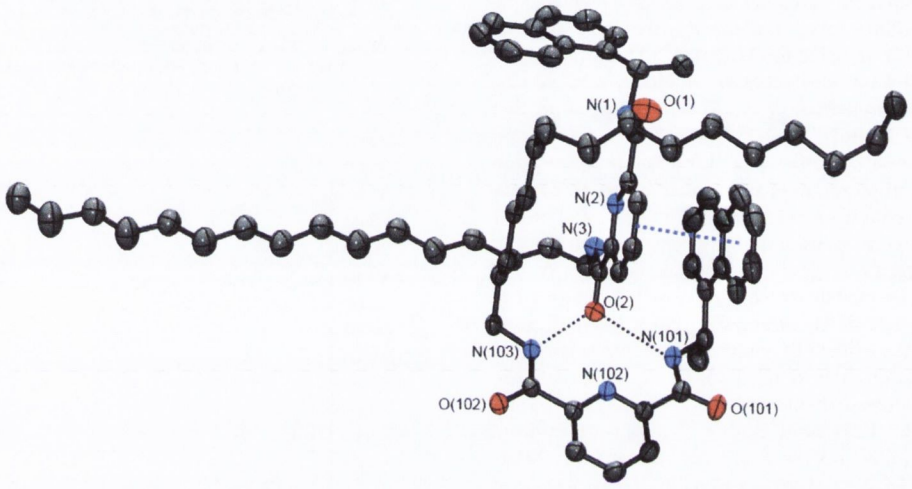

Figure 1. Perspective view of ligand **1** with thermal ellipsoids shown at 50% probability, illustrating dimeric nature of packing. Note that $\pi-\pi$ stacking (blue dotted line) [centroid···centroid = 3.65 Å] and hydrogen bonding (black dotted lines) [see Table 1] exist between the two crystalloraphically independent molecules. Hydrogen atoms have been omitted for clarity.

Table 1. Hydrogen Bonds for 1 [Å and deg]

D−H···A	d(D−H)	d(H···A)	d(D···A)	∠(DHA)
N(1)−H(1X)···O(102)[a]	0.89	2.19	3.0500(18)	162.0
N(3)−H(3X)···O(102)[a]	0.87	2.12	2.9447(18)	158.3
N(101)−H(10X)···O(2)[b]	0.9	2.18	3.0192(18)	154.9
N(103)−H(10Y)···O(2)[b]	0.9	2.15	3.0105(17)	158.2

excitation beam was focused onto the slits of a monochromator (PTI120), which was used to select the appropriate wavelength. The growth and decay of the luminescence at selected wavelengths were detected using a germanium photodiode (Edinburgh instruments, EI-P) and recorded using a digital oscilloscope (Tektronix TDS220) before being transferred to a PC for analysis. Time-resolved emission spectra were obtained by measuring the growth and decay of the luminescence at each of a series of wavelengths. Luminescence lifetimes were obtained by iterative reconvulution of the detector response (obtained using a scatterer) with exponential components for growth and decay of the metal centered luminescence, using a spreadsheet running in Microsoft Excel. The details of this approach have already been discussed.[12]

Langmuir Film Measurements. Surface-pressure isotherms and time stability were measured at 25 °C on a KSV MiniMicro Langmuir−Blodgett trough (KSV, Finland) with a surface area between 1700 and 8700 mm^2. Water was purified with a Milli-Q Integral system (Millipore), and its resistivity was measured to be higher than 18 MΩ cm. A 9:1 mixture of $CHCl_3/CH_3OH$ was used as spreading solvent for complexes $Nd.1_3$ and $Nd.2_3$. Typically drops (20 μL) of the surfactant solution (~2.4×10^{-4} M) were deposited using a microsyringe on the water subphase. After leaving to evaporate for 20 min, the barriers were compressed at 6 mm min^{-1} and the surface pressure was monitored using a platinium Wilhelmy plate. Quartz slides for dipping experiments were immersed in concentrated HNO_3 (30 min), piranha solution (3:1 H_2SO_4/H_2O_2) (30 min) and rinsed well with deionized water immediately prior to use.

■ RESULTS AND DISCUSSION

Synthesis and Characterization. Ligands **1** and **2** were prepared according to our previously reported procedure, as shown in Scheme 1.[28] In addition, colorless, X-ray quality rod shaped single crystals of **1** were obtained from the slow evaporation of a CH_3CN/CH_2Cl_2 solution and the low temperature (123 K) structure determined. Compound **1** crystallized in a chiral monoclinic space group, $P2_1$ and contained two crystallographically independent molecules in the asymmetric unit as shown in Figure 1 (see also the Supporting Information) and Table 1 (CCDC 955698). The two independent molecules differ in the conformation of the hexadecyl chain. In one molecule the chain is relatively trans coplanar (straight chain), while in the second molecule the

chain has a twisted orientation as shown in Figure 1. The two molecules interact through NH···O hydrogen bonding, (see Table 1), and offset face to face $\pi\cdots\pi$ stacking between the pyridyl ring of one molecule and the naphthalene ring of the other (Figure 1). The crystal structure of **2**[28] is isomorphous to that of **1** albeit of the other isomer.

The complexes **Nd.1**$_3$ and **Nd.2**$_3$ ($[Nd(\mathbf{L})_3](CF_3SO_3)_3$) were prepared from **1** and **2**, respectively, by reacting with $Nd(CF_3SO_3)_3$ in 3:1 stoichiometry in CH_3OH for 10 min under microwave irradiation. The pale yellow solutions were then subjected to vapor diffusion of diethyl ether yielding white solids in 50% and 59% yields, respectively. Elemental analysis confirmed the formation of the desired products **Nd.1**$_3$ and **Nd.2**$_3$, whereas ESMS gave dominantly the m/z for the formation of the 1:2 complex formations **Nd.1**$_2$ and **Nd.2**$_2$.

Photophysical Characterization of Nd.1$_3$ and Nd.2$_3$. The photophysical properties of **Nd.1**$_3$ and **Nd.2**$_3$ were first evaluated in CH_3CN and CH_3OH solutions (see Supporting Information Figures S1–S6). The UV–visible absorption spectra of these complexes were dominated by an absorption assigned to the naphthalene antenna $\pi \rightarrow \pi^*$ with λ_{max} = 281 nm, and by the $n \rightarrow \pi^*$ transition of the central pyridyl unit at λ_{max} = 223 nm, with the long wavelength band tailing to ca. 350 nm. Excitation of the naphthalene antennae at 281 nm gave rise on both occasions to Nd(III) centered luminescence indicating effective sensitization of the $^4F_{3/2}$ excited state and subsequent deactivation to the ^4I_J (J = 9/2, 11/2, 13/2) states with line-like emission bands observed at 880 nm ($^4F_{3/2} \rightarrow {}^4I_{9/2}$), 1064 nm ($^4F_{3/2} \rightarrow {}^4I_{11/2}$) and 1334 nm ($^4F_{3/2} \rightarrow {}^4I_{13/2}$). Time resolved emission spectra (TRES) were also recorded for both **Nd.1**$_3$ and **Nd.2**$_3$ in CH_3CN, CH_3OH, and CD_3OD as shown in Figure 2 and Supporting Information Figures S9 and S10. The Nd(III) luminescence decays (excitation at 337 nm) of the three transitions 880 nm ($^4F_{3/2} \rightarrow {}^4I_{9/2}$), 1064 nm ($^4F_{3/2} \rightarrow {}^4I_{11/2}$), and 1334 nm ($^4F_{3/2} \rightarrow {}^4I_{13/2}$) were observed. Lifetime measurements at 1064 nm fitted well to a model in which the data was fitted to components for rise time and decay by reconvolution with the detector response. Similar behavior was observed when measurements were conducted in CH_3OH and CD_3OD, as can be seen from the data in Table 2 and the typical fitted temporal profile shown in Figure 2. The rise time in such systems generally arises from involvement of the triplet state of the donor chromophore in energy transfer to the lanthanide. This is borne out in these data by the differences observed between the rise time in CH_3OH and that in CD_3OD: longer rise times in deuterated media reflect the imperfect overlap between the triplet state of the donor chromophore and phonon assistance involving the solvent vibrational manifold, and the lower energy (and less effective spectral overlap) of C–D and O–D vibrational oscillators relative to analogous C–H and O–H oscillators. It is clear from the data in Table 2 that both Nd(III) containing systems exhibit similar luminescence lifetimes in each of the solvent systems studied.

Due to the profound dependence of the luminescence lifetime of Nd(III) complexes upon ligand structure, it is unwise to use the published equations which were established for aminocarboxylate ligand systems derived from cyclen to calculate the number of inner sphere water molecules (q).[12,15] However, the lifetimes are consistent with a low degree of solvation at the metal center; those in CH_3OH are very long for a Nd(III) complex. If we accept that the NO_2 donor sets of the three dipicolinamide ligands fill the inner coordination sphere, the differences between the values for the decay components of

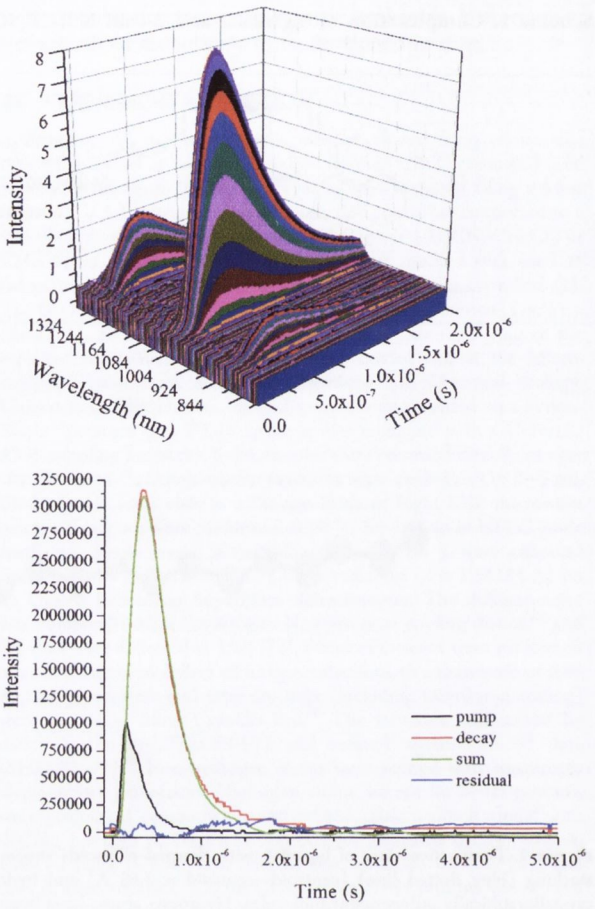

Figure 2. (top) Time-resolved emission spectrum of **Nd.1**$_3$ after excitation at 337 nm, showing sensitized lanthanide-based luminescence. (bottom) Decay curve obtained from **Nd.1**$_3$ in CH_3OH and residuals for fitted curve generated by deconvolution of the instrument response function with a single exponential function.

Table 2. Nd(III) Centered Lifetimes (τ/ns) for Nd($^4F_{3/2}$) in Nd.1$_3$ and Nd.2$_3$ as Measured in in CH_3OH, CD_3OD and CH_3CN, Respectively[a]

	MeOH		CD_3OD		MeCN	
	$\tau_{rise\text{-}time}$ (ns)	τ (ns)	$\tau_{rise\text{-}time}$ (ns)	τ (ns)	$\tau_{rise\text{-}time}$ (ns)	τ (ns)
Nd.1$_3$	16	206	45	775	22	491
Nd.2$_3$	12	251	40	865	22	560

[a]Each measurement is an average of three independent measurements.

the luminescence lifetimes obtained in CH_3OH and CD_3OD are highly instructive. Clearly, two complexes do not constitute a sufficient body of data to establish meaningful relations that define q in dipicolinate systems, but it may be useful to consider an equation of the form:

$$q = A(1/\tau CH_3OH - 1/\tau CD_3OD - B)$$

In a system in which there is no coordinated solvent, the difference between $1/\tau_{CH_3OH}$ and $1/\tau_{CD_3OD}$ should reflect B, the outer sphere solvent contribution to nonradiative deactivation of the excited state. On this basis, **Nd.1**$_3$ and **Nd.2**$_3$ give values of 3.5 ± 0.6 and 2.8 ± 0.5 μs^{-1}, respectively.

dx.doi.org/10.1021/la402274s | Langmuir 2013, 29, 11506–11515

These values are within error of one another and imply that the coordination environments and the nature of the solvation of the two complexes are very similar. It also differs significantly from the value of this outer sphere correction obtained for aminocarboxylate ligand systems ($1.4\ \mu s^{-1}$),[15] suggesting that there may be significant variations in outer sphere solvent effects between different classes of complex.

Circular Dichroism (CD) Studies of 1 and 2 with $Nd(CF_3SO_3)_3$. Circular dichroism spectra were recorded for **1** and **2**, as well as the Nd(III) complexes **Nd.1**$_3$ and **Nd.2**$_3$ in CH_3CN, with the latter being formed in solution upon addition of 0.33 equiv of Nd(III). The ligand CD demonstrated that **1** and **2** are formed as enantiomers, where mirror-image CD was observed, which is consistent with the presence of a single chiral stereoisomer in solution for these two ligands. For ligand **1** (the *S*-enantiomer), positive CD-bands appeared at 206, 229, and 287 nm and a broad shoulder at 250 nm, and a negative CD-band at 218 nm. The *R*-isomer **2** gave the exact opposite signals at these same wavelengths (Figure 3). Equal but

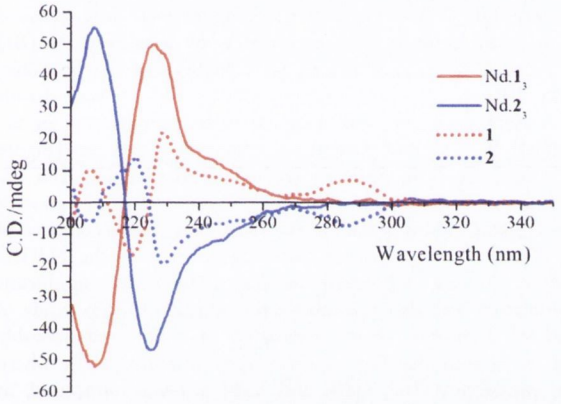

Figure 3. Circular dichroism spectra of ligands **1** and **2** and complexes **Nd.1**$_3$ and **Nd.2**$_3$.

opposite dichroism bands were also observed in the CD spectrum of the two complexes **Nd.1**$_3$ and **Nd.2**$_3$. However, these were structurally different from that seen for their corresponding ligands, as in the case of **Nd.1**$_3$ as only two main bands were observed, a negative band at 207 nm and a positive band centered at 224 nm, respectively. However as before, a positive broad band also occurred, being centered at ca. 250 nm, and unlike that seen for **1**, no long wavelength transition was observed. As expected, **Nd.2**$_3$ gave transitions with equal magnitude and opposite sign, demonstrating that the two complexes were formed as a structurally identical pair of enantiomers. Parker and co-workers[32] have investigated the use of these same chiral antennae (as well as the 2-isomers) in C_4 symmetry based tetranaphthyl based cyclen ligands and Eu(III) complexes. While the structures are quite different to those presented herein, some similarities exists, which enables us to draw some correlations between our results and those obtained in Parker's studies. First, both results indicate the presence of single chiral stereoisomers in solution for the ligands, and second both show the appearance of distinctive bisignate profiles upon formation of the metal ion complexes with crossover points at 218 nm, which is usually indicative of exciton coupling[33] occurring between the naphthyl chromophores. The CD spectra were also recorded at different temperatures between −10 and +25 °C; however, only minor changes were observed in the CD-spectra within this temperature range or both systems, as shown in Supporting Information Figure S8.

Due to the relatively large changes observed between the free ligands **1** and **2** and their corresponding Nd(III) complexes, we next investigated the formation of the complexes in solution by observing the changes in the CD spectra at room temperature. The overall changes in the circular dichroism spectra of **1** and **2** upon the addition of increasing concentrations of $Nd(CF_3SO_3)_3$ were monitored in CH_3CN at RT and are shown in Figure 4, top and bottom, respectively. The results

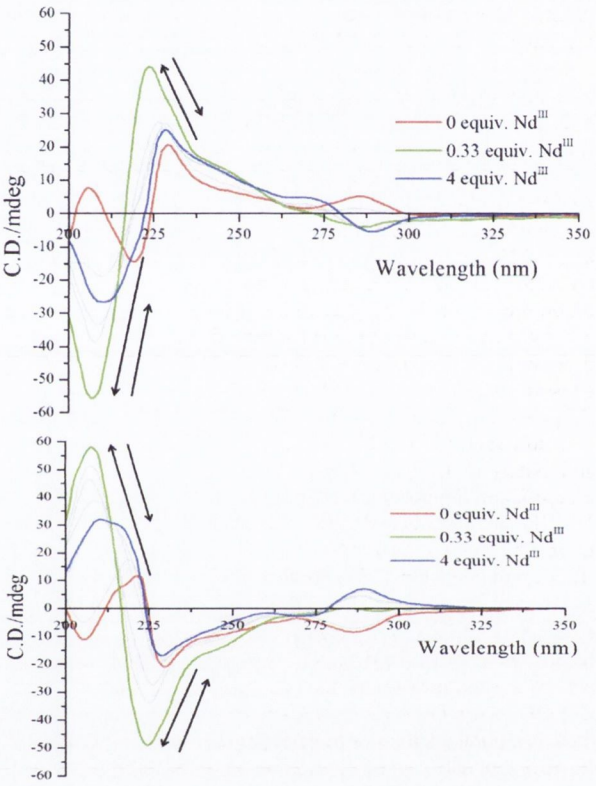

Figure 4. (top) Overall changes in the circular dichroism spectrum of **1** and (bottom) overall changes in the circular dichroism spectrum of **2** upon titrating against increasing concentrations of $Nd(CF_3SO_3)_3$ (0−3 equiv) at RT in CH_3CN.

demonstrate that significant changes occur upon formation of the Nd(III) directed self-assembly with up to 0.33 equiv of the metal ion and the formation of the desired 1:3 (metal/ligand) complex. The aforementioned distinctive bisignate profiles appeared for both; and as above, the two profiles behaved (within experimental error) as previously observed, with equal magnitude and opposite signs, demonstrating that these two self-assemblies are formed in solution as a structurally identical pair of enantiomers. Analyzing the changes observed in Figure 5 further demonstrates that, for **1**, there was an increase in the relative intensity of the positive band located at 229 nm and a shift to 224 nm between the addition of 0−0.33 equiv of $Nd(CF_3SO_3)_3$. Concurrently, a disappearance in the band centered at 218 nm with the emergence of a negative band at 207 nm was evident within the same concentration range.

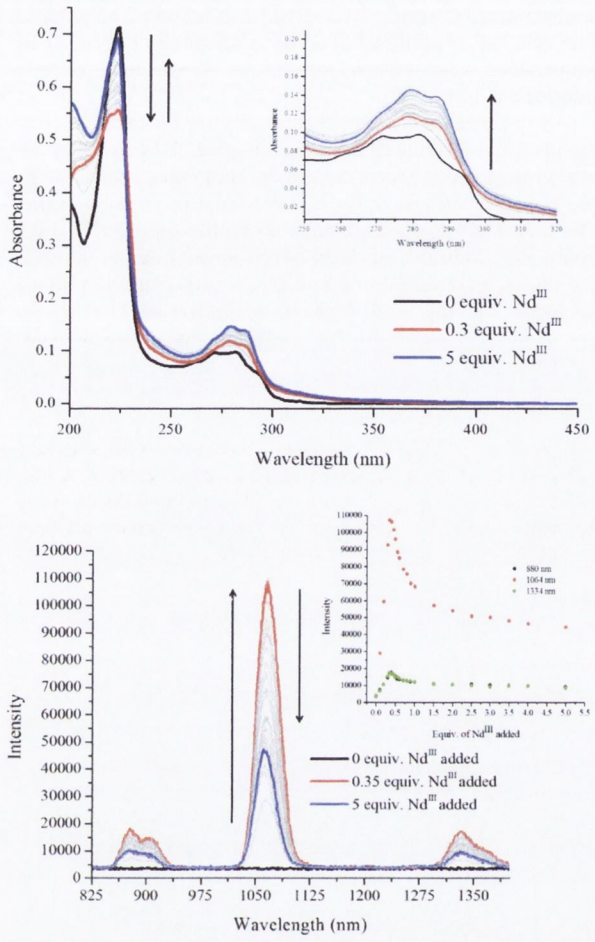

Figure 5. (top) Overall changes in UV–visible absorption spectra and (bottom) overall changes in Nd(III) phosphorescence spectra upon titrating **1** (1×10^{-5} M) against $Nd(CF_3SO_3)_3$ (0–5 equiv) in CH_3CN at room temperature upon excitation at 281 nm.

However, upon addition of Nd(III) between 0.33 and 4 equiv, a decrease was observed in the relative intensities of the 207 and 224 nm bands which was also accompanied with a shift to 210 and 228 nm, respectively. Importantly, the same trend was also seen for **2** (Figure 4, bottom). This would indicate that at higher Nd(III) concentrations the 1:3 complex undergoes structural and stoichiometric changes, most likely resulting in the formation of possibly the 1:2 or the 1:1 complexes (which would obviously have different symmetry to that of the desired 1:3 complex) in solution. We, and others, have observed similar behavior in related work, where initially the 1:3 stoichiometry is rapidly established (ca. 90% within 0.3 equivalents of the lanthanide ion); followed by the formation of the 1:2 species.[34,35] Hence, the above changes provide an additional handle by which to assess the formation of such chiral self-assembly structures in solution; the formation of which was next examined by observing the changes in the absorption, the ligand centered emission and the metal centered NIR emission.

UV–Visible and Luminescence Photophysical Solution Studies of 1 and 2 with $Nd(CF_3SO_3)_3$. A series of photophysical titrations (absorption and luminescence) were carried out in CH_3CN in order to gain an insight into the stoichiometry of the self-assembly process of **1** and **2** with Nd(III) in solution, and to quantify the binding affinity of the various complexes formed, achieved by fitting the changes observed using nonlinear regression analysis (SPECFIT). The overall changes in the UV–visible absorption spectrum of **1** upon titrating against $Nd(CF_3SO_3)_3$ are shown in Figure 5. Here, the high energy absorption band centered at 223 nm experienced a hypochromatic effect within the addition of 0–0.3 equiv of the metal salt. As we had anticipated from the CD results, subsequent addition of Nd(III) then gave rise to a small increase in the absorbance up until the addition of 1 equiv of Nd(III) after which the absorbance began to plateau. Similarly, the longer wavelength absorption band centered at λ_{max} = 281 nm experienced a sharp increase in absorbance between the additions of 0–1 equiv of Nd(III), reaching a plateau after the addition of **1** equivalent of metal salt. Identical behavior was observed upon titrating **2** with Nd(III) (see Supporting Information Figure S11). These changes are similar to that previously observed in our laboratory.[28] The fluorescence emission was also monitored upon excitation at 281 nm, which was quenched upon addition of Nd(III). But both ligands were not strongly fluorescent and the changes were not analyzed further. In contrast, the emergence of long-lived Nd(III) centered luminescence at long wavelengths was clearly visible, with the appearance of characteristic linelike emission bands 880, 1064, and 1334 nm, assigned to the deactivation of the Nd(III) $^4F_{3/2}$ excited state, upon excitation at 281 nm (Figure 5). Here, the NIR emission gradually enhanced between the addition of 0–0.35 equiv of Nd(III), signifying the formation of the 1:3 stoichiometry and, at the same time, the occurrence of an efficient energy transfer from the antenna to the Nd(III) center. As was observed in the CD-spectra, significant modulation was also seen above the addition of 0.35 equiv of Nd(III), indicative of the formation of a new self-assembly species in solution. The corresponding titration profile where the emission at 880, 1064, and 1334 nm was monitored, as shown in the inset in Figure 5, demonstrates this, as after the addition of 0.35 equiv of Nd(III) the emission intensities sharply decrease, reaching a plateau after the addition of ca. 1 equiv of Nd(III). This is indicative of the evolution of the 1:2 species, and eventually the lesser emissive 1:1 species in solution as a function of increased Nd(III) concentrations (see also the Supporting Information).

These changes observed both in the UV–vis absorption and the NIR emission were fitted using a nonlinear regression analysis, the fit to the experimental data at three different wavelengths is shown in Figure 6. The speciation distribution diagram obtained form these fits is also shown in Figure 6, showing that upon the addition of 0–0.33 equiv of Nd(III) the predominant species is the 1:3 **Nd.1**$_3$ species, formed in 79% yield, after the addition of 0.33 equiv of Nd(III). Additional aliquots of Nd(III) drive the formation of the 1:1 species, **Nd.1**, until it becomes the most dominant species in solution. Nearly identical titration behavior was exhibited by **2**, as shown in Supporting Information Figures S11–S16. Binding constants and speciation percentage values obtained for the analyses of the UV–visible titration data are summarized in Table 3, and show that the **Nd.1**$_3$ species is formed with a high binding constant of log $\beta_{1:3}$ of 18.3 ± 0.6 for **1** while for **2** a binding constant of 17.8 ± 0.4 was obtained. Interestingly, the formation of the 2:1 species was not observed, an indication that it is short-lived, but the 1:1 complex formation gave log $\beta_{1:1}$ of 6.0 ± 0.3 for **1** while for **2** log $\beta_{1:1}$ of 6.1 ± 0.2 was obtained. In a similar manner, the changes in the lanthanide-centered

dx.doi.org/10.1021/la402274s | *Langmuir* 2013, 29, 11506–11515

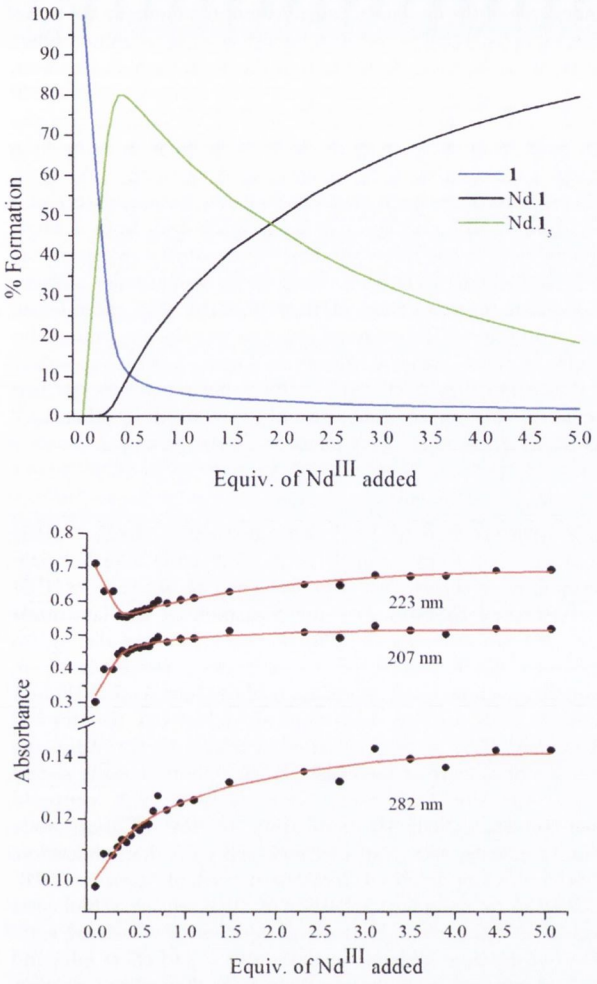

Figure 6. (top) Speciation distribution diagram obtained from UV–visible absorption titration data fit and (bottom) fit of experimental binding isotherms using the nonlinear regression analysis program SPECFIT.

Table 3. Binding Constants and Speciation Distribution Percentages Values Obtained from Both UV–Visible Absorption and Luminescence Titration Data Fits for Both *R* and *S* Enantiomers 1 and 2

	UV–visible		luminescence	
ligand	log $\beta_{1:1}$	log $\beta_{1:3}$	log $\beta_{1:1}$	log $\beta_{1:3}$
1	6.0 ± 0.3	18.3 ± 0.6		
2	6.0 ± 0.2	17.8 ± 0.4		
	% species at M:L = 1:3		% species at M:L = 1:3	
1	4	79	12	53
2	8	74	11	67

emission were analyzed (see fits and speciation diagrams in the Supporting Information). As for the ground state changes, the titration of both **1** and **2** supported the formation of the 3:1 species in solution within the addition of 0.33 equiv, with log $\beta_{1:3}$ of 17.2 ± 0.2 and 17.3 ± 0.8 for **1** and **2**, respectively. These binding constants are comparable to those obtained for other pyridyl amide based self-assembly systems developed in our laboratory.[34] Having established the ability of **1** and **2** to form 3:1 self-assemblies in the presence of Nd(III), we next investigated their self-assembly formation at an air–water interface by forming Langmuir films. Only a small numbers of examples of lanthanide based Langmuir–Blodgett films (LB-films) made from the use of thermodynamically and kinetically stable lanthanide complexes have been developed to date,[36–39] and to the best of our knowledge no examples of NIR emitting LB-films (or NIR luminescent monolayers) have been developed to date, though related systems have been developed,[40,41] but such systems have potential applications in sensing, imaging, and telecommunications.

Langmuir Monolayer Formation. The ability of complexes **Nd.1**$_3$ and **Nd.2**$_3$ to self-assemble at an air–water interface and form Langmuir monolayers was investigated by spreading 20 μL aliquots of each complex (~2.4 × 10^{-4} M) using $CHCl_3/CH_3OH$ (9:1) as the spreading solvent, onto the surface of a water subphase at room temperature. A typical surface pressure–area isotherm was obtained in each case; see Figure 7, in which an exponential increase in surface pressure

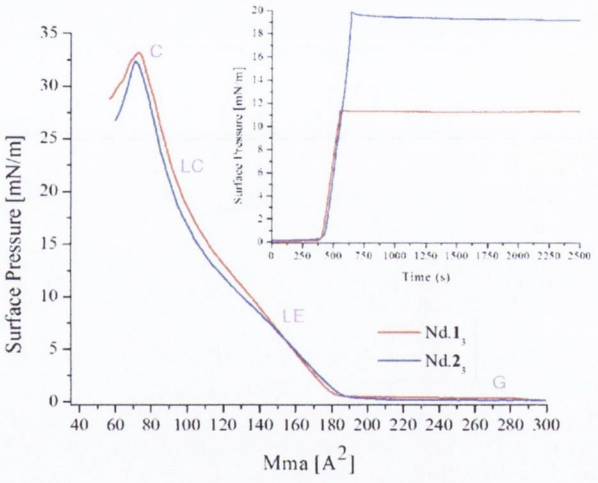

Figure 7. Surface pressure–area isotherm of complexes **Nd.1**$_3$ and **Nd.2**$_3$. Inset: Surface pressure–time stability profiles for **Nd.1**$_3$ and **Nd.2**$_3$. (G = gaseous, LE = liquid expanded, LC = liquid condensed, C = condensed.)

evidenced the different phase transitions, that is, gaseous (G), liquid expanded (LE), liquid condensed (LC), and film collapse (C), upon area decrease. The films collapsed at 33 mN m^{-1} for **Nd.1**$_3$ and 32 mN m^{-1} for **Nd.2**$_3$ with areas of 70 ± 5 Å^2 per molecule. The areas of these Nd(III) complexes are approximately those expected for three alkyl chains (ca. 66 Å^2 per molecule) and indicate that the complexes remain intact at the air–water interface with supramolecular organization into monolayers.[28] The isotherm features as well as the average area per molecule are identical within errors with an Eu(III) system featuring the same ligand,[28] indicating that the supramolecular packing is unaffected by changes in lanthanide ions. This separation of structural aspects from functional ones (lanthanide-specific photophysical applications) provides attractive opportunities for the fabrication of tailored materials. The Langmuir monolayer stability was also assessed by maintaining the monolayers at the liquid-condensed phase for an extended period of time (exceeding 40 min) and monitoring the surface pressure over that same time. The results are shown

dx.doi.org/10.1021/la402274s | *Langmuir* 2013, 29, 11506–11515

in the inset in Figure 7, demonstrating excellent stability properties for both the **Nd.1**$_3$ and the **Nd.2**$_3$ films. Each amphiphilic complex was then transferred onto a quartz slide, generating Langmuir–Blodgett films with good quality (smooth) transfer ratios of ~1 on the emersion of the quartz slide, demonstrating the successful formation of self-assembly monolayer of **Nd.1**$_3$ and **Nd.2**$_3$.

Having successfully formed the Langmuir–Blodgett films of **Nd.1**$_3$ and **Nd.2**$_3$, their photophysical properties were next evaluated. The UV–visible absorption spectra were recorded and their NIR emission properties were probed by recording time resolved emission spectra; see Figure 8 and Supporting Information Figure S17. We were, however, unable to obtain reliable CD spectra of these (single monolayer based) Langmuir–Blodgett films. The absorption spectra of the monolayers matched those seen for the complexes in solution, demonstrating that the films existed as the expected 3:1 complexes. More importantly, for both systems, the NIR centered Nd(III) emission was observed from each film upon excitation at 337 nm with bands centered at λ = 880 and 1064 nm, representing deactivation from the Nd(III) $^4F_{3/2}$ excited state to ground states $^4I_{9/2}$, and $^4I_{11/2}$. The weaker $^4F_{3/2} \rightarrow {}^4I_{13/2}$ transition at 1334 nm was not observed due to significant noise in the spectrum arising from scattered light from the fourth harmonic of the excitation pulse. Attempts to remove the signal arising from scatter by using bandpass or interference filters merely resulted in a diminution of the overall signal. However, it is clear from comparison of the relative intensities of the 880 and 1064 nm peaks in solution and on the surface that the complex symmetry is very similar on both occasions, since the 1064 nm transition is hypersensitive to symmetry (ΔJ = 4). These results are quite significant as they demonstrate that a lanthanide NIR emission can be recoded even from a single monolayer, clearly demonstrating the sensitivity of the system.

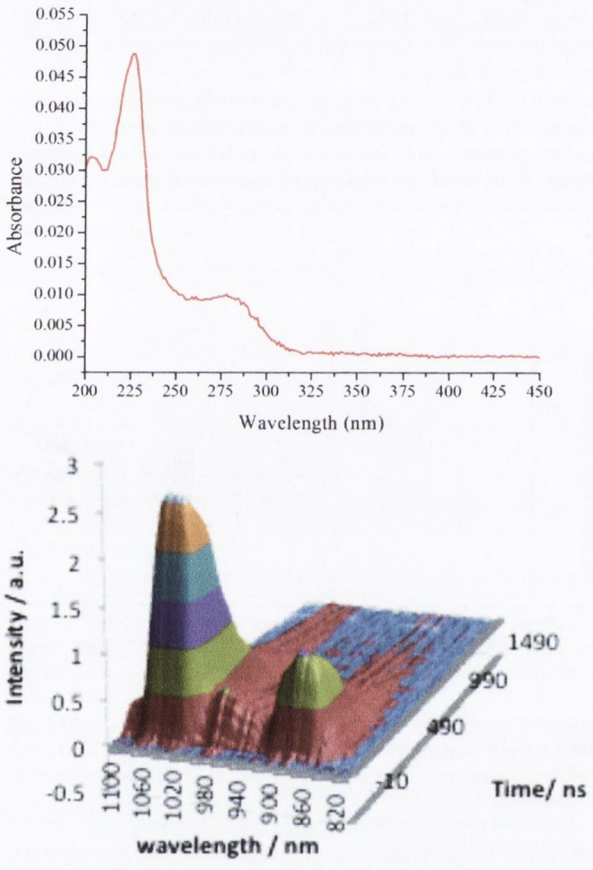

Figure 8. (top) Absorption spectrum of Langmuir–Blodgett **Nd.1**$_3$ monolayer and (bottom) time-resolved emission spectrum of **Nd.1**$_3$ monolayer after excitation at 337 nm, showing sensitized Nd(III)-based luminescence.

The LB films have been found to be stable under ambient conditions over a period of many months. The excited-state decay of the Nd(III) centered emission was also determined for both of these films, as shown in Figure 8 and Supporting Information Figure S17. While this paper represents our first steps in this area, we are currently investigating other Ln^{III} containing amphiphilic complexes for these purposes.

■ CONCLUSION

We have successfully developed amphiphilic, chiral, Nd(III) systems that form through facile lanthanide directed self-assembly processes. We also demonstrate the use of CD-spectroscopy to investigate the formation of the lanthanide directed self-assembly in solution, where we can distinguish between the formation of 1:1 and other stoichiometry in solution such as 1:3. The inclusion of the hexadecyl chain in **1** and **2** leads to the formation of stable and well-formed Langmuir films at an air–water interface. Furthermore, the successful transfer of these onto solid supports (quartz slides) gave, for the first time, time delayed NIR centered luminescence that, by comparing to the solution state measurements, was relatively unaltered upon immobilization. Such NIR immobilized luminescent chiral devices (NIR-ICLDs) have potential application in chiral sensing of biological media as well as in multiple wavelength emissive systems, areas that we are now investing significant time and effort into, and we are currently investigating these and other related systems.

■ ASSOCIATED CONTENT

Supporting Information

Additional table and figures as described in the text. This material is available free of charge via the Internet at http://pubs.acs.org.

■ AUTHOR INFORMATION

Corresponding Authors

*E-mail: gunnlaut@tcd.ie.

*E-mail: j.a.kitchen@soton.ac.uk.

Present Address

[#]Chemistry, Faculty of Natural & Environmental Sciences, University of Southampton, Highfield, Southampton, SO17 1BJ, UK.

Notes

The authors declare no competing financial interest.

■ ACKNOWLEDGMENTS

We thank the Science Foundation Ireland (SFI PI 2010 Award and RFP 2009 Award to T.G.), the Irish Research Council for Science, Engineering & Technology (IRCSET for postdoctoral funding to J.A.K.), and the European Research Council (ERC) for financial support (to M.A. and S.F.). We would also like to

thank Dr. Nicholas G. White for assistance with X-ray data analysis.

■ ABBREVIATIONS

NIR, near-infrared; LB, Langmuir−Blodgett; A-W, air−water; LC, liquid condensed; LE, liquid expanded; G, gaseous; C, collapse; CD, circular dichroism; CPL, circularly polarized luminescence

■ REFERENCES

(1) Binnemans, K. Lanthanide-based Luminescenct Hybrid Materials. *Chem. Rev.* **2009**, *109*, 4283.

(2) Faulkner, S.; Natrajan, L. S.; Perry, W. S.; Sykes, D. Sensitised luminescence in lanthanide containing arrays and *d-f* hybrids. *Dalton Trans.* **2009**, 3890.

(3) Bunzli, J.-C. G.; Piguet, C. Taking advantage of luminescent lanthanide ions. *Chem. Soc. Rev.* **2005**, *34*, 1048.

(4) Lincheneau, C.; Stomeo, F.; Comby, S.; Gunnlaugsson, T. Recent Highlights in the use of Lanthanide-directed Synthesis of Novel Supramolecular (Luminescent) Self-assembly Structures such as Coordination Bundles, Helicates and Sensors. *Aust. J. Chem.* **2011**, *64*, 1315.

(5) Pandya, S.; Yu, J.; Parker, D. Engineering emissive lanthanide complexes for molecular imaging and sensing. *Dalton Trans.* **2006**, 2757.

(6) Eliseeva, S. V.; Bunzli, J.-C. G. Lanthanide luminescence for functional materials and bio-sciences. *Chem. Soc. Rev.* **2010**, *39*, 189.

(7) Bunzli, J.-C. G. Lanthanide Luminescence for Biomedical Analyses and Imaging. *Chem. Rev.* **2010**, *110*, 2729.

(8) Comby, S.; Bünzli, J.-C. G. Lanthanide Near-Infrared Luminescence in Molecular Probes and Devices. In *Handbook on the Physics and Chemistry of Rare Earths*; Gschneider, K. A., Jr., Bünzli, J.-C. G., Pecharsky, V. K., Eds.; Elsevier Science B.V.: Amsterdam, 2007; Vol. 37, Ch. 235, pp 217−470.

(9) Ward, M. D. Mechanisms of sensitization of lanthanide(III)-based luminescence in transition metal/lanthanide and anthracene/lanthanide dyads. *Coord. Chem. Rev* **2010**, *254*, 2634.

(10) de Bettencourt-Dias, A. Lanthanide-based emitting materials in light-emitting diodes. *Dalton Trans.* **2007**, 2229−2241.

(11) Aboshyan-Sorgho, L.; Besnard, C.; Pattison, P.; Kittilstved, K. R.; Aebischer, A.; Bunzli, J.-C. G.; Hauser, A.; Piguet, C. Near-Infrared-Visible Light Upconversion in a Molecular Trinuclear d-f-d Complex. *Angew. Chem., Int. Ed.* **2011**, *50*, 4108.

(12) Beeby, A.; Burton-Pye, B. P.; Faulkner, S.; Motson, G. R.; Jeffery, J. C.; McCleverty, J. A.; Ward, M. D. Synthesis and near-IR luminescence properties of neodymium(III) and ytterbium(III) complexes with poly(pyrazolyl) borate ligands. *Dalton Trans.* **2002**, 1923.

(13) Binnemans, K.; Gorller-Walrand, C. Lanthanide-containing liquid crystals and surfactants. *Chem. Rev.* **2002**, *102*, 2303−2345.

(14) Bunzli, J. C. G.; Piguet, C. Lanthanide-containing molecular and supramolecular polymetallic functional assemblies. *Chem. Rev.* **2002**, *102*, 1897−1928.

(15) Torelli, S.; Imbert, D.; Cantuel, M.; Bernardinelli, G.; Delahaye, S.; Hauser, A.; Bunzli, J. C. G. Piguet, Tuning the decay time of lanthanide-based near infrared luminescence from micro- to milliseconds through d -> f energy transfer in discrete heterobimetallic complexes, C. *Chem.—Eur. J.* **2005**, *11*, 3228−3242.

(16) Wada, Y.; Okubo, T.; Ryo, M.; Nakazawa, T.; Hasegawa, Y.; Yanagida, S. High efficiency near-IR emission of Nd(III) based on low-vibrational environment in cages of nanosized zeolites. *J. Am. Chem. Soc.* **2000**, *122*, 8583.

(17) Yanagida, S.; Hasegawa, Y.; Murakoshi, K.; Wada, Y.; Nakashima, N.; Yamanaka, T. Strategies for enhancing photoluminescence of Nd^{3+} in liquid media. *Coord. Chem. Rev.* **1998**, 461.

(18) Pope, S. J. A.; Coe, B. J.; Faulkner, S.; Bichenkova, E. V.; Yu, X.; Douglas, K. T. Self-Assembly of Heterobimetallic d-f Hybrid Complexes: Sensitization of Lanthanide Luminescence by d-Block Metal-to-Ligand Charge-Transfer Excited States. *J. Am. Chem. Soc.* **2004**, *126*, 9490.

(19) Perry, W. S.; Pope, S. J. A.; Allain, C.; Coe, B. J.; Kenwright, A. M.; Faulkner, S. Synthesis and photophysical properties of kinetically stable complexes containing a lanthanide ion and a transition metal antenna group. *Dalton Trans.* **2010**, *39*, 10974.

(20) Nonat, A. M.; Allain, C. M.; Faulkner, S.; Gunnlaugsson, T. Mixed d-f_3 Coordination Complexes Possessing Improved Near-Infrared (NIR) Lanthanide Luminescent Properties in Aqueous Solution. *Inorg. Chem.* **2010**, *49*, 8449.

(21) Lehr, J.; Bennett, J.; Tropiano, M.; Sørensen, T. J.; Faulkner, S.; Beer, P. D.; Davis, J. J. Reversible recruitment and emission of DO3A-derived lanthanide complexes at ligating molecular films on gold. *Langmuir* **2013**, *29*, 1475.

(22) Truman, L. K.; Comby, S.; Gunnlaugsson, T. pH-Responsive Luminescent Lanthanide-Functionalized Gold Nanoparticles with On-Off Ytterbium Switchable Near-Infrared Emission. *Angew. Chem., Int. Ed.* **2012**, *51*, 9624.

(23) Stomeo, F.; Plush, S. E.; Gunnlaugsson, T. Soft Matter pH Sensing: From Luminescent Lanthanide pH Switches in Solution to Sensing in Hydrogels. *Chem. Mater.* **2006**, *18*, 4336.

(24) Similar work has also been developed by: Qiao, Y.; Lin, Y. Y.; Zhang, S. F.; Huang, J. B. Lanthanide-Containing Photoluminescent Materials: From Hybrid Hydrogel to Inorganic Nanotubes. *Chem.—Eur. J.* **2011**, *17*, 5180−5187.

(25) Massue, J.; Quinn, S. J.; Gunnlaugsson, T. Lanthanide luminescent displacement assays: The sensing of phosphate anions using Eu(III)-cyclen-conjugated gold nanoparticles in aqueous solution. *J. Am. Chem. Soc.* **2008**, *130*, 6900.

(26) Bonnet, C. S.; Massue, J.; Quinn, S. J.; Gunnlaugsson, T. Lanthanide luminescent gold nanoparticles: pH-driven self-assembly formation between Eu(III)-cyclen conjugated AuNPs and sensitising beta-diketonate antenna in water. *Org. Biomol. Chem.* **2009**, 3074.

(27) Similar work has also been developed by: Stasiuk, G. J; Tamang, S.; Imbert, D.; Poillot, C.; Giardiello, M.; Tisseyre, C.; Barbier, E. L.; Fries, P. H.; de Waard, M.; Reiss, P.; Mazzanti, M. Cell-Permeable Ln(III) Chelate-Functionalized InP Quantum Dots As Multimodal Imaging Agents. *ACS Nano* **2011**, *5*, 8193−8201.

(28) Kitchen, J. A.; Barry, D. E.; Mercs, L.; Albrecht, M.; Peacock, R. D.; Gunnlaugsson, T. Circularly Polarized Lanthanide Luminescence from Langmuir-Blodgett Films Formed from Optically Active and Amphiphilic EuIII-Based Self-Assembly Complexes. *Angew. Chem., Int. Ed* **2012**, *51*, 704.

(29) Cosier, J.; Glazer, A. M. A nitrogen gas stream cryostat for general X-ray diffraction studies. *J. Appl. Crystallogr.* **1986**, *19*, 105.

(30) Otwinowski, Z.; Minor, W. Processing of X-ray Diffraction Data Collected in Oscillation Mode. *Methods Enzymol.* **1997**, 276.

(31) Sheldrick, G. M. A short history of SHELX. *Acta Crystallogr., Sect. A* **2008**, *A64*, 112.

(32) Dickins, R. S.; Howard, J. A. K.; Maupin, C. L.; Maloney, J. M.; Parker, D.; Peacock, R. D.; Riehl, J. P.; Siligard, G. Ground and excited state chiroptical properties of enantiopure macrocyclic tetranaphthyl lanthanide complexes: controlled modulation of the frequency and polarisation of emitted light. *New J. Chem.* **1998**, 891.

(33) Satrijo, A.; Meskers, S. C. J.; Swager, T. M. Probing a Conjugated Polymer's Transfer of Organization-Dependent Properties from Solutions to Films. *J. Am. Chem. Soc.* **2006**, *128*, 9030.

(34) Similarly others have seen this effect: Andreiadis, E. S.; Imbert, D.; Pecaut, J.; Demadrille, R.; Mazzanti, M. Self-assembly of highly luminescent lanthanide complexes promoted by pyridine-tetrazolate ligands. *Dalton Trans.* **2012**, *41*, 1268−1277.

(35) We have also seen such effect in double stranded dimetallic helicate formations: Stomeo, F.; Lincheneau, C.; Leonard, J. P.; O'Brien, J. E.; Peacock, R. D.; McCoy, C. P.; Gunnlaugsson, T. Metal-Directed Synthesis of Enantiomerially Pure Dimetallic Lanthanide Luminescent Triple-Stranded Helicates. *J. Am. Chem. Soc.* **2009**, *131*, 9636.

(36) Examples of visibly emitting lanthanide based LB films include: Xu, B.; Zhu, H.-X.; Yan, B. Novel Langmuir−Blodgett film with

ternary europium complex of long chain mono-eicosyl cis-butene dicarboxylate and 1,10-phenanthroline: Cooperative assembly and luminescence. *Inorg. Chem. Commun.* **2010**, *13*, 448 (and reference therein)..

(37) Qian, D.-J.; Yang, K.-Z.; Nakahara, H.; Fukuda, K. Monolayers of Europium Complexes with Different Long Chains and β-Diketonate Ligands and Their Emission Properties in Langmuir-Blodgett Films. *Langmuir* **1997**, *13*, 5925 (and references therein)..

(38) Dutton, P. J.; Conte, L. Terbium Luminescence in Langmuir–Blodgett Films of Octafunctionalized Calix[4]resorcinarenes. *Langmuir* **1999**, *15*, 613.

(39) Gao, L.-H.; Wang, K.-Z.; Cai, L.; Zhang, H.-Z.; Jin, L.-P.; Huang, C.-H.; Gao, H.-J. Studies of Langmuir-Blodgett Films of an Ion Pair Metal Complex Containing Eu(III)-Ru(II) Dual Chromophores. *J. Phys. Chem. B* **2006**, *110*, 7402 (and references therein)..

(40) Matsumoto and co-workers have recently shown that NIR emissive lanthanide doped nanoparticles can be dip-coded onto plastic sheets: Watanabe, S.; Hyodo, H.; Taguchi, H.; Soga, K.; Takanashi, Y.; Matsumoto, M. *J. Oleo Sci.* **2012**, *61*, 565–573.

(41) Hauser, C. P.; Thielemann, D. T.; Adlung, M.; Wickleder, C.; Roesky, P. W.; Weiss, C. K.; Landfester, K. Luminescent Polymeric Dispersions and Films Based on Oligonuclear Lanthanide Clusters. *Macromol. Chem. Phys.* **2011**, *212*, 286–296.